CONSISTENT AND CONSERVATIVE PHASE-FIELD METHOD FOR MULTIPHASE FLOW PROBLEMS

by

Ziyang Huang

A Dissertation

Submitted to the Faculty of Purdue University

In Partial Fulfillment of the Requirements for the degree of

Doctor of Philosophy

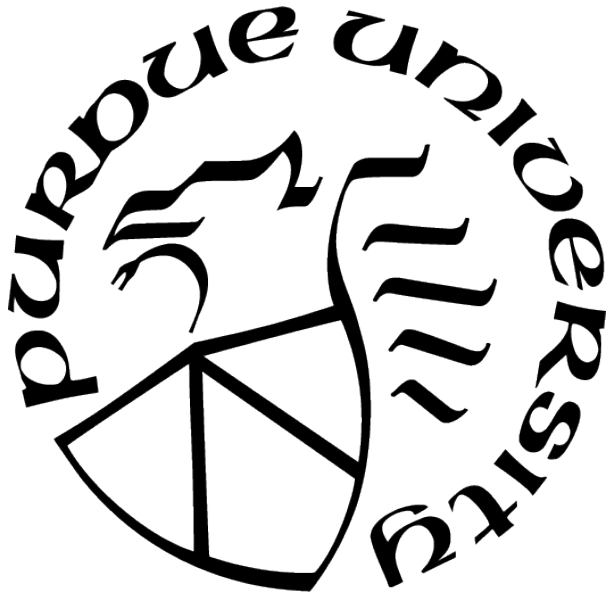

School of Mechanical Engineering

West Lafayette, Indiana

August 2021

THE PURDUE UNIVERSITY GRADUATE SCHOOL
STATEMENT OF COMMITTEE APPROVAL

Dr. Arezoo M. Ardekani, Co-Chair

School of Mechanical Engineering

Dr. Guang Lin, Co-Chair

Department of Mathematics

Dr. Suchuan Dong

Department of Mathematics

Dr. Sadegh Dabiri

Department of Agricultural and Biological Engineering

Approved by:

Dr. Nicole L. Key

ACKNOWLEDGMENTS

I sincerely appreciate the supports from my advisors, Profs. Arezoo M. Ardekani and Guang Lin, as well as their funding sources (National Science Foundation, Brookhaven National Laboratory Subcontract, ARO/MURI grant, and U.S. Department of Energy (DOE) Office). I would also like to acknowledge Lynn Fellowship at Purdue University, which supported my life and study in my first year at Purdue.

My advisors were open to listening to my ideas and encouraged me to proceed with the problems that I believed were important and impactful in my research area. They provided their suggestions and shared their experiences whenever I needed their help. They also cared about my career and provided many opportunities to help my success. Without their supports, I would not be able to accomplish my Ph.D. research. I would like to thank my other two committee members, Profs. Suchuan (Steven) Dong and Sadegh Dabiri, for their inspiring suggestions, especially at the beginning of my Ph.D. research. Their help substantially accelerated my fundamental understanding of my research area. I am also thankful to Profs. Jie Shen and Osman A. Basaran for their impressive courses. Their accomplishments and enthusiasm for sharing their knowledge with students are influencing me. I particularly thank my advisors and Prof. Jie Shen for their recommendation letters when I was looking for a postdoctoral position.

I am grateful for much help from my labmates/colleagues/friends. We discussed difficult problems, attended conferences, and celebrated festivals. These are my treasured memories.

I deeply thank my parents for their unwavering belief that I can finish challenging tasks and can be better and stronger than I think.

This dissertation was partly published in Journal of Computational Physics, Vol 387, Ziyang Huang, Guang Lin, Arezoo M. Ardekani, A mixed upwind/central WENO scheme for incompressible two-phase flows, Page 455-480, Copyright Elsevier (2019); in Journal of Computational Physics, Vol 406, Ziyang Huang, Guang Lin, Arezoo M. Ardekani, Consistent, essentially conservative and balanced-force Phase-Field method to model incompressible two-phase flows, Page 109192, Copyright Elsevier (2019); in Journal of Computational Physics, Vol 420, Ziyang Huang, Guang Lin, Arezoo M. Ardekani, Consistent and conservative scheme

for incompressible two-phase flows using the conservative Allen-Cahn model, Page 109718, Copyright Elsevier (2020); in Journal of Computational Physics, Vol 434, Ziyang Huang, Guang Lin, Arezoo M. Ardekani, A consistent and conservative model and its scheme for N-phase-M-component incompressible flows, Page 110229, Copyright Elsevier (2021); and in International Journal of Multiphase Flow, Vol 142, Ziyang Huang, Guang Lin, Arezoo M. Ardekani, A consistent and conservative volume distribution algorithm and its applications to multiphase flows using Phase-Field models, Page 103727, Copyright Elsevier (2021).

TABLE OF CONTENTS

LIST OF FIGURES

ABSTRACT

This dissertation focuses on a consistent and conservative Phase-Field method for multiphase flow problems, and it includes both model and scheme development. The first general question addressed in the present study is the multiphase volume distribution problem. A consistent and conservative volume distribution algorithm is developed to solve the problem, which eliminates the production of local voids, overfilling, or fictitious phases, but follows the mass conservation of each phase. One of its applications is to determine the Lagrange multipliers that enforce the mass conservation in the Phase-Field equation, and a reduction consistent conservative Allen-Cahn Phase-Field equation is developed. Another application is to remedy the mass change due to implementing the contact angle boundary condition in the Phase-Field equations whose highest spatial derivatives are second-order. As a result, using a 2nd-order Phase-Field equation to study moving contact line problems becomes possible.

The second general question addressed in the present study is the coupling between a given physically admissible Phase-Field equation to the hydrodynamics. To answer this general question, the present study proposes the *consistency of mass conservation* and the *consistency of mass and momentum transport*, and they are first implemented to the Phase-Field equation written in a conservative form. The momentum equation resulting from these two consistency conditions is Galilean invariant and compatible with the kinetic energy conservation, regardless of the details of the Phase-Field equation. It is further illustrated that the 2nd law of thermodynamics and *consistency of reduction* of the entire multiphase system only rely on the properties of the Phase-Field equation. All the consistency conditions are physically supported by the control volume analysis and mixture theory. If the Phase-Field equation has terms that are not in a conservative form, those terms are treated by the proposed consistent formulation. As a result, the proposed consistency conditions can always be implemented. This is critical for large-density-ratio problems.

The consistent and conservative numerical framework is developed to preserve the physical properties of the multiphase model. Several new techniques are developed, including the gradient-based phase selection procedure, the momentum conservative method for the

surface force, the boundedness mapping resulting from the volume distribution algorithm, the "DGT" operator for the viscous force, and the correspondences of numerical operators in the discrete Phase-Field and momentum equations. With these novel techniques, numerical analyses ensure that the mass of each phase and momentum of the multiphase mixture are conserved, the order parameters are bounded in their physical interval, the summation of the volume fractions of the phases is unity, and all the consistency conditions are satisfied, on the fully discrete level and for an arbitrary number of phases. Violation of the consistency conditions results in inconsistent errors proportional to the density contrasts of the phases. All the numerical analyses are carefully validated, and various challenging multiphase flows are simulated. The results are in good agreement with the exact/asymptotic solutions and with the existing numerical/experimental data.

The multiphase flow problems are extended to including mass (or heat) transfer in moving phases and solidification/melting driven by inhomogeneous temperature. These are accomplished by implementing an additional consistency condition, i.e., *consistency of volume fraction conservation*, and the diffuse domain approach. Various problems are solved robustly and accurately despite the wide range of material properties in those problems.

1. INTRODUCTION[1]

Multiphase flows are ubiquitous and have attracted much attention because of their complicated physical nature and widespread applications. For example, the oil spill accident in 2010 [1] has gained worldwide attention due to its dramatic damage to the environment. In order to predict the spread of the oil and to provide remediation strategies, a model that is capable of capturing interactions of the water, oil, and air is needed. Other examples include the enhanced oil recovery, where CO_2 is injected along with the water into oil reservoirs [2]–[4], and dynamics of compound drops [5]–[7], where the drop is composed of different fluids. Interactions among different fluid phases and evolution of their interfaces are strongly coupled and, as a result, introduce complicated dynamics that makes the problems challenging to solve.

In most scenarios of interest, the interface thickness is so small that the sharp interface method [8] is accurate, where fluid motion inside each phase is governed by the Navier-Stokes equation and different phases are connected by boundary conditions at the interfaces. However, in numerical practice, explicitly imposing the boundary conditions at the interfaces, whose locations are unknown, is not a trivial task. The so-called "one-fluid formulation" [9], [10] is one of the most popular alternatives, where the motion of the fluids is governed by a single equation of their mixture and the boundary conditions at the interfaces are implicitly imposed. Lots of efforts have been focused on modeling and simulating two-phase flows under this framework. Many successful numerical models or methods have been developed to specify locations of the interfaces, e.g., the front-tracking method [11]–[14], the level-set method [15]–[20], the conservative level-set method [21]–[25], the volume-of-

[1]This chapter was partly published in Journal of Computational Physics, Vol 387, Ziyang Huang, Guang Lin, Arezoo M. Ardekani, A mixed upwind/central WENO scheme for incompressible two-phase flows, Page 455-480, Copyright Elsevier (2019); in Journal of Computational Physics, Vol 406, Ziyang Huang, Guang Lin, Arezoo M. Ardekani, Consistent, essentially conservative and balanced-force Phase-Field method to model incompressible two-phase flows, Page 109192, Copyright Elsevier (2019); in Journal of Computational Physics, Vol 420, Ziyang Huang, Guang Lin, Arezoo M. Ardekani, Consistent and conservative scheme for incompressible two-phase flows using the conservative Allen-Cahn model, Page 109718, Copyright Elsevier (2020); in Journal of Computational Physics, Vol 434, Ziyang Huang, Guang Lin, Arezoo M. Ardekani, A consistent and conservative model and its scheme for N-phase-M-component incompressible flows, Page 110229, Copyright Elsevier (2021); and in International Journal of Multiphase Flow, Vol 142, Ziyang Huang, Guang Lin, Arezoo M. Ardekani, A consistent and conservative volume distribution algorithm and its applications to multiphase flows using Phase-Field models, Page 103727, Copyright Elsevier (2021).

fluid (VOF) method [26]–[31], and the THINC method [32]–[35]. Recent reviews of various interface-capturing methods and contact angle boundary conditions are available in [36], [37], respectively. The surface tension can be modeled by the smoothed surface stress method [38], the continuous surface force (CSF) [39], the ghost fluid method (GFM) [40], [41], and the conservative and well-balanced surface tension model [42]. The surface tension model is incorporated into the momentum equation by the balanced-force algorithm [43]. A recent review of various numerical models for the surface tension is available in [44]. Recent studies are moving towards problems including three fluid phases or, more generally, an arbitrary number of fluid phases. Compared to the two-phase problems, the three-phase or N-phase flows, where N is the number of phases, cast some additional challenges in locating the phases and interfaces and in modeling interfacial tensions and moving contact lines. The two-phase interface reconstruction schemes in Volume of Fluid (VOF) and Moment of Fluid (MOF) are extended to three-phase cases, e.g., in [45]–[48], and become more involved. One can expect that those schemes will become more and more complicated as the number of phases increases. The level-set method is also extended to three- or multi-phase problems, e.g., in [49]–[52], by simply adding more level-set functions. However, special cares have to be paid on the overlaps or voids introduced by independently advecting the level-set functions, and on the issue of mass conservation.

The present study focuses on the Phase-Field (or Diffuse-Interface) method, which has been popularly used in modeling two-phase flows [53]–[58]. The Phase-Field method is characterized by introducing a small but finite interface thickness. Individual phases are located by a set of order parameters which are governed by the Phase-Field equation (or model). The interface thickness remains constant due to the balance of the intrinsic thermodynamical compression and diffusion, mostly derived (or modified) from a free energy functional, in the Phase-Field equation. The surface tension force can be derived from the energy balance or the least-action principle [54], [59]. The Phase-Field method has also the following advantages. It is globally mass conservative and able to handle topological changes without additional efforts. It doesn't require any explicit interface reconstruction. The surface force calculation of the Phase-Field method doesn't require evaluation of geometrical quantities, e.g., normal vector or curvature of an interface. In addition, it is very easy to include multiple

physical effects by modifying the energy functional. Thus, the Phase-Field method provides a convenient and effective way to model multiphase dynamics. Consequently, the two-phase Phase-Field method has been extended to the three-phase one, e.g., in [60]–[63], and further to the general N-phase one, e.g., in [64]–[70]. Multiphase Allen-Cahn and Cahn-Hilliard Phase-Field equations including the effect of pairwise interfacial tensions are developed in [71], while the hydrodynamics is not included. A series of studies on the Phase-Field modeling of N-phase incompressible flows has been done by Dong [72]–[75]. Most of the existing Phase-Field equations ensure the mass conservation of each phase and the summation of the volume fractions of the phases to be unity. Recent studies have realized the significance of the so-called *consistency of reduction* [60], [64], [74], [75], because this principle avoids producing fictitious phases. It has a significant effect on the flow dynamics, especially when the density ratio or viscosity ratio in the problem is large. For example, in a water-oil-air system, the maximum density and viscosity ratios are of the order of 1000. Violating the *consistency of reduction* can unphysically generate the oil at the interface of a water-air bubble. The bubble becomes much heavier and more viscous than it should be even though only a small amount of the oil is generated. Therefore, the rising motion of the bubble is slowed down due to violating the *consistency of reduction*. This behavior has been demonstrated in [64].

The Phase-Field method is also popular in modeling moving contact line problems. Different from the sharp-interface method, which only includes advection, diffusion in the Phase-Field method regularizes the singularity at contact lines. Such an additional effect can drive contact lines to move even though the no-slip boundary condition is assigned [76], [77]. One commonly used procedure to derive the contact angle boundary conditions in the Phase-Field method is in the context of wall energy relaxation [77]–[81], where the wall energy is minimized by the L^2 gradient flow. Such a procedure has been extended to include surfactant [82], contact angle hysteresis [83], three fluid phases [84]–[86], and N ($N \geqslant 2$) fluid phases [74]. Alternatively, the contact angle boundary conditions can also be geometry-based [87]–[89], where interface orientation is explicitly enforced, and the one in [87] has been extended to model contact lines formed by three fluid phases [90]. Most of these contact angle boundary conditions can be in general written as an inhomogeneous Neumann boundary condition. Among various Phase-Field equations, the Cahn-Hilliard Phase-Field equation [91] is most

popularly used to model moving contact line problems, since the contact angle boundary conditions can be directly applied without influencing the mass conservation. The Cahn-Hilliard equation is a 4th-order partial differential equation (PDE) and therefore it is also called the 4th-order Phase-Field equation here. To uniquely solve it, each boundary requires two boundary conditions, one of which is determined by mass conservation. Flexibility is given to the remaining one to control the morphology of the interface, which is achieved by implementing the contact angle boundary conditions. The popularity of implementing the Cahn-Hilliard equation has motivated several theoretical analyses, e.g., in [77], [78], [92]–[94], and comparison studies, e.g., in [87], [95].

In the present study, the multiphase flow problems having an arbitrary number of immiscible and incompressible fluid phases are considered. Each phase has a constant density and viscosity, and each pair of phases has a surface tension at their interfaces and a contact angle at a wall boundary. To physically model such a kind of problem using the Phase-Field method, several fundamental questions, which have not been aware of or clearly answered, are addressed in the present study.

1.1 Multiphase volume distribution problem

In the present study, the multiphase volume distribution problem is considered, where there can be an arbitrary number of phases. In some previous two-phase studies, this is also called the mass distribution or the mass redistribution. Since the problem is not related to the densities of individual phases, it is more precise to call it the volume distribution. Given the volume changes of individual phases going to be distributed to the domain and a set of order parameters representing the locations of different phases, one needs to specify the volume distribution functions of individual phases at every location of the domain. It should be noted that the domain is fixed. Therefore, before and after the volume distribution, the volume of the domain does not change. This is a kind of inverse problem and its solution is not necessarily unique. However, the admissible solution should not produce any fictitious phases, local voids, or overfilling. In addition to that, the integrals of the volume distribution functions of the solution over the domain should be the given volume

changes correspondingly. These goals are achieved by satisfying the proposed summation and conservation constraints for volume distribution and the *consistency of reduction*, which will be discussed in detail in Section 2.2.2. The volume distribution is called consistent and conservative if it satisfies all the aforementioned physical constraints. It is relatively straightforward to solve the volume distribution problem and to satisfy the physical constraints in two-phase cases, while it becomes non-trivial for general multiphase cases. In a two-phase case, increasing the volume of one of the two phases corresponds to a decrease of the same amount of the volume of another phase from the summation constraint. As a result, only one of the phases is necessarily considered and the volume distribution is solved phase-wise. In a general multiphase case, there can be more than two phases at a specific location. When any one of them changes its volume, the others have to respond to that simultaneously to satisfy the summation constraint. In other words, all the phases have to be considered at the same time. In the two-phase case, the phases inside interfacial regions are fixed. However, the number of phases inside a specific interfacial region is varied from at least two to at most N, and there are lots of different possible combinations of the phases inside that region in the multiphase case. This also casts difficulty to satisfy the *consistency of reduction* in the general multiphase setup. In the present study, the consistent and conservative volume distribution algorithm is proposed to solve the problem.

The first application, motivated the present study to address the multiphase volume distribution problem, is to design the physical and general Lagrange multipliers that enforce the mass conservation for a variety of multiphase Phase-Field equations. As a specific example, a multiphase conservative Allen-Cahn equation that satisfies the *consistency of reduction* is developed in the present work, with the help of the proposed consistent and conservative volume distribution algorithm. Almost all the Phase-Field equations (or models) for multiphase flows are Cahn-Hilliard type [91] since it has a conservative form. Therefore, the mass conservation of each phase is satisfied. However, by adding a Lagrange multiplier, one can obtain the so-called conservative Allen-Cahn equation, which satisfies the mass conservation as well. By appropriately designing the Lagrange multiplier, Brassel and Bretin [96] proposed an equation of this kind that is more suitable than another conservative Allen-Cahn equation [97] for two-phase flow modeling. The two-phase conservative Allen-Cahn equation

[96] is a 2nd-order partial differential equation, while the Cahn-Hilliard equations are usually 4th-order. Therefore, the conservative Allen-Cahn equation [96] is easier to be solved. In addition, it enjoys the maximum principle so that its solution has an upper and lower bound. Both the analysis [96] and numerical comparison [98], [99] suggest that the two-phase conservative Allen-Cahn equation [96] has a better ability than the Cahn-Hilliard equations to preserve under-resolved structures. Therefore, it is attractive to develop a multiphase conservative Allen-Cahn equation for multiphase flows. Such an equation was developed by Kim and Lee [68]. Although they numerically show that small structures are able to be preserved and the solution of their equation is inside the physical interval, their equation violates the *consistency of reduction*, and as a result produces fictitious phases. This will be analyzed in Section 2.2.3 and numerically demonstrated in Section 4.2. Therefore, the proposed multiphase conservative Allen-Cahn equation is the first model of this kind satisfying the *consistency of reduction*.

The second application of the multiphase volume distribution algorithm is to model moving contact line problems using the 2nd-order Phase-Field equations. As mentioned above, the second-order Phase-Field equations, such as the conservative Phase-Field equations [58], [63], [70], [100] and the conservative Allen-Cahn equations [68], [96], become popular in modeling both two-phase flows, e.g., in [57], [58], [101]–[103], and N-phase ($N \geqslant 2$) flows, e.g., in [68]–[70], because they enjoy several desirable properties that the Cahn-Hilliard equations does not have in multiphase flow modeling [68], [96], [98]–[100], [104]. Moreover, they are easier and more efficient to be solved. However, difficulty appears when these 2nd-order Phase-Field equations are used to model problems including moving contact lines, because only a single boundary condition is needed. This boundary condition is always determined by the mass conservation and the homogeneous Neumann boundary condition is normally required. Consequently, only 90^0 contact angle can be assigned at the wall boundary, which strongly restricts the application of the second-order Phase-Field equations. So far, the second-order Phase-Field equations have not been able to share the fruitful progress made in the implementation of the contact angle boundary conditions for moving contact line problems. The idea of addressing this issue is to add a Lagrange multiplier to the original Phase-Field equations, so that the mass change due to the contact angle boundary conditions

is compensated. The Lagrange multiplier needs to be carefully designed to avoid producing voids, overfilling, or fictitious phases, and therefore the consistent and conservative volume distribution algorithm is employed.

The third application related to the multiphase volume distribution problem is to map the order parameters into their physical interval. In multiphase flows, the order parameters are not only indicators of different phases but also used to compute the density and viscosity of the fluid mixture. This computation is based on the assumption that the order parameters have a physical bound. For example, the order parameters should be in $[0, 1]$ if they are the volume fractions. If some of the order parameters are beyond their physical interval, there is no physical interpretation for them, and the density of the fluid mixture, for example, can be smaller than the minimum density of the phases, and can even be negative, resulting in an ill-posed momentum equation. Problems having large density and/or viscosity ratios are less tolerant to the out-of-bound order parameters, and a small out-of-bound error can become problematic in a computation. The out-of-bound order parameters can be generated due to the defect of the Phase-Field equation (or model). For example, the widely-used two-phase Cahn-Hilliard equation [55], with constant mobility and the Ginzburg-Landau double-well potential, admits an out-of-bound solution [105]–[108]. Fortunately, both the asymptotic analysis [56], [109] and the scaling analysis [105] suggest that the out-of-bound issue is controlled by the interface thickness, which is normally as small as the grid size. Another source of the out-of-bound order parameters is from numerical errors, even though the Phase-Field equation has the maximum principle. However, designing a bound-preserving scheme is not a trivial task, especially when the equation is non-linear and complicated. In addition, the bound-preserving scheme usually casts an additional constraint on the time step, e.g., [100] for the two-phase conservative Phase-Field equation [58], and [110] for the Allen-Cahn equation [111]. The out-of-bound issue from the numerical error is the truncation error of the scheme, which again is related to the grid size. Since the out-of-bound error from either the defect of the equation or the numerical error is related to the grid size, which is usually small, a more common practice is to clip the out-of-bound solution, e.g., in [58], [75], [112]. However, a volume distribution algorithm has to be supplemented following the clipping operation. Otherwise, the mass conservation is destroyed [113]. Chiu and Lin [58]

evenly distributed the volume, which is lost from the clipping operation, to the interfacial regions, and this algorithm is applied in [114]. The clipping operation is also commonly used in the volume-of-fluid (VOF) or THINC methods, e.g., [35], [115], [116], and a volume distribution algorithm is required to achieve mass conservation [115]. As discussed, the multiphase volume distribution problem is far more challenging than the two-phase one and, thus, both the clipping operation and the volume distribution have to be carefully designed. Otherwise, fictitious phases, local voids, or overfilling can be artificially produced. The general solution of this problem has not been proposed in previous studies. Thanks to the consistent and conservative volume distribution algorithm, a numerical procedure for multiphase problems, called the boundedness mapping, is developed, which maps the order parameters, obtained numerically from a multiphase model, into their physical interval, and at the same time, the physical properties of the order parameters, i.e., their summation constraint, mass conservation, and *consistency of reduction*, are preserved.

1.2 Coupling to the hydrodynamics

In previous studies, most attention was paid to developing a set of Phase-Field equations that capture locations of individual phases, while the physical coupling between the Phase-Field equation and the hydrodynamics was less studied. The hydrodynamics was included by using a divergence-free flow velocity $\mathbf{u}$ and by simply presuming that the sharp-interface mass conservation equation:

$$\frac{\partial \rho}{\partial t} + \nabla \cdot (\rho \mathbf{u}) = 0, \tag{1.1}$$

is valid for ρ, the density of the fluid mixture. As a result, it directly reaches the Navier-Stokes equation:

$$\frac{\partial (\rho \mathbf{u})}{\partial t} + \nabla \cdot (\rho \mathbf{u} \otimes \mathbf{u}) = -\nabla P + \mathbf{f}, \tag{1.2}$$

or its equivalent form, to govern the motion of the fluid mixture. Here, P is the pressure and $\mathbf{f}$ denotes any forces other than the pressure gradient. Such a strategy of coupling the Phase-Field equations to the hydrodynamics has been popularly used in two-phase models, e.g., [57], [58], [102], [103], [112], [113], [117]–[119], and in more recent three-phase or N-

phase models, e.g., [60]–[70], [86], [90]. This probably attributes to following the conventions of Model H [120] and modified Model H [112], [118], [119].

However, the density of the fluid mixture ρ is never solved from the sharp-interface mass conservation equation Eq.(1.1) but instead computed algebraically from $\sum_{p=1}^{N} \rho_p C_p$ where ρ_p and C_p are the density and volume fraction of Phase p. The present study shows in Section 2.3 that the algebraically computed density along with the divergence-free flow velocity is contradicting to the sharp-interface mass conservation equation Eq.(1.1). Therefore, the Navier-Stokes equation Eq.(1.2) is inconsistent with the actual mass conservation equation of the mulitphase model, and can produce unphysical results. A similar issue was first realized in the sharp-interface methods for two-phase flows on the discrete level, and the so-called consistent schemes were proposed to the Volume-of-Fluid method [28], [121]–[123], to the level-set method [124], [125], and to the THINC method [126]. However, such a consistent scheme is not available for the Phase-Field method. Moreover, this consistency issue in the Phase-Field method is more complicated due to the presence of the thermodynamical effects, and this issue appears not only on the discrete level but also on the continuous (or model) level, see [56], [75] based on the Cahn-Hilliard Phase-Field equation.

The present study proposes the *consistency of mass conservation* and *consistency of mass and momentum transport* to physically couple the Phase-Field equation to the hydrodynamics. These two consistency conditions are general principles that are independent of details of the Phase-Field equation. Therefore, formulations derived from them are generally valid. The effects of these two consistency conditions are first analyzed in the present study with the Phase-Field equation written in a conservative form. It is rigorously proved that violating these two consistency conditions leads to failures of the Galilean invariance and kinetic energy conservation. Therefore, unphysical velocity fluctuations and interface deformations are produced and become more significant as the density ratio of the problem increases. These two consistency conditions result in the optimal coupling in the sense that the 2nd law of thermodynamics (or energy dissipation) or the *consistency of reduction* of the entire multiphase model only relies on the Phase-Field equation. The physical interpretation of the consistency conditions and their formulations are provided using the control volume analysis and mixture theory. For the Phase-Field equation including terms that are not in a

conservative form, like the conservative Allen-Cahn equation, the present study proposes the consistent formulation to resolve this issue, where auxiliary variables governed by a Poisson equation are introduced. As a result, all the mass conservative Phase-Field equations are able to be written in a conservative form, and the analyses of the effects of the consistency conditions are directly applied. Thus, the consistency conditions provide a general, simple, and effective procedure to physically connect various Phase-Field equations to the hydrodynamics. Moreover, the consistency conditions greatly simplified the derivation and analysis of a multiphase flow model since one only needs to pay attention to the development/selection of the Phase-Field equation in which unphysical behaviors are rooted, but directly uses the present formulations from the consistency conditions for the hydrodynamics.

The divergence-free velocity in the present and many existing studies can be interpreted as the "volume-averaged" velocity. Another category of the Phase-Field method for multiphase flows considers the non-divergence-free "mass-averaged" velocity, and examples include [81], [127]–[131] for two-phase flows, [132] for three-phase flows, and [133], [134] for N-phase flows. These models are also called the "quasi-incompressible" models. Lowengrub and colleagues developed both the two- and three-phase flow models [127], [132] of this kind. Recent numerical implementations of this kind of model are restricted to two-phase flows [81], [129]–[131]. The *consistency of reduction*, whose importance has been realized in the studies developing the volume-averaged velocity models, like in [60], [64], [66], [74], [75], has not been explicitly analyzed or discussed based on the mass-averaged velocity models. Such analyses and discussions, however, are outside the scope of the present study. Primary comparisons between the models of volume- and mass-averaged velocities, respectively, were performed in [128], and little difference was observed in two-phase flow applications. This attributes to the fact that the inequality of the two averaged velocities in multiphase flow problems are confined in the small interfacial regions. Of course, further careful qualitative and quantitative comparisons are deserved but this is not the issue to be addressed in the present study. It should be noted that the formulations derived from the proposed consistency conditions are still valid for the mass-averaged velocity models, and related discussions are in Section 2.5.

1.3 Consistent and conservative numerical framework

Another issue to be addressed in the present study is to preserve as many physical properties of the multiphase flow model as possible on the discrete level, in order to eliminate unphysical behaviors, such as generation of fictitious phases, local voids, or overfilling, and unrealistic interface deformations, which will be shown in the numerical tests in Chapter 4. Many progresses have been finished for two-phase problems, e.g., in [55], [112], [113], [117], [135]–[137], but this part is still far from complete for multiphase problems, although some developed schemes are shown to satisfy the energy law on the discrete level, e.g., in [61], [71], [86], and to achieve mass conservation, e.g., in [61], [68]. However, none of the existing schemes have considered the consistency issue introduced above. The consistent scheme for the Phase-Field method, like those [28], [121]–[126] for the sharp-interface methods, has not been developed. This greatly hinders the application of the Phase-Field method to large-density-ratio problems.

The present study focuses on the mass conservation of each phase, the momentum conservation of the multiphase mixture, the summation of the volume fractions of the phases, and on satisfying the consistency conditions on the discrete level. To achieve this goal, several novel techniques valid for an arbitrary number of phases are first reported in the present study.

- The convection term in the Phase-Field equation is written in its conservative form to conserve the mass of each phase, and then the gradient-based phase selection procedure is proposed to avoid generating fictitious phases, local voids, or overfilling.
- The boundedness mapping resulting from the consistent and conservative volume distribution algorithm is implemented to map the out-of-bound order parameters into their physical interval.
- The conservative method is developed to discretize the multiphase surface force that modeling the interfacial tensions. This method contributes the momentum conservation on the discrete level.

- The "DGT" discrete operator is developed for the viscous force to ensure both the *consistency of reduction* and momentum conservation.

- To physically connect the discrete Phase-Field and momentum equations, correspondences of numerical operations in solving both equations are highlighted, which are independent of details of the Phase-Field equation or its discretization. These correspondences are critical to preserve the consistency conditions on the discrete level.

After incorporating those novel techniques, the schemes for the Phase-Field equations and for the momentum equation in the present study have the following provable properties:

- The present schemes for the Phase-Field equations conserve the mass of each phase and therefore the mass of the fluid mixture. They also guarantee the summation of the volume fractions to be unity at every discrete location.

- The present schemes for the Phase-Field equations satisfy the *consistency of reduction*, and therefore the same is true for the discrete momentum equation. This contributes to discretely recovering the single-phase dynamics inside each bulk-phase region.

- The present scheme for the momentum equation is momentum-conservative if the interfacial tensions are either neglected or computed with the conservative method.

- The *consistency of mass conservation* and the *consistency of mass and momentum transport* are satisfied discretely, and, consequently, the scheme for the momentum equation solves advection (or translation) problems exactly (without considering the gravity and interfacial tensions), regardless of the material properties of the fluid phases or the initial shapes of the interfaces.

The aforementioned properties are carefully validated by numerical experiments. Applications of the proposed model and scheme to realistic multiphase flows show their robustness and capability of simulating multiphase dynamics even when there is a significant difference between material properties across the interface.

1.4 N-phase-M-component model

Multiphase and multicomponent flow problems are ubiquitous and have various applications. The problems include strong interactions among phases and components, leading to challenges in developing analytical or numerical solutions. Before the related studies are summarized, the terminology in the present work is first clarified, since "multiphase" and "multicomponent" are commutable in some literature. In the present work, phases are immiscible with each other and the domain is occupied by at least one of the phases, and that components are materials dissolvable in some specific phases and their presence can increase the local density and viscosity based on their amounts (or concentrations).

Despite the active studies on the modeling and simulation of two-/multi-phase flows, the studies including multiple components in a multiphase system are relatively rare, probably because the multiphase problem itself is adequately complicated, and a general and physically plausible multiphase model, e.g., the one in [75], is developed very recently. When there are multiple phases and components in a system, a component can dissolve in several different phases, and, at the same time, there can be different components present in a single phase. It is challenging to incorporate all these relationships between phases and components in a general model. In addition, the phases are moving, deforming, and even experiencing topological changes, and the components inside the phases need to respond to these motions appropriately, which casts another challenge in modeling. The appearance of the components may change the local density, which influences the mass transport and the consistency of the model. Some existing works can be categorized into the two-phase-one-component problems, e.g., the problems including a surfactant [82], [138]–[140], where the concentration of the surfactant changes the surface tension and, as a result, introduces the Marangoni effect, and the problems including phase change [141], [142], where the vapor generated from the liquid is dissolvable in the condensible gas. However, including these additional physics in the problems having multiple phases and components is out of the scope of the present study. The present study is confined to incompressible flows without phase change and assume that the Marangoni effect due to the presence of the components is negligible.

In the present work, a consistent and conservative model for multiphase and multicomponent incompressible flows is developed. The model allows arbitrary numbers of phases and components appearing simultaneously. Each component can exist in different phases. In each phase, there is a background fluid called the pure phase, and multiple components can be dissolved in this pure phase. Therefore, each phase is a "solution" of its pure phase (or background fluid) as the "solvent" and the components dissolved in this phase as the "solutes". Individual pure phases and components have their own densities and viscosities. Each pair of phases has a surface tension and each component has a diffusivity in a given phase. At a wall boundary, each pair of phases has a contact angle. The model is based on the consistent and conservative method for N-phase flows, proposed in the present study, the diffuse domain approach [143], and the consistency analysis developed in the present study. The diffuse domain approach is applied to replace the convection-diffusion equation of a component defined in a specific phase with its mathematical equivalent equation defined in the whole domain. One more consistency condition, i.e., the *consistency of volume fraction conservation*, is proposed. The consistency analysis is performed based on the consistency conditions for multiphase and multicomponent flows, proposed in the present work. It ensures that the flow dynamics is correctly connected with the dynamics of the phases and components, and that no fictitious phases or components are allowed to be generated. The resulting model conserves the mass of individual pure phases, the amount of each component in its dissolvable region, and thus the mass of the fluid mixture, and the momentum of the multiphase and multicomponent flows. It ensures that the summation of the volume fractions of the phases is unity everywhere so that there is no local void or overfilling. It satisfies a physical energy law and it is Galilean invariant. It satisfies all the consistency conditions, which are the *consistency of reduction*, the *consistency of volume fraction conservation*, the *consistency of mass conservation*, and the *consistency of mass and momentum transport*. It should be noted that the consistency conditions play a critical role in avoiding fictitious phases and components, in deriving the energy law, and in proving the Galilean invariance of the model. The model is flexible to allow a component to cross a phase interface with either zero flux or continuous flux based on the property of the phase interface if the component is dissolvable in both sides of the interface. In addition to study the dynamics of the multiphase

and multicomponent flows, the present model is applicable to study some multiphase flows, where the miscibility of each two phases can be different.

The corresponding numerical scheme is developed for the proposed model, which is an extension of the consistent and conservative numerical framework for multiphase flows. The scheme is formally 2nd-order accurate in both time and space and it preserves the properties of the model. The scheme conserves the mass of individual pure phases, the amount of each component in its dissolvable region, and therefore the mass of the fluid mixture. The momentum is exactly conserved by the scheme with the conservative method for the interfacial force, while it is essentially conserved with the balanced-force method. All the consistency conditions are shown to be satisfied on the discrete level by the scheme. This is very important for the problems including large density ratios and to ensure that no fictitious phases or components can be generated by the scheme. The properties and capabilities of the proposed model and scheme are demonstrated numerically. Details of this model is provided in Section 2.6.1.

1.5 Thermo-gas-liquid-solid model including solidification/melting

Liquid-Solid phase change (or solidification/melting) and its interaction with the surrounding air are ubiquitous in various natural and/or industrial processes, e.g., latent thermal energy storage (LTES) systems [144], [145], welding [146]–[149], casting [150], [151], and additive manufacturing (AM) [152]–[154]. This motivates researchers to develop physical and high-fidelity models to further understand the complex physics and dynamics, and accurately predict the behavior of materials in order to produce high-quality products. Such a problem includes many challenging factors, such as a wide range of material properties, evolution of the liquid-solid interface due to solidification/melting, deformation of the gas-liquid interface due to fluid (gas/liquid) motions and surface tension, heat transfer that drives the phase change, and fluid-structure interaction between the fluid and solid, and all these factors are coupled and can be influential. In the present study, this problem is called thermo-gas-liquid-solid flows with liquid-solid phase change.

In spite of the complexity of the problem, it can be separated into two basic problems which are the two-phase incompressible flow and the solidification with convection. Many existing studies have focused on these individual problems. The numerical methods for the two-phase incompressible flows have been introduced above. For the solidification problem with convection, one of the most popular methods is the enthalpy-porosity technique [155]–[159], which can be implemented in a fixed grid. The liquid fraction of the phase change material is algebraically related to the local temperature. Therefore, the enthalpy change due to phase change can be evaluated and becomes a source in the energy equation. A drag force proportional to the velocity is added to the momentum equation to stop the solid motion, which is the same idea as the fictitious domain Brinkman penalization (FD/BP) method for the fluid-structure interaction [160], [161]. The most popularly used drag force in the enthalpy-porosity technique is modified from the Carman-Kozeny equation [162] for the porous medium. Another popular method for solidification is the Phase-Field method [163]–[169], where the liquid-solid interface has a small but finite thickness. Different from the enthalpy-porosity technique using an algebraic relation, the Phase-Field method introduces an additional equation to govern the evolution of the liquid fraction of the phase change material, and therefore is flexible to include more complicated physics, e.g., anisotropy and solute transport in an alloy. After coupling the Phase-Field method with the hydrodynamics, the melt convection can be modeled [170]–[173]. Other methods for modeling the liquid-solid phase change are reviewed in [174]–[180].

Most existing models for the thermo-gas-liquid-solid flows with liquid-solid phase change follow a similar procedure: The deforming gas-liquid interface is located by a certain interface capturing method and the continuous surface tension force is added, while the enthalpy-porosity technique is directly applied without any further changes to adapt to the appearance of a new phase. The volume-of-fluid method is the most popular choice and is used, e.g., in [144], [145], [149], [152], [153], [181], [182]. The level-set and conservative level set methods are recently used in [183] and [154], respectively. Some additional physics are introduced to the models, e.g., the thermo-capillary effect [152]–[154], [183] and recoil pressure [152]–[154]. Another recent model [184] follows the same strategy but instead uses the Phase-Field model in [185] for anisotropic solidification and the conservative Phase-Field method

[58] as the interface capturing method. In spite of its widespread applications, such a well-accepted modeling strategy has the following critical issues. *(i) The volume fractions of the phases are ambiguously defined.* In the models applying the enthalpy-porosity technique, the liquid fraction is meaningful only inside the phase change material, while it directly appears in the energy equation defined in the entire domain including the gas phase. As a result, the meaningless value of the liquid fraction in the gas phase is also counted in the energy equation. Another example is in [184], where two liquid fractions are defined for the same liquid phase, one from the solidification model and the other from the interface capturing method. Since the solidification model and the interface capturing method have no explicit/direct connection, these two liquid fractions may inconsistently label the liquid location. *(ii) The surface tension and drag forces can appear at wrong locations* because the volume fractions, which are not clearly defined, are needed to compute the forces. Based on the formulations, e.g., in [149], [152]–[154], [183], the surface tension at the gas-liquid interface will falsely appear at the gas-solid interface, and the drag force will falsely appear in the gas phase when the local temperature is lower than the solidus temperature. Some artificial operations need to be added but they have seldom been mentioned in the literature. An exception is in [184] where a bounce-back scheme near the gas-solid interface is employed since the gas-solid interface is unable to be effectively labeled by the model, but details of the bounce-back scheme are not provided. *(iii) Physical principles can be violated, depending on the material properties.* The most obvious example is the mass conservation. In, e.g., [152], [153], [159], [181]–[184], the velocity is divergence-free, implying that both the volumes of the gas and phase change material will not change. This restricts the application of the model to problems having matched liquid and solid densities. However, the problems studied in [154], [181] are outside that category, and therefore the volume of the phase change material needs to change in order to satisfy the mass conservation. It should be noted that the volume change in [154] is from evaporation, not solidification/melting, and the velocity is divergence-free without evaporation. As a result, the divergence-free velocity is contradicting the mass conservation. Although the studies in [144], [145], [186], [187] captures the volume change, detail formulations, i.e., the divergence of the velocity, are not provided. Other physical principles, e.g., the momentum and energy conservation and the Galilean invariance of the

models, have never been examined. *(iv) The problem of interest often has a large density ratio*, which can be $O(10^4)$ between the gas and liquid. It has been well-known that the so-called consistent method [28], [121]–[126] needs to be implemented to produce physical results for multiphase flows, while this has never been considered in the existing models for the problem of interest.

The aforementioned issues in the existing models for the problem of interest are originated in simply "combining", not physically "coupling", the models for solidification and two-phase flows. In the present study, those critical issues are properly addressed and a consistent and conservative Phase-Field model is developed for the thermo-gas-liquid-solid flows with liquid-solid phase change. In deriving the model, the consistency conditions proposed in the present study are considered. In the earlier discussions, phase change or temperature variations in the fluids are not included. Here is the first implementation of the consistency conditions to phase change problems, which further demonstrates their generality. All the dependent variables are defined in a fixed regular domain, which is convenient for numerical implementation. The following physical properties are enjoyed by the proposed model:

- The proposed model exactly recovers the consistent and conservative Phase-Field method for incompressible two-phase flows in the present study when the solid phase is absent, the fictitious domain Brinkman penalization (FD/BP) method for fluid-structure interactions [160], [161] when the liquid phase is absent, and the Phase-Field model of solidification of a pure material [163] when the gas phase is absent.

- The proposed model defines the volume fractions of individual phases unambiguously and ensures their summation to be unity everywhere. The local mass conservation is strictly satisfied, from which the divergence of the velocity is non-zero, and therefore the volume change during solidification/melting is captured.

- The momentum is conserved when the solid phase is absent, and the no-slip condition at the solid boundary results in the momentum change. The energy conservation and Galilean invariance are also satisfied by the proposed model.

- The momentum transport is consistent with the mass transport of the gas-liquid-solid mixture, which greatly improves the robustness of the model for large-density-ratio problems and avoids unrealistic interface deformation.

- Isothermal (or temperature equilibrium) solutions are admissible, thanks to satisfying the consistency conditions, which prevents producing any fictitious fluctuations of the temperature.

- Novel continuous surface tension and drag force models are proposed, which are activated only at proper locations. The interpolation function in the solidification model [163] is modified to include the capability of initiating phase change when there is only the liquid/solid-state of the phase change material.

These physical properties of the model are independent of the material properties. The model is validated and its capability is demonstrated with the help of the proposed numerical framework. The proposed model includes all the basic ingredients and challenging aspects of the problem, and additional physics can be incorporated conveniently following the same framework. Details of this model are provided in Section 2.6.2.

2. CONSISTENT AND CONSERVATIVE MODELS FOR MULTIPHASE FLOWS[1]

In this chapter, the consistent and conservative models for immiscible and incompressible multiphase flows are developed, where there can be an arbitrary number of phases. The models are based on the Phase-Field (or Diffuse-Interface) method, which is characterized by introducing a small but finite interface thickness, to locate different phases. Definitions of basic variables of the multiphase problems are first introduced. Then, three consistency conditions are defined to complete the models, along with analyzing their effects on multiphase flows. The physical interpretations to the consistency conditions and the formulations derived from them are provided. At the end of this chapter, the multiphase problems are extended to including mass (heat) transfer, temperature variation, and solidification/melting, with the help of an additionally proposed consistency condition.

2.1 Basic definitions

Inside the domain of interest, denoted by Ω, there are N ($N \geqslant 1$) immiscible and incompressible fluid phases. "Immiscible" means the phases are not capable of combining to form a homogeneous mixture, and "incompressible" means the densities of the phases are constant. Each phase, e.g., Phase p ($1 \leqslant p \leqslant N$), has a volume fraction C_p ($0 \leqslant C_p \leqslant 1$). The volume fraction of Phase p here is defined as the portion of Phase p in a differential volume ($d(vol)_p$) over the same differential volume ($d(vol)$), i.e., $C_p = d(vol)_p/d(vol)$. Since no void or overfilling is allowed to be generated, the summation of the volume fractions should be

[1]This chapter was partly published in Journal of Computational Physics, Vol 387, Ziyang Huang, Guang Lin, Arezoo M. Ardekani, A mixed upwind/central WENO scheme for incompressible two-phase flows, Page 455-480, Copyright Elsevier (2019); in Journal of Computational Physics, Vol 406, Ziyang Huang, Guang Lin, Arezoo M. Ardekani, Consistent, essentially conservative and balanced-force Phase-Field method to model incompressible two-phase flows, Page 109192, Copyright Elsevier (2019); in Journal of Computational Physics, Vol 420, Ziyang Huang, Guang Lin, Arezoo M. Ardekani, Consistent and conservative scheme for incompressible two-phase flows using the conservative Allen-Cahn model, Page 109718, Copyright Elsevier (2020); in Journal of Computational Physics, Vol 434, Ziyang Huang, Guang Lin, Arezoo M. Ardekani, A consistent and conservative model and its scheme for N-phase-M-component incompressible flows, Page 110229, Copyright Elsevier (2021); and in International Journal of Multiphase Flow, Vol 142, Ziyang Huang, Guang Lin, Arezoo M. Ardekani, A consistent and conservative volume distribution algorithm and its applications to multiphase flows using Phase-Field models, Page 103727, Copyright Elsevier (2021).

unity. Another popular choice to locate the phases is the volume fraction contrast, whose definition is

$$\phi_p = C_p - \sum_{q=1,q\neq p}^{N} C_q = 2C_p - 1, \quad 1 \leqslant p \leqslant N, \tag{2.1}$$

and its range is from -1 to 1. Correspondingly, the summation of the volume fraction contrasts is

$$\sum_{p=1}^{N} C_p = \sum_{p=1}^{N} \frac{1+\phi_p}{2} = 1 \quad \text{or} \quad \sum_{p=1}^{N} \phi_p = 2 - N. \tag{2.2}$$

Either the volume fractions $\{C_p\}_{p=1}^{N}$ or the volume fraction contrasts $\{\phi_p\}_{p=1}^{N}$ can be used as the order parameters in a Phase-Field method, and the latter one is considered in the present study unless otherwise specified.

The density and viscosity of fluid phase p are ρ_p ($\rho_p \geqslant 0$) and μ_p ($\mu_p \geqslant 0$), respectively. The density and viscosity of the fluid mixture are defined by

$$\rho = \sum_{p=1}^{N} \rho_p C_p = \sum_{p=1}^{N} \rho_p \frac{\phi_p + 1}{2}, \tag{2.3}$$

$$\mu = \sum_{p=1}^{N} \mu_p C_p = \sum_{p=1}^{N} \mu_p \frac{\phi_p + 1}{2}. \tag{2.4}$$

The interfacial tension between Phases p and q is $\sigma_{p,q}$ ($1 \leqslant p, q \leqslant N$). The interfacial tension between Phases q and p is the same as the one between Phases p and q, i.e., $\sigma_{q,p} = \sigma_{p,q}$, and there is no interfacial tension inside each phase, i.e., $\sigma_{p,p} = 0$. The contact angle of Phases p and q at a wall, measured inside Phase p, is $\theta_{p,q}^{W}$, ($1 \leqslant p, q \leqslant N$). Consequently, $\theta_{p,q}^{W} + \theta_{q,p}^{W} = \boldsymbol{\pi}$ is true.

The flow velocity is denoted by $\mathbf{u}$, which is divergence-free:

$$\nabla \cdot \mathbf{u} = 0. \tag{2.5}$$

Such a velocity is also referred to as the volume-averaged velocity of the fluid mixture and more details related to Eq.(2.5) are provided in Section 2.5. A series of theoretical analyses and discussions related to the volume-averaged velocity and the models based on that is

performed by Brenner, e.g., in [188]–[191]. The divergence-free condition Eq.(2.5) is enforced by a Lagrange multiplier P, called the pressure.

2.2 Consistency of reduction

It should be noted that any N-phase problem is locally a M-phase problem ($1 \leqslant M \leqslant N$), and, in most cases, M is much less than N. Therefore, it is important that the N-phase model recovers the corresponding M-phase model when and where there are only M phases present, so that the local M-phase dynamics is reproduced. Therefore, a multiphase model should satisfies the following principle.

Consistency of reduction*: A N-phase system should be able to recover the corresponding M-phase system ($1 \leqslant M \leqslant N-1$) when ($N-M$) phases don't appear.*

Although the *consistency of reduction* is defined similarly to the one in [64], [75], the understanding of absent phases in the present study needs to be further clarified. In the previous studies, the absence of phases is considered globally, for example, the absence of Phase p means that Phase p dose not appear anywhere, i.e., $\phi_p \equiv -1$. In the present work, the absence of phases is considered locally. As an example, the absence of Phase p means where $\phi_p = -1$ and all its spatial derivatives in its governing equation are zero. Such a consideration in the present study has not only theoretical but also practical values.

It is obvious that if the *consistency of reduction* is true when the absent phases are considered locally, it will be true as well when the absent phases are considered globally, because $\phi_p \equiv -1$ implies all the spatial derivatives of ϕ_p are zero. Therefore, the local consideration in the present study won't contradict with previously developed theories about the *consistency of reduction*, e.g., in [64], [75]. On the other hand, satisfying the *consistency of reduction* in the global sense does not lead to the local case, and examples include the conservative Allen-Cahn equations in [68], [97] for two- and N-phase problems, respectively, as analyzed in the following sections. From a practical point of view, absent phases won't be initiated, because that will increase the cost of computation and the demand of storage. There only exists local absence of phases at different locations of the domain in realistic applications. Therefore, the locally absent case should be considered more carefully.

One of the consequences of violating the *consistency of reduction* is generating fictitious phases in interfacial regions [64], [66]. This has a great influence on the multiphase dynamics even though the amounts of the fictitious phases are small, especially in a problem having a large density or viscosity ratio, which is demonstrated in [64]. Moreover, dynamics inside bulk-phase regions is produced incorrectly if this principle is violated. One shall see that the *consistency of reduction* of the entire multiphase flow model only relies on the Phase-Field equation (or model). Thus, the Phase-Field equation will be first discussed.

When analyzing the *consistency of reduction* in a formal way, without loss of generality and for a clear presentation, a N-phase system ($N \geqslant 2$) is considered and the last phase, i.e., Phase N, is absent in the present study. The analyses are not related to which phase is chosen to be absent, and thus the same conclusion will be drawn by arbitrarily choosing an absent phase among the N phases. Besides, the analyses are repeatable. If the analyses are repeated $(N - M)$ times ($1 \leqslant M \leqslant N - 1$), they produce results of $(N - M)$ absent phases. Therefore, one only needs to consider the case where only a single phase is absent. If the N-phase formulations recover the corresponding $(N-1)$-phase formulations, then the *consistency of reduction* is achieved.

2.2.1 Introduction to the Phase-Field method

The Phase-Field equation (or model) governs the dynamics of the order parameters locating different phases. A general form of the Phase-Field equation for the multiphase incompressible flows is:

$$\frac{\partial \phi_p}{\partial t} + \nabla \cdot (\mathbf{u}\phi_p) = \nabla \cdot \mathbf{J}_p + L_p^R + L_p^c \quad \text{in} \quad \Omega, \quad 1 \leqslant p \leqslant N, \tag{2.6}$$

and the convection term is written in its conservative form, thanks to the divergence-free velocity Eq.(2.5). Here, $\{\mathbf{J}_p\}_{p=1}^N$ are the diffusion fluxes and $\{L_p^R\}_{p=1}^N$ are the reaction terms of the Phase-Field equation, and $\{L_p^c\}_{p=1}^N$ are the Lagrange multipliers supplemented to enforce the mass conservation.

When the fluid phases are in contact with a wall, contact lines are formed there, and the contact angle boundary condition, without lost of generality, can be written as:

$$\mathbf{n}\cdot\nabla\phi_p = \mathcal{F}_p^w[\{\phi_q\}_{q=1}^N;\{\theta_{q,r}^W\}_{q,r=1}^N] \quad \text{at} \quad \partial\Omega, \quad 1\leqslant p\leqslant N. \tag{2.7}$$

Here $\mathbf{n}$ is the unit outward normal at the domain boundary $\partial\Omega$. $\mathcal{F}^w$ is a certain functional with respect to $\{\phi_p\}_{p=1}^N$, and $\{\theta_{p,q}^W\}_{p,q=1}^N$ are its parameters. It should be noted that the notation in Eq.(2.7) is simplified, and $\mathcal{F}^w$ and $\{\theta_{p,q}^W\}_{p,q=1}^N$ can be different at individual wall boundaries in practice. For the 4th-order Phase-Field equations whose highest spatial derivatives are 4th-order, the zero-flux boundary condition, in addition to Eq.(2.7), is usually assigned to the diffusion flux $\mathbf{J}$ for the sake of mass conservation. However, for the 2nd-order ones, only a single boundary condition is needed at the wall boundary and using Eq.(2.7) probably fails to conserve the mass. Therefore, in the present study, the Lagrange multipliers, i.e., L_p^c in Eq.(2.6), are added to compensate the effect of the contact angle boundary condition on mass change.

To be physically admissible in multiphase incompressible flow problems, the Phase-Field equation Eq.(2.6) and the contact angle boundary condition Eq.(2.7) should honor the following basic properties. The first one is the mass conservation:

$$\begin{aligned} \frac{d}{dt}\int_\Omega \phi_p d\Omega + \int_{\partial\Omega}\mathbf{n}\cdot\mathbf{u}\phi_p d\Gamma = 0 \quad \text{or} \\ \int_\Omega L_p^c d\Omega = -\int_\Omega(\nabla\cdot\mathbf{J}_p + L_p^R)d\Omega = S_p^c, \quad 1\leqslant p\leqslant N. \end{aligned} \tag{2.8}$$

After realizing that the mass of individual phases is $\int_\Omega \rho_p(1+\phi_p)/2 d\Omega$, Eq.(2.8) states that the mass of each phase changes only because of injection or removal of that phase at the domain boundary. Notice that the integral of $\nabla\cdot\mathbf{J}$ over the domain is zero for the 4th-order Phase-Field equations but this is probably not true for the 2nd-order ones with non-90^0 contact angles.

The second property is the summation of the order parameters, i.e., Eq.(2.2), which avoids local voids or overfilling. After summing Eq.(2.6), as well as Eq.(2.7), over p, the

constraints for the diffusion fluxes, reaction terms, Lagrange multipliers, and the contact angle boundary condition are:

$$\sum_{q=1}^{N} \mathbf{J}_q = \mathbf{0}, \quad \sum_{q=1}^{N} L_q^R = 0, \quad \sum_{q=1}^{N} L_q^c = 0, \quad \sum_{q=1}^{N} \mathcal{F}_q^W = 0. \tag{2.9}$$

The last property is the *consistency of reduction*. If Phase q ($1 \leqslant q \leqslant N$) is absent, the diffusion flux, reaction term, Lagrange multiplier, and the contact angle boundary condition of Phase q vanish:

$$\mathbf{J}_q = \mathbf{0}, \quad L_q^R = 0, \quad L_q^c = 0, \quad \mathcal{F}_q^W = 0, \tag{2.10}$$

so that Phase q remains absent, i.e., $\partial \phi_q / \partial t = 0$. Their formulations for the rest of the phases reduce to the corresponding ones excluding Phase q.

Various existing studies have considered $\mathbf{J}$, L^R, and $\mathcal{F}^W$ in the three-phase and/or N-phase cases, e.g., those in [60]–[68], [71]–[75], [86], [90], and some of them satisfy the properties in Eq.(2.9) and Eq.(2.10). However, fewer studies consider L^c for an arbitrary number of phases, and a general formulation of L^c satisfying all the properties in Eq.(2.8), Eq.(2.9), and Eq.(2.10) has not been developed. This issue will be addressed in the next section.

2.2.2 Consistent and conservative volume distribution algorithm

The purpose of the consistent and conservative volume distribution algorithm is to specify the volume distribution functions of individual phases, denoted as $\{L_p\}_{p=1}^N$, in a consistent and conservative manner.

Problem statement: *Given a set of order parameters $\{\phi_p\}_{p=1}^N$ that satisfy their summation constraint Eq.(2.2), i.e., $\sum_{p=1}^N \phi_p = (2-N)$, and a set of scalars $\{S_p\}_{p=1}^N$ that satisfy $\sum_{p=1}^N S_p = 0$, determine a set of spatial functions $\{L_p\}_{p=1}^N$ such that*

$$\sum_{q=1}^{N} L_q = 0, \quad \int_\Omega L_p d\Omega = S_p, \quad L_p|_{\phi_p=-1} = 0, \quad 1 \leqslant p \leqslant N. \tag{2.11}$$

Here, $\{S_p\}_{p=1}^N$ are related to the volume changes of individual phases, and the admissible set has a zero summation over p. In other words, the net volume added to the domain is

zero. Therefore, the present algorithm keeps the domain volume fixed but adjusts the phase volumes based on the given values. One may notice that the constraints for L in Eq.(2.11) are the same kind of those in Eq.(2.9), Eq.(2.8), and Eq.(2.10) for L^c if it is assumed that L^c does not include derivatives of the order parameters.

Given $\{S_p\}_{p=1}^N$ only, there can be multiple choices of $\{L_p\}_{p=1}^N$, while not all of them are admissible. Three physical constraints are proposed, which need to be strictly satisfied by $\{L_p\}_{p=1}^N$, and they are formulated in Eq.(2.11). The first constraint is called the summation constraint for volume distribution, which states that the summation of the order parameters after the volume distribution does not change, i.e., $\sum_{p=1}^N(\phi_p + L_p) = (2 - N)$, so that the summation of the volume fractions of the phases is always unity, see Eq.(2.2). In other words, no local void or overfilling can be generated by the volume distribution. The second constraint in Eq.(2.11) is called the conservation constraint for volume distribution, which requires the total amounts of $\{L_p\}_{p=1}^N$ equal to the corresponding given values $\{S_p\}_{p=1}^N$. Otherwise, the volume distribution problem is not solved successfully. It should be noted that the summation and conservation constraints for volume distribution are consistent with each other due to $\sum_{p=1}^N S_p = 0$. The last constraint is related to the *consistency of reduction*. If Phase p is labeled absent by ϕ_p at a specific location, then there should not be any volume of Phase p being distributed at that location. This constraint avoids producing any fictitious phases after the volume distribution at that location. Combining the first and last constraints in Eq.(2.11), one can easily obtain $L_p|_{\phi_p=1} = 0$. In other words, the volume distribution only happens at the interfacial regions, while it is deactivated inside the bulk-phase regions.

Specifying a set of $\{L_p\}_{p=1}^N$ that satisfy all the aforementioned constraints is not a trivial task. A successful algorithm is developed in [96] for two-phase flows. However, it is far more challenging in a general multiphase case. When there are only two phases, the constraints in Eq.(2.11) for L_1 turn into $\int_\Omega L_1 d\Omega = S_1$ and $L_1|_{\phi_1=\pm1} = 0$. Once L_1 is determined, $L_2 = -L_1$ is directly obtained from the first constraint in Eq.(2.11), and $\{L_p\}_{p=1}^2$ satisfy all the constraints in Eq.(2.11). As a result, only phase-wise formulations are needed. On the other hand, if a three-phase example is considered, even though L_1 is specified, one still can not determine L_2 and L_3 directly or uniquely. If L_1 and L_2 are specified independently from phase-wise formulations, there is no guarantee that $L_3 = -(L_1+L_2)$ from the first constraint

in Eq.(2.11) satisfies the rest of the constraints. Due to the complexity of including multiple phases, the volume distribution is unable to be performed phase-wise. Instead, a coupled formulation is proposed for the volume distribution functions, i.e.,

$$L_p = \sum_{q=1}^{N} W_{p,q} B_q, \quad 1 \leqslant p \leqslant N, \tag{2.12}$$

where $W_{p,q}$ is the weight function for volume distribution and should be non-zero only in the interfacial regions including Phases p and q from the *consistency of reduction*. Eq.(2.12) can be conceptually understood as following. B_q, which is related to the total volume of Phase q to be distributed to the domain, can only be distributed to the interfacial regions including Phase q. Therefore, the volume distributed to the interfacial regions including both Phases p and q from B_q is $W_{p,q}B_q$. Then, L_p is obtained by summing all the contributions from the phases. The constraints in Eq.(2.11) for $\{L_p\}_{p=1}^N$ turn into the following for $\{W_{p,q}\}_{p,q=1}^N$, i.e.,

$$\sum_{r=1}^{N} W_{r,q} = 0, \quad \sum_{r=1}^{N} \left(\int_\Omega W_{p,r} d\Omega \right) B_r = S_p, \quad W_{p,q}|_{\phi_p=-1} = 0, \quad 1 \leqslant p, q \leqslant N. \tag{2.13}$$

Based on the *consistency of reduction*, i.e., the third constraint in Eq.(2.13), the weight function for volume distribution is constructed to be

$$W_{p,q} = \begin{cases} -(1+\phi_p)(1+\phi_q), p \neq q, \\ (1+\phi_p)(1-\phi_q), p = q, \end{cases} \quad 1 \leqslant p, q \leqslant N. \tag{2.14}$$

It should be noted that $W_{p,q}$ indicates the interfacial regions including both Phases p and q because it is non-zero only where $-1 < \phi_p, \phi_q < 1$. Moreover, the summation constraint, i.e., the first constraint in Eq.(2.13), is also satisfied by $W_{p,q}$ in Eq.(2.14) given $\sum_{p=1}^N \phi_p = (2-N)$. The remaining step is to satisfy the conservation constraint, i.e., the second constraint in Eq.(2.13). This is achieved by solving the linear system for $\{B_p\}_{p=1}^N$, i.e.,

$$[A_{p,q}]_{N\times N}[B_q]_{N\times 1} = [S_p]_{N\times 1}, \quad A_{p,q} = \int_\Omega W_{p,q} d\Omega. \tag{2.15}$$

The coefficient matrix of the linear system Eq.(2.15), i.e., $[A_{p,q}]_{N\times N}$, includes the integrals of the weight function $W_{p,q}$ $(1 \leqslant p, q \leqslant N)$ over the domain. Since $W_{p,q}$ is symmetric, $[A_{p,q}]_{N\times N}$ is symmetric as well. It should be noted that all the diagonal elements of $[A_{p,q}]_{N\times N}$ are positive while all the off-diagonal ones are negative, and additionally that $\sum_{q=1}^{N} A_{p,q}$ $(1 \leqslant p \leqslant N)$ is zero, from the definition of $W_{p,q}$ in Eq.(2.14). This implies that $\sum_{q=1,q\neq p}^{N} |A_{p,q}| = |A_{p,p}|$ $(1 \leqslant p \leqslant N)$, which shows that the coefficient matrix $[A_{p,q}]_{N\times N}$ in Eq.(2.15) is not only symmetry but also diagonally dominant. Another important observation of Eq.(2.15) is that the rank of $[A_{p,q}]_{N\times N}$ is at most $(N-1)$. After summing Eq.(2.15) over p, an equation of "$0 = 0$" is obtained because both $\sum_{p=1}^{N} W_{p,q}$ and $\sum_{p=1}^{N} S_p$ are zero. As a result, the linear system in Eq.(2.15) has multiple solutions, and implementations show that solving Eq.(2.15) following the scaling argument below is critical to specify the admissible solution and for the success of the algorithm, especially when $\{S_p\}_{p=1}^{N}$ are close to the round-off error. If $[|A_{p,q}|]_{N\times N}$ is in $O(1)$, then $[|B_p|]_{N\times 1}$ should share the same order of magnitude as $[|S_p|]_{N\times 1}$. A robust way to employ this scaling argument is to let B_{q^*} equal to $\max|S_p|$, where q^* is chosen in such a way that the minimum absolute value other than zero of $[A_{p,q}]_{N\times N}$ is in column $[A_{p,q^*}]_{N\times 1}$. Consequently, Eq.(2.15) has a unique solution that honors the scaling argument. A special case is when there is a phase, e.g., Phase p, doesn't have any interfacial regions in the whole domain. Equivalently, Phase p is either globally absent, i.e., $\phi_p \equiv -1$, or filling the entire domain, i.e., $\phi_p \equiv 1$. As a result, both the pth row and column in $[A_{p,q}]_{N\times N}$ are zero, and $B_p = 0$ is set when this happens. In order to obtain $[|A_{p,q}|]_{N\times N} \sim O(1)$, the coefficient matrix $[A_{p,q}]_{N\times N}$ is rescaled by its maximum absolute value, i.e., $\max|A_{p,q}|$, if that value is not zero. Specifically, after obtaining $[A_{p,q}]_{N\times N}$ from the integrals of $\{W_{p,q}\}_{p,q=1}^{N}$, see Eq.(2.15), $[A_{p,q}]_{N\times N}$ is replaced by $[A_{p,q}]_{N\times N}/\max|A_{p,q}|$, and correspondingly $W_{p,q}$ $(1 \leqslant p, q \leqslant N)$ is replaced by $W_{p,q}/\max|A_{p,q}|$. As a result, the final coefficient matrix $[A_{p,q}]_{N\times N}$ is always of $O(1)$, independent of the domain size. Once $\{B_p\}_{p=1}^{N}$ are solved from Eq.(2.15), the volume distribution functions for individual phases $\{L_p\}_{p=1}^{N}$ are obtained from Eq.(2.12).

The volume distribution problem defined at the beginning of this section is solved by the following algorithm:

Applying the weight function $W_{p,q}$ defined in Eq.(2.14) and solving $\{B_p\}_{p=1}^N$ from the $N\times N$ symmetry and diagonally dominant linear system in Eq.(2.15), $\{L_p\}_{p=1}^N$ are determined from Eq.(2.12), which satisfy all the physical constraints in Eq.(2.11).

This algorithm is consistent and conservative in the sense that the resulting $\{L_p\}_{p=1}^N$ satisfy the *consistency of reduction* and their integrals over the domain are equal to the given values $\{S_p\}_{p=1}^N$.

Theorem 2.2.1. *The proposed consistent and conservative volume distribution algorithm is reduction consistent.*

Proof. Without loss of generality and for a clear presentation, the last phase of a N-phase ($N \geqslant 2$) system is absent at the location where $\phi_N = -1$. Then from Eq.(2.12), one has

$$L_N = \sum_{q=1}^{N} W_{N,q} B_q = 0, \quad L_p = \sum_{q=1}^{N} W_{p,q} B_q = \sum_{q=1}^{N-1} W_{p,q} B_q, \quad 1 \leqslant p \leqslant N-1,$$

due to $W_{p,q}|_{\phi_p=-1} = W_{q,p}|_{\phi_p=-1} = 0$ from Eq.(2.14). Therefore, the N-phase formulation of $\{L_p\}_{p=1}^N$ reduces to the corresponding $(N-1)$-phase formulation for the present phases and its value for the absent phase is zero. Notice that one can choose any other phases as the absent phase and reach the same conclusion. By induction, the *consistency of reduction* is true. □

Lastly, the two-phase case is considered, and have $\phi_1 + \phi_2 = 0$ and $S_1 + S_2 = 0$ as the admissible inputs. From Eq.(2.15), one obtains the following equations

$$\begin{cases} S_1 = B_1 \int_\Omega W_{1,1} d\Omega + B_2 \int_\Omega W_{1,2} d\Omega = (B_1 - B_2) \int_\Omega (1-\phi_1^2) d\Omega = (B_1 - B_2) \int_\Omega W_1 d\Omega \\ S_2 = B_1 \int_\Omega W_{2,1} d\Omega + B_2 \int_\Omega W_{2,2} d\Omega = -(B_1 - B_2) \int_\Omega (1-\phi_2^2) d\Omega = -(B_1 - B_2) \int_\Omega W_2 d\Omega \end{cases},$$

and it should be noted that the above two equations are identical due to $S_1 = -S_2$, $\phi_1 = -\phi_2$, and $W_1 = W_2$ where $W_p = W(\phi_p) = (1-\phi_p^2)$. Finally from Eq.(2.12), one obtains

$$\begin{cases} L_1 = B_1 W_{1,1} + B_2 W_{1,2} = (B_1 - B_2)(1-\phi_1^2) = \frac{W_1}{\int_\Omega W_1 d\Omega} S_1, \\ L_2 = B_1 W_{2,1} + B_2 W_{2,2} = -(B_1 - B_2)(1-\phi_2^2) = \frac{W_2}{\int_\Omega W_2 d\Omega} S_2. \end{cases} \tag{2.16}$$

Therefore, the volume distribution algorithm becomes phase-wise in two-phase cases, and Eq.(2.16) is identical to those in [96].

2.2.3 Reduction consistent Phase-Field equations

In this section, two Phase-Field equations, one is the representative of the Cahn-Hilliard type [91] and the other belongs to the conservative Allen-Cahn type [97], [111], are introduced, along with their contact angle boundary condition. The Cahn-Hilliard equation considered in the present study comes from [75] while the conservative Allen-Cahn equation is originally developed, resulting from the consistent and conservative volume distribution algorithm in Section 2.2.2.

Specifically, the multiphase Cahn-Hilliard Phase-Field equation developed in [75] is:

$$\frac{\partial \phi_p}{\partial t} + \nabla \cdot (\mathbf{u}\phi_p) = \sum_{q=1}^{N} \nabla \cdot (M_{p,q} \nabla \xi_q) \quad \text{in} \quad \Omega, \quad 1 \leqslant p \leqslant N, \tag{2.17}$$

$$M_{p,q} = \begin{cases} -M_0(1+\phi_p)(1+\phi_q), p \neq q \\ M_0(1+\phi_p)(1-\phi_q), p = q \end{cases},$$

$$\xi_p = \sum_{q=1}^{N} \lambda_{p,q} \left[\frac{1}{\eta^2} \left(g_1'(\phi_p) - g_2'(\phi_p + \phi_q) \right) + \nabla^2 \phi_q \right],$$

$$\lambda_{p,q} = \frac{3}{2\sqrt{2}} \sigma_{p,q} \eta, \quad g_1(\phi) = \frac{1}{4}(1-\phi^2)^2, \quad g_2(\phi) = \frac{1}{4}\phi^2(\phi+2)^2.$$

In Eq.(2.17), $M_{p,q}$ is the mobility between Phases p and q, and M_0 is a positive constant. ξ_p is the chemical potential of Phase p, and $\{\lambda_{p,q}\}_{p,q=1}^{N}$ are the mixing energy densities, depending on the pairwise interfacial tension $\sigma_{p,q}$ and on the interface thickness η. $\{\lambda_{p,q}\}_{p,q=1}^{N}$ are symmetric and have a zero diagonal. $g_1(\phi)$ and $g_2(\phi)$ are the potential functions, and $g_1'(\phi)$ and $g_2'(\phi)$ are the derivatives of $g_1(\phi)$ and $g_2(\phi)$ with respect to ϕ, respectively.

Multiplying $\frac{1}{2}\xi_p$ to Eq.(2.17) and summing over p, one obtains the free energy equation

$$\begin{aligned}\frac{1}{2}\frac{\partial \mathrm{e}_F}{\partial t}+\sum_{p,q=1}^{N}\frac{\lambda_{p,q}}{4}\nabla\cdot\left(\frac{\partial\phi_p}{\partial t}\nabla\phi_q+\frac{\partial\phi_q}{\partial t}\nabla\phi_p\right)+\mathbf{u}\cdot\frac{1}{2}\sum_{p=1}^{N}\xi_p\nabla\phi_p \\ =\frac{1}{2}\sum_{p,q=1}^{N}\nabla\cdot(\xi_p M_{p,q}\nabla\xi_q)-\frac{1}{2}\sum_{p,q=1}^{N}M_{p,q}\nabla\xi_p\cdot\nabla\xi_q, \\ \mathrm{e}_F=\sum_{p,q=1}^{N}\frac{\lambda_{p,q}}{2}\left[\frac{1}{\eta^2}(g_1(\phi_p)+g_1(\phi_q)-g_2(\phi_p+\phi_q))-\nabla\phi_p\cdot\nabla\phi_q\right],\end{aligned} \tag{2.18}$$

where e_F is the free energy density. It should be noted that the chemical potentials are the functional derivatives of the free energy with respect to the volume fraction contrasts, i.e., $\{\xi_p=\delta E_F/\delta\phi_p\}_{p=1}^N$ where $E_F(=\int_\Omega \mathrm{e}_F d\Omega)$ is the free energy.

It should be noted that $M_{p,q}$ is symmetric positive semi-definite, $\sum_{p=1}^N M_{p,q}=\sum_{q=1}^N M_{p,q}=0$ thanks to Eq.(2.2), and $M_{p,q}=0$ inside bulk-phase regions. Therefore, one can easily check that the diffusion flux in Eq.(2.17) follows the constraints in Eq.(2.9) and Eq.(2.10) for the summation of the order parameters and *consistency of reduction*, respectively. Along with the zero-flux boundary condition, Eq.(2.17) honors the mass conservation as well. More details about Eq.(2.17) should refer to [75].

The multiphase conservative Allen-Cahn equation that satisfies the *consistency of reduction* is developed:

$$\begin{aligned}\frac{\partial\phi_p}{\partial t}+\nabla\cdot(\mathbf{u}\phi_p)=M_0\lambda_0\nabla^2\phi_p-\frac{M_0\lambda_0}{\eta^2}\left(g_1'(\phi_p)-\frac{1+\phi_p}{2}L^s\right)+L_p^c \quad \text{in} \quad \Omega, \\ L^s=\sum_{q=1}^{N}g_1'(\phi_q),\quad S_p^c=\int_\Omega\frac{M_0\lambda_0}{\eta^2}\left(g_1'(\phi_p)-\frac{1+\phi_p}{2}L^s-\eta^2\nabla^2\phi_p\right)d\Omega,\quad 1\leqslant p\leqslant N.\end{aligned} \tag{2.19}$$

Here in Eq.(2.19), λ_0 is the maximum among $\lambda_{p,q}$, i.e., $\lambda_0=\max\lambda_{p,q}$, where $\lambda_{p,q}$ is the same as that in Eq.(2.17). L^s in Eq.(2.19) is the Lagrange multiplier to enforce $\sum_{p=1}^N L_p^R=0$, and $\{L_p^c\}_{p=1}^N$ are obtained from the consistent and conservative volume distribution algorithm in Section 2.2.2. Particularly, the inputs to the algorithm are $\{\phi_p\}_{p=1}^N$ and $\{S_p^c\}_{p=1}^N$. Notice that the summation of $\{S_p^c\}_{p=1}^N$ over p is zero.

One can formally proof that the proposed multiphase conservative Allen-Cahn model Eq.(2.19) satisfies the summation of the order parameters, the mass conservation, and the *consistency of reduction* simultaneously.

Theorem 2.2.2. *The multiphse conservative Allen-Cahn model Eq.(2.19) admits the summation constraint for the order parameters Eq.(2.2), i.e.,*

$$\sum_{p=1}^{N}\phi_p = (2-N) \quad \text{or} \quad \sum_{p=1}^{N} C_p = \sum_{p=1}^{N}\frac{1+\phi_p}{2} = 1.$$

Proof. Summing Eq.(2.19) over p, both sides of the summed equation are zero, given $\sum_{p=1}^{N}\phi_p = (2-N)$, and Eq.(2.5), and Eq.(2.11) are used. □

Theorem 2.2.3. *The multiphse conservative Allen-Cahn model Eq.(2.19) satisfies the conservation constraint for the order parameters Eq.(2.8), i.e.,*

$$\frac{d}{dt}\int_{\Omega}\phi_p d\Omega = 0, \quad 1 \leqslant p \leqslant N,$$

with $\mathbf{n}\cdot\mathbf{u} = 0$ *at the domain boundary or in a periodic domain.*

Proof. Integrating Eq.(2.19) over domain Ω and applying the divergence theorem, the boundary integrals vanish due to the boundary condition, and $\frac{d}{dt}\int_{\Omega}\phi_p d\Omega = 0$ $(1 \leqslant p \leqslant N)$ is obtained with the help of Eq.(2.11). □

Theorem 2.2.4. *The multiphse conservative Allen-Cahn model Eq.(2.19) satisfies the consistency of reduction.*

Proof. Without loss of generality and for a clear presentation, the last phase of a N-phase $(N \geqslant 2)$ system is absent at the location where $\phi_N = -1$ and $|\nabla\phi_N| = |\nabla^2\phi_N| = 0$. From Eq.(2.19), one has

$$\frac{\partial\phi_N}{\partial t} = 0$$

$$\frac{\partial\phi_p}{\partial t} + \nabla\cdot(\mathbf{u}\phi_p) = M_0\lambda_0\nabla^2\phi_p - \frac{M_0\lambda_0}{\eta^2}\left(g_1'(\phi_p) - \frac{1+\phi_p}{2}L^s\right) + L_p^c, \quad 1 \leqslant p \leqslant N-1,$$

where

$$L_p^c = \sum_{q=1}^{N-1} W_{p,q} B_q, \quad L^s = \sum_{p=1}^{N} g_1'(\phi_p) = \sum_{p=1}^{N-1} g_1'(\phi_p),$$

from Theorem 2.2.1 and due to $g_1'(\phi_N) = g_1'(-1) = 0$, respectively. Therefore, the absent phase remains absent while the governing equation for the other phases reduce to the corresponding $(N-1)$-phase one. By induction, Eq.(2.19) satisfies the *consistency of reduction*. □

The proposed consistent and conservative volume distribution algorithm in Section 2.2.2 addresses the difficulty of specifying physical $\{L_p^c\}_{p=1}^N$ in the Phase-Field equation, by noticing that the constraints for $\{L_p^c\}_{p=1}^N$ are the same kind as those in Eq.(2.11) for $\{L_p\}_{p=1}^N$. Kim and Lee [68] developed a similar conservative Allen-Cahn model for multiphase flows. The only difference from the present work is that they defined $\{L_p^c\}_{p=1}^N$ as

$$L_p^c = \frac{\sum_{q=1}^N W_q}{\sum_{q=1}^N \int_\Omega W_q d\Omega} S_p^c, \quad 1 \leqslant p \leqslant N, \tag{2.20}$$

where S_p^c is identically defined in Eq.(2.19). Recall that $W_p = W(\phi_p) = (1-\phi_p^2)$. Although $\{L_p^c\}_{p=1}^N$ defined in Eq.(2.20) satisfy Eq.(2.9) and Eq.(2.8) so that $\sum_{q=1}^N \phi_q = (2-N)$ and $\frac{d}{dt}\int_\Omega \phi_p d\Omega = 0$ $(1 \leqslant p \leqslant N)$, they are not reduction consistent due to violating Eq.(2.10). As a result, fictitious phases can be generated by their model. Consider a three-phase example at the location where Phases 1 and 2 form an interfacial region, i.e., $-1 < \phi_1, \phi_2 < 1$, and Phase 3 is absent around this region, i.e., $\phi_3 = -1$ and $|\nabla\phi_3| = \nabla^2\phi_3 = 0$. In Eq.(2.20), $\sum_{m=1}^3 W_m$ is positive and non-zero, and S_3^c is not necessarily to be zero because (i) Phase 3 can appear somewhere away from the considered interfacial region and (ii) S_3^c defined in Eq.(2.19) is an integral over the entire domain. As a result, around the considered interfacial region, one has $\frac{\partial\phi_3}{\partial t} = L_3^c$ with L_3^c defined in Eq.(2.20) from [68]. If S_3^c is again positive, then from Eq.(2.20), L_3^c is positive, which means Phase 3 is being generated around the interfacial region of Phases 1 and 2. On the other hand, ϕ_3 will be less than -1 if S_3^c is negative. Neither of the results is physical. One can only expect S_3^c to be zero if either $\phi_3 \equiv 1$ or $\phi_3 \equiv -1$ in the entire domain. However, these two cases are meaningless in practice since they restrict the problem to be single- or two-phase. The effect of producing fictitious phases

from the multiphase conservative Allen-Cahn model in [68] is demonstrated in Section 4.2 and the results are shown in Fig.4.12. On the other hand, no fictitious phase is produced by Eq.(2.19), thanks to satisfying the *consistency of reduction*, i.e., Theorem 2.2.4, and see also Section 4.2 and Fig.4.12.

The contact angle boundary condition for multiphase problems developed in [74] is considered at the wall boundary:

$$\mathbf{n}\cdot\nabla\phi_p = \sum_{q=1}^{N}\zeta_{p,q}\frac{1+\phi_p}{2}\frac{1+\phi_q}{2} \quad \text{at} \quad \partial\Omega, \quad 1\leqslant p\leqslant N, \tag{2.21}$$

$$\zeta_{p,q} = \frac{2\sqrt{2}}{\eta}\cos(\theta^W_{p,q}).$$

It is obvious that Eq.(2.21) follows the constraints in Eq.(2.9) and Eq.(2.10). Therefore, the contact angle boundary condition Eq.(2.21) satisfies the summation of the order parameters and *consistency of reduction*. More details about Eq.(2.21) should refer to [74].

When there are only two phases, $\phi = \phi_1$, $\sigma = \sigma_{1,2}$, and $\theta^W = \theta^W_{1,2}$, etc. are used. The two-phase Cahn-Hilliard Phase-Field equation [91] is recovered from the multiphase one Eq.(2.17):

$$\frac{\partial\phi}{\partial t} + \nabla\cdot(\mathbf{u}\phi) = \nabla\cdot(M\nabla\xi) \quad \text{in} \quad \Omega, \quad \xi = \lambda\left(\frac{1}{\eta^2}g_1'(\phi) - \nabla^2\phi\right). \tag{2.22}$$

This Phase-Field equation is the same as the one proposed by Cahn and Hilliard [91], using the H^{-1} gradient flow of the Ginzburg-Landau free energy functional, see also the derivation, e.g., in [55], [59], [192]. It has been widely used in modeling two-phase incompressible flows, e.g., in [54]–[56], [59], [77], [79], [112], [118], [119]. Notice that the mobility in Eq.(2.22) is allowed to be a constant, e.g., $M = M_0$, and this is the case considered in two-phase problems in the present study.

Similarly, the two-phase conservative Allen-Cahn Phase-Field equation recovered from the multiphase one Eq.(2.19) is:

$$\frac{\partial \phi}{\partial t} + \nabla \cdot (\mathbf{u}\phi) = M_0\lambda_0\nabla^2\phi - \frac{M_0\lambda_0}{\eta^2}g_1'(\phi) + L^c \quad \text{in} \quad \Omega, \tag{2.23}$$
$$L^c = \frac{W}{\int_\Omega W d\Omega}S^c, \quad S^c = \int_\Omega \frac{M_0\lambda_0}{\eta^2}\left(g_1'(\phi) - \eta^2\nabla^2\phi\right)d\Omega, \quad W = 1-\phi^2.$$

Eq.(2.23) is exactly the one proposed by Brassel and Bretin [96], further studied in [98], [99], and later on applied to two-phase flows [57], [102], [103]. It should be noted that another two-phase conservative Allen-Cahn equation [97], [193] using $W \equiv 1$ is not reduction consistent, although it has been applied to model two-phase flows [55], [194]. It is obvious that $L^c|_{\phi=\pm1}$ is not zero with $W \equiv 1$, and therefore the discussions below Eq.(2.20) are applied. As shown in [96], the benefit of using $W = 1-\phi^2$ is that not only the conservation constraint, i.e., $\frac{d}{dt}\int_\Omega \phi d\Omega = 0$ is satisfied exactly, but also the conservation of $\frac{d}{dt}\int_{\phi>0}\phi d\Omega$ is of the order of $O(\eta^2)$, better than $O(\eta)$ with $W \equiv 1$. The comparison between the two choices of W can be found in [96], [98], and the comparison among different conservative Allen-Cahn and Cahn-Hilliard equations is available in [99]. It should be noted that the analyses and comparisons in [96], [98], [99] don't include hydrodynamics.

The corresponding two-phase contact angle boundary condition recovered from Eq.(2.21) is:

$$\mathbf{n}\cdot\nabla\phi = \frac{\sqrt{2}}{3\eta}\cos(\theta^W)g_w'(\phi) \quad \text{at} \quad \partial\Omega, \tag{2.24}$$

where $g_w(\phi)$ is the Hermite polynomial, i.e., $g_w(\phi) = \frac{1}{2}\phi(3-\phi^2)$, used, e.g., in [77], [79], [83], [86]. However, for two-phase problems, an alternative $g_w(\phi) = \sin\left(\frac{\pi}{2}\phi\right)$, like [80], [81], [85], is considered. Numerical tests have been performed and do not find distinguishable difference of the two choices of $g_w(\phi)$.

2.3 Consistency of mass conservation

In this section, one only needs to consider the the Phase-Field equation written in a conservative form:

$$\frac{\partial \phi_p}{\partial t} + \nabla\cdot(\mathbf{u}\phi_p) = \nabla\cdot\mathbf{J}_p, \quad 1 \leqslant p \leqslant N. \tag{2.25}$$

The reaction term, Lagrange multiplier, and effect of the contact angle boundary condition can be all included into the "diffusion" term (right-hand side of Eq.(2.1)), after implementing the "consistent formulation" in Section 2.3.1. Therefore, at the moment, the explicit definition of $\{\mathbf{J}_p\}_{p=1}^N$ is not important, but the summation of the order parameters, i.e., Eq.(2.2), and the *consistency of reduction* require $\{\mathbf{J}_p\}_{p=1}^N$ follow the constraints in Eq.(2.9) and Eq.(2.10), respectively.

The *consistency of mass conservation* is proposed to connect the Phase-Field equation to the mass conservation equation, and its definition is:

Consistency of mass conservation*: The mass conservation equation should be consistent with the Phase-Field equation and the density of the fluid mixture. The mass flux in the mass conservation equation should lead to a zero mass source.*

As the density of the fluid mixture is computed from Eq.(2.3), along with the Phase-Field equation Eq.(2.25) and the divergence-free velocity Eq.(2.5), one can, in general, reach the following transport equation for the density of the fluid mixture

$$\frac{\partial \rho}{\partial t} + \nabla \cdot \mathbf{m}^* = S_m^*, \tag{2.26}$$

where $\mathbf{m}^*$ is the mass flux and S_m^* is the mass source. Depending on how the mass flux is defined, the mass source is determined correspondingly. For example, if the mass flux is defined as $\mathbf{m}^* = \rho\mathbf{u}$, then the corresponding mass source is $S_m^* = \sum_{p=1}^N \frac{\rho_p}{2} \nabla \cdot \mathbf{J}_p$. Therefore, the mixture density is not governed by the sharp-interface mass conservation equation Eq.(1.1). Instead, Eq.(2.26) is the "actual" mass conservation equation of the multiphase model, which is derived from Eq.(2.3), Eq.(2.5), and Eq.(2.25).

As the actual mass conservation equation Eq.(2.26) is obtained, the next step is to specify the consistent mass flux $\mathbf{m}$ among various choices of defining the mass flux. The *consistency of mass conservation* is applied, which states that the corresponding mass source of the consistent mass flux is zero. As a result, Eq.(2.26) becomes

$$\frac{\partial \rho}{\partial t} + \nabla \cdot \mathbf{m} = 0, \tag{2.27}$$

after plugging in the consistent mass flux $\mathbf{m}$. The same equation can be obtained using the control volume analysis, see Section 2.5. Applying Eq.(2.27), Eq.(2.3), and Eq.(2.25), the divergence of the consistent mass flux is

$$\nabla \cdot \mathbf{m} = -\frac{\partial \rho}{\partial t} = -\frac{\partial}{\partial t} \sum_{p=1}^{N} \rho_p \frac{1+\phi_p}{2} = -\sum_{p=1}^{N} \frac{\rho_p}{2} \frac{\partial \phi_p}{\partial t} = \nabla \cdot \sum_{p=1}^{N} \frac{\rho_p}{2} (\mathbf{u}\phi_p - \mathbf{J}_p), \tag{2.28}$$

and therefore the consistent mass flux is

$$\mathbf{m} = \sum_{p=1}^{N} \frac{\rho_p}{2} (\mathbf{u} + \mathbf{u}\phi_p - \mathbf{J}_p). \tag{2.29}$$

It should be noted that one more $\mathbf{u}$ is added inside the parentheses of Eq.(2.29), due to the *consistency of reduction* which requires that the N-phase model should recover the corresponding single-phase model if all the phases except, e.g., Phase p, are absent. As a result, the consistent mass flux $\mathbf{m}$ should become $\rho_p \mathbf{u}$ if only Phase p appears, which is true from Eq.(2.29). On the other hand, if the consistent mass flux is defined as $\sum_{p=1}^{N} \frac{\rho_p}{2} (\mathbf{u}\phi_p - \mathbf{J}_p)$, directly from Eq.(2.28), it becomes $\frac{\rho_p}{2}\mathbf{u}$ when only Phase p is present, and violates the *consistency of reduction*. It should also be noted that the definition of the consistent mass flux in Eq.(2.29) is also consistent with the given example of Eq.(2.26) where $\mathbf{m}^* = \rho \mathbf{u}$ and $S_m^* = \sum_{p=1}^{N} \frac{\rho_p}{2} \nabla \cdot \mathbf{J}_p$. Since the velocity is divergence-free, the divergence of the consistent mass flux defined in Eq.(2.29) is still Eq.(2.28), and therefore the *consistency of mass conservation* is held.

To further simplify the formulations, the Phase-Field fluxes $\{\mathbf{m}_{\phi_p}\}_{p=1}^{N}$ that include both the convection and diffusion fluxes of the order parameters are introduced, and one has the following theorem:

Theorem 2.3.1. *Given the Phase-Field fluxes* $\{\mathbf{m}_{\phi_p}\}_{p=1}^{N}$ *that satisfy the Phase-Field equation, i.e.,*

$$\frac{\partial \phi_p}{\partial t} + \nabla \cdot \mathbf{m}_{\phi_p} = 0, \quad 1 \leqslant p \leqslant N, \tag{2.30}$$

the corresponding consistent mass flux that satisfies the ***consistency of mass conservation*** *is*

$$\mathbf{m} = \sum_{p=1}^{N} \frac{\rho_p}{2}(\mathbf{u} + \mathbf{m}_{\phi_p}). \tag{2.31}$$

Applying the formulations in Theorem 2.3.1 is easier to preserve the consistency conditions after discretization, which will be seen in Chapter 3. Hereafter, the (actual) mass conservation equation is referred to Eq.(2.27) and the consistent mass flux is referred to Eq.(2.31). It is worth mentioning that the derivation in the present section doesn't rely on the explicit form of the diffusion fluxes $\{\mathbf{J}_p\}_{p=1}^N$, or the Phase-Field fluxes $\{\mathbf{m}_{\phi_p}\}_{p=1}^N$, in the Phase-Field equation. Therefore, the consistent mass flux defined in Eq.(2.29) or Eq.(2.31) is generally applicable and the *consistency of mass conservation* is always satisfied, as stated in Theorem 2.3.1. The consistent mass flux derived in the present section can be physically interpreted using the mixture theory, see Section 2.5. The significance of the consistent mass flux as well as the *consistency of mass conservation* will be shown in the next section when it is applied to the momentum equation following the *consistency of mass and momentum transport*.

Remark*: Here, the derivation is based on the volume-averaged velocity whose divergence is zero. This property will be further justified in Section 2.5. Some two-phase models, e.g., [81], [127], [128], [130], consider the mass-averaged velocity which is not divergence-free. The consistency of mass conservation is also valid in that situation and this will also be discussed in Section 2.5. The present study except the discussions in Section 2.5 uses the volume-averaged (divergence-free) velocity.*

Although the *consistency of reduction* has been considered when deriving the consistent mass flux in Eq.(2.29), this property of the consistent mass flux is shown in a more formal way, like those in Section 2.2.

Theorem 2.3.2. *If the Phase-Field equation satisfies the* ***consistency of reduction****, then the consistent mass flux in Theorem 2.3.1 is also reduction consistent.*

Proof. Since the Phase-Field equation is reduction consistent, the absent Phase N remains absent, i.e., $\phi_N \equiv -1$, its diffusion flux $\mathbf{J}_N$ is zero, and the other diffusion fluxes reduce to

their $(N-1)$-phase formulation. Then from Theorem 2.3.1, it is obvious that the contribution of Phase N to the consistent mass flux vanishes, i.e.,

$$\mathbf{m} = \sum_{p=1}^{N} \frac{\rho_p}{2}(\mathbf{u} + \mathbf{m}_{\phi_p}) = \sum_{p=1}^{N} \frac{\rho_p}{2}(\mathbf{u} + \mathbf{u}\phi_p - \mathbf{J}_p) = \sum_{p=1}^{N-1} \frac{\rho_p}{2}(\mathbf{u} + \mathbf{m}_{\phi_p}).$$

As a result, the consistent mass flux in Theorem 2.3.1 recovers its $(N-1)$-phase formulation, and it is reduction consistent. □

Therefore, the *consistency of reduction* of the consistent mass flux only depends on whether the same is true for the Phase-Field equation. Since this is the case for Eq.(2.17) and Eq.(2.19), their resulting consistent mass fluxes are reduction consistent.

2.3.1 Consistent formulation

Here, the proposed consistent formulation is introduced, which turns any physically admissible Phase-Field equation, i.e., Eq.(2.6) with the properties in Eq.(2.8), Eq.(2.9), and Eq.(2.10), into a local conservative law. This is critical for the success of implementing the *consistency of mass conservation*. Otherwise, there is always a non-zero mass source, no matter how the terms are arranged, due to the presence of $\{L_p^R\}_{p=1}^N$ and $\{L_p^c\}_{p=1}^N$. As a result, the *consistency of mass conservation* is unable to be satisfied.

To address this issue, the consistent formulation introduces a set of auxiliary variables $\{Q_p\}_{p=1}^N$ whose governing equations are

$$\begin{aligned} \nabla \cdot (W_Q(\phi_p)\nabla Q_p) = L_p^Q \quad \text{in} \quad \Omega, \quad \mathbf{n} \cdot \nabla Q_p = 0 \quad \text{at} \quad \partial\Omega, \\ W_Q(\phi_p) = 1 - \phi_p^2, \quad \int_\Omega L_p^Q d\Omega = 0, \quad 1 \leqslant p \leqslant N. \end{aligned} \tag{2.32}$$

Here, $\{L_p^Q\}_{p=1}^N$ in general can include all the terms on the right-hand side of the Phase-Field equation Eq.(2.6):

$$L_p^Q = \nabla \cdot \mathbf{J}_p + L_p^R + L_p^c. \tag{2.33}$$

From the requirement of mass conservation, integrating of L_p^Q $(1 \leqslant p \leqslant N)$ over the domain is zero, see Eq.(2.8). Therefore, the consistent formulation Eq.(2.32) is eligible and solvable,

along with the homogeneous Neumann (or periodic) boundary condition for Q. If the zero-flux boundary condition is assigned to the diffusion flux $\mathbf{J}$, like the conservative Allen-Cahn equation Eq.(2.19) with 90^0 contact angles and the Cahn-Hilliard equation Eq.(2.17), L^Q can only include the reaction term L^R and the Lagrange multiplier L^c. Choices of $W_Q(\phi)$ in Eq.(2.32) are multiple but the present one is chosen from considering the *consistency of reduction*. Such a choice guarantees $W_Q(\phi_p)\nabla Q_p = \mathbf{0}$ inside bulk phase regions, i.e., $\phi_p = \pm 1$, $(1 \leqslant p \leqslant N)$. As a result, any physically admissible Phase-Field equation, including the reaction term and Lagrange multiplier, and accompanied with the contact angle boundary condition, can be reformulated into a conservative form, thanks to the consistent formulation. Then, one can proceed to implement the *consistency of mass conservation*.

2.4 Consistency of mass and momentum transport

As already indicated in the previous section, i.e., Section 2.3, accompanied with a divergence-free flow velocity, the "actual" mass conservation equation in a Phase-Field model is not in a form like the sharp-interface one, i.e., Eq.(1.1). As a result, the Navier-Stokes equation Eq.(1.2) is incompatible with the "actual" mass conservation equation Eq.(2.27), and can produce unphysical results when using it to govern the motion of the fluid mixture. This will be discussed at the end of this section. To address this issue, the *consistency of mass and momentum transport* is proposed to connect the mass conservation equation and the momentum equation, and its definition is:

***Consistency of mass and momentum transport**: The momentum flux in the momentum equation should be computed as a tensor product between the mass flux and the flow velocity, where the mass flux should be identical to the one in the mass conservation equation.*

Following this consistency condition, the momentum equation governing the motion of the N-phase fluid mixture becomes

$$\frac{\partial(\rho\mathbf{u})}{\partial t} + \nabla\cdot(\mathbf{m}\otimes\mathbf{u}) = -\nabla P + \nabla\cdot\left[\mu(\nabla\mathbf{u} + \nabla\mathbf{u}^T)\right] + \rho\mathbf{g} + \mathbf{f}_s, \tag{2.34}$$

where $\otimes$ denotes the tensor product, $\mathbf{g}$ is the gravity, and $\mathbf{f}_s$ is the surface force modeling the interfacial tensions. It should be noted that the inertia term in Eq.(2.34) is written in its conservative form, which is essential to achieve momentum conservation on the discrete level, and the consistent mass flux $\mathbf{m}$ obtained in Section 2.3 is applied. The *consistency of mass and momentum transport*, as well as Eq.(2.34), will be justified in Section 2.5 using the control volume analysis. The surface force $\mathbf{f}_s$ will be derived from the energy law in Section 2.4.3. As shown in Section 2.4.3, the surface force is equivalent to a conservative form. Therefore, without considering the gravity, the momentum of the multiphase flow is conserved by Eq.(2.34) even including the effect of interfacial tensions. Eq.(2.34) is equivalent to the one in [56], [75], as well as in [191] from GENERIC theory [195].

Like the analyses and discussions in Section 2.2 of the Phase-Field equation, the *consistency of reduction* should also be satisfied by the proposed momentum equation Eq.(2.34) so that correct dynamics including fewer phases is locally reproduced. Since only the density and viscosity of the fluid mixture, the consistent mass flux, and the surface force are related to the number of phases in the momentum equation Eq.(2.34), one has the following theorem:

Theorem 2.4.1. *If the density and viscosity of the fluid mixture, the consistent mass flux, and the surface force are reduction consistent, then the proposed momentum equation Eq.(2.34) is also reduction consistent.*

It is obvious that the density and viscosity of the fluid mixture are reduction consistent since the contributions of the absent phases to them disappear from Eq.(2.3) and Eq.(2.4). The consistent mass flux is reduction consistent as long as the same is true for the Phase-Field equation, as stated in Theorem 2.3.2. One will see in Section 2.4.3 that the surface force Eq.(2.35) used in the present study is also reduction consistent, see Theorem 2.4.5 and Corollary 2.4.5.1. Therefore, the following corollaries for the momentum equation are true in the present study:

Corollary 2.4.1.1. *The momentum equation in the present study, i.e., Eq.(2.34) with the density in Eq.(2.3), the viscosity in Eq.(2.4), the consistent mass flux in Eq.(2.31), the*

Phase-Field fluxes from Eq.(2.17) or Eq.(2.19), and the surface force in Eq.(2.35), satisfies the consistency of reduction.

Corollary 2.4.1.2. *The momentum equation in the present study, i.e., Eq.(2.34) with the density in Eq.(2.3), the viscosity in Eq.(2.4), the consistent mass flux in Eq.(2.31), the Phase-Field fluxes from Eq.(2.17) or Eq.(2.19), and the surface force in Eq.(2.35), recovers inside each bulk-phase region the single-phase Navier-Stokes equation with the corresponding density and viscosity of that phase.*

Although the Navier-Stokes equation Eq.(1.2) is not valid to describe the motion of the fluid mixture in the entire domain, which will be discussed in Sections 2.4.1, 2.4.2, and 2.4.3, it still governs the motion of the single-phase fluids inside individual bulk-phase regions. Thanks to Corollary 2.4.1.2, the single-phase dynamics is correctly reproduced by the present model inside the bulk-phase regions.

***Remark**:*

- *From Theorem 2.3.2, Theorem 2.4.1, and Theorem 2.4.5, the consistency of reduction of the proposed momentum equation Eq.(2.34) majorly relies on the Phase-Field equation. Implementing the consistency of mass conservation and the consistency of mass and momentum transport produces a stronger reliance than using the Navier-Stokes equation Eq.(1.2) in the sense that the consistent mass flux includes the diffusion flux of the Phase-Field equation.*

- *It should be noted that a part of the viscous force, i.e., $\nabla \cdot (\mu \nabla \mathbf{u}^T)$, becomes zero inside the bulk-phase regions because the viscosity is a constant there and $\nabla \cdot (\nabla \mathbf{u}^T)$ is equal to $\nabla(\nabla \cdot \mathbf{u})$, which is zero due to the divergence-free velocity. This relates to the reduction of the momentum equation from two phases to a single phase. Although it is automatically satisfied on the continuous level, this will become an issue after discretization. More details about addressing this issue on the discrete level are given in Theorem 3.5.5 and Theorem 3.5.6, as well as the discussions below them.*

Thanks to satisfying the *consistency of mass conservation* and the *consistency of mass and momentum transport*, the proposed momentum equation Eq.(2.34) additionally has the following properties.

2.4.1 Galilean invariance

The proposed momentum equation Eq.(2.34) derived from the consistency conditions is Galilean invariant.

Theorem 2.4.2. *If both the* ***consistency of mass conservation*** *and the* ***consistency of mass and momentum transport*** *are satisfied, then the proposed momentum equation Eq.(2.34) is Galilean invariant.*

Proof. The Galilean transformation is

$$\mathbf{x}' = \mathbf{x} - \mathbf{u}_0 t, \quad t' = t, \quad \mathbf{u}' = \mathbf{u} - \mathbf{u}_0, \quad f' = f, \quad \nabla' f' = \nabla f, \quad \frac{\partial f'}{\partial t'} = \frac{\partial f}{\partial t} + \mathbf{u}_0 \cdot \nabla f,$$

where $(\mathbf{x}, t)$ is the fixed frame and $(\mathbf{x}', t')$ is the moving frame with respect to the fixed frame with a constant velocity $\mathbf{u}_0$, f is a scalar variable measured in the fixed frame, while f' is the same variable measured in the moving frame. Applying the Galilean transformation, the momentum equation in the moving frame has the same form as the one in the fixed frame:

$$\begin{aligned} &\frac{\partial(\rho'\mathbf{u}')}{\partial t'} + \nabla' \cdot (\mathbf{m}' \otimes \mathbf{u}') + \nabla' P' - \nabla' \cdot \left[\mu'(\nabla'\mathbf{u}' + \nabla'\mathbf{u}'^T)\right] - \rho'\mathbf{g}' - \mathbf{f}_s' \\ &= \underbrace{\frac{\partial(\rho\mathbf{u})}{\partial t} + \nabla \cdot (\mathbf{m} \otimes \mathbf{u}) + \nabla P - \nabla \cdot \left[\mu(\nabla\mathbf{u} + \nabla\mathbf{u}^T)\right] - \rho\mathbf{g} - \mathbf{f}_s}_{\mathbf{0}} - \mathbf{u}_0 \underbrace{\left(\frac{\partial \rho}{\partial t} + \nabla \cdot \mathbf{m}\right)}_{0} = \mathbf{0}. \end{aligned}$$

The underbracket groups the momentum equation Eq.(2.34) and the underbrace groups the mass conservation equation Eq.(2.27) in the fixed frame, both of which are zero. Therefore, the proposed momentum equation Eq.(2.34) is Galilean invariance. □

Corollary 2.4.2.1. *If the mechanical equilibrium in the hydrostatic state is reached, i.e.,*

$$-\nabla P + \rho\mathbf{g} + \mathbf{f}_s = \mathbf{0},$$

then any homogeneous velocity is an admissible solution of the proposed momentum equation Eq.(2.34).

Proof. Suppose the flow velocity in the moving frame, i.e., $\mathbf{u}$, is zero, then the mechanical equilibrium is true in the moving frame. From the Galilean transformation, the flow velocity in the fixed frame becomes $\mathbf{u} = \mathbf{u}_0$, and the mechanical equilibrium is still valid. As a result, the left-hand side of the momentum equation Eq.(2.34) becomes $\mathbf{u}_0$ times the mass conservation equation Eq.(2.27) and is zero. The right-hand side remains the viscous force which is again zero since there is no velocity gradient. Therefore, any homogeneous velocity $\mathbf{u}_0$ is the solution of the proposed momentum equation Eq.(2.34) if the mechanical equilibrium is reached. □

2.4.2 Kinetic energy conservation

The proposed momentum equation Eq.(2.34) derived from the consistency conditions is compatible with the kinetic energy conservation.

Theorem 2.4.3. *If both the* ***consistency of mass conservation*** *and the* ***consistency of mass and momentum transport*** *are satisfied, then the proposed momentum equation Eq.(2.34) implies the following kinetic energy equation:*

$$\frac{\partial \mathrm{e}_K}{\partial t}+\nabla\cdot\left(\mathbf{m}\frac{\mathbf{u}\cdot\mathbf{u}}{2}\right) = -\nabla\cdot(\mathbf{u}P)+\nabla\cdot[\mu(\nabla\mathbf{u}+\nabla\mathbf{u}^T)\cdot\mathbf{u}]-\frac{1}{2}\mu(\nabla\mathbf{u}+\nabla\mathbf{u}^T):(\nabla\mathbf{u}+\nabla\mathbf{u}^T)+\rho\mathbf{u}\cdot\mathbf{g}+\mathbf{u}\cdot\mathbf{f}_s,$$

where

$$\mathrm{e}_K = \frac{1}{2}\rho\mathbf{u}\cdot\mathbf{u},$$

is the kinetic energy density.

Proof. Performing the dot product between $\mathbf{u}$ and Eq.(2.34), and applying the integration by part, the right-hand side (RHS) of the kinetic energy equation is obtained. The left-hand side (LHS) of the kinetic energy equation is obtained from

$$\mathbf{u}\cdot\left(\frac{\partial(\rho\mathbf{u})}{\partial t}+\nabla\cdot(\mathbf{m}\otimes\mathbf{u})\right) = \frac{\partial \mathrm{e}_K}{\partial t}+\nabla\cdot\left(\mathbf{m}\frac{1}{2}\mathbf{u}\cdot\mathbf{u}\right)+\frac{1}{2}\mathbf{u}\cdot\mathbf{u}\underbrace{\left(\frac{\partial\rho}{\partial t}+\nabla\cdot\mathbf{m}\right)}_{0}.$$

The underbraced term is zero because of the mass conservation equation Eq.(2.27). □

Corollary 2.4.3.1. *If all the forces except the pressure gradient are neglected, then the proposed momentum equation Eq.(2.34) implies the kinetic energy conservation, i.e.,*

$$\frac{dE_K}{dt} = \frac{d}{dt}\int_\Omega \mathrm{e}_K d\Omega = 0,$$

with a proper boundary condition.

Proof. Integrating the kinetic energy equation in Theorem 2.4.3 over domain Ω, keeping only the first term on RHS, applying the Divergence theorem, and assuming that all the boundary integrals vanish due to the boundary condition, then the kinetic energy conservation is obtained. □

The significance of satisfying the *consistency of mass conservation* and the *consistency of mass and momentum transport* is illustrated in Theorem 2.4.2, Theorem 2.4.3, and their corollaries. In those proofs, the underbraced terms are zeros because the consistent mass flux that satisfies the *consistency of mass conservation* is applied in the inertia term of the momentum equation, following the *consistency of mass and momentum transport*. Violating either of the consistency conditions results in the failure of proving Theorem 2.4.2, Theorem 2.4.3, or their corollaries, and the resulting momentum equation will not only produce a problematic kinetic energy equation but also be Galilean variant. An informative example will be considering the usage of the Navier-Stokes equation Eq.(1.2) to govern the motion of the fluid mixture, which is equivalent to replacing the consistent mass flux $\mathbf{m}$ in Eq.(2.34) with $\mathbf{m}^* = \rho\mathbf{u}$, and the same in the proofs of Theorem 2.4.2 and Theorem 2.4.3. As a result, the underbraced terms in those proofs become $\frac{\partial \rho}{\partial t} + \nabla \cdot \mathbf{m}^*$, which is $S_m^* = \sum_{p=1}^{N} \frac{\rho_p}{2} \nabla \cdot \mathbf{J}_p$ from Eq.(2.26) and not zero any more. Therefore, Theorem 2.4.2, Theorem 2.4.3 or their corollaries fails. Due to the failure of Corollary 2.4.2.1, circular interfaces will be deformed even in a translation problem. Due to the failure of Corollary 2.4.3.1, the kinetic energy is not conserved in a periodic domain even though all the forces except the pressure gradient are absent. These are some unphysical phenomena that probably appear when the Navier-Stokes equation Eq.(1.2) is applied to describe the motion of the fluid mixture. It is

worth mentioning that proving Theorem 2.4.2, Theorem 2.4.3, and their corollaries only uses the *consistency of mass conservation* and the *consistency of mass and momentum transport*, while does not need to know how the Phase-Field equation (or the diffusion flux) is explicitly defined. Consequently, these consistency conditions, theorems and corollaries are generally valid, regardless of the details of the Phase-Field equation.

***Remark**: One can achieve the consistency of mass and momentum transport without performing the consistent formulation in Section 2.3.1. Given* $\mathbf{m}^*$ *and* S_m^* *that satisfy Eq.(2.26), the consistency of mass and momentum transport is achieved by applying* $\mathbf{m}^*$ *in the inertia term and adding a momentum source* $\mathbf{u}S_m^*$ *on the right-hand side of the momentum equation. One can again show that such a momentum equation is Galilean invariant. However, the momentum conservation is unfortunately destroyed and, as a result, the momentum equation is inconsistent with the kinetic energy conservation. Therefore, it is critical to apply the consistent formulation so that both the consistency of mass conservation and the consistency of mass and momentum transport are satisfied simultaneously.*

2.4.3 Second law of thermodynamics

From the 2nd law of thermodynamics, the total energy of an isothermal multiphase system, including the free energy and kinetic energy, is not increasing, without considering any external energy input. If the diffusion flux of the Phase-Field equation, i.e., $\mathbf{J}_p$ in Eq.(2.25), is appropriately designed, this physical property will be achieved after implementing the proposed momentum equation Eq.(2.34).

Theorem 2.4.4. *Provided the diffusion flux in Eq.(2.25) to be*

$$\mathbf{J}_p = M_p \nabla \xi_p \quad \text{or} \quad \mathbf{J}_p = \sum_{q=1}^{N} M_{p,q} \nabla \xi_q, \quad 1 \leqslant p \leqslant N,$$

where M_p *is non-negative and* $M_{p,q}$ *is symmetric positive semi-definite, and the surface force in Eq,(2.34) to be*

$$\mathbf{f}_s = \sum_{p=1}^{N} \beta \xi_p \nabla \phi_p,$$

where $\beta(>0)$ is to match the two-phase formulation, e.g., in [55], [112], required by the consistency of reduction, the entire multiphase model, including the Phase-Field equation Eq.(2.25) and the proposed momentum equation Eq.(2.34), has the following energy law:

$$\frac{d}{dt}\int_\Omega (\mathrm{e}_K + \beta \mathrm{e}_F) d\Omega = -\frac{1}{2}\int_\Omega \mu(\nabla \mathbf{u} + \nabla \mathbf{u}^T) : (\nabla \mathbf{u} + \nabla \mathbf{u}^T) d\Omega - \mathcal{D}_F,$$

with a proper boundary condition. Here

$$\mathcal{D}_F = \beta \int_\Omega \sum_{p=1}^N M_p \nabla \xi_p \cdot \nabla \xi_p d\Omega \quad \text{or} \quad \mathcal{D}_F = \beta \int_\Omega \sum_{p,q=1}^N M_{p,q} \nabla \xi_p \cdot \nabla \xi_q d\Omega,$$

is the dissipation from the Phase-Field equation and it is non-negative. Recall that ξ_p is the chemical potential of Phase p, i.e., the functional derivative of the free energy with respect to ϕ_p ($\xi_p = \delta E_F / \delta \phi_p$).

Proof. $\mathbf{J}_p = \sum_{q=1}^N M_{p,q} \nabla \xi_q$ is considered. Multiplying $\beta \xi_p$ to Eq,(2.25), summing over p, integrating over domain Ω, performing the integration by part, one obtains

$$\frac{d}{dt}\int_\Omega \beta \mathrm{e}_F d\Omega + \int_\Omega \mathbf{u} \cdot \sum_{p=1}^N \beta \xi_p \nabla \phi_p d\Omega = -\beta \int_\Omega \sum_{p,q=1}^N M_{p,q} \nabla \xi_p \cdot \nabla \xi_q d\Omega.$$

Summing the above equation to the integrated kinetic energy equation (neglecting the gravity) in Theorem 2.4.3 over domain Ω, the energy law is obtained. It has been assumed that the boundary integrals vanish due to the boundary condition. For $\mathbf{J}_p = M_p \nabla \xi_p$, the procedure is the same. □

Remark:

- *Since the proposed momentum equation Eq.(2.34) enjoys Theorem 2.4.3 (for kinetic energy) regardless of the Phase-Field equation, the entire multiphase model satisfying the 2nd law of thermodynamics (or Theorem 2.4.4) only relies on the Phase-Field equation. In other words, as long as the Phase-Field equation (without convection) follows energy dissipation, Theorem 2.4.4 will be true. Failure of Theorem 2.4.4 is totally irrelevant to the proposed momentum equation Eq.(2.34) obtained from the consistency of mass conservation and the consistency of mass and momentum transport.*

- *The suggestions of the diffusion flux in Theorem 2.4.4 are possible options that only consider the 2nd law of thermodynamics. Other physical aspects, i.e., the summation of the order parameters and the consistency of reduction, should be fulfilled at the same time. This requires careful design of the mobility (M_p or $M_{p,q}$) as well as the free energy E_F (determining ξ_p) in Theorem 2.4.4, which is not a simple task. The present study is not attempting to propose general solutions to that question, and related discussions are referred to [60], [61], [64], [66], [71], [74], [75] and the references therein. The present section focuses on coupling any given admissible Phase-Field equation to the hydrodynamics, and on illustrating the significance of implementing the consistency conditions during the coupling.*

- *To include the effect of the contact angles, i.e., the contact angles are other than $\frac{\pi}{2}$, a wall energy functional has to be introduced. However, so far, it is still an open question whether the contact angle boundary condition Eq.(2.21) from [74] corresponds to a multiphase wall functional. But its two-phase correspondence Eq.(2.24) results from a wall energy functional, see, e.g., [77], [79].*

The physical explanation of the surface force in Theorem 2.4.4 is that the amount of work done by the surface force should compensate for the increase of the free energy due to convection [54], [60], [61], [64]. As a result, the total energy, which is the summation of the kinetic energy and the free energy, should not change because of the surface force. The first term on the right-hand side (RHS) of the energy law comes from the viscosity of the fluid mixture and the second term is introduced by the non-equilibrium thermodynamical state. It should be noted that there will be an extra term in the kinetic energy in Theorem 2.4.3 and, therefore, in the energy law in Theorem 2.4.4, if the momentum equation violates the *consistency of mass conservation* and the *consistency of mass and momentum transport*, as discussed in Section 2.4.2. In other words, the total energy of the multiphase system can be changed, even when all the fluids are inviscid and the thermodynamical equilibrium is reached, which is unphysical.

Implementing Theorem 2.4.4 to the Cahn-Hillard Phase-Field equation Eq.(2.17), the resulting multiphase system satisfies the 2nd law of thermodynamics and its total energy is dissipative:

Corollary 2.4.4.1. *The multiphase system, including the Cahn-Hilliard Phase-Field equation Eq.(2.17) and the proposed momentum equation Eq.(2.34) from the consistency conditions, has the following energy law:*

$$\frac{d}{dt}\int_\Omega (\mathrm{e}_K + \frac{1}{2}\mathrm{e}_F)d\Omega = -\frac{1}{2}\int_\Omega \mu(\nabla\mathbf{u} + \nabla\mathbf{u}^T) : (\nabla\mathbf{u} + \nabla\mathbf{u}^T)d\Omega - \frac{1}{2}\int_\Omega \sum_{p,q=1}^{N} M_{p,q}\nabla\xi_p \cdot \nabla\xi_q d\Omega,$$

with a proper boundary condition, where e_F, $M_{p,q}$, *and* ξ_p *are defined in Eq.(2.18) and Eq.(2.17).*

***Remark**: Corollary 2.4.3.1, Theorem 2.4.4, and Corollary 2.4.4.1 require proper boundary conditions (BCs), such as the periodic BC for all the variables, homogeneous Neumann BC for the order parameters, no-flux BC for the diffusion flux in the Phase-Field equation, and no-slip BC for the velocity.*

Correspondingly, the surface force from the Cahn-Hilliard Phase-Field equation Eq.(2.17) is

$$\mathbf{f}_s = \frac{1}{2}\sum_{p=1}^{N}\xi_p\nabla\phi_p, \tag{2.35}$$

where ξ_p is defined in Eq.(2.17).

Then, the *consistency of reduction* of the surface force in Theorem 2.4.4, as well as in Eq.(2.35) from Eq.(2.17), is considered.

Theorem 2.4.5. *The surface force in Theorem 2.4.4 satisfies the consistency of reduction if* ξ_p $(1 \leqslant p \leqslant N,\ p \neq q)$ *recovers the corresponding* $(N-1)$*-phase formulation when Phase* q *is absent.*

Proof. When Phase N is absent, the surface force in Theorem 2.4.4 becomes

$$\mathbf{f}_s = \sum_{p=1}^{N}\beta\xi_p\nabla\phi_p = \sum_{p=1}^{N-1}\beta\xi_p\nabla\phi_p,$$

due to $\nabla\phi_N = \mathbf{0}$. Since ξ_p, $1 \leqslant p \leqslant (N-1)$, recovers the corresponding $(N-1)$-phase formulation, $\mathbf{f}_s$ is reduction consistent. □

It should be noted that it is not necessary to specify the values of the chemical potentials of the absent phases in order to achieve the *consistency of reduction* of the surface force, as stated in Theorem 2.4.5. Again, one has to carefully design the free energy, which leads to the chemical potentials following the requirement in Theorem 2.4.5. However, this is outside the scope of the present study, as pointed out in ***Remark*** below Theorem 2.4.4. With the chemical potentials defined in Eq.(2.17) in Section 2.2.1, the surface force used in the present study, i.e., Eq.(2.35), has the following corollary:

Corollary 2.4.5.1. *The surface force in Eq.(2.35) with the chemical potentials in Eq.(2.17) is reduction consistent.*

Proof. The chemical potentials in Eq.(2.17) becomes

$$\xi_p = \sum_{q=1}^{N} \lambda_{p,q} \left[\frac{1}{\eta^2} \left(g_1(\phi_p) - g_2(\phi_p + \phi_q) \right) + \nabla^2 \phi_q \right] = \sum_{q=1}^{N-1} \lambda_{p,q} \left[\frac{1}{\eta^2} \left(g_1(\phi_p) - g_2(\phi_p + \phi_q) \right) + \nabla^2 \phi_q \right],$$

due to $g_2'(\phi - 1) = g_1'(\phi)$ and $\nabla^2\phi_N = 0$. Recall that $g_1(\phi)$ and $g_2(\phi)$ are the potential functions defined in Eq.(2.17). Therefore, the surface force in Eq.(2.35) is reduction consistent. □

One can also show that the surface force in Eq.(2.35) is equivalent to a conservative form:

Theorem 2.4.6. *The surface force in Eq.(2.35) is equivalent to* $\frac{1}{2}\sum_{p,q=1}^{N} \nabla\cdot(\lambda_{p,q}\nabla\phi_p \otimes \nabla\phi_q)$.

Proof.

$$\begin{aligned}
\frac{1}{2}\sum_{p,q=1}^{N}\nabla\cdot(\lambda_{p,q}\nabla\phi_p\otimes\nabla\phi_q) &= \frac{1}{2}\sum_{p,q=1}^{N}\lambda_{p,q}\nabla^2\phi_q\nabla\phi_p+\frac{1}{4}\sum_{p,q=1}^{N}\lambda_{p,q}\nabla(\nabla\phi_p\cdot\nabla\phi_q)\\
&+\frac{1}{2}\sum_{p,q=1}^{N}\lambda_{p,q}\frac{1}{\eta^2}\nabla g_1(\phi_p)-\sum_{p,q=1}^{N}\frac{1}{4}\lambda_{p,q}\frac{1}{\eta^2}\nabla g_1(\phi_p)-\sum_{p,q=1}^{N}\frac{1}{4}\lambda_{p,q}\frac{1}{\eta^2}\nabla g_1(\phi_q)\\
&+\sum_{p,q=1}^{N}\frac{\lambda_{p,q}}{4}\frac{1}{\eta^2}\nabla g_2(\phi_p+\phi_q)-\sum_{p,q=1}^{N}\frac{1}{2}\lambda_{p,q}\frac{1}{\eta^2}g_2(\phi_p+\phi_q)\nabla\phi_p\\
&=\frac{1}{2}\sum_{p=1}^{N}\underbrace{\sum_{q=1}^{N}\lambda_{p,q}\left(\frac{1}{\eta^2}\left(g_1(\phi_p)-g_2(\phi_p+\phi_q)\right)+\nabla^2\phi_q\right)}_{\xi_p}\nabla\phi_p\\
&-\nabla\underbrace{\frac{1}{2}\sum_{p,q=1}^{N}\frac{\lambda_{p,q}}{2}\left(\frac{1}{\eta^2}\left(g_1(\phi_p)+g_1(\phi_q)-g_2(\phi_p+\phi_q)\right)-\nabla\phi_p\cdot\nabla\phi_q\right)}_{\mathrm{e}_F}\\
&=\mathbf{f}_s-\nabla\frac{\mathrm{e}_F}{2}.
\end{aligned}$$

The gradient term $\nabla\frac{\mathrm{e}_F}{2}$ can be absorbed in to the pressure term, and, as a result, the surface force in Eq.(2.35) is equivalent to $\frac{1}{2}\sum_{p,q=1}^{N}\nabla\cdot(\lambda_{p,q}\nabla\phi_p\otimes\nabla\phi_q)$. □

Theorem 2.4.6 supports the statement in Section 2.4 that the momentum of the multi-phase flow is conserved by the proposed momentum equation Eq.(2.34), without the gravity. Compared to $\frac{1}{2}\sum_{p,q=1}^{N}\nabla\cdot(\lambda_{p,q}\nabla\phi_p\otimes\nabla\phi_q)$, the surface force defined in Eq.(2.35) is more convenient to be numerically implemented. First, the number of terms in Eq.(2.35) doesn't change with the dimension of the problem. Second, it doesn't need to evaluate the mixed derivatives. The only second derivative comes from the Laplace operator in ξ_p, which can be conveniently computed in any dimension. Lastly, writing the surface force in a gradient form, i.e., Eq.(2.35), the balanced-force algorithm [43] can be applied to reduce the spurious current caused by the numerical force imbalance.

***Remark**:*

- *In the general N-phase cases, there is no explicit proof in the present study that the conservative Allen-Cahn equation Eq.(2.19) follows the energy dissipation, and, as a result, Theorem 2.4.4 may not hold. However, one can show that the 2nd law of*

thermodynamics is honored when there are only two phases, and the proof is the same as the one for Theorem 2.4.4 after multiplying [right-hand side of Eq.(2.23)]$/M_0$ *to both sides of Eq.(2.23).*

- *The surface force in Eq.(2.35) from Theorem 2.4.4 and Eq.(2.17) is also called the free-energy-based surface tension model, which has been used even the Phase-Field equation is different from Eq.(2.17), e.g., in [70], [196], [197]. An alternative choice of modeling the interfacial tensions is called the generalized continuous surface tension force formulation which is a geometry-based model [65], [67], [69].*

2.5 Physical interpretation of the consistency conditions and alternative models

Here, the physical interpretation to the consistency conditions and their formulations are provided. First, the *consistency of mass conservation* and the *consistency of mass and momentum transport* are justified using the control volume analysis. The Reynolds transport theorem (Lemma 2.5.1) and Divergence (Gauss's) theorem (Lemma 2.5.2) [8] are to be implemented. Given an arbitrary control volume $\Omega(t)$ whose boundary is $\partial\Omega(t)$. The velocity and outward unit normal on $\partial\Omega(t)$ are $\mathbf{u}_{\partial\Omega(t)}$ and $\mathbf{n}$, respectively. Then, the Reynolds transport theorem and Divergence theorem on a scalar (vector or tensor) function $\mathcal{F}$ are written as

Lemma 2.5.1 (Reynolds transport theorem)**.**

$$\frac{d}{dt}\int_{\Omega(t)}\mathcal{F}d\Omega=\int_{\Omega(t)}\frac{\partial\mathcal{F}}{\partial t}d\Omega+\int_{\partial\Omega(t)}\mathcal{F}(\mathbf{n}\cdot\mathbf{u}_{\partial\Omega(t)})d\Gamma.$$

Lemma 2.5.2 (Divergence (Gauss's) theorem)**.**

$$\int_{\Omega(t)}\nabla\cdot\mathcal{F}d\Omega=\int_{\partial\Omega(t)}\mathbf{n}\cdot\mathcal{F}d\Gamma.$$

The mass, momentum, and force in $\Omega(t)$ are

$$\int_{\Omega(t)}\rho d\Omega,\quad\int_{\Omega(t)}\rho\mathbf{u}d\Omega,\quad\int_{\Omega(t)}\mathbf{f}d\Omega. \tag{2.36}$$

Notice that ρ is the mixture density defined in Eq.(2.3) and that the forces acting on $\partial\Omega(t)$ have been included in $\mathbf{f}$ after using the Divergence theorem (Lemma 2.5.2). Suppose the mass flux on $\partial\Omega(t)$ is $\mathbf{m}$, then the mass and momentum leaving the control volume boundary per unit time are

$$\begin{aligned} &\int_{\partial\Omega(t)} \mathbf{n}\cdot\mathbf{m} d\Gamma - \int_{\partial\Omega(t)} \rho\mathbf{n}\cdot\mathbf{u}_{\partial\Omega(t)} d\Gamma, \\ &\int_{\partial\Omega(t)} (\mathbf{n}\cdot\mathbf{m})\mathbf{u} d\Gamma - \int_{\partial\Omega(t)} (\rho\mathbf{n}\cdot\mathbf{u}_{\partial\Omega(t)})\mathbf{u} d\Gamma. \end{aligned} \tag{2.37}$$

Provided Eq.(2.36) and Eq.(2.37), one obtains the mass and momentum balances of $\Omega(t)$:

$$\begin{aligned} \frac{d}{dt}\int_{\Omega(t)} \rho d\Omega &= -\left[\int_{\partial\Omega(t)} \mathbf{n}\cdot\mathbf{m} d\Gamma - \int_{\partial\Omega(t)} \rho\mathbf{n}\cdot\mathbf{u}_{\partial\Omega(t)} d\Gamma\right], \\ \frac{d}{dt}\int_{\Omega(t)} \rho\mathbf{u} d\Omega &= -\left[\int_{\partial\Omega(t)} (\mathbf{n}\cdot\mathbf{m})\mathbf{u} d\Gamma - \int_{\partial\Omega(t)} (\rho\mathbf{n}\cdot\mathbf{u}_{\partial\Omega(t)})\mathbf{u} d\Gamma\right] + \int_{\Omega(t)} \mathbf{f} d\Omega. \end{aligned} \tag{2.38}$$

After implementing the Reynolds transport theorem (Lemma 2.5.1) and then the Divergence theorem (Lemma 2.5.2) to Eq.(2.38), one obtains:

$$\begin{aligned} &\int_{\Omega(t)} \left(\frac{\partial\rho}{\partial t} + \nabla\cdot\mathbf{m}\right) d\Omega = 0, \\ &\int_{\Omega(t)} \left(\frac{\partial(\rho\mathbf{u})}{\partial t} + \nabla\cdot(\mathbf{m}\otimes\mathbf{u}) - \mathbf{f}\right) d\Omega = 0. \end{aligned} \tag{2.39}$$

Notice that the control volume is arbitrary. Consequently, Eq.(2.39) is true everywhere, and the obtained mass and momentum equations are identical to Eq.(2.27) and Eq.(2.34), respectively, derived from the *consistency of mass conservation* and *consistency of mass and momentum transport*. So far, only the Reynolds transport theorem (Lemma 2.5.1) and Divergence theorem (Lemma 2.5.2) are used without any further assumptions. For a clear presentation, the volume fractions $\{C_p\}_{p=1}^N$ are considered as the order parameters in the following discussions. As pointed out in [198]–[201], one has the flexibility to choose the governing equation for the volume fractions. Here, the following two cases are considered:

$$\frac{\partial C_p}{\partial t} + \nabla\cdot(\mathbf{u}C_p) = \nabla\cdot\mathbf{J}_p^C, \quad 1 \leqslant p \leqslant N, \tag{2.40}$$

$$\frac{\partial C_p}{\partial t} + \mathbf{u} \cdot \nabla C_p = \nabla \cdot \mathbf{J}_p^C, \quad 1 \leqslant p \leqslant N. \tag{2.41}$$

where $\{\mathbf{J}_p^C\}_{p=1}^N$ are the diffusion fluxes of the volume fractions. The only difference in Eq.(2.40) and Eq.(2.41) is in the convection term since a divergence-free velocity need not to be assumed at the moment.

Next, the assumption that the densities of the fluid phases are constant is supplemented, which is the case considered in the present study as pointed out in Section 2.1. Under this assumption, the mass conservation equation can be obtained algebraically, starting from Eq.(2.40) or Eq.(2.41). After appropriately arranging the terms, the mass flux $\mathbf{m}$ in Eq.(2.39) can be finalized. This is exactly the procedure stated in the *consistency of mass conservation*. After multiplying Eq.(2.40) or Eq.(2.41) by ρ_p, summing over p, and comparing to Eq.(2.27) (or the first equation of Eq.(2.39)), one has the following four options.

- *Option 1*: Provided Eq.(2.40) and $\sum_{p=1}^N \mathbf{J}_p^C = \mathbf{0}$,

$$\frac{\partial \rho}{\partial t} + \nabla \cdot \left(\sum_{p=1}^N \rho_p (\mathbf{u} C_p - \mathbf{J}_p^C) \right) = 0 \quad \text{or} \quad \nabla \cdot \mathbf{u} = 0 \quad \text{and} \quad \mathbf{m} = \sum_{p=1}^N \rho_p (\mathbf{u} C_p - \mathbf{J}_p^C).$$

  To satisfy the 2nd-law of thermodynamics, the diffusion fluxes can be

$$\mathbf{J}_p^C = M_p^C \nabla \xi_p^C \quad \text{or} \quad \mathbf{J}_p^C = \sum_{q=1}^N M_{p,q}^C \nabla \xi_q^C, \quad 1 \leqslant p \leqslant N.$$

- *Option 2*: Provided Eq.(2.40) and $\sum_{p=1}^N \rho_p \mathbf{J}_p^C = \mathbf{0}$,

$$\frac{\partial \rho}{\partial t} + \nabla \cdot (\rho \mathbf{u}) = 0 \quad \text{or} \quad \nabla \cdot \mathbf{u} = \nabla \cdot \sum_{p=1}^N \mathbf{J}_p^C \quad \text{and} \quad \mathbf{m} = \rho \mathbf{u}.$$

  To satisfy the 2nd-law of thermodynamics, the diffusion fluxes can be

$$\mathbf{J}_p^C = M_p^C \nabla \left(\beta_C \xi_p^C + P \right) \quad \text{or} \quad \mathbf{J}_p^C = \sum_{q=1}^N M_{p,q}^C \nabla \left(\beta_C \xi_q^C + P \right), \quad 1 \leqslant p \leqslant N.$$

- *Option 3*: Provided Eq.(2.41) and $\sum_{p=1}^{N} \mathbf{J}_p^C = \mathbf{0}$,

$$\frac{\partial \rho}{\partial t} + \nabla \cdot \left(\sum_{p=1}^{N} \rho_p (\mathbf{u} C_p - \mathbf{J}_p^C) \right) = \rho \nabla \cdot \mathbf{u} \quad \text{or} \quad \nabla \cdot \mathbf{u} = 0 \quad \text{and} \quad \mathbf{m} = \sum_{p=1}^{N} \rho_p (\mathbf{u} C_p - \mathbf{J}_p^C).$$

To satisfy the 2nd-law of thermodynamics, the diffusion fluxes can be

$$\mathbf{J}_p^C = M_p^C \nabla \xi_p^C \quad \text{or} \quad \mathbf{J}_p^C = \sum_{q=1}^{N} M_{p,q}^C \nabla \xi_q^C, \quad 1 \leqslant p \leqslant N.$$

- *Option 4*: Provided Eq.(2.41) and $\sum_{p=1}^{N} \mathbf{J}_p^C = \mathbf{0}$,

$$\frac{\partial \rho}{\partial t} + \nabla \cdot (\rho \mathbf{u}) = \rho \nabla \cdot \mathbf{u} + \nabla \cdot \sum_{p=1}^{N} \rho_p \mathbf{J}_p^C \quad \text{or} \quad \nabla \cdot \mathbf{u} = -\frac{1}{\rho} \nabla \cdot \sum_{p=1}^{N} \rho_p \mathbf{J}_p^C \quad \text{and} \quad \mathbf{m} = \rho \mathbf{u}$$

To satisfy the 2nd-law of thermodynamics, the diffusion fluxes can be

$$\mathbf{J}_p^C = M_p^C \nabla \left(\beta_C \xi_p^C - \frac{\rho_p}{\rho} P \right) \quad \text{or} \quad \mathbf{J}_p^C = \sum_{q=1}^{N} M_{p,q}^C \nabla \left(\beta_C \xi_q^C - \frac{\rho_q}{\rho} P \right), \quad 1 \leqslant p \leqslant N.$$

Here, $\xi_p^C (= \delta E_F / \delta C_p)$ and M_p^C (or $M_{p,q}^C$) are the chemical potential and mobility, respectively, based on the volume fractions. $\beta_C (> 0)$ is the coefficient for matching the two-phase formulation, like β in Theorem 2.4.4.

Option 1 is equivalent to the results in Section 2.3. The only difference is that $\{\phi_p\}_{p=1}^N$ are the order parameters in Section 2.3 but $\{C_p\}_{p=1}^N$ here. A divergence-free velocity is obtained but the mass conservation equation is different from the sharp-interface one Eq.(1.1), as pointed out in Chapter 1. *Option 2*, on the other hand, recovers the form of the sharp-interface mass conservation equation Eq.(1.1) but results in a non-divergence-free velocity. Similar formulations are presented in [128] for the two-phase case and in [133] for the N-phase case. *Option 3* is identical to *Option 1*, both of which have a divergence-free velocity. As a result, Eq.(2.40) and Eq.(2.41) have no difference since the convection terms of them are equal. *Option 4* is similar to *Option 2* in the sense that it reproduces the form of the sharp-interface mass conservation equation Eq.(1.1) with a non-divergence-free velocity. However,

it does not conserve $(\rho_p C_p)$, or the mass of Phase p $(1 \leqslant p \leqslant N)$, due to $\nabla \cdot \mathbf{u} \neq 0$ in Eq.(2.41), although it conserves ρ, or the mass of the fluid mixture. Therefore, *Option 4* is not suitable for the present problem. The divergence of the velocity in *Options 1 and 2* is obtained by summing Eq.(2.40) over p and notice that $\sum_{p=1}^{N} C_p = 1$ as in Eq.(2.2). In order to satisfy the 2nd law of thermodynamics, the diffusion fluxes in *Options 2 and 4* include the pressure, which is used to compensate the work done by the pressure due to volume change, i.e., $P\nabla \cdot \mathbf{u}$, from the momentum equation Eq.(2.34) (or the second equation of Eq.(2.39)). Since *Options 1 and 3* are identical and *Option 4* is unphysical, only *Options 1 and 2* are discussed in the following.

To further illustrate the physical meaning of the velocity and mass flux in *Options 1 and 2*, the mixture theory [202], [203] is used. The volume fractions are advected by the corresponding phase velocity:

$$\frac{\partial C_p}{\partial t} + \mathbf{u}_p \cdot \nabla C_p = 0, \quad \nabla \cdot \mathbf{u}_p = 0, \quad 1 \leq p \leq N. \tag{2.42}$$

Here, $\{\mathbf{u}_p\}_{p=1}^{N}$ are the phase velocities and they are divergence-free since the density of each phase is a constant. From Eq.(2.42), one can easily derive the mass conservation equation of the mixture:

$$\frac{\partial \rho}{\partial t} + \nabla \cdot \left(\sum_{p=1}^{N} \rho_p C_p \mathbf{u}_p \right) = 0. \tag{2.43}$$

After comparing Eq.(2.42) to Eq.(2.40), the diffusion flux should be interpreted as $\mathbf{J}_p^C = (\mathbf{u} - \mathbf{u}_p)C_p$, the volume transported by the relative velocity. Provided the condition in *Option 1*, i.e., $\sum_{p=1}^{N} \mathbf{J}_p^C = \mathbf{0}$, one obtains $\mathbf{u} = \sum_{p=1}^{N} C_p \mathbf{u}_p$, which is the volume-averaged velocity. *Option 1* tells that the volume-averaged velocity is divergence-free, which has been pointed out in Section 2.1. An alternative way to show this is from its definition and Eq.(2.42), i.e., $\nabla \cdot \mathbf{u} = \sum_{p=1}^{N} \nabla \cdot (\mathbf{u}_p C_p) = \sum_{p=1}^{N} \mathbf{u}_p \cdot \nabla C_p = -\sum_{p=1}^{N} \frac{\partial C_p}{\partial t} = 0$, presented in [56] for the two-phase case and in [75] for the N-phase case. The mass flux in *Option 1* now is $\mathbf{m} = \sum_{p=1}^{N} \rho_p (\mathbf{u} C_p - \mathbf{J}_p^C) = \sum_{p=1}^{N} \rho_p C_p \mathbf{u}_p$, the same as the one in Eq.(2.43) from the mixture theory. Since *Option 1* is equivalent to the case in Section 2.3, the consistent mass flux in Theorem 2.3.1 is actually the mass flux from the mixture theory. The failure of using $\rho\mathbf{u}$

as the mass flux in the volume-averaged velocity case is because it only considers the mass transport by the averaged velocity but misses those by the relative velocity (or motion) of the phases. *Option 2* requires $\sum_{p=1}^{N} \rho_p \mathbf{J}_p^C = \mathbf{0}$, and therefore one has $\mathbf{u} = (\sum_{p=1}^{N} \rho_p C_p \mathbf{u}_p)/\rho$, which is the mass-averaged velocity. Therefore, the mass-averaged velocity is non-divergence-free although each phase is incompressible, which has also been realized in [127], [128] for the two-phase case, [132] for the three-phase case, and [133], [134] for the N-phase case. The mass flux in *Option 2* is $\mathbf{m} = \rho\mathbf{u} = \sum_{p=1}^{N} \rho_p C_p \mathbf{u}_p$, correspondingly, which is again identical to the mass flux in Eq.(2.43) from the mixture theory. Interestingly, both *Options 1 and 2* reproduce the mass flux of the mixture theory although the physical interpretation of the velocity in them are different.

Finally, the *consistency of reduction* is considered. Provided Eq.(2.40), the *consistency of reduction* requires $\mathbf{J}_p^C|_{C_p \equiv 0} = \mathbf{0}$. Due to $\sum_{p=1}^{N} \mathbf{J}_p^C = \mathbf{0}$ in *Option 1* or to $\sum_{p=1}^{N} \rho_p \mathbf{J}_p^C = \mathbf{0}$ in *Option 2*, it can be inferred that $\mathbf{J}_p^C|_{C_p \equiv 1} = \mathbf{0}$. In other words, $\mathbf{J}_p^C$ is zero inside bulk phase regions. This can be interpreted again from the mixture theory where the diffusion flux is interpreted as $\mathbf{J}_p^C = (\mathbf{u} - \mathbf{u}_p)C_p$. Obviously, $\mathbf{J}_p^C$ vanishes when Phase p is absent (or $C_p = 0$). On the other hand, both the volume-averaged velocity in *Option 1* and the mass-averaged velocity in *Option 2* have the property: $\mathbf{u} = \mathbf{u_p}$ inside Phase p (or $C_p = 1$) from their definitions. As a result, $\mathbf{J}_p^C$ vanishes inside bulk-phase regions from the mixture theory, as required by the *consistency of reduction*. It should be noted that the suggested diffusion fluxes in *Options 1-4* only consider the 2nd law of thermodynamics. Additional care has to be paid to satisfy the conditions, i.e., $\sum_{p=1}^{N} \mathbf{J}_p^C = \mathbf{0}$ in *Option 1* and $\sum_{p=1}^{N} \rho_p \mathbf{J}_p^C = \mathbf{0}$ in *Option 2*, and the *consistency of reduction*. The present study considers the volume-averaged velocity, i.e., *Option 1*, and implement the Phase-Field equations in Eq.(2.17) and Eq.(2.19). The diffusion flux in Eq.(2.17) satisfies all the aforementioned requirements, while the one in Eq.(2.19) misses the energy dissipation, as discussed in Section 2.4.3. There are several two-phase [81], [127], [128], [130], three-phase [132], and N-phase [133], [134] models considering the mass-averaged velocity as presented in *Option 2*, and these models are also called the "quasi-incompressible" models. Although part of the aforementioned requirements is considered, explicit discussions about whether the diffusion flux in those models meets all

the required aspects simultaneously are not found. Such discussions are outside the scope of the present study.

Remark: *The consistent and conservative volume distribution algorithm in Section 2.2.2 is used to determine* $\{L_p^c\}_{p=1}^N$ *in Eq.(2.6), and it can also be used to obtain* $\{L_p^{mc}\}_{p=1}^N$, *corresponding to* $\{L_p^c\}_{p=1}^N$, *in the mass-averaged velocity models based on* $\{C_p\}_{p=1}^N$. *Similar to the constraints for* $\{L_p^c\}_{p=1}^N$ *in Eq.(2.8) and Eq.(2.10),* $(\int_\Omega L_p^{mc} d\Omega = S_p^{mc})$ *and* $(L_p^{mc}|_{C_p=0} = 0)$ *should be followed by* $\{L_p^{mc}\}_{p=1}^N$, *but the summation constraint becomes* $(\sum_{p=1}^N \rho_p L_p^{mc} = 0)$, *different from the one for* $\{L_p^c\}_{p=1}^N$ *in Eq.(2.9). Note that* $\{S_p^{mc}\}_{p=1}^N$ *are known, like their correspondences* $\{S_p^c\}_{p=1}^N$ *in Eq.(2.8), and that* $C_p = 0$ *is the same as* $\phi_p = -1$, *see Eq.(2.1). One can first determine* $\{(\rho_p L_p^{mc})\}_{p=1}^N$ *that satisfy*

$$\sum_{q=1}^{N}(\rho_q L_q^{mc}) = 0, \quad \int_\Omega (\rho_p L_p^{mc}) d\Omega = \rho_p S_p^{mc}, \quad (\rho_p L_p^{mc})|_{C_p=0} = 0, \quad 1 \leqslant p \leqslant N,$$

following the consistent and conservative volume distribution algorithm proposed in Section 2.2.2, because the above constraints for $\{(\rho_p L_p^{mc})\}_{p=1}^N$ *are equivalent to those in Eq.(2.11) for* $\{L_p\}_{p=1}^N$. *Finally,* $\{L_p^{mc}\}_{p=1}^N$ *are obtained from* $\{(\rho_p L_p^{mc})/\rho_p\}_{p=1}^N$.

In summary, the physical insights of the consistency conditions and their formulations in the present study are provided using the control volume analysis and the mixture theory. The *consistency of mass and momentum transport* are a direct consequence of the control volume analysis. Without priorly interpreting the velocity, one can straightforwardly obtain the mass flux as well as the divergence of the velocity following the *consistency of mass conservation* under provided conditions. These formulations can be further physically explained with the mixture theory, and the obtained mass flux is always identical to the one from the mixture theory regardless of the interpretation of the velocity. The *consistency of reduction* is supported by the mixture theory as well. It is illustrated that these consistency conditions are general for both models using the volume-averaged and mass-averaged velocities, respectively, although the present study focuses on the former case. In practice, these consistency conditions provide a "shortcut" of developing physical models that couple the Phase-Field equation to the hydrodynamics, without explicitly exploring their physical background.

2.6 Consistency of volume fraction conservation

A new consistency condition, called the *consistency of volume fraction conservation*, is developed to include component transports in moving and deforming phases. This consistency condition is accompanied with the diffuse domain approach [143] which extends a partial differential equation (PDE) for the component defined in a time-dependent domain to in a larger and fixed domain. Then, the component equation is finalized using the following consistency condition.

Consistency of volume fraction conservation*: The conservation equation of the volume fractions derived from the component equation should be consistent with the one derived from the Phase-Field equation when the component is homogeneous.*

In the original diffuse domain approach [143], it replaces the exact (or sharp) indicator function with the smoothed one, and presumes that the smoothed indicator function has the same sharp-interface dynamics as the exact one, i.e., the phase interface is advected by the flow velocity only. However, this is not the case when the smoothed indicator function is chosen from the Phase-Field method. There are allowable thermodynamical compression and diffusion, which models the transport of the phases by the relative motion of the phases, in addition to the flow advection, inside the interfacial region. This casts a discrepancy between the Phase-Field method and the original diffuse domain approach, which has not been realized before. The *consistency of volume fraction conservation* aims to remove the discrepancy by incorporating those thermodynamical effects in the Phase-Field method to the component equation. This consistency condition is essential to eliminate unphysical fluctuations of the components.

2.6.1 Extend to mass (heat) transfer

The problem considered allows N ($N \geqslant 1$) phases and M ($M \geqslant 0$) components appearing simultaneously. Therefore, the model is called the N-phase-M-component model. Each component can exist in different phases. In each phase, there is a background fluid called the pure phase, and multiple components can be dissolved in this pure phase. Therefore, each phase is a "solution" of its pure phase (or background fluid) as the "solvent" and the

components dissolved in this phase as the "solutes". ρ_p^ϕ and μ_p^ϕ denote the density and viscosity, respectively, of pure Phase p. The Marangoni effect due to the appearance of the components is assumed to be negligible, and consequently, the pairwise surface tensions and contact angles are identical to those of the pure phases. Notice that the volume fraction of the phases are denoted by $\{\chi_p\}_{p=1}^N$ here, and they are obtained from the Phase-Field equation Eq.(2.30):

$$\begin{aligned} &\frac{\partial \chi_p}{\partial t} + \nabla \cdot \mathbf{m}_{\chi_p} = 0, \quad 1 \leqslant p \leqslant N, \\ &\chi_p = \frac{1+\phi_p}{2}, \quad \mathbf{m}_{\chi_p} = \frac{\mathbf{u} + \mathbf{m}_{\phi_p}}{2}. \end{aligned} \tag{2.44}$$

Here, $\{\phi_p\}_{p=1}^N$ can be governed by the Cahn-Hilliard Eq.(2.17) or the conservative Allen-Cahn Eq.(2.19) equation, and the former case is used.

The M components are represented by a set of concentrations $\{C_p\}_{p=1}^M$. Individual components have their densities $\{\rho_p^C\}_{p=1}^M$ and viscosities $\{\mu_p^C\}_{p=1}^M$. Each component can be dissolved inside different phases. On the other hand, there can be multiple components inside a specific phase. To indicate the dissolvabilities among the components and the phases, the dissolvability matrix with dimension $M \times N$ is defined as

$$I_{p,q}^M = \begin{cases} 1, \text{if Component } p \text{ is dissolvable in Phase } q, \\ 0, \text{else.} \end{cases} \tag{2.45}$$

The diffusion coefficient of Component p in Phase q is denoted by $D_{p,q}$. Noted that values of $\{C_p\}_{p=1}^M$ are meaningful only inside the corresponding phases they dissolve in. To obtain a meaningful value in the entire domain of interest, one needs to use, e.g., $I_{p,q}^M \chi_q C_p$, to represent the amount of Component p in Phase q. As pointed out in [204], there are two commonly used ways to interpret concentration. The first case is to quantify the amount of a dissolved solute of a solution such as the "molar concentration" of salt in a salt water solution. The second case is to quantify the composition of miscible fluids such as the "volume fraction" of ethanol in a water-ethanol system. Here, the components act like "solutes" while the pure phases behave as "solvents". Therefore, the concentrations of the components are interpreted

as the first case, e.g., the "molar concentration". It is further assumed that inside each phase the "solution" compound of the pure phase (as the "solvent") and the components (as the "solutes") dissolved in that phase is dilute. In other words, in a specific phase, the volume fractions of the components dissolved in it are negligibly small compared to the volume fraction of the pure phase or the background fluid of that phase. Therefore, the volume of each phase will not be changed by either the appearance or cross-interface transport of the components. This assumption of diluteness is also consistent with neglecting the Marangoni effect of the components. It should be noted that the concentrations in the proposed model can also be interpreted as the second case, e.g., the "volume fraction", in a subset of problems where each phase has a single diffusion coefficient shared by all the components dissolved in it and the cross-interface transport of those components is prohibited. Although the assumption of diluteness can be removed in these problems, one has to be cautious about the assumption of neglecting the Marangoni effect of the components when applying the proposed model to those problems. In the present work, $\{\rho_p^C\}_{p=1}^M$ and $\{\mu_p^C\}_{p=1}^M$ are loosely called densities and viscosities, respectively, regardless of which interpretation of the concentrations is employed. The actual meaning of $\{\rho_p^C\}_{p=1}^M$ depends on the concrete definition of the concentrations. For example, ρ_p^C is the molar mass of Component p when the concentrations are "molar concentration", while it is the density of pure Component p minus the density of the pure phase the component dissolves in when the concentrations mean "volume fraction". The same works for $\{\mu_p^C\}_{p=1}^M$.

The consistent component equation: Suppose Component p is dissolvable in Phase q, i.e., $I_{p,q}^M = 1$, the dynamics of Component p is modeled by the convection-diffusion equation:

$$\frac{\partial C_p}{\partial t} + \nabla \cdot (\mathbf{u} C_p) = \nabla \cdot (D_{p,q} \nabla C_p), \tag{2.46}$$

defined in Ω_q, which is the part of the domain occupied by Phase q. The boundary condition of Component p at $\Gamma_{q,r}$, i.e., the boundary between Ω_q and Ω_r, is

$$\mathbf{n}_{q,r} \cdot (D_{p,q} \nabla C_p) = \begin{cases} 0, \text{if } I_{p,r}^M = 0 \\ -\mathbf{n}_{r,q} \cdot (D_{p,r} \nabla C_p), \text{if } I_{p,r}^M = 1, \end{cases}, \quad q \neq r, \tag{2.47}$$

where $\mathbf{n}_{q,r}$ is the unit normal vector pointing from Ω_q to Ω_r, and it is obvious that $\mathbf{n}_{q,r} = -\mathbf{n}_{r,q}$. The boundary condition Eq.(2.47) tells that if Component p is unable to dissolve in Ω_r, i.e., $I^M_{p,r} = 0$, no diffusive flux is allowed across $\Gamma_{q,r}$. On the other hand, if Component p is also dissolvable in Ω_r, i.e., $I^M_{p,r} = 1$, the diffusive flux is continuous at $\Gamma_{q,r}$. The convective flux is zero at $\Gamma_{q,r}$ by considering that the velocities of the flow and of $\Gamma_{q,r}$ are the same. The effect of cross-interface transports of components, i.e., Eq.(2.47), on changing phase volumes is not counted, thanks to the assumption of diluteness. In addition, by an appropriate setup, the proposed model allows to remove the cross-interface transports of components without modifying Eq.(2.47). Related details are provided later.

After implementing the diffuse domain approach [143] and the *consistency of volume fraction conservation*, the consistent component equation is:

$$\frac{\partial(\chi^M_p C_p)}{\partial t} + \nabla \cdot (\mathbf{m}_{\chi^M_p} C_p) = \nabla \cdot (D_p \nabla C_p), \quad 1 \leqslant p \leqslant M, \tag{2.48}$$

where

$$\chi^M_p = \sum_{q=1}^{N} I^M_{p,q} \chi_q, \quad 1 \leqslant p \leqslant M, \tag{2.49}$$

$$\mathbf{m}_{\chi^M_p} = \sum_{q=1}^{N} I^M_{p,q} \mathbf{m}_{\chi_q}, \quad 1 \leqslant p \leqslant M, \tag{2.50}$$

$$D_p = \sum_{q=1}^{N} I^M_{p,q} \chi_q D_{p,q}, \quad 1 \leqslant p \leqslant M. \tag{2.51}$$

Provided C_p is homogeneous, Eq.(2.44) is obtained from Eq.(2.48). Unless otherwise specified, the homogeneous Neumann boundary condition is applied to Eq.(2.48) at the boundary of domain Ω. It is obvious that the total amount of Component p inside its dissolvable region χ^M_p is conserved, i.e., $\frac{d}{dt}\int_\Omega (\chi^M_p C_p) d\Omega = 0$. After defining the component flux as

$$\mathbf{m}_{C_p} = \mathbf{m}_{\chi^M_p} C_p - D_p \nabla C_p, \quad 1 \leqslant p \leqslant M, \tag{2.52}$$

Eq.(2.48) can be written as

$$\frac{\partial(\chi_p^M C_p)}{\partial t} + \nabla \cdot \mathbf{m}_{C_p} = 0, \quad 1 \leqslant p \leqslant M. \tag{2.53}$$

Density and viscosity: Phase p is composed of its pure phase and the components dissolved in it, both of which contribute to the mass in Ω_p. As a result, the density of Phase p in Ω_p, denoted by ρ_p, is

$$\rho_p = \rho_p^\phi + \sum_{q=1, I_{q,p}^M=1}^{M} \rho_q^C C_q = \rho_p^\phi + \sum_{q=1}^{M} I_{q,p}^M \rho_q^C C_q. \tag{2.54}$$

The density of the fluid mixture in Ω, denoted by ρ, is the volume average of $\{\rho_p\}_{p=1}^N$:

$$\rho = \sum_{p=1}^{N} \rho_p \chi_p = \sum_{p=1}^{N} \rho_p^\phi \chi_p + \sum_{p=1}^{M} \rho_p^C \chi_p^M C_p, \tag{2.55}$$

where the first term in the rightmost is contributed from the pure phases (or the background fluids) and the second term appears due to the components. Similarly, the viscosity of the fluid mixture in Ω is

$$\mu = \sum_{p=1}^{N} \mu_p^\phi \chi_p + \sum_{p=1}^{M} \mu_p^C \chi_p^M C_p. \tag{2.56}$$

The consistent mass flux: The momentum equation is identical to Eq.(2.34) in Section 2.4, and the consistent mass flux there is derived from the *consistency of mass conservation* using the Phase-Field equation Eq.(2.30) and the consistent component equation Eq.(2.53), like the one in Section 2.3. Specifically, it reads

$$\mathbf{m} = \sum_{p=1}^{N} \rho_p^\phi \mathbf{m}_{\chi_p} + \sum_{p=1}^{M} \rho_p^C \mathbf{m}_{C_p}. \tag{2.57}$$

The above mass flux and the density in Eq.(2.55) follow Eq.(2.27).

consistency of reduction: The *consistency of reduction* is enriched from the N-phase one by adding the component part. It assures that no fictitious component is generated by the model. Any components that are absent at $t = 0$ will not appear at $\forall t > 0$, without

considering any sources or injection, if the model satisfies the *consistency of reduction*. For a specific p and from Eq.(2.48), one can obtain $C_p \equiv 0, \forall t > 0$, if $C_p = 0$ initially. As a result, the contribution of C_p to the density Eq.(2.55), the viscosity Eq.(2.56), and the mass flux Eq.(2.31) disappears. Consequently, the M-component system with the absence of Component p reduces to the corresponding $(M-1)$ system. One can repeat the procedure $(M-M')$ times so that the M-component system reduces to the corresponding M'-component system $(0 \leqslant M' \leqslant M-1)$. Combining with the analysis in Section 2.2 for the N-phase models, the proposed N-phase-M-component model satisfies the *consistency of reduction*.

Energy law: The proposed consistent component equation Eq.(2.48) follows the energy dissipation.

Theorem 2.6.1. *The proposed consistent component equation satisfies the following energy law:*

$$\frac{d}{dt}\int_\Omega \mathrm{e}_C d\Omega = -\sum_{p=1}^{M}\int_\Omega \gamma_{C_p} D_p \nabla C_p \cdot \nabla C_p d\Omega,$$

where e_C *is the component energy density*

$$\mathrm{e}_C = \sum_{p=1}^{M} \frac{1}{2}\gamma_{C_p}\chi_p^M C_p^2,$$

and $\{\gamma_{C_p}\}_{p=1}^M$ *are positive dimensional constants so that* e_C *has a unit* $[\mathrm{J/m^3}]$.

Proof. After multiplying Eq.(2.48) with $\gamma_{C_p} C_p$ and then summing over all the components p, the governing equation for the component energy density is obtained:

$$C_p\left(\frac{\partial(\chi_p^M C_p)}{\partial t} + \nabla\cdot(\mathbf{m}_{\chi_p^M} C_p) = \nabla\cdot(D_p\nabla C_p)\right)$$

$$C_p\left(\chi_p^M\frac{\partial C_p}{\partial t} + \mathbf{m}_{\chi_p^M}\cdot\nabla C_p\right) + C_p^2\underbrace{\left(\frac{\partial \chi_p^M}{\partial t} + \nabla\cdot\mathbf{m}_{\chi_p^M}\right)}_{0} = \nabla\cdot(D_pC_p\nabla C_p) - D_p\nabla C_p\cdot\nabla C_p$$

$$\chi_p^M\frac{\partial \frac{1}{2}C_p^2}{\partial t} + \mathbf{m}_{\chi_p^M}\cdot\nabla\frac{1}{2}C_p^2 + \frac{C_p^2}{2}\underbrace{\left(\frac{\partial \chi_p^M}{\partial t} + \nabla\cdot\mathbf{m}_{\chi_p^M}\right)}_{0} = \nabla\cdot(D_pC_p\nabla C_p) - D_p\nabla C_p\cdot\nabla C_p$$

$$\frac{\partial(\frac{1}{2}\chi_p^M C_p^2)}{\partial t} + \nabla\cdot\left(\mathbf{m}_{\chi_p^M}\frac{1}{2}C_p^2\right) = \nabla\cdot(D_pC_p\nabla C_p) - D_p\nabla C_p\cdot\nabla C_p.$$

Thanks to the *consistency of volume fraction conservation*, the volume fraction equation, i.e., the terms with under-brace, is recovered. Integrating the above equation over the domain and assuming that all the boundary integrals vanish, the component energy dissipation is obtained. □

Combining Theorem 2.4.4 (or Corollary 2.4.4.1) in Section 2.4.3 for the N-phase model, one obtains the following corollaries:

Corollary 2.6.1.1. *If the N-phase model follows the 2nd law of thermodynamics (or energy decay), the same will be true for the N-phase-M-component model with the consistent component equation Eq.(2.48).*

Corollary 2.6.1.2. *If the Cahn-Hilliard equation Eq.(2.17) and the consistent component equation Eq.(2.48) are used, the N-phase$M$-component model satisfies the 2nd law of thermodynamics (or energy decay):*

$$\frac{d}{dt}\left(E_K + \frac{1}{2}\mathrm{e}_F + \mathrm{e}_C\right) = -\int_\Omega \frac{1}{2}\sum_{p,q=1}^{M} M_{p,q}\nabla\xi_p\cdot\nabla\xi_q d\Omega$$
$$-\int_\Omega \sum_{p=1}^{M}\gamma_{C_p}D_p\nabla C_p\cdot\nabla C_p d\Omega - \int_\Omega \frac{1}{2}\mu(\nabla\mathbf{u}+\nabla\mathbf{u}^T):(\nabla\mathbf{u}+\nabla\mathbf{u}^T)d\Omega$$

The total energy of the N-phase-M-component system, which includes the free energy, the component energy, and the kinetic energy, is not increasing with time without any external input. Three factors are to reduce the total energy of the multiphase and multicomponent system. The first one comes from the thermodynamical non-equilibrium, contributed by the Phase-Field equation. The second one results from the inhomogeneity of the components in their dissolvable regions, contributed by the component equation. It should be noted that D_p is zero where C_p is not dissolvable so there is no contribution from those regions to the total energy. The last one is due to the viscosity of the fluids, contributed from the momentum equation. If the consistency conditions are violated, some additional terms will be added to the total energy of the multiphase and multicomponent system. In other words, even though all the phases are in their thermodynamical equilibrium, all the components are homogeneous in their dissolvable region, and all the fluids are inviscid, the total energy of

the multiphase and multicomponent system could still change due to the additional terms introduced by the inconsistency. Such a behavior of the total energy is not physically plausible. Thus, the consistency conditions are playing an essential role in the physical behavior of the system.

Galilean invariance: The consistent component equation Eq.(2.48) also enjoys the Galilean invariance, and the proof is similar to the one in Section 2.4.1. Combining Theorem 2.4.2, the N-phase-M-component model is Galilean invariant as well, and therefore Corollary 2.4.2.1 is still true.

Theorem 2.6.2. *The consistent component equation Eq.(2.48) is Galilean invariant.*

Corollary 2.6.2.1. *The proposed N-phase-M-component model satisfies the Galilean invariance.*

The proposed N-phase-M-component model can be applied to study some multiphase flows where the miscibilities of each pair of phases are different. For example, to model a three-phase system where Phases 01 and 02 are miscible while Phases 01 and 03 are immiscible, as well as Phases 02 and 03, one can define a 2-phase-1-component system, where Phase 1 without Component 1 represents Phase 01, Phase 1 with a specific amount, e.g., $1\text{mol}/\text{m}^3$, of Component 1 represents Phase 02, and Phase 2 represents Phase 03. One can set $I^M_{1,1} = 1$ and $I^M_{1,2} = 0$. As a result, Phase 1, with/without Component 1, is immiscible with Phase 2, and the immisciblities between Phases 01 and 03 and between Phases 02 and 03 are properly modeled. Component 1 is only dissolvable in Phase 1. When Phase 1 with Component 1 moves to locations where Phase 1 has no Component 1, Component 1 starts to be transported by both convection and diffusion to those locations, which models the miscible behavior of Phases 01 and 02. However, the proposed model is not ready for the problems where the miscible phases have significantly different surface tensions with respect to a phase that they are immiscible with or where a phase is miscible with several other phases that are immiscible with each other, since neither the Marangoni effect due to the presence of the components nor the change of phase volumes due to the transport of components has been considered.

The proposed N-phase-M-component model is flexible to model the cross-interface transport of a component which is dissolvable in both sides of the interface. Although the diffusive flux is continuous across the phase interfaces if the component is dissolvable in both of the phases, the proposed model works in the scenario where the component is not allowed to cross the phase interfaces even though it is dissolvable in both sides of the interface. For example, Component 01 is dissolvable in both Phases p and q but is unable to cross the phase interfaces between Phases p and q. One can set Component 1 with $I^M_{1,p} = 1$ and $I^M_{1,q} = 0$, and Component 2 with $I^M_{2,p} = 0$ and $I^M_{2,q} = 1$. Consequently, Component 1 is only allowed to be dissolved in Phase p but not in Phase q, and Component 2 is the opposite. Neither Component 1 nor 2 can cross the phase interface between Phases p and q. Consequently, the concentration of Component 01 in its dissolvable region $\chi^M_{01}C_{01}$ is represented by $\chi^M_1 C_1 + \chi^M_2 C_2$.

In addition to the N-phase-M-component model, more importantly, the present model illustrate a general framework that physically connects the phases, components, and fluid flows, with the help of the proposed consistency conditions. Thus, it can be implemented to incorporate many other models for locating the phases or transporting the components. One can freely choose another physical model, instead of Eq.(2.17), to govern the order parameters. Also, one can replace the convection-diffusion equation Eq.(2.46) with other transport equation that more accurately produces the dynamics of the components, and obtain the component equation following the diffuse domain approach and the *consistency of volume fraction conservation*, as described above. These result in changing the definitions of the Phase-Field flux and component flux in Eq.(2.30) and Eq.(2.53), while the rest of the equations, e.g., the density of the fluid mixture Eq.(2.55), the consistent mass flux Eq.(2.57), and the momentum equation Eq.(2.34) remain unchanged. The Galilean invariance of the momentum equation (Theorem 2.4.2) and the kinetic energy equation in Theorem 2.4.3 are always valid, regardless of the concrete definitions of the Phase-Field flux and component flux which depend on the equations for the order parameters and components. However, the free energy, the component energy, and the Galilean invariance of the order parameters and components may be affected.

2.6.2 Extend to solidification (melting)

A consistent and conservative thermo-gas-liquid-solid model including solidification/melting is developed with the help of the consistency conditions. The problem considered includes two materials, which are a gas "G" and a phase change material "M" experiencing solidification or melting. Therefore, in the entire domain Ω, there are three phases: the gas phase including only "G", and the liquid and solid phases of "M". The liquid-solid phase change is driven by temperature. The part of Ω occupied by "G" is denoted by Ω_G, and similarly, Ω_M, Ω_M^L, and Ω_M^S denote the domains occupied by "M", the liquid phase, and the solid phase of "M", respectively. As a result, one has $\Omega = \Omega_G \cup \Omega_M = \Omega_G \cup \Omega_M^L \cup \Omega_M^S$. In addition, boundaries of the domains are denoted with "∂" in front of the corresponding domains, for example, $\partial\Omega$ is the boundary of Ω. The material properties of the gas phase "G" and the liquid and solid phases of "M" are assumed to be constant and denoted by β_G, β_M^L, and β_M^S, respectively, where β can be density ρ, viscosity μ, specific heat C_p, and heat conductivity κ.

Here, φ is the volume fraction of the phase change material "M" in Ω. It can be governed by the two-phase Cahn-Hilliard Eq.(2.22) or conservative Allen-Cahn Eq.(2.23) equation, and the former case is considered. It should be noted that the velocity is not divergence-free because the phase change can induce the volume change. Therefore, the convection term is written as $(\mathbf{u} \cdot \nabla\varphi)$. Unless otherwise specified, the homogeneous Neumann boundary condition is applied.

The phase change equation: In the present study, the Allen-Cahn Phase-Field model for the solidification of a pure material [163] is considered and the convection term is added:

$$\begin{aligned}
\frac{\partial\phi}{\partial t} + \nabla\cdot(\mathbf{u}\phi) = -M_\phi\left(\frac{\lambda_\phi}{\eta_\phi^2}g'(\phi) - \lambda_\phi\nabla^2\phi + \frac{\rho_M^L L}{T_M}p'(\phi)(T_M - T)\right) \\
+\phi\nabla\cdot\mathbf{u} \quad \text{in} \quad \Omega_M, \\
\lambda_\phi = \frac{3\sqrt{2}\rho_M^L L}{T_M}\Gamma_\phi\eta_\phi, \quad M_\phi = \frac{\mu_\phi\Gamma_\phi}{\lambda_\phi}, \\
p(\phi) = \phi^3(6\phi^2 - 15\phi + 10), \\
\mathbf{n}\cdot\nabla\phi = 0 \quad \text{at} \quad \partial\Omega_M.
\end{aligned} \tag{2.58}$$

Notice that Eq.(2.58) is defined in Ω_M. Here, ϕ is considered as the volume fraction of the liquid phase of "M" in Ω_M. M_ϕ is the mobility of ϕ. Γ_ϕ and μ_ϕ are the Gibbs-Thomson and linear kinetic coefficients, respectively, in the Gibbs-Thomson equation of the liquid-solid interface. λ_ϕ is the mixing energy density of ϕ, which is related to the thickness of the liquid-solid interface η_ϕ. L is the latent heat of the liquid-solid phase change. T is the temperature and T_M is the melting temperature of the phase change. $p(\phi)$ is the interpolation function, monotonically increasing from 0 to 1 and having extreme points at $\phi = 0$ and $\phi = 1$, and $p'(\phi)$ is the derivative of $p(\phi)$ with respect to ϕ. $g(\phi) = \phi^2(1-\phi)^2$ is the double-well potential function. Unless otherwise specified, the homogeneous Neumann boundary condition is applied. This solidification/melting model Eq.(2.58) is the basis of many more complicated models including, e.g., components and/or anisotropy [163], [164], [166], [168], [172], [173]. The model can be derived either thermodynamically from a free energy functional using the L^2 gradient flow or geometrically from the Gibbs-Thomson equation, and details are available in [111], [163], [171]. The first two terms in the parentheses on the right-hand side of Eq.(2.58) models the curvature driven effect on the phase change, while they are, at the same time, competing with each other to maintain the thickness of the liquid-solid interface. The effect of the temperature is modeled by the last term in the parentheses.

After implementing the diffuse domain approach [143] and the *consistency of volume fraction conservation*, the phase change equation is:

$$
\begin{aligned}
\frac{\partial(\varphi\phi)}{\partial t} + \nabla\cdot(\mathbf{m}_\varphi\phi) &= -M_\phi\xi_\phi + \varphi\phi\nabla\cdot\mathbf{u} \quad \text{in} \quad \Omega, \\
\xi_\phi &= -\lambda_\phi\nabla\cdot(\varphi\nabla\phi) + \frac{\lambda_\phi}{\eta_\phi^2}\varphi g(\phi) + \frac{\rho_M^L L}{T_M}\varphi\tilde{p}(\phi)(T_M - T), \\
\lambda_\phi &= \frac{3\sqrt{2}\rho_M^L L}{T_M}\Gamma_\phi\eta_\phi, \quad M_\phi = \frac{\mu_\phi\Gamma_\phi}{\lambda_\phi}, \\
p(\phi) = \phi^3(6\phi^2 - 15\phi + 10), \quad \tilde{p}'(\phi) &= \begin{cases} 1, & \phi = 0 \quad \text{and} \quad T \geqslant T_M, \\ 1, & \phi = 1 \quad \text{and} \quad T \leqslant T_M, \\ p'(\phi), & \text{else}, \end{cases} \\
\mathbf{m}_{\varphi\phi} &= \mathbf{m}_\varphi\phi, \\
\mathbf{n}\cdot\nabla\phi &= 0, \quad \text{at} \quad \partial\Omega.
\end{aligned}
\tag{2.59}
$$

Here, ξ_ϕ is called the chemical potential of ϕ, $\tilde{p}'(\phi)$ is modified from $p'(\phi)$ to initiate the phase change, and $\mathbf{m}_{\varphi\phi}$ is the Phase-Field flux of $(\varphi\phi)$.

Eq.(2.59) admits the existence of fully liquid/solid state of "M". For example, given, $\phi = 1$ and $T > T_M$, one obtains $\phi \equiv 1$ from Eq.(2.59), after noticing that the two-phase Cahn-Hilliard eqaution Eq.(2.22) is recovered. In other words, Eq.(2.59) admits the existence of fully liquid state of "M", when the temperature is larger than the melting temperature and there is no solid phase at the beginning. This property is inherited from Eq.(2.58), thanks to satisfying the *consistency of volume fraction conservation*. The same will also be true for the solid state of "M".

Another issue addressed is about initiating the phase change. It should be noted that the terms in the parentheses on the right-hand side of Eq.(2.58), which are the driving forces for the phase change, are nonzero only at $0 < \phi < 1$. In other words, given "M" in fully solid (liquid) state at the beginning, melting (solidification) will never happen no matter how high (low) the temperature is. This issue is originated in the definition of $p(\phi)$ in Eq.(2.58) whose extreme points are $\phi = 0$ and $\phi = 1$, i.e., $p'(0) = p'(1) = 0$. These extreme points are the same as the equilibrium states of ϕ. Defining $p(\phi)$ in this way, as mentioned in [163], is an improvement from using $p(\phi) = \phi$, e.g., in [205], in the sense that the equilibrium state of ϕ is always 0 or 1, independent of the temperature. However, defining $p(\phi) = \phi$ preserves the driving force from the temperature when $\phi = 0$ or $\phi = 1$. The equilibrium states of ϕ should depend on the temperature. If the temperature is larger than the melting point, the equilibrium state should be $\phi = 1$ (liquid), while it should be $\phi = 0$ (solid) if $T < T_M$. To achieve this property, $\tilde{p}'(\phi)$ defined in Eq.(2.59) is proposed in the present study, which combines the advantages of $p(\phi) = \phi^3(6\phi^2 - 15\phi + 10)$ in [163] and $p(\phi) = \phi$ in [205], but avoids their disadvantages. Only when $\phi = 1$ (liquid) and $T < T_M$ (undercool) or when $\phi = 0$ (solid) and $T > T_M$ (overheat), $\tilde{p}'(\phi)$ is 1, so that the effect of the temperature on the phase change is included. In other cases, $\tilde{p}'(\phi)$ is the same as $p'(\phi)$ with $p(\phi) = \phi^3(6\phi^2 - 15\phi + 10)$. As a result, the equilibrium state of ϕ when $T < T_M$ is $\phi = 0$ (solid), and it is $\phi = 1$ (liquid) when $T > T_M$.

The volume fractions and material properties: Based on the Phase-Field equation Eq.(2.30) and the phase change equation Eq.(2.59), the volume fractions of the gas, liquid,

and solid phases in the proposed model are defined unambiguously. The volume fraction of the gas phase (or "G") in Ω is $\alpha_G = (1-\varphi)$, and they are $\alpha_L = (\varphi\phi)$ and $\alpha_S = (\varphi - \varphi\phi)$ for the liquid and solid phases, respectively. The volume fraction of "M" in Ω is $\alpha_M = \alpha_L + \alpha_S = \varphi$. It is clear that $\alpha_G + \alpha_M = \alpha_G + \alpha_L + \alpha_S = 1$ is always true in the entire domain.

With the volume fractions of the phases in hand, the material properties of the gas-liquid-solid mixture and their fluxes are computed as

$$\begin{aligned} \beta &= \beta_G + (\beta_M^S - \beta_G)\varphi + (\beta_M^L - \beta_M^S)(\varphi\phi), \\ \mathbf{m}_\beta &= \beta_G \mathbf{u} + (\beta_M^S - \beta_G)\mathbf{m}_\varphi + (\beta_M^L - \beta_M^S)\mathbf{m}_{\varphi\phi}. \end{aligned} \tag{2.60}$$

Here, β represents a certain material property, e.g., density ρ, and $\mathbf{m}_\varphi$ and $\mathbf{m}_{\varphi\phi}$ are the Phase-Field fluxes defined in Eq.(2.30) and Eq.(2.59), respectively.

The mass conservation including solidification/melting: To determine the mass transport of the model, the *consistency of mass conservation* in Section 2.3 is applied. First, the density of the multiphase mixture is obtained following Eq.(2.60)

$$\rho = \rho_G + (\rho_M^S - \rho_G)\varphi + (\rho_M^L - \rho_M^S)(\varphi\phi). \tag{2.61}$$

After combining Eq.(2.61) with the Phase-Field equation equation, Eq.(2.30), and the phase change equation, Eq.(2.59), the mass of the multiphase mixture is governed by

$$\frac{\partial \rho}{\partial t} + \nabla \cdot \mathbf{m}_\rho = \rho \nabla \cdot \mathbf{u} - M_\phi(\rho_M^L - \rho_M^S)\xi_\phi, \tag{2.62}$$

where $\mathbf{m}_\rho$ is the consistent mass flux defined in Eq.(2.60). Finally, to obtain a zero mass source in Eq.(2.62), the divergence of the velocity should satisfy

$$\nabla \cdot \mathbf{u} = \frac{M_\phi(\rho_M^L - \rho_M^S)}{\rho}\xi_\phi. \tag{2.63}$$

Eq.(2.63) illustrates the volume change due to the liquid-solid phase change. As a result, the mass conservation equation of the model is also Eq.(2.27). Therefore, the mass of the gas-liquid-solid mixture is locally conserved, even though the phase change happens. This is

achieved at the expense of changing the volume of "M", as indicated in Eq.(2.63). On the other hand, if the densities of the liquid and solid phases of "M" are the same, the volume of "M" remains the same, and therefore the divergence of the velocity is zero, which can also be seen in Eq.(2.63). It should be noted that the mass conservation equation Eq.(2.27) is not an independent equation in the model. Instead, it is derived from Eq.(2.60) and Eq.(2.63), as elaborated here. Therefore, one does not need to explicitly solve the mass conservation equation Eq.(2.27).

The energy equation: The enthalpy of the multiphase mixture is

$$\int_{\Omega} \left((\rho C_p) T + \rho_M^L L(\varphi\phi) \right) d\Omega,$$

and only the heat conductivity is considered in the present study. After considering the consistency conditions, the following energy equation is obtained:

$$\frac{\partial((\rho C_p)T)}{\partial t} + \nabla \cdot (\mathbf{m}_{(\rho C_p)} T) + \rho_M^L L \left(\frac{\partial(\varphi\phi)}{\partial t} + \nabla \cdot \mathbf{m}_{\varphi\phi} \right) = \nabla \cdot (\kappa \nabla T) + Q_T. \tag{2.64}$$

Here, (ρC_p) and κ denote the volumetric heat and the heat conductivity, respectively, and they are computed from Eq.(2.60). Q_T is the heat source, and is neglected unless otherwise specified. The terms in the parenthesis on the left-hand side of Eq.(2.64) represents the effect of the phase change on the enthalpy. Therefore, without the phase change, i.e., $\phi \equiv 1$ and $T > T_M$ or $\phi \equiv 0$ and $T < T_M$, these terms should disappear. This is true due to the *consistency of volume fraction conservation*. As a result, the terms in the parenthesis in Eq.(2.64) are identical to those on the left-hand side of Eq.(2.59).

Further, Eq.(2.64) admits isothermal solutions (or temperature equilibrium) when the phase change does not happen. Plugging $T \equiv T_0$ in Eq.(2.64), one obtains $T_0 \left[\frac{\partial(\rho C_p)}{\partial t} + \nabla \cdot \mathbf{m}_{(\rho C_p)} \right]$ on the left-hand side and 0 on the right-hand side. Following the derivation from the *consistency of mass conservation* and replacing ρ with (ρC_p), one can show that $\left[\frac{\partial(\rho C_p)}{\partial t} + \nabla \cdot \mathbf{m}_{(\rho C_p)} \right]$ is zero, where $\mathbf{m}_{(\rho C_p)}$ is the flux of volumetric heat defined in Eq.(2.60), by noticing that the velocity is divergence-free when there is no phase change. Therefore, isothermal solutions are admissible.

As all the gas-liquid, gas-solid, and liquid-solid interfaces are immersed in Ω, their effects are modeled as volumetric forces, i.e., $\mathbf{f}_s$ and $\mathbf{f}_d$, in the momentum equation Eq.(2.34). $\mathbf{f}_s$ is the surface tension force, modeling the surface tension at the gas-liquid interface, while $\mathbf{f}_d$ is the drag force, modeling the no-slip boundary condition at the gas-solid and liquid-solid interfaces by enforcing $\mathbf{u} = \mathbf{u}_S$ in the solid phase, where $\mathbf{u}_S$ is the given solid velocity and is set to be zero unless otherwise specified. Note that the consistent mass flux $\mathbf{m}_\rho$ in Eq.(2.62) is applied in the momentum equation, following the *consistency of mass and momentum transport*.

Surface tension force: To model the surface tension at the gas-liquid interface, the commonly used Phase-Field formulation $\xi_\varphi \nabla\varphi$ is applied, which can be derived from either the energy balance [54] or the least-action principle [55], [59]. However, $\xi_\varphi \nabla\varphi$ is activated at all "*G-M*" interfaces, including both the gas-liquid and gas-solid interfaces. To remove its contribution at the gas-solid interface, $\xi_\varphi \nabla\varphi$ is multiplied by ϕ so that the surface tension force remains to be $\xi_\varphi \nabla\varphi$ at the gas-liquid interface and smoothly reduces to zero away from it. As a result, the surface tension force in the momentum equation Eq.(2.34) is:

$$\mathbf{f}_s = \phi \xi_\varphi \nabla\varphi. \tag{2.65}$$

To more clearly illustrate the distribution of the surface tension force, a gas bubble at the center of a unit domain with a radius 0.2 is considered, the bottom half of which is in contact with the solid phase while the upper half is in contact with the liquid phase. Fig.2.1 schematically shows the magnitude of the surface tension forces. It should be noted that the thermo-capillary effect has not been considered in the present study and the surface tension σ is treated as a constant.

Drag force: To model the no-slip boundary condition at both the gas-solid and liquid-solid interfaces, the velocity inside the solid phase needs to be the given value $\mathbf{u}_S$. A drag force, formulated as

$$\mathbf{f}_d = A_d(\mathbf{u}_S - \mathbf{u}), \quad A_d = C_d \frac{\alpha_S^2}{(1-\alpha_S)^3 + \mathrm{e}_d}, \tag{2.66}$$

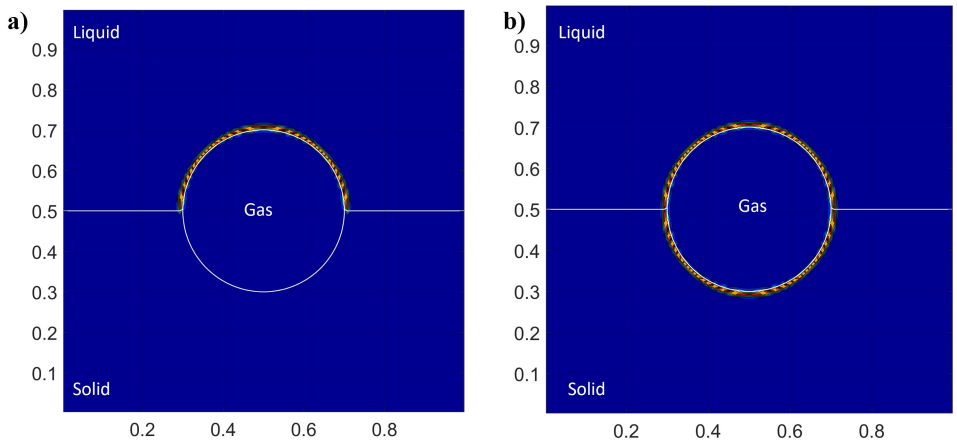

Figure 2.1. Magnitude of the surface tension force $|\mathbf{f}_s|$. a) The proposed surface tension force $\mathbf{f}_s = \phi\xi_\varphi\nabla\varphi$, b) The original surface tension force $\mathbf{f}_s = \xi_\varphi\nabla\varphi$. The proposed surface tension force shown in a) removes its contribution at the gas-solid interface, compared to the original formulation shown in b).

is added to the momentum equation Eq.(2.34), where the drag coefficient A_d can be considered as the Lagrange multiplier that enforces $\mathbf{u} = \mathbf{u}_S$ inside the solid phase. A_d should depend on the volume fraction of the solid phase in such a way that it is zero away from the solid phase and increases to a large enough value that overwhelms the inertia and viscous effects inside the solid phase. As a result, around the gas-solid and liquid-solid interfaces, the momentum equation Eq.(2.34) reduces to Darcy's law [155]. Voller and Prakash [156] modified the well-known Carman-Kozeny equation [162], by adding a small constant, denoted by e_d here, at the denominator to avoid division by zero, and obtained $A_d = C_d\frac{(1-\phi)^2}{\phi^3+\mathrm{e}_d}$ in Ω_M, where C_d should be a large number and ϕ is the volume fraction of the liquid phase of "M" in Ω_M as a reminder. Such a definition of A_d has been popularly used, e.g., in [144], [145], [152], [157], [159]. It should be noted that Voller and Prakash [156] did not consider the gas phase and formulated A_d in terms of the volume fraction of the liquid phase. Therefore, their formulation is only applicable in Ω_M. To obtain A_d in Ω, the volume fraction of the solid phase in Ω is directly used as the dependent variable of A_d, i.e., $A_d = C_d\frac{\alpha_S^2}{(1-\alpha_S)^3+\mathrm{e}_d}$, as shown in Eq.(2.66). Another popular option of enforcing $\mathbf{u} = 0$ is to assign a large viscosity inside the solid phase, e.g., in [155], [182], [183]. Although it looks simpler, the numerical tests indicate that this is not an effective choice and adding a drag force is recommended.

Eq.(2.22), Eq.(2.59), Eq.(2.60), Eq.(2.63), Eq.(2.34), and Eq.(2.64) complete the consistent and conservative model for thermo-gas-liquid-solid flows including liquid-solid phase change, and the proposed model honors many physical properties. From Eq.(2.27), Eq.(2.34), and Eq.(2.64), it is obvious that the mass and enthalpy of the multiphase mixture are conserved, and the momentum (neglecting the gravity) is conserved without the appearance of the solid phase, by noticing that $\mathbf{f}_s = \xi_\varphi \nabla\varphi$ is equivalent to $\nabla\cdot(-\lambda_\varphi \nabla\varphi\otimes\nabla\varphi)$, see [54], [55], [206], and $\mathbf{f}_d = \mathbf{0}$, in this circumstance. When there is the solid phase, the momentum is not necessarily conserved due to the no-slip boundary condition at the solid boundary. The Galilean invariance is also satisfied by the proposed model. The proof is straightforward, using the Galilean transformation, like the one in Section 2.4.1.

More importantly, the proposed model is reduction consistent with (i) the isothermal consistent and conservative Phase-Field method for two-phase incompressible flows in the present study when the solid phase is absent and the initial homogeneous temperature is larger than the melting temperature, (ii) the isothermal fictitious domain Brinkman penalization (FD/BP) method for fluid-structure interaction in [160], [161] when the liquid phase is absent and the initial homogeneous temperature is lower than the melting temperature, and (iii) the Phase-Field model of solidification in [163] when the gas phase and flow are absent and the material properties of the liquid and solid phases are matched (except the thermal conductivity).

Theorem 2.6.3. *The proposed thermo-gas-liquid-solid model including solidification/melting is consistent with the isothermal consistent and conservative Phase-Field method for two-phase incompressible flows.*

Proof. Given $\phi = 1$ and $T = T_0 > T_M$ at $t = 0$, as already analyzed below Eq.(2.59), one obtains $\phi = 1$ and therefore $\mathbf{m}_{\varphi\phi} = \mathbf{m}_\varphi$ and $\xi_\phi = 0$ from Eq.(2.59), and $T = T_0$ from Eq.(2.64), at $\forall t > 0$. As a result, the velocity is divergence-free from Eq.(2.63), and the convection term of the two-phase Cahn-Hilliard equation Eq.(2.22) can be written in its conservative form. From Eq.(2.60), one obtains $\beta = \beta_G + (\beta_M^L - \beta_G)\varphi$ and $\mathbf{m}_\beta = \beta_G\mathbf{u} + (\beta_M^L - \beta_G)\mathbf{m}_\varphi$, showing that the contribution of β_M^S disappears. Finally in Eq.(2.65) and Eq.(2.66), $\mathbf{f}_s$ becomes $\xi_\varphi\nabla\varphi$, and $\mathbf{f}_d = \mathbf{0}$ due to $\alpha_S = (\varphi - \varphi\phi) = 0$. Therefore,

the temperature remains its homogeneous initial value, and the simplified system from the proposed model with the given condition is equivalent to the consistent and conservative Phase-Field method for two-phase incompressible flows, by noticing that $\tilde{\varphi} = \frac{1+\varphi}{2}$ is the order parameter of the two-phase Cahn-Hilliard equation. □

Theorem 2.6.4. *The proposed thermo-gas-liquid-solid model including solidification/melting is consistent with the isothermal fictitious domain Brinkman penalization (FD/BP) method for fluid-structure interaction in [160], [161].*

Proof. Given $\phi = 0$ and $T = T_0 < T_M$ at $t = 0$, one obtains $\phi = 0$ and therefore $\mathbf{m}_{\varphi\phi} = \mathbf{0}$ and $\xi_\phi = 0$ from Eq.(2.59), and $T = T_0$ from Eq.(2.64), at $\forall t > 0$. As a result, the velocity is divergence-free from Eq.(2.63), and the convection term of the two-phase Cahn-Hilliard equation Eq.(2.22) can be written in its conservative form. In Eq.(2.65) and Eq.(2.66), $\mathbf{f}_s$ becomes $\mathbf{0}$, and $\mathbf{f}_d = A_d(\mathbf{u}_S - \mathbf{u})$ with $\alpha_S = \varphi$. In this case, the gas phase should be understood as an arbitrary incompressible fluid and the solid phase represents the fictitious domain, where the material properties are the same as the fluid ones without loss of generality. As a result, one obtains $\beta = \beta_G$ and $\mathbf{m}_\beta = \beta_G \mathbf{u}$ from Eq.(2.60). Therefore, the temperature remains its initial homogeneous value, and the simplified system with the given condition is equivalent to the FD/BP method for fluid-structure interaction in [160], [161]. Notice that A_d is defined proportional to α_S in [160], [161], different from the one in Eq.(2.66), and the level-set method, instead of the two-phase Cahn-Hilliard equation, is used in [161] for the volume fraction of the fictitious domain (or the solid phase). □

Theorem 2.6.5. *The proposed thermo-gas-liquid-solid model including solidification/melting is consistent with the Phase-Field model of solidification in [163].*

Proof. Given $\varphi = 1$ and $\mathbf{u} = \mathbf{0}$ at $t = 0$, one has $\xi_\varphi = 0$ and therefore $\partial\varphi/\partial t = 0$ from Eq.(2.22), which implies $\varphi = 1$ and $\mathbf{m}_\varphi = \mathbf{u}$ at $\forall t > 0$. Further requiring that the material properties of the liquid and solid phases of "M" are identical, one obtains $\nabla \cdot \mathbf{u} = 0$ and $\partial\mathbf{u}/\partial t = \mathbf{0}$ from Eq.(2.63) and Eq.(2.34), respectively. Therefore, one obtains $\mathbf{u} = \mathbf{0}$ at $\forall t > 0$, and all the convection terms are dropped. Putting all these to the phase change equation Eq.(2.59) and the energy equation Eq.(2.64), they become the same as those in [163], except that $p'(\phi)$ is replaced with $\tilde{p}'(\phi)$ in the present study. □

Remark: *In the proofs of Theorem 2.6.3, Theorem 2.6.4, and Theorem 2.6.5, the given conditions are assumed to be true at* $t = 0$ *in the entire domain for convenience. Actually, one only needs those conditions to be true locally at any moment, and Theorem 2.6.3, Theorem 2.6.4, and Theorem 2.6.5 will again be valid. In other words, the proposed model including solidification/melting will automatically reduce to the corresponding multiphase models whenever one of the phases is locally absent.*

3. CONSISTENT AND CONSERVATIVE NUMERICAL FRAMEFORK[1]

In this chapter, the consistent and conservative numerical framework is proposed. General theorems are developed to honor the *consistency of mass conservation* and *consistency of mass and momentum transport* on the discrete level, regardless of the details of the Phase-Field equation and its scheme. The *consistency of reduction* of the multiphase flow model majorly relies on the Phase-Field equation, as demonstrated in Chapter 2, and the reduction-consistent and mass-conservative schemes for Eq.(2.17) and Eq.(2.19), as well as their two-phase correspondences, i.e., Eq.(2.22) and Eq.(2.23), are developed. The momentum equation Eq.(2.34) is solved from a momentum-conservative projection scheme, along with the balanced-force method or the conservative method for the surface force. Both the schemes for the Phase-Field and momentum equations are formally 2nd-order accurate in both time and space.

3.1 Grid arrangement and discrete operators

For a clear presentation, in the present study, the discrete operators are defined in two dimensions, while extension to three dimensional problems is straightforward. The collocated grid arrangement is used and shown in Fig.3.1. Cell centers are denoted by $(x_{\mathrm{i}}, y_{\mathrm{j}})$ and cell faces are denoted by $(x_{\mathrm{i}+1/2}, y_{\mathrm{j}})$ and $(x_{\mathrm{i}}, y_{\mathrm{j}+1/2})$. The nodal values of a scalar function f are stored at the cell centers $(x_{\mathrm{i}}, y_{\mathrm{j}})$ and are denoted by $f_{\mathrm{i,j}}$. The nodal values of a vector function $\mathbf{f}$ are stored at the cell faces $(x_{\mathrm{i}+1/2}, y_{\mathrm{j}})$ and $(x_{\mathrm{i}}, y_{\mathrm{j}+1/2})$, and are denoted by $f^x_{\mathrm{i}+1/2,\mathrm{j}}$

[1]This chapter was partly published in Journal of Computational Physics, Vol 387, Ziyang Huang, Guang Lin, Arezoo M. Ardekani, A mixed upwind/central WENO scheme for incompressible two-phase flows, Page 455-480, Copyright Elsevier (2019); in Journal of Computational Physics, Vol 406, Ziyang Huang, Guang Lin, Arezoo M. Ardekani, Consistent, essentially conservative and balanced-force Phase-Field method to model incompressible two-phase flows, Page 109192, Copyright Elsevier (2019); in Journal of Computational Physics, Vol 420, Ziyang Huang, Guang Lin, Arezoo M. Ardekani, Consistent and conservative scheme for incompressible two-phase flows using the conservative Allen-Cahn model, Page 109718, Copyright Elsevier (2020); in Journal of Computational Physics, Vol 434, Ziyang Huang, Guang Lin, Arezoo M. Ardekani, A consistent and conservative model and its scheme for N-phase-M-component incompressible flows, Page 110229, Copyright Elsevier (2021); and in International Journal of Multiphase Flow, Vol 142, Ziyang Huang, Guang Lin, Arezoo M. Ardekani, A consistent and conservative volume distribution algorithm and its applications to multiphase flows using Phase-Field models, Page 103727, Copyright Elsevier (2021).

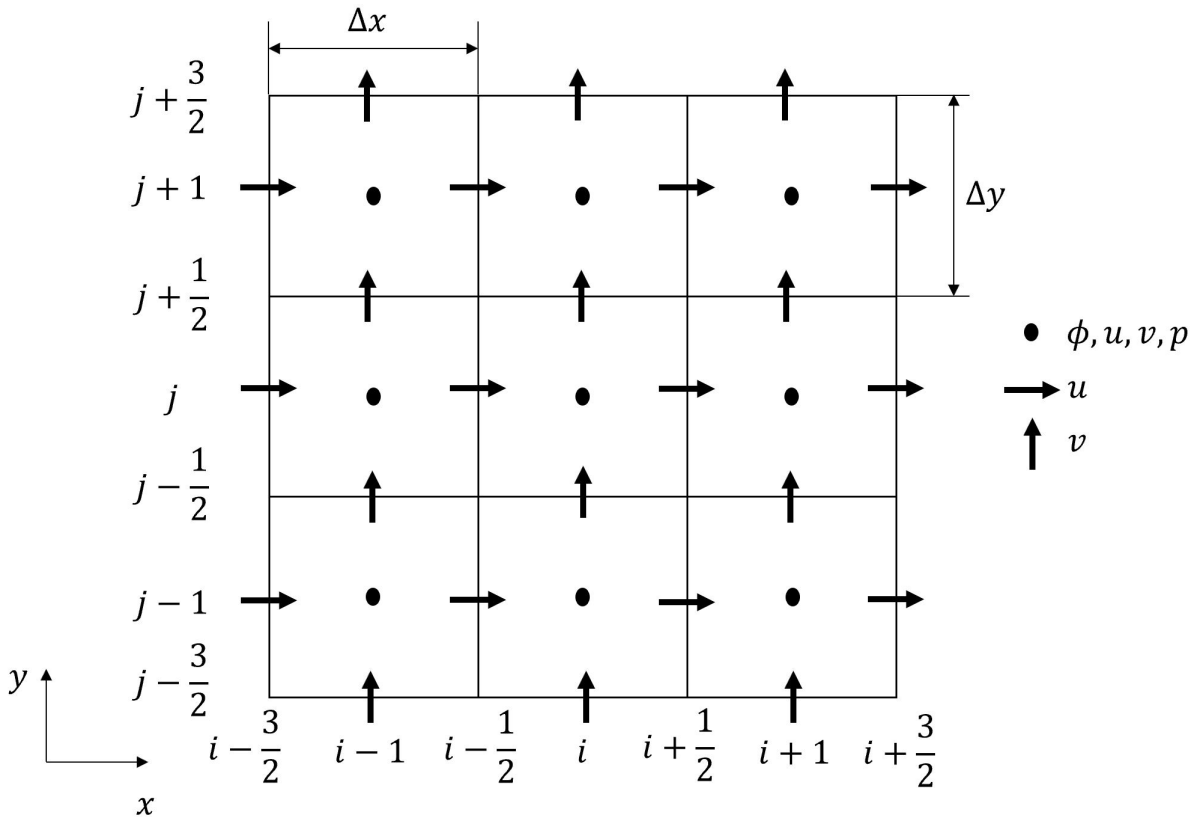

Figure 3.1. Schematic of the collocated grid arrangement. All the scalar variables, including the components of the cell-center velocity, are stored at the center of each cell. All the vector variables, including the cell-face velocity, are stored at the centers of the cell faces

and $f^y_{\mathrm{i,j+1/2}}$, where f^x and f^y are the components of the vector function. It should be noted that the gradient of a scalar function is also a vector function. In the collocated grid arrangement, one has a cell-center velocity, whose individual components are considered as a scalar function defined at the cell centers $(x_{\mathrm{i}}, y_{\mathrm{j}})$. In addition, a cell-face velocity is stored at the cell faces $(x_{\mathrm{i+1/2}}, y_{\mathrm{j}})$ and $(x_{\mathrm{i}}, y_{\mathrm{j+1/2}})$, as a vector function. Discretized differential and interpolation operators are denoted with superscript $\tilde{(\cdot)}$. For example, $\tilde{\nabla}$ represents the discretized gradient operator, and $\tilde{f}_{\mathrm{i+1/2,j}}$ means an interpolation of function f at $(x_{\mathrm{i+1/2}}, y_{\mathrm{j}})$ from its nodal values. f^n denotes the function value of f at time t^n, and $f^{*,n}$ denotes an extrapolation of f at t^n from previous time levels. Δx and Δy denote the cell/grid size, along the x and y axes, respectively, and Δt denotes the time step size. Close to the domain boundary, the ghost points outside the computational domain are assigned so that one does

not need to modify the discrete operators. The ghost-point values are determined, based on the boundary conditions. For the periodic boundary condition, the ghost-point values are assigned by copying their corresponding ones inside the computational domain. For the other boundary conditions, the linear extrapolation or the 2nd-order central difference is used unless otherwise specified. The discrete operators defined below are formally 2nd-order accurate, discretely conservative, and easy to be implemented. Most of them have compact stencils. It is worth mentioning that higher order schemes are probably to be used in the present framework as long as they are conservative on the discrete level.

Time discretization: The time derivative, without loss of generality, can be denoted by

$$\frac{\partial f}{\partial t} \approx \frac{\tilde{\partial} f}{\tilde{\partial} t} = \frac{\gamma_t f^{n+1} - \hat{f}}{\Delta t}. \tag{3.1}$$

Here, $\hat{(\cdot)}$ is an operator including f^n, f^{n-1}, etc., and has $\gamma_t f_0 = \hat{f}_0$ provided $f^n = f^{n-1} = ... = f_0$. The present study majorly considers the 2nd-order backward difference scheme where $\gamma_t = 1.5$, $\hat{f} = 2f^n - 0.5f^{n-1}$, and correspondingly $f^{*,n+1} = 2f^n - f^{n-1}$. Notice that Eq.(3.1) can conceptually represent various time discretization schemes, like the Crank-Nicolson, linear multistep, and Runge-Kutta methods.

Numerical integration: Domain Ω is partitioned by non-overlapping cells, and the integral of a function f over Ω is approximated by a quadrature rule in each cell and then summing the values up. Unless otherwise specified, the mid-point rule is used in the present study. Specifically,

$$\int_\Omega f d\Omega \approx \sum_{\mathrm{i,j}} [f \Delta\Omega]_{\mathrm{i,j}}, \tag{3.2}$$

where $\Delta\Omega$ ($= \Delta x \Delta y$ in the present study) is the cell volume.

Lagrangian interpolation: The Lagrangian interpolation is denoted as

$$[\bar{f}]^{x,p,q}_{\mathrm{i,j}} = \overline{(f_{\mathrm{i}-p,\mathrm{j}}, f_{\mathrm{i}-p+1,\mathrm{j}}, ..., f_{\mathrm{i}+q,\mathrm{j}})}, \tag{3.3}$$

where f is a scalar function defined at $(x_{\mathrm{i}-p+k}, y_{\mathrm{j}})_{k=0}^{p+q}$. Eq(3.3) denotes the Lagrangian interpolation along the x axis at point $(x_{\mathrm{i}}, y_{\mathrm{j}})$ with a p-left-bias and q-right-bias stencil. The frequently-used linear interpolation with $p = q = \frac{1}{2}$ at point $(x_{\mathrm{i}}, y_{\mathrm{j}})$ is denoted as

$$[\bar{f}]^x_{\mathrm{i,j}} \equiv [\bar{f}]^{x,1/2,1/2}_{\mathrm{i,j}} = \overline{(f_{\mathrm{i}-1/2,\mathrm{j}}, f_{\mathrm{i}+1/2,\mathrm{j}})}. \tag{3.4}$$

The interpolation along the other axis can be defined in the same manner.

Discrete divergence operator: The discrete divergence operator is defined as

$$\begin{aligned}[\tilde{\nabla} \cdot (\mathbf{f}_1 \tilde{f}_2)]_{\mathrm{i,j}} = &\frac{f^x_{1,\mathrm{i}+1/2,\mathrm{j}} \tilde{f}_{2,\mathrm{i}+1/2,\mathrm{j}} - f^x_{1,\mathrm{i}-1/2,\mathrm{j}} \tilde{f}_{2,\mathrm{i}-1/2,\mathrm{j}}}{\Delta x} \\ &+ \frac{f^y_{1,\mathrm{i,j}+1/2} \tilde{f}_{2,\mathrm{i,j}+1/2} - f^y_{1,\mathrm{i,j}-1/2} \tilde{f}_{2,\mathrm{i,j}-1/2}}{\Delta y},\end{aligned} \tag{3.5}$$

where $\mathbf{f}_1$ is a vector function defined at the cell face while f_2 is a scalar function defined at the cell center. In this case, the nodal values of $\mathbf{f}_1$ is directly used, while numerical evaluation has to be performed to specify $\tilde{f}_2$ from its nodal values f_2. Here, the present study use the 5th-order WENO scheme [207], which is very robust and accurate. It should be noted that the discrete divergence operator should be formally 2nd-order accurate even when a high-order numerical scheme is implemented to evaluate $\tilde{f}_2$. However, the error would be smaller when a high-order scheme is used [208]. To achieve higher order of accuracy, a more sophisticated interpolation has to be performed on $f^x_{1,\mathrm{i}\pm1/2,\mathrm{j}}$ and $f^y_{1,\mathrm{i,j}\pm1/2}$, and readers can refer to [208]–[210].

Discrete gradient operators: Two discrete gradient operators are defined. One is at the cell face

$$[\tilde{f}_2 \tilde{\nabla}^x f_1]_{\mathrm{i}+1/2,\mathrm{j}} = \tilde{f}_{2,\mathrm{i}+1/2,\mathrm{j}} \frac{f_{1,\mathrm{i}+1,\mathrm{j}} - f_{1,\mathrm{i,j}}}{\Delta x}, \tag{3.6}$$

and the other is at the cell center

$$[\overline{\tilde{f}_2 \tilde{\nabla}^x f_1}]^x_{\mathrm{i,j}} = \overline{([\tilde{f}_2 \tilde{\nabla}^x f_1]_{\mathrm{i}-1/2,\mathrm{j}}, [\tilde{f}_2 \tilde{\nabla}^x f_1]_{\mathrm{i}+1/2,\mathrm{j}})}, \tag{3.7}$$

where f_1 and f_2 are both scalar functions defined at the cell center. $\tilde{f}_{2,\mathrm{i}+1/2,\mathrm{j}}$ has to be numerically evaluated from the nodal values of f_2. Unless otherwise specified, the linear

interpolation, i.e., $\tilde{f}_{2,\mathrm{i}+1/2,\mathrm{j}} = [\overline{f_2}]^x_{\mathrm{i}+1/2,\mathrm{j}}$, is used. The discrete gradient operators along the other axes can be similarly defined. These discrete gradient operators are formally 2nd-order accurate due to the 2nd-order central difference and linear interpolation in Eq.(3.6) and Eq.(3.7).

Discrete Laplace operator: The discrete Laplace operator successively uses the discrete divergence operator Eq.(3.5) and the discrete gradient operator Eq.(3.6), which results in

$$\begin{aligned}[\tilde{\nabla}\cdot(\tilde{f}_2\tilde{\nabla}f_1)]_{\mathrm{i,j}} = &\frac{1}{\Delta x}\Big(\tilde{f}_{2,\mathrm{i}+1/2,\mathrm{j}}\frac{f_{1,\mathrm{i}+1,\mathrm{j}}-f_{1,\mathrm{i,j}}}{\Delta x} - \tilde{f}_{2,\mathrm{i}-1/2,\mathrm{j}}\frac{f_{1,\mathrm{i,j}}-f_{1,\mathrm{i}-1,\mathrm{j}}}{\Delta x}\Big)\\ &+\frac{1}{\Delta y}\Big(\tilde{f}_{2,\mathrm{i,j}+1/2}\frac{f_{1,\mathrm{i,j}+1}-f_{1,\mathrm{i,j}}}{\Delta y} - \tilde{f}_{2,\mathrm{i,j}-1/2}\frac{f_{1,\mathrm{i,j}}-f_{1,\mathrm{i,j}-1}}{\Delta y}\Big),\end{aligned} \tag{3.8}$$

where both f_1 and f_2 are scalar functions defined at the cell center. Unless otherwise specified, $\tilde{f}_2$ is evaluated by the linear interpolation and this discrete operator should be formally 2nd-order accurate. Special attention should be paid to the Dirichlet boundary condition, where an $O(1)$ error will appear when linear extrapolation is used to specify the ghost-point values outside the domain. This can be easily shown by Taylor expansion. To resolve this error while maintaining a compact stencil, a parabolic extrapolation, whose stencil consists of the boundary and the two cells nearest to the boundary, is used to specify the ghost point value.

Discrete Divergence-Gradient-Transpose operator: The present study names the operator $\nabla\cdot(f_2(\nabla\mathbf{f_1})^T)$ the Divergence-Gradient-Transpose operator. With $f_2=\mu$ and $\mathbf{f_1}=\mathbf{u}$, it is a part of the viscous term in the momentum equation Eq.(2.34). This discrete operator is related to the *consistency of reduction* of the momentum equation, see the second remark below Corollary 2.4.1.2 in Section 2.4.

The same discrete divergence Eq.(3.5) and gradient Eq.(3.6) operators are used, and the discrete Divergence-Gradient-Transpose operator is

$$\begin{aligned}[\tilde{\nabla}\cdot(\tilde{f}_2(\tilde{\nabla}\tilde{\mathbf{f}}_1)^T)]^x_{\mathrm{i,j}} = &\frac{1}{\Delta x}\Big(\tilde{f}_{2,\mathrm{i}+1/2,\mathrm{j}}\frac{\tilde{f}^x_{1,\mathrm{i}+1,\mathrm{j}}-\tilde{f}^x_{1,\mathrm{i,j}}}{\Delta x} - \tilde{f}_{2,\mathrm{i}-1/2,\mathrm{j}}\frac{\tilde{f}^x_{1,\mathrm{i,j}}-\tilde{f}^x_{1,\mathrm{i}-1,\mathrm{j}}}{\Delta x}\Big)\\ +\frac{1}{\Delta y}\Big(\tilde{f}_{2,\mathrm{i,j}+1/2}&\frac{\tilde{f}^y_{1,\mathrm{i}+1/2,\mathrm{j}+1/2}-\tilde{f}^y_{1,\mathrm{i}-1/2,\mathrm{j}+1/2}}{\Delta x} - \tilde{f}_{2,\mathrm{i,j}-1/2}\frac{\tilde{f}^y_{1,\mathrm{i}+1/2,\mathrm{j}-1/2}-\tilde{f}^y_{1,\mathrm{i}-1/2,\mathrm{j}-1/2}}{\Delta x}\Big),\end{aligned} \tag{3.9}$$

where $\mathbf{f}_1$ is a vector function defined at the cell face, f_2 is a scalar function defined at the cell center, and $\tilde{f}_2$, unless otherwise specified, is evaluated by the linear interpolation. Eq.(3.9) is formally 2nd-order accurate. $[\tilde{\nabla}\cdot(\tilde{f}_2(\tilde{\nabla}\tilde{\mathbf{f}}_1)^T)]^y_{\mathrm{i,j}}$ can be similarly defined. $\tilde{f}_1$ in Eq.(3.9) are computed by

$$\begin{aligned}\tilde{f}^x_{1,\mathrm{i,j}} &= [\overline{f^x_1}]^x_{\mathrm{i,j}} = \frac{1}{2}(f^x_{1,\mathrm{i+1/2,j}} + f^x_{1,\mathrm{i-1/2,j}}),\\ \tilde{f}^y_{1,\mathrm{i+1/2,j+1/2}} &= [\overline{f^y_1}]^x_{\mathrm{i+1/2,j+1/2}} = \frac{1}{2}(f^y_{1,\mathrm{i,j+1/2}} + f^y_{1,\mathrm{i+1,j+1/2}}).\end{aligned} \tag{3.10}$$

Special care has to be paid to the discrete cells close to the boundary. Consider the boundary cell where $f^x_{1,\mathrm{i-3/2,j}}$ and $f^y_{1,\mathrm{i-1,j\pm1/2}}$ in Eq.(3.9) are outside of the domain and are replaced by the ghost-point values $\tilde{f}^x_{1,\mathrm{i-3/2,j}}$ and $\tilde{f}^y_{1,\mathrm{i-1,j\pm1/2}}$. These ghost-point values are defined carefully by

$$\begin{aligned}\tilde{f}^x_{1,\mathrm{i-3/2,j}} &= [\overline{f^x_1}]^{x,-1,3}_{\mathrm{i-3/2,j}} = 3f^x_{1,\mathrm{i-1/2,j}} - 3f^x_{1,\mathrm{i+1/2,j}} + f^x_{1,\mathrm{i+3/2,j}},\\ \tilde{f}^y_{1,\mathrm{i-1,j\pm1/2}} &= [\overline{f^y_1}]^{x,-1,2}_{\mathrm{i-1,j\pm1/2}} = 2f^y_{1,\mathrm{i,j\pm1/2}} - f^y_{1,\mathrm{i+1,j\pm1/2}}.\end{aligned} \tag{3.11}$$

Except replacing $f^x_{1,\mathrm{i-3/2,j}}$ and $f^y_{1,\mathrm{i-1,j\pm1/2}}$ with those in Eq.(3.11), the other terms in Eq.(3.9) are computed following Eq.(3.10).

Thanks to the careful definition of $\tilde{\mathbf{f}}_1$ in Eq.(3.10) and Eq.(3.11), the discrete Divergence-Gradient-Transpose operator Eq.(3.9) has the following property:

Lemma 3.1.1. *Provided f_2 a constant around $(x_\mathrm{i}, y_\mathrm{j})$, the discrete Divergence-Gradient-Transpose operator Eq.(3.9) becomes:*

$$[\tilde{\nabla}\cdot(\tilde{f}_2(\tilde{\nabla}\tilde{\mathbf{f}}_1)^T)]_{\mathrm{i,j}} = \left\{f_2[\tilde{\partial}^x(\tilde{\nabla}\cdot\mathbf{f}_1)]_{\mathrm{i,j}}, f_2[\tilde{\partial}^y(\tilde{\nabla}\cdot\mathbf{f}_1)]_{\mathrm{i,j}}\right\}.$$

Here, $\tilde{\mathbf{f}}_1$ is computed from Eq.(3.10) for the interior cells and uses Eq.(3.11) for the boundary cells. $\tilde{\partial}^q$ is a numerical operator approximating the partial derivative with respect to the q axis. For the interior cells, it is the central difference ($\tilde{\partial}^{q,CD}$), and for the boundary cells, it can be the forward ($\tilde{\partial}^{q,FD}$) or backward difference ($\tilde{\partial}^{q,BD}$) depending on the location of the boundary relative to the cell center.

Proof. Consider the x component and the interior cell first. Combining Eq.(3.9) and Eq.(3.10), one obtains

$$\begin{aligned}[\tilde{\nabla}\cdot(\tilde{f}_2(\tilde{\nabla}\tilde{\mathbf{f}}_1)^T)]^x_{\mathrm{i,j}} = \frac{1}{2}\frac{1}{\Delta x}f_2\Big(&\frac{f^x_{1,\mathrm{i}+3/2,\mathrm{j}}-f^x_{1,\mathrm{i}+1/2,\mathrm{j}}}{\Delta x}+\frac{f^y_{1,\mathrm{i}+1,\mathrm{j}+1/2}-f^y_{1,\mathrm{i}+1,\mathrm{j}-1/2}}{\Delta y}\\ &-\frac{f^x_{1,\mathrm{i}-1/2,\mathrm{j}}-f^x_{1,\mathrm{i}-3/2,\mathrm{j}}}{\Delta x}-\frac{f^y_{1,\mathrm{i}-1,\mathrm{j}+1/2}-f^y_{1,\mathrm{i}-1,\mathrm{j}-1/2}}{\Delta y}\Big)\\ &= f_2\frac{[\tilde{\nabla}\cdot\mathbf{f}_1]_{\mathrm{i}+1,\mathrm{j}}-[\tilde{\nabla}\cdot\mathbf{f}_1]_{\mathrm{i}-1,\mathrm{j}}}{2\Delta x}\\ &= f_2[\tilde{\partial}^{x,CD}(\tilde{\nabla}\cdot\mathbf{f_1})]_{\mathrm{i,j}}.\end{aligned}$$

This works for all the interior cells. Then, the boundary cell next to the left boundary is considered. The ghost point values are from Eq.(3.11) and the rest of $\tilde{\mathbf{f}}_1$ is computed from Eq.(3.10). After doing that, one obtains

$$[\tilde{\nabla}\cdot(\tilde{f}_2(\tilde{\nabla}\tilde{\mathbf{f}}_1)^T)]^x_{\mathrm{i,j}} = f_2\frac{1}{\Delta x}\Big([\tilde{\nabla}\cdot\mathbf{f}_1]_{\mathrm{i}+1,\mathrm{j}}-[\tilde{\nabla}\cdot\mathbf{f}_1]_{\mathrm{i,j}}\Big) = f_2[\tilde{\partial}^{x,FD}(\tilde{\nabla}\cdot\mathbf{f}_1)]_{\mathrm{i,j}},$$

The same result can be obtained at the other side of the boundary except that $\tilde{\partial}^{x,FD}$ is replaced by $\tilde{\partial}^{x,BD}$. The proof along the other axes is the same and not repeated here. □

Discrete conservation: The present study calls a discrete operator conservative in the sense that its summation over all the grid points is zero when the domain considered is periodic.

Lemma 3.1.2. *Provided f_2 a constant, the gradient operators defined in Eq.(3.6) and Eq.(3.7) are conservative.*

Proof. Consider $\tilde{\nabla}^x f$ in Eq.(3.6) first (f_1 is replaced with f for simplicity), and its summation over all the grid points is

$$\sum_{\mathrm{i,j}}[\tilde{\nabla}^x f]_{\mathrm{i}+1/2,\mathrm{j}} = \sum_{\mathrm{j}}\frac{\sum_{\mathrm{i}} f_{\mathrm{i}+1,\mathrm{j}}-\sum_{\mathrm{i}} f_{\mathrm{i,j}}}{\Delta x} = \sum_{\mathrm{j}}\frac{\sum_{\mathrm{i}} f_{\mathrm{i,j}}-\sum_{\mathrm{i}} f_{\mathrm{i,j}}}{\Delta x} = \sum_{\mathrm{j}} 0 = 0.$$

By replacing the summation order, $\sum_{\mathrm{i,j}}[\tilde{\nabla}^y f]_{\mathrm{i,j}+1/2} = 0$ is shown. Since the order of summation and linear interpolation is interchangeable, $\sum_{\mathrm{i,j}}[\overline{\tilde{\nabla} f}]_{\mathrm{i,j}} = 0$ is shown. □

Lemma 3.1.3. *The divergence operator defined in Eq.(3.5) (or Eq.(3.8) or Eq.(3.9)) is conservative.*

Proof.

$$\sum_{\mathrm{i,j}} [\tilde{\nabla} \cdot \mathbf{f}]_{\mathrm{i,j}} = \sum_{\mathrm{j}} \frac{\sum_{\mathrm{i}} f^x_{\mathrm{i+1/2,j}} - \sum_{\mathrm{i}} f^x_{\mathrm{i-1/2,j}}}{\Delta x} + \sum_{\mathrm{i}} \frac{\sum_{\mathrm{j}} f^y_{\mathrm{i,j+1/2}} - \sum_{\mathrm{j}} f^y_{\mathrm{i,j-1/2}}}{\Delta y}$$
$$= \sum_{\mathrm{j}} \frac{\sum_{\mathrm{i}} f^x_{\mathrm{i+1/2,j}} - \sum_{\mathrm{i}} f^x_{\mathrm{i+1/2,j}}}{\Delta x} + \sum_{\mathrm{i}} \frac{\sum_{\mathrm{j}} f^y_{\mathrm{i,j+1/2}} - \sum_{\mathrm{j}} f^y_{\mathrm{i,j+1/2}}}{\Delta y} = \sum_{\mathrm{j}} 0 + \sum_{\mathrm{i}} 0 = 0.$$

Here, $\mathbf{f}$ is $(\mathbf{f}_1 \tilde{f}_2)$ in Eq.(3.5), $(\tilde{f}_2 \tilde{\nabla} f_1)$ in Eq.(3.8), and $(\tilde{f}_2 (\tilde{\nabla} \tilde{\mathbf{f}}_1)^T)$ in Eq.(3.9). □

***Remark**: Lemma 3.1.2 is true with the zero-gradient boundary condition, and Lemma 3.1.3 is true with the zero-flux boundary condition.*

3.2 Consistency analysis on the discrete level

The *consistency of reduction* of the Phase-Field equation requires the constraints in Eq.(2.10) satisfied after discretization, which strongly depends on the specific form of the Phase-Field equation and the scheme to solve it. This will be considered in detail in Sections 3.3.3 and 3.3.4. This section analyzes the effects of the consistency conditions on the discrete level, provided that that the *consistency of reduction* is satisfied discretely by the Phase-Field equation. General theorems are proposed to ensure those consistency conditions after discretization, which are unrelated to the specific form or scheme of the Phase-Field equation.

In order to illustrate the effects of the consistency conditions on the discrete level, a simple one-dimensional two-phase advection problem is first analyzed, and the two-phase Cahn-Hilliard equation Eq.(2.22) is used as an example. As one shall see, the following analyses are not restricted to this specific example. In this problem, the physical and the only admissible solution that satisfies the divergence-free condition is $u \equiv u_0$, where u_0 is a constant. This implies that the interface is moving along the x direction with a constant velocity u_0, and that the mechanical equilibrium is reached, i.e., the right-hand side of the momentum equation Eq.(2.34) is zero. As will be shown in the following, without delicate

consideration of the consistency conditions on the discrete level, the numerical solution fails to reproduce the physical one even in such a simple problem.

Assuming that all the cell-center and cell-face velocities are equal to the exact value u_0 and the mechanical equilibrium is reached up to t^n, the solution of u^{n+1} is investigated. As a result, the fully discretized Phase-Field and momentum equations at cell (x_i) are

$$\begin{aligned}\frac{\gamma_t^{(1)}\phi_\mathrm{i}^{n+1}-\hat{\phi}_\mathrm{i}^{(1)}}{\Delta t}+u_0\frac{\tilde{\phi}_{\mathrm{i}+1/2}^{(1)}-\tilde{\phi}_{\mathrm{i}-1/2}^{(1)}}{\Delta x}&=\frac{(M\tilde{\nabla}^{x,(1)}\xi^*)_{\mathrm{i}+1/2}-(M\tilde{\nabla}^{x,(1)}\xi^*)_{\mathrm{i}-1/2}}{\Delta x},\\ \frac{\gamma_t^{(2)}\rho_\mathrm{i}^{n+1}u_\mathrm{i}^{n+1}-u_0\hat{\rho}_\mathrm{i}^{(2)}}{\Delta t}+u_0\frac{\tilde{m}_{\mathrm{i}+1/2}^{x}-\tilde{m}_{\mathrm{i}-1/2}^{x}}{\Delta x}&=0.\end{aligned}\tag{3.12}$$

Here, the discrete differential and interpolation operators can be arbitrary, different from those in Section 3.1. To distinguish different schemes for the same differential or interpolation operators, a superscript is added, like $\gamma_t^{(l)}$ and $\tilde{\nabla}^{(l)}$ etc. ξ^* is the numerical chemical potential, whose definition depends on the specific scheme to solve the Phase-Field equation, possibly different from the one in Eq.(2.22). The right-hand side of discrete momentum equation is zero because of the mechanical equilibrium (or force-free condition). Then, the solutions of the order parameter and cell-center velocity at t^{n+1} are:

$$\begin{aligned}\phi_\mathrm{i}^{n+1}&=\frac{\hat{\phi}_\mathrm{i}^{(1)}}{\gamma_t^{(1)}}-\frac{\Delta t}{\gamma_t^{(1)}}\Big[u_0\frac{\tilde{\phi}_{\mathrm{i}+1/2}^{(1)}-\tilde{\phi}_{\mathrm{i}-1/2}^{(1)}}{\Delta x}-\frac{(M\tilde{\nabla}^{x,(1)}\xi^*)_{\mathrm{i}+1/2}-(M\tilde{\nabla}^{x,(1)}\xi^*)_{\mathrm{i}-1/2}}{\Delta x}\Big],\\ \rho_\mathrm{i}^{n+1}&=\frac{\rho_1+\rho_2}{2}+\frac{\rho_1-\rho_2}{2}\phi_\mathrm{i}^{n+1},\\ \rho_\mathrm{i}^{*}&=\frac{\rho_1+\rho_2}{2}+\frac{\rho_1-\rho_2}{2}\frac{\hat{\phi}_\mathrm{i}^{(2)}}{\gamma_t^{(2)}}-\frac{\Delta t}{\gamma_t^{(2)}}\frac{\tilde{m}_{\mathrm{i}+1/2}^{x}-\tilde{m}_{\mathrm{i}-1/2}^{x}}{\Delta x},\\ u_\mathrm{i}^{n+1}&=\frac{\rho_\mathrm{i}^{*}}{\rho_\mathrm{i}^{n+1}}u_0.\end{aligned}\tag{3.13}$$

Obviously, if $\rho_\mathrm{i}^{*}=\rho_\mathrm{i}^{n+1}$, the exact solution $u_\mathrm{i}^{n+1}=u_0$ is obtained. However, ρ_i^{*} depends on the discrete mass flux $\tilde{m}^x$, and three discrete mass fluxes are going to be discussed:

$$\begin{aligned}\tilde{m}^{IC,x}&=\tilde{\rho}^{(2)}u_0,\\ \tilde{m}^{CC,x}&=\frac{\rho_1+\rho_2}{2}u_0+\frac{\rho_1-\rho_2}{2}(u_0\tilde{\phi}^{(3)}-M\tilde{\nabla}^{x,(3)}\xi),\\ \tilde{m}^{DC,x}&=\frac{\rho_1+\rho_2}{2}u_0+\frac{\rho_1-\rho_2}{2}(u_0\tilde{\phi}^{(1)}-M\tilde{\nabla}^{x,(1)}\xi^*).\end{aligned}\tag{3.14}$$

The first one in Eq.(3.14) is the discrete inconsistent mass flux, which violates the *consistency of mass conservation* even on the continuous level, see Section 2.3. The second one is the direct discretization of the consistent mass flux in Section 2.3. The last one is the discrete consistent mass flux, which achieves the *consistency of mass conservation* on the discrete level. Notice that the discrete differential and interpolation operators and the numerical chemical potential in $\tilde{m}^{DC,x}$ are identical to those in the fully-discretized Phase-Field equation in Eq.(3.12), but this is not necessary the case in $\tilde{m}^{IC,x}$ or $\tilde{m}^{CC,x}$. The difference between the corresponding ρ_{i}^{*} and ρ_{i}^{n+1} from the discrete mass flux defined in Eq.(3.14) are:

$$
\begin{aligned}
\rho_{\mathrm{i}}^{*,IC} - \rho_{\mathrm{i}}^{n+1} &= \frac{\rho_1-\rho_2}{2}\Big(\frac{\hat{\phi}_{\mathrm{i}}^{(2)}}{\gamma_t^{(2)}} - \frac{\hat{\phi}_{\mathrm{i}}^{(1)}}{\gamma_t^{(1)}}\Big) \\
&-\frac{u_0\Delta t}{\Delta x}\Big(\frac{\tilde{\rho}_{\mathrm{i}+1/2}^{(2)} - \tilde{\rho}_{\mathrm{i}-1/2}^{(2)}}{\gamma_t^{(2)}} - \frac{\rho(\tilde{\phi}_{\mathrm{i}+1/2}^{(1)}) - \rho(\tilde{\phi}_{\mathrm{i}-1/2}^{(1)})}{\gamma_t^{(1)}}\Big) \\
&-\frac{\rho_1-\rho_2}{2}\frac{\Delta t}{\gamma_t^{(1)}}\frac{(M\tilde{\nabla}^{x,(1)}\xi^{*})_{\mathrm{i}+1/2} - (M\tilde{\nabla}^{x,(1)}\xi^{*})_{\mathrm{i}-1/2}}{\Delta x}, \\
\rho_{\mathrm{i}}^{*,CC} - \rho_{\mathrm{i}}^{n+1} &= \frac{\rho_1-\rho_2}{2}\Big(\frac{\hat{\phi}_{\mathrm{i}}^{(2)}}{\gamma_t^{(2)}} - \frac{\hat{\phi}_{\mathrm{i}}^{(1)}}{\gamma_t^{(1)}}\Big) \\
&-\frac{\rho_1-\rho_2}{2}\frac{u_0\Delta t}{\Delta x}\Big(\frac{\tilde{\phi}_{\mathrm{i}+1/2}^{(3)} - \tilde{\phi}_{\mathrm{i}-1/2}^{(3)}}{\gamma_t^{(2)}} - \frac{\tilde{\phi}_{\mathrm{i}+1/2}^{(1)} - \tilde{\phi}_{\mathrm{i}-1/2}^{(1)}}{\gamma_t^{(1)}}\Big) \\
&+\frac{\rho_1-\rho_2}{2}\frac{\Delta t}{\Delta x}\Big(\frac{(M\tilde{\nabla}^{x,(3)}\xi)_{\mathrm{i}+1/2} - (M\tilde{\nabla}^{x,(3)}\xi)_{\mathrm{i}-1/2}}{\gamma_t^{(2)}} \\
&\qquad -\frac{(M\tilde{\nabla}^{x,(1)}\xi^{*})_{\mathrm{i}+1/2} - (M\tilde{\nabla}^{x,(1)}\xi^{*})_{\mathrm{i}-1/2}}{\gamma_t^{(1)}}\Big), \\
\rho_{\mathrm{i}}^{*,DC} - \rho_{\mathrm{i}}^{n+1} &= \frac{\rho_1-\rho_2}{2}\Big(\frac{\hat{\phi}_{\mathrm{i}}^{(2)}}{\gamma_t^{(2)}} - \frac{\hat{\phi}_{\mathrm{i}}^{(1)}}{\gamma_t^{(1)}}\Big) \\
&-\frac{\rho_1-\rho_2}{2}\Delta t\Big(\frac{1}{\gamma_t^{(2)}} - \frac{1}{\gamma_t^{(1)}}\Big)\Big(u_0\frac{\tilde{\phi}_{\mathrm{i}+1/2}^{(1)} - \tilde{\phi}_{\mathrm{i}-1/2}^{(1)}}{\Delta x} \\
&\qquad -\frac{(M\tilde{\nabla}^{x,(1)}\xi^{*})_{\mathrm{i}+1/2} - (M\tilde{\nabla}^{x,(1)}\xi^{*})_{\mathrm{i}-1/2}}{\Delta x}\Big).
\end{aligned}
\tag{3.15}
$$

From Eq.(3.15), none of the discrete mass fluxes reproduce the physical solution ($u^{n+1} = u_0$ or equivalently $\rho^{*} = \rho^{n+1}$) unconditionally. The error can be categorized into four parts. The first part comes from using different time discretization schemes in the Phase-Field and

momentum equations. This is the first term in all $(\rho^* - \rho^{n+1})$ in Eq.(3.15). If the same time discretization schemes are used, i.e., $\gamma_t^{(1)} = \gamma_t^{(2)}$ and $\hat{\phi}^{(1)} = \hat{\phi}^{(2)}$, this part of error is removed. Under this circumstance, the second term on the right-hand side of $(\rho^{*,DC} - \rho^{n+1})$ also becomes zero due to $\left(\frac{1}{\gamma_t^{(1)}} - \frac{1}{\gamma_t^{(2)}}\right) = 0$. The second part is introduced by the mismatch of the discrete differential and interpolation operators in the fully discretized Phase-Field equation and in computing the discrete mass flux. The second terms of $(\rho^{*,IC} - \rho^{n+1})$ and $(\rho^{*,CC} - \rho^{n+1})$ belong to this category. It is easy to resolve this inconsistency in $(\rho^{*,CC} - \rho^{n+1})$ by requiring $\tilde{\phi}^{(3)} = \tilde{\phi}^{(1)}$ and $\tilde{\nabla}^{(3)} = \tilde{\nabla}^{(1)}$. However, it becomes more complicated in $(\rho^{*,IC} - \rho^{n+1})$ when a nonlinear interpolation scheme is used, since $\tilde{\rho}^{(2)}$ is not necessarily equal to $\rho(\tilde{\phi}^{(2)})$ in general. In other words, $\tilde{\phi}^{(2)} = \tilde{\phi}^{(1)}$ doesn't guarantee to resolve the inconsistency in $(\rho^{*,IC} - \rho^{n+1})$. The only guaranteed way is to compute $\tilde{\rho}$ by $\rho(\tilde{\phi}^{(1)})$. The third part results from using the chemical potential in Eq.(2.22) instead of the numerical one appearing in the fully discretized Phase-Field equation. The third term of $(\rho^{*,CC} - \rho^{n+1})$ is this case. Even if the first and the second sources of inconsistency are removed, this term remains because $(\xi - \xi^*)$ is in general of the order of the truncation error which is non-zero. The last part is the "model" error due to violating the *consistency of mass conservation* on the contiuous level, which is the last term in $(\rho^{*,IC} - \rho^{n+1})$.

The analysis shows that the physical solution of such a simple problem is only obtained when using the discrete consistent mass flux $\tilde{\mathbf{m}}^{DC}$ and using the same time discretization schemes for both the Phase-Field and momentum equations. Another observation is that all the inconsistent errors are proportional to the density difference between the two fluids, i.e., $(\rho_1 - \rho_2)$, implying that these errors could be more significant as the density ratio of the fluids increases. The consistency on the discrete level is more involved because, unlike on the continuous level, there are multiple ways to approximate a particular differential operator. This requires additional careful consideration. Otherwise, inconsistent errors are produced, and can become dominant in problems having large density ratios.

In the following, several general theorems that are independent of the form of the Phase-Field equation and the details of its discretization are newly proposed to help to satisfy the consistency conditions on the discrete level, so that the physical connection between the Phase-Field and momentum equations is still true after discretization.

Consistency of mass conservation on the discrete level is achieved by following Theorem 3.2.1:

Theorem 3.2.1. *Given the discrete Phase-Field fluxes* $\{\tilde{\mathbf{m}}_{\phi_p}\}_{p=1}^{N}$ *that satisfy the fully discretized Phase-Field equation:*

$$\frac{\gamma_t \phi_p^{n+1} - \hat{\phi}_p}{\Delta t} + \tilde{\nabla} \cdot \tilde{\mathbf{m}}_{\phi_p} = 0, \quad 1 \leqslant p \leqslant N,$$

and a cell-face velocity $\mathbf{u}$ *that is discretely divergence-free:*

$$\tilde{\nabla} \cdot \mathbf{u} = 0,$$

the corresponding discrete consistent mass flux is

$$\tilde{\mathbf{m}} = \sum_{p=1}^{N} \frac{\rho_p}{2} (\mathbf{u} + \tilde{\mathbf{m}}_{\phi_p}),$$

and it satisfies the consistency of mass conservation on the discrete level:

$$\frac{\gamma_t \rho^{n+1} - \hat{\rho}}{\Delta t} + \tilde{\nabla} \cdot \tilde{\mathbf{m}} = 0,$$

where γ_t, $\hat{(\cdot)}$, *and* $\tilde{\nabla} \cdot (\cdot)$ *are identical to those in the fully discretized Phase-Field equation.*

Proof.

$$\begin{aligned}
\frac{\gamma_t \rho^{n+1} - \hat{\rho}}{\Delta t} + \tilde{\nabla} \cdot \tilde{\mathbf{m}} &= \sum_{p=1}^{N} \frac{\rho_p}{2} \frac{\gamma_t (1 + \phi_p^{n+1}) - \widehat{(1 + \phi_p)}}{\Delta t} + \tilde{\nabla} \cdot \sum_{p=1}^{N} \frac{\rho_p}{2} (\mathbf{u} + \tilde{\mathbf{m}}_{\phi_p}) \\
&= \sum_{p=1}^{N} \frac{\rho_p}{2} \left(\frac{\gamma_t - \overbrace{\hat{1}}^{\gamma_t}}{\Delta t} + \underbrace{\tilde{\nabla} \cdot \mathbf{u}}_{0} \right) + \sum_{p=1}^{N} \frac{\rho_p}{2} \underbrace{\left(\frac{\gamma_t \phi_p^{n+1} - \hat{\phi}_p}{\Delta t} + \tilde{\nabla} \cdot \tilde{\mathbf{m}}_{\phi_p} \right)}_{0} = 0.
\end{aligned}$$

It should be noted that the same time discretization scheme and discrete divergence operator as those in the fully discretized Phase-Field equation need to be used so that the fully dis-

cretized Phase-Field equation is recovered. Therefore, the *consistency of mass conservation on the discrete level* is satisfied . □

Consistency of mass and momentum transport on the discrete level is achieved by following Theorem 3.2.2:

Theorem 3.2.2. *Given the fully discretized Phase-Field equation, i.e.,*

$$\frac{\gamma_t \phi_p^{n+1} - \hat{\phi}_p}{\Delta t} + \tilde{\nabla} \cdot \tilde{\mathbf{m}}_{\phi_p} = 0, \quad 1 \leqslant p \leqslant N,$$

the consistency of mass and momentum transport on the discrete level is satisfied by discretizing the left-hand side of the momentum equation Eq.(2.34) as

$$\frac{\gamma_t \rho^{n+1} \mathbf{u}^{n+1} - \widehat{\rho \mathbf{u}}}{\Delta t} + \tilde{\nabla} \cdot (\tilde{\mathbf{m}} \otimes \tilde{\mathbf{u}}),$$

where γ_t, $\hat{(\cdot)}$, and $\tilde{\nabla} \cdot (\cdot)$ are the same as those in the fully discretized Phase-Field equation, and the discrete consistent mass flux $\tilde{\mathbf{m}}$ is determined from Theorem 3.2.1.

Theorem 3.2.2 follows the definition of the *consistency of mass and momentum conservation* in Section 2.4 but additionally highlights the correspondences of the numerical operators in the fully discretized Phase-Field and momentum equations.

Consistency of reduction on the discrete level of the discrete consistent mass flux in Theorem 3.2.1 is achieved by following Theorem 3.2.3:

Theorem 3.2.3. *If the Phase-Field equation satisfies the consistency of reduction on the discrete level, then the discrete consistent mass flux from Theorem 3.2.1 is also reduction consistent, only when the cell-face velocity in Theorem 3.2.1 is evaluated in the same manner as the one in the convection fluxes of the discrete Phase-Field fluxes.*

Proof. The discrete Phase-Field flux $\tilde{\mathbf{m}}_{\phi_p}$ includes both the convection ($\mathbf{u}^{(2)}\tilde{\phi}_p$) and numerical diffusion $\mathbf{J}_p^*$ fluxes, i.e., $\tilde{\mathbf{m}}_{\phi_p} = \mathbf{u}^{(2)}\tilde{\phi}_p - \mathbf{J}_p^*$. The discrete divergence-free cell-face velocity is $\mathbf{u}^{(1)}$. From Theorem 3.2.1, the discrete consistent mass flux is $\tilde{\mathbf{m}} = \sum_{p=1}^{N} \frac{\rho_p}{2}(\mathbf{u}^{(1)} + \tilde{\mathbf{m}}_{\phi_p})$. Following the proof for Theorem 2.3.2, the contribution from absent Phase N to the discrete

consistent mass flux becomes $\frac{\rho_N}{2}(\mathbf{u}^{(1)} - \mathbf{u}^{(2)})$. Only when $\mathbf{u}^{(1)}$ and $\mathbf{u}^{(2)}$ are the same, i.e., $\mathbf{u}^{(1)} = \mathbf{u}^{(2)}$, does the contribution from absent Phase N to the discrete consistent mass flux disappear, and therefore the *consistency of reduction* is achieved by the discrete consistent mass flux in Theorem 3.2.1. □

***Remark**: Theorem 3.2.1, Theorem 3.2.2, and Theorem 3.2.3 are general. First, they do not rely on the details of the Phase-Field equation. Second, they do not rely on the details of discretizing the Phase-Field equation. They illustrate the correspondences of the numerical operations in the schemes for the Phase-Field and momentum equations. These correspondences discretely reproduce the physical connection of the Phase-Field equation, the mass conservation, and the momentum transport.*

3.3 Reduction-consistent and mass-conservative schemes

In this section, the schemes solving the Cahn-Hilliard Eq.(2.17) and conservative Allen-Cahn Eq.(2.19) equations, as well as their two-phase correspondences in Eq.(2.22) and Eq.(2.23), are introduced. Before that, several novel techniques are developed to help to ensure the order parameters in their physical interval, the summation of the order parameters, mass conservation, and the *consistency of reduction*.

3.3.1 Gradient-based phase selection procedure

The gradient-based phase selection procedure is developed for computing the convection term in the Phase-Field equation, i.e., $\{\tilde{\nabla}\cdot(\mathbf{u}\tilde{\phi}_p)\}_{p=1}^N$, where $\tilde{\nabla}\cdot(\cdot)$ is the discrete divergence operator in Eq.(3.5) and $\tilde{(\cdot)}$ represents a certain interpolation from cell-center values to cell-face ones. Written the convection term in its conservative form helps to conserve the mass due to $\sum_{\mathrm{i,j}}[\tilde{\nabla}\cdot(\mathbf{u}\tilde{\phi}_p)]_{\mathrm{i,j}} = 0$ in a periodic domain from Lemma 3.1.3. The critical requirements of computing $\{\tilde{\nabla}\cdot(\mathbf{u}\tilde{\phi}_p)\}_{p=1}^N$ is to ensure its summation over p, i.e., $\sum_{p=1}^N \tilde{\nabla}\cdot(\mathbf{u}\tilde{\phi}_p)$, to be $\tilde{\nabla}\cdot(\mathbf{u}(2-N))$ from Eq.(2.2), and the *consistency of reduction*, i.e., $[\tilde{\nabla}\cdot(\mathbf{u}\tilde{\phi}_p)]_{\mathrm{i,j}} = [-\tilde{\nabla}\cdot\mathbf{u}]_{\mathrm{i,j}}$ provided $\phi_p = -1$ around $(x_{\mathrm{i}}, y_{\mathrm{j}})$. However, these two requirements are not automatically true on the discrete level, although it is on the continuous level, since, in practice, the interpolation operator $\tilde{(\cdot)}$ is usually non-linear and performed on each phase independently.

Even though one has $\sum_{p=1}^{N}\phi_p = (2-N)$, there is nothing to guarantee $\sum_{p=1}^{N}\tilde{\phi}_p = (2-N)$. The gradient-based phase selection procedure is proposed to address the issue and it works for any interpolation operator.

The gradient-based phase selection procedure consists of the following steps at each cell face:

- *Step 1:* Compute the convection flux $\{\mathbf{u}\tilde{\phi}_p\}_{p=1}^{N}$ with any interpolation operator $\tilde{(\cdot)}$.
- *Step 2:* Compute the normal gradient of the order parameters, i.e., $\{\tilde{\nabla}^n\phi_p\}_{p=1}^{N}$.
- *Step 3:* Specify Phase q such that $|\tilde{\nabla}^n\phi_q|$ is maximum among all the phases.
- *Step 4:* Correct the convection flux of Phase q using

$$\mathbf{u}\tilde{\phi}_q = (2-N)\mathbf{u} - \sum_{p=1,p\neq q}^{N}\mathbf{u}\tilde{\phi}_p.$$

It is obvious that the summation of the convection flux over p, i.e., $\sum_{p=1}^{N}\mathbf{u}\tilde{\phi}_p$, is always $(2-N)\mathbf{u}$ at each cell face after implementing the gradient-based phase selection procedure. Therefore, one automatically obtains $\sum_{p=1}^{N}\tilde{\nabla}\cdot(\mathbf{u}\tilde{\phi}_p) = \tilde{\nabla}\cdot(\mathbf{u}(2-N))$, and the summation requirement is achieved. Provided $\phi_p = -1$ around $(x_{\mathrm{i}}, y_{\mathrm{j}})$, its normal gradient there is $|\tilde{\nabla}^n\phi_p| = 0$. Therefore, Phase p won't be selected to correct its convection flux, and this guarantees $\tilde{\nabla}\cdot(\mathbf{u}\tilde{\phi}_p) = -\tilde{\nabla}\cdot\mathbf{u}$. As a result, the requirement of *consistency of reduction* is satisfied.

It should be noted that the gradient-based phase selection procedure plays an essential role in the numerical solution of the order parameters satisfying their summation and the *consistency of reduction*. Failure of the convection term satisfying the aforementioned requirements results in the same failure of the final solution, see the analyses in Section 3.3.1, and the numerical studies in Section 4.9.

3.3.2 Boundedness mapping

The consistent and conservative volume distribution algorithm described in Section 2.2.2 is used to develop a numerical procedure, called the boundedness mapping, to tackle out-

of-bound order parameters that commonly appear in numerical practice, while the physical properties of the order parameters remain intact.

Problem statement: *Given a set of spatially discretized order parameters* $\{\phi_p\}_{p=1}^N$ *that satisfies the summation constraint Eq.(2.2), i.e.,* $\sum_{p=1}^N \phi_p = (2-N)$*, and a set of scalars* $\{S_{\phi_p}\}_{p=1}^N$ *that are the total amounts of individual order parameters in the domain, determine a mapping from* $\{\phi_p\}_{p=1}^N$ *to* $\{\phi_p^b\}_{p=1}^N$*, such that*

$$\sum_{q=1}^{N} \phi_q^b = 2-N, \quad \sum_{\mathrm{i,j}} [\phi_p^b \Delta\Omega]_{\mathrm{i,j}} = S_{\phi_p}, \quad \phi_p^b|_{\phi_p \leqslant -1} = -1, \quad \phi_p^b \in [-1,1], \quad 1 \leqslant p \leqslant N. \tag{3.16}$$

The first two constraints in Eq.(3.16) corresponds to the summation and conservation constraints of the order parameters, i.e., Eq.(2.2) and Eq.(2.8), respectively. It should be noted that admissible $\{S_{\phi_p}\}_{p=1}^N$ satisfy $\sum_{p=1}^N S_{\phi_p} = (2-N)|\Omega|$, where $|\Omega| = \sum_{\mathrm{i,j}} [\Delta\Omega]_{\mathrm{i,j}}$ is the volume of the entire domain, so that the first two constraints in Eq.(3.16) are consistent. $\{\phi_p^b\}_{p=1}^N$ are reduction consistent with $\{\phi_p\}_{p=1}^N$ in the sense that locations labeled as Phase p absent by ϕ_p are also labeled as Phase p absent by ϕ_p^b $(1 \leqslant p \leqslant N)$. This is formulated in the third constraint in Eq.(3.16). In addition, the order parameters after the mapping stay in their physical interval, which is the last constraint in Eq.(3.16).

The boundedness mapping includes the clipping step, the rescaling step, and the conservation step, which are preformed sequentially.

The clipping step is

$$\phi_p^{b*} = \begin{cases} 1, \phi_p \geqslant 1, \\ -1, \phi_p \leqslant -1, \\ \phi_p, \text{else}, \end{cases} \qquad 1 \leqslant p \leqslant N. \tag{3.17}$$

The rescaling step is

$$C_p^{b*} = \frac{1+\phi_p^{b*}}{2}, \quad C_p^{b**} = \frac{C_p^{b*}}{\sum_{q=1}^N C_q^{b*}}, \quad \phi_p^{b**} = 2C_p^{b**} - 1, \quad 1 \leqslant p \leqslant N. \tag{3.18}$$

The conservation step is

$$\phi_p^b = \phi_p^{b**} + \mathcal{L}_p^b, \quad 1 \leqslant p \leqslant N, \tag{3.19}$$

where, from Eq.(3.16), $\{\mathcal{L}_p^b\}_{p=1}^N$ have the following constraints

$$\sum_{q=1}^{N} \mathcal{L}_q^b = 0, \quad \sum_{\mathrm{i,j}} [\mathcal{L}_p^b \Delta\Omega]_{\mathrm{i,j}} = S_{\phi_p} - \sum_{\mathrm{i,j}} [\phi_p^{b**} \Delta\Omega]_{\mathrm{i,j}} = S_p^b, \quad \mathcal{L}_p^b|_{\phi_p^{b**}=-1} = 0. \tag{3.20}$$

Notice that the constraints in Eq.(3.20) for $\{\mathcal{L}_p^b\}_{p=1}^N$ are the same kind as those in Eq.(2.11) for $\{L_p\}_{p=1}^N$ in Section 2.2.2. Therefore, $\{\mathcal{L}_p^b\}_{p=1}^N$ are determined from the consistent and conservative volume distribution algorithm in Section 2.2.2 with inputs $\{\phi_p^{b**}\}_{p=1}^N$ and $\{S_p^b\}_{p=1}^N$, and the resulting $\{\mathcal{L}_p^b\}_{p=1}^N$ satisfies Eq.(3.20). It should be noted that the inputs $\{\phi_p^{b**}\}_{p=1}^N$ and $\{S_p^b\}_{p=1}^N$ are admissible because $\sum_{p=1}^N \phi_p^{b**} = (2-N)$ from the rescaling step Eq.(3.18) and $\sum_{p=1}^N S_p^b = 0$.

The clipping step Eq.(3.17) removes the out-of-bound error from the input order parameters, and the rescaling step Eq.(3.18) enforces the summation constraint for the order parameters. The intermediate results $\{\phi_p^{b**}\}_{p=1}^N$ satisfy the first and last constraints in Eq.(3.16). The conservation step Eq.(3.19) is supplemented so that the final results $\{\phi_p^b\}_{p=1}^N$ additionally satisfy the second constraint in Eq.(3.20), i.e., the amounts of the order parameters in the entire domain match the given values. After performing the boundedness mapping, i.e., the three steps above, it is obvious that the first two constraints for $\{\phi_p^b\}_{p=1}^N$ in Eq.(3.16) are enforced. The third constraint in Eq.(3.16) is also true. Given $\phi_p \leqslant -1$, from the clipping step Eq.(3.17), one obtains $\phi_p^{b*} = -1$. Therefore, both C_p^{b*} and C_p^{b**} are zero and ϕ_p^{b**} is again -1 after the rescaling step Eq.(3.18). Thanks to Eq.(3.20), one finally has $\mathcal{L}_p^b = 0$ and obtain $\phi_p^b = \phi_p^{b**} = -1$ from the conservation step Eq.(3.19). Therefore, the third constraint for $\{\phi_p^b\}_{p=1}^N$ in Eq.(3.16) is satisfied. Although the last constraint in Eq.(3.16), i.e., $\{\phi_p^b\}_{p=1}^N \in [-1, 1]$, is not explicitly enforced in the conservation step Eq.(3.19), it should be noted that out-of-bound ϕ_p^b $(1 \leqslant p \leqslant N)$, if there are any, most probably appears where $|\phi_p^{b**}|$ is close to one, due to $\mathcal{L}_p^b|_{\phi_p^{b**}=\pm 1} = 0$ and $\phi_p^{b**} \in [-1, 1]$. On the other hand, $\mathcal{L}_p^b$ is close to zero at those locations, see the formulations and analysis in Section 2.2.2. In

practice, the last constraint in Eq.(3.16), i.e., $\{\phi_p^b\}_{p=1}^N \in [-1,1]$, is found after performing the boundedness mapping. If the out-of-bound issue appears in $\{\phi_p^b\}_{p=1}^N$, one can iteratively apply the boundedness mapping, letting $\{\phi_p^b\}_{p=1}^N$ as the new input, until the boundedness constraint, i.e., $\{\phi_p^b\}_{p=1}^N \in [-1,1]$, is achieved.

One can formally proof that the proposed boundedness mapping is reduction consistent.

Theorem 3.3.1. *The boundedness mapping, including the clipping step Eq.(3.17), the rescaling step Eq.(3.18), and the conservation step Eq.(3.19), satisfies the consistency of reduction.*

Proof. Without loss of generality and for a clear presentation, the last phase of a N-phase ($N \geqslant 2$) system is absent at the location where $\phi_N = -1$. From the clipping step Eq.(3.17), one has

$$\phi_N^{b*} = -1, \quad \phi_p^{b*} = \begin{cases} 1, \phi_p \geqslant 1, \\ -1, \phi_p \leqslant -1, \\ \phi_p, \text{else}, \end{cases} \quad 1 \leqslant p \leqslant N-1.$$

From the rescaling step Eq.(3.18), one has

$$\begin{aligned} C_N^{b*} = \frac{1+\phi_N^{b*}}{2} = 0, \quad C_p^{b*} = \frac{1+\phi_p^{b*}}{2}, \quad 1 \leqslant p \leqslant N-1, \\ C_N^{b**} = \frac{C_N^{b*}}{\sum_{q=1}^N C_q^{b*}} = 0, \quad C_p^{b**} = \frac{C_p^{b*}}{\sum_{q=1}^N C_q^{b*}} = \frac{C_p^{b*}}{\sum_{q=1}^{N-1} C_q^{b*}}, \quad 1 \leqslant p \leqslant N-1, \\ \phi_N^{b**} = 2C_N^{b**} - 1 = -1, \quad \phi_p^{b**} = 2C_p^{b**} - 1, \quad 1 \leqslant p \leqslant N-1. \end{aligned}$$

From the conservation step Eq.(3.19) along with the constraints in Eq.(3.20), one has

$$\phi_N^b = \phi_N^{b**} = -1, \quad \phi_p^b = \phi_p^{b**} + \mathcal{L}_p^b, \quad 1 \leqslant p \leqslant N-1.$$

Noticing that $\{\mathcal{L}_p^b\}_{p=1}^N$ is determined by the consistent and conservative volume distribution algorithm in Section 2.2.2, which has been shown to be reduction consistent, see Theorem 2.2.1.

Therefore, the absent phase remains absent while the N-phase formulations for the other phases reduce to the corresponding $(N-1)$-phase ones. Iterating the above three steps by letting the output $\{\phi_p^b\}_{p=1}^N$ become the new input does not change the conclusion. By

induction, it concludes that the boundedness mapping satisfies the *consistency of reduction*.

□

Following the analysis in Section 2.2.2 and Eq.(2.16), the two-phase correspondence of the proposed boundedness mapping is:

$$\phi^{b*} = \begin{cases} 1, \phi \geqslant 1, \\ -1, \phi \leqslant -1, \\ \phi, \text{else}, \end{cases} \tag{3.21}$$

$$\phi^{b**} = \phi^{b*}, \quad W(\phi) = 1 - \phi^2,$$

$$\phi^b = \phi^{b**} + \frac{W(\phi^{b**})}{\sum_{\text{i,j}} [W(\phi^{b**})\Delta\Omega]_{\text{i,j}}} \left(S_\phi - \sum_{\text{i,j}} [\phi^{b**}\Delta\Omega]_{\text{i,j}} \right).$$

This is a phase-wise formulation and the rescaling step Eq.(3.18) is not needed because one can directly obtain ϕ_2^b from ϕ^b, i.e., $\phi_2^b = -\phi^b$.

In summary, the boundedness mapping, which is a numerical procedure, is developed, with the help of the consistent and conservative volume distribution algorithm in Section 2.2.2. It includes the clipping step Eq.(3.17), the rescaling step Eq.(3.18), and the conservation step Eq.(3.19), and is shown to be reduction consistent. Given a set of out-of-bound order parameters, the output of the mapping, i.e., $\{\phi_p^b\}_{p=1}^N$, not only are bounded by their physical interval, i.e., $[-1, 1]$ in the present work, but also satisfy the summation constraint for the order parameters Eq.(2.2), i.e., $\sum_{p=1}^N \phi_p^b = (2 - N)$, match the given amounts of the order parameters in the entire domain $\{S_{\phi_p}\}_{p=1}^N$, and is reduction consistent with the input order parameters $\{\phi_p\}_{p=1}^N$ in the sense that Phase p $(1 \leqslant p \leqslant N)$ won't be mapped to the location where Phase p is labeled absent by ϕ_p. This mapping is directly applicable to numerical solutions of various multiphase models.

3.3.3 Scheme for the Cahn-Hilliard equation

This section introduces the schemes to solve the Cahn-Hilliard Phase-Field equation Eq.(2.17) and its two-phase correspondence Eq.(2.22), and analyzes the physical properties of the schemes.

The solution of the Cahn-Hilliard Phase-Field equation Eq.(2.17) is obtained by solving the following two Helmholtz equations successively for each phase, i.e., $1 \leqslant p \leqslant N$.

Step 1: Solve for an auxiliary variable ψ_p^{n+1} from

$$\begin{aligned}\tilde{\nabla}\cdot(\tilde{\nabla}\psi_p^{n+1}) - (\alpha+S)\psi_p^{n+1} = \left[\tilde{\nabla}\cdot(\tilde{\nabla}\psi_p^{*,n+1}) - (\alpha+S)\tilde{\nabla}\cdot(\tilde{\nabla}\phi_p^{*,n+1})\right] \\ +\frac{1}{\gamma_0}\left[\frac{\hat{\phi}_p}{\Delta t} - \tilde{\nabla}\cdot\left(\mathbf{u}^{*,n+1}\tilde{\phi}_p^{*,n+1}\right) + \sum_{q=1}^{N}\tilde{\nabla}\cdot\left(\overline{M_{p,q}^{*,n+1}}\tilde{\nabla}\xi_q^{*,n+1}\right) + S_{\phi_p}^{n+1}\right],\end{aligned} \tag{3.22}$$

where α satisfies

$$\alpha^2 + S\alpha + \frac{\gamma_t}{\gamma_0\Delta t} = 0, \tag{3.23}$$

or explicitly, $\alpha = \frac{1}{2}\left[-S + \sqrt{S^2 - \frac{4\gamma_t}{\gamma_0\Delta t}}\right]$ with $S \geqslant \sqrt{\frac{4\gamma_t}{\gamma_0\Delta t}}$, and $\gamma_0 = NM_0\sum_{p,q=1}^{N}\lambda_{p,q}$. The source term $S_{\phi_p}^{n+1}$ is only non-zero in the manufactured solution problem, i.e., in Section 4.1.

Step 2: Solve for the order parameter at $n+1$ time level, ϕ_p^{n+1}, from

$$\tilde{\nabla}\cdot(\tilde{\nabla}\phi_p^{n+1}) + \alpha\phi_p^{n+1} = \psi_p^{n+1}. \tag{3.24}$$

The boundary conditions, unless otherwise specified, for ϕ_p^{n+1} and ψ_p^{n+1} are

$$\mathbf{n}\cdot\tilde{\nabla}\phi_p^{n+1} = \sum_{q=1}^{N}\zeta_{p,q}\frac{1+\phi_p^{*,n+1}}{2}\frac{1+\phi_q^{*,n+1}}{2}, \tag{3.25}$$

$$\mathbf{n}\cdot\tilde{\nabla}\psi_p^{n+1} = \mathbf{n}\cdot\tilde{\nabla}\left[\psi_p^{*,n+1} + (\alpha+S)(\phi_p^{n+1} - \phi_p^{*,n+1})\right] + \frac{1}{\gamma_0}\sum_{q=1}^{N}\mathbf{n}\cdot\left(\overline{M_{p,q}^{*,n+1}}\tilde{\nabla}\xi_q^{*,n+1}\right),$$

where $\zeta_{p,q}$ is computed from Eq.(2.21) with $\{\theta_{p,q}^W\}_{p,q=1}^N = \frac{\pi}{2}$, unless otherwise specified.

The scheme is originated in [75] while several modifications are proposed in the present work to fix the issues of the original one. First, to achieve the mass conservation discretely, the convection term is computed from its conservative form, i.e., $\nabla\cdot(\mathbf{u}\phi_p)$, while in [75], it is computed from its non-conservative form, i.e., $\mathbf{u}\cdot\nabla\phi_p$. Second, to honor the *consistency of reduction*, all the order parameters are computed from Eq.(3.22) and Eq.(3.24). However, in [75], only the first $(N-1)$ order parameters are solved from Eq.(3.22) and Eq.(3.24), and the last one is obtained algebraically from their summation Eq.(2.2). Such an implementation in

[75] can easily violate the *consistency of reduction* and produce fictitious phases numerically, see Theorem 3.3.4 and the numerical studies in Section 4.9. Third, to avoid generating local voids or overfilling, the gradient-based phase selection procedure in Section 3.3.1 is implemented so that the summation of the order parameters, i.e., Eq.(2.2), is satisfied, and the *consistency of reduction* remains intact.

The fully discretized Cahn-Hilliard Phase-Field equation is

$$\begin{aligned}\frac{\gamma_t\phi_p^{n+1}-\hat{\phi}_p}{\Delta t}+\tilde{\nabla}\cdot\left(\mathbf{u}^{*,n+1}\tilde{\phi}_p^{*,n+1}\right)=\sum_{q=1}^{N}\tilde{\nabla}\cdot\overline{M_{p,q}^{*,n+1}}\tilde{\nabla}\xi_q^{*,n+1}+S_{\phi_p}^{n+1}\\ -\gamma_0\tilde{\nabla}\cdot\tilde{\nabla}\left[(\psi_p^{n+1}-\psi_p^{*,n+1})-(\alpha+S)(\phi_p^{n+1}-\phi_p^{*,n+1})\right].\end{aligned}\tag{3.26}$$

The last term on the right-hand side of Eq.(3.26) is newly introduced. It comes from decoupling the Cahn-Hilliard Phase-Field equation in Eq.(2.17) and is zero on the continuous level. To consider the formal order of accuracy, one has assumed that the solution of Eq.(3.26) is smooth enough in both time and space such that their Taylor expansions exist. As mentioned in Section 3.1, all the discrete operators are 2nd-order accurate and the 2nd-order backward difference is used for time discretization. If all the terms in Eq.(3.26) are evaluated at the time level $n+1$, the proposed scheme is 2nd-order accurate in time. However, this leads to a fully-coupled and non-linear system, which is difficult and cost to solve. Instead, some of the terms, denoted with a superscript "$*, n+1$", are evaluated explicitly and the difference between $f^{*,n+1}$ and f^{n+1} is $O(\Delta t^2)$, where f is a smooth function. As a result, the 2nd-order accuracy in time is maintained in Eq.(3.26). Thus, the proposed scheme is formally 2nd-order accurate in both time and space. Additionally, the scheme including the newly proposed gradient-based phase selection procedure in Section 3.3.1 has the following physical properties on the discrete level:

- It satisfies the mass conservation, see Theorem 3.3.2 and its corollary.
- It satisfies the summation of the order parameters at every discrete cell, see Theorem 3.3.3.
- It satisfies the *consistency of reduction*, see Theorem 3.3.4.

Theorem 3.3.2. *The scheme for the Cahn-Hilliard Phase-Field equation Eq.(2.17) satisfies the mass conservation of each phase,i.e.,*

$$[\text{Mass}]_p^n = [\text{Mass}]_p^0, \quad 1 \leqslant p \leqslant N,$$

where $[\text{Mass}]_p^n = \sum_{\text{i,j}} \left[\rho_p \frac{1+\phi_p^n}{2}\right]_{\text{i,j}} \Delta x \Delta y$.

Proof. Given $\sum_{\text{i,j}} [\phi_p]_{\text{i,j}}^n = \sum_{\text{i,j}} [\phi_p]_{\text{i,j}}^{n-1} = ... = \sum_{\text{i,j}} [\phi_p]_{\text{i,j}}^0$, one immediately obtains $\sum_{\text{i,j}} [\hat{\phi}_p]_{\text{i,j}} = \widehat{\sum_{\text{i,j}} [\phi_p]_{\text{i,j}}} = \gamma_t \sum_{\text{i,j}} [\phi_p]_{\text{i,j}}^0$. Summing the fully-discretized Phase-Field equation Eq.(3.26) over all the cells and applying Lemma 3.1.3, one reaches

$$\sum_{\text{i,j}} [\phi_p^{n+1}]_{\text{i,j}} = \frac{1}{\gamma_t} \sum_{\text{i,j}} [\hat{\phi}_p]_{\text{i,j}} = \sum_{\text{i,j}} [\phi_p]_{\text{i,j}}^0, \quad 1 \leqslant p \leqslant N.$$

Therefore the total masses of individual phases, i.e., $[\text{Mass}]_p = \sum_{\text{i,j}} \left[\rho_p \frac{1+\phi_p}{2}\right]_{\text{i,j}} \Delta x \Delta y, 1 \leqslant p \leqslant N$, are time-independent. □

Corollary 3.3.2.1. *The scheme for the Cahn-Hilliard Phase-Field equation Eq.(2.17) conserves the total mass of the fluid mixture,i.e.,*

$$[\text{Mass}]^n = [\text{Mass}]^0$$

where, $[\text{Mass}]^n = \sum_{\text{i,j}} [\rho^n]_{\text{i,j}} \Delta x \Delta y$.

Proof. From Eq.(2.3),

$$\begin{aligned}[\text{Mass}]^n = \sum_{\text{i,j}} [\rho^n]_{\text{i,j}} \Delta x \Delta y &= \sum_{\text{i,j}} \sum_{p=1}^{N} \left[\rho_p \frac{1+\phi_p^n}{2}\right]_{\text{i,j}} \Delta x \Delta y \\ &= \sum_{p=1}^{N} [\text{Mass}]_p^n = \sum_{p=1}^{N} [\text{Mass}]_p^0 = [\text{Mass}]^0.\end{aligned}$$

Another way to proof is to consider the fully-discretized mass conservation equation in Theorem 3.2.1 and apply Lemma 3.1.3. □

Theorem 3.3.3. *The scheme for the Cahn-Hilliard Phase-Field equation Eq.(2.17) guarantees Eq.(2.2), i.e.,*

$$\sum_{p=1}^{N}\phi_p = 2-N \quad \text{or} \quad \sum_{p=1}^{N}\frac{\phi_p+1}{2}=1,$$

and therefore no local void or overfilling is produced numerically.

Proof. For a clear presentation, $\sum_{p=1}^{N}[\phi_p]_{\mathrm{i,j}}$ and $\sum_{p=1}^{N}[\psi_p]_{\mathrm{i,j}}$ are denoted as $\Phi_{\mathrm{i,j}}$ and $\Psi_{\mathrm{i,j}}$, respectively, and all the subscripts are dropped in the following analysis since it works for every $(x_{\mathrm{i}}, y_{\mathrm{j}})$. Given $\Phi^n = \Phi^{n-1} = ... = \Phi^0 = 2-N$, one immediately obtains $\Phi^{*,n+1} = 2-N$, $\hat{\Phi} = \gamma_t(2-N)$, $\Psi^{*,n+1} = \alpha(2-N)$ from Eq.(3.24), $\sum_{p=1}^{N}\overline{M_{p,q}^{*,n+1}} = \overline{\sum_{p=1}^{N}M_{p,q}^{*,n+1}} = 0$ from Eq.(2.17). With the help of the proposed gradient-based phase selection procedure and the discretely divergence-free cell-face velocity, the summation of the convective term over p is $\sum_{p=1}^{N}\tilde{\nabla}\cdot(\mathbf{u}^{*,n+1}\tilde{\phi}_p^{*,n+1}) = (2-N)\tilde{\nabla}\cdot\mathbf{u}^{*,n+1} = 0$. Summing Eq.(3.22) over p and combining everything together, one reaches the equation for Ψ^{n+1}, i.e.,

$$\tilde{\nabla}\cdot(\tilde{\nabla}\Psi^{n+1}) - (\alpha+S)\Psi^{n+1} = \frac{\gamma_t(2-N)}{\gamma_0\Delta t},$$

and $\Psi^{n+1} = \alpha(2-N)$ is the solution after noting that α satisfies Eq.(3.23). The equation for Φ is obtained by summing Eq.(3.24) over p, i.e.,

$$\tilde{\nabla}\cdot(\tilde{\nabla}\Phi^{n+1}) + \alpha\Phi^{n+1} = \Psi^{n+1},$$

and the solution of Φ^{n+1} is $(2-N)$ after plugging in $\Psi^{n+1} = \alpha(2-N)$. Finally one has $\Phi^{n+1} = \sum_{p=1}^{N}\phi_p = 2-N$, as well as $\sum_{p=1}^{N}\frac{1+\phi_p^{n+1}}{2} = 1$, at every (i,j). □

Remark: *The proposed gradient-based phase selection procedure is essential in the proof. Without performing this procedure, the summation of the convection term in Eq.(3.22) over p is not zero, and the proof of Theorem 3.3.3 fails. The numerical test in Section 4.9 shows that although the difference between Φ^{n+1} and Φ^n is tiny when the WENO scheme is used to compute all $\{\tilde{\phi}_p\}_{p=1}^{N}$ but without performing the gradient-based phase selection procedure to correct the convection flux, its accumulation makes the difference between Φ^{n+1} and Φ^0 noticeable in long-time simulations. Physically speaking, this corresponds to generating local*

voids or overfilling. One may notice that the proof requires the discretely divergence-free cell-face velocity. This is true in the present study, see Section 3.5

Theorem 3.3.4. *The scheme for the Cahn-Hilliard Phase-Field equation Eq.(2.17) satisfies the consistency of reduction on the discrete level.*

Proof. Given Phase N absent up time level n, i.e., $\phi_N^n, \phi_N^{n-1}, ..., \phi_N^0 \equiv -1$, one immediately has $\phi_N^{*,n+1} \equiv -1$, $M_{N,q}^{*,n+1} = M_{q,N}^{*,n+1} = 0$ from Eq.(2.17), $\hat{\phi}_N = -\gamma_t$ from Section 3.1, and $\psi_N^{*,n+1} = -\alpha$ from Eq.(3.24).

In the first part, the scheme for $p = N$ is considered. Since the gradient of $\phi_N^{*,n+1} \equiv -1$ is zero, the proposed gradient-based phase selection procedure does not choose Phase N to correct its convection flux. Then, any admissible interpolation operator should return $\tilde{\phi}_N^{*,n+1} = -1$ and the convection term $\tilde{\nabla} \cdot \left(\mathbf{u}^{*,n+1}\tilde{\phi}_N^{*,n+1}\right)$ is zero, thanks to satisfying the divergence-free condition discretely at all the previous time levels. Combining everything together, Eq.(3.22) for $p = N$ becomes

$$\tilde{\nabla} \cdot (\tilde{\nabla}\psi_N^{n+1}) - (\alpha + S)\psi_N^{n+1} = -\frac{\gamma_t}{\gamma_0 \Delta t},$$

and its solution is $\psi_N^{n+1} = -\alpha$ after noting that α satisfies Eq.(3.23). Plugging this into Eq.(3.24), it is obvious that $\phi_N^{n+1} = -1$ is the solution. Therefore, Phase N, which is absent initially, won't be generated numerically by the scheme, and the first part of the analysis is completed.

In the second part, the scheme for Phase p ($p \neq N$) is considered and it reduces to the corresponding $(N-1)$-phase one. From Eq.(3.22) and Eq.(3.24), the only coupling term between different phases is $\sum_{q=1}^{N} \tilde{\nabla} \cdot \left(\overline{M_{p,q}^{*,n+1}}\tilde{\nabla}\xi_q^{*,n+1}\right)$. As $M_{p,N}^{*,n+1} = 0$ from Eq.(2.17), the coupling term reduces to $\sum_{q=1}^{N-1} \tilde{\nabla} \cdot \left(\overline{M_{p,q}^{*,n+1}}\tilde{\nabla}\xi_q^{*,n+1}\right)$. As $g_2(\phi-1) = g_1(\phi)$ and $\tilde{\nabla}\cdot(\tilde{\nabla}\phi_N^{*,n+1}) = 0$ are still true on the discrete level, the chemical potentials recover the corresponding $(N-1)$-phase formulation, which has been shown in Corollary 2.4.5.1. Therefore, the scheme for p ($p \neq N$) reduces to the one excluding Phase N.

In conclusion, the *consistency of reduction* is satisfied by the scheme for the Cahn-Hilliard Phase-Field equation Eq.(2.17). □

Remark: *Solving all the order parameters from their Phase-Field equation and applying the proposed gradient-based phase selection procedure are essential to achieve the consistency of reduction on the discrete level. In many previous studies, e.g., in [65], [66], [68], [72]–[75], only the first* $(N-1)$ *phases are solved from their Phase-Field equation, and the last phase is obtained from their summation, i.e., Eq.(2.2). This is equivalent to always correcting the convection flux of Phase* N*. Such a strategy can violate the consistency of reduction and, as a result, generate fictitious phases. Continuing the example where Phase* N *is absent,* $\{\tilde{\phi}_p\}_{p=1}^{N-1}$ *in the convection flux are computed independently with probably a non-linear interpolation. Therefore,* $\sum_{p=1}^{N-1}\tilde{\phi}_p$ *is not necessary to be* $3-N$*. Since* $\sum_{p=1}^{N}\tilde{\phi}_p = 2-N$ *is always enforced by adjusting the convection flux of Phase* N*, one finally has* $\tilde{\phi}_N \neq -1$*. As a result, the convection term becomes a numerical source to produce the absent phase. The behavior of producing fictitious phases is demonstrated in the numerical test in Section 4.9.*

The scheme to solve the two-phase Cahn-Hilliard Phase-Field equation Eq.(2.22) (with a constant mobility) is the same as the convex splitting scheme in [79], [112]:

Step 1: Solve for an auxiliary variable ψ from

$$\begin{aligned}\tilde{\nabla}\cdot(\tilde{\nabla}\psi) - \Big(\alpha + \frac{S}{\eta^2}\Big)\psi = \frac{1}{\lambda M}\Big[\frac{\hat{\phi}}{\Delta t} - \tilde{\nabla}\cdot(\mathbf{u}^{*,n+1}\tilde{\phi}^{*,n+1}) + S_\phi^{n+1}\Big] \\ + \frac{1}{\eta^2}\Big[\tilde{\nabla}\cdot(\tilde{\nabla}g_1'(\phi^{*,n+1})) - S\tilde{\nabla}\cdot(\tilde{\nabla}\phi^{*,n+1})\Big],\end{aligned} \tag{3.27}$$

where α and S are

$$\alpha = -\frac{S}{2\eta^2}\Big[1 + \sqrt{1 - \frac{4\gamma_t}{\lambda M\Delta t}\frac{\eta^4}{S^2}}\Big], \quad \frac{S}{\eta^2} \geq \sqrt{\frac{4\gamma_t}{\lambda M\Delta t}}.$$

Step 2: Solve for ϕ^{n+1} from

$$\tilde{\nabla}\cdot(\tilde{\nabla}\phi^{n+1}) + \alpha\phi^{n+1} = \psi. \tag{3.28}$$

The boundary conditions, unless otherwise specified, for ϕ^{n+1} and ψ are

$$\mathbf{n}\cdot\tilde{\nabla}\phi^{n+1} = \frac{\sqrt{2}}{3\eta}\cos(\theta^W)g'_w(\phi^{*,n+1}), \tag{3.29}$$
$$\mathbf{n}\cdot\tilde{\nabla}\psi = \mathbf{n}\cdot\tilde{\nabla}\left[\frac{1}{\eta^2}g'_1(\phi^{*,n+1}) - \frac{S}{\eta^2}\phi^{*,n+1}\right] + (\alpha+\frac{S}{\eta^2})(\mathbf{n}\cdot\tilde{\nabla}\phi^{n+1}),$$

where θ^W is 90^0 unless otherwise specified.

This scheme leads to the following fully discretized Phase-Field equation:

$$\frac{\gamma_t\phi^{n+1}-\hat{\phi}}{\Delta t} + \tilde{\nabla}\cdot(\mathbf{u}^{*,n+1}\tilde{\phi}^{*,n+1}) = M\tilde{\nabla}\cdot(\tilde{\nabla}\xi^*) + S_\phi^{n+1}, \tag{3.30}$$
$$\xi^* = \lambda\Big(\frac{1}{\eta^2}g'_1(\phi^{*,n+1}) - \tilde{\nabla}\cdot(\tilde{\nabla}\phi^{n+1})\Big) + \frac{\lambda S}{\eta^2}(\phi^{n+1}-\phi^{*,n+1}).$$

The scheme for the two-phase Cahn-Hilliar Phase-Field equation Eq.(2.22) is formally 2nd-order accurate and mass conservative, and the analyses are similar to those of the scheme for Eq.(2.17). The *consistency of reduction* is obvious because ξ^* is zero when $\phi\equiv\pm1$.

3.3.4 Scheme for the conservative Allen-Cahn equaiton

This section introduces the schemes to solve the conservative Allen-Cahn Phase-Field equation Eq.(2.19) and its two-phase correspondence Eq.(2.23), and analyzes the physical properties of the schemes.

The scheme to solve the conservative Allen-Cahn Phase-Field equation Eq.(2.19) is:

Step 1: Solve the Allen-Cahn equation, i.e., Eq.(2.19) excluding all the Lagrange multiplies L^s and L^c_p, from

$$\frac{\gamma_t\phi_p^*-\hat{\phi}_p}{\Delta t} + \tilde{\nabla}\cdot(\mathbf{u}^{*,n+1}\tilde{\phi}_p^{*,n+1}) = M_0\lambda_0\tilde{\nabla}\cdot\tilde{\nabla}\phi_p^* - \frac{M_0\lambda_0}{\eta^2}\tilde{g}'_1(\phi_p^*), \quad 1\leqslant p\leqslant N, \tag{3.31}$$

where $\tilde{g}_1(\phi_p^*)$ is the linear approximation of $g_1(\phi_p^*)$ from its Taylor expansion at ϕ_p^n, i.e.,

$$\tilde{g}'_1(\phi_p^*) = g'_1(\phi_p^n) + g''_1(\phi_p^n)(\phi_p^*-\phi_p^n), \quad 1\leqslant p\leqslant N. \tag{3.32}$$

Notice that the gradient-based phase selection procedure in Section 3.3.1 is implemented when computing the convection term.

Step 2: Compute the discrete Lagrange multiplier $\tilde{L}_s$ from

$$\tilde{L}^s = \sum_{p=1}^{N} \left(\tilde{g}_1'(\phi_p^*) - \eta^2 \tilde{\nabla} \cdot \tilde{\nabla} \phi_p^* \right). \tag{3.33}$$

Compared to Eq.(2.19), the appearance of $\tilde{\nabla} \cdot \tilde{\nabla} \phi_p^*$ in Eq.(3.33) is due to $\sum_{p=1}^{N} \phi_p^* \neq (2-N)$.

Step 3: Compute the discrete Lagrange multipliers $\{\tilde{L}_p^c\}_{p=1}^N$ from the consistent and conservative volume distribution algorithm in Section 2.2.2, and the inputs are $\{\phi_p^n\}_{p=1}^N$ and $\{\tilde{S}_p^c\}_{p=1}^N$. Here

$$\tilde{S}_p^c = \sum_{\mathrm{i,j}} \left[\frac{M_0 \lambda_0}{\eta^2} \left(\tilde{g}_1'(\phi_p^*) - \frac{1+\phi_p^n}{2} \tilde{L}^s \right) \Delta\Omega - M_0 \lambda_0 (\tilde{\nabla} \cdot \tilde{\nabla} \phi_p^*) \Delta\Omega \right]_{\mathrm{i,j}}, \quad 1 \leqslant p \leqslant N. \tag{3.34}$$

The resulting $\{\tilde{L}_p^c\}_{p=1}^N$ not only are reduction consistent, see Theorem 2.2.1, but also satisfy Eq.(2.11) on the discrete level, i.e.,

$$\sum_{q=1}^{N} \tilde{L}_q^c = 0, \quad \sum_{\mathrm{i,j}} [\tilde{L}_p^c \Delta\Omega]_{\mathrm{i,j}} = \tilde{S}_p^c, \quad \tilde{L}_p^c|_{\phi_p^n = -1} = 0, \quad 1 \leqslant p \leqslant N. \tag{3.35}$$

Notice that the Laplacian in Eq.(3.34) can be excluded when the contact angles are 90^0.

Step 4: Obtain the solution at time level $n+1$ from

$$\frac{\gamma_t \phi_p^{n+1} - \gamma_t \phi_p^*}{\Delta t} = \frac{M_0 \lambda_0}{\eta^2} \frac{1+\phi_p^n}{2} \tilde{L}^s + \tilde{L}_p^c, \quad 1 \leqslant p \leqslant N. \tag{3.36}$$

The boundary condition for ϕ is identical to the one in Eq.(3.25) unless otherwise specified.

The fully discretized equation of the conservative Allen-Cahn Phase-Field equation Eq.(2.19) from the proposed scheme is

$$\frac{\gamma_t \phi_p^{n+1} - \hat{\phi}_p}{\Delta t} + \tilde{\nabla} \cdot (\mathbf{u}^{*,n+1} \tilde{\phi}_p^{*,n+1}) = M_0 \lambda_0 \tilde{\nabla} \cdot \tilde{\nabla} \phi_p^* - \frac{M_0 \lambda_0}{\eta^2} \left(\tilde{g}_1(\phi_p^*) - \frac{1+\phi_p^n}{2} \tilde{L}^s \right) + \tilde{L}_p^c. \tag{3.37}$$

Outside the interfacial region, there is no contribution from the Lagrange multipliers, and one has $\phi_p^{n+1} = \phi_p^*$. In Eq.(3.31), $(\phi^{n+1} - \phi^{*,n+1}) \sim O(\Delta t^2)$ and from Eq.(3.32) $(\tilde{g}'(\phi^*) - g'(\phi^*)) \sim O(\phi^* - \phi^n)^2 \sim O(\Delta t^2)$. The correction introduced by the Lagrange multipliers is effective only in the interfacial region, which occupies a small portion of the domain, and is expected to be small in one time step. As a result, the scheme for the conservative Allen-Cahn equation Eq.(2.19) is expected to be 2nd-order accurate, which will be examined numerically in Section 4.1. Additionally, the scheme including the newly proposed gradient-based phase selection procedure in Section 3.3.1 has the following physical properties on the discrete level:

- It satisfies the mass conservation, see Theorem 3.3.5.
- It satisfies the summation of the order parameters at every discrete cell, see Theorem 3.3.6.
- It satisfies the *consistency of reduction*, see Theorem 3.3.7.

Theorem 3.3.5. *The scheme for the conservative Allen-Cahn equation Eq.(2.19) satisfies the mass conservation of each phase:*

$$\sum_{\mathrm{i,j}} [\rho_p \frac{1+\phi_p^n}{2} \Delta\Omega]_{\mathrm{i,j}} = \sum_{\mathrm{i,j}} [\rho_p \frac{1+\phi_p^0}{2} \Delta\Omega]_{\mathrm{i,j}}, \quad 1 \leqslant p \leqslant N.$$

Proof. Given $\sum_{\mathrm{i,j}} [\phi_p^n \Delta\Omega]_{\mathrm{i,j}} = \sum_{\mathrm{i,j}} [\phi_p^{n-1} \Delta\Omega]_{\mathrm{i,j}} = \cdots = \sum_{\mathrm{i,j}} [\phi_p^0 \Delta\Omega]_{\mathrm{i,j}}$, and summing Eq.(3.37) over all the cells after multiplying it to $\Delta\Omega$, one has $\sum_{\mathrm{i,j}} [\hat{\phi}_p \Delta\Omega]_{\mathrm{i,j}} = \sum_{nC} \widehat{[\phi_p \Delta\Omega]}_{\mathrm{i,j}} = \gamma_t \sum_{\mathrm{i,j}} [\phi_p^0 \Delta\Omega]_{\mathrm{i,j}}$. All the terms having the discrete divergence operator in Eq.(3.37) vanish after the summation, as proofed in Section 3.1. From Eq.(3.34) and the second property of $\{\tilde{L}_p^c\}_{p=1}^N$ in Eq.(3.35), the right-hand side of the summed Eq.(3.37) over i, j becomes zero. At the end, one reaches

$$\sum_{\mathrm{i,j}} [\phi_p^{n+1} \Delta\Omega]_{\mathrm{i,j}} = \frac{1}{\gamma_t} \sum_{\mathrm{i,j}} [\hat{\phi}_p \Delta\Omega]_{\mathrm{i,j}} = \sum_{\mathrm{i,j}} [\phi_p^0 \Delta\Omega]_{\mathrm{i,j}}, \quad 1 \leqslant p \leqslant N.$$

Therefore, the mass conservation of each phase is true. □

***Remark**: From Theorem 3.3.5, Corollary 3.3.2.1 is again true.*

Theorem 3.3.6. *The scheme for the conservative Allen-Cahn equation Eq.(2.19) satisfies the summation of the order parameters Eq.(2.2), i.e.,*

$$\sum_{p=1}^{N} \phi_p = (2 - N),$$

at every discrete location and time level.

Proof. Given $\sum_{p=1}^{N} \phi_p^n = \sum_{p=1}^{N} \phi_p^{n-1} = \cdots = \sum_{p=1}^{N} \phi_p^0 = (2 - N)$ at every discrete cell in the domain, and summing Eq.(3.37) over all p, one has $\sum_{p=1}^{N} \hat{\phi}_p = \widehat{\sum_{p=1}^{N} \phi_p} = \gamma_t(2 - N)$, $\sum_{p=1}^{N} \tilde{\nabla} \cdot (\mathbf{u}^{*,n+1} \tilde{\phi}_p^{*,n+1}) = 0$, and $\sum_{p=1}^{N} \frac{1+\phi_p^n}{2} = 1$. From Eq.(3.33) and the first property of $\{\tilde{L}_p^c\}_{p=1}^{N}$ in Eq.(3.35), the right-hand side of the summed Eq.(3.37) over p becomes zero. At the end, one reaches

$$\sum_{p=1}^{N} \phi_p^{n+1} = \frac{1}{\gamma_t} \sum_{p=1}^{N} \hat{\phi}_p = (2 - N),$$

at every discrete location. By induction, $\sum_{p=1}^{N} \phi_p = (2 - N)$ is true at every time level. □

Theorem 3.3.7. *The scheme for the conservative Allen-Cahn equation Eq.(2.19) satisfies the consistency of reduction on the discrete level.*

Proof. Without loss of generality and for a clear presentation, the last phase of a N-phase ($N \geqslant 2$) system is absent globally, i.e., $\phi_N = -1$ in the entire domain.

Consider the absent phase, i.e., Phase N, first, and one has $\phi_N^n = \phi_N^{*,n+1} = -1$, $\hat{\phi}_N = -\gamma_t$, $\tilde{\nabla} \cdot (\mathbf{u}^{*,n+1} \tilde{\phi}_N^{*,n+1}) = -\tilde{\nabla} \cdot \mathbf{u}^{*,n+1} = 0$, and $\tilde{g}_1'(\phi_N^*) = 2(\phi_N^* + 1)$. Then $\phi_N^* = -1$ is the solution of **Step 1** Eq.(3.31). One does not need to consider **Step 2** at this moment. From **Step 3**, i.e., the last property of $\{\tilde{L}_p^c\}_{p=1}^{N}$ in Eq.(3.35), one has $\tilde{L}_N^c = 0$, and finally from **Step 4** Eq.(3.36) one obtains $\phi_N^{n+1} = \phi_N^* = -1$.

For the rest of the phases, **Step 1** Eq.(3.31) does not include any coupling among the phases so it automatically satisfies the *consistency of reduction*. The contribution of Phase N to $\tilde{L}^s$ in **Step 2** disappears due to $\tilde{\nabla} \cdot \tilde{\nabla} \phi_N^* = \tilde{g}_1'(\phi_N^*) = 0$, and, as a result, the summation in Eq.(3.33) is only from $p = 1$ to $p = N - 1$. $\{\tilde{L}_p^c\}_{p=1}^{N}$ in **Step 3** is determined by the consistent and conservative volume distribution algorithm in Section 2.2.2, and therefore it

is reduction consistent, see Theorem 2.2.1. Consequently, all the terms in **Step 4** Eq.(3.36) for the rest of the phases reduce to the corresponding $(N-1)$-phase ones.

In summary, the absent phase, i.e., Phase N, remains absent, and the rest of the phases are updated from the formulations that reduce to the corresponding $(N-1)$-phase ones, without any influences from the absent phase. By induction, the *consistency of reduction* is satisfied by the proposed scheme on the discrete level. □

Remark:

- *When discussing the consistency of reduction on the discrete level, Phase N is absent globally for convenience. It becomes more involved when considering the local absence because there is a matrix inversion, which couples all the information in the domain, in* ***Step 1*** *Eq.(3.31). If a fully explicit scheme is used in* ***Step 1*** *Eq.(3.31), then at the location where $\phi_N^n = \phi_N^{*,n+1} = -1$ and $|\tilde{\nabla}\tilde{\phi}_N^{*,n+1}| = \tilde{\nabla}\cdot\tilde{\nabla}\phi_N^n = 0$, the consistency of reduction can be proof in the same manner. The difference of the solutions from the present scheme in* ***Step 1*** *Eq.(3.31) and the fully explicit scheme is of the order of $\frac{\partial\phi_N^*}{\partial t}\Delta t$, where $\frac{\partial\phi_N^*}{\partial t}$ is the time derivative of the Allen-Cahn equation. As a result, the highest spatial derivative in the difference of the schemes is $\tilde{\nabla}\cdot\tilde{\nabla}(\tilde{\nabla}\cdot\tilde{\nabla}\phi_N^n)$. It is reasonable to expect that Theorem 3.3.7 is still valid at the location where $\phi_N^n = \phi_N^{*,n+1} = -1$ and $|\tilde{\nabla}\tilde{\phi}_N^{*,n+1}| = \tilde{\nabla}\cdot\tilde{\nabla}\phi_N^n = |\tilde{\nabla}\cdot\tilde{\nabla}(\tilde{\nabla}\tilde{\phi}_N^{*,n+1})| = \tilde{\nabla}\cdot\tilde{\nabla}(\tilde{\nabla}\cdot\tilde{\nabla}\phi_N^n) = 0$. A similar argument can be made for Theorem 3.3.4. The numerical implementation in Section 4.2 demonstrates that the consistency of reduction on the discrete level holds locally and the results are shown in Fig.4.12.*

- *It is suggested in [66] that the prefactor $\frac{1+\phi_p}{2}$ of L^s in Eq.(2.19) is replaced by $\left(\frac{1+\phi_p}{2}\right)^{\gamma_s}$, where γ_s is larger than 1, in order to reduce the amount of fictitious phases. The numerical results in [66] indicate that by increasing γ_s by 1, the peak of the fictitious phase is about two orders of magnitude smaller. However, as shown in Theorem 2.2.4 and Theorem 3.3.7, both the proposed conservative Allen-Cahn equation Eq.(2.19) using $\frac{1+\phi_p}{2}$ ahead of L^s and its numerical scheme developed in this section are reduction consistent. Therefore, the production of any fictitious phases is eliminated, since the absent phases remain absent in the proofs. This property is demonstrated in Chapter 4.*

With the same procedure of the proofs of Theorem 2.2.4 and Theorem 3.3.7, choosing $\left(\frac{1+\phi_p}{2}\right)^{\gamma_s}$ $(\gamma_s \geqslant 1)$ *ahead of* L^s *in Eq.(2.19) does not change the consistency of reduction of the proposed conservative Allen-Cahn equation and its numerical scheme. The reason for generating fictitious phases in [66] is that the scheme in [66] does not satisfy the consistency of reduction.*

The scheme to solve the two-phase conservative Allen-Cahn equation Eq.(2.23) is identical to the one for Eq.(2.19) except that **Step 2** or Eq.(3.33) is missed since $\tilde{L}^s$ is zero, and that the computation of $\tilde{L}^c$ is simplified using Eq.(2.16). Thus, Theorem 3.3.5, Theorem 3.3.6, and Theorem 3.3.7 are still valid in the two-phase cases. An alternative scheme developed to solve the two-phase conservative Allen-Cahn equation Eq.(2.23) honors the maximum principle of the equation [211]. This scheme is modified from [110] where a maximum-principle-preserving finite difference scheme for the Allen-Cahn equation with convection and variable mobility is proposed but does not include the Lagrange multiplier to enforce mass conservation.

The maximum-principle-preserving and conservative scheme for the two-phase conservative Allen-Cahn equation Eq.(2.23):

$$\begin{aligned} &\phi^{n+1} - \Delta t\left(M_0\lambda_0\tilde{\nabla}\cdot\tilde{\nabla}\phi^{n+1} - \tilde{\nabla}\cdot(\mathbf{u}^n\tilde{\phi}^{n+1})\right) \\ &= \phi^n - \frac{M_0\lambda_0\Delta t}{\eta^2}g_1'(\phi^n) + \frac{M_0\lambda_0\Delta t}{\eta^2}\frac{W(\phi^n)}{\sum_{\mathrm{i,j}}[W(\phi^n)\Delta\Omega]_{\mathrm{i,j}}}\sum_{\mathrm{i,j}}[g_1'(\phi^n)\Delta\Omega]_{\mathrm{i,j}}, \end{aligned} \tag{3.38}$$

where $\tilde{\phi}$ represents the 1st-order upwind scheme.

Theorem 3.3.8. *The scheme in Eq.(3.38) for the two-phase conservative Allen-Cahn equation Eq.(2.23) satisfies the maximum principle on the discrete level:*

$$\|\phi\|_\infty \leqslant 1$$

at every discrete location and time level if $\|\phi\|_\infty \leqslant 1$ *at* $t = 0$ *and* $\frac{M_0\lambda_0\Delta t}{\eta^2} \leqslant \frac{1}{4}$. *Here,* $\|\cdot\|_\infty$ *denotes the standard infinity norm of a function, a matrix, or a vector.*

Proof. The left-hand side (LHS) of Eq.(3.38) can be represented as $A\phi^{n+1} = (I - B)\phi^{n+1}$, where B is the discrete Laplace operator minus the 1st-order upwind operator and is a NDD matrix, see Lemma 3.3.10. The right-hand side (RHS) of Eq.(3.38) is $f(\phi^n)$, where $f(\phi)$ is defined in Lemma 3.3.11. Given $\|\phi\|_\infty \leqslant 1$ up to time level n and $\frac{M_0\lambda_0\Delta t}{\eta^2} \leqslant \frac{1}{4}$, $\|\phi^{n+1}\|_\infty = \|A^{-1}f(\phi^n)\|_\infty \leqslant \|A^{-1}\|_\infty\|f(\phi^n)\|_\infty \leqslant 1$ with the help of Lemma 3.3.10 and Lemma 3.3.11. Thus, the maximum principle is preserved in the discrete level. □

Theorem 3.3.9. *The scheme in Eq.(3.38) for the two-phase conservative Allen-Cahn equation Eq.(2.23) satisfies the mass conservation on the discrete level:*

$$\sum_{\mathrm{i,j}} [\phi^n \Delta\Omega]_{\mathrm{i,j}} = \sum_{\mathrm{i,j}} [\phi^0 \Delta\Omega]_{\mathrm{i,j}}.$$

Proof. After summing Eq.(3.38) over all the cells, the remaining term on the left-hand side (LHS) is $\sum_{\mathrm{i,j}} [\phi^{n+1}\Delta\Omega]_{\mathrm{i,j}}$ and the remaining term on the right-hand side (RHS) is $\sum_{\mathrm{i,j}} [\phi^n\Delta\Omega]_{\mathrm{i,j}}$. Consequently, $\sum_{\mathrm{i,j}} [\phi^{n+1}\Delta\Omega]_{\mathrm{i,j}} = \sum_{\mathrm{i,j}} [\phi^n\Delta\Omega]_{\mathrm{i,j}}$. If the mass is conserved up to time level n, i.e., $\sum_{\mathrm{i,j}} [\phi^n\Delta\Omega]_{\mathrm{i,j}} = \sum_{\mathrm{i,j}} [\phi^0\Delta\Omega]_{\mathrm{i,j}}$, then one has $\sum_{\mathrm{i,j}} [\phi^{n+1}\Delta\Omega]_{\mathrm{i,j}} = \sum_{\mathrm{i,j}} [\phi^0\Delta\Omega]_{\mathrm{i,j}}$, which implies the mass conservation on the discrete level. □

Lemma 3.3.10. *Let $B = (b_{rs}) \in R^{N\times N}$ and $A = aI - B$, where a is a positive constant and I is the identity matrix. If B is a negative diagonally dominant (NDD) matrix, i.e.,*

$$b_{rr} \leqslant 0, b_{rr} + \sum_{s\neq r} |b_{rs}| \leqslant 0, \forall r,$$

then A is invertible and its inverse satisfies

$$\|A^{-1}\|_\infty \leqslant \frac{1}{a}.$$

The proof of Lemma 3.3.10 is available in [110].

Lemma 3.3.11. *Let $f(\phi)$ to be*

$$f(\phi) = \phi - \frac{M_0\lambda_0\Delta t}{\eta^2} g_1'(\phi) + \frac{M_0\lambda_0\Delta t}{\eta^2} \frac{W(\phi)}{\sum_{\mathrm{i,j}} [W(\phi)\Delta\Omega]_{\mathrm{i,j}}} \sum_{\mathrm{i,j}} [g_1'(\phi)\Delta\Omega]_{\mathrm{i,j}}.$$

If $\phi \in [-1, 1]$ *and* $\frac{M_0\lambda_0\Delta t}{\eta^2} \leqslant \frac{1}{4}$*, then*

$$\|f(\phi)\|_\infty \leqslant 1.$$

Proof. The summation term $\frac{\sum_{\mathrm{i,j}}[g_1'(\phi)\Delta\Omega]_{\mathrm{i,j}}}{\sum_{\mathrm{i,j}}[W(\phi)\Delta\Omega]_{\mathrm{i,j}}}$ is bounded.

$$\begin{aligned}\left|\frac{\sum_{\mathrm{i,j}}[g_1'(\phi)\Delta\Omega]_{\mathrm{i,j}}}{\sum_{\mathrm{i,j}}[W(\phi)\Delta\Omega]_{\mathrm{i,j}}}\right| &= \left|\frac{\sum_{\mathrm{i,j}}[\phi(\phi^2-1)\Delta\Omega]_{\mathrm{i,j}}}{\sum_{\mathrm{i,j}}[(1-\phi^2)\Delta\Omega]_{\mathrm{i,j}}}\right| \\ \leqslant \frac{\sum_{\mathrm{i,j}}[|\phi|(1-\phi^2)\Delta\Omega]_{\mathrm{i,j}}}{\sum_{\mathrm{i,j}}[(1-\phi^2)\Delta\Omega]_{\mathrm{i,j}}} &\leqslant \frac{\sum_{\mathrm{i,j}}[(1-\phi^2)\Delta\Omega]_{\mathrm{i,j}}}{\sum_{\mathrm{i,j}}[(1-\phi^2)\Delta\Omega]_{\mathrm{i,j}}} = 1.\end{aligned}$$

As a result, $f(\phi)$ is bounded by $f_+(\phi)$ and $f_-(\phi)$, i.e., $f_-(\phi) \leqslant f(\phi) \leqslant f_+(\phi)$, where

$$f_\pm(\phi) = \phi - \frac{M_0\lambda_0\Delta t}{\eta^2}g_1'(\phi) \pm \frac{M_0\lambda_0\Delta t}{\eta^2}W(\phi) = \phi + \frac{M_0\lambda_0\Delta t}{\eta^2}(1-\phi^2)(\phi \pm 1).$$

Notice that $f_\pm(\pm 1) = \pm 1$, so if $f_\pm$ are monotonically increasing functions for $\phi \in [-1, 1]$, then $-1 \leqslant f_-(\phi) \leqslant f(\phi) \leqslant f_+(\phi) \leqslant 1$, or equivalently $\|f(\phi)\|_\infty \leqslant 1$. The derivative of $f_+(\phi)$ is

$$f_+'(\phi) = 1 - 3\frac{M_0\lambda_0\Delta t}{\eta^2}\left((\phi + \frac{1}{3})^2 - \frac{4}{9}\right),$$

and its minimum for $\phi \in [-1, 1]$ is $\left(1 - \frac{4M_0\lambda_0\Delta t}{\eta^2}\right)$ at $\phi = 1$. With a similar procedure, the minimum of $f_-'(\phi)$ for $\phi \in [-1, 1]$ is $\left(1 - \frac{4M_0\lambda_0\Delta t}{\eta^2}\right)$ at $\phi = -1$. Thus $f_\pm(\phi)$ are monotonic increasing when $\frac{M_0\lambda_0\Delta t}{\eta^2} \leqslant \frac{1}{4}$. As a result, $\|f(\phi)\|_\infty \leqslant 1$. □

Although the scheme in Eq.(3.38) preserves the maximum principle and mass conservation, it is only 1st-order accurate. Weng and Zhuang [212] proposed an operator splitting scheme along with the Fourier spectral method to solve the two-phase conservative Allen-Cahn equation without convection. They show that their scheme satisfies the maximum principle, while it does not conserve mass exactly. Joshi and Jaiman [102], [103] introduced the positivity preserving stabilization term to the variational form of the two-phase conservative Allen-Cahn equation in order to enforce the maximum principle with the finite element method (FEM). Designing a higher-order scheme that preserves the maximum principle is non-trivial and could be a future direction of study.

3.3.5 Implementation of the boundedness mapping

It should be noted that $\{\phi_p^{n+1}\}_{p=1}^N$, obtained from the schemes in Section 3.3.3 and Section 3.3.4, are possibly outside their physical interval, i.e., $[-1, 1]$ in the present study. The boundedness mapping in Section 3.3.2 is implemented to finalize the order parameters at the new time level. Specifically, input $\{\phi_p^{n+1}\}_{p=1}^N$ and $\{S_{\phi_p^{n+1}}\}_{p=1}^N$ into the mapping and obtain $\{\phi_p^b\}_{p=1}^N$ that satisfy Eq.(3.16). Here, $\{\phi_p^{n+1}\}_{p=1}^N$ are the solution of the schemes in Section 3.3.3 and Section 3.3.4, and $\{S_{\phi_p^{n+1}}\}_{p=1}^N$ are

$$S_{\phi_p^{n+1}} = \sum_{\mathrm{i,j}} [\phi_p^{n+1} \Delta\Omega]_{\mathrm{i,j}}, \quad 1 \leqslant p \leqslant N, \tag{3.39}$$

because the schemes in Section 3.3.3 and Section 3.3.4 satisfy the mass conservation, see Theorem 3.3.2 and Theorem 3.3.5. Both $\{\phi_p^{n+1}\}_{p=1}^N$ and $\{S_{\phi_p^{n+1}}\}_{p=1}^N$ are the admissible inputs of the boundedness mapping algorithm in Section 3.3.2 due to $\sum_{p=1}^N \phi_p^{n+1} = (2 - N)$, see Theorem 3.3.3 and Theorem 3.3.6.

In summary, the order parameters at the new time level $\{\phi_p^b\}_{p=1}^N$, which is mapped from $\{\phi_p^{n+1}\}_{p=1}^N$, have the following properties:

- They satisfy the mass conservation, see Theorem 3.3.2 (Theorem 3.3.5) and the second constraint for $\{\phi_p^b\}_{p=1}^N$ in Eq.(3.16).
- They satisfy the summation of the order parameters, see Theorem 3.3.3 (Theorem 3.3.6) and the first constraint for $\{\phi_p^b\}_{p=1}^N$ in Eq.(3.16).
- They satisfy the *consistency of reduction*, see Theorem 3.3.4 (Theorem 3.3.7) and Theorem 3.3.1.
- They satisfy the boundedness constraint, i.e., $\{\phi_p^b\}_{p=1}^N \in [-1, 1]$, see the last constraint for $\{\phi_p^b\}_{p=1}^N$ in Eq.(3.16).

Remark:

- *From Theorem 3.3.3 and Theorem 3.3.4 (or Theorem 3.3.6 and Theorem 3.3.7), one can deduce that* $\{\phi_p^{n+1}\}_{p=1}^N$ *are either* 1 *or* -1 *inside bulk-phase regions. As a result,*

the out-of-bound error only possibly appears at interfacial regions. Therefore, the clipping step Eq.(3.17) of the boundedness mapping in Section 3.3.2 is only effective in interfacial regions but does not modify any existing bulk-phase regions labeled by $\{\phi_p^{n+1}\}_{p=1}^N$.

- *The out-of-bound error in* $\{\phi_p^{n+1}\}_{p=1}^N$ *is normally small. The largest out-of-bound error observed in the present study is usually of* $O(10^{-5})$ *in one time step even in problems including strong interactions among the phases. In all the results reported in the present study, one only needs to perform the boundedness mapping in Section 3.3.2 once in each time step, and the resulting* $\{\phi_p^b\}_{p=1}^N$ *already satisfy all the constraints in Eq.(3.16).*

The effect of the boundedness mapping is quantified as Lagrange multipliers:

$$\tilde{L}_p^b = \frac{\gamma_t \phi_p^b - \gamma_t \phi_p^{n+1}}{\Delta t}, \quad 1 \leqslant p \leqslant N. \tag{3.40}$$

Notice that $\sum_{\mathrm{i,j}} [\tilde{L}_p^b \Delta\Omega]_{\mathrm{i,j}}$ $(1 \leqslant p \leqslant N)$ is zero due to $\sum_{\mathrm{i,j}} [\phi_p^b \Delta\Omega]_{\mathrm{i,j}} = \sum_{\mathrm{i,j}} [\phi_p^{n+1} \Delta\Omega]_{\mathrm{i,j}}$. As a result, the final fully discretized Phase-Field equation, including the effect of the boundedness mapping, is

$$\frac{\gamma_t \phi_p^{n+1} - \hat{\phi}_p}{\Delta t} + \tilde{\nabla} \cdot (\mathbf{u}^{*,n+1} \tilde{\phi}_p^{*,n+1}) = \tilde{\nabla} \cdot \mathbf{J}_p^* + \tilde{L}_p^R + \tilde{L}_p^c + \tilde{L}_p^b, \quad 1 \leqslant p \leqslant N. \tag{3.41}$$

Here, $\{\phi_p^b\}_{p=1}^N$ are renamed as $\{\phi_p^{n+1}\}_{p=1}^N$ in the rest of the study for convenience, and the numerical diffusion fluxes $\{\mathbf{J}_p^*\}_{p=1}^N$ and reaction terms $\{\tilde{L}_p^R\}_{p=1}^N$ depend on the specific scheme to solve the Phase-Field equation, like those in Section 3.3.3 and Section 3.3.4.

3.4 Discrete consistent mass flux

After solving the Phase-Field equation, the next critical step is to determine the discrete consistent mass flux, which reproduces the physical coupling between the Phase-Field and momentum equations from the consistency conditions in Section 2.3 and Section 2.4. As analyzed in Section 3.2, discretizing the consistent mass flux needs special care, so that the consistency conditions are preserved on the discrete level, while directly following the

formulations on the continuous level usually fails to achieve the goal. The correct way should follow Theorem 3.2.1 and Theorem 3.2.3.

The first step from Theorem 3.2.1 is to determine the discrete Phase-Filed fluxes $\{\tilde{\mathbf{m}}_{\phi_p}\}_{p=1}^N$ such that the fully-discretized Phase-Field equation is

$$\frac{\gamma_t \phi_p^{n+1} - \hat{\phi}_p}{\Delta t} + \tilde{\nabla} \cdot \tilde{\mathbf{m}}_{\phi_p} = 0, \quad 1 \leqslant p \leqslant N, \tag{3.42}$$

which is the discrete counter part of Eq.(2.30). In other words, one needs to turn the fully discretized Phase-Field equation in Eq.(3.41) into Eq.(3.42). This is accomplished by performing the consistent formulation in Section 2.3.1 discretely. Specifically, $\{Q_p\}_{p=1}^N$ are solved from

$$\begin{aligned} \tilde{\nabla} \cdot \left(\overline{W_{Q_p}^{n+1}} \tilde{\nabla} Q_p \right) = \tilde{L}_p^Q \quad \text{in} \quad \Omega, \quad \mathbf{n} \cdot \tilde{\nabla} Q_p = 0 \quad \text{at} \quad \partial\Omega, \\ W_{Q_p}^{n+1} = W_Q(\phi_p^{n+1}) = 1 - (\phi_p^{n+1})^2, \quad \tilde{L}_p^Q = \tilde{\nabla} \cdot \mathbf{J}_p^* + \tilde{L}_p^R + \tilde{L}_p^c + \tilde{L}_p^b, \quad 1 \leqslant p \leqslant N, \end{aligned} \tag{3.43}$$

which is the discrete counterpart of Eq.(2.32) and Eq.(2.33). It should be noted that $\tilde{L}_p^Q$ contains all the terms on the right-hand side of Eq.(3.41), including $\{\tilde{L}_p^b\}_{p=1}^N$, representing the effect of the boundedness mapping. This term does not appear in Eq.(2.33). Notice that $\tilde{\nabla} \cdot \mathbf{J}_p^*$ can be excluded from $\tilde{L}_p^Q$ when using the Cahn-Hilliard equation or the conservative Allen-Cahn equation with 90^0 contact angles. In order to successfully implement the consistent formulation, as discussed in Section 2.3.1, $\sum_{\mathrm{i,j}} [\tilde{L}_p^Q \Delta\Omega]_{\mathrm{i,j}}$ $(1 \leqslant p \leqslant N)$ needs to be zero. This condition is true, see Theorem 3.3.2 (Theorem 3.3.5) and the analysis below Eq.(3.40). After solving $\{Q_p\}_{p=1}^N$ from Eq.(3.43), the discrete Phase-Field fluxes in Eq.(3.42) are obtained.

It should be noted that both sides of Eq.(3.43) are zero away from the interface, which leads to all-zero rows in the coefficient matrix of the discretized linear system of Eq.(3.43). In practice, to avoid getting all-zero rows, W_Q in Eq.(3.43) is set to be a small value δ_Q where $|\phi^{n+1}|$ is larger than $(1-\delta_Q)$, due to $W_Q(\phi = 1-\delta_Q) \sim \delta_Q$. Consequently, Eq.(3.43) reduces to the Laplace equation, i.e., $\tilde{\nabla} \cdot \tilde{\nabla} Q = 0$, away from the interface, and the gradient of Q becomes zero there. It should be noted that such a modification of W_Q is effective only far away from the interface and it does not change the behavior of Eq.(3.43) there since $\overline{W_Q} \tilde{\nabla} Q$ is still

zero away from the interface. Although Eq.(3.43) is a variable-coefficient elliptic equation, after the modification of W_Q, most of the rows in the coefficient matrix is representing the discretized Laplace equation, which has constant coefficients and is diagonally dominant, since the domain is majorly occupied by the bulk-phase regions away from the interface. δ_Q is chosen to be 10^{-6} since the locations where $|\phi^{n+1}|$ is larger than $(1-10^{-6})$ are about 10η away from the interface. This is adequately far away from the interface, considering that the length scale of the computational domain is about 100η normally.

The second step is to use Theorem 3.2.3. Since $\mathbf{u}^{*,n+1}$ is used in all the convection terms $(\tilde{\nabla}\cdot(\mathbf{u}^{*,n+1}\tilde{\phi}_p^{*,n+1}))$ in the present study when solving the Phase-Field equation, see Eq.(3.41), the discrete consistent mass flux finally is

$$\tilde{\mathbf{m}} = \sum_{p=1}^{N} \frac{\rho_p}{2}(\mathbf{u}^{*,n+1} + \tilde{\mathbf{m}}_{\phi_p}). \tag{3.44}$$

Remark:

- *The discrete consistent mass flux in Eq.(3.44) satisfies the consistency of mass conservation on the discrete level, see Theorem 3.2.1.*
- *The discrete consistent mass flux in Eq.(3.44) satisfies the consistency of reduction on the discrete level, see Theorem 3.2.3.*

3.5 Momentum-conservative projection scheme

In this section, the scheme to solve the momentum equation Eq.(2.34) is introduced. The hydrostatic ($\mathbf{u} \equiv \mathbf{0}$) is first considered and the balanced-force algorithm [43] is extended to the surface force from the Phase-Field method. Then, two methods are developed to compute the surface force in Eq.(2.35), one of which contributes to the momentum conservation on the discrete level. At the end, the momentum-conservative projection scheme is constructed and its properties are analyzed.

3.5.1 Balanced-Force algorithm

When the flow is stationary, i.e., $\mathbf{u} = \mathbf{0}$, the momentum equation Eq.(2.34) reduces to

$$\mathbf{G} = -\frac{1}{\rho}\nabla p + \mathbf{g} + \frac{1}{\rho}\mathbf{f}_s + \frac{1}{\rho}\mathbf{S}_\mathbf{u} = \mathbf{0}, \tag{3.45}$$

which represents the force balance (or mechanical equilibrium) between the pressure gradient, gravity, surface tension, and other external forces $\mathbf{S}_\mathbf{u}$. The residual of Eq.(3.45) after discretization unphysically drives the flow to move, and generates the so-called spurious current. The balanced-force algorithm is developed by [43] for both the continuous surface force [39] and the ghost fluid method (GFM) [40]. Here, this idea is followed and applied to the surface force from the Phase-Field method.

The x-component of Eq.(3.45) is first discretized at $(x_{\mathrm{i}+1/2}, y_{\mathrm{j}})$ as

$$\begin{aligned} G^x_{s,\mathrm{i}+1/2,\mathrm{j}} &= g^x + \frac{1}{\tilde{\rho}_{\mathrm{i}+1/2,\mathrm{j}}}[f^x_s]_{\mathrm{i}+1/2,\mathrm{j}} + \frac{1}{\tilde{\rho}_{\mathrm{i}+1/2,\mathrm{j}}} S^x_{\mathbf{u},\mathrm{i}+1/2,\mathrm{j}}, \\ G^x_{\mathrm{i}+1/2,\mathrm{j}} &= -\frac{1}{\tilde{\rho}_{\mathrm{i}+1/2,\mathrm{j}}}[\tilde{\nabla}^x p]_{\mathrm{i}+1/2,\mathrm{j}} + G^x_{s,\mathrm{i}+1/2,\mathrm{j}}, \end{aligned} \tag{3.46}$$

where, unless otherwise specified, $\tilde{\rho}$ is evaluated by the linear interpolation from its cell-center values. Here, $\mathbf{G}$ denotes the discretized net force per unit mass and $\mathbf{G}_s$ is the net force per unit mass excluding the pressure gradient. The y-component is similarly discretized at $(x_{\mathrm{i}}, y_{\mathrm{j}+1/2})$. The cell-center $\overline{\mathbf{G}}$ at $(x_{\mathrm{i}}, y_{\mathrm{j}})$ is linearly interpolated from $G^x_{\mathrm{i}+1/2,\mathrm{j}}$ and $G^y_{\mathrm{i},\mathrm{j}+1/2}$:

$$[\overline{\mathbf{G}}]_{\mathrm{i},\mathrm{j}} = \left\{ [\overline{G^x}]^x_{\mathrm{i},\mathrm{j}}, [\overline{G^y}]^y_{\mathrm{i},\mathrm{j}} \right\}. \tag{3.47}$$

3.5.2 Discretization methods for the surface force

In this section, two methods to discretize the surface force $\mathbf{f}_s$ defined in Eq.(2.35) are introduced and analyzed. As shown in Section 3.5.1, one only needs to determine the surface force at the cell faces. To avoid repeated algebra, only the x-component of the surface force is presented, and the other components are computed following the same manner.

The balanced-force method: The first method proposed is called the balanced-force method, which was developed in [43] for the sharp interface surface tension models. Since the surface force in Eq.(2.35) share a similar form as the continuous surface force [39], the same strategy is used and the discretization of the surface force reads

$$[f_s^x]_{\mathrm{i+1/2,j}} = \frac{1}{2}\sum_{p=1}^{N} [\overline{\xi_p}]^x_{\mathrm{i+1/2,j}} [\tilde{\nabla}^x \phi_p]_{\mathrm{i+1/2,j}}. \tag{3.48}$$

This formulation is applied in [196] to the two-phase steady drop problem and the results show that the spurious current is reduced by more than an order of magnitude and with a better convergence rate than those using the continuum surface force [39]. In the present study, its property of numerical force balance in multiphase flows will be further examined.

The conservative method: The surface force $\mathbf{f}_s$ in Eq.(2.35) is first rewritten into an equivalent form:

$$\begin{aligned}
\mathbf{f}_s &= \frac{1}{2}\sum_{p=1}^{N} \xi_p \nabla\phi_p = \frac{1}{2}\sum_{p,q=1}^{N} \lambda_{p,q}\left[\frac{1}{\eta^2}\left(g_1(\phi_p) - g_2(\phi_p+\phi_q)\right) + \nabla^2\phi_q\right]\nabla\phi_p \\
&= \frac{1}{2}\sum_{p,q=1}^{N} \lambda_{p,q}\left[\frac{1}{\eta^2}\left(\nabla g_1(\phi_p) - \frac{1}{2}\nabla g_2(\phi_p+\phi_q)\right) + \nabla^2\phi_q\nabla\phi_p\right].
\end{aligned}$$

The x-component of the surface force is discretized as:

$$\begin{aligned}
[f_s^x]_{\mathrm{i+1/2,j}} = \frac{1}{2}\sum_{p,q=1}^{N} \lambda_{p,q}\Bigg[\frac{1}{\eta^2}\Big([\tilde{\nabla}^x g_1(\phi_p)]_{\mathrm{i+1/2,j}} - \frac{1}{2}[\tilde{\nabla}^x g_2(\phi_p+\phi_q)]_{\mathrm{i+1/2,j}}\Big) \\
+[\overline{\tilde{\nabla}\cdot(\tilde{\nabla}\phi_q)}]^x_{\mathrm{i+1/2,j}}[\tilde{\nabla}^x\phi_p]_{\mathrm{i+1/2,j}}\Bigg].
\end{aligned} \tag{3.49}$$

The only difference between the balanced-force method Eq.(3.48) and the conservative method Eq.(3.49) is in the discretizations of ∇g_1 and ∇g_2. In the conservative method Eq.(3.49), these two terms are discretized directly using the gradient operator defined in Eq.(3.6), while in the balanced-force method Eq.(3.48), the chain rule was applied first and then the gradient operator is applied on ϕ_p instead. On the continuous level, both of them are equivalent while on the discrete level, their difference is of the order of the truncation error. However, such a difference has influences on the discrete conservation and force balance.

***Remark**:*

- *The conservative method is a general momentum-conservative numerical model for interfaceial tensions that can include an arbitrary number of phases, see Theorem 3.5.1.*
- *The balanced-force method Eq.(3.48) is not proofed conservative. However, the surface force is a local force, which is zero everywhere except close to interfaces, and the difference of the balanced-force method from the conservative method is of the order of the truncation error. As a result, the summation of the balanced-force method over all the cells is excepted to be small and reduce after grid refinement.*
- *Both the balanced-forece method and the conservative method are reduction consistent on the discrete level, see Theorem 3.5.2.*

Theorem 3.5.1. *The surface force Eq.(2.35) computed with the conservative method Eq.(3.49) is conservative:*

$$\sum_{\mathrm{i,j}} [f_s^x]_{\mathrm{i+1/2,j}} = 0, \quad \sum_{\mathrm{i,j}} [f_s^y]_{\mathrm{i,j+1/2}} = 0,$$

in a periodic domain.

Proof. Following the definition of the gradient operator Eq.(3.6), the mixed derivative evaluated at cell corners $(\mathrm{i}+1/2, \mathrm{j}+1/2)$ is commutable, i.e.,

$$\left[\tilde{\nabla}^y(\tilde{\nabla}^x\phi)\right]_{\mathrm{i+1/2,j+1/2}} = \left[\tilde{\nabla}^x(\tilde{\nabla}^y\phi)\right]_{\mathrm{i+1/2,j+1/2}}.$$

After defining

$$\left[\widetilde{(\nabla^x\phi_p)(\nabla^x\phi_q)}\right]_{\mathrm{i,j}} = [\overline{\tilde{\nabla}^x\phi_p}]^x_{\mathrm{i,j}}[\overline{\tilde{\nabla}^x\phi_q}]^x_{\mathrm{i,j}},$$

$$\left[\widetilde{(\nabla^y\phi_p)(\nabla^x\phi_q)}\right]_{\mathrm{i+1/2,j+1/2}} = [\overline{\tilde{\nabla}^y\phi_p}]^x_{\mathrm{i+1/2,j+1/2}}[\overline{\tilde{\nabla}^x\phi_q}]^y_{\mathrm{i+1/2,j+1/2}},$$

$$[\widetilde{\nabla\phi_p\cdot\nabla}\phi_q]_{\mathrm{i,j}}=[\overline{(\tilde{\nabla}^x\phi_p)(\tilde{\nabla}^x\phi_q)}]^x_{\mathrm{i,j}}+[\overline{(\tilde{\nabla}^y\phi_p)(\tilde{\nabla}^y\phi_q)}]^y_{\mathrm{i,j}},$$

$$[(\nabla^x\phi_p)\widetilde{\nabla^x(\nabla^x\phi_q)}]_{\mathrm{i,j}}=[\overline{\tilde{\nabla}^x\phi_p}]^x_{\mathrm{i,j}}[\tilde{\nabla}^x(\tilde{\nabla}^x\phi_q)]_{\mathrm{i,j}},$$

$$[(\nabla^y\phi_p)\widetilde{\nabla^x(\nabla^y\phi_q)}]_{\mathrm{i+1/2,j+1/2}}=[\overline{\tilde{\nabla}^y\phi_p}]^x_{\mathrm{i+1/2,j+1/2}}[\tilde{\nabla}^x(\tilde{\nabla}^y\phi_q)]_{\mathrm{i+1/2,j+1/2}},$$

one obtains the following two identities

$$\begin{aligned}[\overline{\tilde{\nabla}\cdot(\tilde{\nabla}\phi_p)}]^x_{\mathrm{i+1/2,j}}[\tilde{\nabla}^x\phi_q]_{\mathrm{i+1/2,j}}=&\left[\tilde{\nabla}^x\left((\nabla^x\widetilde{\phi_p)(\nabla^x}\phi_q)\right)\right]_{\mathrm{i+1/2,j}}+\left[\tilde{\nabla}^y\left((\nabla^y\widetilde{\phi_p)(\nabla^x}\phi_q)\right)\right]_{\mathrm{i+1/2,j}}\\&-\overline{[(\nabla^x\phi_p)\widetilde{\nabla^x(\nabla^x\phi_q)}]}^x_{\mathrm{i+1/2,j}}-\overline{[(\nabla^y\phi_p)\widetilde{\nabla^x(\nabla^y\phi_q)}]}^y_{\mathrm{i+1/2,j}},\end{aligned}$$

$$\begin{aligned}[\tilde{\nabla}^x(\widetilde{\nabla\phi_p\cdot\nabla}\phi_q)]_{\mathrm{i+1/2,j}}=&\overline{[(\nabla^x\phi_p)\widetilde{\nabla^x(\nabla^x\phi_q)}]}^x_{\mathrm{i+1/2,j}}+\overline{[(\nabla^y\phi_p)\widetilde{\nabla^x(\nabla^y\phi_q)}]}^y_{\mathrm{i+1/2,j}}\\&+\overline{[(\nabla^x\phi_q)\widetilde{\nabla^x(\nabla^x\phi_p)}]}^x_{\mathrm{i+1/2,j}}+\overline{[(\nabla^y\phi_q)\widetilde{\nabla^x(\nabla^y\phi_p)}]}^y_{\mathrm{i+1/2,j}}.\end{aligned}$$

Multiplying them with $\lambda_{p,q}$ and summing over p and q, one obtains

$$\begin{aligned}\sum_{p,q=1}^{N}\lambda_{p,q}[\overline{\tilde{\nabla}\cdot(\tilde{\nabla}\phi_q)}]^x_{\mathrm{i+1/2,j}}[\tilde{\nabla}^x\phi_p]_{\mathrm{i+1/2,j}}=&\sum_{p,q=1}^{N}\lambda_{p,q}\left[\tilde{\nabla}^x\left((\nabla^x\widetilde{\phi_p)(\nabla^x}\phi_q)\right)\right]_{\mathrm{i+1/2,j}}\\&+\sum_{p,q=1}^{N}\lambda_{p,q}\left[\tilde{\nabla}^y\left((\nabla^y\widetilde{\phi_p)(\nabla^x}\phi_q)\right)\right]_{\mathrm{i+1/2,j}}-\frac{1}{2}\sum_{p,q=1}^{N}\lambda_{p,q}[\tilde{\nabla}^x(\widetilde{\nabla\phi_p\cdot\nabla}\phi_q)]_{\mathrm{i+1/2,j}}.\end{aligned}$$

Finally, summing the conservative method Eq.(3.49) over all the cells and applying Lemma 3.1.2, one has

$$\sum_{\mathrm{i,j}}[f^x_s]_{\mathrm{i+1/2,j}}=0.$$

Performing a similar analysis, one has $\sum_{\mathrm{i,j}} [f_s^y]_{\mathrm{i,j+1/2}} = 0$. □

Theorem 3.5.2. *Both the balanced-force method Eq.(3.48) and the conservative method Eq.(3.49) for discretizing the surface force in Eq.(2.35) are reduction consistent.*

Proof. Consider the last phase of the N-phase system is absent. Since $\nabla\phi_N = \mathbf{0}$, $\nabla^2\phi_N = 0$, and $g_2'(\phi - 1) = g_1'(\phi)$ are true after discretization, the proof of the balanced-force method Eq.(3.48) is identical to the one for Theorem 2.4.5 and Corollary 2.4.5.1.

The conservative method Eq.(3.49) becomes

$$\begin{aligned}\mathbf{f}_s &= \frac{1}{2}\sum_{p,q=1}^{N}\lambda_{p,q}\left[\frac{1}{\eta^2}\left(\tilde{\nabla}^x g_1(\phi_p) - \frac{1}{2}\tilde{\nabla}^x g_2(\phi_p+\phi_q)\right) + \overline{\tilde{\nabla}\cdot(\tilde{\nabla}\phi_q)}\tilde{\nabla}\phi_p\right] \\ &= \frac{1}{2}\sum_{p,q=1}^{N-1}\lambda_{p,q}\left[\frac{1}{\eta^2}\left(\tilde{\nabla} g_1(\phi_p) - \frac{1}{2}\tilde{\nabla} g_2(\phi_p+\phi_q)\right) + \overline{\tilde{\nabla}\cdot(\tilde{\nabla}\phi_q)}\tilde{\nabla}\phi_p\right],\end{aligned}$$

by noticing that $g_1(\phi) = g_2(\phi - 1)$, $g_1(-1) = 0$, $\tilde{\nabla}\phi_N = \mathbf{0}$, and $\tilde{\nabla}\cdot(\tilde{\nabla}\phi_N) = 0$. Recall that $g_1(\phi)$ and $g_2(\phi)$ are the potential functions defined in Eq.(2.17). Therefore both the balanced-force method Eq.(3.48) and the conservative method Eq.(3.49) for discretizing the surface force Eq.(2.35) are reduction consistent. □

3.5.3 Scheme for the momentum equation

The projection scheme to decouple the pressure and velocity of the momentum equation Eq.(2.34) is constructed. Both the cell-center and cell-face velocities and the pressure are updated in the following 7 steps.

Step 1: Solve for the provisional velocity $\mathbf{u}^*$ at the cell centers from

$$\frac{\gamma_t\rho^{n+1}\mathbf{u}^* - \widehat{\rho\mathbf{u}}}{\Delta t} + \tilde{\nabla}\cdot(\tilde{\mathbf{m}}\otimes\tilde{\mathbf{u}}^{*,n+1}) = \rho^{n+1}\overline{\mathbf{G}^n} + \tilde{\nabla}\cdot(\tilde{\mu}^{n+1}\tilde{\nabla}\mathbf{u}^*) + \tilde{\nabla}\cdot(\tilde{\mu}^{n+1}(\tilde{\nabla}\tilde{\mathbf{u}}^{*,n+1})^T). \quad (3.50)$$

Step 2: Solve for another provisional velocity $\mathbf{u}^{**}$ at the cell centers from

$$\frac{\gamma_t\mathbf{u}^{**} - \gamma_t\mathbf{u}^*}{\Delta t} = -\overline{\mathbf{G}^n}. \quad (3.51)$$

Step 3: Solve the provisional velocity $\mathbf{u}^*$ at the cell faces from

$$\frac{\gamma_t \mathbf{u}^* - \gamma_t \overline{\mathbf{u}^{**}}}{\Delta t} = -\frac{1}{\overline{\overline{\rho^{n+1}}}} \tilde{\nabla} P^n + \mathbf{G}_s^{n+1}. \tag{3.52}$$

Here, $\mathbf{u}^{**}$ is linearly interpolated from the cell centers to the cell faces, and the "Rhie-Chow" interpolation [43], [213]–[215] is applied to address the odd-even decoupling of the pressure in the collocated grid arrangement.

Step 4: Solve for the pressure correction P' at the cell centers from

$$\frac{\gamma_t}{\Delta t}(\tilde{\nabla} \cdot \mathbf{u}^{n+1} - \tilde{\nabla} \cdot \mathbf{u}^*) = -\tilde{\nabla} \cdot \left(\frac{1}{\overline{\overline{\rho^{n+1}}}} \tilde{\nabla} P' \right). \tag{3.53}$$

Step 5: Solve for P^{n+1} at the cell centers from

$$P^{n+1} = P^n + P'. \tag{3.54}$$

Step 6: Solve for $\mathbf{u}^{n+1}$ at the cell faces from

$$\frac{\gamma_t \mathbf{u}^{n+1} - \gamma_t \mathbf{u}^*}{\Delta t} = -\frac{1}{\overline{\overline{\rho^{n+1}}}} \tilde{\nabla} P', \tag{3.55}$$

Step 7: Solve for $\mathbf{u}^{n+1}$ at the cell centers from

$$\frac{\gamma_t \mathbf{u}^{n+1} - \gamma_t \mathbf{u}^{**}}{\Delta t} = \overline{\mathbf{G}^{n+1}}. \tag{3.56}$$

Recall that $\mathbf{G}$ and $\mathbf{G}^s$ are defined in Eq.(3.46). The density ρ^{n+1} and viscosity μ^{n+1} of the fluid mixture are obtained from Eq.(2.3) and Eq.(2.4), respectively, the discrete consistent mass flux $\tilde{\mathbf{m}}$ is computed from Section 3.4, and the surface force $\mathbf{f}_s$ in $\mathbf{G}^s$ is computed from either the balanced-force or conservative methods in Section 3.5.2, after solving for ϕ^{n+1} in Section 3.3. The cell-face velocity at the new time level $n+1$ is divergence-free discretely:

$$\tilde{\nabla} \cdot \mathbf{u}^{n+1} = 0, \tag{3.57}$$

and this is used in **Step 4**. The boundary conditions for the velocity and pressure are problem-dependent and will be specified in individual cases in Chapters 4 and 5.

The fully discretized momentum equation is from the above projection scheme is:

$$\begin{aligned}\frac{\gamma_t\rho^{n+1}\mathbf{u}^{n+1}-\widehat{\rho\mathbf{u}}}{\Delta t}+\tilde{\nabla}\cdot(\tilde{\mathbf{m}}\otimes\tilde{\mathbf{u}}^{*,n+1})=\rho^{n+1}\overline{\mathbf{G}^{n+1}}\\ +\tilde{\nabla}\cdot(\tilde{\mu}^{n+1}\tilde{\nabla}\mathbf{u}^{*})+\tilde{\nabla}\cdot(\tilde{\mu}^{n+1}(\tilde{\nabla}\tilde{\mathbf{u}}^{*,n+1})^{T}),\end{aligned}\tag{3.58}$$

In order to satisfy the *consistency of mass and momentum transport* on the discrete level, the 2nd-order backward difference is used for time discretization, and the discrete divergence operator is from Eq.(3.5), the same as those for the Phase-Field equation, see Theorem 3.2.2. In terms of the formal order of accuracy, $(\mathbf{u}^{*,n+1}-\mathbf{u}^{n+1})\sim O(\Delta t^2)$ is true. From **Step 5**, one has $P'\sim O(\Delta t)$, resulting in, at the cell faces, $(\mathbf{u}^{*}-\mathbf{u}^{n+1})\sim O(\Delta t^2)$ from **Step 6**. By combining **Step 2**, **Step 7**, and $P'\sim O(\Delta t)$, one has $(\mathbf{u}^{*}-\mathbf{u}^{n+1})\sim O(\Delta t^2)$ at the cell centers. Finally, all the terms in Eq.(3.58) that are not evaluated at $(n+1)$ time level are different from their corresponding ones evaluating at $(n+1)$ time level in $O(\Delta t^2)$. Combined with the 2nd-order backward difference for time discretization, the overall temporal accuracy is 2nd-order. Additionally, the scheme for the momentum equation has the following provable properties on the discrete level:

- It satisfies the momentum conservation, see Theorem 3.5.3 and its corollaries.
- It satisfies the *consistency of mass and momentum transport*, see Theorem 3.2.2.
- It produces the exact solution of advection (or translation) problems, independent of the material properties of the fluid phases or the initial shapes of the interfaces, see Theorem 3.5.4.
- It satisfies the *consistency of reduction* and the single-phase dynamics is recovered, see Theorem 3.5.6 and its corollaries.
- It satisfies the kinetic energy conservation on the semi-discrete level when all the forces are neglected, see Theorem 3.5.7.

Theorem 3.5.3. *If the discrete surface force is conservative, the scheme for the momentum equation Eq.(2.34) conserves the momentum of the multiphase mixture:*

$$[\mathbf{Momentum}]^n = [\mathbf{Momentum}]^0,$$

where $[\mathbf{Momentum}]^n = \sum_{\mathrm{i,j}} [\rho^n \mathbf{u}^n]_{\mathrm{i,j}} \Delta x \Delta y$.

Proof. Given $\sum_{\mathrm{i,j}} [\rho^n \mathbf{u}^n]_{\mathrm{i,j}} = \sum_{\mathrm{i,j}} [\rho^{n-1} \mathbf{u}^{n-1}]_{\mathrm{i,j}} = \ldots = \sum_{\mathrm{i,j}} [\rho^0 \mathbf{u}^0]_{\mathrm{i,j}}$, one immediately has $\sum_{\mathrm{i,j}} [\widehat{\rho \mathbf{u}}]_{\mathrm{i,j}} = \widehat{\sum_{\mathrm{i,j}} [\rho \mathbf{u}]_{\mathrm{i,j}}} = \gamma_t \sum_{\mathrm{i,j}} [\rho^0 \mathbf{u}^0]_{\mathrm{i,j}}$. Note that the summation of $\rho^{n+1} \overline{\mathbf{G}^{n+1}}$ in Eq.(3.58) over all the cells is zero if the discrete surface force is conservative. As an example, consider the x component, and one has

$$\begin{aligned}\sum_{\mathrm{i,j}} [\rho^{n+1} \overline{G^{x,n+1}}^x]_{\mathrm{i,j}} &= \sum_{\mathrm{i,j}} \frac{\rho^{n+1}_{\mathrm{i,j}}}{2} (G^{x,n+1}_{\mathrm{i+1/2,j}} + G^{x,n+1}_{\mathrm{i-1/2,j}}) = \sum_{\mathrm{i,j}} \frac{\rho^{n+1}_{\mathrm{i,j}} + \rho^{n+1}_{\mathrm{i+1,j}}}{2} G^{x,n+1}_{\mathrm{i+1/2,j}} \\ &= \sum_{\mathrm{i,j}} \overline{\rho^{n+1}_{\mathrm{i+1/2,j}}}^x G^{x,n+1}_{\mathrm{i+1/2,j}} = \sum_{\mathrm{i,j}} [\, - \tilde{\nabla}^x P + f_s^x]^{n+1}_{\mathrm{i+1/2,j}} = \sum_{\mathrm{i,j}} [f_s^x]^{n+1}_{\mathrm{i+1/2,j}} = 0,\end{aligned}$$

after applying Eq.(3.46) and Lemma 3.1.2. The same is true for the y component. Summing the fully discretized momentum equation Eq.(3.58) over all the cells and applying Lemma 3.1.3 and $\sum_{\mathrm{i,j}} [\rho^{n+1} \overline{\mathbf{G}^{n+1}}]_{\mathrm{i,j}} = \mathbf{0}$, one has

$$\sum_{\mathrm{i,j}} [\rho^{n+1} \mathbf{u}^{n+1}]_{\mathrm{i,j}} = \frac{1}{\gamma_t} \sum_{\mathrm{i,j}} [\widehat{\rho \mathbf{u}}]_{\mathrm{i,j}} = \sum_{\mathrm{i,j}} [\rho^0 \mathbf{u}^0]_{\mathrm{i,j}}.$$

Therefore, the momentum of the multiphase mixture, i.e., $[\mathbf{Momentum}] = \sum_{\mathrm{i,j}} [\rho \mathbf{u}]_{\mathrm{i,j}} \Delta x \Delta y$, is conserved. □

Corollary 3.5.3.1. *If the surface force Eq.(2.35) is computed by the conservative method Eq.(3.49), the scheme for the momentum equation Eq.(2.34) conserves the momentum of the multiphase mixture:*

$$[\mathbf{Momentum}]^n = [\mathbf{Momentum}]^0,$$

where $[\mathbf{Momentum}]^n = \sum_{\mathrm{i,j}} [\rho^n \mathbf{u}^n]_{\mathrm{i,j}} \Delta x \Delta y$.

Corollary 3.5.3.2. *Without considering the surface force, the scheme for the momentum equation Eq.(2.34) conserves the momentum of the multiphase mixture:*

$$[\textbf{Momentum}]^n = [\textbf{Momentum}]^0,$$

where $[\textbf{Momentum}]^n = \sum_{\mathrm{i,j}} [\rho^n \mathbf{u}^n]_{\mathrm{i,j}} \Delta x \Delta y$.

Theorem 3.5.4. *If the* ***consistency of mass conservation*** *and the* ***consistency of mass and momentum transport*** *are satisfied* ***on the discrete level****, the gravity, viscosity, surface force, and any other external momentum sources are neglected, and the initial velocity and pressure are homogeneous, then the same homogeneous velocity and pressure are the solution of the momentum equation solved from the scheme.*

Proof. Given initial homogeneous velocity $\mathbf{u}_0$ and pressure P_0, and suppose they are still true up to time level n, the scheme for the momentum equation Eq.(2.34) is followed.

From **Step 1**, its right-hand side (RHS) is zero, and as a result, one has

$$\mathbf{u}^* = \frac{1}{\gamma_t \rho^{n+1}} \underbrace{\left(\hat{\rho} - \Delta t \tilde{\nabla} \cdot \tilde{\mathbf{m}}\right)}_{\rho^{n+1}} \mathbf{u}_0 = \mathbf{u}_0.$$

The terms inside the parentheses becomes ρ^{n+1} due to the *consistency of mass conservation*, see Theorem 3.2.1. Since $\overline{\mathbf{G}^n} = \mathbf{0}$, from **Step 2**, one obtains $\mathbf{u}^{**} = \mathbf{u}^* = \mathbf{u}_0$ and further $\overline{\mathbf{u}^{**}} = \mathbf{u}_0$. From **Step 3**, one has $\mathbf{u}^*$ at the cell faces is again $\mathbf{u}_0$, by noticing that both $\tilde{\nabla} P^n$ and $\mathbf{G}_s^{n+1}$ are zero. From **Step 4**, one has $\tilde{\nabla} \cdot \mathbf{u}^* = \tilde{\nabla} \cdot \mathbf{u}_0 = 0$, and further P' is a constant. Without loss of generality, $P' = 0$ is set. After that, one has $P^{n+1} = P_0$ from **Step 5**, and $\mathbf{u}^{n+1}$ at the cell faces is $\mathbf{u}_0$ from **Step 6**. Finally, $\overline{\mathbf{G}^{n+1}}$ is zero and from **Step 7**, $\mathbf{u}^{n+1}$ at the cell centers is $\mathbf{u}_0$. □

Remark*:*

- *Theorem 3.5.4 corresponds to the pure translation problem, and it holds no matter how many phases appear, what material properties of the fluid phases and initial shapes of the interfaces could be. This is consistent with the physical configuration.*

- *If the consistency conditions are violated, the terms inside the parentheses from* ***Step 1*** *is not* ρ^{n+1} *anymore, resulting in* $\mathbf{u}^* \neq \mathbf{u}_0$*. This error will be transferred into the upcoming steps of the scheme for the momentum equation, leading to a non-homogeneous* P'*. As a result,* $\mathbf{u}^{n+1}$ *is not equal to* $\mathbf{u}_0$*. Such unphysical velocity and pressure fluctuations depend on the densities of the phases and probably become a source of numerical instability. Thanks to Theorem 3.5.4, these unphysical behaviors will not appear, and a comparison study is performed in Section 4.8 to numerically illustrate the effect of the consistency conditions. A simplified two-phase 1D analysis considering* ***Step 1*** *only are available in Section 3.2. Theorem 3.5.4 considers a more general problem, and its proof is in a more formal way and more complete.*

- *One can again show that the initial homogeneous velocity is preserved if the hydrostatic mechanical equilibrium is always satisfied numerically, i.e.,* $\mathbf{G} \equiv 0$*. Recall that* $\mathbf{G}$ *is defined in Eq.(3.46). The proof is similar and the only difference is that* P' *can be non-homogeneous. However, by combining* ***Step 3*** *and* ***Step 6****, the right-hand side recovers* $\mathbf{G}^{n+1}$*, which is zero, and one still has* $\mathbf{u}^{n+1} = \overline{\mathbf{u}}^{**} = \mathbf{u}_0$ *at the cell faces. It should be noted that* $\mathbf{G} \equiv \mathbf{0}$ *is seldom achievable in numerical practice.*

Theorem 3.5.5. *If the density and viscosity of the fluid mixture, the discrete consistent mass flux, and the discrete surface force are reduction consistent, then the momentum equation is essentially reduction consistent on the discrete level such that the* N*-phase discretized equation recovers the corresponding* M*-phase one* $(2 \leqslant M \leqslant N-1)$ *when* $(N-M)$ *phases are absent.*

Theorem 3.5.6. *If the density and viscosity of the fluid mixture, the discrete consistent mass flux, and the discrete surface force are reduction consistent, and the discretized* $\nabla \cdot (\mu \nabla \mathbf{u}^T)$ *is exactly zero when* μ *is a constant, then the momentum equation is reduction consistent on the discrete level.*

Corollary 3.5.6.1. *the scheme for the momentum equation Eq.(2.34) satisfies the consistency of reduction on the discrete level.*

Corollary 3.5.6.2. *the scheme for the momentum equation Eq.(2.34) recovers inside each bulk-phase region the fully discretized single-phase Navier-Stokes equation with the corresponding density and viscosity of that phase. For example, in the bulk-phase region of Phase p, the fully discretized momentum equation becomes*

$$\frac{\gamma_t \rho_p \mathbf{u}^{n+1} - \rho_p \widehat{\mathbf{u}}}{\Delta t} + \tilde{\nabla} \cdot (\rho_p \mathbf{u}^{*,n+1} \otimes \tilde{\mathbf{u}}^{*,n+1}) = \overline{(-\tilde{\nabla} P^{n+1} + \rho_p \mathbf{g} + \mathbf{S}_\mathbf{u})} + \mu_p \tilde{\nabla} \cdot (\tilde{\nabla} \mathbf{u}^*).$$

***Remark**: Although only the density and viscosity of the fluid mixture, the discrete consistent mass flux, and the discrete surface force in the fully discretized momentum equation Eq.(3.58) are related to the number of phases, there is one more issue from the viscous term $\nabla \cdot (\mu (\nabla \mathbf{u})^T)$, which should be zero inside the bulk-phase regions because of the divergence-free velocity there, as discussed in Section 2.4. This is not an issue on the continuous level but things change after discretization. That's why one more constraint about the viscous term is added in Theorem 3.5.6, compared to Theorem 2.4.1 and Theorem 3.5.5. In some studies, e.g., [216], the viscous term $\nabla \cdot (\mu \nabla \mathbf{u}^T)$ is first transformed to $\nabla \mu \cdot \nabla \mathbf{u}^T$ ($\nabla \cdot (\mu (\nabla \mathbf{u})^T) = \nabla \mu \cdot (\nabla \mathbf{u})^T + \mu \nabla (\nabla \cdot \mathbf{u}) = \nabla \mu \cdot (\nabla \mathbf{u})^T$), and then discretization is performed. Although this helps the consistency of reduction discretely, it unfortunately destroys the momentum conservation. As introduced in Section 3.1, a special method is developed for this viscous term and it has the property that $\tilde{\nabla} \cdot (\tilde{\nabla} \tilde{\mathbf{u}}^T) = \overline{\tilde{\nabla} (\tilde{\nabla} \cdot \mathbf{u})}$, see Lemma 3.1.1. Therefore, $\tilde{\nabla} \cdot (\tilde{\nabla} \tilde{\mathbf{u}}^T)$ will be exactly zero if the cell-face velocity is discretely divergence-free. This is exactly the case in the present scheme, and the momentum conservation is honored on the discrete level as well, see Theorem 3.5.3. Thanks to this method, the scheme for the momentum equation Eq.(2.34) enjoys Corollary 3.5.6.1 and Corollary 3.5.6.2.*

Theorem 3.5.7. *If the **consistency of mass conservation** and the **consistency of mass and momentum transport** are satisfied, all the forces are neglected, and the central difference and linear interpolation are applied, then the semi-discrete momentum equation:*

$$\frac{\partial (\rho \mathbf{u})}{\partial t} + \tilde{\nabla} \cdot (\tilde{\mathbf{m}} \otimes \bar{\mathbf{u}}) = \mathbf{0},$$

implies the kinetic energy conservation:

$$\frac{d}{dt}\left(\sum_{\mathrm{i,j}}[\mathrm{e}_K]_{\mathrm{i,j}}\Delta x\Delta y\right)=0.$$

Proof. Performing the dot product between $\mathbf{u}$ and the semi-discrete momentum equation, one obtains

$$\frac{\partial \mathrm{e}_K}{\partial t}+\tilde{\nabla}\cdot\left(\tilde{\mathbf{m}}\frac{\widetilde{\mathbf{u}\cdot\mathbf{u}}}{2}\right)+\frac{\mathbf{u}\cdot\mathbf{u}}{2}\underbrace{\left(\frac{\partial\rho}{\partial t}+\nabla\cdot\tilde{\mathbf{m}}\right)}_{0}=0,$$

where $[\widetilde{\frac{\mathbf{u}\cdot\mathbf{u}}{2}}]_{\mathrm{i+1/2,j}}=\frac{1}{2}(\mathbf{u}_{\mathrm{i+1,j}}\cdot\mathbf{u}_{\mathrm{i,j}})$ and $[\widetilde{\frac{\mathbf{u}\cdot\mathbf{u}}{2}}]_{\mathrm{i,j+1/2}}=\frac{1}{2}(\mathbf{u}_{\mathrm{i,j+1}}\cdot\mathbf{u}_{\mathrm{i,j}})$. The underbraced term is zero thanks to satisfying the consistency conditions. Summing the above equation over all the cells and applying Lemma 3.1.3, one obtains

$$\frac{d}{dt}\left(\sum_{\mathrm{i,j}}[\mathrm{e}_K]_{\mathrm{i,j}}\Delta x\Delta y\right)=0.$$

□

***Remark**:*

- *Since the WENO scheme is applied in the present study, numerical dissipation is added to the system and the kinetic energy will decay even satisfying the condition in Theorem 3.5.7.*

- *Including the pressure gradient is expected to dissipate the kinetic energy. It is unable to show $-\rho\mathbf{u}\cdot[\frac{1}{\rho}\tilde{\nabla}P]=-\tilde{\nabla}\cdot(\widetilde{\mathbf{u}P})$, where $(\widetilde{\mathbf{u}P})$ denotes a certain numerical operator applied to $\mathbf{u}$ and P. Numerical experiments have been performed in [209], where a single-phase collocated scheme was analyzed and tested, and it was discovered that $-\mathbf{u}\cdot\overline{[\tilde{\nabla}P]}$ dissipates the kinetic energy. In multiphase problems, ρ, the prefactor, is not a constant any more, which makes the analysis more involved. However, since ρ is always positive, it should not change the dissipative property of $-\mathbf{u}\cdot\overline{[\tilde{\nabla}p]}$. This point is confirmed by the numerical experiments in Section 4.9.*

- *It is challenging to achieve the secondary conservation, i.e., the kinetic energy conservation, on the (fully) discrete level, especially in multiphase problems. First, all the schemes should be central type so that no numerical dissipation is added. Both the WENO scheme and the 2nd-order backward difference in time used in the present study introduce numerical dissipation. Second, the time discretization scheme should follow* $\mathbf{u}\cdot\frac{\partial(\rho\mathbf{u})}{\partial t}=\frac{\partial(\rho\frac{1}{2}\mathbf{u}\cdot\mathbf{u})}{\partial t}+\frac{1}{2}\mathbf{u}\cdot\mathbf{u}\frac{\partial\rho}{\partial t}$ *for variable density, which is non-trivial. Third, the inertia term* $\tilde{\nabla}\cdot(\tilde{\mathbf{m}}\otimes\tilde{\mathbf{u}})$ *may have to be evaluated implicitly, which increases the computational cost.*

- *When the surface forces are present, one needs to additionally consider the free energy related to the Phase-Field equation. The analysis of the total energy dissipation, e.g., Corollary 2.4.4.1, on the discrete level is very complicated and this point will be examined and discussed using numerical experiments in Section 4.9.*

3.6 Scheme for the component equation

After solving the Phase-Field equation, the volume fractions as well as the volumetric fluxes are algebraically obtained based on the definitions from Eq.(3.42):

$$\frac{\gamma_t\chi_p^{n+1}-\hat{\chi_p}}{\Delta t}+\tilde{\nabla}\cdot\tilde{\mathbf{m}}_{\chi_p}=\frac{1}{2}\left(\underbrace{\frac{\gamma_t-\overbrace{\hat{1}}^{\gamma_t}}{\Delta t}}_{0}+\underbrace{\tilde{\nabla}\cdot\mathbf{u}}_{0}+\underbrace{\frac{\gamma_t\phi_p^{n+1}-\hat{\phi_p}}{\Delta t}+\tilde{\nabla}\cdot\tilde{\mathbf{m}}_{\phi_p}}_{0}\right)=0, \tag{3.59}$$
$$\chi_p=\frac{1+\phi_p}{2},\quad \tilde{\mathbf{m}}_{\chi_p}=\frac{\mathbf{u}^{*,n+1}+\tilde{\mathbf{m}}_{\phi_p}}{2},\quad 1\leqslant p\leqslant N,$$

which is the discrete counterpart of Eq.(2.44).

The scheme for solving the consistent component equation Eq.(2.48) is

$$\frac{\gamma_t\chi_p^{M,n+1}C_p^{n+1}-\widehat{\chi_p^M C_p}}{\Delta t}+\tilde{\nabla}\cdot(\tilde{\mathbf{m}}_{\chi_p^M}\tilde{C}_p^{*,n+1})=\tilde{\nabla}\cdot(D_p\tilde{\nabla}C_p^{n+1}),\quad 1\leqslant p\leqslant M, \tag{3.60}$$

where $\{\chi_p^M\}_{p=1}^M$, $\{\tilde{\mathbf{m}}_{\chi_p^M}\}_{p=1}^M$, and $\{D_p\}_{p=1}^M$ are computed from Eq.(2.49), Eq.(2.50), and Eq.(2.51), respectively, using $\{\chi_p^{n+1}\}_{p=1}^N$ and $\{\tilde{\mathbf{m}}_{\chi_p}\}_{p=1}^N$ in Eq.(3.59). As a result, the *con-*

sistency of volume fraction conservation is satisfied on the discrete level by noticing that Eq.(3.59) can be derived from Eq.(3.60) provided homogeneous C_p.

The 2nd-order backward difference scheme is applied in Eq.(3.60) for the temporal discretization but C^{n+1} is replaced by $C^{*,n+1}$ in the convection term. Note that the difference between C^{n+1} and $C^{*,n+1}$ is $O(\Delta t^2)$, so the scheme is still formally 2nd-order accurate in time. The application of the 2nd-order spatial discretization results in formally 2nd-order accuracy of the scheme in space. The scheme Eq.(3.60) additionally has the following properties.

Theorem 3.6.1. *The scheme Eq.(3.60) conserves the total amount of Component p in its dissolvable region:*

$$\sum_{\mathrm{i,j}} [(\chi_p^M C_p)^{n+1} \Delta\Omega]_{\mathrm{i,j}} = \sum_{\mathrm{i,j}} [(\chi_p^M C_p)^0 \Delta\Omega]_{\mathrm{i,j}}, \quad 1 \leqslant p \leqslant M,$$

if there is no source of the components at the boundary of the domain.

Proof. After multiplying $\Delta\Omega$ to Eq.(3.60) and then summing it over all the cells, both the convection and diffusion terms vanish due to the property of the discrete divergence operator, see Lemma 3.1.3 in Section 3.1. As a result, $\sum_{\mathrm{i,j}} [(\chi_p^M C_p)\Delta\Omega]_{\mathrm{i,j}}$ doesn't change as time advances. □

Theorem 3.6.2. *The consistency of reduction on the discrete level is satisfied by the scheme Eq.(3.60).*

Proof. Suppose C_p is zero up to time level n and there is no source of the component at the boundary of the domain, then the convection term and $\widehat{\chi_p^M C_p}$ vanish. The resulting equation is a discretized homogeneous Helmholtz equation. Thus, C_p remains to be zero at time level $n+1$. In other words, if Component p is absent at $t = 0$ and it doesn't have any sources at the boundary of the domain, it won't appear at $\forall t > 0$. Therefore the *consistency of reduction* is satisfied. □

The discrete component fluxes are

$$\tilde{\mathbf{m}}_{C_p} = \tilde{\mathbf{m}}_{\chi_p^M} \tilde{C}_p^{*,n+1} - D_p \tilde{\nabla} C_p^{n+1}, \quad 1 \leqslant p \leqslant M, \tag{3.61}$$

and it also satisfies the *consistency of reduction* since it becomes zero if C_p is zero up to time level $n+1$. Once $\{\chi_p^{M,n+1}C_p^{n+1}\}_{p=1}^M$ and $\{\tilde{\mathbf{m}}_{C_p}\}_{p=1}^M$ are available, the density, viscosity and mass flux are computed from Eq.(2.55), Eq.(2.56) and Eq.(2.57), respectively, and one can proceed to solve the momentum equation.

Thanks to Eq.(3.59), Eq.(3.60), and Eq.(3.61), one obtains

$$\frac{\gamma_t\rho^{n+1}-\hat{\rho}}{\Delta t}+\tilde{\nabla}\cdot\tilde{\mathbf{m}}=\sum_{p=1}^{N}\rho_p^{\phi}\underbrace{\left(\frac{\gamma_t\chi_p^{n+1}-\hat{\chi_p}}{\Delta t}+\tilde{\nabla}\cdot\tilde{\mathbf{m}}_{\chi_p}\right)}_{0} \tag{3.62}$$
$$+\sum_{p=1}^{M}\rho_p^{C}\underbrace{\left(\frac{\gamma_t\chi_p^{M,n+1}C_p^{n+1}-\widehat{\chi_p^M C_p}}{\Delta t}+\tilde{\nabla}\cdot\tilde{\mathbf{m}}_{C_p}\right)}_{0}=0,$$

which is the discrete counterpart of the mass conservation equation Eq.(2.27). Therefore, the *consistency of mass conservation* is satisfied by the discrete mass flux $\tilde{\mathbf{m}}$, and thus, the *consistency of mass and momentum transport* is satisfied in the momentum equation as well.

3.7 Scheme for the phase change problems

The numerical procedure to solve the proposed thermo-gas-liquid-solid model including solidification/melting in Section 2.6.2 is introduced in this section.

First, the two-phase Cahn-Hilliard equation Eq.(2.22) is solved along with the boundedness mapping. As a result, one obtains φ^{n+1} and the discrete Phase-Field flux $\tilde{\mathbf{m}}_{\varphi}$ with the help of the consistent formulation, and they satisfy

$$\frac{\gamma_t\varphi^{n+1}-\hat{\varphi}}{\Delta t}+\tilde{\nabla}\cdot\tilde{\mathbf{m}}_{\varphi}=\varphi^{*,n+1}\tilde{\nabla}\cdot\mathbf{u}^{*,n+1}. \tag{3.63}$$

Second, the phase change equation Eq.(2.59) is solved. To preserve the *consistency of volume fraction conservation* on the discrete level, it should be noted that φ^{n+1} and $\tilde{\mathbf{m}}_{\varphi}$ in

Eq.(3.63) are inputs to solve the phase change equation. The fully-discretized phase change equation is

$$\frac{\gamma_t(\varphi^{n+1}\phi^{n+1}) - \widehat{(\varphi\phi)}}{\Delta t} + \tilde{\nabla}\cdot(\tilde{\mathbf{m}}_\varphi\tilde{\phi}^{*,n+1}) = -M_\phi\tilde{\xi}_\phi + \varphi^{*,n+1}\phi^{*,n+1}\tilde{\nabla}\cdot\mathbf{u}^{*,n+1}, \quad (3.64)$$

$$\tilde{\xi}_\phi = -\lambda_\phi\tilde{\nabla}\cdot(\overline{\varphi^{n+1}}\tilde{\nabla}\phi^{n+1}) + \frac{\lambda_\phi}{\eta_\phi^2}\varphi^{n+1}\tilde{g}'(\phi^{n+1}) + \frac{\rho_M^L L}{T_M}\varphi^{n+1}\tilde{p}'(\phi^{*,n+1})(T_M - T^{*,n+1}),$$

$$\tilde{\mathbf{m}}_{\varphi\phi} = \tilde{\mathbf{m}}_\varphi\tilde{\phi}^{*,n+1},$$

where $\tilde{g}'(\phi^{n+1})$ is linearized $g'(\phi^{n+1})$ around $\phi^{*,n+1}$ from Taylor expansion. As a result, one obtains $(\varphi\phi)^{n+1}$ and $\tilde{\mathbf{m}}_{\varphi\phi}$.

The next step is to obtain (ρC_p), $\tilde{\mathbf{m}}_{(\rho C_p)}$, and κ from Eq.(2.60), noticing that $\mathbf{u}^{*,n+1}$ is applied to Eq.(2.60) due to the *consistency of reduction*, see Theorem 3.2.3. Then, the temperature is updated from the following fully-discretized energy equation:

$$\frac{\gamma_t(\rho C_p)^{n+1}T^{n+1} - \widehat{(\rho C_p)T}}{\Delta t} + \tilde{\nabla}\cdot(\tilde{\mathbf{m}}_{(\rho C_p)}\tilde{T}^{*,n+1}) \quad (3.65)$$

$$+\rho_M^L L\left[\frac{\gamma_t(\varphi^{n+1}\phi^{n+1}) - \widehat{(\varphi\phi)}}{\Delta t} + \tilde{\nabla}\cdot\tilde{\mathbf{m}}_{\varphi\phi}\right] = \tilde{\nabla}\cdot(\overline{\kappa^{n+1}}\tilde{\nabla}T^{n+1}) + Q_T^{n+1}.$$

It should be noted that the terms in the bracket in Eq.(3.65) are identical to the left-hand side of the fully-discretized phase change equation in Eq.(3.64). This numerical correspondence is consistent with the derivation in Section 2.6.2.

Finally, the momentum equation Eq.(2.34) is solved, majorly based on the 2nd-order projection scheme on a collocated grid in Section 3.5.3. Again, ρ, $\tilde{\mathbf{m}}_\rho$, and μ in the momentum equation are directly computed from Eq.(2.60) and the surface tension force $\mathbf{f}_s^{n+1}$ is computed from its definition in Eq.(2.65) with the balanced-force method in Section 3.5.2, while the drag force $\mathbf{f}_d$ in Eq.(2.66) is treated implicitly. As mentioned in Section 2.6.2, $\mathbf{f}_d$ should be predominant over either the inertial or viscous effect inside the solid phase. In other words, from Eq.(2.34), $A_d|_{\alpha_S=1} = C_d/\mathrm{e}_d$ should be much larger than $\rho/\Delta t$ (inertia) or μ/h^2 (viscous). Here h denotes the grid size. To achieve this goal, C_d is set to be $(\rho^{n+1}/\Delta t + \mu^{n+1}/h^2)$, and e_d is fixed to be 10^{-3}. Therefore, $\mathbf{f}_d$ will always be thousand times larger than both the inertial and viscous effects inside the solid phase, regardless of the numerical setup or material

properties. The divergence of the velocity at the new time level, which appears in **Step 4** of the projection scheme in Section 3.5.3, is determined from Eq.(2.63), i.e.,

$$\tilde{\nabla} \cdot \mathbf{u}^{n+1} = \frac{M_\phi(\rho_M^L - \rho_M^S)}{\rho^{n+1}} \xi_\phi^{n+1}, \tag{3.66}$$

where ξ_ϕ^{n+1} is obtained from its definition in Eq.(2.59). On the continuous level, as discussed in Section 2.6.2, with ρ and $\mathbf{m}_\rho$ from Eq.(2.60) and $\nabla \cdot \mathbf{u}$ in Eq.(2.63), Eq.(2.27) is implied. However, this is not necessarily true after discretization when the phase change happens and the densities of the liquid and solid phases are not the same. As a result, the *consistency of mass conservation* and *consistency of mass and momentum transport* are violated. In order to remedy this issue, a momentum source $S_m \mathbf{u}^{*,n+1}$ is added to the momentum equation, where S_m is the residual of the fully-discretized mass conservation equation, i.e.,

$$S_m = \frac{\gamma_t \rho^{n+1} - \hat{\rho}}{\Delta t} + \tilde{\nabla} \cdot \tilde{\mathbf{m}}_\rho. \tag{3.67}$$

It should be noted that S_m only appears on the discrete level due to discretization errors, and it is exactly zero away from the liquid-solid interface.

Following the above steps, the physical connections among different parts of the proposed model are correctly captured at the discrete level. With similar analyses to those in the proofs of Theorem 2.6.3, Theorem 2.6.4, and Theorem 2.6.5 in Section 2.6.2, one can easily show that those theorems remain intact on the discrete level. This will be numerically validated in Chapter 4.

3.8 Stability of the schemes

The proposed scheme is decoupled, semi-implicit, and formally 2nd-order accurate in both time and space. It conserves the mass of individual pure phases, the total amount of the components inside their corresponding dissolvable regions, and, as a result, the total mass of the fluid mixture. The momentum is conserved if the conservative method for the interfacial forces is applied. All the consistency conditions, i.e., the *consistency of reduction*, the *consistency of volume fraction conservation*, the *consistency of mass conservation*, and

the *consistency of mass and momentum transport*, are satisfied on the discrete level. The scheme also eliminates any generation of local void or overfilling. Therefore, the scheme is consistent and conservative.

One of the advantages of the decoupled semi-implicit scheme is that one solves the complicated system part by part and only needs to solve linear systems in every part. This avoids solving a huge non-linear coupled system from a fully implicit scheme and is probably more efficient in a single time step. However, the scheme is only conditionally stable and the time step size Δt is restricted. Rigorous proofs of the stability of the schemes are non-trivial but some empirical criteria are used here. Since all the convection terms are treated explicitly, the CFL condition needs to be considered, i.e., $\Delta t \leqslant \Delta t_{\text{CFL}} \sim \frac{h}{U_m}$ where h is the grid size and U_m is the scale of the maximum velocity. Another restriction comes from the surface tension [39], [43], i.e., $\Delta t \leqslant \Delta t_\sigma \sim \sqrt{\frac{h^3}{4\pi} \min(\frac{\rho_p+\rho_q}{\sigma_{p,q}})_{p\neq q}}$. The dominant part of the viscous term, i.e., $\nabla \cdot (\mu \nabla \mathbf{u})$, has been treated implicitly, which greatly removes the dependency of stability on the Reynolds number. As stated in [214], explicitly treating the remaining part of the viscous term is reasonable because it contributes in only a minor way to the viscous force, and a more careful analysis is available in [217]. The aforementioned criteria have been commonly used in computational fluid dynamics, and interested readers can refer to [16], [39], [43], [75], [79], [214], [217], [218]. The effect of M_0 in the Cahn-Hilliard equation Eq.(2.17) on the stability of the scheme in Section 3.3.3 has been discussed in [75], and it is observed that a large M_0 could lead to instability. On the other hand, the scheme in Section 3.3.4 for the conservative Allen-Cahn equation Eq.(2.19) allows a much larger M_0. The choice of M_0 in the present study is based on the practices in [75], so that it won't be the dominant factor of numerical instability but provides reasonably good results.

In addition to stability, accuracy is another important aspect when determining the time step size, since most interests are in the dynamical behavior of the multiphase and multicomponent problems. Therefore, a smaller time step size is necessary to produce accurate dynamical data. The efficiency of the scheme is not a major concern at the moment. Most attention is paid on developing a scheme that honors the physical properties of the proposed model.

4. VALIDATION[1]

This chapter performs various numerical benchmark tests to validate the basic properties of the models in Chapter 2 and the schemes in Chapter 3. For brevity, CH and CAC denote the models using the Cahn-Hilliard Eq.(2.17) and conservative Allen-Cahn Eq.(2.19) equations, respectively. If the boundedness mapping is supplemented, those models are denoted by CHB and CACB. The L_2 error of f, or L_2 norm of $(f - f^E)$, is the root mean square of $(f - f^E)$. The L_∞ error of f, or the L_∞ norm of $(f - f^E)$, is $\max|f - f^E|$. Here, f is the variable of interest and f^E is its exact (or reference) value. Moreover, h denotes the grid/cell size. All the results are reported in their dimensionless forms.

4.1 Manufactured solutions

The formal order of accuracy of the schemes described in Chapter 3 is examined using the manufactured solution problem. The idea is to first assume the exact solution and then plug it into the governing equations. The residuals of the the governing equations become the known source terms added to the discretized governing equations. Therefore, the numerical solution should approximate the "assumed" exact solution. Specifically, the source terms

[1]This chapter was partly published in Journal of Computational Physics, Vol 387, Ziyang Huang, Guang Lin, Arezoo M. Ardekani, A mixed upwind/central WENO scheme for incompressible two-phase flows, Page 455-480, Copyright Elsevier (2019); in Journal of Computational Physics, Vol 406, Ziyang Huang, Guang Lin, Arezoo M. Ardekani, Consistent, essentially conservative and balanced-force Phase-Field method to model incompressible two-phase flows, Page 109192, Copyright Elsevier (2019); in Journal of Computational Physics, Vol 420, Ziyang Huang, Guang Lin, Arezoo M. Ardekani, Consistent and conservative scheme for incompressible two-phase flows using the conservative Allen-Cahn model, Page 109718, Copyright Elsevier (2020); in Journal of Computational Physics, Vol 434, Ziyang Huang, Guang Lin, Arezoo M. Ardekani, A consistent and conservative model and its scheme for N-phase-M-component incompressible flows, Page 110229, Copyright Elsevier (2021); and in International Journal of Multiphase Flow, Vol 142, Ziyang Huang, Guang Lin, Arezoo M. Ardekani, A consistent and conservative volume distribution algorithm and its applications to multiphase flows using Phase-Field models, Page 103727, Copyright Elsevier (2021).

added to the right-hand side of the Phase-Field equation, the consistent formulation, and the momentum equation, respectively, are.

$$S_{\phi_p} = \frac{\partial \phi_p^E}{\partial t} + \nabla \cdot (\mathbf{u}^E \phi_p^E) - \nabla \cdot \mathbf{J}_p^E - L_p^{R,E} - L_p^{c,E}, \quad 1 \leqslant p \leqslant N,$$

$$S_{Q_p} = \nabla \cdot (W^E \nabla Q_p^E) - L_p^{Q,E}, \quad 1 \leqslant p \leqslant N,$$

$$\mathbf{S_u} = \frac{\partial (\rho^E \mathbf{u}^E)}{\partial t} + \nabla \cdot (\mathbf{m}^E \otimes \mathbf{u}^E) + \nabla P^E - \nabla \cdot \left[\mu^E (\nabla \mathbf{u}^E + (\nabla \mathbf{u}^E)^T)\right] - \rho^E \mathbf{g} - \mathbf{f}_s^E$$

Here, the superscript "E" represents the exact values of the equations in Chapter 2, resulting from the "assumed" exact solution.

The domain considered is $[-\pi, \pi] \times [-\pi, \pi]$ with the free-slip boundary that is consistent with the "assumed" exact solution or simply the exact solution in the following. The initial condition is from the exact solution by setting $t = 0$, and all the tests are stopped at $t = 1$. The cell size h is ranging from $\frac{2\pi}{8}$ to $\frac{2\pi}{128}$ along each axis.

4.1.1 Two-phase results

For the two-phase flow models using two-phase CH and two-phase CAC, the assumed exact solution is

$$\phi^E = Q^E = P^E = \cos(x)\cos(y)\sin(t),$$

$$u^E = \sin(x)\cos(y)\cos(t), \quad v^E = -\cos(x)\sin(y)\cos(t).$$

This exact solution is infinitely differentiable with respect to space and time, so it is suitable to valid the formal order of accuracy. Notice that u^E and v^E satisfy the divergence-free condition, and the integral of ϕ^E over the domain is independent of time. The material properties and parameters are $\rho_1 = 3$, $\rho_2 = 1$, $\mu_1 = 0.02$, $\mu_2 = 0.01$, $\mathbf{g} = \{1, -2\}$, $\eta = 0.1$, $\lambda = 0.001$ and $M_0 = 0.001$.

Using two-phase CH-B, the formal order of accuracy in space is first studied by fixing the time step size to be $\Delta t = 10^{-3}$. The L_2 and L_∞ errors of ϕ, u, v, and P are plotted in Fig.4.1. The 2nd-order convergence is clearly observed in both the L_2 and L_∞ errors

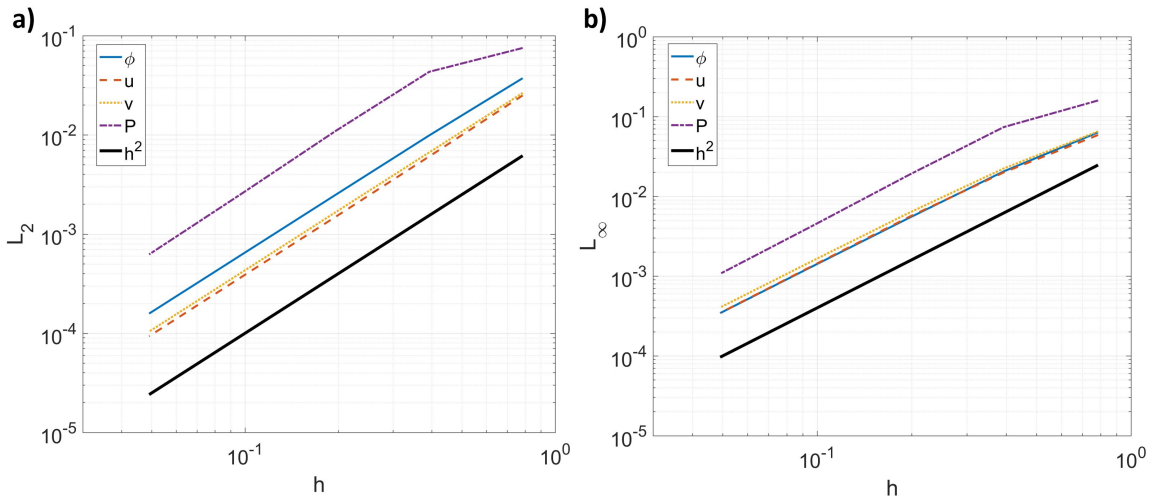

Figure 4.1. Results of the manufactured solution with two-phase CH-B and fixed Δt. a) L_2 errors of ϕ, u, v, and P with respect to the cell size. b) L_∞ errors of ϕ, u, v, and P with respect to the cell size.

as expected. One can conclude that the proposed scheme for two-phase CH-B is formally 2nd-order accurate in space.

In addition, the discrete divergence $\tilde{\nabla}\cdot\mathbf{u}$ and the discrete Divergence-Gradient-Transpose $\tilde{\nabla}\cdot(\tilde{\nabla}\tilde{\mathbf{u}})^T$ of the velocity are plotted in Fig.4.2. The discrete divergence-free condition is satisfied to machine precision, and because of this, $\tilde{\nabla}\cdot(\tilde{\nabla}\tilde{\mathbf{u}})^T$ reaches the machine zero, as expected in Lemma 3.1.1. This ensures the *consistency of reduction* of the viscous term on the discrete level, see ***Remark*** below Corollary 3.5.6.2.

Next the temporal convergence is tested by reducing the time step size as fast as the cell size, i.e., $\Delta t = h/(2\pi)$. The results are plotted in Fig.4.3. Since it has been validated that the scheme is 2nd-order accurate in space, and Δt is set proportional to h, the overall 2nd-order convergence observed in Fig.4.3 implies 2nd-order convergence of the temporal error, which matches the analysis in Chapter 3.

The same procedures are repeated using two-phase CAC-B and CAC-C, and the results are shown in Fig.4.4, Fig.4.5, Fig.4.6, and Fig.4.7. All the results suggest the 2nd-order accuracy.

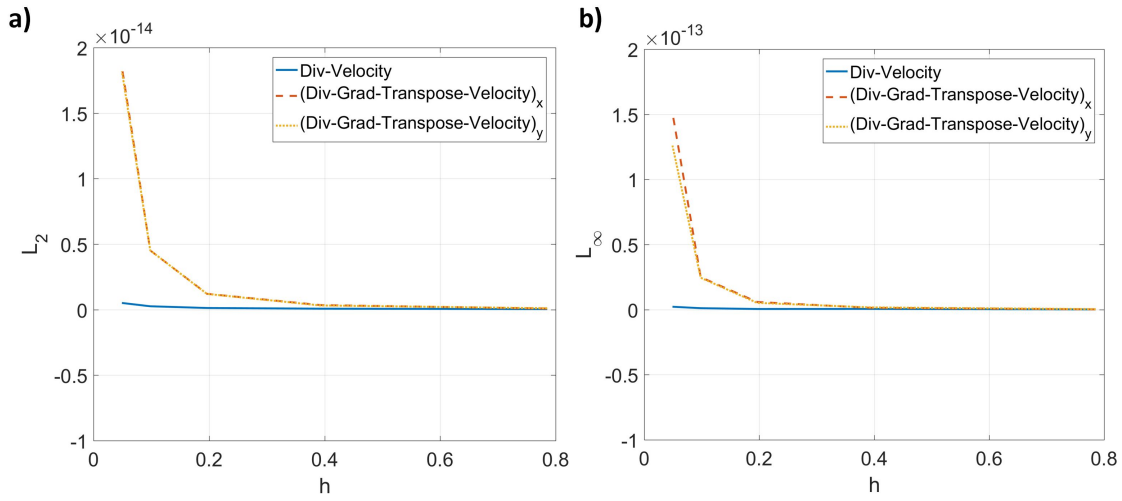

Figure 4.2. Results of the manufactured solution with two-phase CH-B and fixed Δt. a) L_2 errors of $\tilde{\nabla} \cdot \mathbf{u}$ and $\tilde{\nabla} \cdot (\tilde{\nabla}\tilde{\mathbf{u}})^T$ with respect to the cell size. b) L_∞ errors of $\tilde{\nabla} \cdot \mathbf{u}$ and $\tilde{\nabla} \cdot (\tilde{\nabla}\tilde{\mathbf{u}})^T$ with respect to the cell size.

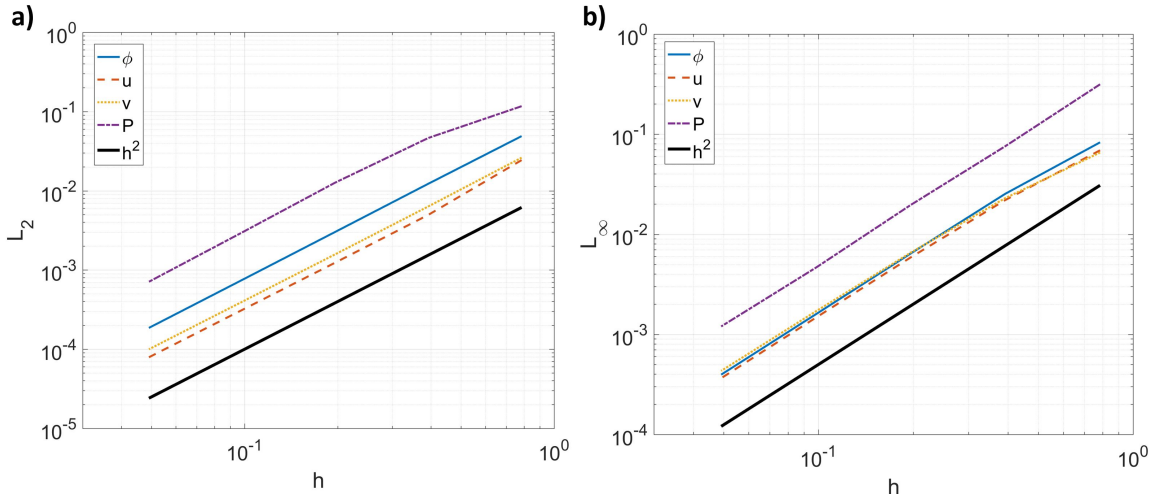

Figure 4.3. Results of the manufactured solution with two-phase CH-B and Δt proportional to the cell size. a) L_2 errors of ϕ, u, v, and P with respect to the cell size. b) L_∞ errors of ϕ, u, v, and P with respect to the cell size.

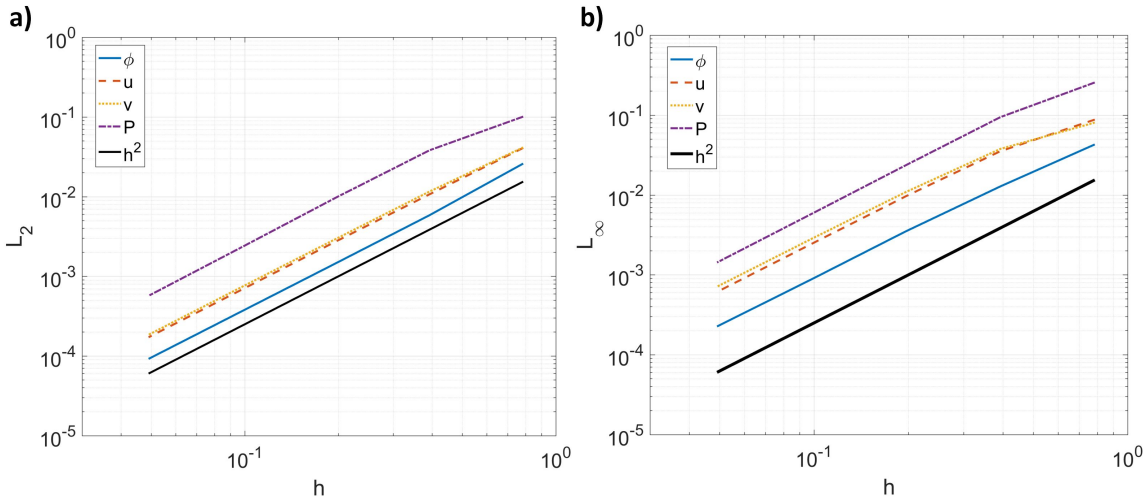

Figure 4.4. Results of the manufactured solution with two-phase CAC-B and fixed Δt. a) L_2 errors of ϕ, u, v, and P with respect to the cell size. b) L_∞ errors of ϕ, u, v, and P with respect to the cell size.

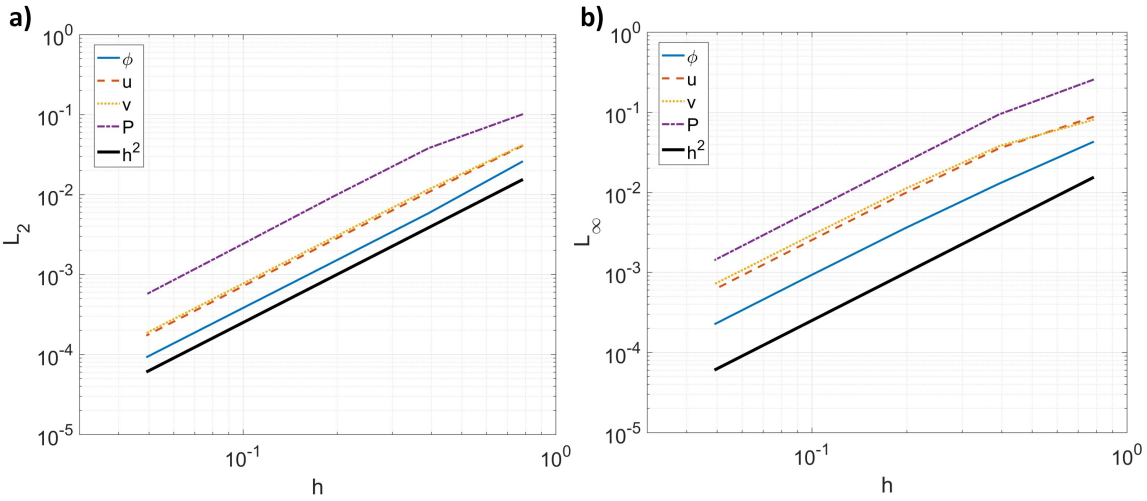

Figure 4.5. Results of the manufactured solution with two-phase CAC-C and fixed Δt. a) L_2 errors of ϕ, u, v, and P with respect to the cell size. b) L_∞ errors of ϕ, u, v, and P with respect to the cell size.

4.1.2 Multiphase results

Here, CH-B and CH-C are considered, and the assumed exact solution is

$$\phi_1^E = \frac{1}{3}\cos(x)\cos(y)\sin(t) - \frac{2}{3}, \quad \phi_2^E = \frac{1}{3}\cos(x)\cos(y)\sin(2t) - \frac{2}{3},$$
$$\phi_3^E = \frac{1}{3}\cos(x)\cos(y)\sin\left(\frac{1}{2}t\right) - \frac{2}{3}, \quad \phi_4^E = -\frac{1}{3}\cos(x)\cos(y)\left[\sin(t) + \sin(2t) + \sin\left(\frac{1}{2}t\right)\right],$$
$$u^E = \sin(x)\cos(y)\cos(t), \quad v^E = -\cos(x)\sin(y)\cos(t), \quad P^E = \cos(x)\cos(y)\sin(t).$$

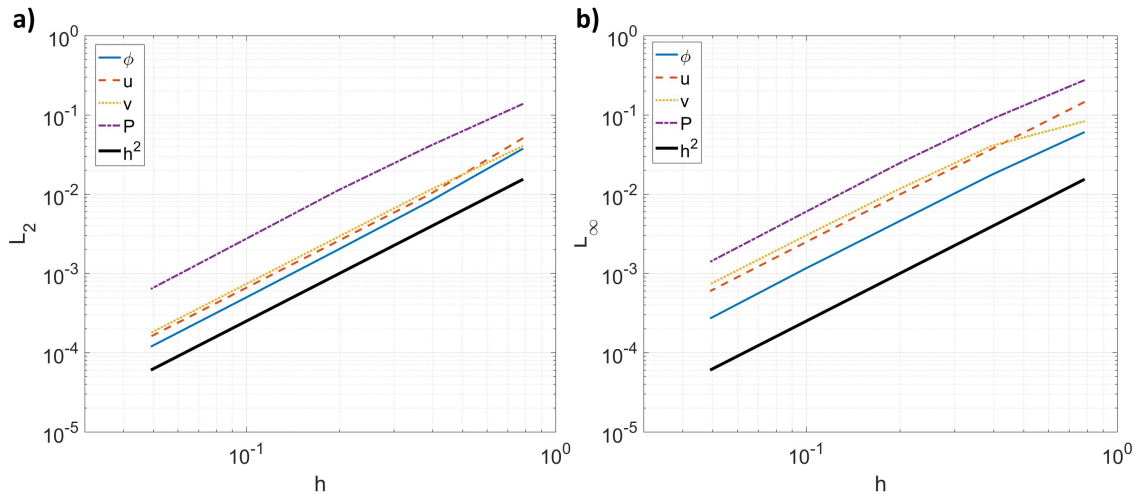

Figure 4.6. Results of the manufactured solution with two-phase CAC-B and Δt proportional to the cell size. a) L_2 errors of ϕ, u, v, and P with respect to the cell size. b) L_∞ errors of ϕ, u, v, and P with respect to the cell size.

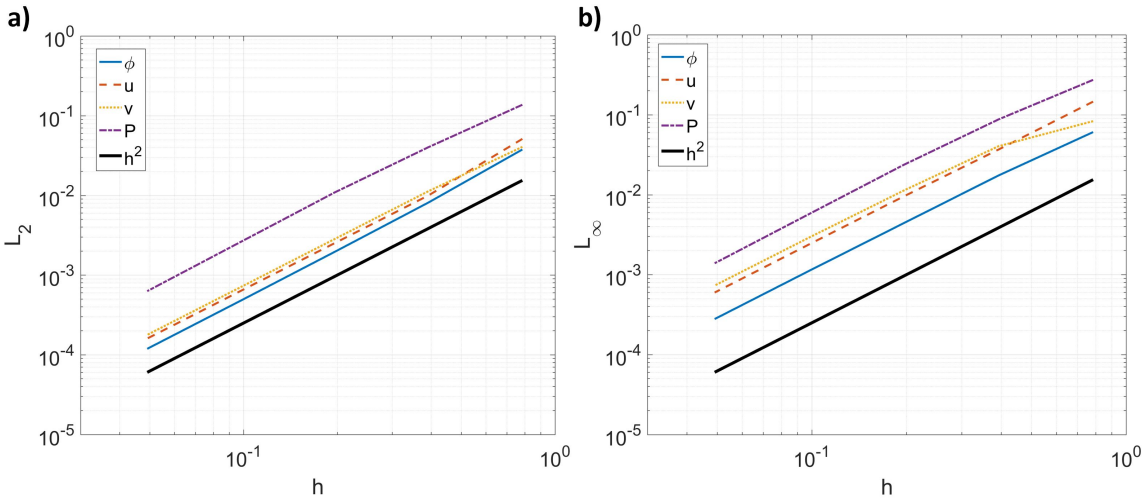

Figure 4.7. Results of the manufactured solution with two-phase CAC-C and Δt proportional to the cell size. a) L_2 errors of ϕ, u, v, and P with respect to the cell size. b) L_∞ errors of ϕ, u, v, and P with respect to the cell size.

Notice that $\nabla \cdot \mathbf{u}^E = 0$ and $\sum_{p=1}^{N} \phi_p^E = 2 - N$ are satisfied. The material properties and parameters are $\rho_1 = 1$, $\rho_2 = 5$, $\rho_3 = 10$, $\rho_4 = 15$, $\mu_1 = 0.01$, $\mu_2 = 0.02$, $\mu_3 = 0.05$, $\mu_4 = 0.10$, $\sigma_{1,2} = 0.01$, $\sigma_{1,3} = 0.02$, $\sigma_{1,4} = 0.03$, $\sigma_{2,3} = 0.04$, $\sigma_{2,4} = 0.05$, $\sigma_{3,4} = 0.06$, $\mathbf{g} = \{1, -2\}$, $\eta = 0.1$, and $M_0 = 0.001$.

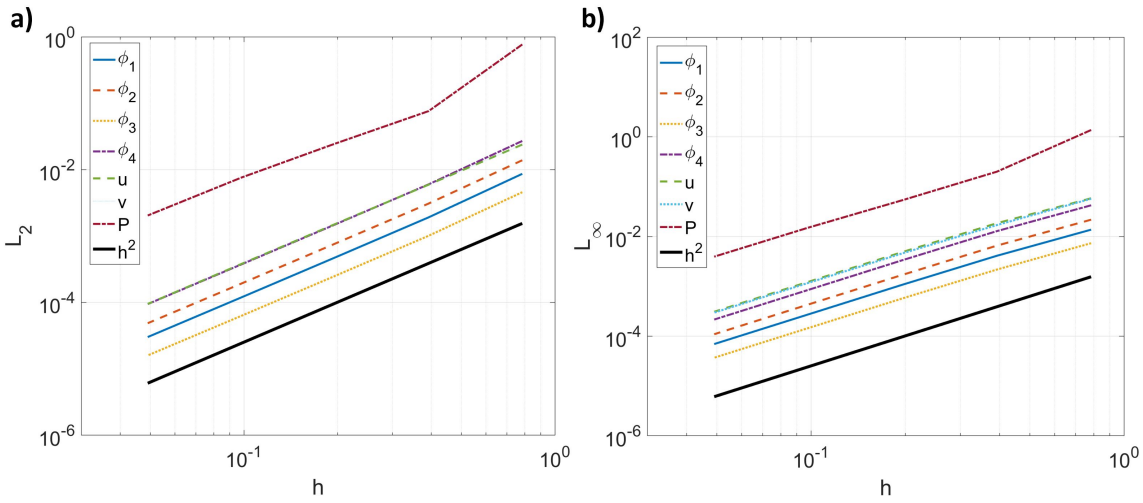

Figure 4.8. Results of the manufactured solution with CH-B and fixed Δt. a) L_2 errors of $\{\phi_p\}_{p=1}^4$, u, v, and P with respect to the cell size. b) L_∞ errors of $\{\phi_p\}_{p=1}^4$, u, v, and P with respect to the cell size.

The 2nd-order convergences of both the L_2 and L_∞ errors are observed in all the unknowns in Fig.4.8. Thus, the formal order of accuracy in space of the proposed scheme is 2nd-order accurate. Since the scheme for the momentum equation does not change in the multiphase problems, both $\tilde{\nabla}\cdot\mathbf{u}$ and $\tilde{\nabla}\cdot(\tilde{\nabla}\tilde{\mathbf{u}})^T$ are machine zero, like in the two-phase cases. Next, the time step is set proportional to the cell size, i.e., $\Delta t = \frac{h}{2\pi}$, and run the simulations again. The results obtained from CH-B are plotted in Fig.4.9. Again 2nd-order convergences of both the L_2 and L_∞ errors are observed. This implies that the formal order of accuracy of the proposed scheme in time is 2nd-order as well. Fig.4.10 and Fig.4.11 plots the results from CH-C and the same conclusions are drawn.

In summary, the proposed scheme in Chapter 3 is formally 2nd-order accurate in both time and space, and it satisfies $\tilde{\nabla}\cdot\mathbf{u} = 0$ and $\tilde{\nabla}\cdot(\tilde{\nabla}\tilde{\mathbf{u}}^T) = \overline{\tilde{\nabla}(\tilde{\nabla}\cdot\mathbf{u})} = \mathbf{0}$ on the discrete level. CAC (Eq.(2.19)) is not considered because it seems impossible to obtain $L_p^{c,E}$ in the equation. Since the schemes for CAC and for its two-phase correspondence (two-phase CAC) are almost the same, it is reasonable to infer that the same properties of two-phase CAC are followed.

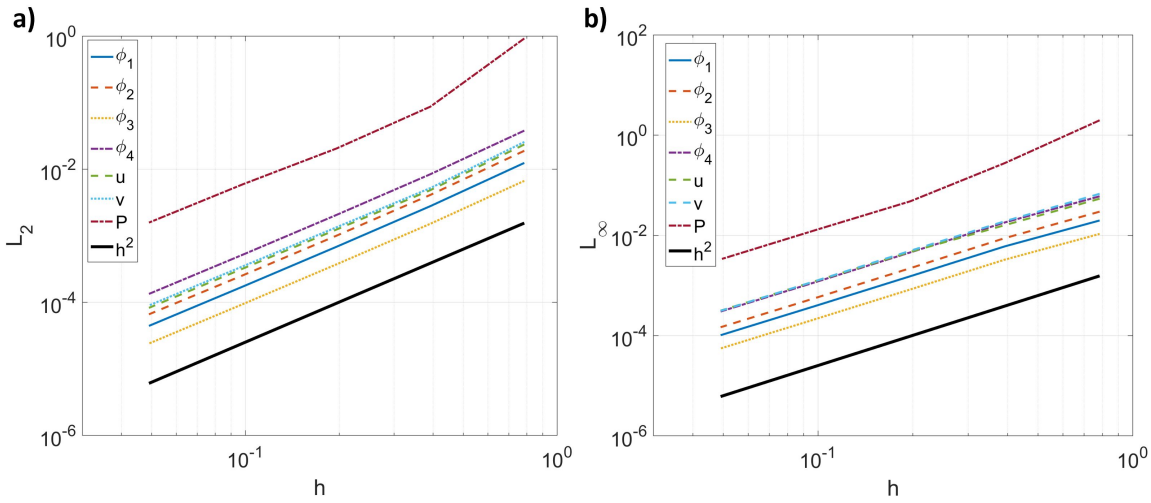

Figure 4.9. Results of the manufactured solution with CH-B and Δt proportional to the cell size. a) L_2 errors of $\{\phi_p\}_{p=1}^4$, u, v, and P with respect to the cell size. b) L_∞ errors of $\{\phi_p\}_{p=1}^4$, u, v, and P with respect to the cell size.

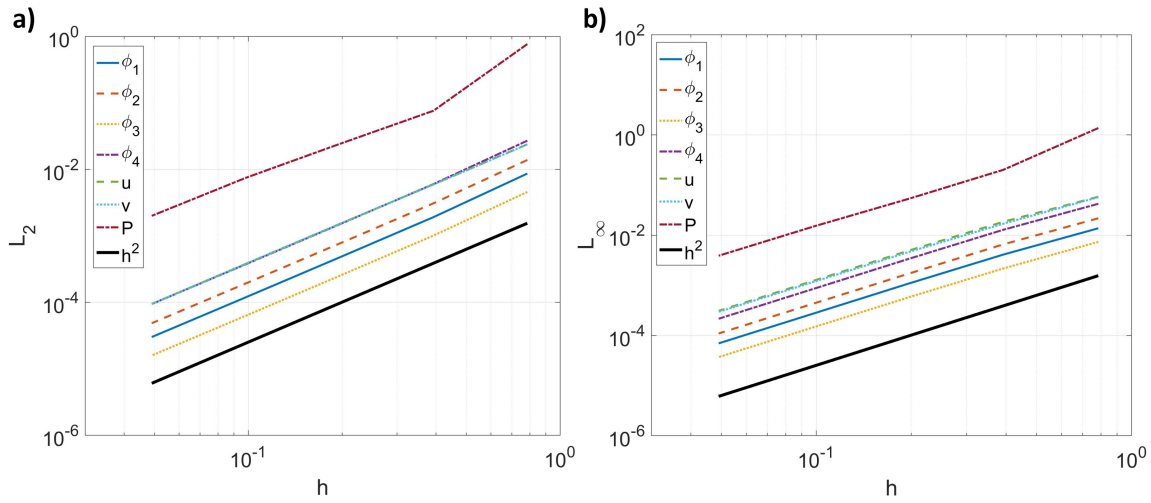

Figure 4.10. Results of the manufactured solution with CH-C and fixed Δt. a) L_2 errors of $\{\phi_p\}_{p=1}^4$, u, v, and P with respect to the cell size. b) L_∞ errors of $\{\phi_p\}_{p=1}^4$, u, v, and P with respect to the cell size.

4.2 Fictitious phases

To illustrate the importance of satisfying the *consistency of reduction*, the numerical equilibrium state of the Phase-Field equations without coupling to the flow, i.e., $\mathbf{u} \equiv \mathbf{0}$, are compared. In addition to CH, CHB, CAC, and CACB, the multiphase conservative

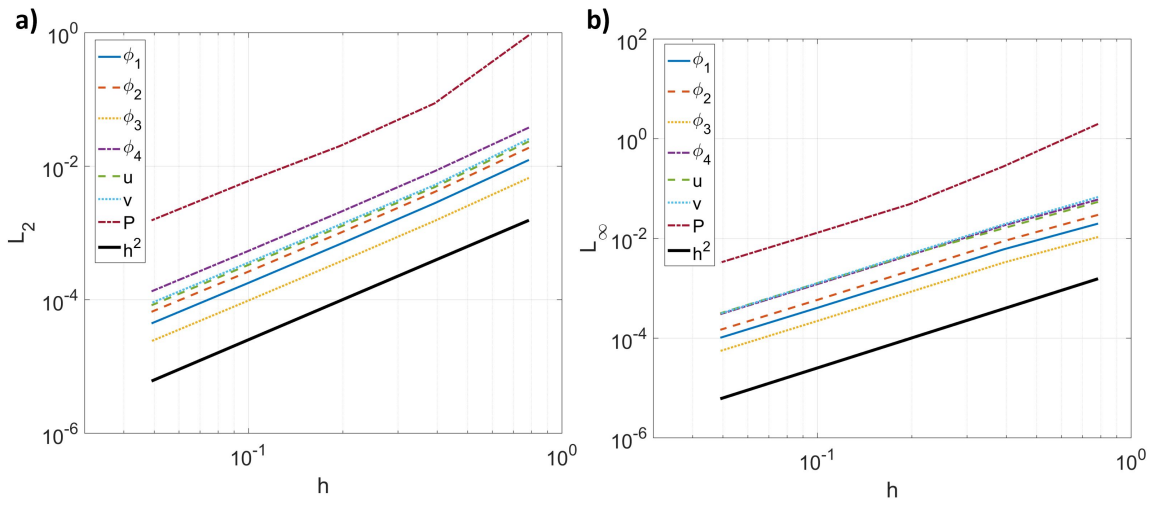

Figure 4.11. Results of the manufactured solution with CH-C and Δt proportional to the cell size. a) L_2 errors of $\{\phi_p\}_{p=1}^4$, u, v, and P with respect to the cell size. b) L_∞ errors of $\{\phi_p\}_{p=1}^4$, u, v, and P with respect to the cell size.

Allen-Cahn equation, proposed in [68], is supplemented, and it is called CACN in this case. CACN is solved by the same scheme in Section 3.3.4 for CAC except that $\{L_p^c\}_{p=1}^N$ follow the definition in Eq.(2.20) from [68]. Therefore, all the differences shown here between CAC and CACN are rooted in the different definitions of $\{L_p^c\}_{p=1}^N$. As analyzed in Section 2.2.3, CACN is not reduction consistent and can generate fictitious phases.

The domain considered is $[1 \times 1]$ with homogeneous Neumann boundaries. The domain is discretized by $[128 \times 128]$ cells and the time step is $\Delta t = 10h$. $\eta = 0.015$ are set and the off-diagonal elements of $\lambda_{p,q}$ are $\frac{3}{2\sqrt{2}}\eta$. M_0 is (η^2/λ_0) for CAC, CACB, and CACN, and is $10^{-3}\eta^2$ for CH and CHB due to numerical stability. The circle of Phase 1 is at $(0.25, 0.25)$ with a radius 0.1. The circle of Phase 2 is at $(0.5, 0.75)$ with a radius 0.1. The circle of Phase 3 is at $(0.75, 0.25)$ with a radius 0.1. Phase 4 occupies the rest of the domain. The circles of Phases 1, 2, and 3 are separated far enough, so there are no intersections among them. Therefore, $\eta^3|\nabla\phi_1||\nabla\phi_2||\nabla\phi_3|$ should be zero.

Fig.4.12 shows the equilibrium profiles from different Phase-Field equations, along with $\eta^3|\nabla\phi_1||\nabla\phi_2||\nabla\phi_3|$. It can be observed from Fig.4.12 **a)** that some amounts of Phase 1 from CACN are generated at the interfacial regions of Phases 2 and 4, and of Phases 3 and 4.

Phases 2 and 3 from CACN behave similarly to Phase 1. More clearly, $\eta^3|\nabla\phi_1||\nabla\phi_2||\nabla\phi_3|$ is non-zero at all the interfacial regions. Unphysically generating fictitious phases is because CACN violates the *consistency of reduction*, as analyzed in Section 2.2.3. On the other hand, the results from CH, CHB, CAC, and CACB do not generate any fictitious phases, and $\eta^3|\nabla\phi_1||\nabla\phi_2||\nabla\phi_3|$ from those equations is machine zero, since the *consistency of reduction* is satisfied by those equations and their schemes. In addition, there is little difference in the profiles from CH, CHB, CAC, and CACB.

4.3 Under-resolved structures

The comparison study in [99] shows that the two-phase CAC has a better ability to preserve under-resolved structures than CH. Here, the multiphase version of that study is performed and CH, CHB, CAC, and CACB are considered. Again, the velocity is set to be zero, i.e., $\mathbf{u} \equiv \mathbf{0}$.

The domain considered is $[1 \times 1]$ with homogeneous Neumann boundaries. The number of cells to discretize the domain is $[128 \times 128]$ and the time step is $\Delta t = 10h$. $\eta = h$ and $M_0 = 10^{-3}\eta^2$ are set, and the off-diagonal elements of $\lambda_{p,q}$ are $\frac{3}{2\sqrt{2}}\eta$. Phase 1 is enclosed by a circle at $(0.5, 0.5)$ with a diameter 0.2. Phase 2 is enclosed by a circle at $(0.2, 0.2)$ with a diameter 0.1. Phase 3 is enclosed by a circle at $(0.8, 0.8)$ with a diameter 0.05. Phase 4 occupies the rest of the domain.

The number of grid points across the circles, i.e., D/h, is 25.6 for Phase 1, 12.8 for Phase 2, and 6.4 for Phase 3. If the interfacial region is defined as $-0.995 < \phi < 0.995$, the number of grid points across the interfacial region is $n_I = 2\sqrt{2}\tanh^{-1}(0.995)\eta/h \approx 8.5$. Therefore, about 17 gird points across the circle of Phase 1 are inside the bulk-phase region of Phase 1. Inside the bulk-phase region of Phase 2, there are 5 grid points across the circle of Phase 2, while there is none inside the bulk-phase region of Phase 3. Evolutions of individual circles are quantified by measuring their diameters for a long period of time, and the results are shown in Fig.4.13. It is clear that the diameter of the smallest circle (Phase 3) decreases and it finally disappears at about $t = 750$ for CH and CHB. The shrinkage of the other two circles is negligible, considering the long period of simulation time. On the other hand, all

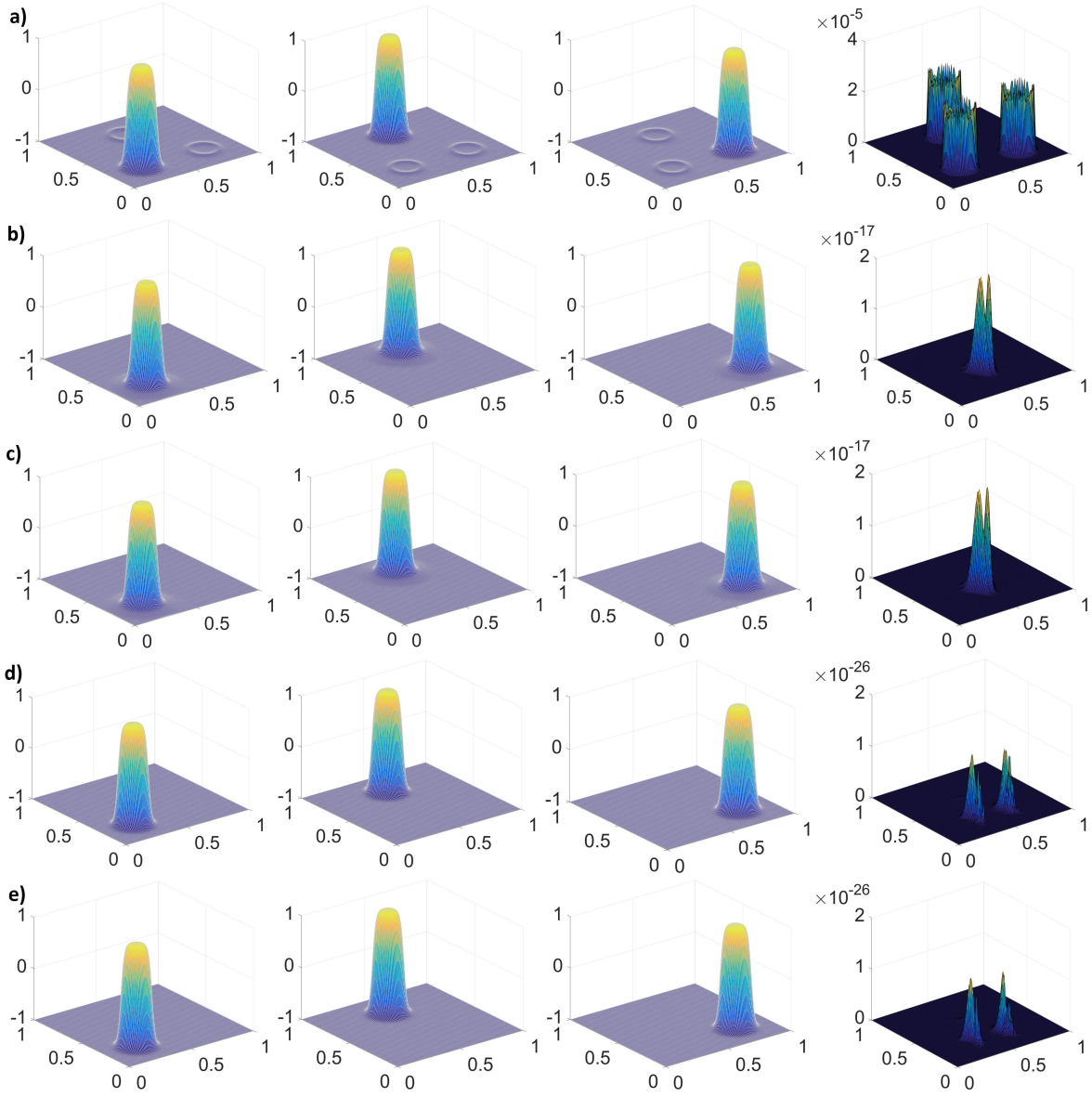

Figure 4.12. Results of the fictitious phases from a) CACN, b) CH, c) CHB, d) CAC, and e) CACB. The first column: Profile of phase 1. The second column: Profile of phase 2. The third column: Profile of phase 3. The fourth column: $\eta^3|\nabla\phi_1||\nabla\phi_2||\nabla\phi_3|$.

the circles are preserved and their diameters do not change with time for CAC and CACB. The maximum ϕ_3 less than 1 at $t = 0$, see the second column of Fig.4.13 c) or d), represents the poor resolution of the smallest circle in the sense that there is no bulk-phase region of Phase 3 at the beginning. Nevertheless, unlike CH and CHB, both CAC and CACB preserve this under-resolved structure very well.

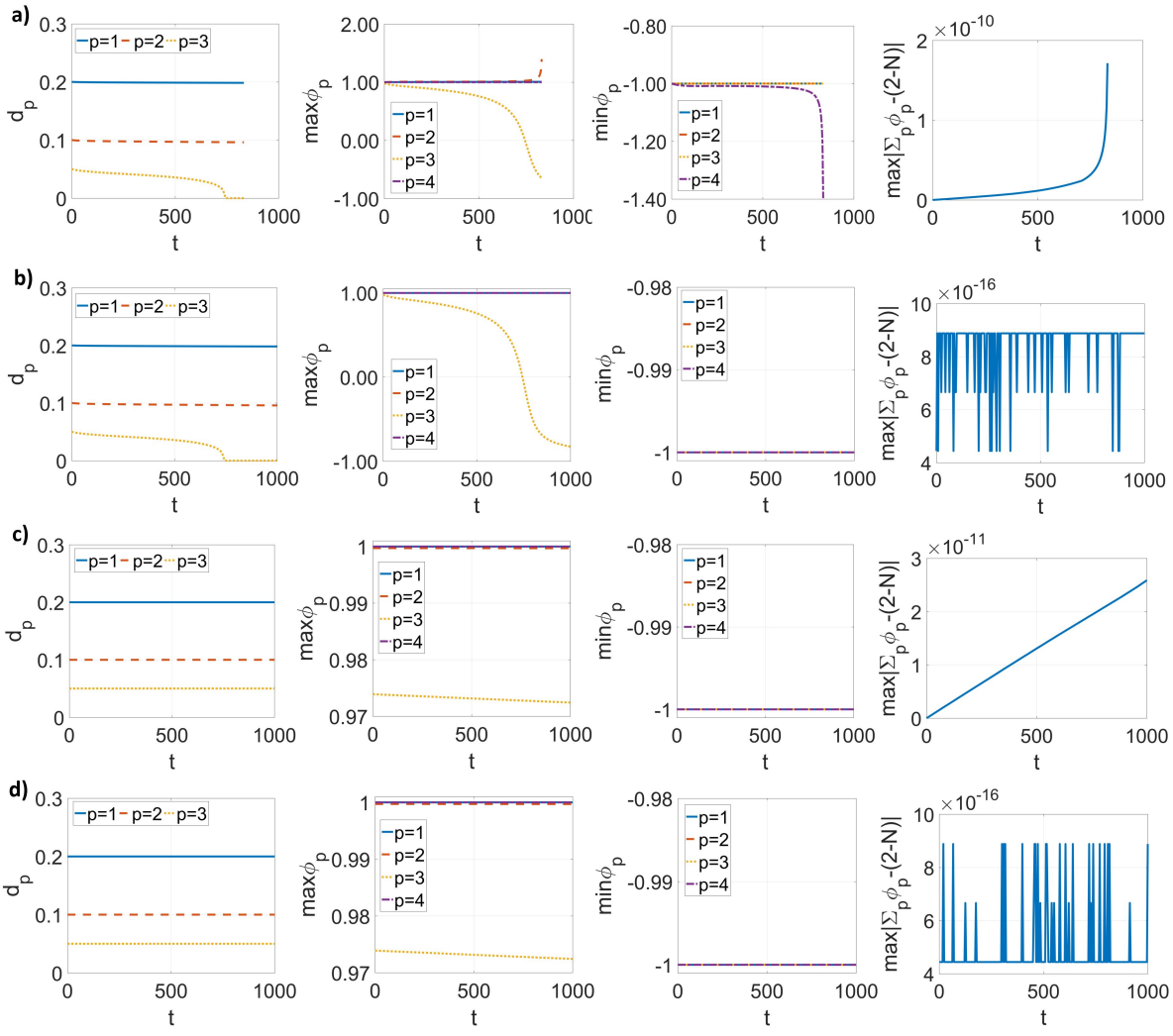

Figure 4.13. Results of the under-resolved structures from a) CH, b) CHB, c) CAC, and d) CACB. The first column: Diameter of the circles. The second column: Maximum of the order parameters. The third column: Minimum of the order parameters. The fourth column: Error of the summation constraint for the order parameters.

Without the boundedness mapping, the result using CH becomes unstable after the smallest circle disappears. One can observe that the maximum of ϕ_2 is larger than 1 and increases with a dramatic rate, see the second column of Fig.4.13 a). Due to the summation constraint for the order parameters, the minimum of ϕ_4 decreases beyond -1 with a similar behavior, see the third column of Fig.4.13 a). One can infer that the out-of-bound error appears at the interfacial region between Phases 2 and 4. Fig.4.14 **a)** shows the profiles of

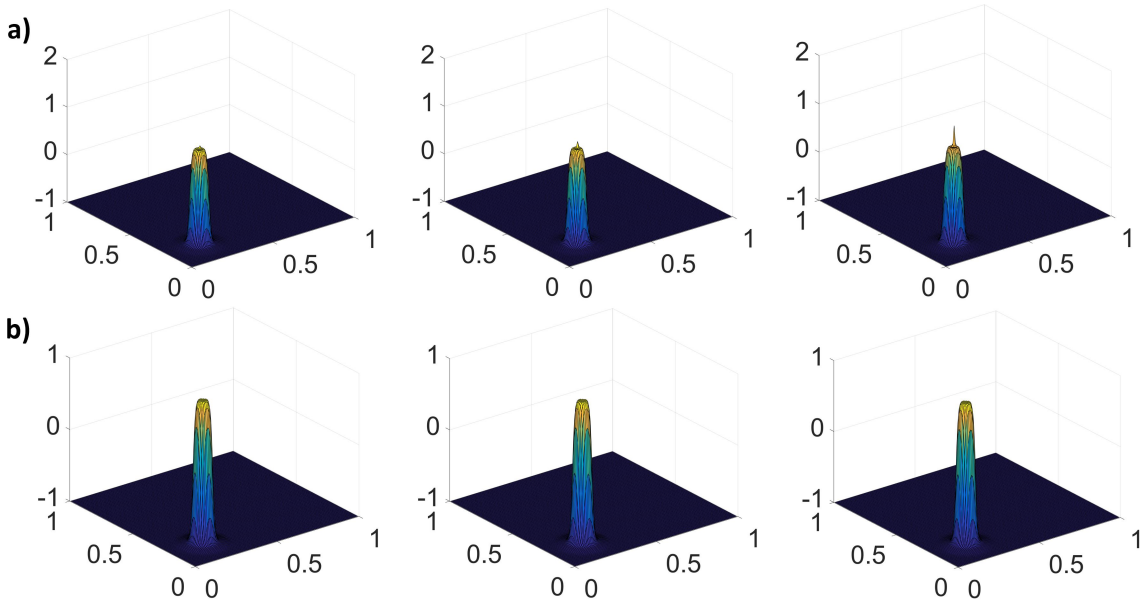

Figure 4.14. Profiles of ϕ_2 at selected moments of the under-resolved structures from a) CH and b) CHB. The first column: $t = 781.2500$. The second column: $t = 820.3125$. The third column: $t = 832.0313$.

ϕ_2 at selected moments from CH. At the interfacial region of Phases 2 and 4, an out-of-bound error initializes, which is consistent with the remark in Section 3.3.5. As time goes on, the out-of-bound error keeps growing and becomes a spike. As a result, the profile of ϕ_2 is significantly contaminated and becomes unphysical. Eventually, numerical instability is triggered due to the large out-of-bound error. Profiles of ϕ_2 using CHB at the same moments are supplemented in Fig.4.14 **b)**. Thanks to the boundedness mapping, the out-of-bound error is eliminated. Consequently, the physical profile of ϕ_2 is preserved and the computation is stable. The out-of-bound error from CAC is of the order of the round-off error. Thus, the difference between CAC and CACB is negligible. Although the summation constraint for the order parameters is satisfied, as shown in the last column of Fig.4.13, it is enforced more accurately when the boundedness mapping is included, i.e., in the last column of Fig.4.13 b) and d).

In summary, CAC has a better ability to preserve under-resolved structures than CH. The boundedness mapping is beneficial to improve the robustness of the scheme and to provide a physical solution.

4.4 Reversed single vortex

This case evaluates the performance of the Phase-Field equations as an interface-capturing method with a given velocity. Following the case setup in [219], the domain is $[1 \times 1]$ and a circle with a radius $r = 0.15$ is initially at $(x_r, y_r) = (0.5, 0.75)$. The velocity is defined from the stream function

$$\psi_s = \frac{1}{\pi}\sin^2(\pi x)\sin^2(\pi y)\cos(\frac{\pi t}{T}),$$

where $T = 2$ as that in [219]. The circle is stretched by the flow and reaches its maximum deformation at $t = \frac{T}{2}$. After that, the flow begins to reverse and the circle should return to its initial location and shape at $t = T$. The cell size of each direction is successively decreased from $h = 1/25$ to $h = 1/200$, and the time step is determined by the CFL constraint, i.e., CFL $= |u|_{\max}\Delta t/h = 0.1$. η and M_0 are $\eta = \eta_0(h/h_0)$ and $M_0 = M_{00}(\eta/\eta_0)$, with $\eta_0 = h_0 = 1/32$ and $M_{00} = 10^{-7}$. The error of the solution is defined as

$$Er = r - \sqrt{(x_s - x_r)^2 + (y_s - y_r)^2},$$

where (x_s, y_s) are the points at the zero contour of the order parameter at $t = T$, i.e., $\phi(x_s, y_s, T) = 0$. The L_2 error is defined as the root mean square of Er.

Fig.4.15 and Fig.4.16 show the results of the reversed single vortex problem using two-phase CH and CAC equations, respectively, at $t = 0$, $t = \frac{T}{2}$ and $t = T$. It can be clearly observed that the quality of the numerical solution is improved and the solution converges to the exact one as the cell size is reduced. Fig.4.17 **a)** shows the L_2 norm of Er and the convergence rate is around 1.5 from both equations.

4.5 Zalesak's disk

This case evaluates the performance of the Phase-Field equations as an interface-capturing method with a given velocity. Following the case setup in [220], the domain is $[1 \times 1]$ and there is a notched circle initially at $(x_r, y_r) = (0.5, 0.75)$ with a radius $r = 0.15$. The width

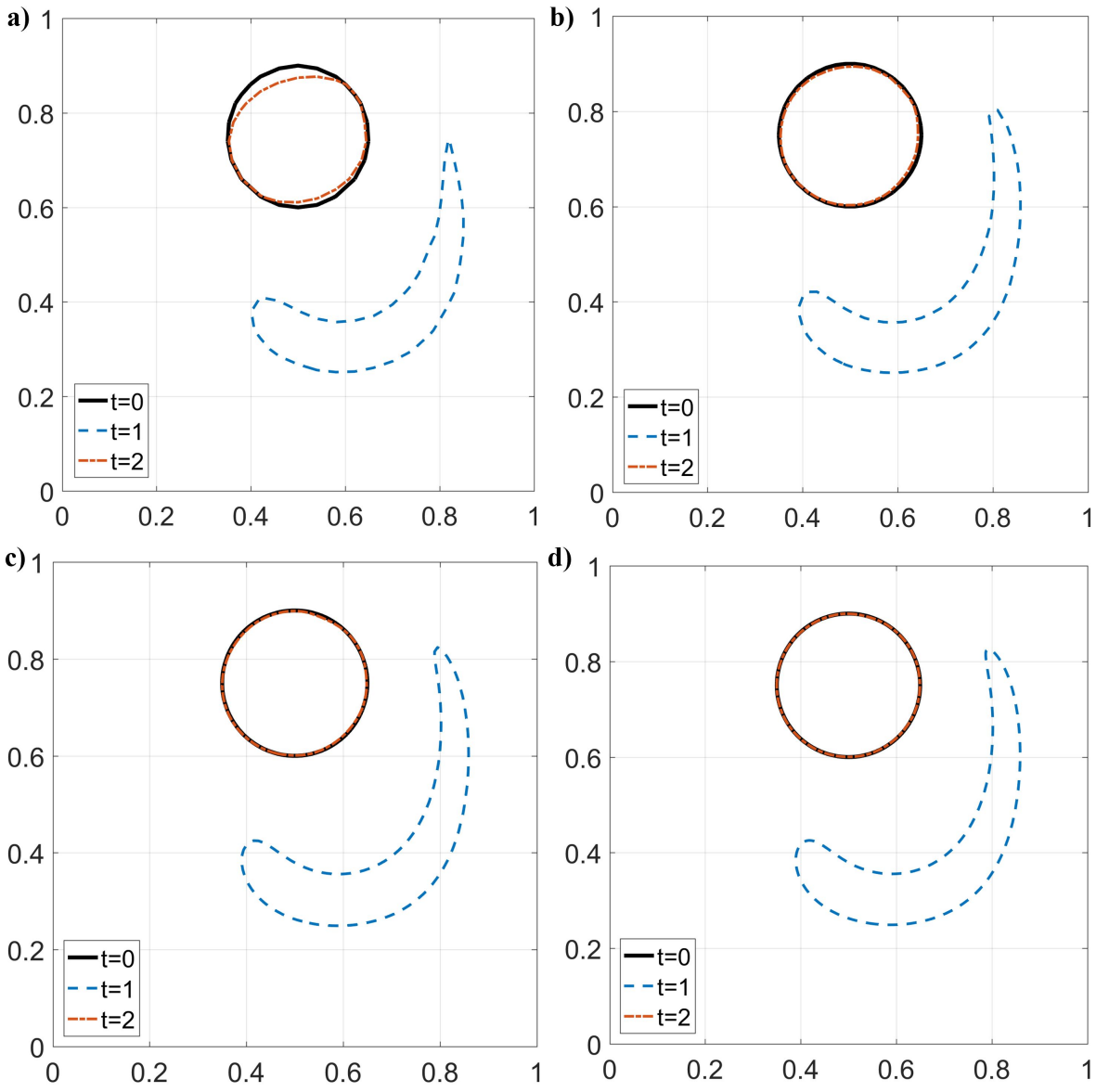

Figure 4.15. Results of the reversed single vortex problem using two-phase CH at $t = 0$ (black solid line), $t = T/2$ (blue dashed line), $t = T$ (red dashed line). a) $h = 1/25$, b) $h = 1/50$, c) $h = 1/100$ and d) $h = 1/200$.

of the notch and the distance from the top of the notch to the center of the circle are both 0.05. The velocity of rigid body rotation is defined from the stream function

$$\psi_s = \frac{1}{2}\Omega_0[(x - x_0)^2 + (y - y_0)^2],$$

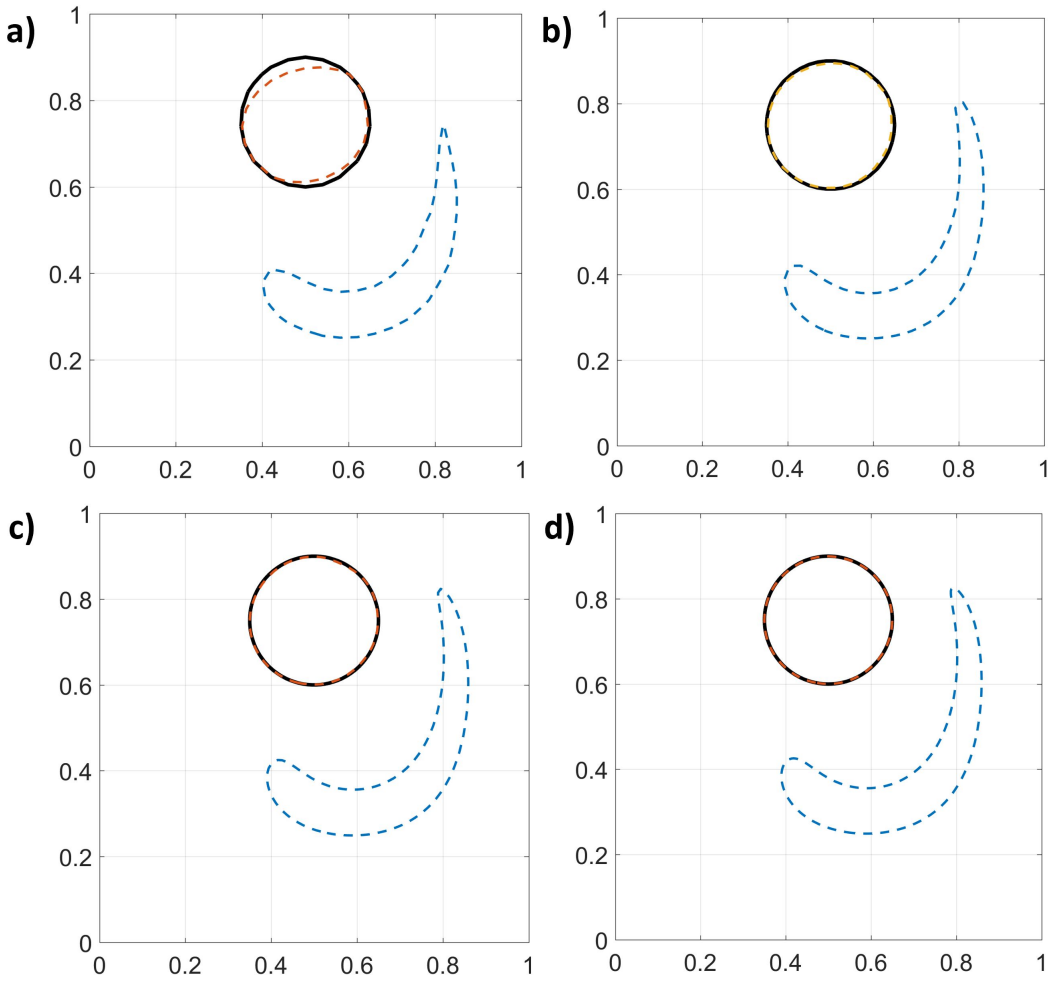

Figure 4.16. Results of the reversed single vortex problem using two-phase CAC at $t = 0$ (black solid line), $t = T/2$ (blue dashed line), $t = T$ (red dashed line). a) $h = 1/25$, b) $h = 1/50$, c) $h = 1/100$ and d) $h = 1/200$.

where $\Omega_0 = 1$, and $x_0 = y_0 = 0.5$ as those in [219]. The notched circle is going to rotate around (x_0, y_0) without changing its shape. At $t = 2\pi$, the notched circle should return to its initial location without any deformation. The cell size h is successively decreased from $h = 1/25$ to $h = 1/200$, and the time step is determined from the CFL constraint, i.e., $\text{CFL} = \Omega_0 \Delta t/h = 0.1$. η and M_0 are $\eta = \eta_0(h/h_0)$ and $M_0 = M_{00}(\eta/\eta_0)$ with $\eta_0 = h_0 = 1/32$ and $M_{00} = 10^{-7}$. The error of the solution is defined as

$$Er = \sqrt{[x_I(s; t = 2\pi) - x_I(s; t = 0)]^2 + [y_I(s; t = 2\pi) - y_I(s; t = 0)]^2},$$

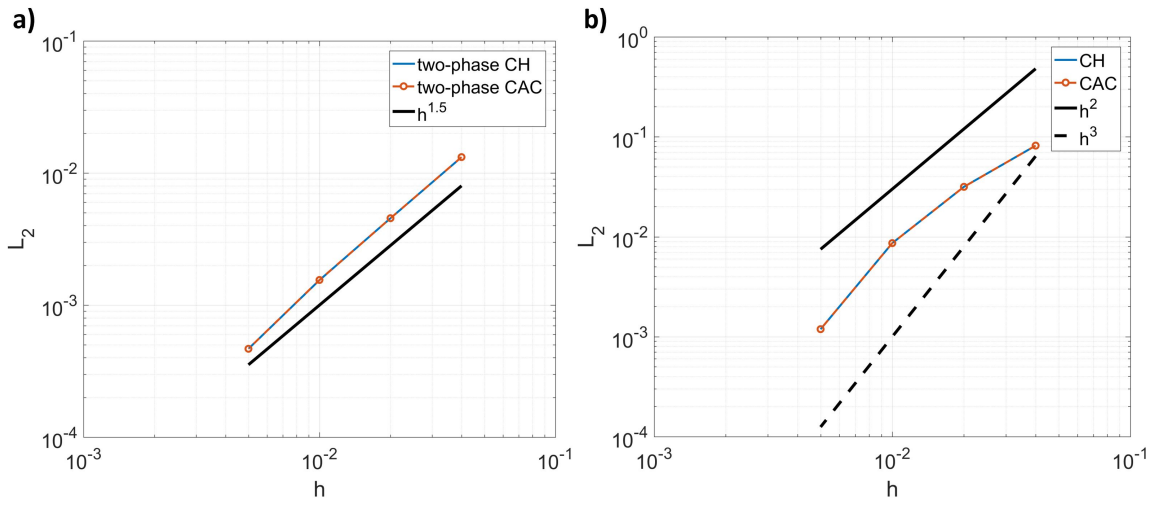

Figure 4.17. Convergence in the interface capturing problems using two-phase CH and CAC. a) The reverse single vortex problem. b) The Zalesak's disk problem.

where $x_I(s;t)$ and $y_I(s;t)$ are the cubic spline interpolants using the points (x_s, y_s) at time t satisfying $\phi(x_s, y_s, t) = 0$, and s is the parameter of the cubic splines ranging from 0 to 1. When evaluating Er, s is discretized by 1000 points equally.

Fig.4.18 and Fig.4.19 show the results of the Zalesak's disk problem using two-phase CH and CAC, respectively, at $t = 0$, $t = 2$, $t = 4$ and $t = 2\pi$. The convergence of the numerical solution to the exact solution can be obviously observed. Fig.4.17 **b)** shows the L_2 norm of Er and the convergence rate is fast. This can be attributed to the rigid body motion of the notched circle that is lack of deformation.

4.6 Two diffusion problems

Two diffusion problems are performed to demonstrate that the proposed N-phase-M-component model is capable of modeling different circumstances of cross-interface transports of a component that is dissolvable in both sides of the interface. The domain considered is $[1 \times 1]$ with periodic boundaries along the x axis and free-slip boundaries along the y axis. The domain is discretized by 128×128 cells and the time step size is $\Delta t = 10^{-3}$. Phase 1, whose pure phase density is 1000 and viscosity is 10^{-3}, is at the bottom below $y = 0.3$, while the rest of the domain is filled by Phase 2, whose pure phase density and viscosity are 1 and

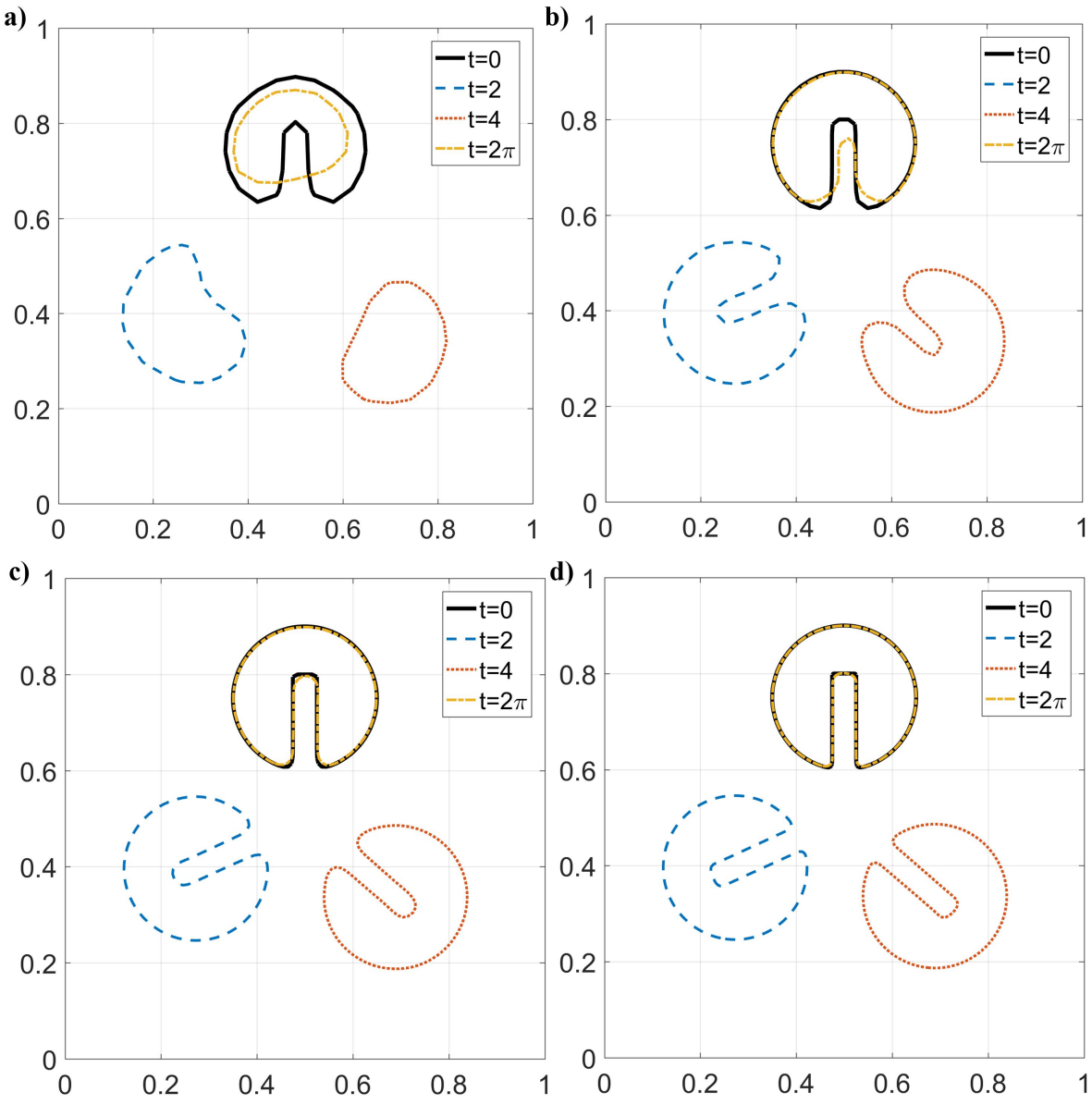

Figure 4.18. Results of the Zalesak's disk problem using two-phase CH at $t = 0$ (black solid line), $t = 2$ (blue dashed line), $t = 4$ (red dashed line), and $t = 2\pi$ (yellow dashed line). a) $h = 1/25$, b) $h = 1/50$, c) $h = 1/100$ and d) $h = 1/200$.

2×10^{-5}, respectively. The surface tension between the phases is 0.0728 and no gravity is considered. Component 01 with density 50 and viscosity 10^{-4} is dissolvable in both of the phases with diffusivity 0.02 inside Phase 1 and 0.08 inside Phase 2. Initially, there is no

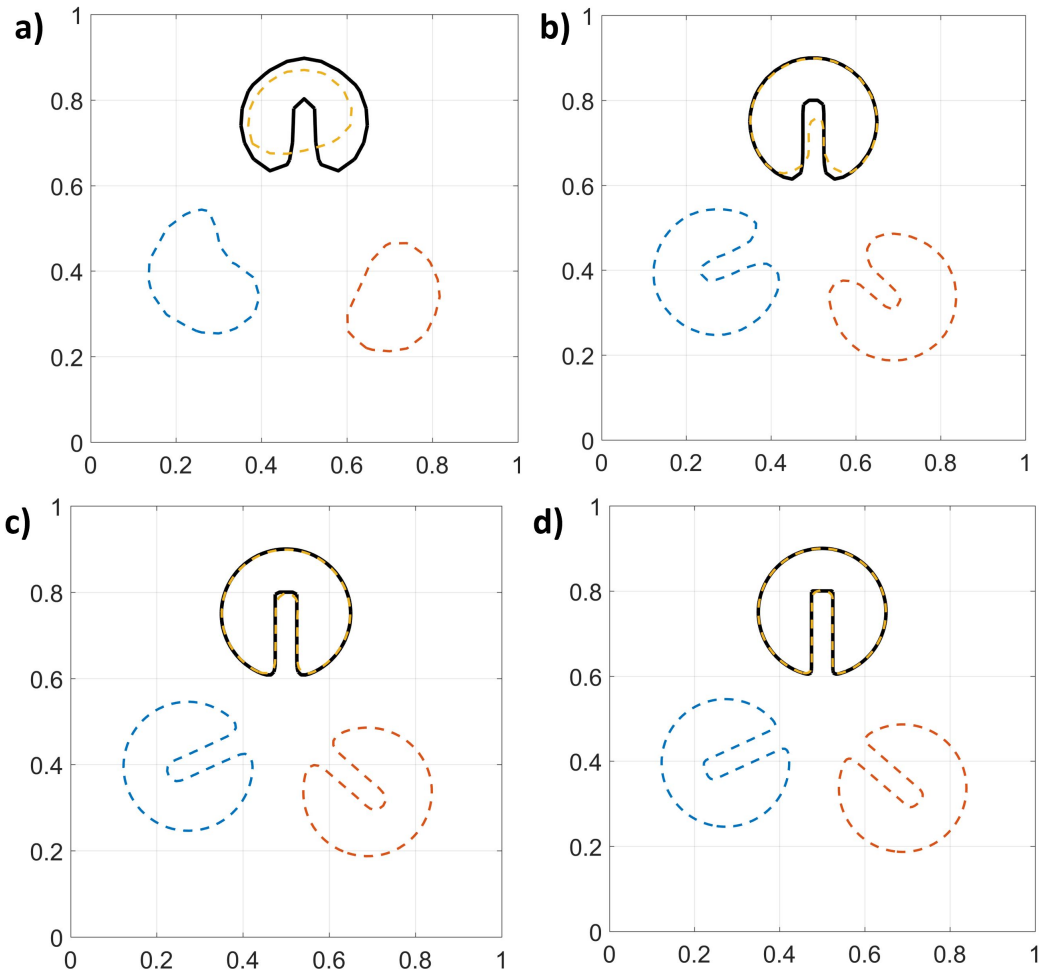

Figure 4.19. Results of the Zalesak's disk problem using two-phase CAC at $t = 0$ (black solid line), $t = 2$ (blue dashed line), $t = 4$ (red dashed line), and $t = 2\pi$ (yellow dashed line). a) $h = 1/25$, b) $h = 1/50$, c) $h = 1/100$ and d) $h = 1/200$.

Component 01 inside the domain, while its concentrations are 1 at the bottom wall and 0.1 at the top wall.

In the first case, Component 01 is unable to cross the phase interface between Phases 1 and 2. As discussed in Section 2.6.1, one needs to define Component 1 and Component 2 such that Component 1 is dissolvable only in Phase 1 and Component 2 is dissolvable only in Phase 2. Consequently, the concentration of Component 01 is represented by $\chi_{01}^{M} C_{01} = \chi_{1}^{M} C_1 + \chi_{2}^{M} C_2$. The sharp-interface steady solution is a step function jumping from 1 to 0.1 at $y = 0.3$. In the second case, Component 01 is able to cross the phase interface between

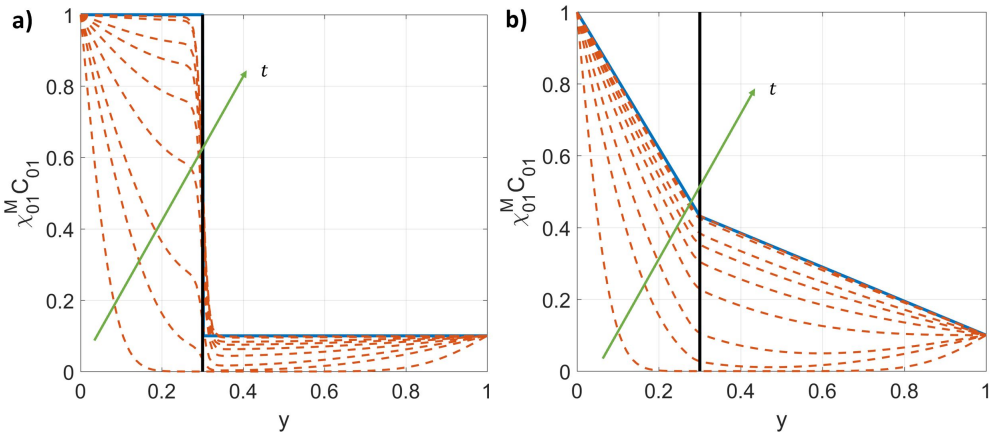

Figure 4.20. Profiles of the concentrations, blue solid line: the sharp-interface steady solution, red dashed lines: the numerical solution at $t = 0.1$, 0.5, 1, 2, 3, 4, 5, 8, 10, black solid line: interface. a) results of the first case of the two diffusion problems. b) results of the second case of the two diffusion problems.

Phases 1 and 2. Then one only needs to define a single component, i.e., Component 1, sharing the same material properties with Component 01 and dissolving in both Phases 1 and 2. As a result, the concentration of Component 01 is $\chi_{01}^{M}C_{01} = \chi_{1}^{M}C_{1}$. The sharp-interface steady solution is two straight segments with different slopes connecting at $y = 0.3$, i.e.,

$$C^{S}(y) = \begin{cases} -\frac{36}{19}y + 1, & y \leqslant 0.3 \\ -\frac{9}{19}(y-1) + 0.1, & y \geq 0.3 \end{cases}$$

The profiles of $\chi_{01}^{M}C_{01}$ at selected moments in the two cases are shown in Fig.4.20, along with the corresponding sharp-interface steady solutions. As time goes on, the numerical solutions successfully approach the corresponding sharp-interface steady solutions, even though the background phases have a density ratio of 1000 and a viscosity ratio of 50. Due to the diffuse domain approach, one can observe that the profiles change smoothly across the interface instead of a sharp transition. The results in this section demonstrate that the proposed model is capable of modeling whether a component is allowed to cross a phase interface when it is dissolvable in both sides of the interface.

4.7 Steady drops

The steady drop problem is performed to quantify the numerical force balance between the pressure gradient and the surface force which is discretized by either the balanced-force method or the conservative method. With a circular interface surrounded by quiescent fluids, on the continuous level, the surface tension should be exactly balanced by the pressure jump, and thus the fluid remains stationary. However, such an exact force balance is seldom achievable on the discrete level, and the force imbalance introduced by the discretization drives the fluid to move, generating the so-called spurious current. Ample studies of the two-phase spurious current have been performed in, e.g., [39], [43], [44], [113], [118], [196], [206], [221]–[224], based on the continuous surface [39] and/or the ghost fluid method (GFM) [40]. This section investigates the performance of the surface force from the Phase-Field method.

The domain size is $[1 \times 1]$ with the free-slip boundary. The cell size is ranging from $\frac{1}{16}$ to $\frac{1}{128}$ along each axis, and the time step size is $\Delta t = 10^{-3}$. The Phase-Field parameters are set up as those in [221], i.e., $\eta = \eta_0(h/h_0)^{2/3}$ and $M_0 = M_{00}(\eta/\eta_0)^{3/2}$, where $\eta_0 = h_0 = 1/32$ and $M_{00} = 10^{-7}$. The strength of the spurious current is evaluated at $t = 10$, by measuring the L_2 and L_∞ norms of the total velocity, i.e., $V = \sqrt{u^2 + v^2}$.

4.7.1 Two-phase results

The fluid inside the drop is referred to as Phase 1 with density ρ_1 and viscosity μ_1, while the one outside the drop is named Phase 2 with density ρ_2 and viscosity μ_2. A circular drop with a radius $D = 0.4$ is placed at the center of the domain and the velocity and pressure are initially zero.

First, the effects of the density ratio, viscosity ratio, and surface tension on the convergence behaviors of the spurious current under grid refinement are investigated using two-phase CH-B. Six cases are considered, whose material properties are

- Case 0: $\rho_1 = 1000$, $\rho_2 = 1000$, $\mu_1 = 0$, $\mu_2 = 0$, $\sigma = 10^{-12}$
- Case 1: $\rho_1 = 1000$, $\rho_2 = 1000$, $\mu_1 = 0$, $\mu_2 = 0$, $\sigma = 1$

- Case 2: $\rho_1 = 1000$, $\rho_2 = 1000$, $\mu_1 = 0.1$, $\mu_2 = 0.1$, $\sigma = 1$
- Case 3: $\rho_1 = 1000$, $\rho_2 = 1$, $\mu_1 = 0.1$, $\mu_2 = 0.1$, $\sigma = 1$
- Case 4: $\rho_1 = 1000$, $\rho_2 = 1000$, $\mu_1 = 0.1$, $\mu_2 = 0.0001$, $\sigma = 1$
- Case 5: $\rho_1 = 1000$, $\rho_2 = 1000$, $\mu_1 = 0.1$, $\mu_2 = 0.1$, $\sigma = 10$

Case 0 is a numerical check, such that the output is zero when the input is zero. For a clear presentation, the results of case 0 are not shown. Both the L_2 and L_∞ norms of V in case 0 are in the order of 10^{-14} for all the cell sizes considered.

The results of cases 1 to 5 are shown in Fig.4.21. One can see that the spurious current decreases in all the cases as a result of grid refinement, with the convergent rate in between 1st and 2nd order. Case 5, which has the largest surface tension, produces the largest spurious current, while converges slower at the rate very close to 1st order. Case 1, which is the inviscid case, has the second largest spurious current, while converges faster at the rate close to 2nd order. This implies that the physical viscosity helps to suppress the spurious current. The large viscosity ratio (Case 4) slightly increases the strength of the spurious current, while the effect of large density ratio (Case 3) is very small. Interestingly, one obtains the smallest spurious current in Case 3, which includes a large density ratio. In general, the tests show that the strengths of the spurious current in cases 1 to 5 are in the same order of magnitude.

Next, the performances of the balanced method and the conservative method are investigated using two-phase CAC-B and CAC-C. The material properties are $\rho_1 = \rho_2 = 1000$, $\mu_1 = \mu_2 = 0.1$, and $\sigma = 1$. Fig.4.22 shows the convergence behavior of the total velocity in L_2 and L_∞ norms. One can observe that the spurious current is small and converges to zero as the cell is refined, no matter which method is used. The balanced-force method has a better performance in achieving the numerical force balance. The spurious current is smaller than the one from the conservative method. In addition, the spurious current converges to zero with a rate that is close to 2nd-order when using the balanced-force method, while it is closer to 1st-order when the conservative method is applied.

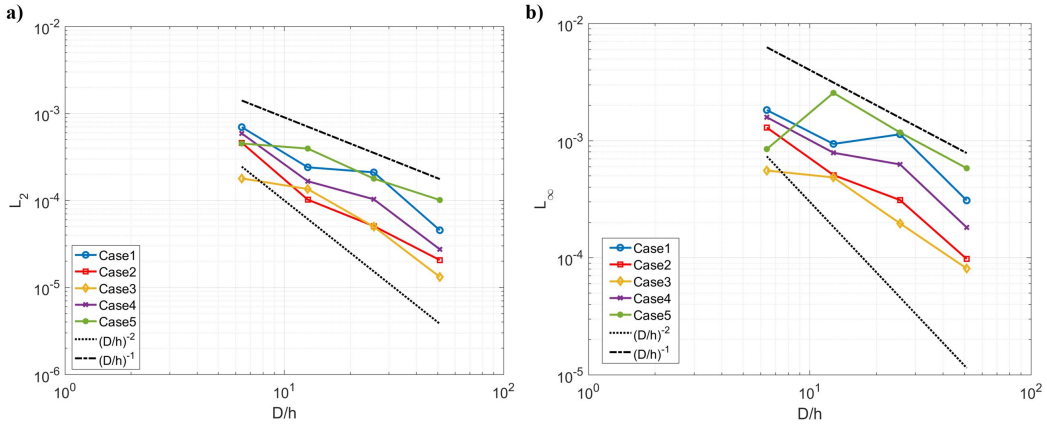

Figure 4.21. Results of the steady drop using two-phase CH-B. a) The L_2 error. b) The L_∞ error.

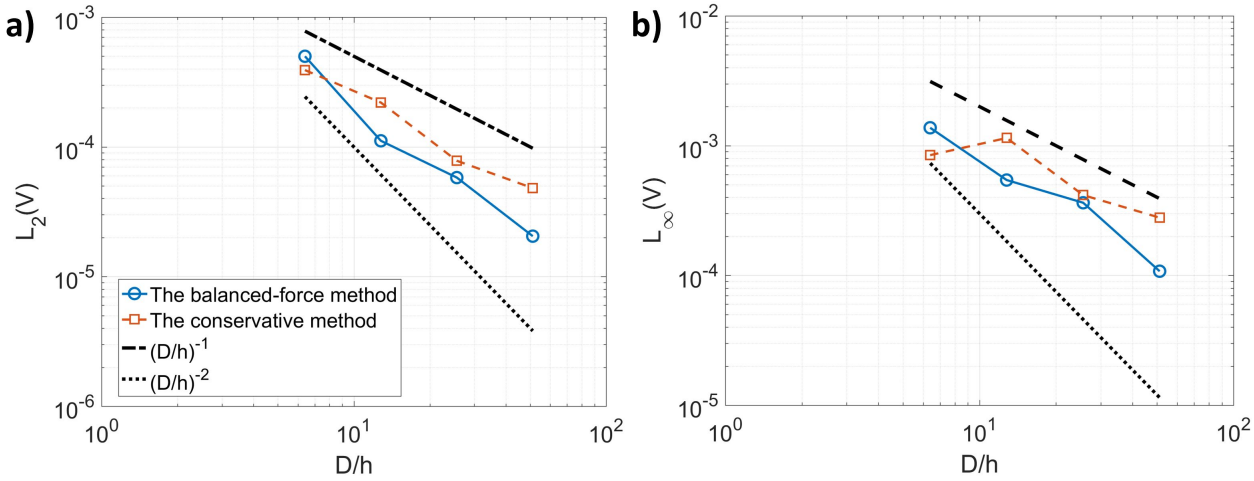

Figure 4.22. Results of the steady drop using two-phase CAC-B and CAC-C. a) The L_2 error. b) The L_∞ error.

4.7.2 Multiphase results

Here, the three-phase steady drops is investigated using CH-B and CH-C, which is unable to be easily modeled by previous two-phase methods. Initially, the drop (Phase 1) at $(0.5, 0.5)$ with a radius 0.15 is surrounded by a circular ring (Phase 2) whose outer radius is 0.3. The material properties are $\rho_1 = 1000$, $\rho_2 = 100$, $\rho_3 = 1$, $\sigma_{1,2} = 0.5$, $\sigma_{1,3} = 0.1$, $\sigma_{2,3} = 1$. Both the inviscid and viscous cases are considered and the performances of the balanced-force method

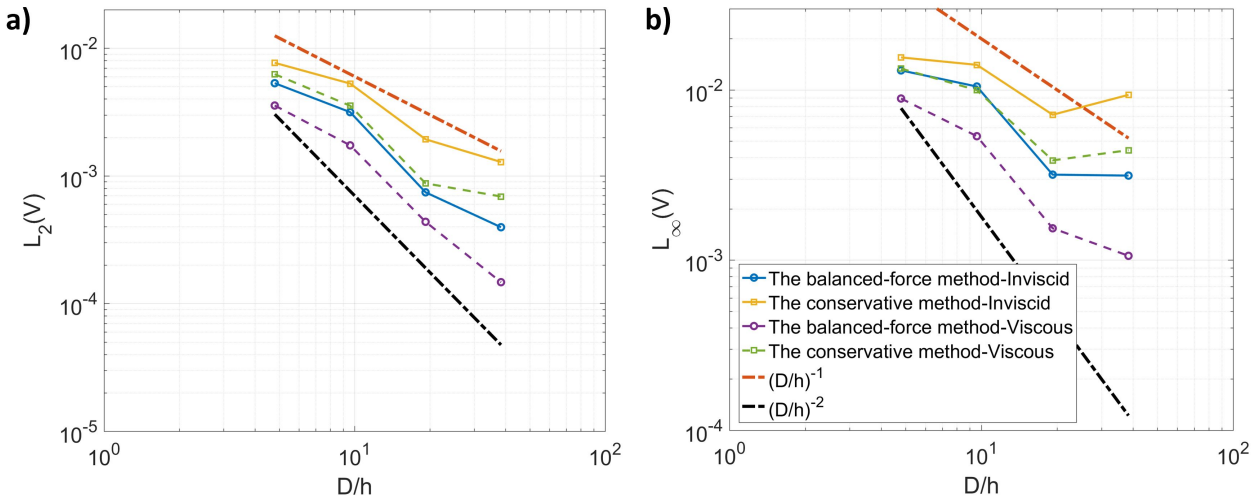

Figure 4.23. Results of the three-phase steady drops using CH-B and CH-C. a) The L_2 error. b) The L_∞ error. a) and b) share the same legend. (D/h) represents the spatial resolution where D is the diameter of the Phase 1 drop and h denotes the grid size.

to that of the conservative method are compared. In the viscous case, $\mu_1 = 0.1$, $\mu_2 = 0.005$, and $\mu_3 = 0.0001$. The results are shown in Fig.4.23.

It can be observed that the balanced-force method performs better than the conservative method. It generates smaller spurious current and the norms of the spurious current reduce faster during the grid refinement. Its L_2 norm reduces with a rate close to 2nd order, while the convergence rate of its L_∞ norm is about 1st order. In the cases using the conservative method, both the L_2 and L_∞ norms converge at a rate close to 1st order. In addition, the spurious currents in the viscous cases are smaller than those in the inviscid cases. However, the appearance of viscosity doesn't change the convergence rate.

In summary, the spurious currents generated by the balanced-force method and by the conservative method are in an acceptable range. However, the balanced-force method achieves better numerical force balance than the conservative method.

4.8 Large-Density-Ratio advection

The appropriate coupling between the Phase-Field equation and the momentum equation should satisfy the *consistency of mass conservation* and the *consistency of mass and*

momentum transport. The large-density-ratio advection is performed to demonstrate that the consistency conditions are achieved on the discrete level, and to validate Theorem 3.5.4. Only the discrete consistent mass flux and the discrete inconsistent mass flux (computed as $\overline{\rho}\mathbf{u}$) are considered in the following discussions.

Unless otherwise specified, in this section, the domain considered is $[1 \times 1]$ with the periodic boundary condition. Initially, a homogeneous velocity is given, i.e., $u = u_0$ and $v = v_0$. The domain is discretized by 128×128 cells, and the time step is $\Delta t = 0.1h$. The parameters are $\eta = 3h$, $M_0 = 10^{-7}$, $u_0 = 1$, and $v_0 = 1$. All the computations are stopped at $t = 1$ or before the computation becomes unstable. Based on Theorem 3.5.4, the interface should return to its original location at $t = 1$ without any deformation, and the velocity should not be changed, thanks to satisfying the *consistency of mass conservation* and the *consistency of mass and momentum transport* on the discrete level.

4.8.1 One-dimensional results

First, the analysis in Section 3.2 of the one-dimensional advection under the force-free condition is numerically reproduced using two-phase CH. The governing equations to be solved are simplified, such that the right-hand side of the momentum equation Eq.(2.34) is set to zero. The physical solution is that the velocity maintains its initial value u_0 all the time. However, the analysis shows that, numerically, only satisfying the consistency conditions on the discrete level leads to the physical solution.

The computational domain is $[0, 1]$ with the periodic boundary condition. A one-dimensional drop is initially located at the center of the domain with a diameter $D = 0.5$. Phase 1, which is inside the drop, is denser than Phase 2, which is outside the drop. Both the cell-center and cell-face velocities are initially equal to $u_0 = 1$. The cell-face velocity is given to be u_0 at $\forall t > 0$ instead of being computed in this case, and only the error of the cell-center velocity, i.e., $(u - u_0)$, is analyzed. By doing so, the actual equations needed to be solved numerically are Eq.(3.27) and Eq.(3.28) for ϕ, and Eq.(3.50) with zero right-hand side for u, and u^* in Eq.(3.50) becomes u^{n+1} in this case. The other parameters are $\eta = 1/32$, $M_0 = 10^{-7}$ and $CFL = u_0 \Delta t / h = 0.2$. The computations are stopped at $t = 2$, when the drop returns to its

initial location for the second time. The number of cells is in the range of 64 to 512. The L_2 and L_∞ norms of $(u^{n+1} - u_0)$ are used to quantified the results.

The results obtained from the discrete consistent mass flux is labeled as "C", and those from the discrete inconsistent mass flux ($\overline{\rho}u$) are labeled as "I", and they are shown in Fig.4.24. The number following "C" or "I" represents the density ratio. The cases of C-1 and I-1 are identical, and their errors are zero so they cannot be seen in the log-log plot. As expected, the cases using the discrete consistent mass flux reproduce the physical results accurately. Both the L_2 and L_∞ errors are below 10^{-6} no matter what the cell size and density ratio are. The errors do not reach the machine zero because of the round-off error of the computer, which will be further explained in the two-dimensional advection problem. In spite of the simplicity of the problem and the idealized numerical implementation, a large error is introduced by the inconsistency of mass and momentum transport when $\overline{\rho}u$ is used as the mass flux. In addition, the error increases as the density ratio increases. Although the error is reduced as a result of the grid refinement, it is still larger than 10^{-2} for the finest grid. It should be noted that there are about 256 cells across the drop in the finest grid, which is seldom achievable in practical computations of bubbly flows. These numerical tests not only match the analysis in Section 3.2, but also emphasis the significance of achieving consistency on the discrete level to obtain physical solutions in practical computations.

4.8.2 Two-phase results

Since only the simplified equations are solved and the cell-face velocity is given its exact value in the one-dimensional advection case, the error of the cell-center velocity has no chance to contaminate the cell-face velocity to consequently create unphysical interface distortion and pressure fluctuations. To validate this statement, the two-dimensional advection problem is performed, where the governing equations without any simplifications are solved numerically, following the scheme in Chapter 3. This also corresponds to Theorem 3.5.4 and its corollary.

A circular drop with a radius $D = 0.2$ is initially located at the center of the domain. The density ratios considered are 1, 10^3, 10^6, and 10^9, and the fluid inside the drop (Phase

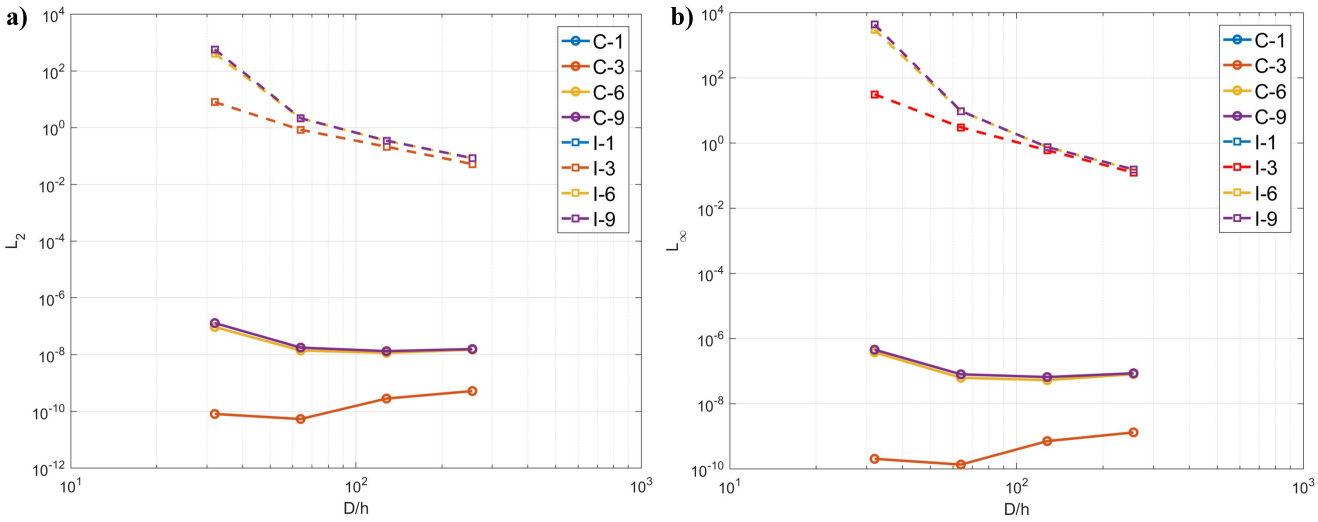

Figure 4.24. Results of the one-dimensional advection of a drop using two-phase CH and the simplified momentum equation. a) The L_2 error of the cell-center velocity. b) The L_∞ error of the cell-center velocity.

1) is denser than the surrounded fluid (Phase 2). Fig.4.25 shows the initial drop shape and the streamline. The solution at $t = 1$ should be identical to the initial configuration. Results from two-phase CH are reported. Fig.4.26 shows the cases without the surface tension ($\sigma = 10^{-12}$) at $t = 1$ by using either the discrete consistent or inconsistent mass fluxes. One can obtain a stable solution for a density ratio of 10^9 when using the discrete consistent mass flux, and the physical solution is well reproduced. The streamlines are parallel to each other along the 45^0 line. The shape of the interface remains a circle and the its location lays on the initial one. However, 10^3 is the highest density ratio to have stable results when using the discrete inconsistent mass flux. Even in that case, although the solution is stable, it is incorrect. The streamlines are oscillatory and the shape of the interface is highly deformed by the perturbed velocity, which is unphysical. Fig.4.27 shows the results including the surface tension ($\sigma = 1$). Again, one obtains the physical results for density ratio 10^9 by using the discrete consistent mass flux. Unphysical velocity perturbation and interface deformation is again observed in the case of a density ratio of 10^3 using the discrete inconsistent mass flux. Because of the surface tension, the interface deformation is restricted and it looks like an ellipse.

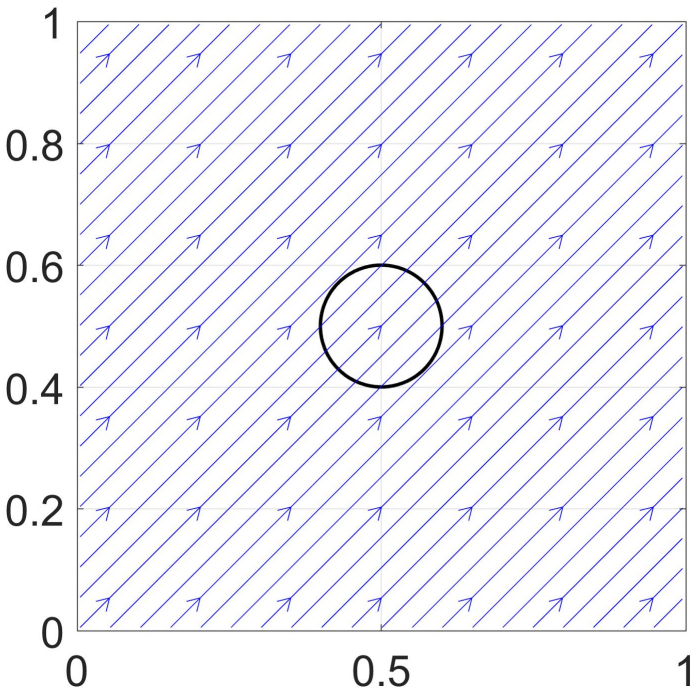

Figure 4.25. Initial configuration of the two-dimensional advection of a circular drop. Solid black line: Interface at $t = 0$; Blue arrow line: Streamlines at $t = 0$.

The L_2 and L_∞ errors of u and v are measured to quantify the importance of achieving the consistency on the discrete level. In addition, for the cases without surface tension, the L_2 and L_∞ errors of P are measured, whose reference value is zero. $(\Delta p)_{\text{avg}} = |\int_\Omega p d\Omega| / \int_\Omega 0.5(1+\phi) d\Omega$ and $(\Delta p)_{\max} = p_{\max} - p_{\min}$ are defined to quantify the pressure jump when there is a surface tension. Label "*" represents the results before the computation becomes unstable. Fig.4.28 plots the results without the surface tension. It is observed that the errors from the cases using the discrete consistent mass flux are very small, while it seems proportional to the density ratio. This can be understood by considering that the round-off error introduces an additional inconsistent error. Following the analysis in Section 3.2, one can estimate that its magnitude is in the order of $(\rho_1 - \rho_2)/2$ times the round-off error. When the density ratio is large, the factor $(\rho_1 - \rho_2)/2$ is close to be proportional to the density ratio. One can see that the errors obtained in Fig.4.28 behave similarly to the estimation. The errors from the cases using the discrete inconsistent mass flux are very large, compared to those obtained from the consistent one. The pressure error grows dramatically as the density

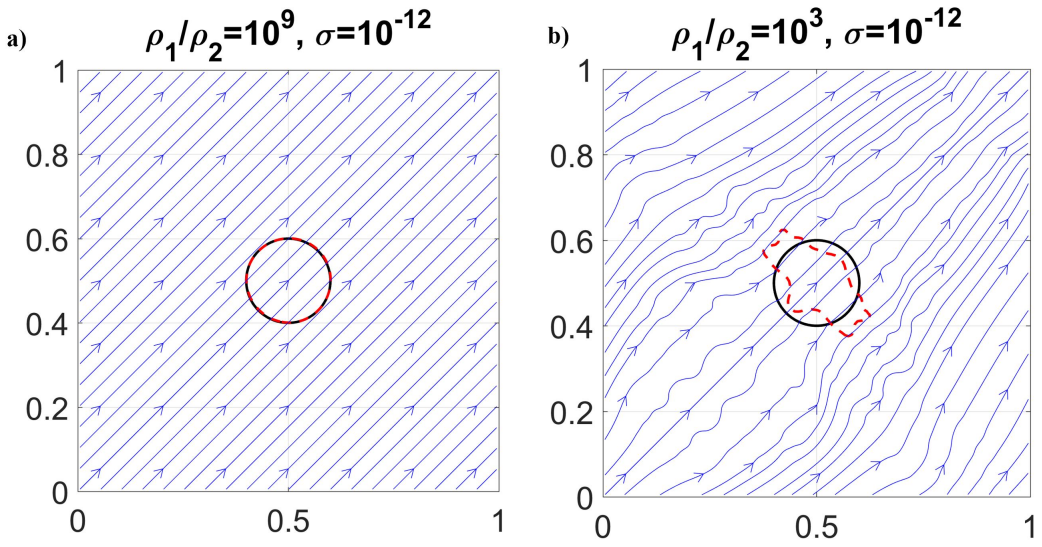

Figure 4.26. Results of the two-dimensional advection of a circular drop without surface tension using two-phase CH. Solid black line: Interface at $t = 0$; Red dash line: Interface at $t = 1$; Blue arrow line: Streamlines at $t = 1$. a) Using the discrete consistent mass flux. b) Using the discrete inconsistent mass flux.

ratio increases and finally triggers numerical instability. The largest pressure is in front of the interface, where the inconsistent error is most significant. This large pressure value hinders the movement of the interface and results in unphysical interface deformation such that the interface is compressed along its advection direction. Fig 4.29 plots the results including the surface tension. The errors of different density ratios for the cases using the discrete consistent mass flux slightly change, while they are larger than their correspondences without the surface tension. These errors are majorly introduced by the numerical imbalance of the surface tension and the pressure, i.e., the spurious current, instead of the round-off error. Both $(\Delta p)_{\text{avg}}$ and $(\Delta p)_{\text{max}}$ have the values close to the pressure jump from the Young-Laplace equation, i.e., $2\sigma/D = 10$ in this case. The errors for the cases using the discrete inconsistent mass flux, on the other hand, is majorly introduced by inconsistency instead of numerical imbalance, and they behave similarly to their corresponding ones without surface tension.

The inviscid and surface-tension-free case is repeated using the two-phase CAC, where the consistent formulation is implemented to obtain the discrete consistent mass flux. Fig.4.30

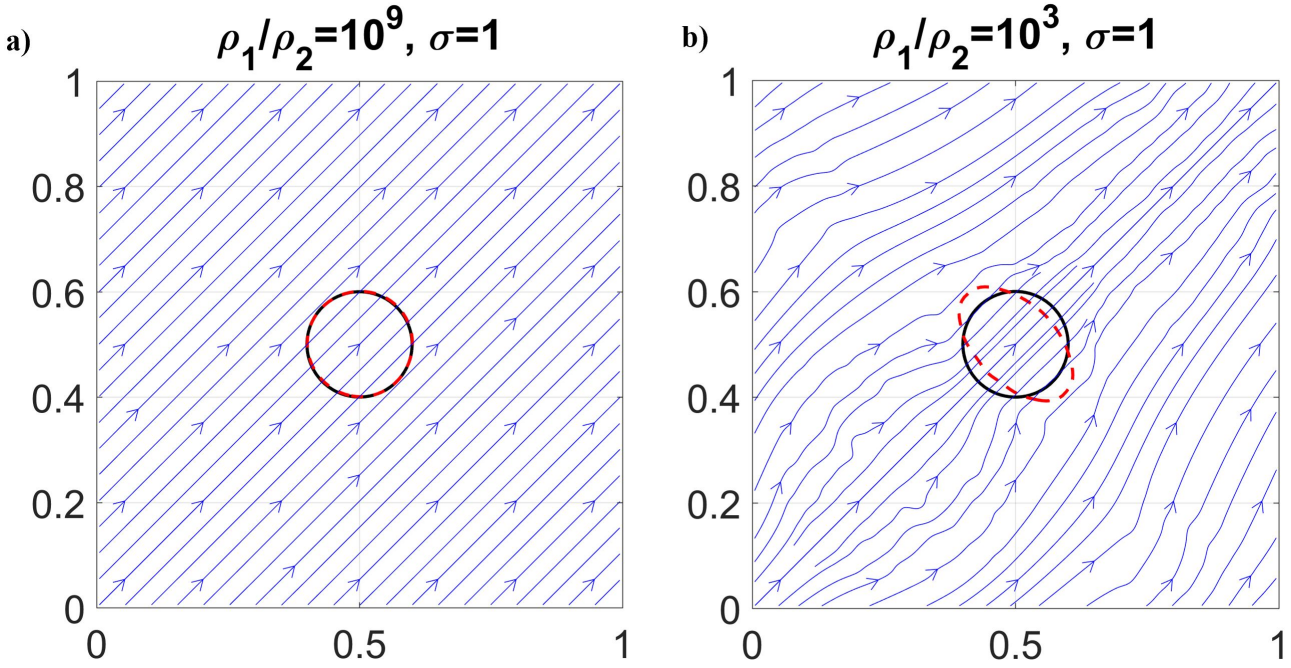

Figure 4.27. Results of the two-dimensional advection of a circular drop with surface tension using two-phase CH. Solid black line: Interface at $t = 0$; Red dash line: Interface at $t = 1$; Blue arrow line: Streamlines at $t = 1$. a) Using the discrete consistent mass flux. b) Using the discrete inconsistent mass flux.

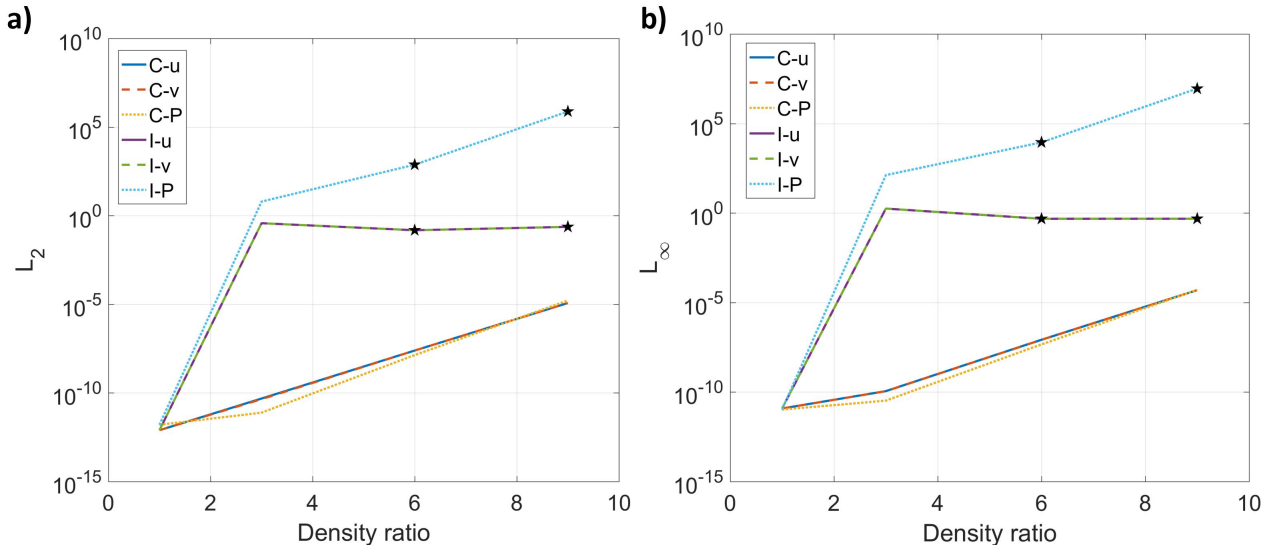

Figure 4.28. Results of the two-dimensional advection of a circular drop without surface tension using two-phase CH. "*" represents data before numerical instability.

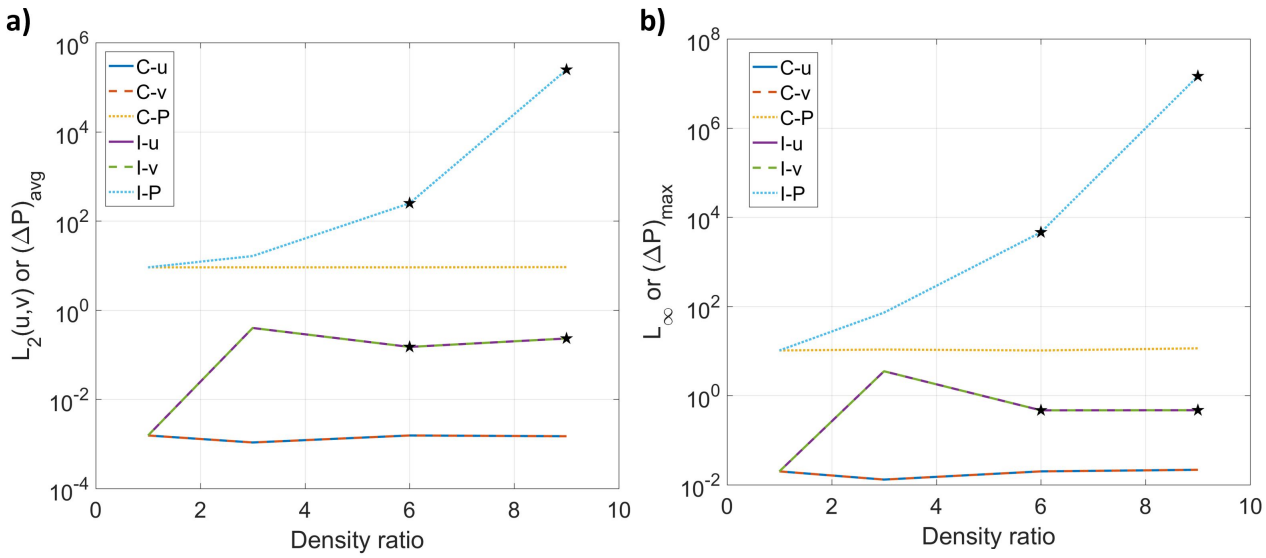

Figure 4.29. Results of the two-dimensional advection of a circular drop with surface tension using two-phase CH-B. "*" represents data before numerical instability.

a) shows the result of the density ratio 10^9 from the proposed consistent scheme at $t = 1$. The physical solution is well reproduced. The interface at $t = 1$ is on top of the one at $t = 0$, and the velocity vectors are all pointing towards 45^0 from the x axis. For comparison, the result of the density ratio 10^3 from the discrete inconsistent mass flux is depicted in Fig.4.30 b). One can observe strong compression of the interface along the flow direction and the streamlines are distorted. This case demonstrate the effectiveness of the consistent formulation.

4.8.3 Multiphase results

The two-phase advection problem is extended to the multiphase one, and CH is first considered. The material properties are $\rho_1 = 10^9$, $\rho_2 = 10^6$, and $\rho_1 = 1$, and there is neither viscosity nor interfacial tension. Initially, a circular drop (Phase 1) with a radius 0.1 is at $(0.5, 0.5)$, surrounded by Phase 2, whose outer interface is an ellipse with its semi-major axis 0.3 along the y axis and with its semi-minor axis 0.25 along the x axis. Fig.4.31 a) and c) shows the result from the discrete consistent mass flux. It can be observed that the interfaces, as expected, return to their initial location without any deformation, and all the

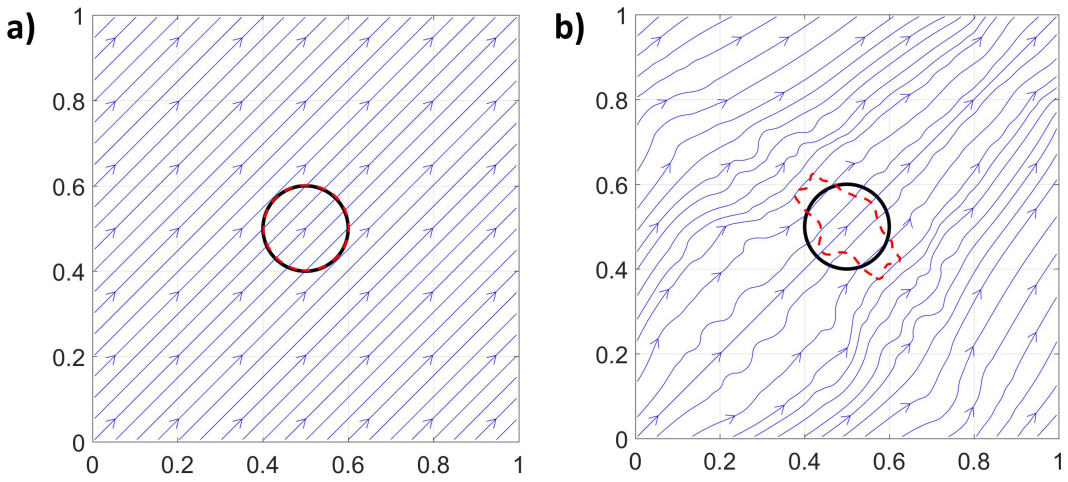

Figure 4.30. Results of the two-dimensional advection problem using two-phase CAC. a) Result from the discrete consistent mass flux with a density ratio 10^9. b) Result from the discrete inconsistent mass flux with a density ratio 10^3. Black solid line: interface at $t = 0$, blue arrow lines: streamlines at $t = 1$, red dashed line: interface at $t = 1$.

streamlines are pointing towards 45^0. Fig.4.31 b) and d) shows the result from the discrete inconsistent mass flux, i.e., $\overline{\rho}u$. Due to violating the consistency conditions, the interfaces experienced significant unphysical deformation and the streamlines are fluctuating. It should be noted that the densities are 1000, 10, and 1 in the case using the discrete inconsistent mass flux, in order to have a stable solution.

Next, CHB and CACB are considered to demonstrate that including the boundedness mapping will not affect the consistency of the scheme after implementing the consistent formulation. The densities of Phases 1, 2, and 3 are 10^6, 10^3, and 1, respectively. The off-diagonal elements of $\lambda_{p,q}$ are $\frac{0.03}{2\sqrt{2}}\eta$. Phase 1 is enclosed by a circle at $(0.65, 0.65)$ with a radius 0.15. Phase 2 is enclosed by a circle at $(0.3, 0.4)$ with a radius 0.1. Phase 3 occupies the rest of the domain. As shown in Fig.4.32, at $t = 1$, the interfaces return to their original locations without any deformation and the velocity preserves its initial value, even though the maximum density ratio is 10^6.

The critical factor in the problem is to satisfy the *consistency of mass conservation* and the *consistency of mass and momentum transport*. Thanks to the consistent formulation in Section 2.3.1, the fully discretized Phase-Field equation including the boundedness mapping

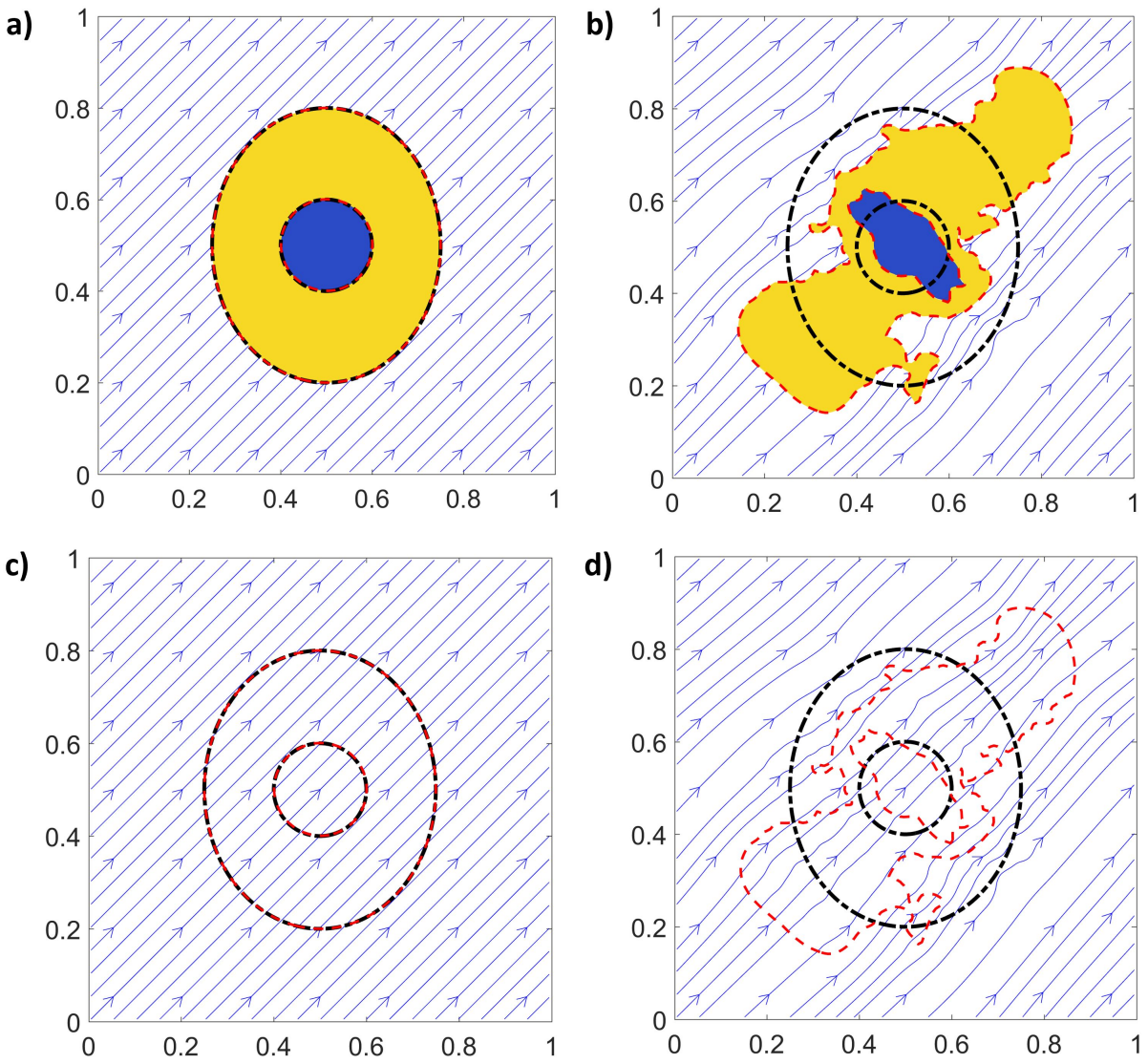

Figure 4.31. Results of two-dimensional advection using CH. a) and c) Results from the discrete consistent mass flux with densities $\rho_1 = 10^9$, $\rho_2 = 10^6$, and $\rho_1 = 1$. b) and d) Results of using the discrete inconsistent mass flux with densities $\rho_1 = 10^3$, $\rho_2 = 10$, and $\rho_1 = 1$. Blue arrow lines: Streamlines at $t = 1$, Black dash-dotted lines: Interfaces at $t = 0$, Red dashed lines: Interfaces at $t = 1$, Blue: Phase 1, Yellow: Phase 2, Background: Phase 3.

is able to be written in a conservative form, see Section 3.4. As a result, the discrete mass conservation equation in Theorem 3.2.1 is satisfied as well after using the discrete consistent mass flux which is applied in the momentum equation. Fig.4.33 shows the residues of the fully discretized Phase-Field equation Eq.(3.41) and the discrete mass conservation equation

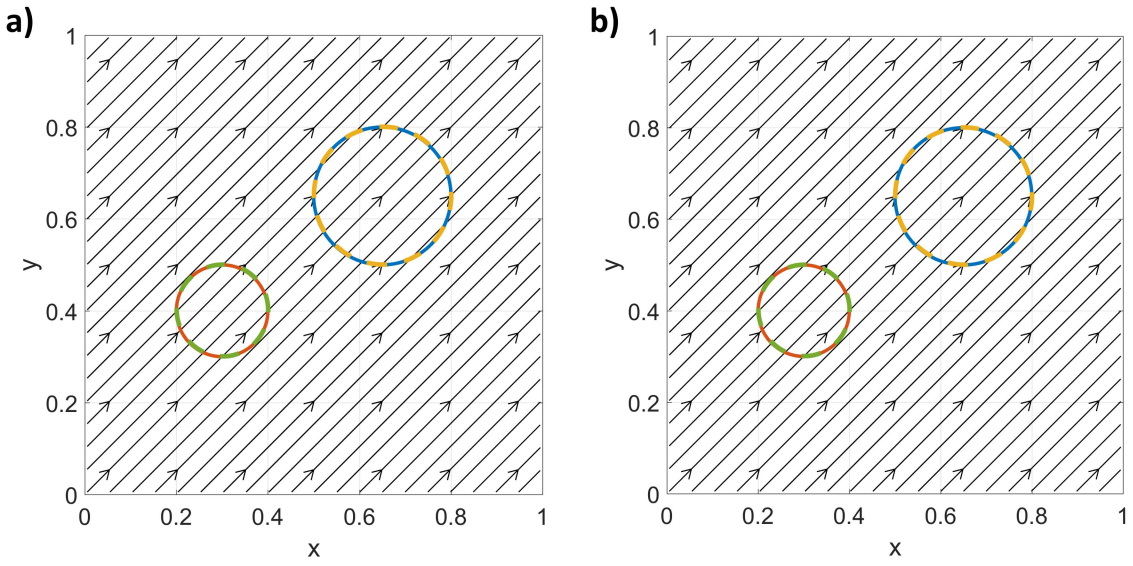

Figure 4.32. Results of the two dimensional advection from a) CHB and b) CACB. Blue solid line: Interface of phase 1 at $t = 0$. Red solid line: Interface of phase 2 at $t = 0$. Yellow dashed line: Interface of phase 1 at $t = 1$. Green dashed line: Interface of phase 2 at $t = 1$. Black arrow: Stream lines at $t = 1$.

in Theorem 3.2.1 from CHB and CACB. The residue of the fully discretized Phase-Field equation from either CHB or CACB is in the order of the round-off error. The residue of the discrete mass conservation equation is in the order of the maximum density ratio of the problem times the residue of the fully discretized Phase-Field equation.

In summary, the proposed scheme satisfies the *consistency of mass conservation* and the *consistency of mass and momentum transport* on the discrete level, even though the reaction terms and Lagrange multipliers of the Phase-Field equation and the boundedness mapping are included, and the analysis in Section 3.2 and Theorem 3.5.4 are validated.

4.9 Horizontal shear layer

The horizontal shear layer in [113], [225] and its variations of including multiple fluid phases are performed to validate the physical properties of the schemes of the present study in Chapter 3. Different layers of fluids are moving horizontally at different speeds. A vertical velocity perturbation is applied and the fluids begin to interact with each other. The domain

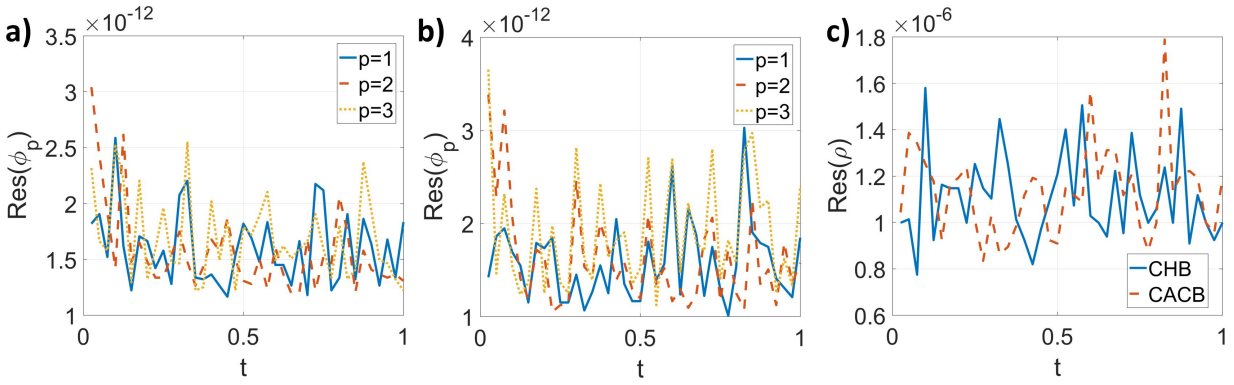

Figure 4.33. Residues of the fully discretized Phase-Field equation Eq.(3.41) and the discrete mass conservation equation in Theorem 3.2.1 of the two-dimensional advection from CHB and CACB. a) Residue of the fully discretized Phase-Field equation from CHB. b) Residue of the fully discretized Phase-Field equation from CACB. c) Residue of the discrete mass conservation equation from CHB ant CACB.

considered is $[1 \times 1]$ and all its boundaries are periodic. The cell size h is $\frac{1}{128}$ in default and the time step is $\Delta t = \text{CFL}h$, with $\text{CFL} = 0.1$.

4.9.1 Two-phase results

The two-phase cases is first investigated using two-phase CH-B. Initially, the horizontal shear layer along with a vertical perturbation is

$$u|_{t=0} = \begin{cases} \tanh(\frac{y-y_1}{\delta_1}), y \leq y_0, \\ \tanh(\frac{y_2-y}{\delta_1}), y > y_0, \end{cases} \qquad v|_{t=0} = \delta_2 \sin(kx).$$

The parameters are $y_0 = 0.5$, $y_1 = 0.25$, $y_2 = 0.75$, $\delta_1 = 1/30$, $\delta_2 = 0.05$, and $k = 2\pi$, the same as those in [113], [225], and as a result, $\eta = \delta_1/\sqrt{2}$. The initial order parameter $\phi|_{t=0}$ is the same as $u|_{t=0}$, meaning that Phase 1 is initially at the center of the domain with unperturbed velocity 1, while Phase 2 has -1 velocity next to Phase 1. Six cases are presented:

- Case 1: $\rho_1 = 1$, $\rho_2 = 1$, $\mu_1 = 0$, $\mu_2 = 0$, $\sigma = 10^{-12}$
- Case 2: $\rho_1 = 10$, $\rho_2 = 1$, $\mu_1 = 0$, $\mu_2 = 0$, $\sigma = 10^{-12}$

- Case 3: $\rho_1 = 1$, $\rho_2 = 1$, $\mu_1 = 0.01$, $\mu_2 = 0.001$, $\sigma = 10^{-12}$
- Case 4: $\rho_1 = 10$, $\rho_2 = 1$, $\mu_1 = 0.01$, $\mu_2 = 0.001$, $\sigma = 10^{-12}$
- Case 5: $\rho_1 = 1$, $\rho_2 = 1$, $\mu_1 = 0$, $\mu_2 = 0$, $\sigma = 0.1$
- Case 6: $\rho_1 = 10$, $\rho_2 = 1$, $\mu_1 = 0$, $\mu_2 = 0$, $\sigma = 0.1$

The first two cases are inviscid and without the surface force. The third and fourth cases are viscous while without the surface force. The last two cases are inviscid but include the surface force. The cases with odd IDs have matched densities while the other cases have a density ratio 10. Whenever viscous effects are included, the viscosity ratio is 10. As analyzed in Section 3.3, the mass of the fluid mixture is conserved on the discrete level, i.e., $\sum_{\mathrm{i,j}} [\rho \Delta\Omega]_{\mathrm{i,j}} = \sum_{\mathrm{i,j}} [\rho|_{t=0} \Delta\Omega]_{\mathrm{i,j}}$, no matter whether the viscous or surface forces are present. With matched densities, while without the surface force, e.g., Cases 1 and 3, the momentum of the fluid mixture is conserved as well, i.e., $\sum_{\mathrm{i,j}} [\rho \mathbf{u} \Delta\Omega]_{\mathrm{i,j}} = \sum_{\mathrm{i,j}} [(\rho \mathbf{u})|_{t=0} \Delta\Omega]_{\mathrm{i,j}}$, as proofed in Section 3.5.3. The kinetic energy, on the continuous level, is conserved in Cases 1 and 2, see Section 2.4.2. However, because of numerical dissipation, the kinetic energy on the discrete level, $E_K = \sum_{\mathrm{i,j}} \frac{1}{2} [\rho \mathbf{u} \cdot \mathbf{u} \Delta\Omega]_{\mathrm{i,j}}$, should be decreased, i.e., $E_K(t) \leq E_K(t = 0)$, as discussed in the remarks below Theorem 3.5.7. In the presence of the surface force, e.g., Cases 5 and 6, there is energy transfer between the kinetic energy and the free energy. The total energy, which is the sum of the kinetic energy and the free energy, however, does not increase on the continuous level even when the flow is inviscid, see Section 2.4.3 or [56]. It is desired that the discrete forms of the energies reproduce this property, i.e., $E_K(t) + E_F(t) \leq E_K(t = 0) + E_F(t = 0)$, where $E_F(t) = \sum_{\mathrm{i,j}} [\lambda \left(\frac{1}{\eta^2} g_1(\phi) + \frac{1}{2} \widetilde{\nabla\phi \cdot \nabla\phi} \right) \Delta\Omega]_{\mathrm{i,j}}$.

Fig.4.34 shows the results of cases 1-4, where the surface force is neglected and as a result the free energy is zero. Fig.4.34 a) shows the change of the mass which is machine zero. Therefore, cases 1-4 conserve the mass on the discrete level, no matter whether viscous effects are included. Fig.4.34 c) and d) show the change of the momentum in the x and y directions, respectively. The momentum is conserved on the discrete level no matter whether the densities of the phases are the same or not. Fig.4.34 b) shows the time history of the change of the kinetic energy. Cases 1 and 2 do not include physical viscosities, and as a result

the kinetic energies in these two cases are almost unchanged, compared to those in cases 3 and 4, where physical viscosities are included. The inset plot shows that the kinetic energies in cases 1 and 2 decay although these two cases are inviscid. To further confirm that the decay of the kinetic energy is caused by numerical dissipation, finer-grid solutions of cases 2 and 4 are supplemented. Numerical dissipation should be reduced after grid refinement while physical dissipation should not be changed. After reducing the grid size by half, the change of the kinetic energy in case 2 (inviscid case) is reduced from 0.1166% to 0.0223%. Opposite to that, there is no observable difference in case 4 (viscous case) after refining the grid, indicating that the kinetic energy is dissipated dominantly by physical viscosity in case 2.

Cases 1,2,5, and 6 are next considered, where cases 5 and 6 include the surface force and cases 1 and 2 do not. The mass is again conserved on the discrete level, as shown in Fig.4.35, a), even when the surface force is included. Fig.4.35 c) and d) show the change of the momentum. Case 6, where the densities are not matched and the surface force is present, has the most noticeable momentum reduction in the x direction, due to using the balanced-force method. However, when compared to its initial value 3.9, the reduction of the momentum in the x direction is only 0.0058%, which is still insignificant. Since there is the surface force in case 5, the free energy appears, and Fig.4.35 b) shows the time histories of the kinetic energy, free energy and total energy of that case. It is observed that the decrease of the kinetic energy corresponds to the increase of the free energy. However, the total energy, which is the summation of them, decays, and this can be observed more clearly in the inset plot. The same behavior is obtained in case 6 (not shown). It should be noted that, although cases 5 and 6 are inviscid, the total energy decay doesn't result from numerical dissipation but is actually the property of the Phase-Field method. To confirm this, results for the finer grid is included, which is almost on top of that of the default grid.

This case is repeated using two-phase CAC-B and CAC-C. The material properties become $\rho_1 = 10$, $\rho_2 = 1$, $\mu_1 = 0.01$, $\mu_2 = 0.001$, $\sigma = 0.1$. The time histories of $\Phi = \sum_{\mathrm{i,j}} [\phi \Delta\Omega]_{\mathrm{i,j}}$, $\mathrm{Momentum}_x = \sum_{\mathrm{i,j}} [\rho u \Delta\Omega]_{\mathrm{i,j}}$ and $\mathrm{Momentum}_y = \sum_{\mathrm{i,j}} [\rho v \Delta\Omega]_{\mathrm{i,j}}$ minus their initial values are shown in Fig.4.36. It is clear that the mass is conserved on the discrete level due to Φ is conserved. Since the setup of the problem is symmetric with respect to the y axis, the

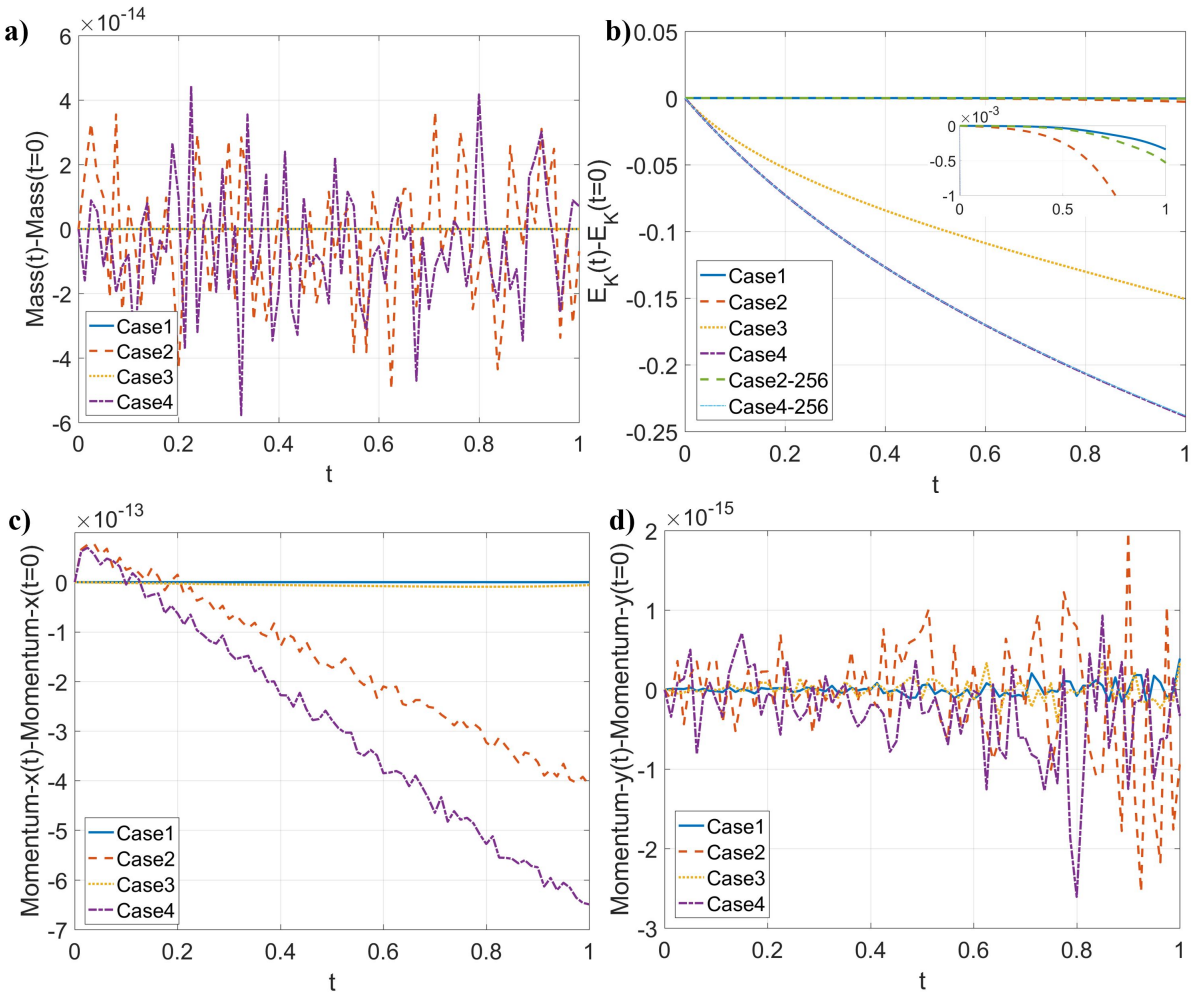

Figure 4.34. Results of the horizontal shear layer in Cases 1-4 using two-phase CH-B. a) Change of the mass, b) change of the kinetic energy, c) change of the momentum-x, and d) change of the momentum-y with respect to time. "256" in the legend represents the results from a finer grid $h = 1/256$.

Momentum$_y$ is also conserved no matter whether the balanced-force method or the conservative method is used. However, Momentum$_x$ is conserved only when the conservative method is used, as expected. A finer grid resolution of the balanced-force method is performed, and the momentum non-conservative error is greatly reduced. Considering the initial value of Momentum$_x$ is 3.9, the maximum change of Momentum$_x$ is less than 0.05% from the default-grid solution. As a result, the scheme using the balanced-force method leads to the essential conservation of momentum. The results in Fig.4.36 are consistent with our analyses in Chapter 3.

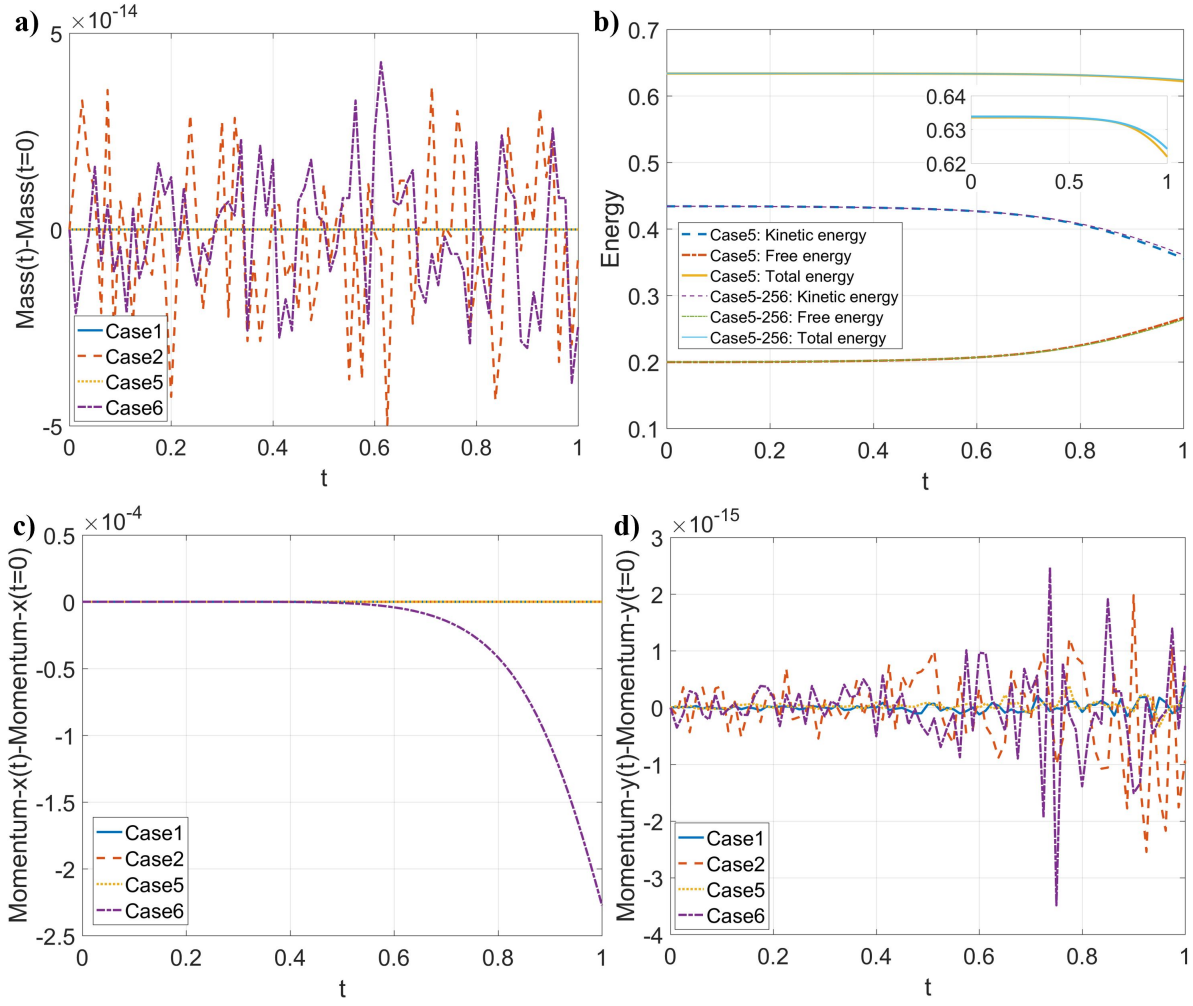

Figure 4.35. Results of the horizontal shear layer in Cases 1,2,5,6 using two-phase CH-B. a) Change of the mass, b) the energies, c) change of the momentum-x, and d) change of the momentum-y with respect to time. "256" in the legend represents the results from a finer grid $h = 1/256$.

The time histories of the kinetic energy, $E_K = \sum_{i,j} \left[\frac{1}{2}\rho \mathbf{u} \cdot \mathbf{u} \Delta\Omega\right]_{i,j}$, the free energy, $E_F = \sum_{i,j} \left[\lambda \left(\frac{1}{\eta^2} g_1(\phi) + \frac{1}{2}\widetilde{\nabla\phi \cdot \nabla\phi}\right) \Delta\Omega\right]_{i,j}$, and the total energy, $E_T = E_K + E_F$, are shown in Fig.4.37. Fig.4.37 a) considers the case without viscosity and surface tension. As a result, the free energy is zero, and total energy (or the kinetic energy) should not change with time. The decay of the total energy, as well as the kinetic energy, in Fig.4.37 a) is attributed to the numerical dissipation introduced by the backward difference for time discretization, the WENO scheme for the convection terms, and the linear interpolation of the pressure gradient in the momentum equation, as discussed in the remarks below Theorem 3.5.7. The

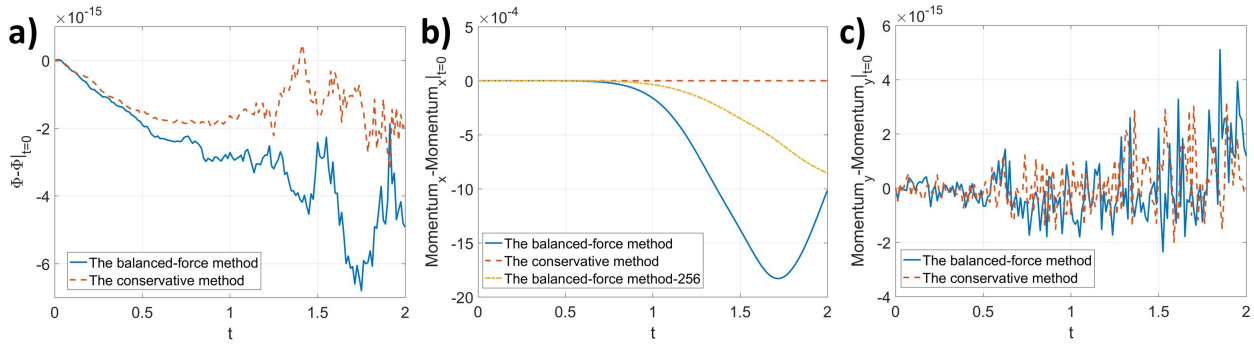

Figure 4.36. Time histories of the changes of the mass and momentum in the horizontal shear layer problem using two-phase CAC-B and CAC-C. a) Change of $\Phi = \sum_{i,j} [\phi \Delta\Omega]_{i,j}$ versus t, b) change of Momentum$_x$ versus t, c) change of Momentum$_y$ versus t. "256" in the legend represents the results from a finer grid size $h = 1/256$.

numerical dissipation should be reduced after the grid size is refined, and one can observe that the decay of the energy happens latter and its amount is smaller in a fine-grid solution. The second case is inviscid but includes the surface tension. The results are shown in Fig.4.37 b). In this case, the total energy decays only due to deviating from the thermodynamical equilibrium defined by the Phase-Field equation, see Theorem 2.4.4. It can be observed that the decrease of the kinetic energy is always larger than the increase of the free energy, leading to the decay of the total energy. Fig.4.37 c) shows the results of the case including both the viscosity and surface tension. The energy transfer from the kinetic energy to the free energy and the decay of the total energy are again observed. The results from a finer grid are also included in Fig.4.37 b) and c), and the difference between the fine-grid solution and the default-grid solution is small. Thus, the contribution of the numerical dissipation to the energy decay is negligible. The balanced-force method gives almost identical results so only the results from the conservative method are presented. In summary, the energy law in Section 2.4.3 is reproduced by the scheme on the discrete level.

The effectiveness of the boundedness mapping algorithm is illustrated using two-phase CACB-C in Fig.4.38, where the time history of $\max(|\phi| - 1)$ is shown. From the maximum principle of two-phase CAC, ϕ should be in the range of $[-1, 1]$. Thus, $\max(|\phi| - 1)$ should always be negative. It can be observed that before $t = 1.5$, ϕ satisfies the maximum principle,

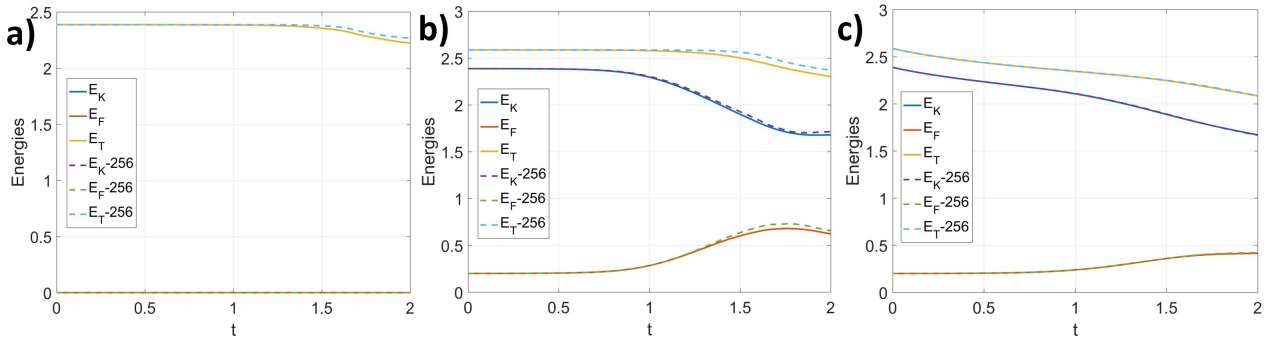

Figure 4.37. Time histories of the kinetic energy, free energy, and total energy in the horizontal shear layer problem using two-phase CAC-C. a) without viscosity and surface tension, b) without viscosity but surface tension, c) with viscosity and surface tension. "256" in the legend represents the results from a finer grid size $h = 1/256$.

and the boundedness mapping is not activated. After $t = 1.5$, ϕ slightly goes beyond the interval $[-1, 1]$ without the boundedness mapping. When the grid is refined, ϕ stays in $[-1, 1]$ longer and the out-of-bound error becomes smaller. In Fig.4.38 b), which is the zoom of Fig.4.38 a), it is observed that before $t = 1.5$, there is no difference between the solutions with and without the boundedness mapping since the mapping is not activated. After $t = 1.5$, ϕ remains to be in $[-1, 1]$ with the help of the boundedness mapping while it is outside $[-1, 1]$ without the boundedness mapping. Two-phase CACB-B gives almost identical results so only the results from the conservative method (two-phase CACB-C) are presented. The changes of Φ ($\Phi = \sum_{i,j} [\phi \Delta\Omega]_{i,j}$) and momentum ($\sum_{i,j} [\rho \mathbf{u} \Delta\Omega]_{i,j}$) versus time are shown in Fig.4.39 and the boundedness mapping is included. The boundedness mapping doesn't change the properties of the mass and momentum conservation of the scheme, which is consistent with the analysis in Section 3.3.2. The time histories of the kinetic energy, free energy, and total energy using two-phase CACB-C are shown in Fig.4.40, along with the corresponding results (from two-phase CAC-C) without the boundedness mapping. The energy law is preserved when the boundedness mapping is included, and there is no observable difference between the results with and without the boundedness mapping. The balanced-force method gives almost identical results so only the results from the conservative method are presented.

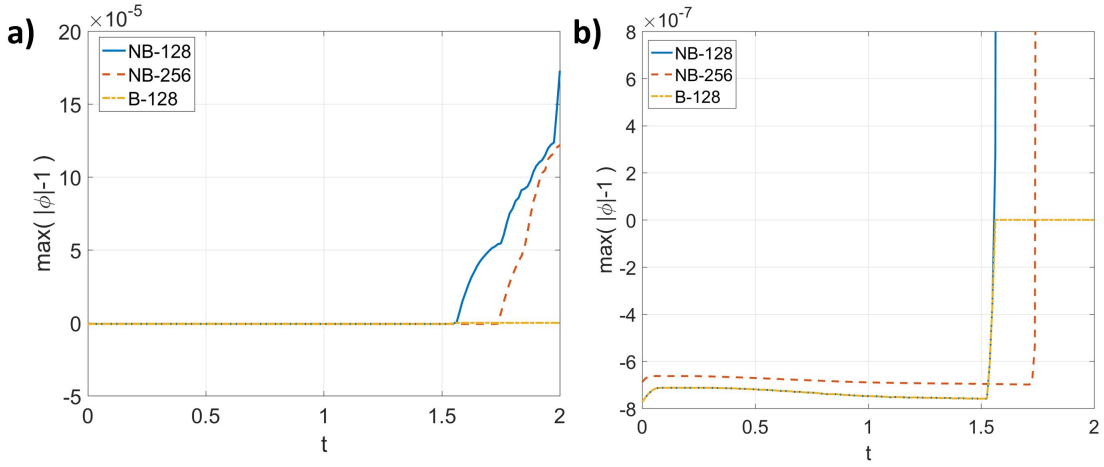

Figure 4.38. Effectiveness of the boundedness mapping using two-phase CAC-C and CACB-C. a) Time histories of $\max(|\phi| - 1)$, b) zoom of a). NB: the boundedness mapping is not activated, B: the boundedness mapping is activated. "128" in the legend represents the results from a grid size $h = 1/128$. "256" in the legend represents the results from a grid size $h = 1/256$.

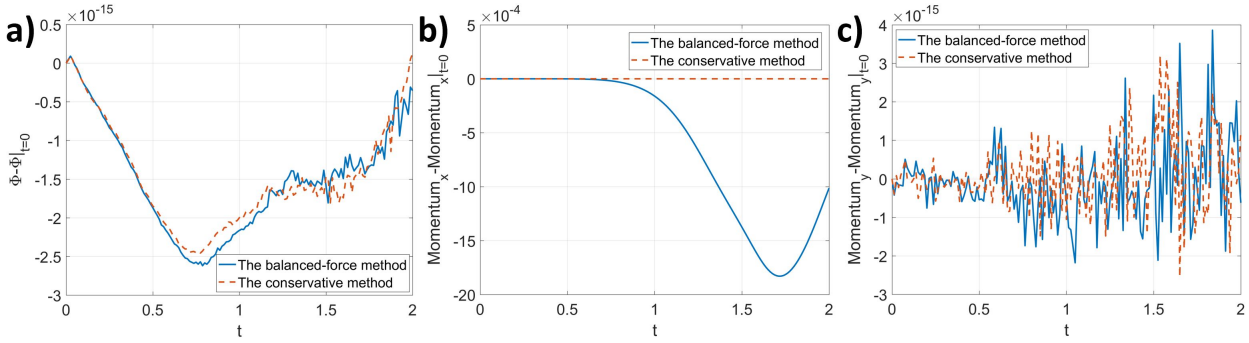

Figure 4.39. Time histories of the changes of the mass and momentum in the horizontal shear layer problem using two-phase CACB-C (including the boundedness mapping). a) Change of $\Phi = \sum_{i,j} [\phi \Delta\Omega]_{i,j}$ versus t, b) change of $\text{Momentum}_x = \sum_{i,j} [\rho u \Delta\Omega]_{i,j}$ versus t, c) change of $\text{Momentum}_y = \sum_{i,j} [\rho v \Delta\Omega]_{i,j}$ versus t.

4.9.2 Multiphase results

The horizontal shear layer problem is further extended to including multiple phases, and CH-B and CH-C are first investigated. The material properties, unless otherwise specified, are $\rho_1 = 50$, $\rho_2 = 10$, $\rho_3 = 1$, $\rho_4 = 0.5$, $\mu_1 = 0.01$, $\mu_2 = 0.1$, $\mu_3 = 0.05$, $\mu_4 = 0.08$, $\sigma_{1,2} = 0.05$, $\sigma_{1,3} = 0.01$, $\sigma_{1,4} = 0.08$, $\sigma_{2,3} = 0.1$, $\sigma_{2,4} = 0.02$, $\sigma_{3,4} = 0.2$. η and M_0 are $\frac{1}{128}$ and 10^{-7},

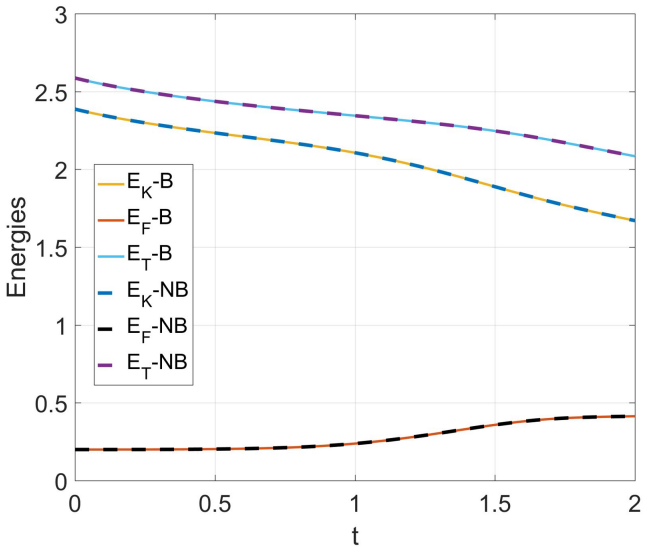

Figure 4.40. Time histories of the kinetic energy, free energy, and total energy in the horizontal shear layer problem using two-phase CAC-C and CACB-C. B: the boundedness mapping is activated, NB: the boundedness mapping is not activated.

respectively. Initially, Phase 1 is stationary in $y_0 < y < y_2$, Phase 2 is in $y_1 < y < y_0$, moving from left to right at a unity speed, and Phase 3 moves in the opposite direction, filling the rest of the domain. Phase 4 is absent, i.e., $\phi_4|_{t=0} \equiv -1$. $y_0 = 0.5$, $y_1 = 0.25$, and $y_2 = 0.75$ are set. This configuration is perturbed by a vertical velocity the same as the two-phase case.

The *consistency of reduction* on the discrete level is first validated. ϕ_4, which is absent at the beginning of the computation, should not appear during the computation, i.e., $\phi_4 \equiv -1$. In addition, since Phase 4 is absent, the problem considered is actually a three-phase problem. The result from setting $N = 4$ and $\phi_4|_{t=0} = -1$ should be the same as that from setting $N = 3$. Fig.4.41 a) shows the time history of the maximum value of $|\phi_4+1|$. It is clear that ϕ_4 equals to -1 up to round off error. Fig.4.41 b) shows the time histories of the kinetic energy E_K, the free energy E_F, and the total energy E_T $(= E_K + \frac{1}{2}E_F)$ (see Corollary 2.4.4.1) from the 4-phase and 3-phase solutions, and they are indistinguishable from each other. Fig.4.41 c) and d) show the snapshots of the three phases at $t = 2$ from the 4-phase and 3-phase

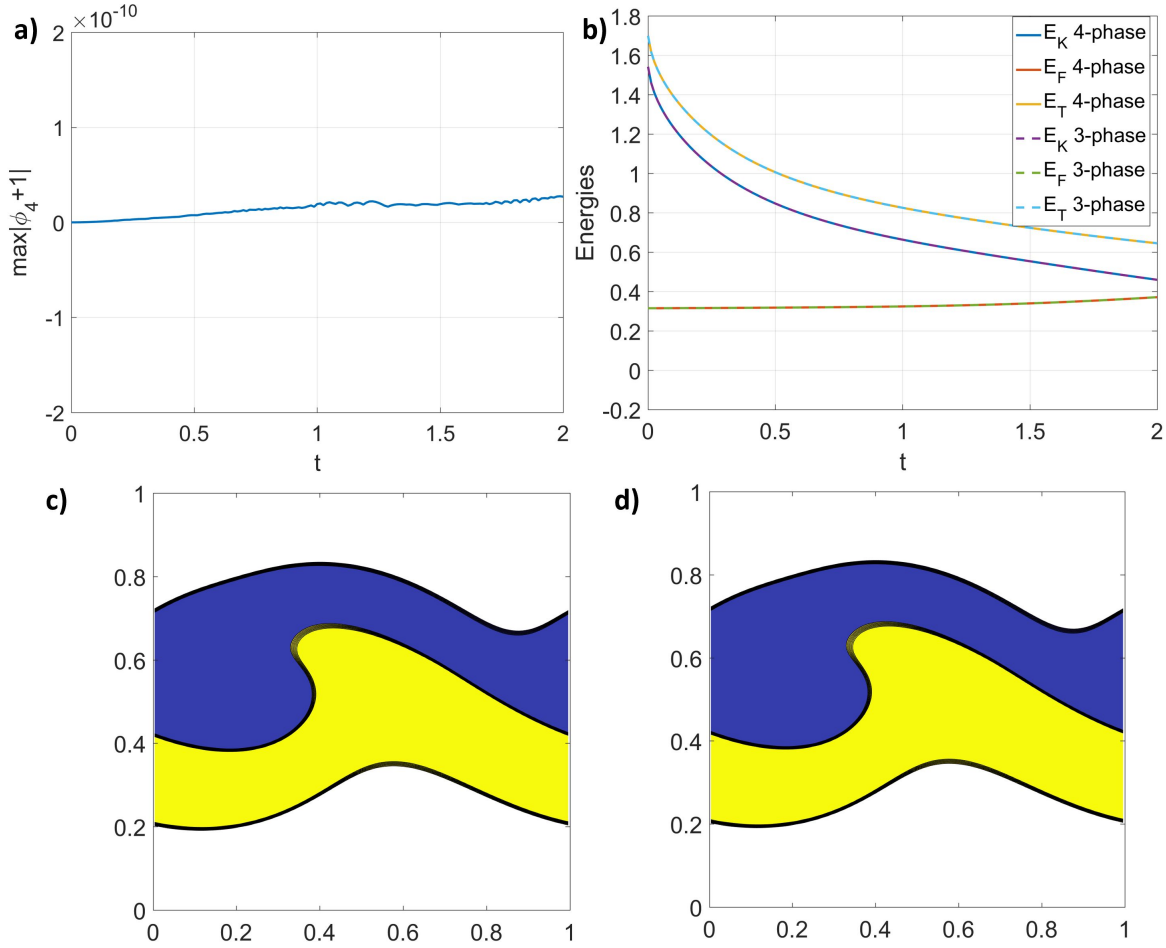

Figure 4.41. Validation of the *consistency of reduction* using CH-B. a) Time history of $\max|\phi_4+1|$. b) Time histories of the kinetic, free, and total energies from the 4-phase and 3-phase solutions. c) Snapshot of the phases at $t = 2$ from the 4-phase solution. d) Snapshot of the phases at $t = 2$ from the 3-phase solution. Blue: Phase 1, Yellow: Phase 2, White: Phase 3.

solutions, respectively, and they are identical. The results validate that the *consistency of reduction* is satisfied on the discrete level.

Instead of applying the proposed scheme, where all the order parameters are solved from their Phase-Field equation, the 4-phase setup is repeated and the practice in [75] is followed, where only ϕ_1, ϕ_2, and ϕ_3 are solved from their Phase-Field equation numerically and ϕ_4 is obtained from their summation, i.e., $\phi_4 = -2 - (\phi_1 + \phi_2 + \phi_3)$. The result is shown in Fig.4.42. It can be observed that Phase 4, which is absent at the beginning, is being generated unphysically, and, therefore, the *consistency of reduction* is violated on

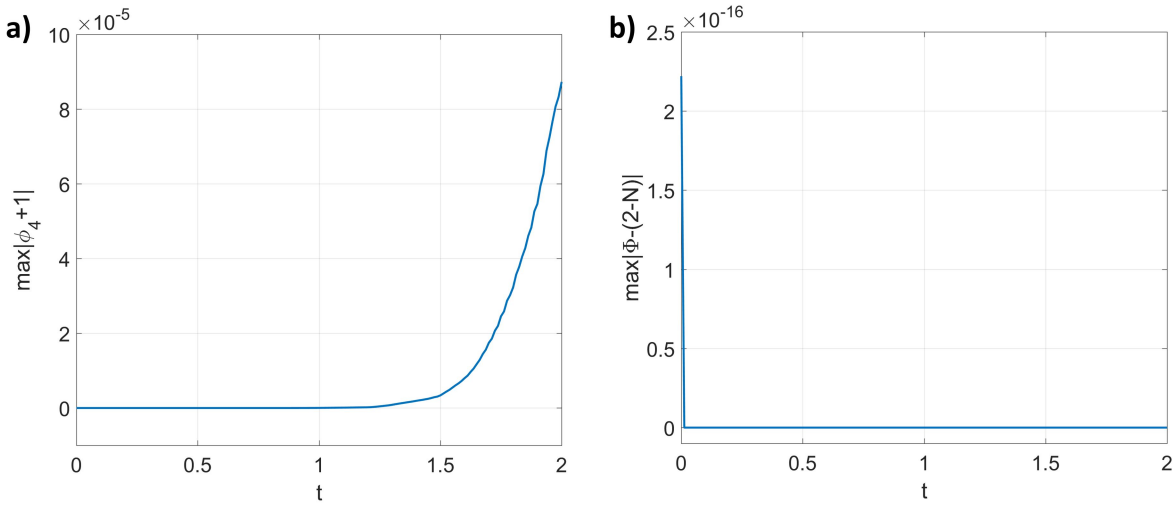

Figure 4.42. Generation of fictitious phases from a reduction inconsistent scheme: solving ϕ_1, ϕ_2, and ϕ_3 from their Phase-Field equation (CH-B) numerically and obtaining ϕ_4 from $\phi_4 = -2 - (\phi_1 + \phi_2 + \phi_3)$. a) Time history of $\max|\phi_4 + 1|$. b) Time history of $\max|\Phi - (2 - N)|$ ($\Phi = \sum_{p=1}^{N} \phi_p$).

the discrete level, although the summation of the volume fraction contrasts, i.e., Eq.(2.2), is exactly enforced. As discussed in Section 3.3, $\{\tilde{\phi}_p\}_{p=1}^{3}$ in the convection term of the Phase-Field equation are computed independently from the WENO scheme. As a result, there is nothing to guarantee $\sum_{p=1}^{3} \tilde{\phi}_p = -1$. This error contributes to $\sum_{p=1}^{3} \phi_p \neq -1$. Consequently, $\phi_4 = -2-(\phi_1+\phi_2+\phi_3)$ can be larger than -1. In other words, ϕ_4 is generated numerically. Even though the Phase-Field equation satisfy the *consistency of reduction*, its numerical scheme still needs to be carefully designed in order to preserve this property and, consequently, to avoid generating fictitious phases numerically. Since it has been validated that the proposed scheme satisfies the *consistency of reduction*, in the following, only the 3-phase setup is used unless otherwise specified.

Next, the mass conservation on the discrete level is considered. As shown in Section 3.3, the total mass, i.e., Mass $= \sum_{\mathrm{i,j}} [\rho \Delta\Omega]_{\mathrm{i,j}}$, and the amounts of individual volume fraction contrasts, i.e., $\mathrm{M}_p = \sum_{\mathrm{i,j}} [\phi_p \Delta\Omega]_{\mathrm{i,j}}$, are globally conserved. In addition, Φ $(= \sum_{p=1}^{N} \phi_p)$ is $(2 - N)$ at every discrete cell, which avoids generating local void or overfilling. Fig.4.43 a) and b) show the changes of Mass and M_p, respectively, and their changes are machine zero. These results confirm that the mass conservation is satisfied on the discrete level. Fig.4.43

c) and d) show the results including the gradient-based phase selection procedure (Present) and using the WENO scheme only (WENO), respectively. Because of the non-linearity of the WENO scheme, the summation and the interpolation are not commutable. As a result, $\sum_{p=1}^{N} \tilde{\nabla} \cdot (\mathbf{u}\tilde{\phi}_p)$ is not zero, which results in $\Phi \neq (2-N)$. Besides, the difference between Φ and $(2-N)$ increases with time, as shown in Fig.4.43 c). On the contrary, the proposed scheme, which implements the gradient-based phase selection procedure, guarantees Φ to be $(2-N)$ all the time. Fig.4.43 d) shows the spatial distribution of $\Phi - (2-N)$ at $t = 2$. The present scheme guarantees $\Phi = (2-N)$ to be satisfied at every discrete cell, while only using the WENO scheme generates local void or overfilling at about one third of the total discrete cells.

Now, the momentum conservation on the discrete level is considered. As shown in Section 3.5.3, Momentum$_x$ $(=\sum_{\mathrm{i,j}} [\rho u \Delta\Omega]_{\mathrm{i,j}})$ and Momentum$_y$ $(=\sum_{\mathrm{i,j}} [\rho v \Delta\Omega]_{\mathrm{i,j}})$ are conserved if the conservative method (CH-C) is used. However, this is not necessarily true when the balanced-force method (CH-B) is implemented. The results in Fig.4.44 a) and b) confirm the analysis. The momentum from the balanced-force method increases with time, although it is not significant. Specifically, the change of Momentum$_x$ is less than 0.04% of its initial value. However, the momentum from the conservative method doesn't change with time. Since the difference between the balanced-force method and the conservative method is in the order of truncation error, the non-conservation of momentum from the balanced-force method should be reduced under grid refinement, and this is also shown in Fig.4.44 a) and b). Fig.4.44 c) and d) show the snapshots of the three phases from the balanced-force method and the conservative method, respectively. The difference is very small. One can summarize that, on the discrete level, the momentum is conserved if the conservative method is used, while it is essentially conserved if the balanced-force method is used.

Finally, the energy dissipation on the discrete level is considered, which is discussed in Theorem 3.5.7 and the remarks below. CH follows the energy law in Corollary 2.4.4.1, which states that the total energy of the multiphase system, without external energy input, should not increase with time, and the following numerical experiments show that the proposed scheme respects the energy law on the discrete level.

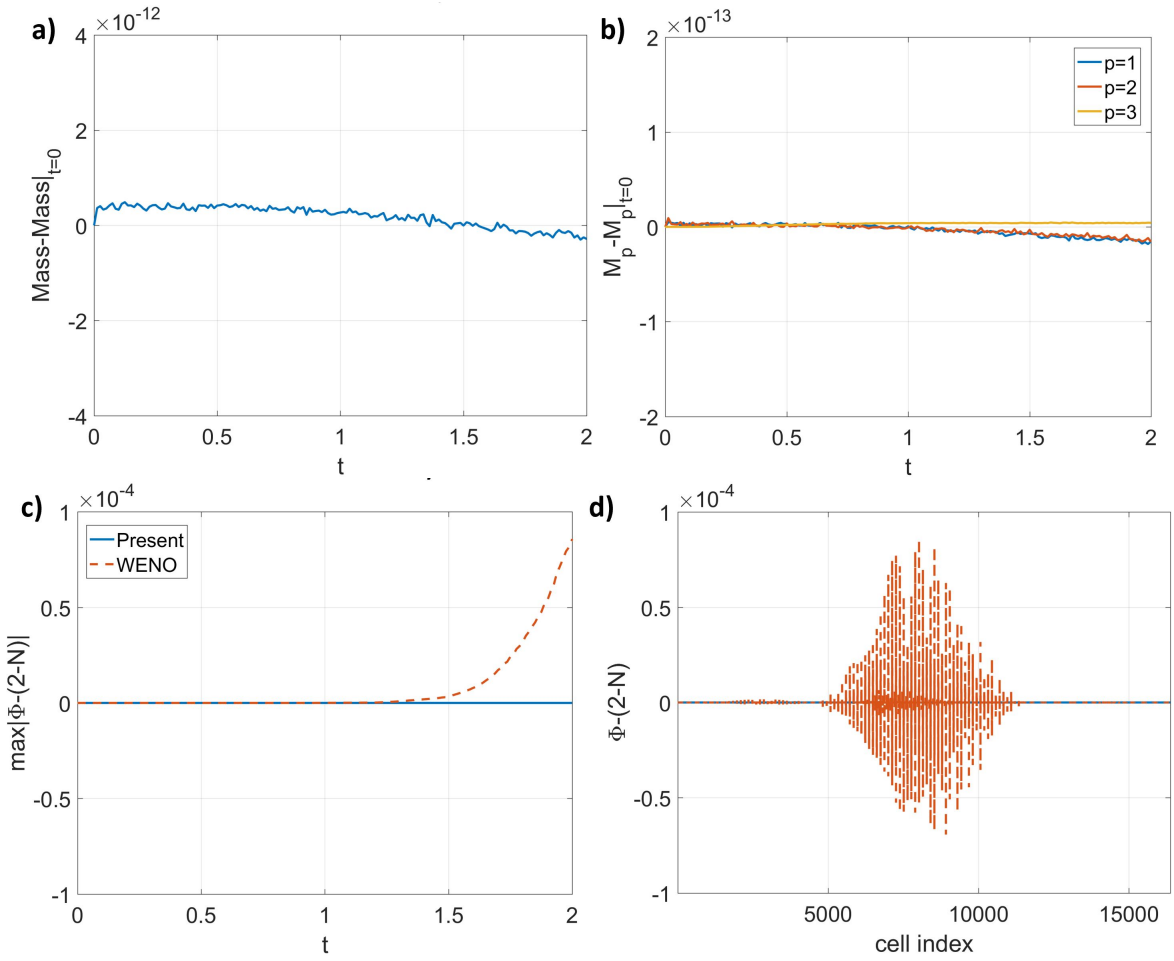

Figure 4.43. Validation of the mass conservation and summation of the order parameters using CH-B. a) Time history of the change of Mass($= \sum_{i,j} [\rho \Delta \Omega]_{i,j}$). b) Time histories of the change of M_p($= \sum_{i,j} [\phi_p \Delta_\Omega]_{i,j}$). c) Time histories of $\max|\Phi - (2-N)|$ ($\Phi = \sum_{p=1}^{N} \phi_p$) from the present scheme including the gradient-based phase selection procedure (Present) and the scheme using WENO only (WENO). d) The spatial distributions of $\Phi - (2-N)$ at $t = 2$ from the present scheme (Present) and the scheme using WENO only (WENO). c) and d) share the same legend.

In the first case, where there is neither viscosity nor interfacial tension, the free energy is zero so the total energy is the same as the kinetic energy. From the energy law in Corollary 2.4.4.1, the total energy, as well as the kinetic energy, does not change with time. However, in practice, the total energy is decreased due to numerical dissipation. Fig.4.45 shows the time histories of the kinetic, free, and total energies. The free energy is identically zero. The kinetic energy and the total energy are the same. When the cell is refined,

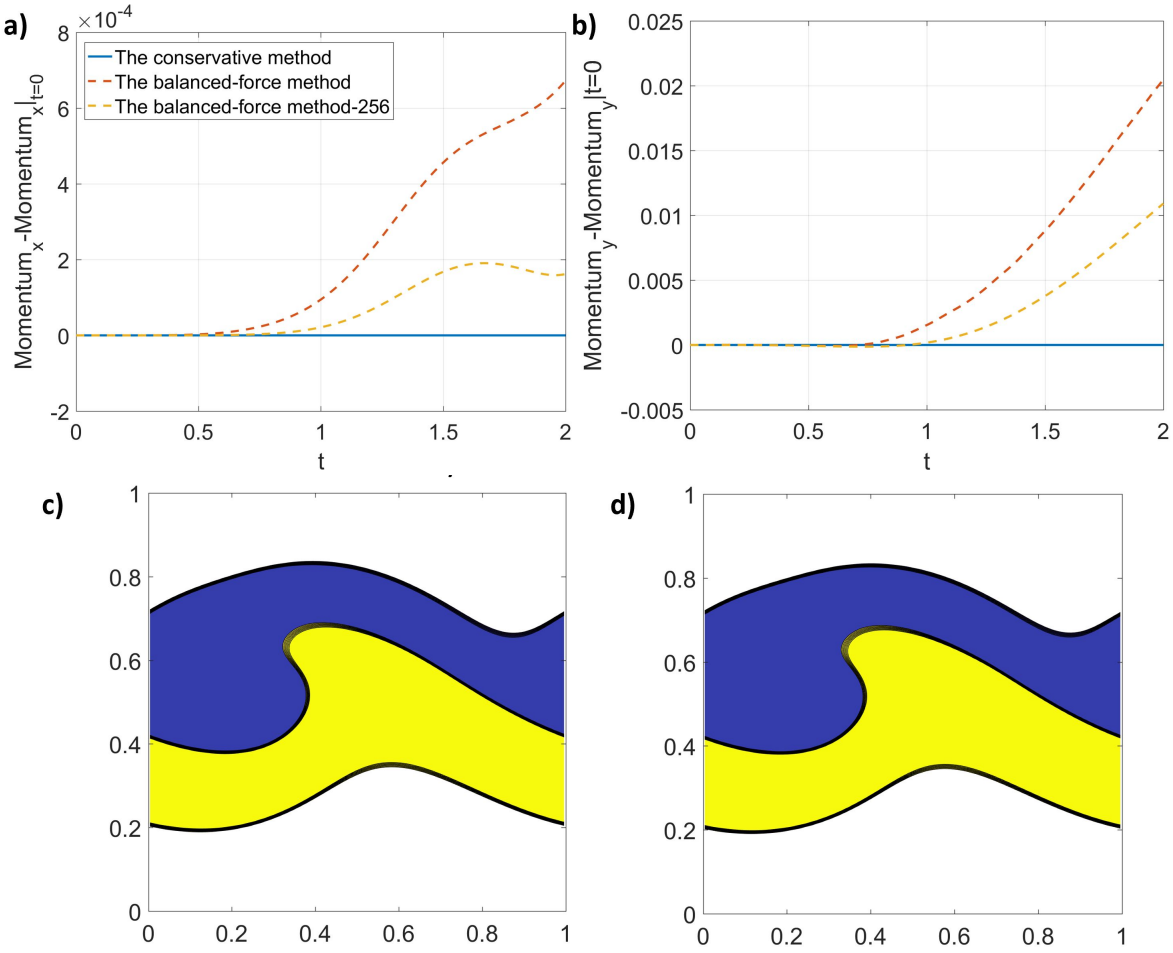

Figure 4.44. Validation of the momentum conservation using CH-B and CH-C. a) Time history of the change of Momentum$_x$($=\sum_{\mathrm{i,j}}[\rho u \Delta\Omega]_{\mathrm{i,j}}$). b) Time histories of the change of Momentum$_y$($=\sum_{\mathrm{i,j}}[\rho v \Delta\Omega]_{\mathrm{i,j}}$). a) and b) share the same legend, and "256" in the legend represents the results obtained from a finer cell size $h = 1/256$. c) Snapshot of the phases at $t = 2$ from the balanced-force method (CH-B). d) Snapshot of the phases at $t = 2$ from the conservative method (CH-C). Blue: Phase 1, Yellow: Phase 2, White: Phase 3.

the change of the kinetic energy is reduced, implying that the numerical dissipation is the source of changing the kinetic energy. The numerical dissipation comes from the backward difference time discretization, the WENO scheme for the inertia term, and the linearly interpolated pressure gradient term in Eq.(3.58), like the two-phase case, as discussed in the remarks below Theorem 3.5.7.

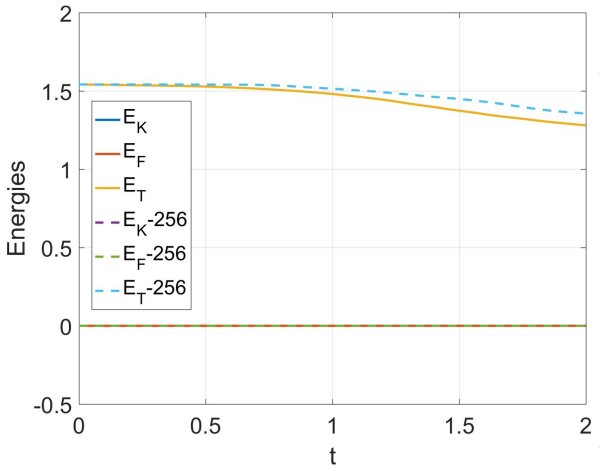

Figure 4.45. Time histories of the kinetic (E_K), free (E_F), and total (E_T) energies in the case without viscosity and interfacial tensions using CH-B. "256" in the legend represents the results obtained from a finer cell size $h = 1/256$.

The second case has no viscosity but interfacial tension. From Corollary 2.4.4.1, there is energy transfer between the kinetic energy and the free energy in this case, while the total energy should decrease. Fig.4.46 shows the results from the balanced-force method (CH-B) and the conservative method (CH-C). Both methods respect the energy law on the discrete level, i.e., the total energy decreases with time, as shown in Fig.4.46 a) and b). one can also observe the energy transfer from the kinetic energy to the free energy due to the deformation of the initially flat interfaces. In Fig.4.46 c), although the total energies from the two methods are very close to each other, the kinetic energy from the conservative method decreases more than the one from the balanced-force method at a later time. As a result, the free energy from the conservative method increases faster than the one from the balanced-force method. The difference between the two methods is much less after the cell size is refined, as shown in Fig.4.46 d).

The last case considered includes both the viscosity and interfacial tension, corresponding to the complete form of Corollary 2.4.4.1. The results are shown in Fig.4.47, and Corollary 2.4.4.1 is satisfied on the discrete level by both the balanced-force method (CH-B) and the conservative method (CH-C), as shown in Fig.4.47 a) and b). There is little difference between the default and the fine grid solutions, implying that the decay of the total energy

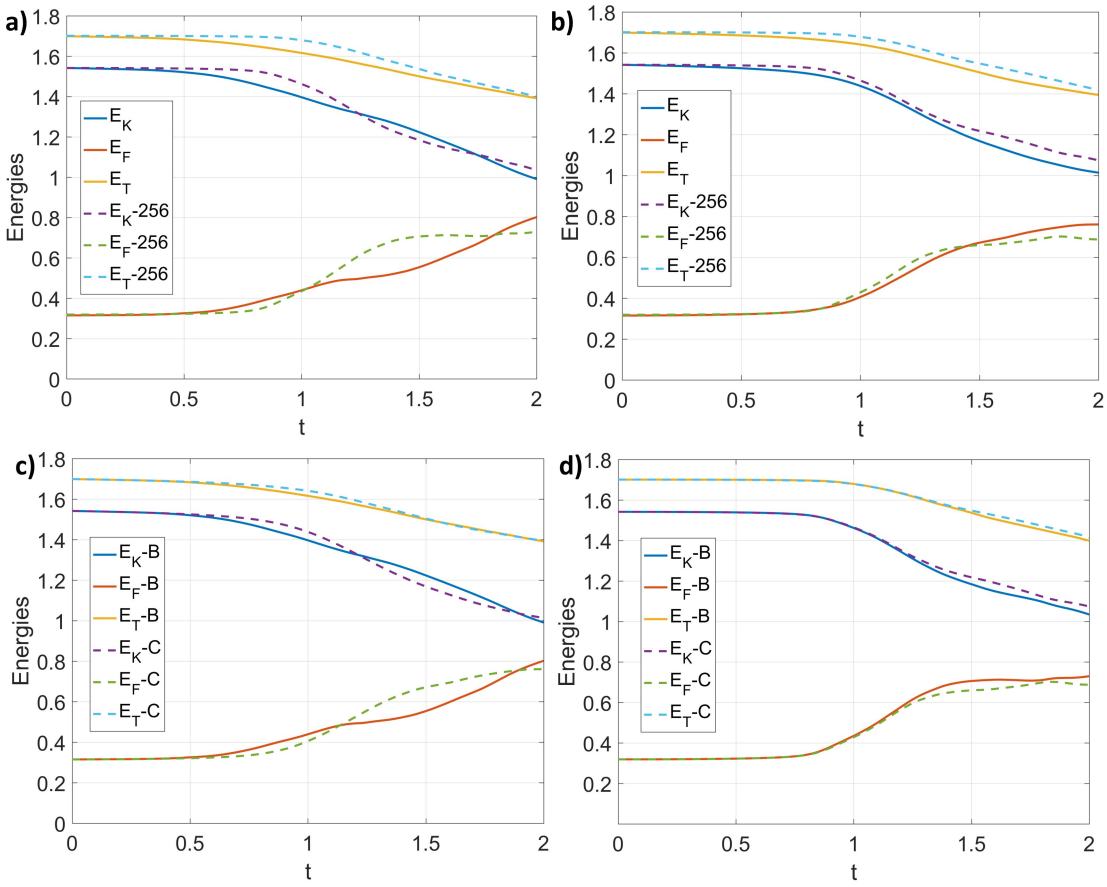

Figure 4.46. Time histories of the kinetic (E_K), free (E_F), and total (E_T) energies in the case without viscosity but with interfacial tensions using CH-B and CH-C. a) from the balanced-force method (CH-B). b) from the conservative method (CH-C). c) from the cell size $h = 1/128$. d) from the cell size $h = 1/256$. B: The balanced-force method (CH-B), C: The conservative method (CH-C), "256" represents the results from a finer cell size $h = 1/256$.

results from the physical interaction in the Phase-Field method, instead of numerical dissipation. In addition, the difference between the two methods is hardly observable in both the default and the find grid solutions, as shown in Fig.4.47 c) and d).

At the end of this case, the boundedness mapping is included, and CH-B, CHB-B, CAC-B, and CACB-B are considered together. The mass conservation of individual phases, the maximum and minimum of the order parameters, and the summation of the order parameters are first investigated, and the results are shown in Fig.4.48. It is clear that all the results satisfy the mass conservation and the summation of the order parameters, no matter whether

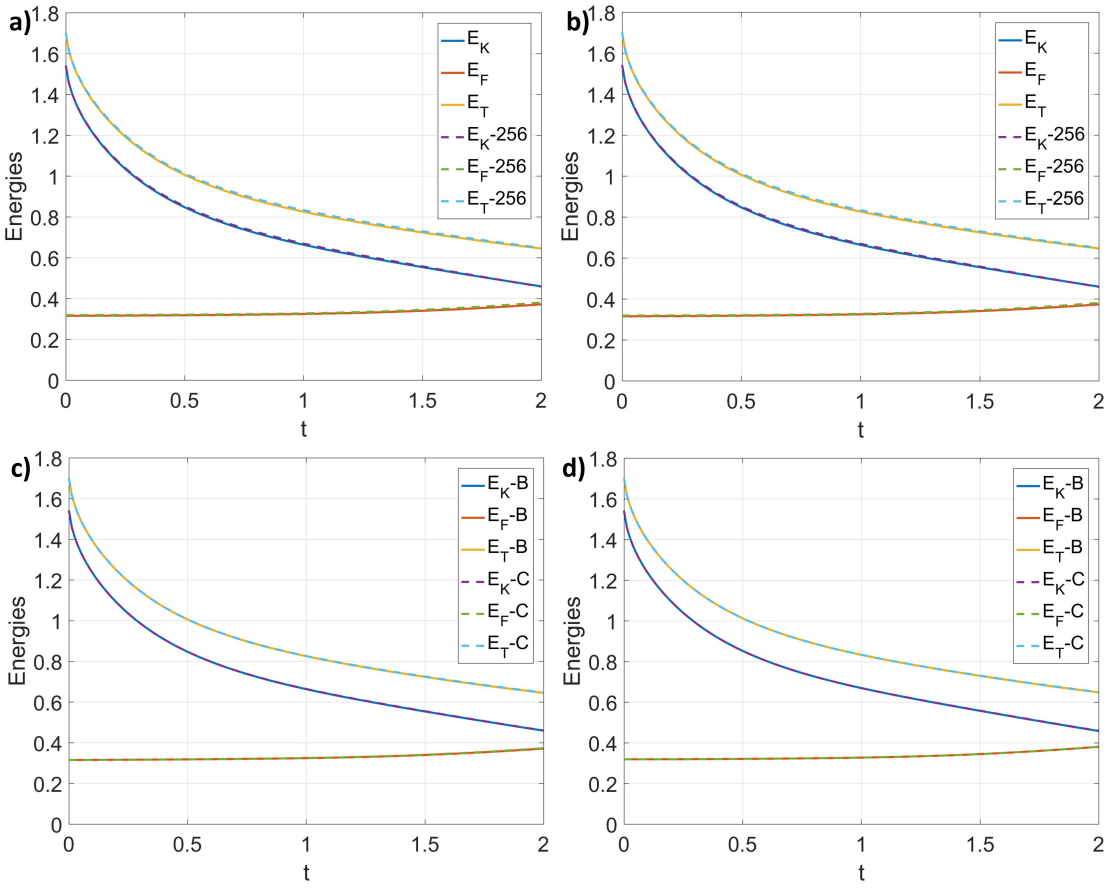

Figure 4.47. Time histories of the kinetic (E_K), free (E_F), and total (E_T) energies in the case with viscosity and interfacial tensions using CH-B and CH-C. a) from the balanced-force method (CH-B). b) from the conservative method (CH-C). c) from the cell size $h = 1/128$. d) from the cell size $h = 1/256$. B: The balanced-force method (CH-B), C: The conservative method (CH-C), "256" represents the results from a finer cell size $h = 1/256$.

the boundedness mapping is included. However, without the boundedness mapping, i.e., from CH-B and CAC-B, the order parameters do not stay in the physical interval $[-1, 1]$. The out-of-bound error appears at about $t = 0.4$. It grows with time and finally reaches $O(10^{-4})$. On the other hand, with the help of the boundedness mapping, none of the order parameters go beyond the physical interval $[-1, 1]$.

Next, the problem is quantified by the time histories of the kinetic energy (E_K), the free energy (E_F), and the total energy (E_T), see Corollary 2.4.4.1, and they are shown in Fig.4.49. The results with/without the boundedness mapping are on top of each other since

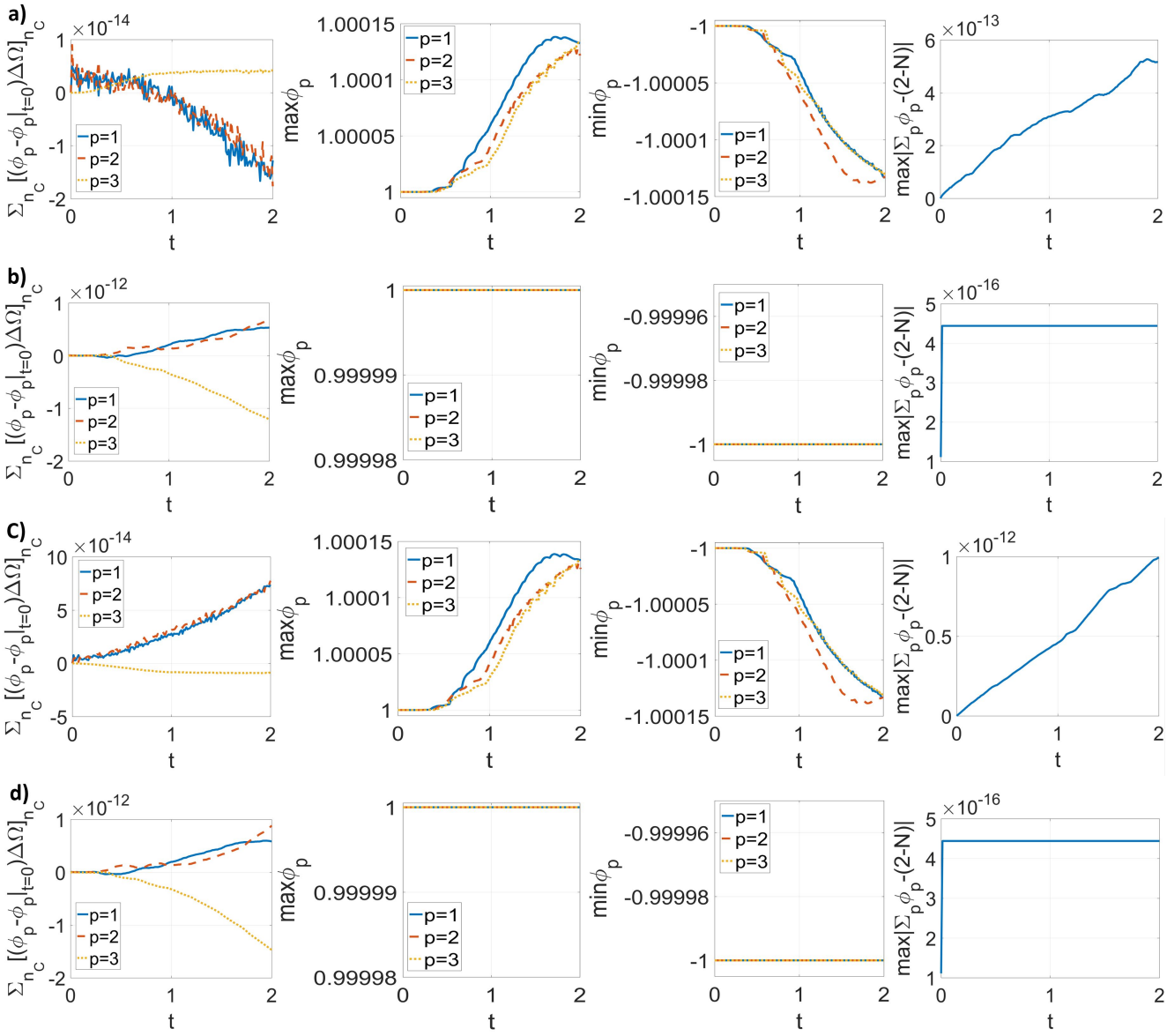

Figure 4.48. Results of the three-phase horizontal shear layer from a) CH-B, b) CHB-B, c) CAC-B, and d) CACB-B. The first column: Errors of the mass conservation of individual phases. The second column: Maximum of the order parameters. The third column: Minimum of the order parameters. The fourth column: Error of the summation of the order parameters.

the out-of-bound error is small. In addition, the difference between CHB-B and CACB-B is unobservable in this case. The decay of the total energy is consistent with the energy law in Corollary 2.4.4.1.

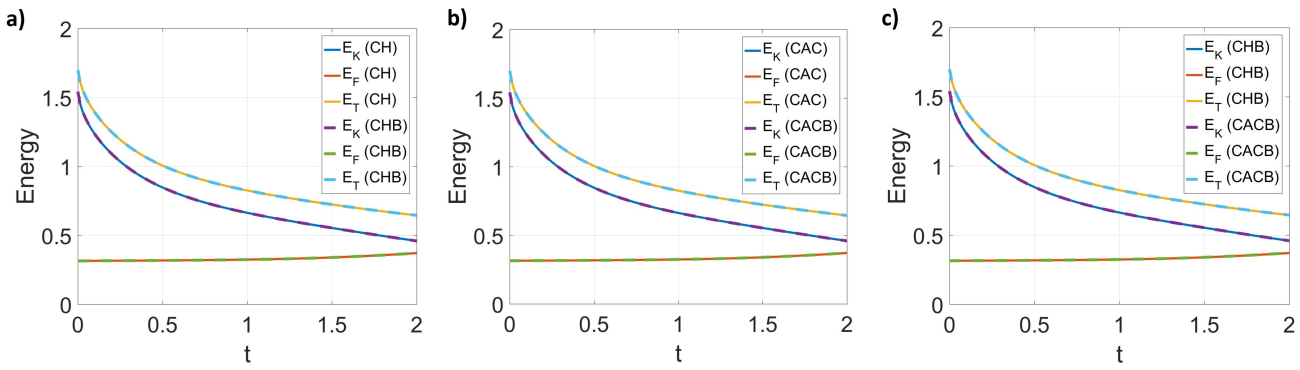

Figure 4.49. Time histories of the energies from a) CH-B and CHB-B, b) CAC-B and CACB-B, and c) CHB-B and CACB-B.

The *consistency of reduction* is revisited by adding the 4th phase, whose density is 0.5, viscosity is 0.08, and surface tensions are $\sigma_{1,4} = 0.08$, $\sigma_{2,4} = 0.02$, and $\sigma_{3,4} = 0.2$. However, Phase 4 is absent at the beginning, i.e., $\phi_4|_{t=0} = -1$. Therefore, it should not appear during the computation. The results from CHB-B and CACB-B are shown in Fig.4.50. The mass conservation and the summation of the order parameters are again satisfied. ϕ_4 from CHB-B is exact -1 at every cell and every time step. However, the difference between ϕ_4 from CACB-B and -1 is the round-off error. Therefore, both the Phase-Field equations along with the boundedness mapping do not generate any fictitious phases. Then the energies from the three-phase case are compared to those from the 4-phase case in Fig.4.51, and the difference between them is unobservable. The three-phase dynamics is reproduced by the four-phase setup with a phase absent. Therefore the *consistency of reduction* is satisfied.

The results shown here validate the analyses and discussions in Chapter 3. In summary, the proposed scheme satisfies the summation of the order parameters, the mass conservation of each phase, the *consistency of reduction*, unconditionally. Additionally, the order parameters are bounded in their physical interval if the boundedness mapping is supplemented. The momentum is conserved unconditionally if the conservative method is used for the surface force, while it becomes essentially conserved with the balanced-force method. The energy transfer between the kinetic and free energies is well captured by the scheme and the total energy is dissipated either by the intrinsic physical dissipation of the Phase-Field method, or by numerical dissipation which is usually very small compared to the physical one.

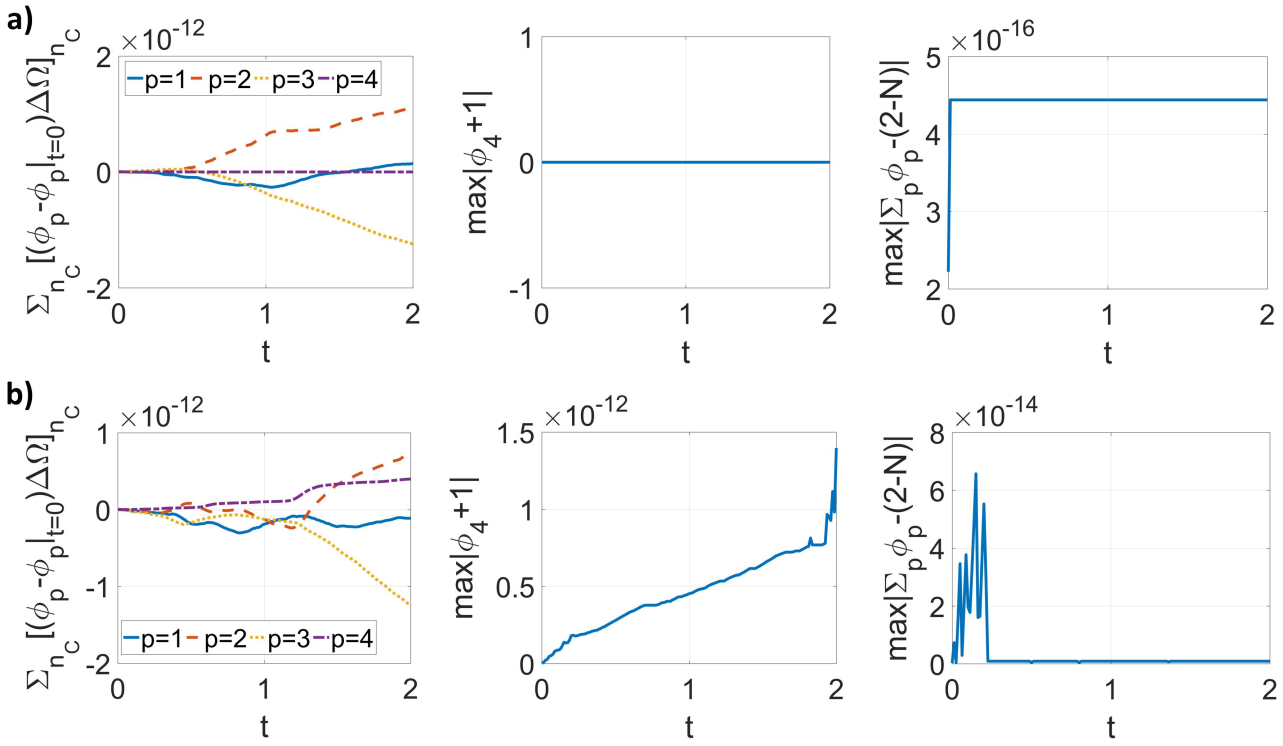

Figure 4.50. Results of the four-phase horizontal shear layer from a) CHB-B and b) CACB-B. The first column: Errors of the mass conservation of individual phases. The second column: Error of ϕ_4. The third column: Error of the summation constraint for the order parameters.

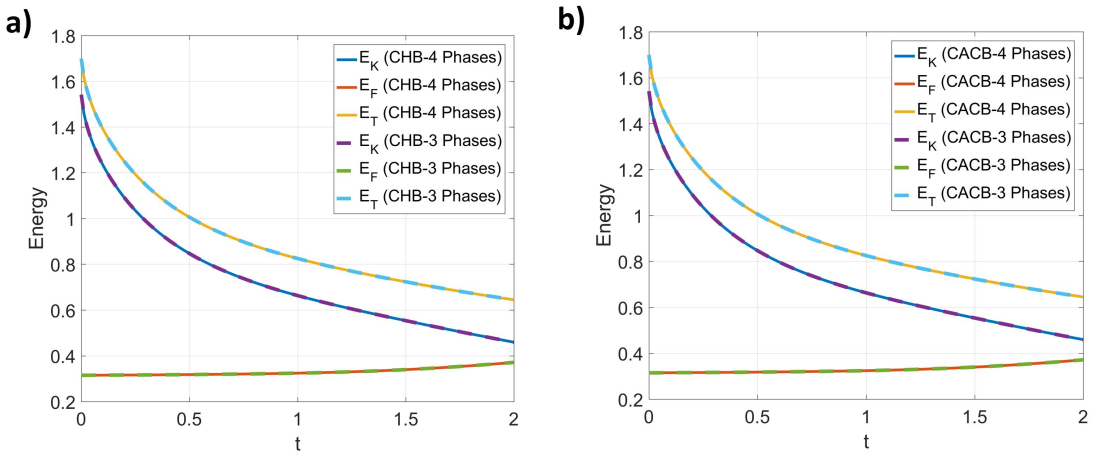

Figure 4.51. Time histories of the energies from a) CHB-B and b) CACB-B.

4.9.3 Multiphase and multicomponent results

The mass conservation, momentum conservation, and energy law are discussed using the N-phase-M-component model. Phase 1, whose pure phase density is 10 and viscosity is 10^{-2}, is initially in $0.25 \leqslant y \leqslant 0.75$. Phase 2, whose pure phase density is 1 and viscosity is 10^{-3}, fills the rest of the domain. The surface tension between them is 0.1 and no gravity is considered. η is $\frac{1}{30\sqrt{2}}$ in this case, like the two-phase setup. Component 1, whose density is 20 and viscosity is 10^{-3}, is dissolvable in Phase 2 only, with diffusivity 10^{-3}. It initially occupies $0 \leqslant y \leqslant 0.125$ and $0.875 \leqslant y \leqslant 1$, with a homogeneous concentration 1. The initial velocity is identical to the two-phase one as well. In this case, both the balanced-force method (B) and the conservative method (C) is used to discretize the interfacial force.

Fig.4.52 shows the time histories of the total volumes of individual phases, the total amount of Component 1 inside its dissolvable region, and the total mass of the fluid mixture. It is clear that all the quantities shown in Fig.4.52 have little change as time goes on, and they have been checked that the changes of them with respect to their initial values are below 10^{-12}, which matches the analysis in Chapter 3. The results demonstrate that the proposed scheme conserves the mass of individual pure phases, i.e., $\left\{\rho_p^\phi \sum_{\mathrm{i,j}} [\chi_p \Delta\Omega]_{\mathrm{i,j}}\right\}_{p=1}^{N}$, conserves the amount of each component in its dissolvable region, i.e., $\left\{\sum_{\mathrm{i,j}} [\chi_p^M C_p \Delta\Omega]_{\mathrm{i,j}}\right\}_{p=1}^{M}$, and, thus, conserves the mass of the fluid mixture, i.e., $\sum_{\mathrm{i,j}} [\rho\Delta\Omega]_{\mathrm{i,j}} = \sum_{p=1}^{N} \rho_p^\phi \sum_{\mathrm{i,j}} [\chi_p \Delta\Omega]_{\mathrm{i,j}} + \sum_{p=1}^{M} \rho_p^C \sum_{\mathrm{i,j}} [\chi_p^M C_p \Delta\Omega]_{\mathrm{i,j}}$ from Eq.(2.55), on the discrete level.

Fig.4.53 shows the time histories of the changes of the momentum. Using the conservative method, the momentum is conserved on the discrete level. On the other hand, using the balanced-force method doesn't conserve the momentum exactly. However, the change of the momentum is small, which is less than 0.25% of its initial value in this case. Therefore, the momentum is essentially conserved by the balanced-force method. The obtained results are consistent with the results of the multiphase flows without components, and they demonstrate that including components doesn't change the property of momentum conservation of the scheme.

Fig.4.54 shows the time histories of the kinetic energy E_K, the free energy E_F, the component energy E_C and the total energy $E_T = E_K + \frac{1}{2}E_F + E_C$. Both the balanced-force

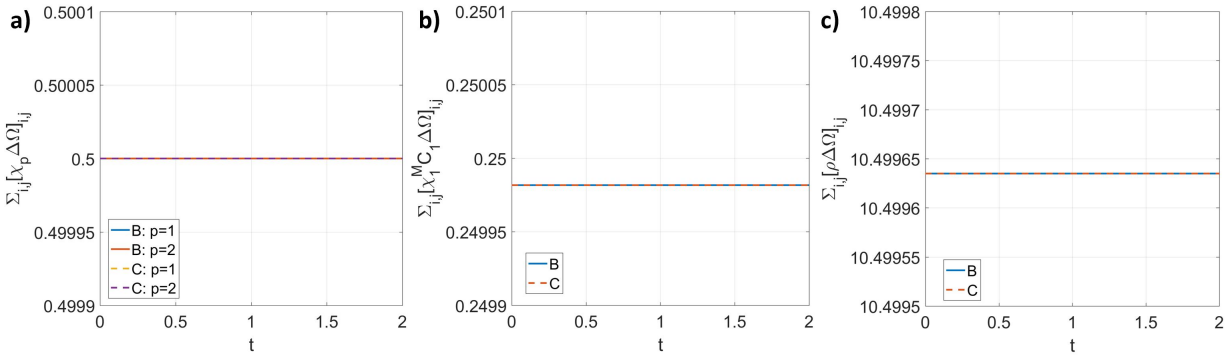

Figure 4.52. Time histories of the quantities related to mass conservation in the horizontal shear layer. a) Time histories of total volumes of individual phases. b) Time histories of the total amount of Component 1 in its dissolvable region. c) Time histories of the total mass of the fluid mixture.

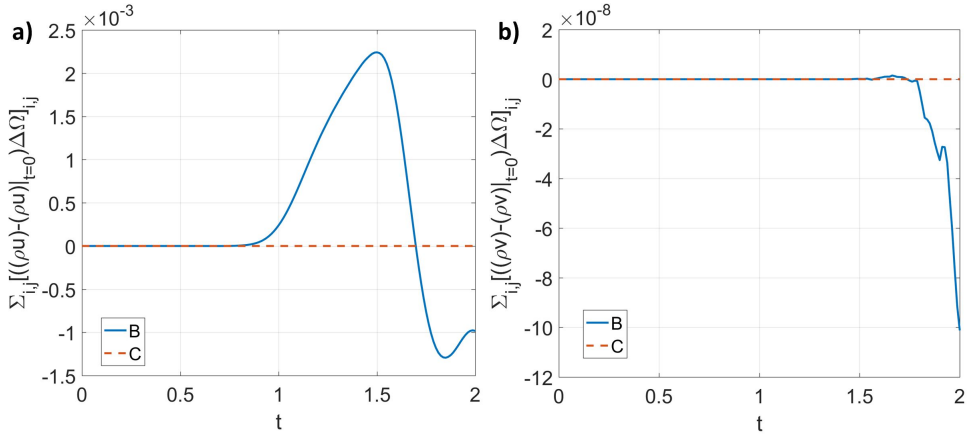

Figure 4.53. Time histories of the momentum in the horizontal shear layer. a) Time histories of the x component of the momentum. b) Time histories of the y component of the momentum.

method and the conservative method give similar results. In this case, the contribution from the component energy is negligibly small. One can observe from Fig.4.54 **a)** that the kinetic energy is decaying due to both the viscous effect and the energy transfer to the free energy. Therefore, the free energy is increased. The total energy is always decaying, demonstrating that the energy law of the N-phase$M$-component model in Corollary 2.6.1.2 is honored at the discrete level by the scheme. Fig.4.54 **b)** shows that the component energy is also decaying all the time.

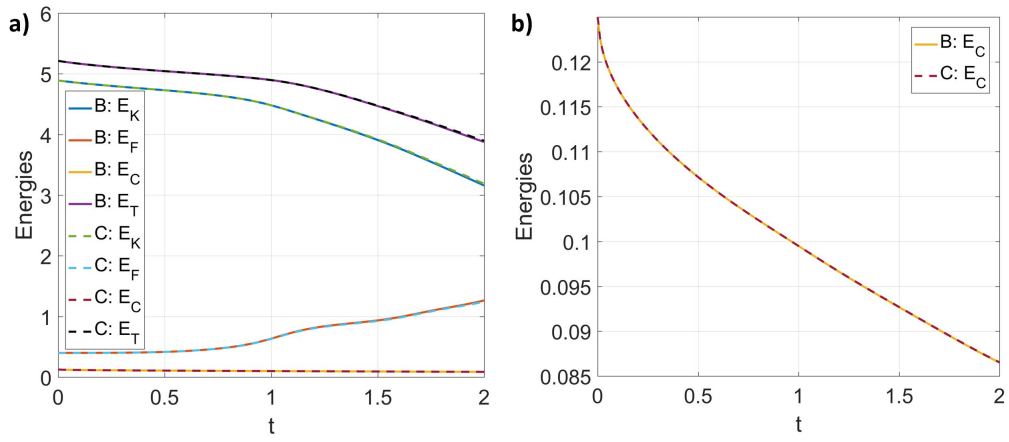

Figure 4.54. Time histories of the energies in the horizontal shear layer. a) Time histories of the kinetic energy, free energy, component energy, and total energy. b) Time histories of the component energy.

4.10 Rising bubble: convergence tests

The convergence behavior of the numerical solution of the Phase-Field method to the sharp-interface solution is studied in a problem including large density ratio, large viscosity ratio, surface tension, and gravity. There are two convergence behaviors when numerically applying a Phase-Field method to mutliphase problems. The first one is the convergence of the numerical solution to the exact solution of the Phase-Field method with fixed interface thickness η by reducing the cell size, which has been studied in Section 4.1. The second one is the convergence of the exact solution of the Phase-Field method to the sharp-interface one by reducing the interface thickness η. In numerical implementations, it is more common and practical to consider those two together by decreasing both the cell size and the interface thickness at the same time, and then to evaluate how fast the numerical solution converges to the sharp-interface solution. Such a discussion in the Phase-Field community focuses only on the matched density case, while careful and systematic discussions in the problem of large density and viscosity ratios have not yet been seen, although it is a common situation in two-phase flows. This section focuses on addressing this gap in the literature.

The rising bubble case is considered. The domain considered is $[1 \times 2]$ and it has no-slip boundaries at the top and bottom but free-slip at the lateral. The cell size h is ranging from

$\frac{1}{16}$ to $\frac{1}{256}$, and the time step size is $\Delta t = 0.128h$. A circular bubble (Phase 1) of diameter 0.5 is initially released at $(0.5, 0.5)$ inside a quiescent fluid (Phase 2). The density and viscosity of Phase 1 inside the bubble are 1 and 0.1, respectively, while they are 1000 and 10 for Phase 2 outside the bubble. These lead to a density ratio 1000 and viscosity ratio 100. The surface tension is 1.96 and gravitational acceleration is $\mathbf{g} = \{0, -0.98\}$. All the computations are stopped at $t = 1$. Three benchmark quantities are used: the circularity ψ_c, the center of mass y_c and the rising velocity v_c to quantify the results, and their definitions are as follows:

$$\psi_c = \frac{P_a}{P_b} = \frac{2\sqrt{\int_{\phi>0} \pi d\Omega}}{P_b}, \quad y_c = \frac{\int_\Omega y \frac{1+\phi}{2} d\Omega}{\int_\Omega \frac{1+\phi}{2} d\Omega}, \quad v_c = \frac{\int_\Omega v \frac{1+\phi}{2} d\Omega}{\int_\Omega \frac{1+\phi}{2} d\Omega},$$

where P_a is the perimeter of the circle whose area is identical to the bubble, and P_b is the perimeter of the bubble. The circularity ψ_c quantifies the shape of the bubble. It is 1 when the bubble is a circle, and less than 1 when the bubble deforms. The center of mass y_c and rising velocity v_c quantify the dynamics of the bubble. The sharp interface solution under the same setup are available in [226], where the Level-Set and Arbitrary-Lagrange-Euler (ALE) methods are used and excellent agreement is reached in the time zone considered. The same benchmark quantities are defined in [226] and they are considered as the reference. If the benchmark quantities at time t are not directly available, the cubic spline interpolation is used to specify them.

4.10.1 Two-phase results

First, two-phase CH-B is first considered. η is related to the cell size h as $\eta = \eta_0(h/h_0)^{\chi_\eta}$ and the mobility M_0 is related to η as $M_0 = M_{00}(\eta/\eta_0)^{\chi_M}$, where $\eta_0 = h_0 = 1/32$ and $M_{00} = 10^{-7}$. The exponent χ_η should be less than or equal to 1 so that at least there are the same number of grid points across the interface during grid refinement. The exponent χ_M should be larger than or equal to 1 but smaller than 2, based on the analysis in [54]. The effect of χ_η on the convergence rate is first considered by fixing $\chi_M = 1$ and by choosing χ_η to be 0, 1/3, 1/2, 2/3, and 1. The results are shown in Fig.4.55-Fig.4.59. When $\chi_\eta = 0$, the interface thickness η doesn't change during grid refinement, one can see that the numerical solutions quickly converge to the exact solution of the Phase-Field method with parameters

$\eta = \eta_0$ and $M_0 = M_{00}$. Since the interface thickness η is not reduced, the numerical solutions are unable to converge to the sharp interface solution. When χ_η is larger than zero, one can see that all the numerical solutions converge to the sharp interface solution during grid refinement. However, the convergence rate is different for different χ_η. For example, the discrepancy between the numerical solution of $\chi_\eta = 1/3$ and the sharp interface solution is very obvious even with the finest grid ($h = 1/256$), while the numerical solution of $\chi_\eta = 1$ with the grid size ($h = 1/128$) is almost on top of the sharp interface solution. To quantify the convergence rate, the L_2 errors of the benchmark quantities are measured and plotted in Fig.4.61. For the case where $\chi_\eta = 0$, since the numerical solution does not converge to the sharp interface solution, it does not make sense to use that as the reference to compute the L_2 error. As convergence can be observed, the finest-grid solution is used as the reference instead for this case. For the other cases where $\chi_\eta > 0$, the sharp interface solution in [226] is used as the reference solution when computing the L_2 error. However, it should be noted that the reference solution is still a numerical approximation of the exact sharp interface solution. The computed L_2 error includes the errors of the present Phase-Field solution and of the reference solution. The error of the reference solution is negligible, compared to the error of the present Phase-Field solution, when the grid is coarse. However, it becomes more significant as the present Phase-Field solution gets closer to the exact sharp interface solution during grid refinement, and, as a result, interferes the evaluation of the convergence rate. Consequently, the finest-grid results are skipped when evaluating the convergence rate. It is observed that the convergence rate is better than 2nd-order when η is fixed and is close to 0.6, 0.9, 1.2 and 1.5 when χ_η is 1/3, 1/2, 2/3, and 1, respectively. Next the case where $\chi_\eta = 2/3$ and $\chi_M = 3/2$, which leads to $M_0 \sim h$, is considered. The results are given in Fig.4.60 and the L_2 errors of the benchmark quantities are plotted in Fig.4.61, as well. The convergence to the sharp interface solution is observed in Fig.4.60 and both the errors and the convergence rates have little change, compared to the corresponding one with $\chi_M = 1$. This implies that the effect of χ_M on the numerical solution is small.

For all the cases that have been discussed, no matter how χ_η is chosen, the magnitude of η is still on the same order of the grid size h, and our numerical practice shows this is a good choice for η. However, the magnitude of the mobility depends on M_0 while there is no clear

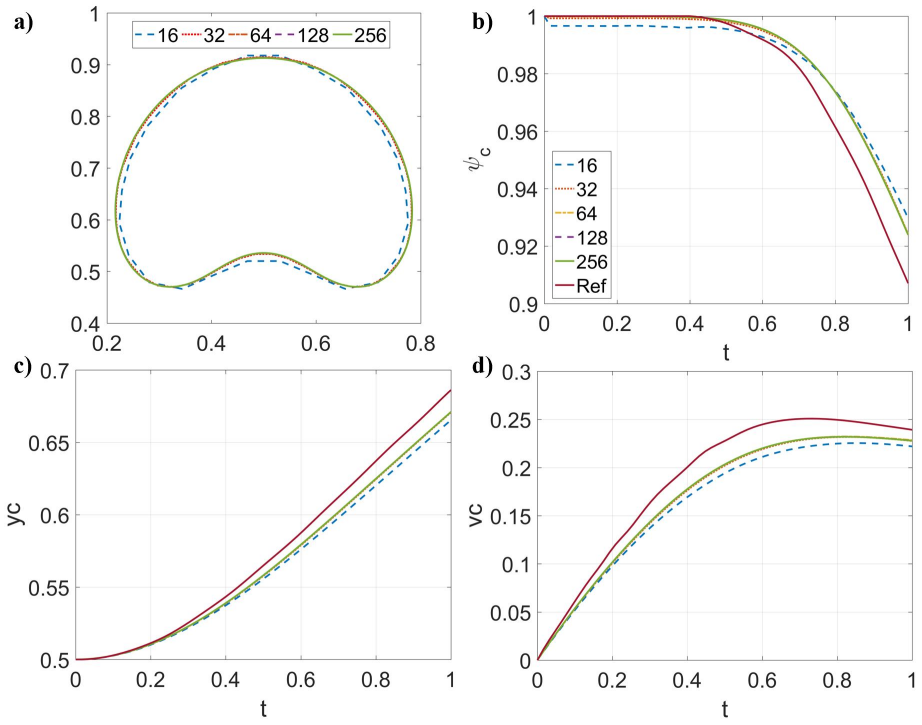

Figure 4.55. Results of the rising bubble with $\chi_\eta = 0$ and $\chi_M = 1$ using two-phase CH-B. a) The shape of the bubble at $t = 1$, b) the circularity ψ_c vs. t, c) the center of mass y_c vs. t, and d) the rising velocity v_c vs. t.

guideline to specify that. To figure out the effect of M_0, a series numerical experiments are performed by fixing $\chi_\eta = 1$, $\chi_M = 1$, $h = 1/128$ and choosing M_0 from 10^{-4} to 10^{-9}. The results are shown in Fig.4.62. There is little difference between the cases with different M_0, and all the cases in Fig.4.62 are almost on top of the sharp interface solution. This implies that the numerical solution is strongly tolerant to the magnitude of the mobility. This also explain why the effect of χ_M on the numerical solution is small.

Next, two-phase CAC-B and CAC-C are investigated. Here, the interface thickness reduces as fast as the cell size, i.e., $\eta = \eta_0(h/h_0)$, where $\eta_0 = h_0 = 1/32$, and the mobility is $M_0 = M_{00}(\eta/\eta_0)$ with $M_{00} = 10^{-7}$. Figs.4.63 and 4.64 show the results from the balanced-force method (two-phase CAC-B) and the conservative method (two-phase CAC-C), respectively. No matter which method is used, the convergence of the numerical Phase-Field solution to the sharp-interface solution (the Reference) can be clearly observed during successive cell refinement. To quantify the convergence behavior, the L_2 errors of the circularity ψ_c, the

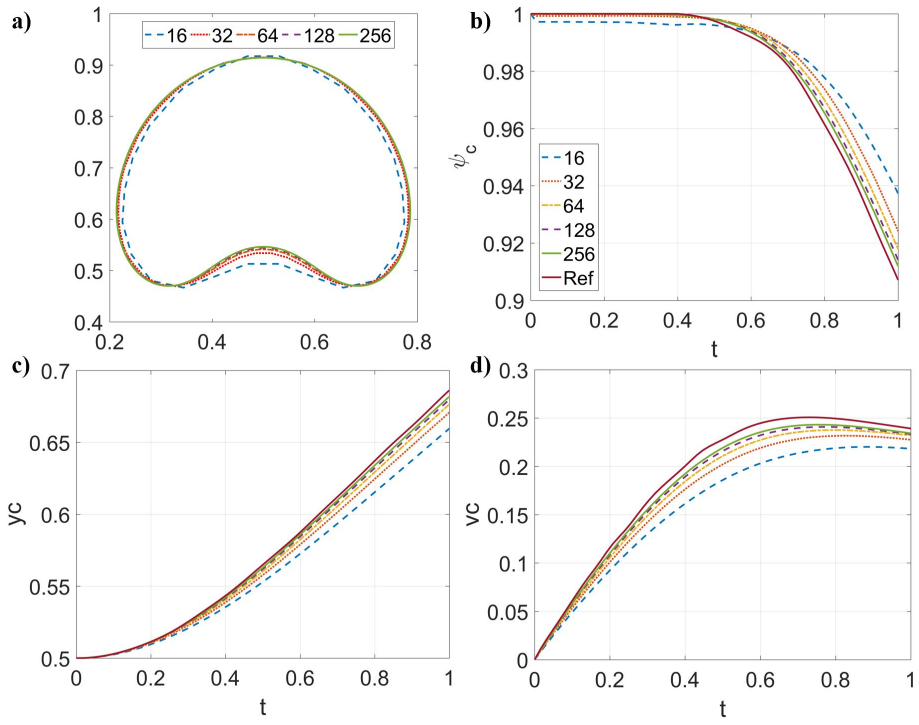

Figure 4.56. Results of the rising bubble with $\chi_\eta = 1/3$ and $\chi_M = 1$ using two-phase CH-B. a) The shape of the bubble at $t = 1$, b) the circularity ψ_c vs. t, c) the center of mass y_c vs. t, and d) the rising velocity v_c vs. t.

center of mass y_c, and the rising velocity y_c are computed, considering the sharp-interface solutions as the reference values, and they are plotted in Fig.4.65. The difference between the two methods is tiny although the conservative method (two-phase CAC-C) slightly outperforms the balanced-force method (two-phase CAC-B). The circularity, which quantifies the shape of the bubble, has a convergence rate close to 2nd-order, while it is around 1.6th-order for the center of mass and the rising velocity. In summary, the numerical Phase-Field solution converges to the sharp-interface solution with a rate between 1.5th- and 2nd-order.

In Section 4.1, it is demonstrated that the scheme is formally 2nd-order accurate although $W(\phi^n)$ is used when computing $\tilde{L}^c$ in two-phase CAC. To further investigate its effect on the accuracy of the scheme in a realistic two-phase flow problem, the convergence test is repeated but fix both η and M_0, i.e., $\eta = \eta_0$ and $M_0 = M_{00}$, as the grid is refined. As a result, the numerical solution converges to the exact solution of the Phase-Field method. L_2 errors

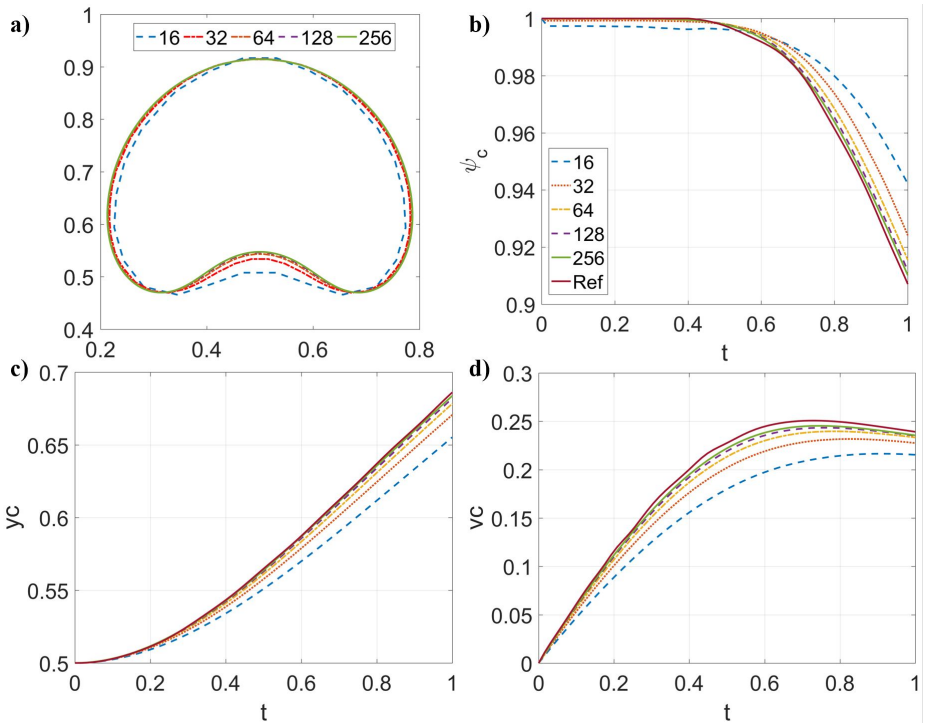

Figure 4.57. Results of the rising bubble with $\chi_\eta = 1/2$ and $\chi_M = 1$ using two-phase CH-B. a) The shape of the bubble at $t = 1$, b) the circularity ψ_c vs. t, c) the center of mass y_c vs. t, and d) the rising velocity v_c vs. t.

of the benchmark quantities are computed using the finest-grid solution as the reference and are plotted in Fig.4.66 a). Again 2nd-order convergence is observed. Therefore, using $W(\phi^n)$ has little effect on the accuracy of the scheme. The slowing down of the convergence rate in Fig.4.65 is attributed to approximating a sharp-interface problem with a Phase-Field method.

Then, the effect of the mobility in two-phase CAC is considered. the grid size is fixed to be $h = \frac{1}{128}$ but change M_0 from 10^{-3} to 10^{-9}. The results are shown in Fig.4.67. Although the mobility changes in a wide range, the difference among the solutions is negligible. Therefore, the two-phase flow model shows good tolerance to the value of the mobility. Since the asymptotic analysis of the two-phase flow model using CAC is not available, the analysis of the one using two-phase CH [54], [77] is borrowed and the mobility is related to the interface thickness as $M_0 = M_{00}(\eta/\eta_0)$, whose results are shown in Fig.4.63, Fig.4.64, and Fig.4.67. The convergence of the numerical solution to the sharp-interface solution has been observed

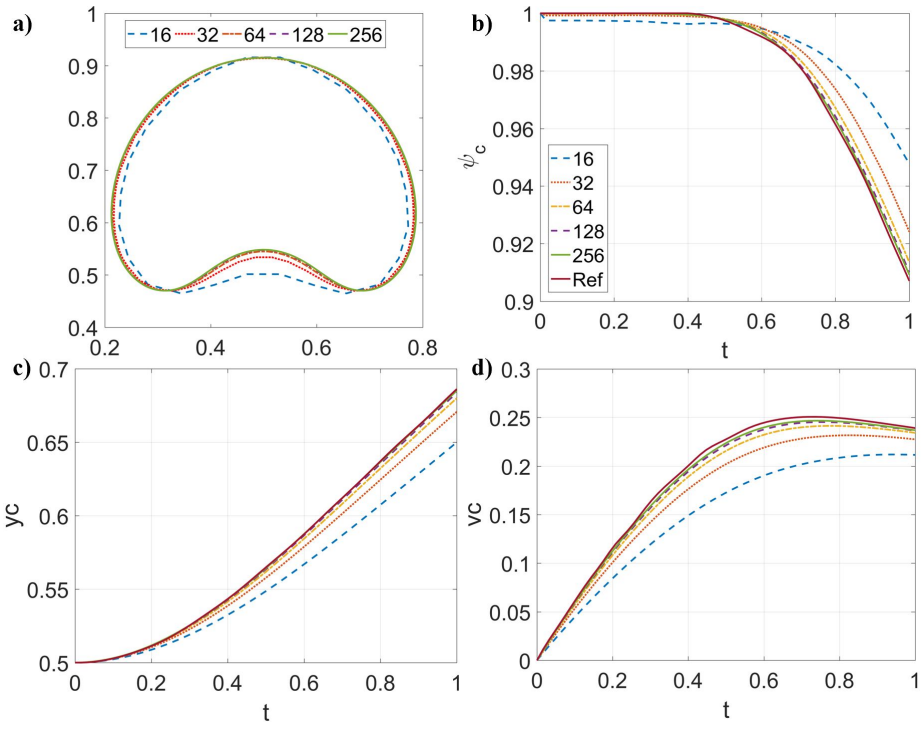

Figure 4.58. Results of the rising bubble with $\chi_\eta = 2/3$ and $\chi_M = 1$ using two-phase CH-B. a) The shape of the bubble at $t = 1$, b) the circularity ψ_c vs. t, c) the center of mass y_c vs. t, and d) the rising velocity v_c vs. t.

and quantified. Another suggestion is to relate M_0 to η as $M_0 = M_{00}(\eta/\eta_0)^2$ [94], [109]. Since the model is not sensitive to the mobility, one can infer that changing the correlation of the mobility will not make a big difference in the convergence behavior to the sharp-interface solution, and the results, obtained from $M_0 = M_{00}(\eta/\eta_0)^2$ with $M_{00} = 10^{-3}$, in Fig.4.66 b), confirm the statement. It should be noted that these observations are based on a practical and numerically affordable setup and the interface thickness considered is probably not small enough to reach the asymptotic regime. Therefore, they are useful for numerical implementation but not necessarily representing the behavior of the method in the asymptotic regime. Numerically reaching the asymptotic regime is challenging since it normally requires a tremendous number of grid points to resolve the interface thickness which can be a million times smaller than the length scale of the problem [92]. Therefore, the asymptotic analysis is a more appropriate tool to study the behavior of the method inside that regime, but it is outside the scope of the present study. Fortunately, it is demonstrated

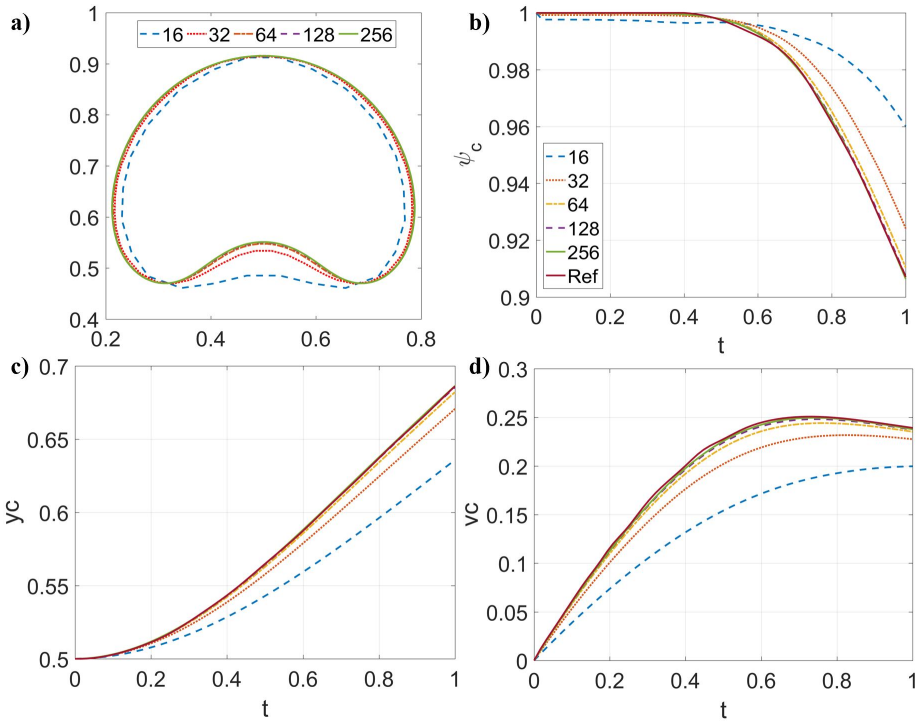

Figure 4.59. Results of the rising bubble with $\chi_\eta = 1$ and $\chi_M = 1$ using two-phase CH-B. a) The shape of the bubble at $t = 1$, b) the circularity ψ_c vs. t, c) the center of mass y_c vs. t, and d) the rising velocity v_c vs. t.

that satisfactory results can be obtained even outside the asymptotic regime, which makes the two-phase CAC method practical and computationally affordable to study two-phase flows numerically.

4.10.2 Multiphase results

The same case is repeated using the multiphase Phase-Field equations, i.e., CH-B and CH-C. $\eta = \eta_0 \frac{h}{h_0}$, where η_0=$h_0 = \frac{1}{32}$, and $M_0 = 10^{-7} \frac{\eta}{\eta_0}$ are set, so that both of them decrease as the cell is refined. Fig.4.68 and Fig.4.69 show the results using the balanced-force method (CH-B) and the conservative method (CH-C), respectively. It is clear that the Phase-Field solution converges to the sharp interface solution (labeled as "Reference" in the figures) as the cell size h, as well as the interface thickness η, reduces. To quantify the convergence rate, the L_2 errors, i.e, the root mean square of the difference between the Phase-Field and the sharp-interface solutions, of the three benchmark quantities are computed. The results are

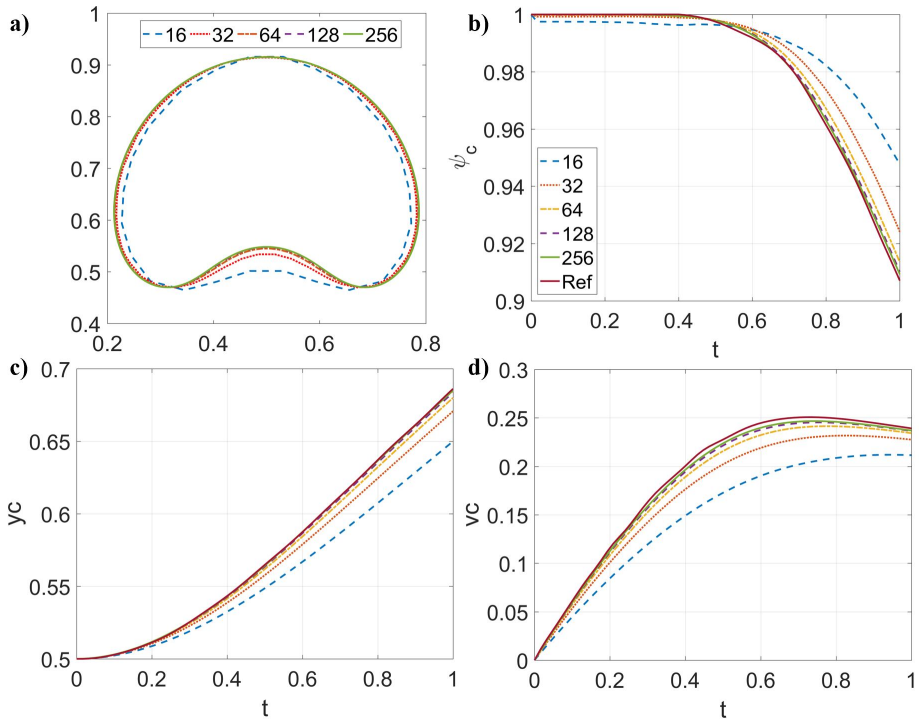

Figure 4.60. Results of the rising bubble with $\chi_\eta = 2/3$ and $\chi_M = 3/2$ using two-phase CH-B. a) The shape of the bubble at $t = 1$, b) the circularity ψ_c vs. t, c) the center of mass y_c vs. t, and d) the rising velocity v_c vs. t.

plotted in Fig.4.70. There is no significant difference between the two methods, although the conservative method performs slightly better, giving smaller errors and faster convergence rates. Overall, both the circularity ψ_c and the center of mass converge to their sharp-interface solutions with a rate close to 2nd order, while the convergence rate of the rising velocity is about 1.5th order, which is slightly slower.

Next, the boundedness mapping is included and CHB-B and CACB-B are considered. In the first test, η and M_0 are fixed in order to study the convergence of the numerical solutions to the exact solutions of the Phase-Field methods. This test is related to the truncation error and should be able to indicate the formal order of accuracy of the schemes. In the second test, η and M_0 are correlated to the grid/cell size h. The interface thickness η is reduced when the cell is refined, and the convergence of the numerical solutions of the Phase-Field methods to the sharp-interface solution can be studied.

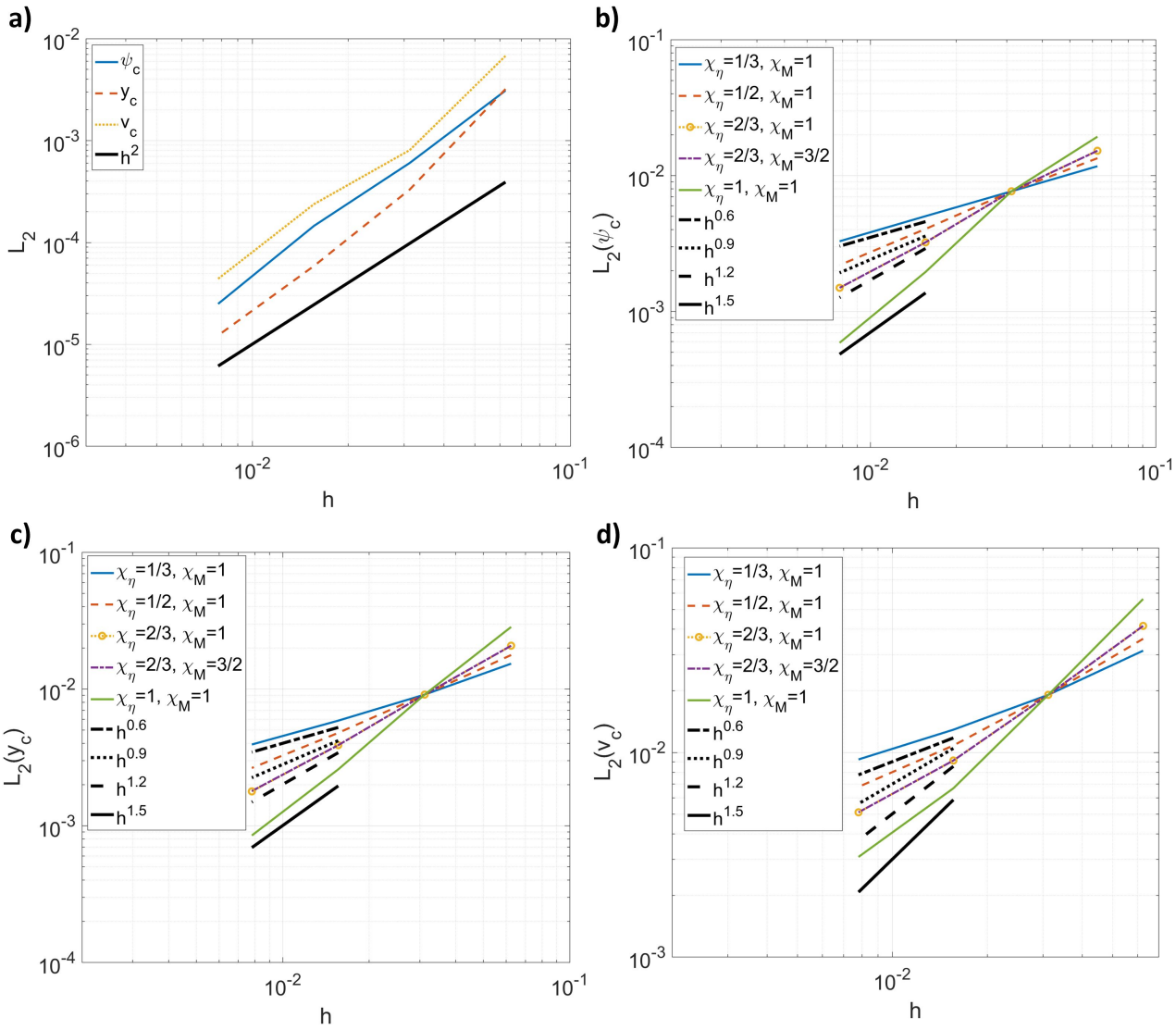

Figure 4.61. L_2 errors of the benchmark quantities from two-phase CH-B. a) $\chi_\eta = 0$ and $\chi_M = 1$ (or fixed η and M_0). b) L_2 errors of ψ_c with different χ_η and χ_M. c) L_2 errors of y_c with different χ_η and χ_M. d) L_2 errors of v_c with different χ_η and χ_M.

Fig.4.71 and Fig.4.72 show the results from CHB-B and CACB-B, respectively, using fixed $\eta = \eta_0 = \frac{1}{32}$ and $M_0 = 10^{-7}$. As the cell size becomes smaller, the numerical solutions gradually approach the exact solutions of the Phase-Field methods, which is different from the sharp-interface solution, since the interface thickness is not reducing. To quantify the convergence behavior, the L_2 errors, i.e., the root-mean-square errors, of the three benchmark quantities are computed. The solutions from the finest grid is used as the exact solutions

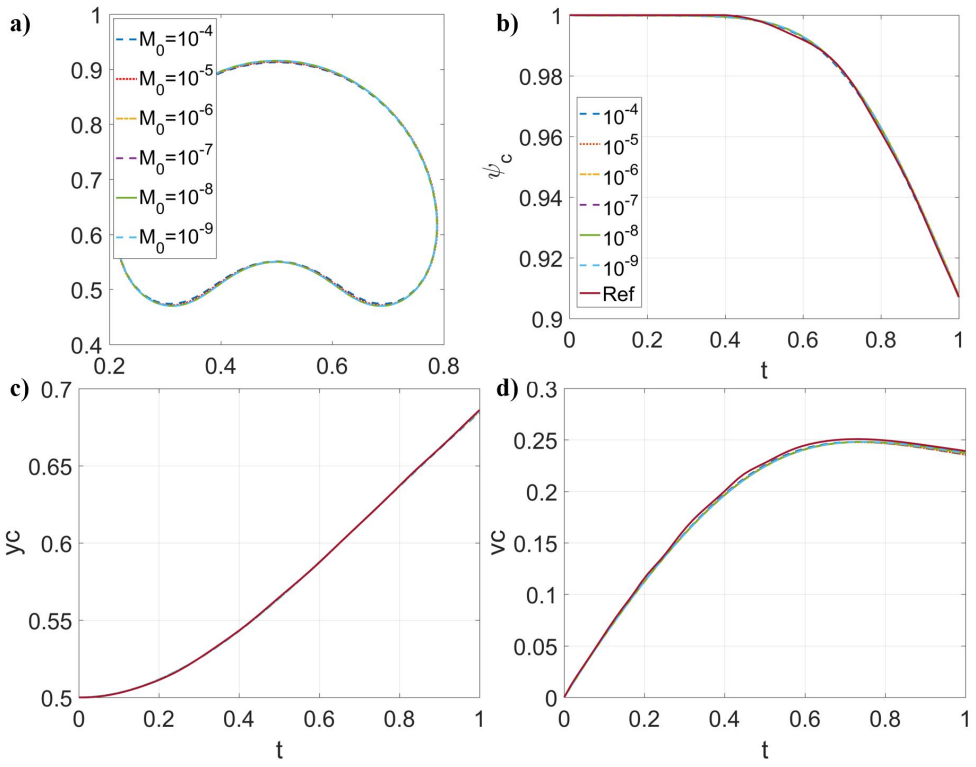

Figure 4.62. Results of the rising bubble with different M_0 using two-phase CH-B. a) The shape of the bubble at $t = 1$, b) the circularity ψ_c vs. t, c) the center of mass y_c vs. t, and d) the rising velocity v_c vs. t.

of the Phase-File methods. The errors are plotted in Fig.4.73 a), and the convergence rates are 2nd-order. Therefore, the schemes for CHB and CACB are formally 2nd-order accurate. This supplements the formal accuracy of CAC that is missed validated in Section 4.1.

Fig.4.74 and Fig.4.75 show the results from CHB-B and CACB-B, respectively, using $\eta = h$ and $M_0 = 10^{-7}(\eta/\eta_0)$. The convergence of the numerical solutions from the Phase-Field methods to the sharp-interface solution is observed, as the cell size, as well as the interface thickness, is refined. The L_2 errors of the three benchmark quantities are computed using the sharp-interface solution. The errors are plotted in Fig.4.73 b), and both CHB-B and CACB-B share a similar convergence behavior. The circularity ψ_c, which quantifies the shape of the bubble, converges to the sharp-interface solution at a rate close to 2nd-order. The convergence rate is around 1.5th-order for the dynamics of the bubble, quantified by

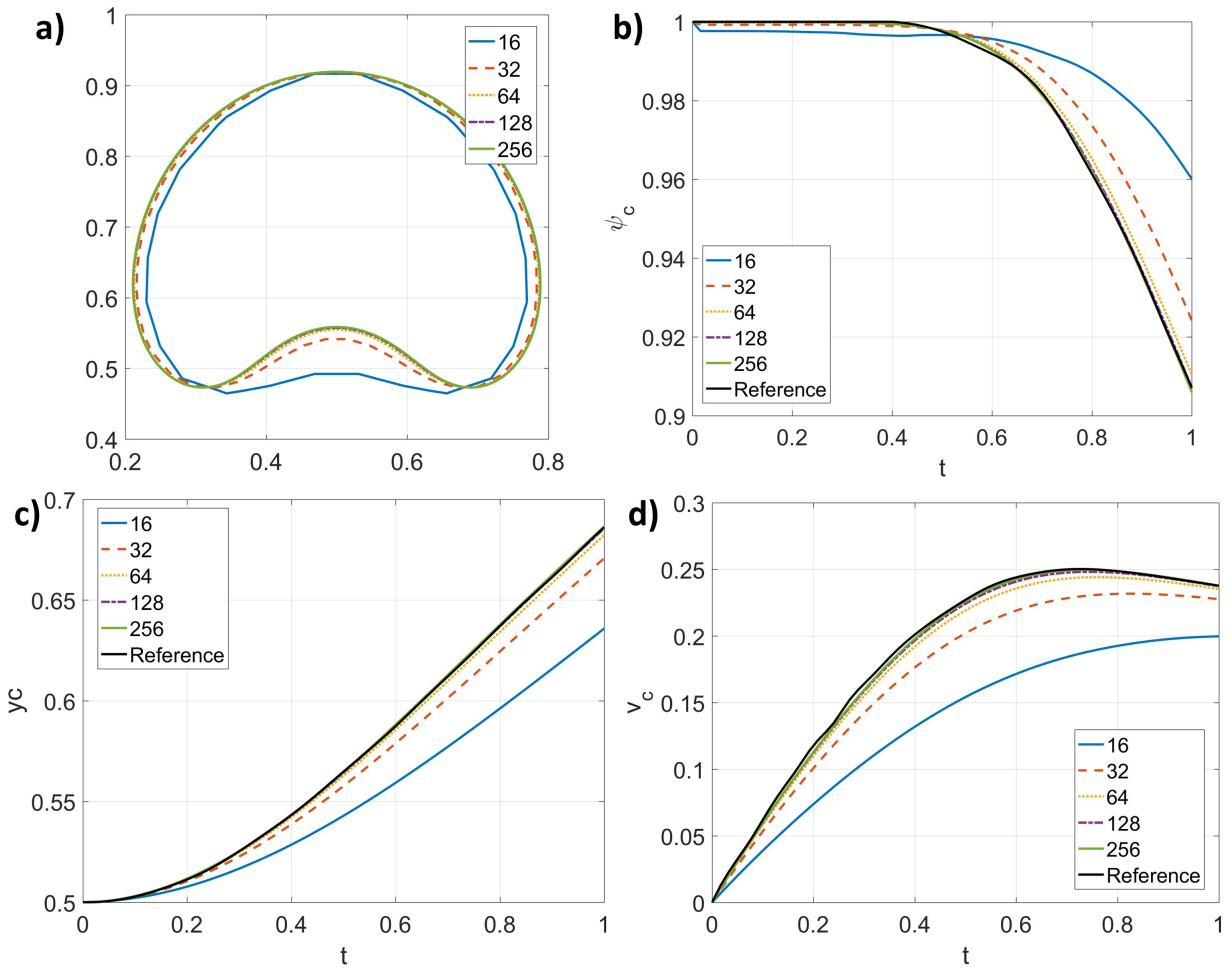

Figure 4.63. Results of the convergence test from the balanced-force method (two-phase CAC-B). a) The bubble shape at $t = 1$, b) ψ_c versus t, c) y_c versus t, and d) v_c versus t.

both y_c and v_c. Therefore, the numerical solutions of the Phase-Field methods converge to the sharp-interface solution.

Compared to the results from two-phase CH and CAC and multiphase CH, one can conclude that the boundedness mapping has little effect on either the formal order of accuracy or the convergence rate to the sharp-interface solution. In summary, the numerical solution of the Phase-Field methods using either the balanced-force or the conservative method for the surface force converges to the sharp-interface solution, even in a case including large density and viscosity ratios. The convergence rate is between 1.5th- and 2nd-order.

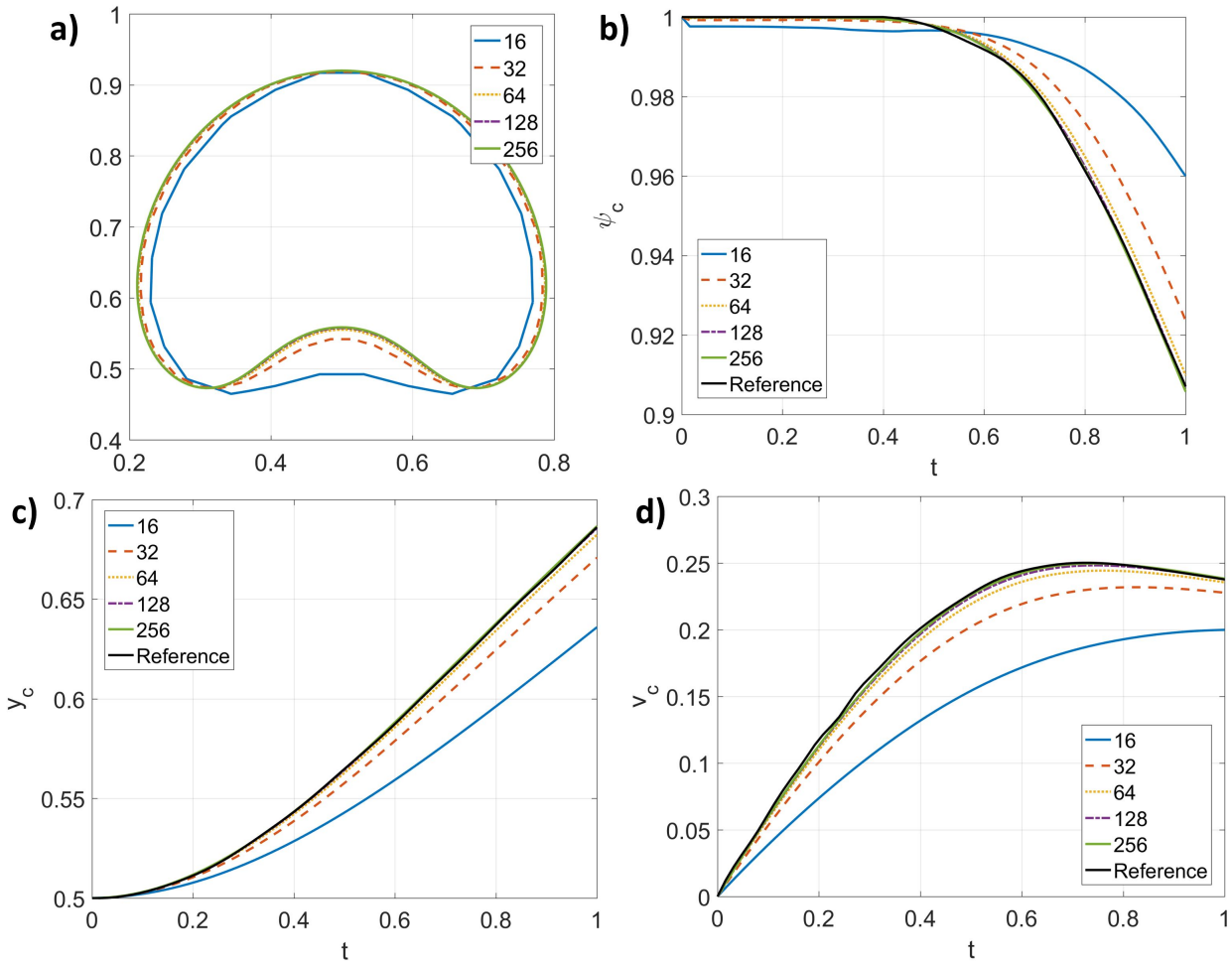

Figure 4.64. Results of the convergence test from the conservative method (two-phase CAC-C). a) The bubble shape at $t = 1$, b) ψ_c versus t, c) y_c versus t, and d) v_c versus t.

4.10.3 Multiphase and multicomponent results

This case is performed to demonstrate the capability of the proposed N-phase-M-component model and scheme of producing sharp-interface solutions, to illustrate the effect of the proposed consistency of volume fraction conservation, and to quantify the convergence of the entire scheme. Additional two components are added. Component 1, having a density 0.5 and viscosity 0.05, is only dissolvable in Phase 1 with a diffusivity 0.01. Component 2 is only dissolvable in Phase 2 with a diffusivity 0.05 and has a density 1600 and viscosity 14.

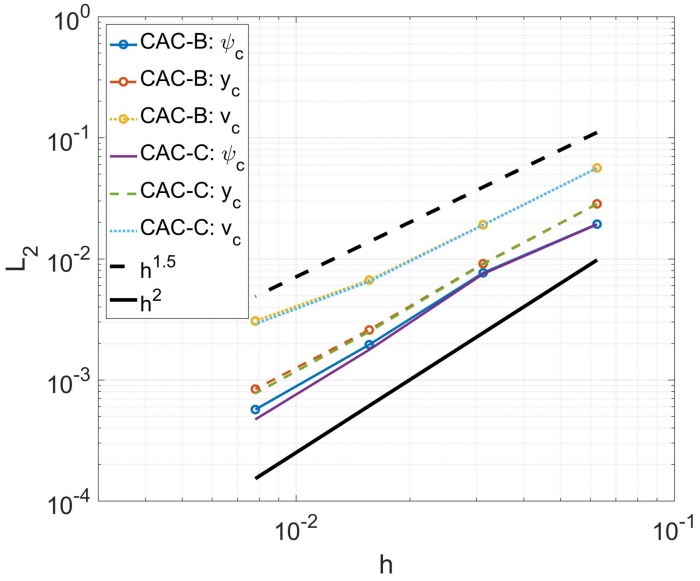

Figure 4.65. L_2 errors of the benchmark quantities using two-phase CAC-B and CAC-C.

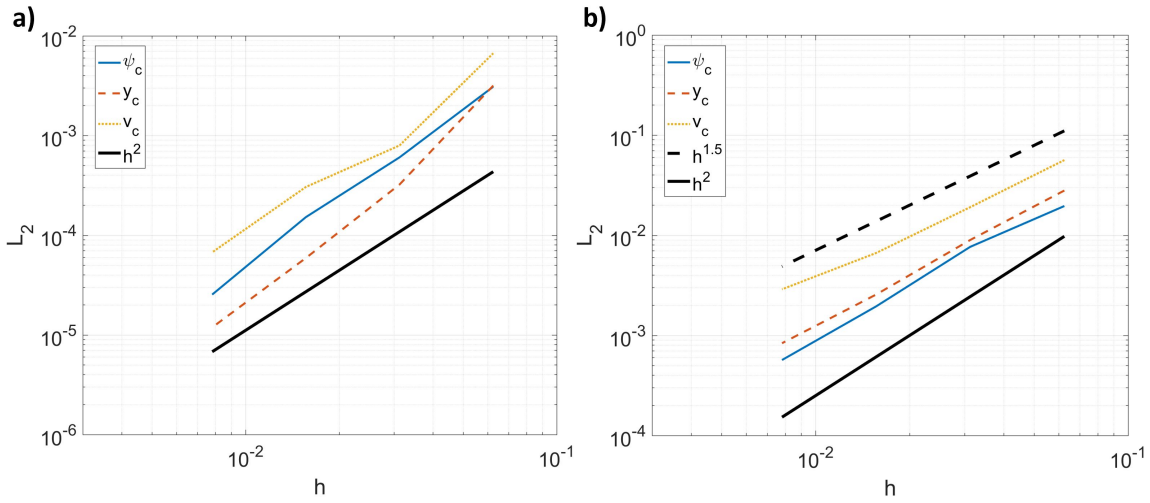

Figure 4.66. L_2 errors of the benchmark quantities using two-phase CAC-B. a) Fixed η and M_0. b) $M_0 \sim \eta^2$.

First, the results from the proposed N-phase-M-component model and scheme are compared with the sharp-interface ones in [226] using the following two setups.

- *Setup 1:* The bubble is represented by Phase 1, while the liquid is Phase 2. The components are absent, by giving their concentrations to be zeros at $t = 0$. Therefore, the densities, viscosities, and surface tension of the phases are the same as the given

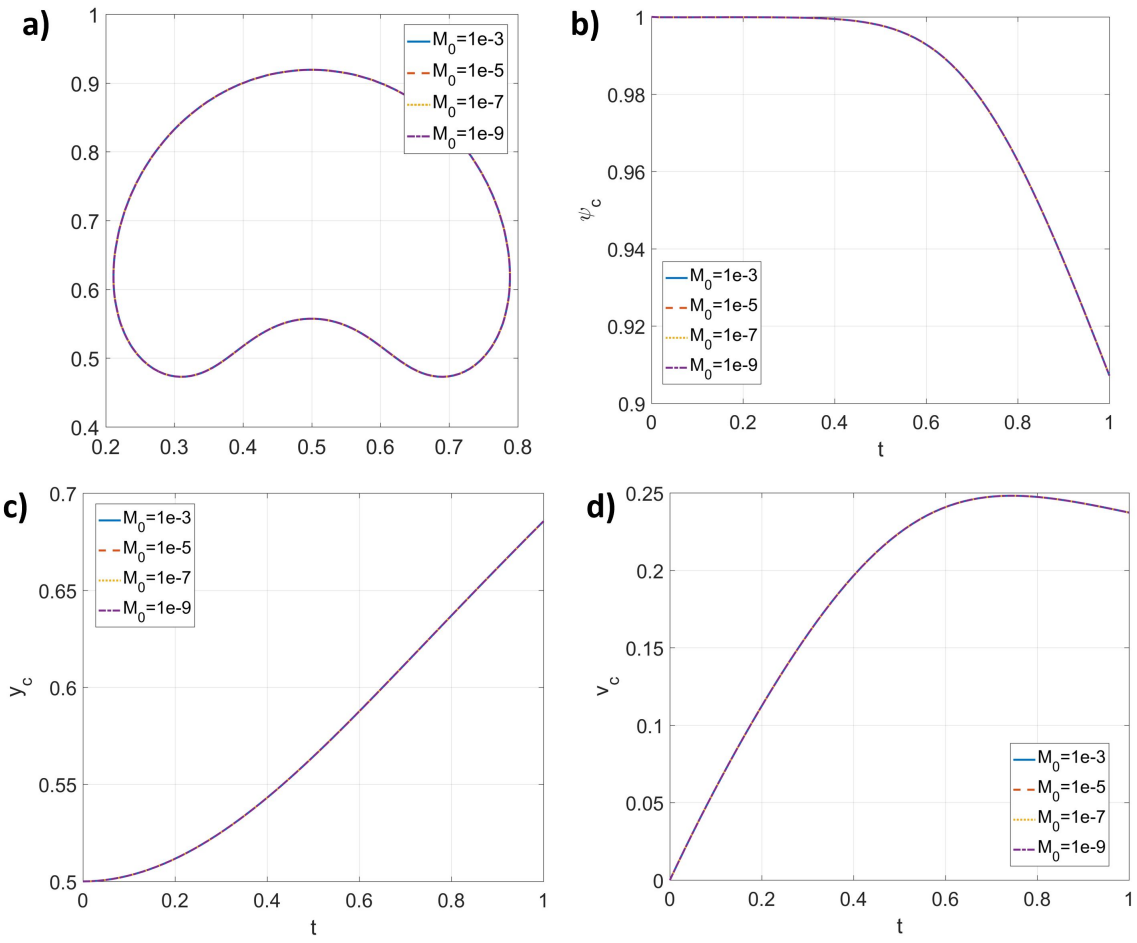

Figure 4.67. Results of the convergence test with fixed grid size $h = 1/128$ but different M_0 using two-phase CAC-B. a) The bubble shape at $t = 1$, b) ψ_c versus t, c) y_c versus t, and d) v_c versus t.

values for the bubble and liquid, and χ_b equals χ_1. The domain is discretized by a grid size of $h = \frac{1}{128}$. The time step size is $\Delta t = 0.128h$ and η is the same as h.

- *Setup 2:* The bubble is represented by Phase 1 with Component 1 having a homogeneous concentration 1 dissolved in it. On the other hand, the liquid is composed of Phase 2 and Component 2 with a homogeneous concentration 0.5. Thus, the concentrations are initially 1 and 0.5 for Components 1 and 2, respectively. The material properties of Phase 1 become 0.5 for the density and 0.05 for the viscosity, while they are 200 for the density and 3 for the viscosity of Phase 2. The rest is the same as Setup 1.

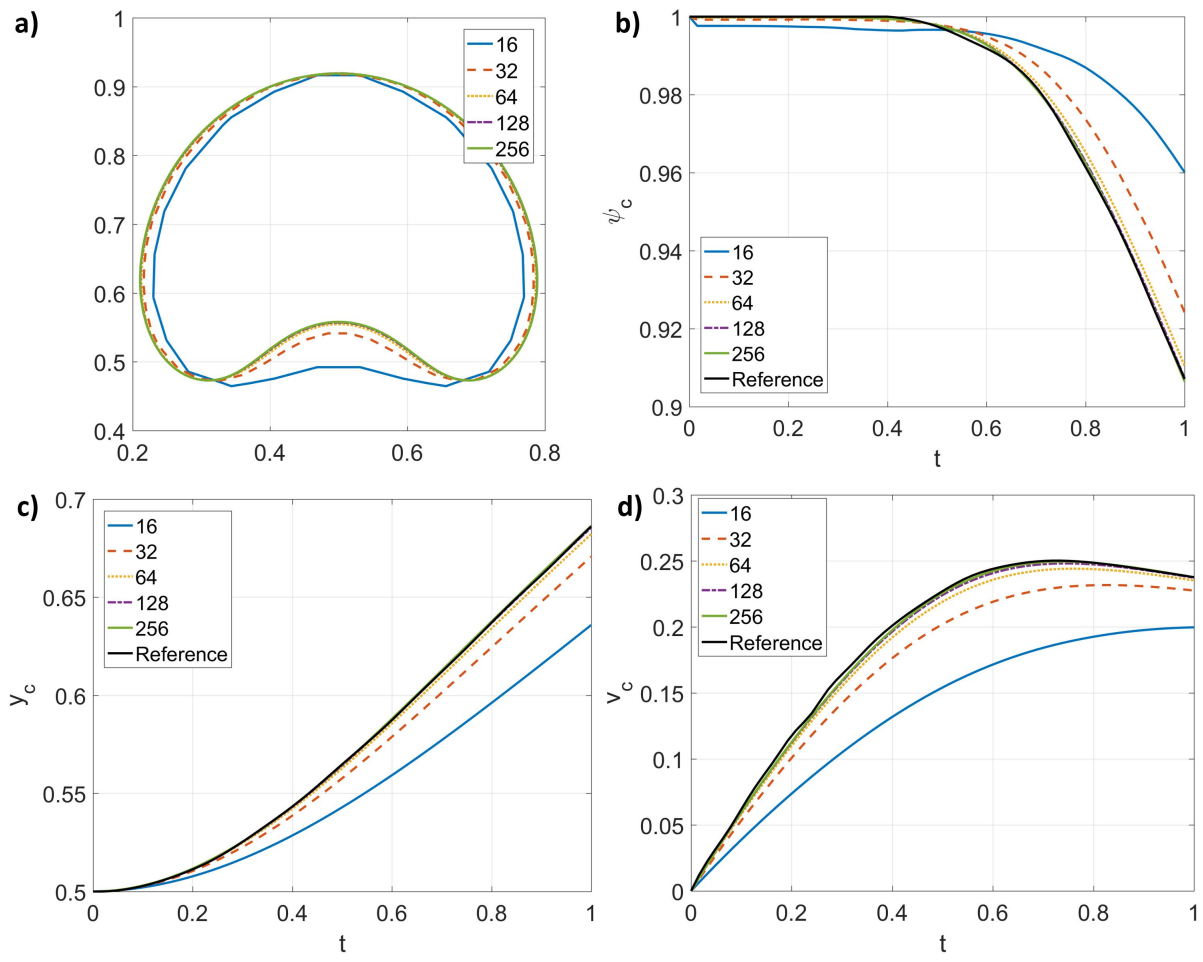

Figure 4.68. Results of the convergence test using the balanced-force method (CH-B). a) Bubble shape at $t = 1$. b) Circularity ψ_c vs. t. c) Center of mass y_c vs. t. d) Rising velocity v_c vs. t. The legend shows the number of grid cells per unit length, and "Reference" is the sharp-interface solution.

As pointed out in Section 2.6.1, any pure phase can be modeled as another pure phase dissolving components with homogeneous concentrations. For example, one can model a salt water as a pure phase or as a solution of water, which is the pure phase (or the background fluid), and salt, which is the component, with a homogeneous concentration. Therefore, Setups 1 and 2 should produce the same results. Fig.4.76 shows the results from Setups 1 and 2, along with the sharp-interface results from [226]. The results from both setups are indistinguishable from each other and agree well with the sharp-interface results. In addition, under Setup 1, the concentrations of the components, which are zero initially, are

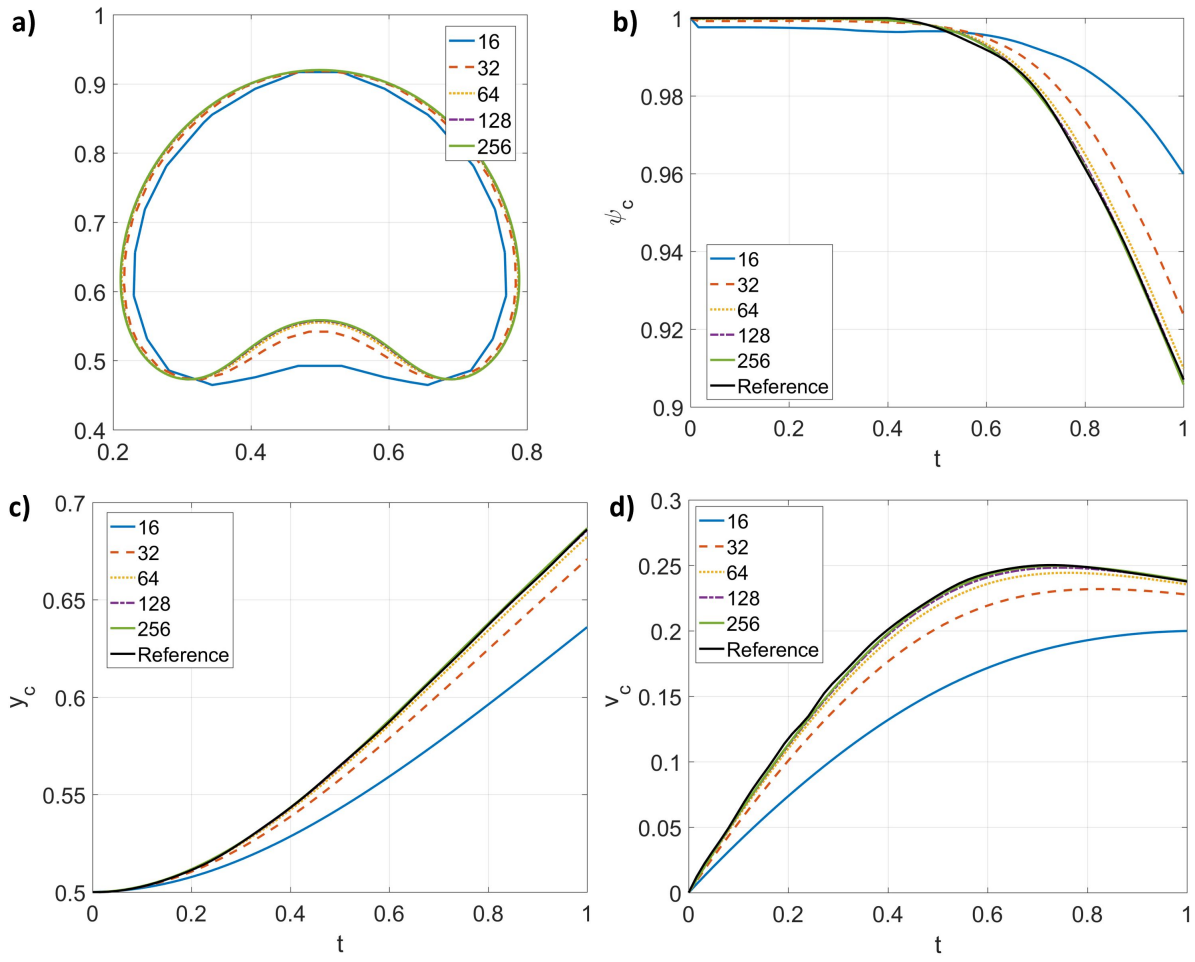

Figure 4.69. Results of the convergence test using the conservative method (CH-C). a) Bubble shape at $t = 1$. b) Circularity ψ_c vs. t. c) Center of mass y_c vs. t. d) Rising velocity v_c vs. t. The legend shows the number of grid cells per unit length, and "Reference" is the sharp-interface solution.

always zero during the computation. This confirms the *consistency of reduction* of the model and scheme.

Next, the effect of the newly proposed consistency condition, i.e., the *consistency of volume fraction conservation* is considered. The effects of the other consistency conditions have been discussed in the previous cases. Setup 2 is repeated but the concentrations of the components are solved from the original diffuse domain approach [143], without considering the *consistency of volume fraction conservation*. Those Results are labeled as "IC" which means inconsistent. Since Setups 1 and 2 are equivalent, the profile of $\chi_p^M C_p$ should be

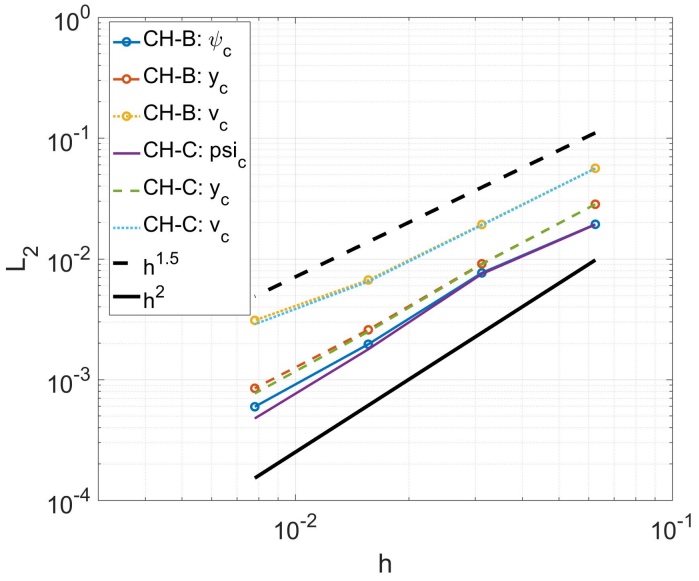

Figure 4.70. L_2 errors of the benchmark quantities using CH-B and CH-C.

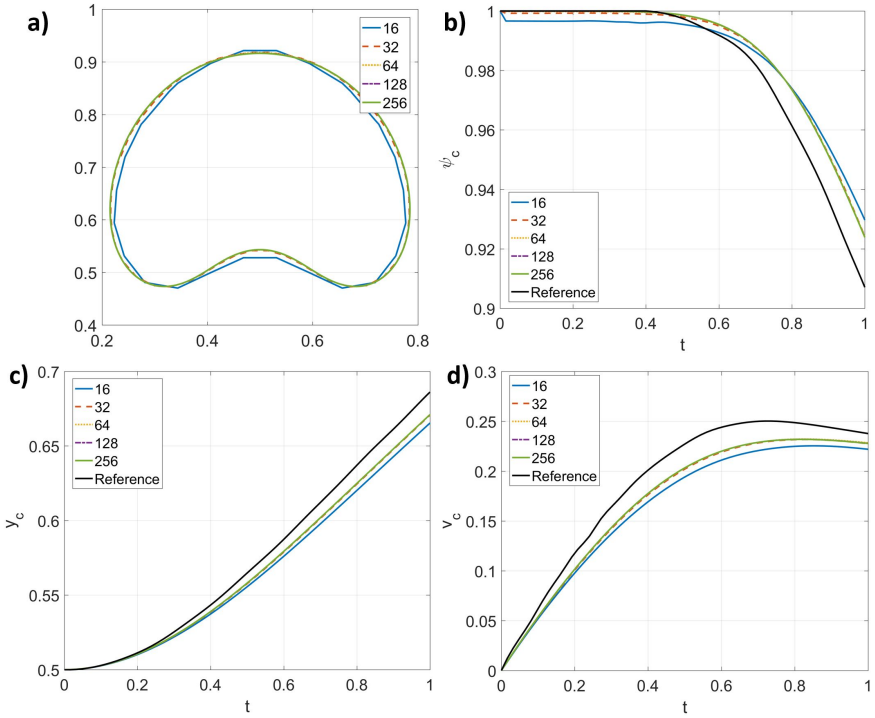

Figure 4.71. Results of the convergence test with $\eta = \eta_0$ from CHB-B. a) Shape of the bubble at $t = 1$. b) Circularity. c) Center of mass. d) Rising velocity. 16, 32, 64, 128, and 256 are the numbers of cells on a unite length of the domain. Reference is the sharp-interface solution from [226].

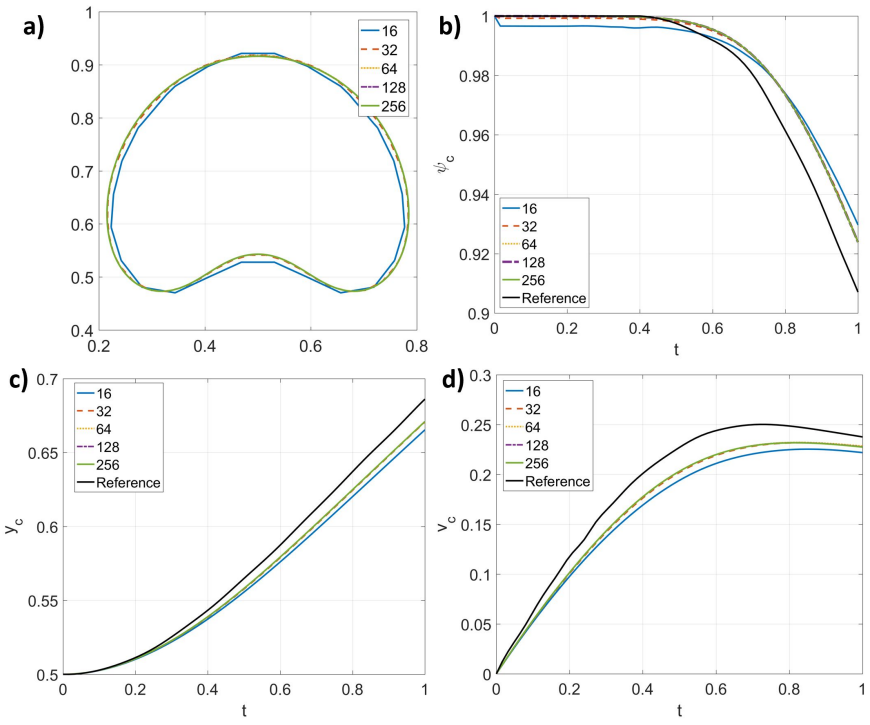

Figure 4.72. Results of the convergence test with $\eta = \eta_0$ from CACB-B. a) Shape of the bubble at $t = 1$. b) Circularity. c) Center of mass. d) Rising velocity. 16, 32, 64, 128, and 256 are the numbers of cells on a unite length of the domain. Reference is the sharp-interface solution from [226].

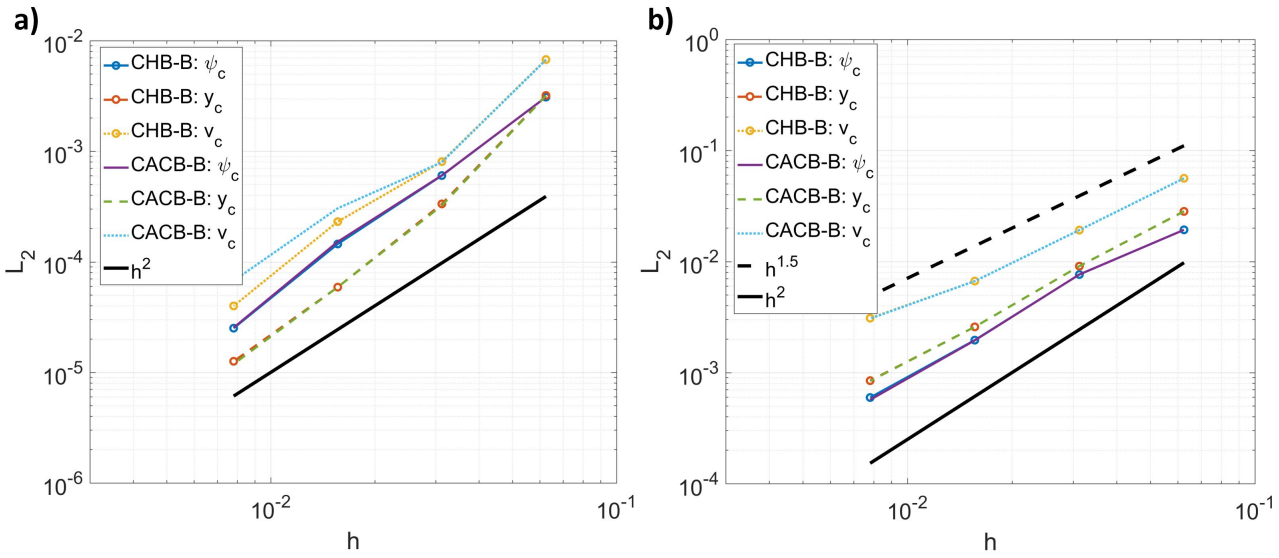

Figure 4.73. L_2 errors of the benchmark quantities using CHB-B and CACB-B. a) $\eta = \eta_0$. b) $\eta = h$.

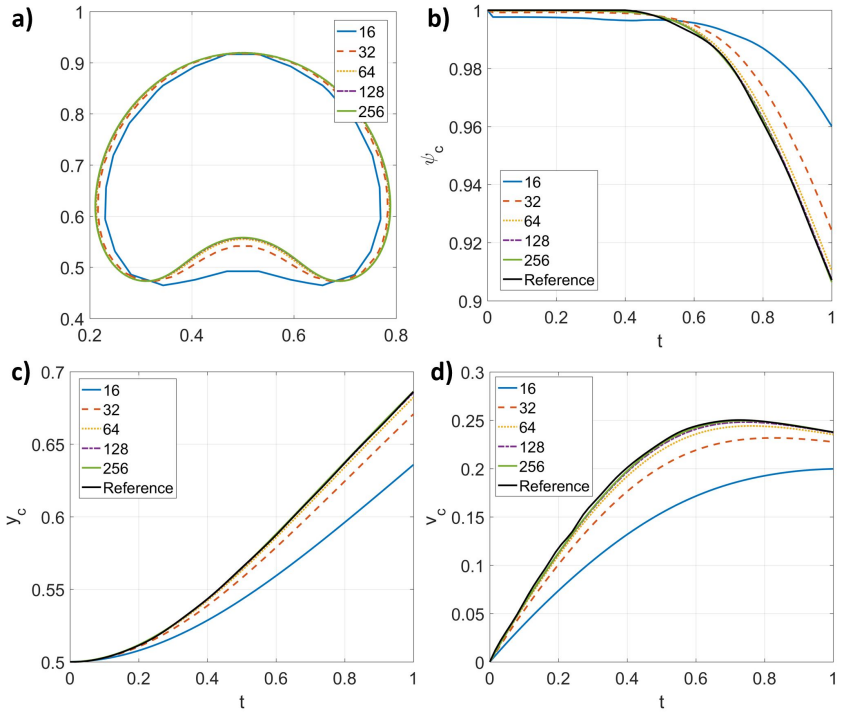

Figure 4.74. Results of the convergence test with $\eta = h$ from CHB-B. a) Shape of the bubble at $t = 1$. b) Circularity. c) Center of mass. d) Rising velocity. 16, 32, 64, 128, and 256 are the numbers of cells on a unite length of the domain. Reference is the sharp-interface solution from [226].

the same as $\chi_p^M(C_p|_{t=0})$. Fig.4.77 shows the difference between $\chi_1^M C_1$ and χ_1^M at $x = 0.5$ at different moments. Due to violating the *consistency of volume fraction conservation*, it is observed from the "IC" results that the concentration of Component 1 is suffering from unphysical oscillations around the boundary of the bubble. Even worse, the oscillations are growing with time, which probably becomes an origin of numerical instability in highly dynamical problems. On the other hand, the difference is less than 10^{-11} at $t = 1$ from the proposed consistent model and scheme. The concentration of Component 2 behaviors in a similar manner, and therefore they are not shown here.

Finally, the convergence of the entire scheme is considered using Setups 3 and 4, modified from Setup 2, such that the concentrations of the components are not homogeneous initially.

- *Setup 3*: The concentration of Component 1 is unity inside a circle at $(0.5, 0.5)$ with a radius 0.1 but zero elsewhere initially. The concentration of Component 2 is 0.5 above

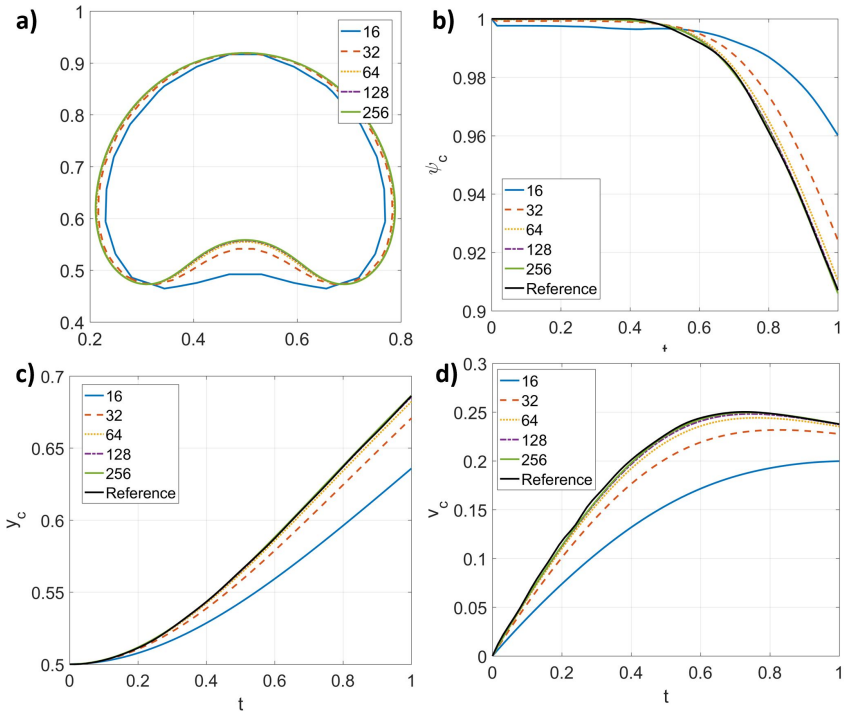

Figure 4.75. Results of the convergence test with $\eta = h$ from CACB-B. a) Shape of the bubble at $t = 1$. b) Circularity. c) Center of mass. d) Rising velocity. 16, 32, 64, 128, and 256 are the numbers of cells on a unite length of the domain. Reference is the sharp-interface solution from [226].

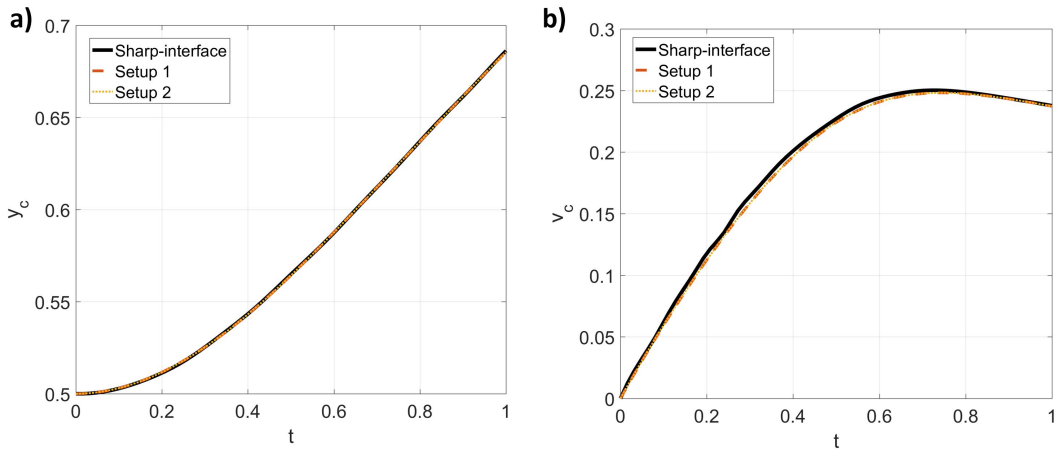

Figure 4.76. Results of the rising bubble problem under Setups 1 and 2. a) The trajectory of the bubble center versus time. b) The rising speed of the bubble versus time. The sharp-interface results are from [226].

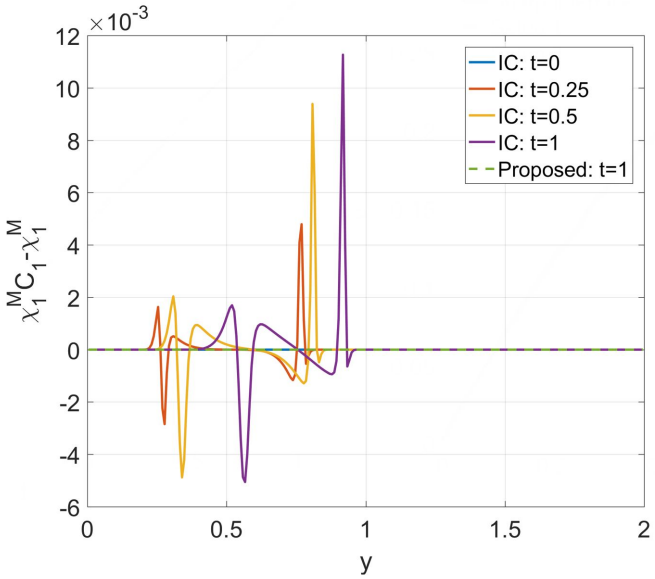

Figure 4.77. Differences between $\chi_1^M C_1$ and χ_1^M under Setup 2 at $x = 0.5$. IC: the concentrations are solved from the original diffuse domain approach [143], without considering the *consistency of volume fraction conservation*. Proposed: the concentrations are solved from the proposed Eq.(2.48) that satisfies the *consistency of volume fraction conservation*.

$y = 0.85$ but zero elsewhere initially. The grid size is ranging from $\frac{1}{16}$ to $\frac{1}{256}$, and η is fixed to be $\frac{1}{32}$. The solution from the finest grid is considered as the reference solution.

- *Setup 4*: The same as Setup 3 but η is changing with the grid size, i.e., $\eta = h$.

The solutions from different grid sizes in Setup 3 are approximating the same exact solution of the model with a fixed η. Therefore, its convergence behavior represents the formal order of accuracy of the proposed scheme. On the other hand, the solutions in Setup 4 converge to a series of solutions that approach the one with zero η, i.e., the sharp-interface solution. It usually converges slower than the formal order of accuracy of the scheme but is more related to practical applications. Fig.4.78 shows the results of Setups 3 and 4, and convergences of the results are evident after successively refining the grid size under both setups. Fig.4.79 shows the L_2 norms, i.e., the root mean square, of y_c and v_c minus their corresponding reference solutions from the finest grid. The convergence under Setup 3 is close to but better than 2nd order, which validates the formally 2nd-order accuracy of the proposed scheme.

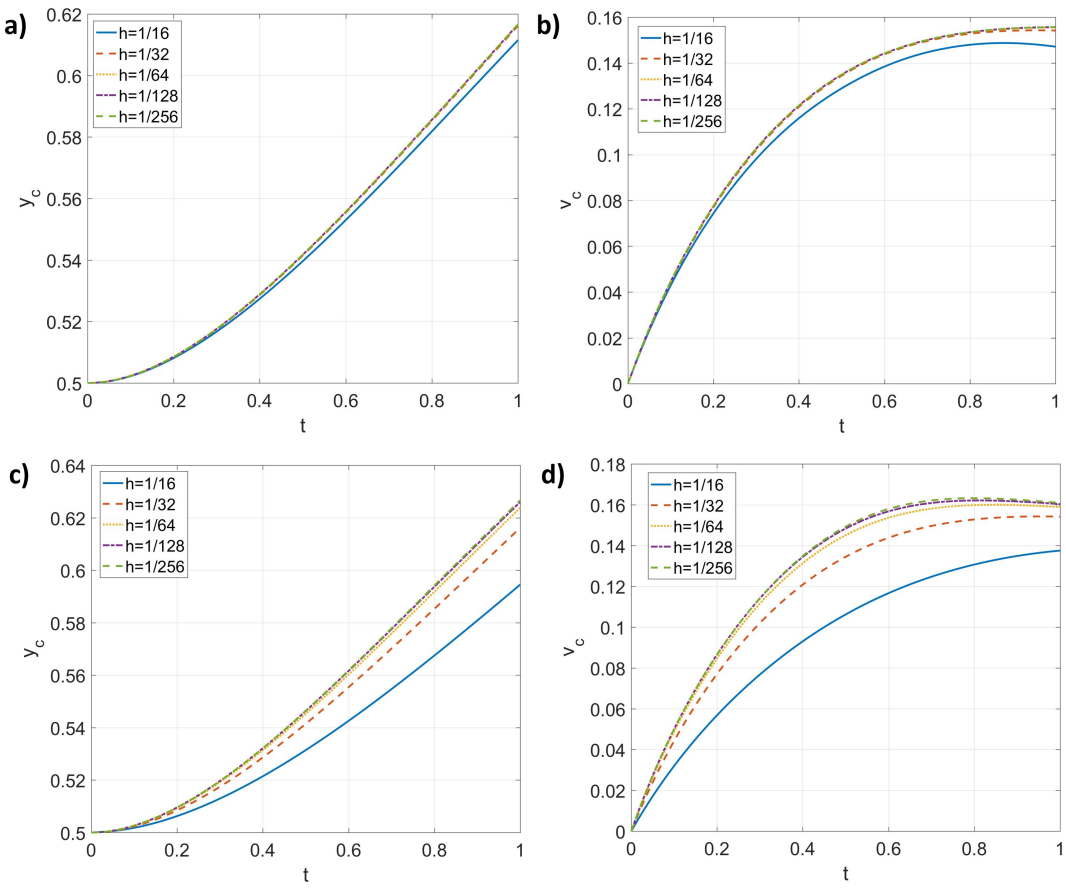

Figure 4.78. Results of the rising bubble problem under Setups 3 and 4 using different grid sizes. a) The trajectory of the bubble center versus time under Setup 3. b) The rising speed of the bubble versus time under Setup 3. c) The trajectory of the bubble center versus time under Setup 4. d) The rising speed of the bubble versus time under Setup 4.

The convergence in Setup 4 is a little slower than that in Setup 3 but still close to 2nd order.

The present case demonstrates that the proposed N-phase-M-component model and scheme are able to produce sharp-interface solutions. The proposed *consistency of volume fraction conservation* is essential to eliminate unphysical fluctuations of components around phase interfaces. The formal order of accuracy of the entire scheme is 2nd-order, and the convergence behavior towards the sharp interface solution is reasonably satisfactory with a rate close to 2nd order.

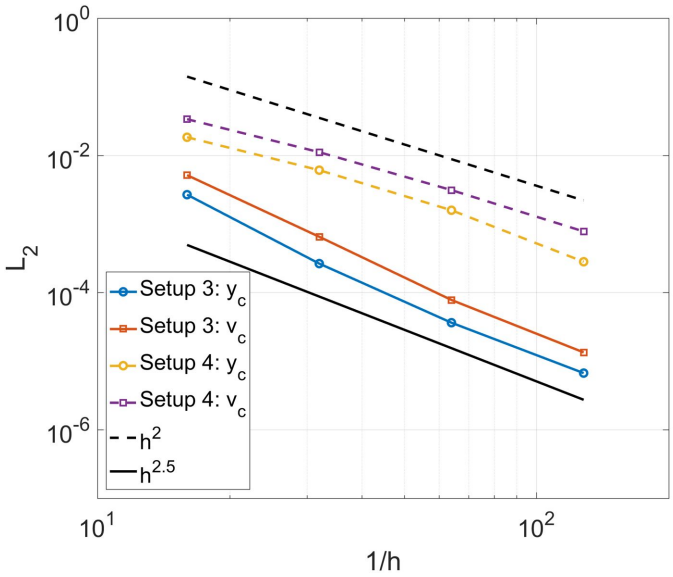

Figure 4.79. The L_2 norms of y_c and v_c minus their corresponding reference solutions form the finest grid versus the grid sizes under Setups 3 and 4.

4.11 Couette flow

The Couette flow problem is solved to validate Theorem 2.6.4 of the thermo-gas-liquid-solid model including solidification/melting, where the liquid phase is absent and the temperature is below the melting temperature, and to demonstrate the drag force in Section 2.6.2. The unit domain considered is periodic along the x axis while is no-slip along the y axis. Both the top and bottom boundaries are adiabatic but the top one is moving with a unit horizontal velocity, i.e., $u_{top} = 1$. The solid phase is at the bottom below $y = 0.3$, while the gas phase fills the rest of the domain. The input parameters are $\rho = 1$, $\mu = 0.15$, $C_p = 10^3$, $\kappa = 0$, $\Gamma_\phi = 2.41 \times 10^{-7}$, $\mu_\phi = 2.6 \times 10^{-5}$, $T_M = 2$, $L = 100$, $\sigma = 10^{-2}$, and $\mathbf{g} = \mathbf{0}$. The liquid phase is initially absent, i.e., $\alpha_L = \varphi\phi = 0$, and therefore one has $\phi = 0$. The initial temperature is $T_0 = 1$ which is lower than the melting temperature $T_M = 2$. The domain is discretized by 128×128 grid cells, and the time step is determined by $u_{top}\Delta t/h = 0.1$.

The above setup is equivalent to the following Couette flow:

$$\frac{\partial u}{\partial t} = \nu \frac{\partial^2 u}{\partial y^2}, \quad u = u_0 \quad \text{at} \quad y = y_0, \quad u = u_1 \quad \text{at} \quad y = y_1, \quad u|_{t=0} = 0, \quad \nu = 0.15,$$

where $u_0 = 0$, $u_1 = u_{top} = 1$, $y_0 = 0.3$, and $y_1 = 1$. The exact solution of the above equation is

$$u_E = \begin{cases} \sum_{\alpha=1}^{\infty} \frac{2(u_1 \cos(\alpha\pi) - u_0)}{\alpha\pi} \exp\left[-\nu \left(\frac{\alpha\pi}{y_1 - y_0}\right)^2 t\right] \sin\left[\frac{\alpha\pi}{y_1 - y_0}(y - y_0)\right] \\ \qquad + \frac{u_1 - u_0}{y_1 - y_0}(y - y_0) + u_0, \quad y_0 \leqslant y \leqslant y_1, \\ 0, \quad \text{else}, \end{cases}$$

derived from separation of variables. Theorem 2.6.4 implies that the liquid phase remains absent, i.e., $\alpha_L = \varphi\phi = 0$ or $\phi = 0$ at $\forall t > 0$, the temperature remains homogeneous, i.e., $T = T_0$ at $\forall t > 0$, and the exact solution is produced (or approximated) by the FD/BP FSI formulation, with the present setup. Expected results are obtained and shown in Fig.4.80. First in Fig.4.80 a), the profile of the solid fraction ($\alpha_S = \varphi - \varphi\phi = \varphi$) at $t = 1$ overlaps the one at $t = 0$, representing that the solid phase is stationary. Moreover, the profiles of the solution from the proposed model are indistinguishable from the exact solution, noticing that the summation in the exact solution is from $\alpha = 1$ to $\alpha = 10^6$. Theorem 2.6.4 is true, as shown in Fig.4.80 b) that $\phi = 0$ and $T = T_0$ at $\forall t > 0$. In addition, the unidirectional condition, which is required to obtain the Couette flow, is also demonstrated, as shown in Fig.4.80 b) that $v = 0$ at $\forall t > 0$.

4.12 Stefan problem

The Stefan problem is performed to validate Theorem 2.6.5 of the thermo-gas-liquid-solid model including solidification/melting, where both the gas phase and the flow are absent and the liquid and solid phases have matched material properties (except the thermal conductivities). The setup in [205] is followed. The unit domain is periodic along the x direction. Both the top and bottom boundaries are free-slip and adiabatic. The material properties are: $\rho = 1$, $\mu = 1$, $C_p = 1$, $\kappa_M^L = 0.05$, $\kappa_M^S = 1$, $T_M = 1$, $L = 0.53$, and $\mathbf{g} = \mathbf{0}$. Other parameters are $\eta_\phi = \sqrt{2a_\phi}\zeta_\phi$, $M_\phi = 1/(\nu_\phi \zeta_\phi^2 L)$, and $\lambda_\phi = 1/(\nu_\phi M_\phi)$, where $a_\phi = 0.0625$, $\nu_\phi = 1$, and $\zeta_\phi = 0.002$, the same as those in [205]. Initially, the liquid-solid interface is at $y = s_0 = 0.2$, above which there is the solid phase having a temperature $T_0^S = 1.1$, while below which there is the liquid phase having a temperature $T_0^L = 1.53$. The domain is discretized by 5×2000 grid cells, and the time step is $\Delta t = 5 \times 10^{-6}$.

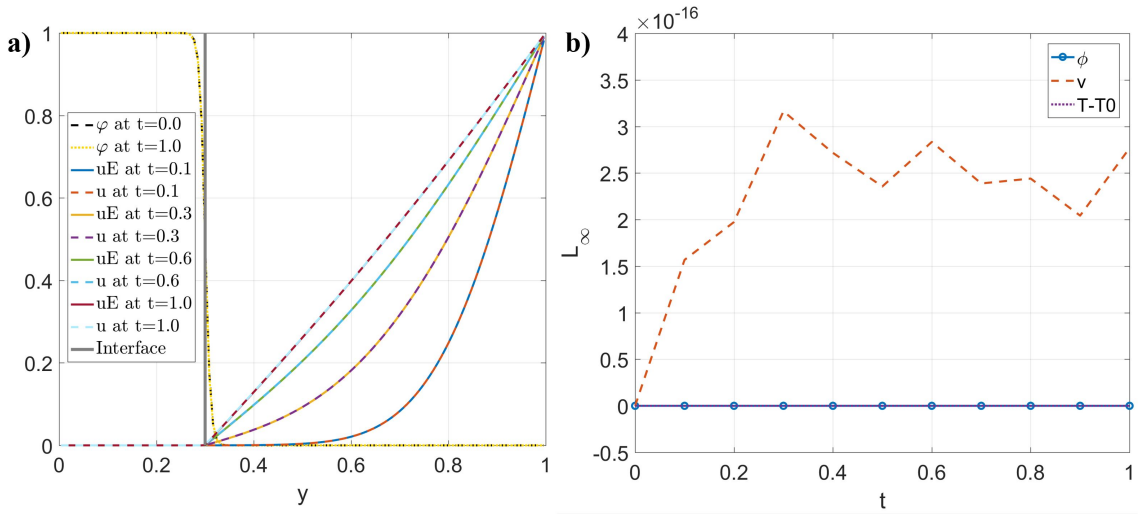

Figure 4.80. Results of the Couette flow. a) Profile of φ at $t = 0$ and $t = 1$, and profiles of u_E and u at $t = 0$, $t = 0.1$, $t = 0.3$, $t = 0.6$, and $t = 1$. Here, u_E is the exact solution of the Couette flow, and the numerical predictions and analytical solutions are overlapped. b) L_∞ norms of ϕ, v, and $(T - T_0)$ versus time. The liquid phase remains absent, the temperature equilibrium is preserved, and the unidirectional flow condition is produced, which validate Theorem 2.6.4.

The above setup is to produce the following Stefan problem [205] (based on $\Delta T = T - T_M$):

$$\frac{\partial \Delta T}{\partial t} = \frac{\partial}{\partial y}\left(\kappa_M^L \frac{\partial \Delta T}{\partial y}\right) \quad y \in (-\infty, s(t)), \qquad \frac{\partial \Delta T}{\partial t} = \frac{\partial}{\partial y}\left(\kappa_M^S \frac{\partial \Delta T}{\partial y}\right) \quad y \in (s(t), +\infty),$$

$$\Delta T = T_0^L - T_M \quad \text{at} \quad y \to -\infty, \qquad \Delta T = T_0^S - T_M \quad \text{at} \quad y \to +\infty,$$

$$\Delta T = 0, \quad \text{at} \quad y = s(t),$$

$$L\frac{ds}{dt} = \kappa_M^S \frac{\partial \Delta T}{\partial y}|_{y=s^+} - \kappa_M^L \frac{\partial \Delta T}{\partial y}|_{y=s^-},$$

where $s(t)$ is the location of the liquid-solid interface. The above equation has an analytical self-similar solution [205], [227]:

$$s_E(t) = s_0 + 2\alpha\sqrt{t},$$

$$T_E - T_M = \begin{cases} (T_0^L - T_M)\left[\dfrac{\operatorname{erfc}\left(\frac{y-s_0}{2\sqrt{\kappa_M^L t}}\right) - \operatorname{erfc}\left(\frac{\alpha}{\sqrt{\kappa_M^L}}\right)}{2 - \operatorname{erfc}\left(\frac{\alpha}{\sqrt{\kappa_M^L}}\right)}\right] & y < s(t), \\ (T_0^S - T_M)\left[1 - \dfrac{\operatorname{erfc}\left(\frac{y-s_0}{2\sqrt{\kappa_M^S t}}\right)}{\operatorname{erfc}\left(\frac{\alpha}{\sqrt{\kappa_M^S}}\right)}\right] & y > s(t), \end{cases}$$

$$\alpha = \frac{\sqrt{\kappa_M^S}}{\sqrt{\pi}L}\frac{T_M^S - T_M}{\operatorname{erfc}(\alpha/\sqrt{\kappa_M^S})}\exp\left(-\frac{\alpha^2}{\kappa_M^S}\right) + \frac{\sqrt{\kappa_M^L}}{\sqrt{\pi}L}\frac{T_M^L - T_M}{2 - \operatorname{erfc}\left(\alpha/\sqrt{\kappa_M^L}\right)}\exp\left(-\frac{\alpha^2}{\kappa_M^L}\right).$$

Numerical results are compared to the exact solution, and shown in Fig.4.81. The interface location is specified as the 0.5 contour of $(\varphi\phi)$ from the numerical results. Both the temperature and interface location agree with the exact solution very well. Minor discrepancy is observed near the domain boundary at $t = 0.1$ in Fig.4.81 a) because in practice the domain is not infinite. Moreover, the L_∞ norms of $(\varphi - 1)$, u, and v are on the orders of 10^{-16}, 10^{-33}, and 10^{-34}, respectively, at the end of the simulation, which demonstrates Theorem 2.6.5.

4.13 The mass conservation and volume change

Here, the effect of the mass conservation of the thermo-gas-liquid-solid model including solidification/melting is discussed, which leads to the non-divergence-free velocity, i.e., Eq.(2.63), when the phase change happens and the liquid and solid phases have different densities. Such an effect has been overlooked by many existing models. The unit domain considered is periodic along the x axis. The bottom boundary is no-slip and has a fixed temperature $T_{bottom} = 5$, while the top one is an outflow boundary having a fixed pressure $P_{top} = 0$ and zero heat flux. At the bottom of the domain below $y = 0.3$ is the liquid phase, whose material properties are $\rho_M^L = 1000$, $\mu_M^L = 1 \times 10^{-3}$, $(C_p)_M^L = 1$, and $\kappa_M^L = 200$. Floating on the liquid phase is the solid phase, whose material properties are $\rho_M^S = 900$, $\mu_M^S = 1 \times 10^{-3}$, $(C_p)_M^S = 1$, and $\kappa_M^S = 300$. Above $y = 0.6$ is the gas phase, whose material

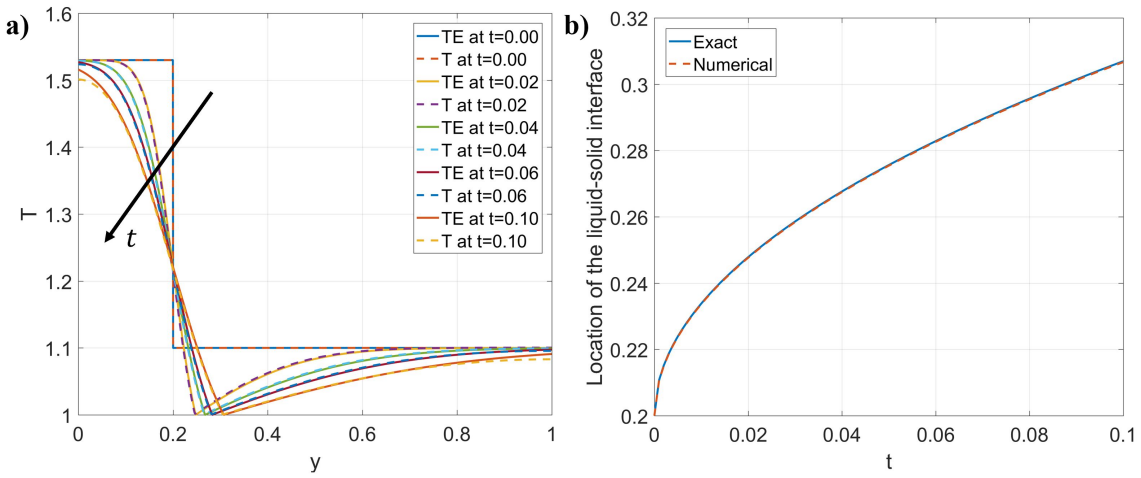

Figure 4.81. Results of the Stefan problem. a) Profiles of the temperature at different time. Here, T_E is the exact solution of the Stefan problem . b) Location of the liquid-solid interface versus time. The numerical prediction agrees well with the analytical solution, which validates Theorem 2.6.5.

properties are $\rho_G = 1$, $\mu_G = 2 \times 10^{-5}$, $(C_p)_G = 0.1$, and $\kappa_G = 100$. Other parameters are $T_M = 1$, $L = 20$, $\sigma = 0.0728$, $\rho_M^L L\Gamma_\phi / T_M = 10$, $M_\phi = 5 \times 10^{-4}$, and $\mathbf{g} = (0, -9.8)$. The initial temperature is $T_0 = 0.5$. The domain is discretized by 128×128 grid cells, and the time step is $\Delta t = 10^{-3}$.

The materials are heated by the bottom wall whose temperature is higher than the melting temperature. As a result, the solid phase will melt and finally disappear. Since the liquid density is 10% larger than the solid phase, the final volume of the phase change material should be smaller than its initial value, in order to honor the mass conservation. Results are shown in Fig.4.82 and match the expectation. From Fig.4.82 a), the liquid-solid interface is moving upward while at the same time the gas-solid interface is moving downward. At the beginning, the volume (area) of "M", including its liquid and solid phases, is 0.6. At the end of the simulation, there is only the liquid phase of "M" in the domain, and the gas-liquid interface stays horizontally below $y = 0.6$, indicating that the volume of "M" is smaller than its initial value.

Quantitative data are reported in Fig.4.82 b) where the displacements of the liquid-solid and gas-solid interfaces versus time are plotted. The gas-solid interface is defined as the 0.5

contour of φ, while the liquid-solid interface is the 0.5 contour of $(\varphi\phi)$. One can observe that the liquid-solid interface actually moves downward at the very beginning because the initial temperature is below the melting temperature. As a result, solidification happens in that period. As the materials are heated from the bottom wall, the solid melts, leading to the rise of the liquid-solid interface but fall of the gas-solid interface, as expected. The melting process ends before $t = 4$. The mass of the phase change material "M" is estimated simply by $[\rho_M^L s_{LS} + \rho_M^S(s_{GS} - s_{LS})]$, where s_{LS} and s_{GS} denote the locations of the liquid-solid and gas-solid interfaces, respectively, illustrated in the first snapshot in Fig.4.82 a). As plotted in Fig.4.82 b), the change of $[s_{GS} + (\rho_M^L/\rho_M^S - 1)s_{LS}]$ is negligible, which implies that the movements of the interfaces are constrained by the mass conservation. One can expect a more obvious displacement of the gas-solid interface, induced by the phase change, to appear if the density difference of the liquid and solid phases of the phase change material is larger than the present setup.

Although the proposed model strictly satisfies the mass conservation, i.e., Eq.(2.27), the present scheme does not always do, as discussed in Section 3.7. Fig.4.82 c) shows the relative changes of the total mass $(\int_\Omega \rho d\Omega)$ and the mass of "M" $(\int_\Omega \rho_M d\Omega)$ versus time. Here, $\rho_M = \rho_M^L(\varphi\phi) + \rho_M^S(\varphi - \varphi\phi)$ and the integral is computed from the mid-point rule. It should be noted that the total mass in this case is not conserved, and its change is related to the volume change of "M" during the phase change. The initial decrease of the total mass corresponds to the solidification process, where the volume of "M" expands and therefore the gas is squeezed out. As melting occurs, the total mass increases because the volume of "M" reduces, and the gas moves into the domain. When melting is completed, the total mass stops changing as well. On the other hand, the mass of "M" should be conserved even though the phase change happens, while it is not exactly true due to numerical errors. Nonetheless, its relative change is very small, in the order of 10^{-5}, which is satisfactory. It should be noted that as long as the velocity is divergence-free, i.e., the phase change is absent or the densities of the liquid and solid phases are the same, the present scheme exactly conserves the mass of "M" as well as "G" on the discrete level.

In summary, the proposed model automatically and physically captures the volume change induced by the phase change, and therefore the mass conservation, thanks to the

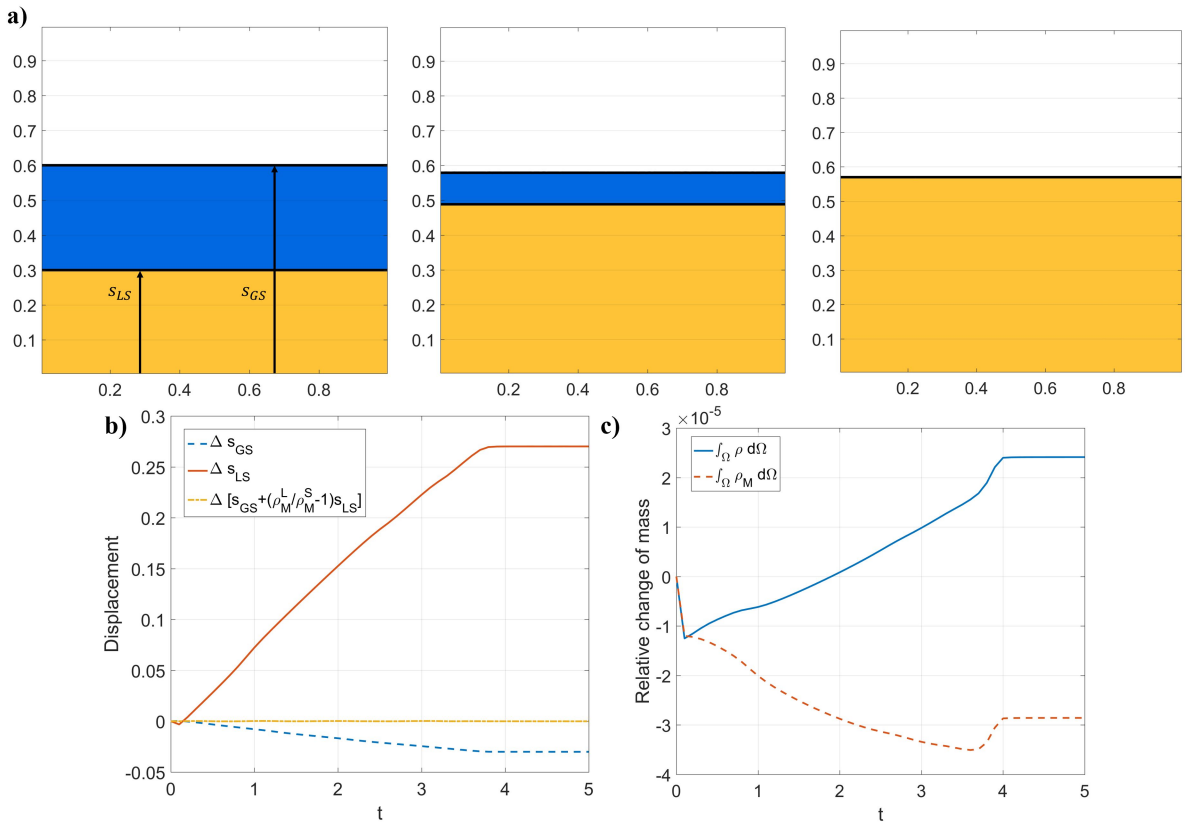

Figure 4.82. Results of the mass conservation and volume change. a) Snapshots of the phases at $t = 0.0$, $t = 2.5$, and $t = 5.0$, and schematic of the locations of the liquid-solid (s_{LS}) and gas-solid (s_{GS}) interfaces. White: the gas phase, Orange: the liquid phase, Blue: the solid phase. b) Displacements of the gas-solid and liquid-solid interfaces versus time. The displacements of the interfaces are constrained by the mass conservation, quantified by $\Delta[s_{GS} + (\rho^L_M/\rho^S_M - 1)s_{LS}] = 0$. c) Relative changes of the total mass and the mass of the phase change material "M" versus time. The total mass is changing because the gas moves in and out of the domain following the volume change of the phase change material. The mass of the phase change material changes slightly (less than 0.004%) due to numerical errors.

consistency of mass conservation. This physical behavior is not correctly captured in many existing models, where the velocity is assumed to be divergence-free.

5. APPLICATION[1]

The proposed models in Chapter 2 and schemes in Chapter 3 are applied to various challenging realistic multiphase flow problems. All the results are reported in their dimensionless forms.

5.1 Floating liquid lens

The floating liquid lens problem is performed. A liquid drop (Phase 2) is floating on the interface between Phase 1 at the bottom and Phase 3 at the top. Because the forces are imbalanced at the triple points of the three phases, the drop is stretched horizontally while compressed vertically and finally reaches its equilibrium state.

If there is no gravity, one can derive an exact solution based on the force balance at the triple points, the normal stress balance at the interfaces, and the volume conservation. At the equilibrium state, the free energy of the floating lens is minimized. In other words, the area (or the length in 2D) of the drop interface should be minimized under the volume constraint (or the area constraint in 2D), the force balance at the triple points, and the normal stress balance at the interfaces. As a result, in 2D, the equilibrium shape of the drop is a combination of two circular segments, which satisfies the aforementioned constraints. As illustrated in Fig.5.1, the drop, called Phase 2, has an initial radius R_0. The interfacial tensions between Phases 1 and 2, Phases 1 and 3, and Phases 2 and 3 are $\sigma_{1,2}$, $\sigma_{1,3}$, and $\sigma_{2,3}$, respectively. When the drop reaches its equilibrium shape, the radius of the upper circular segment is $R_{2,3}$ and the angle between the circular segment and the horizontal line is $\theta_{2,3}$, while they are denoted by $R_{1,2}$ and $\theta_{1,2}$ for the lower circular segment. The force balance at

[1]This chapter was partly published in Journal of Computational Physics, Vol 387, Ziyang Huang, Guang Lin, Arezoo M. Ardekani, A mixed upwind/central WENO scheme for incompressible two-phase flows, Page 455-480, Copyright Elsevier (2019); in Journal of Computational Physics, Vol 406, Ziyang Huang, Guang Lin, Arezoo M. Ardekani, Consistent, essentially conservative and balanced-force Phase-Field method to model incompressible two-phase flows, Page 109192, Copyright Elsevier (2019); in Journal of Computational Physics, Vol 420, Ziyang Huang, Guang Lin, Arezoo M. Ardekani, Consistent and conservative scheme for incompressible two-phase flows using the conservative Allen-Cahn model, Page 109718, Copyright Elsevier (2020); in Journal of Computational Physics, Vol 434, Ziyang Huang, Guang Lin, Arezoo M. Ardekani, A consistent and conservative model and its scheme for N-phase-M-component incompressible flows, Page 110229, Copyright Elsevier (2021); and in International Journal of Multiphase Flow, Vol 142, Ziyang Huang, Guang Lin, Arezoo M. Ardekani, A consistent and conservative volume distribution algorithm and its applications to multiphase flows using Phase-Field models, Page 103727, Copyright Elsevier (2021).

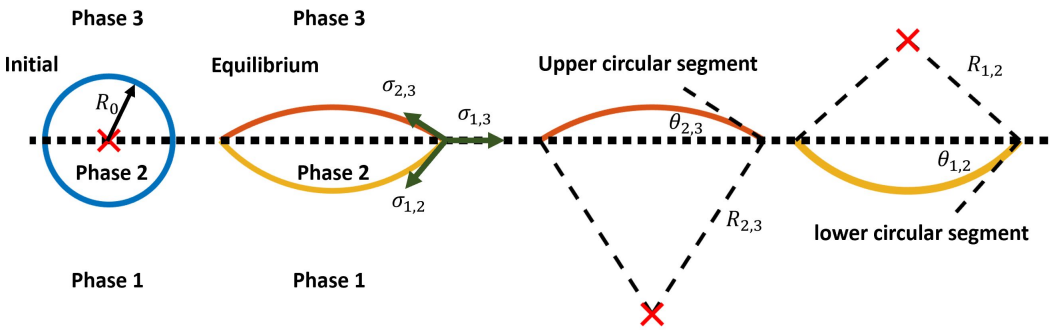

Figure 5.1. Schematic of a floating liquid lens.

the triple points is

$$\sigma_{2,3}\cos(\theta_{2,3}) + \sigma_{1,2}\cos(\theta_{1,2}) = \sigma_{1,3}$$
$$\sigma_{2,3}\sin(\theta_{2,3}) = \sigma_{1,2}\sin(\theta_{1,2}),$$

and its solutions for $\theta_{1,2}$ and $\theta_{2,3}$ are

$$\theta_{1,2} = \cos^{-1}\left(\frac{\sigma_{1,3}^2 + \sigma_{1,2}^2 - \sigma_{2,3}^2}{2\sigma_{1,2}\sigma_{1,3}}\right),$$
$$\theta_{2,3} = \sin^{-1}\left(\frac{\sigma_{1,2}}{\sigma_{2,3}}\sin(\theta_{1,2})\right).$$

Second, the areas of the two circular segments are

$$S_{1,2} = R_{1,2}^2\left(\theta_{1,2} - \sin(\theta_{1,2})\cos(\theta_{1,2})\right)$$
$$S_{2,3} = R_{2,3}^2\left(\theta_{2,3} - \sin(\theta_{2,3})\cos(\theta_{2,3})\right).$$

The area constraint requires that

$$S_{1,2} + S_{2,3} = \pi R_0^2.$$

Third, the normal stress balances at the upper and lower circular segments are considered. By applying the Young-Laplace Law at the two circular segments, one has

$$\frac{\sigma_{1,2}}{R_{1,2}} = p_{1,2} = p_{drop} = p_{2,3} = \frac{\sigma_{2,3}}{R_{2,3}},$$

where $p_{1,2}$ is the pressure inside the drop and right beside the lower circular segment, $p_{2,3}$ is the pressure inside the drop and right beside the upper circular segment, and p_{drop} is the pressure inside the drop. By combining the area constraint and the normal stress balances, $R_{1,2}$ and $R_{2,3}$ are obtained:

$$R_{2,3} = R_0 \sqrt{\frac{\pi}{(\theta_{2,3} - \sin(\theta_{2,3})\cos(\theta_{2,3})) + (\frac{\sigma_{1,2}}{\sigma_{2,3}})^2(\theta_{1,2} - \sin(\theta_{1,2})\cos(\theta_{1,2}))}}$$

$$R_{1,2} = R_{2,3}\frac{\sigma_{1,2}}{\sigma_{2,3}}.$$

Finally, it's straightforward to obtain the equilibrium thickness of the drop when the gravity is zero,

$$\mathrm{e}_d = R_{2,3}\,(1 - \cos(\theta_{2,3})) + R_{1,2}\,(1 - \cos(\theta_{1,2}))$$

If the gravity is dominant, asymptotic analyses from Langmuir and de Gennes [228], [229] give the final thickness of the drop as

$$\mathrm{e}_d = \sqrt{\frac{2(\sigma_{2,3} + \sigma_{1,2} - \sigma_{1,3})\rho_1}{\rho_2(\rho_1 - \rho_2)|\mathbf{g}|}}.$$

In the present case, the material properties are $\rho_1 = 998.207\mathrm{kg/m^3}$, $\rho_2 = 557\mathrm{kg/m^3}$, $\rho_3 = 1.2041\mathrm{kg/m^3}$, $\mu_1 = 1.002 \times 10^{-3}\mathrm{Pa \cdot s}$, $\mu_2 = 9.15 \times 10^{-2}\mathrm{Pa \cdot s}$, $\mu_3 = 1.78 \times 10^{-5}\mathrm{Pa \cdot s}$, $\sigma_{1,2} = 0.04\mathrm{N/m}$, $\sigma_{1,3} = 0.0728\mathrm{N/m}$, $\sigma_{2,3} = 0.055\mathrm{N/m}$. The density and viscosity ratios are about 1000 and 5000. Three different magnitudes of the gravity are 0, 5, and 9.8 $\mathrm{m/s^2}$, and their directions are pointing downward. The governing equations are non-dimensionalized by a density scale $1.2041\mathrm{kg/m^3}$, a length scale 0.04m, and a acceleration scale $1\mathrm{m/s^2}$. The rest of the setup and the results are reported in their dimensionless forms. The domain considered is $[-1, 1] \times [0, 0.8]$ with the periodic boundaries at the lateral and the no-slip

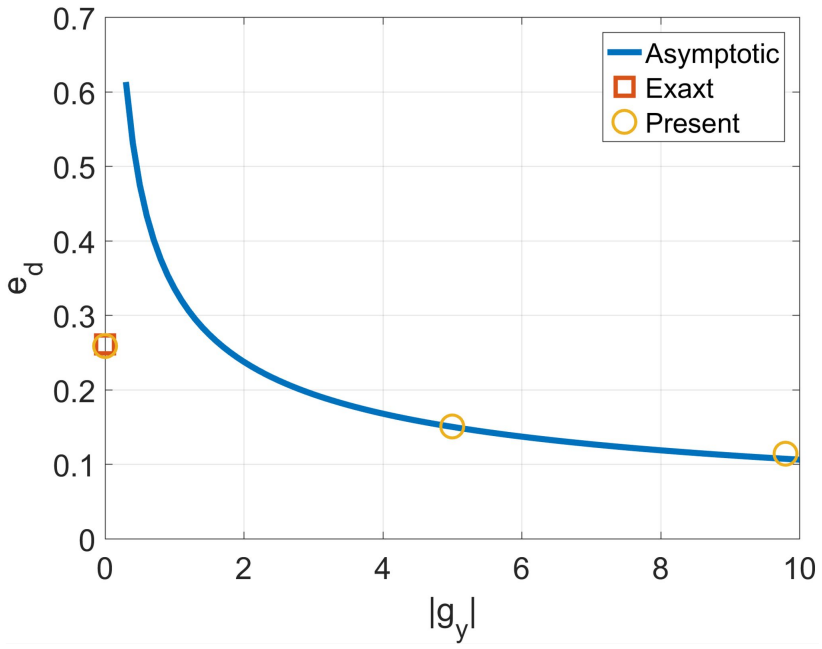

Figure 5.2. Final thickness of the drop vs. gravity in the floating liquid lens problem.

walls at the top and bottom. The domain is discretized by $[201 \times 81]$ cells and the time step is $\Delta t = 10^{-5}$. η and M_0 are set to be 0.01 and 10^{-7}. Initially, a circular drop (Phase 2) of a radius 0.2 is at $(0, 0.4)$, floating on the horizontal interface between Phases 1 and 3 at $y = 0.4$.

Fig.5.2 shows the final thickness of the drop (Phase 2) with respect to the magnitude of gravity, along with the exact solution for zero gravity and with the asymptotic solution for gravity dominant cases. The numerical results match both the exact and asymptotic solutions in two limits very well. Fig.5.3 shows the initial and final shapes of the three phases. When there is no gravity, the drop becomes a combination of two circular segments, which agrees well with the exact solution. As gravity increases, the drop is horizontally elongated and vertically compressed. Both the proposed model and scheme are able to reproduce the equilibrium state of the N-phase flows even including interfacial tensions.

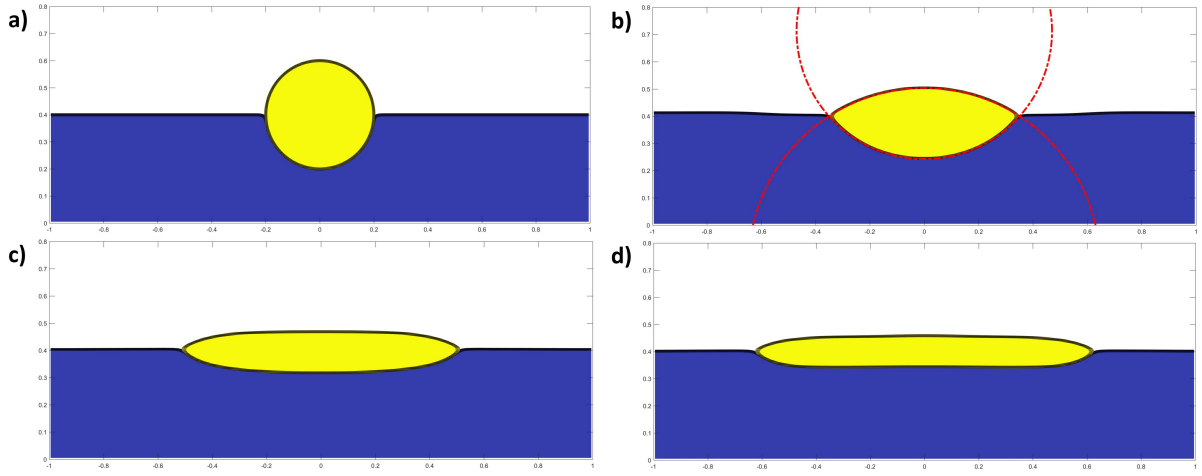

Figure 5.3. Initial and final shapes of the three phases in the floating liquid lens problem using CH-B. a) Initial configuration. b) Final shapes with $|\mathbf{g}| = 0$. c) Final shapes with $|\mathbf{g}| = 5$. d) Final shapes with $|\mathbf{g}| = 9.8$. Blue: Phase 1, Yellow: Phase 2, White: Phase 3. Red dash-dotted lines in b): Exact solution for $|\mathbf{g}| = 0$.

5.2 Rayleigh-Taylor instability

The Rayleigh-Taylor instability is considered as a benchmark problem for two-phase flows, and it also is extended to including multiple phases here. A heavier fluid is initially on the top of a lighter one. These two fluids are separated by a horizontal interface. The interface is unconditionally unstable after it is perturbed. During the penetration of the fluids, complex interface dynamics is observed due to the appearance of small-scale flow patterns.

5.2.1 Two-phase results

The domain considered is $[1 \times 4]$ with the free-slip boundary condition at the top and bottom of the domain while the periodic boundary condition is imposed at the two lateral boundaries. The domain is discretized by 128×512 cells, and the time step size Δt is $5 \times 10^{-4}/\sqrt{At}$. The material properties are $\rho_1 = 3$, $\rho_2 = 1$, $\mu_1 = \mu_2 = 0.001$, $\sigma = 10^{-12}$, and $\lambda M = 10^{-15}$. As a result, the Atwood number in this case is $At = \frac{\rho_1 - \rho_2}{\rho_1 + \rho_2} = 0.5$. The gravity $\mathbf{g}$ points downwards and its magnitude is unity, i.e., $\mathbf{g} = \{0, -1\}$. The initial

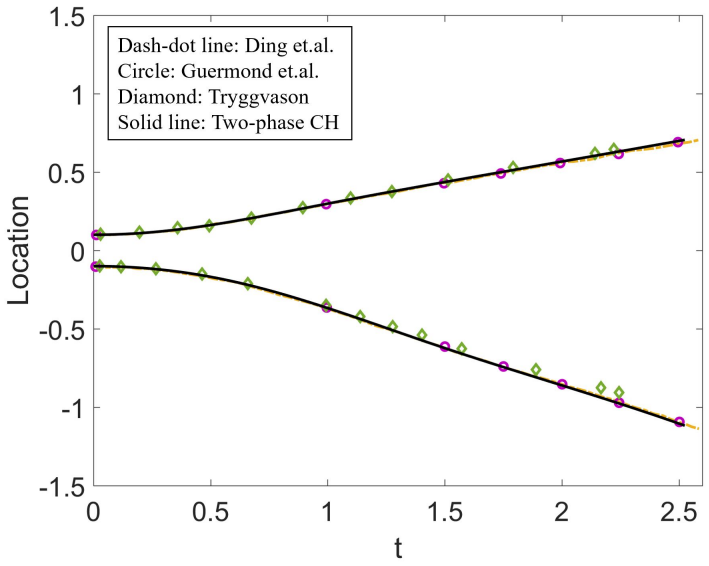

Figure 5.4. Locations of the interface of the Rayleigh-Taylor instability with density ratio 3 using two-phase CH.

horizontal perturbation is modeled by a sinusoidal wave at $y = 2$, whose amplitude is 0.1 and wavelength is 2π, and the initial velocity is zero.

The present result using two-phase CH is compared to those by Ding et al. [119], Guermond and Quartapelle [117], and Tryggvason [230] for verification. The viscosities of the phases are identical to those in [117], [119], while the flow considered in [230] is inviscid. Quantitative comparison can be achieved by measuring the transient locations of the interface at the center and at the lateral edge of the domain, as shown in Fig.5.4. The present result is almost on top of the published one. The snapshots of the interface at different times are compared against those in [119] in Fig.5.5. Both the interface structure and its temporal evolution agree very well with those in [119]. In addition, larger density ratios, i.e., 30, 1000, and 3000, are explored, whose results are shown in Fig.5.6. As the density ratio increases, the interface moves faster while its evolution is simpler. In addition, the results of the density ratio 1000 and 3000 are almost identical since the Atwood numbers in these two cases are very close to unity. The long-time dynamics of the Rayleigh-Taylor instability with $At = 0.5$ (density ratio 3) is shown in Fig.5.7, where very complicated interface evolution can be observed. The mainstream in the middle of the domain is moving downward, trans-

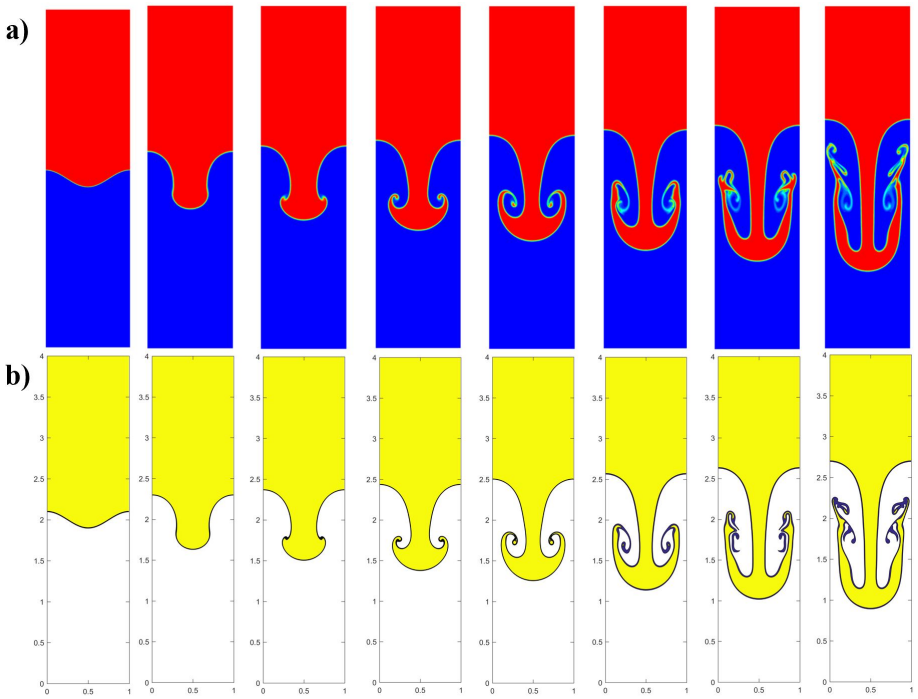

Figure 5.5. Snapshots of the interface of the Rayleigh-Taylor instability with density ratio 3 using two-phase CH. From left to right, $t \times \text{sqrt}(At) = 0$, 1, 1.25, 1.5, 1.75, 2, 2.25, 2.5. a) is from Ding et al. [119], and b) is from the present scheme.

porting the heavier fluid from top to bottom. When the heavier fluid reaches the bottom wall, it spreads towards the lateral walls and then moves upward along them. The flow in the middle and in the side of the domain are in the opposite direction and it further triggers instability, and the expansion and contraction of the middle fluid column can be observed. As the instability grows, it interacts with other flow structures or generates small droplets and filaments, resulting in a sophisticated interface pattern. Despite the complicated interface evolution, the numerical solution maintains symmetry. Since the viscous effects, in this case, is small, the problem reaches equilibrium after a very long time which is outside our simulation time.

The same case is performed using two-phase CAC. The early dynamics of the problem is quantified by measuring the locations of the interface at the center and at the lateral edge of the domain versus time, which is presented in Fig.5.8, along with the results from [117], [119], [230] and two-phase CH. The present results agree very well with the previous studies. The

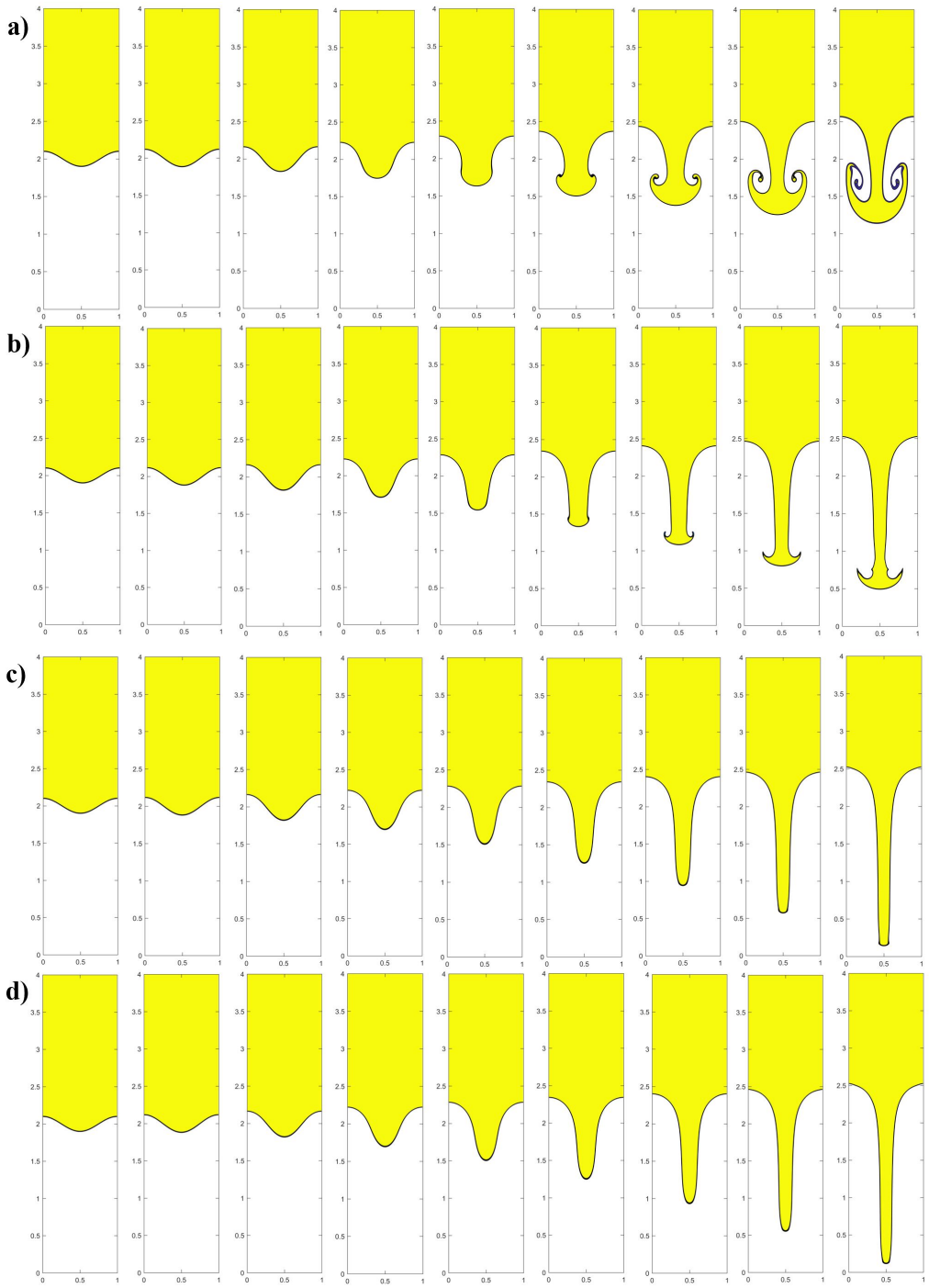

Figure 5.6. Snapshots of the interface of the Rayleigh-Taylor instability using two-phase CH with density ratio a) 3, b) 30, c) 1000, and d) 3000. From left to right, $t \times \text{sqrt}(At) = 0$, 0.25, 0.5, 0.75, 1, 1.25, 1.5, 1.75, 2.

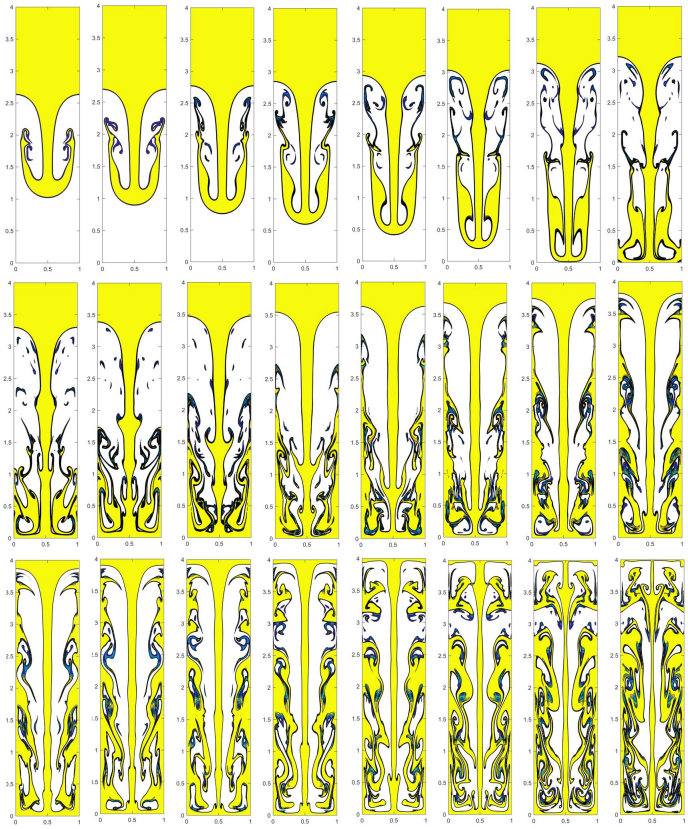

Figure 5.7. Snapshots of the interface of the Rayleigh-Taylor instability with density ratio 3 using two-phase CH (continued from Fig.5.6 a)). From left to right, top to bottom, $t \times \text{sqrt}(At)$ is from 2.25 to 8 with 0.25 increment.

evolution of the interface is shown in Fig.5.9 up to $t\sqrt{At} = 10$. The amplitude of the initial perturbation keeps growing, and a secondary instability is triggered at the two sides of the front of the heavier fluid after $t\sqrt{At} = 1.25$. As a result, the interface has a mushroom-like shape. As the heavier fluid moves downward, some small structures are generated by the instability. Further, there are new instabilities appearing on the small structures, resulting in topological changes. Consequently, one can observe a complicated interface configuration in the long-time dynamics of the problem.

5.2.2 Multiphase results

The three-phase Rayleigh-Taylor instability problem is considered using CH, where the heaviest phase (Phase 1), stays on the top of Phase 2, whose density is in the middle. At the

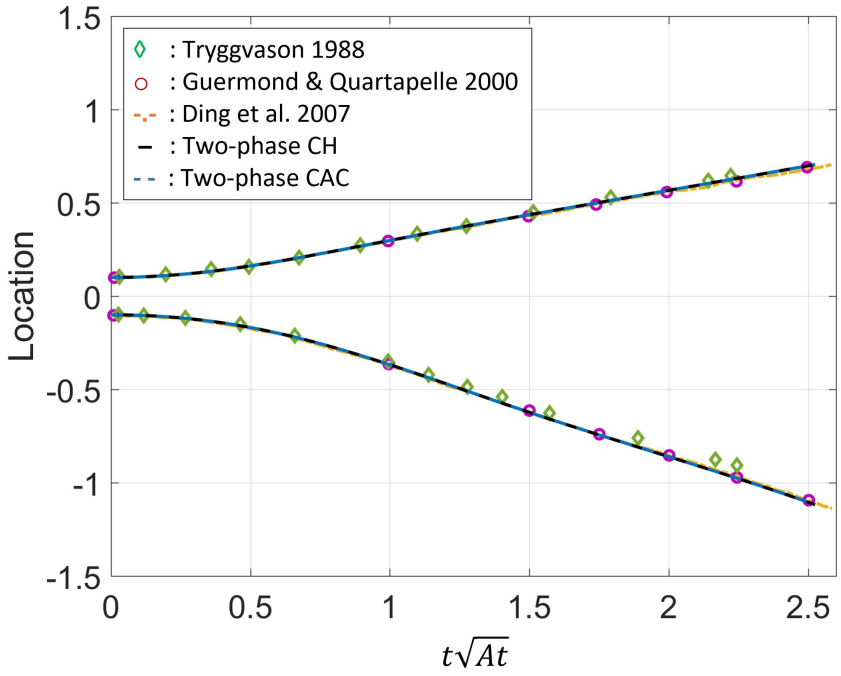

Figure 5.8. The locations of the interface at the center and the lateral edge of the domain for the Rayleigh-Taylor instability problem using two-phase CAC.

bottom, there is the lightest phase (Phase 3). The Atwood number between Phases p and q is defined as $At_{p,q} = \frac{\rho_p - \rho_q}{\rho_p + \rho_q}$. The domain of interest is 1×6. Its left and right boundaries are periodic while the top and bottom boundaries are free-slip. 128×768 cells are used to discretize the domain and the time step is $\Delta t = 10^{-3}$. The densities of the fluids are $\rho_1 = 4.5, \rho_2 = 3, \rho_3 = 1$, and their dynamic viscosities are all 10^{-3}. As a result, one has $At_{1,2} = 0.2$ and $At_{2,3} = 0.5$. The pairwise interfacial tensions are $\sigma_{p,q} = 10^{-12}, p \neq q$. The gravity is pointing downward with unity magnitude, i.e., $\mathbf{g} = \{0, -1\}$. Initially, the flow is stationary, and the interface between Phases 1 and 2 is at $y = 4$ and that between 2 and 3 is at $y = 2$. A horizontal sinusoidal perturbation is applied to both of the interfaces, whose amplitude is 0.1 and wavelength is 2π.

Since the interfaces are initially far away separated, there is no interaction between them at the beginning of the simulation. As a result, one can compare the locations of the interface between Phases 2 and 3 at the center and at the lateral edge of the domain to the two-phase results, where the Atwood number At is 0.5, by Tryggvason [230], Guermond and Quartapelle

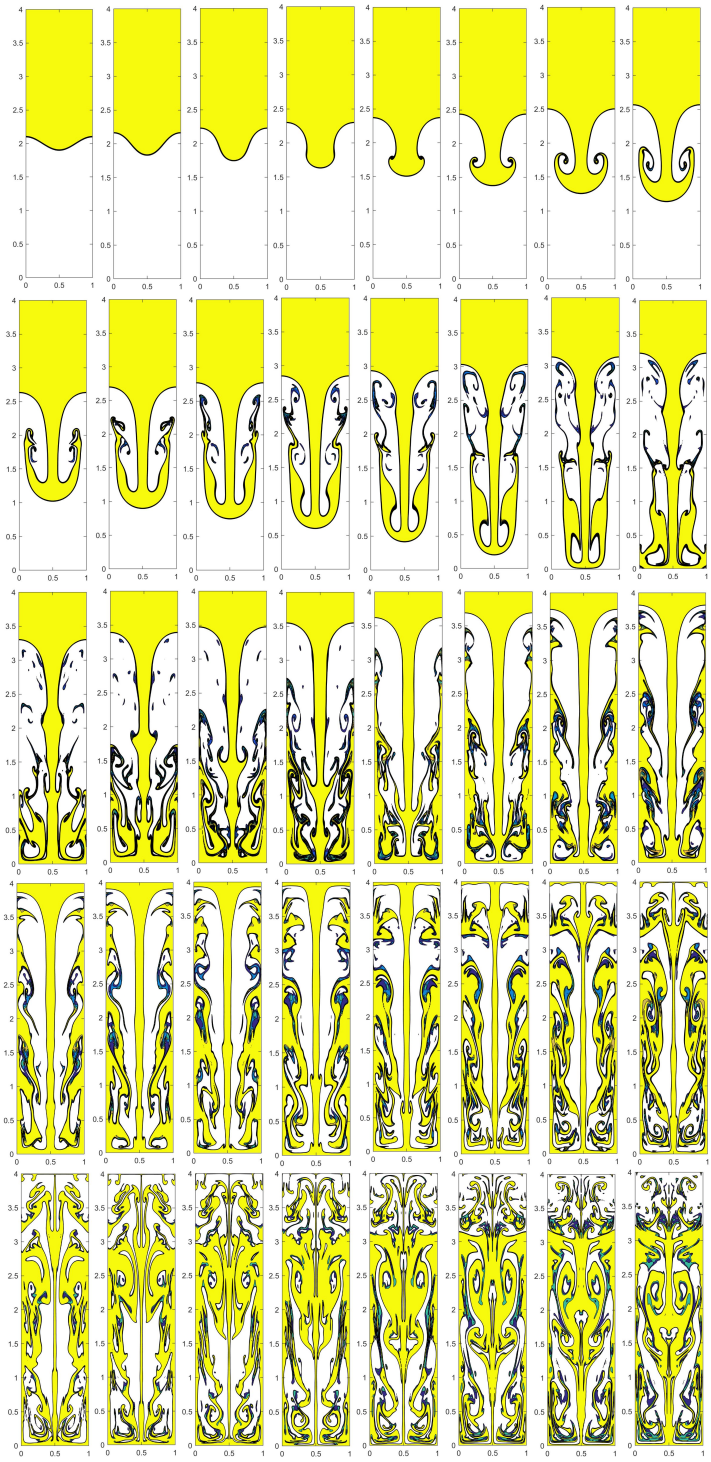

Figure 5.9. The evolution of the interface of the Rayleigh-Taylor instability problem using two-phase CAC at $t \times \text{sqrt}(At) = 0$, 0.5, 0.75, 1,..., 10 from left to right and from top to bottom.

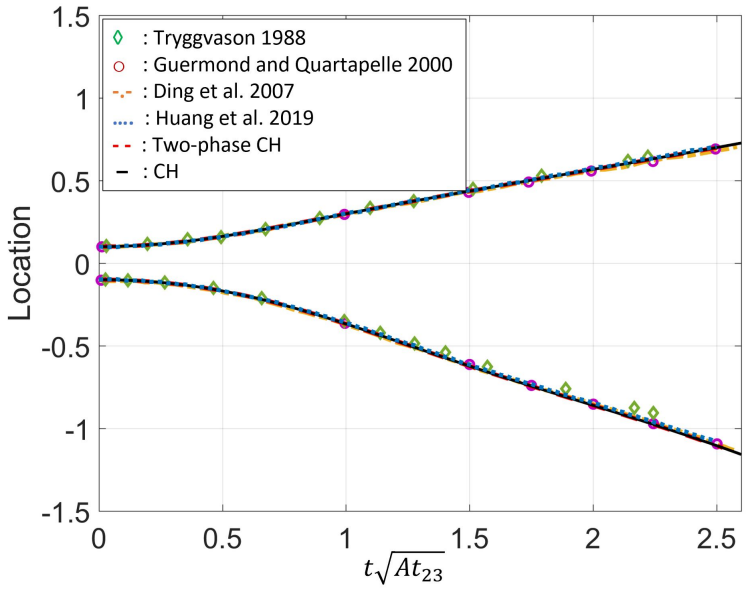

Figure 5.10. Locations of the interface between Phases 2 and 3 in the three-phase Rayleigh-Taylor instability problem using CH.

[117], Ding et al. [119], Huang et al. [113] and two-phase CH. The comparisons are shown in Fig.5.10, and the present results under a three-phase setup are almost indistinguishable from the published ones under a two-phase setup. The evolution of the three phases is presented in Fig.5.11 up to $t = 10$. Before $t = 5$, the three-phase dynamics is not observed, and the interfaces between Phases 1 and 2 and between Phases 2 and 3 evolve like two independent Rayleigh-Taylor instability problems with $At = 0.2$ at the top and with $At = 0.5$ at the bottom. The configurations of the individual interfaces are almost identical to those reported in [113], [119] and two-phase CH where only two phases were present. Phase 2 moves downward faster than Phase 1 because the Atwood number between Phases 2 and 3 is larger than that between Phases 1 and 2. One can observe multiple drops and filaments being generated from Phase 2 before it reaches the bottom of the domain. After $t = 5$, the three-phase dynamics begins. Phase 2 accumulates at the bottom of the domain, and then moves upward along the lateral edge of the domain. A channel of Phase 2 is built up in the middle of the domain and Phase 1 tries to move downward along this channel. As a result, the configuration of the interface between Phases 1 and 2 is shrunk compared to the two-phase one in [113]. Phase 1 gradually fills up the middle channel, along with

complex instability patterns resulting from its complex interactions with the other phases. Since Phase 1 is the heaviest, it takes the place of Phase 2 at the bottom and the lateral edge of the domain at the end of the simulation. As a result, Phase 2 is pushed to aggregate between the middle and lateral columns of Phase 1. The long-time dynamics of this problem is highly sophisticated because of the strong interactions between different phases.

5.3 Dam break

The dam break (or collapse of water column) problem is performed and the numerical results are compared to the experimental measurements by Martin and Moyce [231]. In the experiment, a water column, which is initially stationary, collapses due to gravity, after the holding is removed. Martin and Moyce [231] measured the locations of the front and the height of the water column at different instants, and scaled them with the initial width of the water column a. The scaled locations of the front and the height are denoted by Z and H, respectively. The computational domain is $[4a \times 2a]$ and is discretized by 256×128 cells. The no-slip/penetration boundary condition is applied at all the boundaries. A square of water column initially is in $[0, a] \times [0, a]$ of the domain, with $a = 2.25$ inch, i.e., 5.715cm, and is surrounded by the air. The material properties of water and air are:

- Air: $\rho_{air} = 1.204$ kg/m^3, $\mu_{air} = 1.78 \times 10^{-5}$kg/(m $\cdot$ s)
- Water: $\rho_{water} = 998.207$kg/m^3, $\mu_{water} = 1.002 \times 10^{-3}$ kg/(m $\cdot$ s)
- Surface tension: $\sigma = 7.28 \times 10^{-2}$ kg/s^2
- Gravitational acceleration: $g_x = 0$m/s^2, $g_y = -9.8$ m/s^2.

The density ratio is about 830 while the viscosity ratio is about 56.

5.3.1 Two-phase results

In this case, two-phase CH-B is used, and the water is labeled as Phase 1 and the air is labeled as Phase 2. The governing equations are non-dimensionalized by the density scale ρ_{air}, the length scale a, and the time scale $\sqrt{a/|g_y|}$. The results are reported in their

dimensionless form. Following the same calibration in [231], $Z = 1.44$ when $t = 0.8$ and $H = 1$ when $t = 0$. Quantitative comparisons of the numerical results to the experimental results in [231] are shown in Fig.5.12. Both the the front and height of the interface obtained from our scheme agree with the measurements very well. In addition, the case of density ratio 100,000 is performed for the same setup to test the capability of the represent scheme dealing with extremely large density ratios. The front and height from this case are also plotted in Fig.5.12, from which one can see that the interface moves a little faster than the one for the water-air case. The snapshots of the interfaces for both cases are shown in Fig.5.13. The long-time dynamics of the water-air case is included in Fig.5.14 and one can observe the complicated interface evolution. The water is pushed to rise on the vertical wall at the right of the domain. Because of gravity, the rising motion on the wall is slowed down and the water on the vertical wall tends to move backward. However, the water at the bottom is still moving from left to right because of inertia, and as a result, a bump of water appears on the vertical wall. This bump grows, and finally collapse with the water at the bottom. After that, a hydraulic jump is generated, moving from right to left, along with small filaments and droplets. This hydraulic jump hits the left vertical wall and then the water is pushed to move again to the right.

The same case is repeated using two-phase CAC-B and CAC-C. The early dynamics of the problem is quantified by measuring the front and the height of the water column versus time, which is presented in Fig.5.15, along with the experimental data from [231]. The results from the balanced-force method (two-phase CAC-B) and from the conservative method (two-phase CAC-C) overlap with each other, and both of them agree well with the experimental measurements. The evolution of the interface is shown in Fig.5.16 up to $t = 10$, where both of the results from the two methods are presented. The water column collapses towards the right of the domain and climbs up the right wall. The rising motion is slowed down by gravity, while the water at the bottom is still pushed upward. As a result, there is a bump in the middle of the climbing water. This bump collapses onto the bottom water and pushes it moving backward. Consequentially, a water jump is developed and moves toward the left, along with complicated interface configurations. At the end of the simulation, the water jump reaches the left wall and the bottom water is pushed to move to the right

again. Although both the balanced-force method and the conservative method give a similar physical picture of the problem, it can be observed that the balanced-force method tends to break the interface when the length scale of the interfacial structure is close to the cell size. As a result, more topological changes are observed in the results using the balanced-force method. The present results also show that the conservative method is more stable than the balanced-force method. A time step that is 5 times larger can be used, and the conservative method is stable for the whole simulation, while the balanced-force method is only stable before the water touches the top wall.

5.3.2 Multiphase results

The three-phase dam break problem is considered using CHB-B and CACB-B. The three phases considered are water (Phase 1), whose density is 998.207kg/m^3 and viscosity is 1.002×10^{-3}Pa $\cdot$ s, oil (Phase 2), whose density is 557kg/m^3 and viscosity is 9.15×10^{-2}Pa $\cdot$ s, and air (Phase 3), whose density is 1.2041kg/m^3 and viscosity is $1.78\times 10^{-5}\times 10^{-2}$Pa $\cdot$ s. The surface tensions between them are $\sigma_{1,2} = 0.04$N/m, $\sigma_{1,3} = 0.0728$N/m, and $\sigma_{2,3} = 0.055$N/m. The gravity is pointing downward with a magnitude 9.8m/s^2. The governing equations are non-dimensionalized by a density scale 1.204kg/m^3, a length scale 5.715cm, and an acceleration scale 9.8m/s^2. The rest of the setup and the results are reported in their dimensionless forms. The domain considered is $[8 \times 2]$ and all the boundaries are no-slip. The domain is discretized by $[512 \times 128]$ cells. η and M_0 are 0.01 and 10^{-7}, respectively. The time step is $\Delta t = 5 \times 10^{-4}$. Initially, the flow is stationary, a square water column with a width 1 is at the left of the domain, and an oil column with the same size is at the right of the domain.

The initial dynamics is quantified by measuring the front Z and height H of the water column. Since the water and oil are far away separated at the beginning, there is no interaction between them and one can compare the numerical solutions from both CHB-B and CACB-B to the experimental data from Martin and Moyce [231]. The numerical results are calibrated by setting Z equal to 1.44, when t is 0.8, and H equal to 1, when t is 0, as those in [231]. The results are shown in Fig.5.17. The difference between CHB and CACB is unobservable and both results agree well with the experimental data.

Fig.5.18 and Fig.5.19 show the configurations of the interfaces from CHB-B and CACB-B, respectively, up to $t = 10$. Both models give a similar picture of the problem. The water and oil columns collapse at the beginning and start sliding along the bottom wall. The water is moving faster than the oil since the oil is about 100 times more viscous than the water. Due to the high viscosity, the oil close to the lateral wall is falling down more slowly than other parts of it. When the fronts of the water and oil meet together, the oil, which is lighter and moving slower, is squeezed upward by the water, and the water climbs along the bottom of the oil. The front of the oil, squeezed by the water, collapses again and lays above the water, along with breaking up into small droplets and filaments. At the same time, the water keeps moving toward the right and pushing the oil at the bottom moving backward. It can be observed that the interactions among different phases are very complicated. Even though the problem is challenging, the mass conservation and the summation constraint for the order parameters are always satisfied, as shown in Fig.5.20.

Fig.5.21 shows the results from CHC-B, which is CH-B but including only the clipping and rescaling steps in the boundedness mapping in Section 3.3.2. The results are compared to those from CHB-B. Thanks to adding the rescaling step, the summation constraint for the order parameters are satisfied from CHC-B. The mass change due to simply clipping and rescaling the order parameters is significant, although the out-of-bound error is small, in the order of 10^{-5}, in one time step. This problem is sensitive to the out-of-bound errors since it has a maximum density ratio of about 1000 and a maximum viscosity ratio of about 5000. Both the clipping operation in previous studies and the boundedness mapping proposed in the present work improve the robustness of the scheme, which is important for the success of the simulation. Moreover, the boundedness mapping additionally enforces the mass conservation of each phase, which is also important for long-time simulation.

5.4 Rising bubble

Cases in this section include large density ratios, gravity, surface tension force, and moving contact lines, which are challenging factors in multiphase flows. Lighter fluids are released inside a closed water tank. Because of the buoyancy effect, those lighter fluids move

upward and at the same time they deform. Contact lines between the water, the lighter fluids, and the top wall appear after the lighter fluids touch the top wall. The contact lines slide along the top wall with the oscillation of the lighter fluids. As a result, the lighter fluids may touch the lateral walls. The material properties of the air, water, and oil:

- Air: $\rho_{air} = 1.204$ kg/m^3, $\mu_{air} = 1.78 \times 10^{-5}$kg/(m $\cdot$ s)
- Water: $\rho_{water} = 998.207$kg/m^3, $\mu_{water} = 1.002 \times 10^{-3}$ kg/(m $\cdot$ s)
- Oil: $\rho_{oil} = 557$kg/m^3, $\mu_{oil} = 9.15 \times 10^{-2}$Pa $\cdot$ s
- Surface tension: $\sigma_{water-air} = 7.28 \times 10^{-2}$ kg/s^2, $\sigma_{water-oil} = 0.04$N/m, $\sigma_{oil-air} = 0.055$N/m.
- Gravitational acceleration: $g_x = 0$m/s^2, $g_y = -9.8$ m/s^2.

The governing equations are non-dimensionalized by a density scale 1.204kg/m^3, a length scale 0.01m, and an acceleration scale 1m/s^2. The rest of the setup and the results are reported in their dimensionless forms. The domain considered is $[-0.5, 0.5] \times [0, 1.5]$ and its boundaries are all no-slip. $[100 \times 150]$ cells are used to discretize the domain and the time step is $\Delta t = 2.5 \times 10^{-5}$.

5.4.1 Two-phase results

The two-phase air-water case is first considered using two-phase CH-B. An air bubble is initially at $(0, 0.5)$ with a radius 0.25 and the velocity is zero. Different steady contact angles are assigned at the right, left, and top walls. The cases are named by "R#L#T#", where"R","L", and "T" represent the right, left and top wall of the domain and the numbers following them denote the steady contact angles (in degree) at those walls, respectively. Four cases are considered which are R90L90T90, R30L150T90, R150L120T90 and R30L60T120.

The selected snapshots of the 4 cases are shown in Fig.5.22-Fig.5.25. Little difference is observed in the 4 cases before the bubble touches the top wall. This is reasonable since the contact angle should not interfere with the dynamics far away from the wall. It can be observed that the bubble begins to rise because of the buoyancy effect and deforms by

horizontally spreading and vertically shrinking. A large curvature at the left and right of the bubble appears due to the deformation of the bubble. The surface energy is strong due to large curvatures. To prevent further increase in the surface energy, the bubble expands vertically while shrinks horizontally. In addition, a surface wave along the interface is formed. When the bubble touches the top wall, some amount of water is trapped by the bubble and the top wall. Multiple contact lines formed by the water, air and top wall begin to move from the center to the lateral walls, due to the inertia of the bubble.

R90L90T90, R30L150T90, and R150L120T90 share the same dynamics before the contact lines reach the lateral walls. In R90L90T90 Fig.5.22, the bubble touches both of the lateral walls because of the symmetric set up. A new surface wave propagates and reflects between the centerline of the domain and the lateral walls. However, the amplitude is attenuated by the viscous effect and the interface gradually becomes horizontal. The present result of R90L90T90 is comparable to those in [112], [113], where only the 90^0 contact angle was considered and the same behavior was reported. Different from R90L90T90, the bubbles in R30L150T90 Fig.5.23 and R150L120T90 Fig.5.24 only touch the lateral wall that has a smaller steady contact angle. The bubble in R30L150T90 touches the right wall while the one in R150L120T90 touches the left wall. This is reasonable since, with a smaller steady contact angle, the attraction between the wall and the air is stronger. Because of the effect of steady contact angle, the bubbles have different equilibrium shapes and locations. Again, different dynamics is observed when the steady contact angle of the top wall is changed from 90^0 to 120^0, which corresponds to R150L120T90 case in Fig.5.24. The bubble is unable to reach either of the lateral walls in this case so the steady contact angles of the lateral walls are not important. After the bubble reaches the top wall, it begins to spread and then shrink along the top wall until its energy is attenuated by the viscous effects.

5.4.2 Mutliphase results

Using CH-B, one can investigate the multiphase dynamics. Both the air bubble and the oil drop are circular, whose radii are 0.15 and 0.3, respectively. Three different sets of contact angles at the top wall are considered, which are $\theta^T_{water-oil} = \theta^T_{oil-air} = \frac{\pi}{2}$ in the first

case, $\theta^T_{water-oil} = \frac{\pi}{2}, \theta^T_{oil-air} = \frac{2\pi}{3}$ in the second case, and $\theta^T_{water-oil} = \frac{\pi}{6}, \theta^T_{oil-air} = \frac{2\pi}{3}$ in the last case. The evolutions of the three phases of the three cases are shown in Fig.5.26, Fig.5.27, and Fig.5.28, respectively, up to $t = 2.5$.

There is no significant difference among Fig.5.26, Fig.5.27, and Fig.5.28 before $t = 1.8$. This makes sense since the contact angle boundary condition should only influence the dynamics close to the top wall. At the beginning, the air bubble moves upward, relative to the oil drop, driven by the buoyancy effect. The drag introduced by the relative motion between the air bubble and the oil drop, along with the buoyancy effect between the oil and the water, drives the oil drop moving upwards. Since the density contrast between the air and the oil is much larger than that between the water and the oil, the motion of the air bubble is more pronounced, and as a result, the air bubble crosses the water-oil interface. After that, the triple points between the air, oil, and water is formed, and the three phases gradually reach an equilibrium configuration. This equilibrium configuration keeps moving upward without observable deformation until the air bubble touches the top wall. After touching the top wall, the air bubble quickly spreads along the top wall and is further compressed along the vertical direction because of the rising motion of the oil drop. The difference among the three cases begins with the oil drop touching the top wall, i.e., right after $t = 1.8$, since the contact angle between the water and oil at the top wall varies from case to case. In Fig.5.26 and Fig.5.27, the spreading length of the oil drop is larger than that of the air bubble, and the compressed air bubble is relaxed to a shape close to a semi circle. In Fig.5.28, the spreading length of the oil drop is very close to that of the air bubble, and the relaxation of the air bubble is not obvious. Finally, both the air bubble and the oil drop stay at the top wall with the assigned contact angles.

5.4.3 Axisymmetric results

The two-phase axisymmetric rising bubble is presented using two-phase CACB-B and CACB-C to demonstrate the effectiveness of the boundedness mapping and the consistent formulation in a coordinate system other than the Cartesian one. A spherical bubble with a radius R is released at $z = 2R$ in an axisymmetric domain $[4R \times 8R]$ with a free-slip

boundary condition at $z = 0$, $z = 8R$, and $r = 4R$, where $R = 0.01$m. The density of the liquid is $\rho_L = 1000\text{kg/m}^3$, and the gravity along the negative z axis is $g_z = 10\text{m/s}^2$. Other parameters are specified as the density ratio 1000, the viscosity ratio 100, the Bond number $Bo = \frac{\rho_L g_z R^2}{\sigma} = 200$, and the Reynolds number $Re = \frac{\rho_L R\sqrt{g_z R}}{\mu_L} = 100$. The equations are non-dimensionalized by using R, ρ_L and g_z as the length, density and acceleration scales. The domain is discretized by $[200 \times 400]$ cells, and the time step is $\Delta t = 10^{-3}$.

Figs.5.29 and 5.30 show the results from the balanced-force method (two-phase CACB-B) and the conservative method (two-phase CACB-C), respectively. In this case, both of the methods give the same evolution of the bubble. The buoyancy effect drives the bubble upward. The bottom part of the bubble moves faster, and at the end catches up with its top. As a result, the topological change happens, and the bubble becomes a band ring. The present results are comparable to those in [232], where the same case is considered using the Level-Set method.

5.5 Moving contact lines

Moving contact lines are popularly modeled by the 4th-order Phase-Field methods, like CH and its two-phase correspondence, where the highest spatial derivative in the methods is 4th-order. These methods require two boundary conditions at the wall. Usually, one is for the mass conservation and the other is for the contact angle. On the other hand, difficulties appear when the 2nd-order Phase-Field methods, like CAC and its two-phase correspondence, are used, because only a single boundary condition is needed. Thanks to the consistent and conservative volume distribution algorithm developed in Section 2.2.2, such difficulties are removed. In the following, results from CH-B or two-phase CH-B are briefly validated and more results from CAC-B or two-phase CAC-B are reported.

5.5.1 Results from the Cahn-Hilliard equations

Two-phase cases using two-phase CH-B are first considered. Following the setup in [79], the domain is $[-3, 3] \times [0, 2]$ and there is a semicircular drop initially at $(x_r, y_r) = (0, 0)$ with a radius $r = 1$. The velocity components are all zero at the beginning. The left and

right boundaries of the domain are periodic, while the top and the bottom are considered as walls. The no-slip and no-penetration boundary condition for velocity is applied at the walls and a 90^0 contact angle is imposed at the top wall. Different steady contact angles θ^W, between the drop and the bottom wall, which are 45^0, 60^0, 90^0, 120^0, and 135^0, are imposed through the contact angle boundary condition Eq. (2.24), although initially the contact angle between them is 90^0. The drop will spread or contract along the bottom wall because of the mismatch between the initial 90^0 contact angle and the imposed contact angle, and finally the drop should reach the equilibrium state, where the mismatch disappears. The purpose of this case is to validate Eq. (2.24). The two fluids have the same density 1 and viscosity 1. The surface tension between the fluids is 100, η is 0.02, and M_0 is determined from the Peclet number 1.061×10^2 as that defined in [79]. The domain is discretized by 385×128 cells and the time step is $\Delta t = 5 \times 10^{-5}$. The computations are stopped at $t = 1$, which is long enough for the drop to reach its equilibrium state under different contact angels considered.

When the drop is at its equilibrium state with a contact angle θ^W, the free energy of the drop is minimized. In other words, the area (or the length in 2D) of the drop interface should be minimized under the volume constraint (or the area constraint in 2D) and the contact angle constraint. As a result, in 2D, the equilibrium shape of the drop is a circular segment, which intersects the homogeneous flat surface with the given contact angle, and the enclosed area is the same as the initial one. As illustrated in Fig.5.31, the area enclosed by the circular segment is

$$S_d = R_d^2 \left(\theta^W - \sin(\theta^W) \cos(\theta^W) \right),$$

where R_d is the radius of the circular segment and θ^W is the contact angle between the drop and the surface. The area constraint requires that $S_d = \frac{\pi}{2} R_0^2$, where R_0 is the radius of the initial semi-circular drop. Thus, one can obtain

$$R_d = R_0 \sqrt{\frac{\pi/2}{\theta^W - \sin(\theta^W) \cos(\theta^W)}}.$$

Once R_d is found by given R_0 and θ^W, the height and the spreading length of the equilibrium drop can be computed as

$$H_d = R_d\left(1-\cos(\theta^W)\right), \quad L_d = 2R_d\sin(\theta^W).$$

It should be noted that θ^W is measured by radian. The numerical height and length of the drop is measured based on the zero contour of the Phase-Field function, which is considered as the location of the interface.

Fig.5.32 shows the initial and the equilibrium shapes of the drop under different contact angles θ^W. Fig.5.33 compares the height and the half spreading length of the drop, obtained from the numerical result, to the exact solution, and excellent agreements are achieved.

Next, the contact angle boundary condition Eq.(2.21) for multiple phases is validated. Three phases appear in the domain, where Phase 1 is in contact with the bottom wall, Phase 2 is in contact with the top wall and Phase 3 fills the remaining space of the domain. Although the equilibrium state does not depend on the material properties of the phases, significant density and viscosity differences are considered to make the problem more challenging. The material properties of the phases are $\rho_1 = 998.209\text{kg/m}^3$, $\rho_2 = 870\text{kg/m}^3$, $\rho_3 = 1.2041\text{kg/m}^3$, $\mu_1 = 1.002\times10^{-3}\text{Pa}\cdot\text{s}$, $\mu_2 = 9.15\times10^{-2}\text{Pa}\cdot\text{s}$, $\mu_3 = 1.78\times10^{-4}\text{Pa}\cdot\text{s}$, $\sigma_{1,2} = 0.04\text{N/m}$, $\sigma_{1,3} = 0.0728\text{N/m}$, $\sigma_{2,3} = 0.055\text{N/m}$. Both the density and viscosity ratios are about 1000. The governing equations are non-dimensionalized by a density scale 1.2041kg/m^3, a length scale 0.04m and an acceleration scale 1m/s^2. The rest of the setup and the results are reported in their dimensionless forms. The domain considered is $[-1,1]\times[0,0.5]$ with periodic boundaries at the lateral and no-slip walls at the top and bottom. The domain is discretized by $[200\times50]$ cells and the time step is $\Delta t = 10^{-4}$. η and M_0 are set to be 0.01 and 10^{-7}. The contact angles between Phases 1 and 3 at the bottom wall and between Phases 2 and 3 at the top wall are $(45^0, 135^0)$, $(120^0, 60^0)$, and $(75^0, 105^0)$. Initially, the centers of Phases 1 and 2 are at $(-0.5, 0)$ and $(0.5, 0.5)$, respectively, and both of them are semi-circular with radius $R_0 = 0.2$.

Fig.5.34 shows the heights and the spreading lengths obtained from the numerical solutions under different contact angles, along with the exact solution. The present numerical

results agree well with the exact solution. The proposed scheme is able to include the effect of contact angle accurately even there are significant contrasts of material properties. Fig.5.35 shows the initial and final shapes of the drops, along with the circular segments determined from the exact solution. The interfaces between Phases 1 and 3 and between Phases 2 and 3 overlap onto the circular segments, which are the exact shapes of the drops.

5.5.2 Results from the conservative Allen-Cahn equations

Three cases including moving contact lines using CAC-B or two-phase CAC-B are presented, which are seldom reported in the literature. $M_0\lambda_0 = 10^{-3}$ and $\eta = h$ are set unless otherwise specified.

Equilibrium drop: Here, the equilibrium drop problem is investigated again using both CAC-B and two-phase CAC-B. The "SI" unit system is used here, and the units are skipped presenting when reporting the setup and results in this case for the sake of brevity. The water (Phase 1) has a density $\rho_1 = 829$ and dynamic viscosity $\mu_1 = 2.08$, while the values of density and viscosity are $\rho_2 = 1$ and $\mu_2 = 0.0185$ for the air (Phase 2). The surface tension between them is $\sigma = 37.8$, and the gravity is pointing downward. The domain is $[-0.5, 0.5] \times [0, 0.3]$, and its lateral boundaries are periodic while they are no-slip walls at the top and bottom. A semicircle water drop having a radius 0.2 is initially on the middle of the bottom wall, and the air surrounds the drop. Different contact angles are assigned at the bottom wall. 150×45 grid cells are used and the time step is $\Delta t = 1 \times 10^{-4}$ to discretize the space and time, respectively.

Fig.5.36 shows the evolution of the drop with $\theta^W = 60^0$ and $\theta^W = 135^0$ and $|\mathbf{g}| = 0$, along with the corresponding exact final solution. As expected, the drop starts with the semicircle shape, gradually approaches the final exact solution. The equilibrium shape agrees with the exact solution very well. As shown in Fig.5.37 a), a good agreement with the exact solution is obtained. Note that the height of the domain is changed to 0.5 for $\theta^W = 135^0$ and $\theta^W = 150^0$, while the grid size remains unchanged. To investigate the convergence with respect to grid refinement, the errors of the height and spreading length of the water drop versus the grid

size is shown in Fig.5.38, using data from $\theta^W = 60^0$. The observed convergence rate is close to 2nd-order.

Then, the effect of gravity is included, and the domain is changed to $[-0.6, 0.6] \times [0, 0.24]$ without changing the grid size. Based on the asymptotic analysis for gravity-dominant cases [229], the final height of the drop becomes

$$H_d = 2\sqrt{\frac{\sigma_{la}}{\rho_l |\mathbf{g}|}} \sin(\theta/2),$$

where ρ_l, σ_{la}, and $|\mathbf{g}|$ are the liquid density, surface tension between the liquid and air, and the magnitude of the gravity, respectively. Fig.5.39 shows the evolution of the drop with $|\mathbf{g}| = 10$ and $|\mathbf{g}| = 15$, along with the prediction from the asymptotic solution. The contact angle is $\theta^W = 135^0$. One can observe that the drop is flattened, having a pancake-like shape, when the gravity is added. The final height of the drop matches the asymptotic prediction. Fig.5.37 b) shows the final height of the drop versus the gravity, and the present numerical prediction overall agrees well with both the exact solution without gravity and the asymptotic solution with dominant gravity. Further, Fig.5.40 a) demonstrates the mass conservation of the proposed formulation, where the relative changes of Φ ($\Phi = \int_\Omega \phi d\Omega$) of the four cases reported in Fig.5.36 and Fig.5.39 are in the order of the round-off error.

Next, the N-phase results from CAC-B are supplemented. The oil phase (Phase 3) is introduced, whose density is $\rho_3 = 722.5$ and viscosity is $\mu_3 = 9.5$. The surface tensions between the oil and air and between oil and water are $\sigma_{3,2} = 28.55$ and $\sigma_{3,1} = 20.76$, respectively. The domain size is $[-1, 1] \times [0, 0.5]$ while the grid size is the same as the two-phase cases. The water drop right now is on the bottom wall with a contact angle $\theta^W_{1,2} = 60^0$, while the oil drop is attached to the top wall with a contact angle $\theta^W_{3,2} = 120^0$. Evolution of the drops is shown in Fig.5.41. Not only both the water and oil drops finally match the exact solution but also the shape of the water drop at different moments is indistinguishable from the two-phase solution in the left column of Fig.5.36. The final heights and spreading lengths of the two drops are measured and plotted in Fig.5.37 a) as well, and good agreement is obtained with both the exact and two-phase solutions. Fig.5.38 also shows the convergence

behavior of the N-phase results from CAC-B, which is similar to the two-phase one (two-phase CAC-B).

Then, the gravity is added and CAC-B is again used. The surface tension between the oil and air becomes $\sigma_{3,2} = 37.48$ so that the final heights of both the water and oil drops, predicted from the asymptotic solution, are the same. The domain is $[-1, 1] \times [0, 0.3]$, and the magnitude of the gravity is $|\mathbf{g}| = 10$. The contact angle of the water drop on the bottom wall is $\theta^W_{1,2} = 135^0$, while it is $\theta^W_{3,2} = 120^0$ for the oil drop. Evolution of the drops are shown in Fig.5.42. Both of the drops are compressed vertically and finally reach a similar height to the asymptotic prediction. Again, the water drop behaves identically to the two-phase solution in the left column of Fig.5.39. Fig.5.37 b) also includes the final heights of the two drops in this case, and they are in good agreement with both the asymptotic and two-phase solutions. The mass conservation of the phases is investigated, and the relative changes of Φ_p, where p is the index of the phases, are in the order of the round-off error, as shown in Fig.5.40 b). In additional to that, the summation of the order parameters exactly satisfies Eq.(2.2), which is shown in Fig.5.40 c).

The last property the N-phase results should satisfy is the *consistency of reduction*. The N-phase case with $|\mathbf{g}| = 10$ is repeated but only consider the left half of the domain, i.e., $-1 \leqslant x \leqslant 0$. Therefore, the oil drop disappears at the beginning, i.e., $\phi_3|_{t=0} = -1$. Evolution of the water drop from CAC-B is shown in the left column of Fig.5.39 as well using the cyan dashed line, and the difference from the two-phase solution is negligible. This also suggests that choosing $g_w(\phi)$ in Eq.(2.24) as a Sine or Hermite polynomial function has a negligible effect on the solution. Fig.5.43 quantitatively validates that not only the mass conservation and the summation of the order parameters are exactly satisfied by CAC-B but also the *consistency of reduction* since $\phi_3 = -1$ is true at $\forall t > 0$.

Bouncing drop: Here, a falling drop bouncing back after it contacts the bottom wall is considered, using the two-phase CAC-B. The density of the water (Phase 1) is 998.207kg/m^3 and the viscosity is $1.002 \times 10^{-3}\text{Pa} \cdot \text{s}$. They are 1.2041kg/m^3 and $1.78 \times 10^{-5}\text{Pa} \cdot \text{s}$ for the air (Phase 2). The surface tension is $7.28 \times 10^{-2}\text{N/m}$ and the gravity is $\mathbf{g} = \{0, -9.8\}\text{m/s}^2$. Non-dimensionalization is performed to the governing equations based on the density scale 1.2041kg/m^3, length scale $5 \times 10^{-3}\text{m}$, and acceleration scale 1m/s^2. The density scale is the

same as the air density. The length scale is the initial height of releasing the drop, which is also the horizontal length of the domain. It is 4 times the initial radius of the drop to prevent the drop from touching the lateral sides of the domain in the investigated cases of $\theta^W > 90^0$. The acceleration scale is chosen for convenience so that the dimensionless value of the gravity is the same as the dimensional one. The dimensionless grid size and time step are $h = 0.01$ and $\Delta t = 5 \times 10^{-5}$, respectively. The water is inside a circle having a radius 0.25 at $(0, 1)$ in the dimensionless domain $[-0.5, 0.5] \times [0, 1.5]$. The boundaries are periodic at the lateral sides while no-slip at the top and bottom walls.

Fig.5.44 and Fig.5.45 show results with contact angle $\theta^W = 165^0$ at the bottom wall. The drop remains circular as it is falling down. After the drop impacts on the bottom wall, it is strongly deformed to reduce the downward velocity and finally reaches a "dumbbells-like" shape. Then, the drop tries to restore the circular shape and jumps upward, leaving the bottom wall and finally arriving at a height lower than where it is initially released. This process repeats and the velocity is gradually reduced to zero. Finally, the drop settles down on the bottom wall and the equilibrium shape deviates slightly from the circular one because of the gravity.

Different contact angles at the bottom wall are considered. it is observed that the drop is unable to bounce back when the contact angle is less than or equal to 120^0 and the water finally fills the bottom of the domain when the contact angle is less than or equal to 90^0. The same behaviors are also reported in [79]. Fig.5.46 shows shapes of the drops from different contact angles at $t = 0.46$, right after the first impact to the bottom wall, and at $t = 4.00$. The (y-component) center of mass of the drop y_c ($y_c = \int_\Omega y \frac{1+\phi}{2} d\Omega / \int_\Omega \frac{1+\phi}{2} d\Omega$) versus time is shown in Fig.5.47 a). Until the second impact to the bottom wall, the centers of mass from $\theta^W = 165^0$ and $\theta^W = 150^0$ move very similarly, as shown in Fig.5.47 a). However, with a smaller contact angle, length of the drop in contact with the bottom wall is larger, as shown in Fig.5.46. This can provide more dissipation, and as a result, the drop have a less chance to bounce back. On the other hand, each time when the drop impacts to the wall induces a large deformation of the drop, which also produces a strong dissipation due to the viscosity of the water. Therefore, from Fig.5.47 a), peaks of the curves describing the motion of center of mass decay very fast for the drops that bounce back, e.g., those with $\theta^W = 165^0$ and 150^0.

For the drop that is unable to bounce back, e.g., the one with $\theta^W = 120^0$, it oscillates on the bottom wall, and its center of mass curve has a higher frequency but there is less attenuation between the two neighboring peaks. For the drop that will finally fill the bottom, e.g., those with $\theta^W = 90^0$ and $\theta^W = 60^0$, a long-term but small-amplitude oscillation of the center of mass is observed. This is caused by the capillary wave on the horizontal water-air interface, as shown in Fig.5.46.

Finally, the effect of the mobility M_0 is considered. Fig.5.48 shows shapes of the drops with different mobilities (or $M_0\lambda_0$), and the mass centers (y component) are shown in Fig.5.47 b). With a larger mobility, the drop becomes more "rigid" and therefore less deforms, as shown in Fig.5.48. On the other hand, a too "soft" drop, resulting from a small mobility, suffers from fictitious oscillation on the side close to the bottom wall. Even worse, the oscillation destroys the symmetry of the solution, and at the end produces a non-symmetry drop staying biased to left half of the domain. The drop with the smallest mobility finally is floating above the bottom wall because the interface is over-thickened. However, these unphysical behaviors are not observed in the cases with a larger mobility. As shown in Fig.5.47 b), there is no significant difference due to the mobility before the first impact of the drop to the bottom wall. The one with the largest mobility can only bounce back once and settles down very fast. The one with the smallest mobility bounces back multiple times although the height it returns to after the first impact is lowest among the three cases. These behaviors suggest that a larger mobility produces more dissipation.

Compound drops: Here, the compound drops sliding on a horizontal solid wall is reported using CAC-B. The material properties of the three phases are $\rho_1 = \rho_2 = \rho_3 = 1\text{kg/m}^3$, $\mu_1 = \mu_2 = 1\text{Pa}\cdot\text{s}$, $\mu_3 = 1\times10^{-3}\text{Pa}\cdot\text{s}$, and $\sigma_{1,2} = \sigma_{1,3} = \sigma_{2,3} = 100\text{N/m}$, the contact angles at the bottom wall are $\theta_{1,2} = 120^0$, $\theta_{1,3} = 90^0$ and $\theta_{2,3} = 60^0$, and the gravity is neglected. The density, length, and velocity scales for non-dimensionalizing the governing equations are 1kg/m^3, 1m, and 10m/s, respectively. The density scale is the same as the density of Phase 1, and the length scale is the initial radius of the Phase 1 drop, denoted by R_{01}. The velocity scale, denoted by U, is determined from the inertial-capillary time scale $T = \sqrt{\rho_1 R_{01}^3/\sigma_{1,2}}$, i.e., $U = R_{01}/T$. As a result, the Reynolds number is $Re = \rho_1 U R_{01}/\mu_1 = 10$ and the Weber number is $We = \rho_1 U^2 R_{01}/\sigma_{1,2} = 1$ in this case. The dimensionless domain

size is $[-2, 2] \times [0, 1.2]$, and the periodic and no-slip boundary conditions are assigned along the x and y axes, respectively. The space and time are discretized by 200×60 grid cells and $\Delta t = 1 \times 10^{-4}$. Initially, two quarter-circular drops compound a semi-circular with a radius 1 on the middle of the bottom wall, left half of which is full of Phase 1 and the other half is Phase 2. Phase 3 occupies the remaining domain. Evolution of the drops are shown in Fig.5.49, along with the exact solution from [90] for the equilibrium state. The drops move towards the equilibrium shape, which agrees well with the exact solution. Quantitatively, the spreading lengths of Phases 1 and 2 are 1.0547 and 1.6871, respectively, and the relative errors are 1.614% and 1.166% after comparing to the exact ones 1.0720 and 1.7070 from [90].

Next, the sliding motion of the compound drops on a translating wall is investigated. The setup is slightly changed as follows: $\mu_2 = 0.67\text{Pa} \cdot \text{s}$, $\mu_3 = 0.33 \times 10^{-3}\text{Pa} \cdot \text{s}$, and $\sigma_{1,2} = \sigma_{1,3} = \sigma_{2,3} = 888\text{N/m}$. The velocity scale for non-dimensionalizing the governing equations is 66.6m/s, which is the velocity of the bottom wall. As a result, the Reynolds number and Weber number become $Re = 66.6$ and $We = 5$. The dimensionless height of the domain becomes 1.5, while the grid size remains the same. The bottom wall is moving backward with a unit dimensionless velocity. Results are shown in Fig.5.50 and Fig.5.51, and the behaviors of the drops are significantly different from those on a stationary wall. It is observed that the Phase 1 (yellow) drop climbs onto the Phase 2 (blue) drop, and thoroughly leave the bottom wall, sitting on the Phase 2 drop. Then, it crosses the Phase 2 drop and returns on the bottom wall. At the end, the Phase 1 drop is still in contact with the Phase 2 drop but moves in front of it.

5.6 Miscible falling drop

A liquid drop, initially in the air, falls down into another liquid at the bottom, and gradually mixing with the bottom liquid, and the proposed N-phase-M-component model is used. This is a three-phase case where the liquid drop (Phase 01) is miscible with the other bottom liquid (Phase 02) while the air (Phase 03) is not miscible with either of the liquids (Phases 01 or 02). The densities and viscosities of Phases 01, 02, and 03 are $\rho_{01} =$

3000kg/m^3, $\mu_{01} = 1.5 \times 10^{-3}$Pa $\cdot$ s, $\rho_{02} = 1000$kg/m^3, $\mu_{02} = 1 \times 10^{-3}$Pa $\cdot$ s, $\rho_{03} = 1$kg/m^3, and $\mu_{03} = 2 \times 10^{-5}$Pa $\cdot$ s. The surface tension between the immiscible pairs is 0.0728N/s and the diffusivity between the miscible pair is 1×10^{-5}m^2/s. The gravity is pointing downward with a magnitude 9.8m/s^2.

As mentioned in Section 2.6.1, this three-phase case can be turned into a 2-phase-1-component setup, where Phase 01 is represented by Phase 1 with 1mol/m^3 Component 1, Phase 02 is represented by pure Phase 1, Phase 03 is represented by pure Phase 2, and Component 1 is only dissolvable in Phase 1, i.e., $\{I^M_{p,q}\} = \{1, 0\}$. As a result, one has $\rho^\phi_1 = 1000$kg/m^3, $\mu^\phi_1 = 1 \times 10^{-3}$Pa $\cdot$ s, $\rho^\phi_2 = 1$kg/m^3, $\mu^\phi_2 = 2 \times 10^{-5}$Pa $\cdot$ s, $\sigma_{1,2} = 0.0728$N/s, $\rho^C_1 = 2000$kg/mol, $\mu^C_1 = 5 \times 10^{-4}$Pa $\cdot$ s $\cdot$ m^3/mol, $D_{1,1} = 1 \times 10^{-5}$m^2/s. The governing equations are non-dimensionalized by a length scale 0.01m, a density scale 1kg/m^3, an acceleration scale 1m/s^2, and a concentration scale 1mol/m^3. Consequently, Phase 01 is represented by Phase 1 with unity concentration of Component 1 in the results reported.

The domain considered is $[1 \times 1]$ with periodic boundaries along the x axis and with free-slip boundaries along the y axis. The domain is discretized by $[128 \times 128]$ cells and the time step size is $\Delta t = 10^{-4}$. Initially, the circular drop of Phase 1 is at $(0.5, 0.75)$ with a radius 0.15, and there is Component 1 with a homogeneous unity concentration inside it. The bottom of the domain below $y = 0.3$ is filled with pure Phase 1. The rest of the domain is occupied by Phase 2.

The results are shown in Fig.5.52 by the configurations of the phases and components at selected moments. Phase 1 is filled by the yellow color and Phase 2 is represented by the white color. Component 1 is shown by its concentration along with the yellow lines representing the interfaces between Phases 1 and 2. Due to both the heaviness of the drop, which is 3000 times heavier than its surrounded air, and the strong surface tension, the drop is falling without obvious deformation until it is close to the bottom liquid tank. At this moment, the bottom of the drop is flattened slightly. During the falling of the drop, Component 1 inside the drop preserves to be homogeneous. As a result, Phase 01 is well represented by the combination of Phase 1 and Component 1 with unity concentration. After the drop merges to the bottom tank, Component 1 starts to be transported, by both convection and diffusion, inside the liquid tank, and this process is modeling the mixing

between Phases 01 and 02. one can observe that Component 1 is first transported along the phase interface. Due to the inertia of the drop, the interface reaches a large "U" shape before it bounces back. Most of Component 1 is transported to the bottom of the domain. Since the vertical velocity close to the bottom free-slip boundary is small, and Component 1 is heaviest among all the phases and components, the major part of Component 1 stays at the bottom, and only small amount of it moves upward following the movement of the interface. As the interface moves upward, the Rayleigh-Taylor instability occurs. It should be noted that the appearance of Component 1 makes the fluid denser. Consequently, the fluid with a larger amount of Component 1, is penetrating to the fluid with less amount of Component 1, and the Rayleigh-Taylor instability is triggered. The interface keeps moving upward then downward while the amplitude is attenuated by the viscous effect. In the meanwhile, Component 1 becomes more homogeneous inside the bottom tank as time goes on. At the end of the simulation, one can observe that the movement of the interface is not significant and Component 1 is distributed homogeneously inside Phase 1 (the bottom liquid tank). Fig.5.53 shows the time histories of the total volumes of individual phases and the total amount of Component 1 in its dissolvable region. All the quantities in Fig.5.53 are conserved exactly even though the problem is highly complicated and dynamical.

5.7 Falling drops with moving contact lines

To demonstrate the capability of the N-phase-M-component model and scheme, an example that includes three phases and three components, large density and viscosity ratios, multiphase interfacial tensions, and the effect of contact angles and moving contact lines, is presented.

The densities and viscosities of the 3 pure phases are $\rho_1^\phi = 1000\text{kg/m}^3$, $\mu_1^\phi = 10^{-3}\text{Pa}\cdot\text{s}$, $\rho_2^\phi = 500\text{kg/m}^3$, $\mu_2^\phi = 10^{-1}\text{Pa}\cdot\text{s}$, $\rho_3^\phi = 1\text{kg/m}^3$, and $\mu_3^\phi = 2\times10^{-5}\text{Pa}\cdot\text{s}$. The interfacial tensions are $\sigma_{1,2} = 0.04\text{N/m}$, $\sigma_{1,3} = 0.0728\text{N/m}$, and $\sigma_{2,3} = 0.055\text{N/m}$, and the gravity is $\mathbf{g} = \{0, -9.8\}\text{m/s}^2$. The contact angle between Phases 1 and 2 at the right boundary is 135^0 and the other is 90^0. The densities and viscosities of the 3 components are $\rho_1^C = 500\text{kg/mol}$, $\mu_1^C = 5\times10^{-4}\text{Pa}\cdot\text{s}\cdot\text{m}^3/\text{mol}$, $\rho_2^C = 100\text{kg/mol}$, $\mu_2^C = 1\times10^{-3}\text{Pa}\cdot\text{s}\cdot\text{m}^3/\text{mol}$, $\rho_3^C = 1\text{kg/mol}$,

$\mu_3^C = 1 \times 10^{-4}\text{Pa} \cdot \text{s} \cdot \text{m}^3/\text{mol}$. Component 1 is only dissolvable in Phase 1 with diffusivity $1\times10^{-5}\text{m}^2/\text{s}$, Component 2 is dissolvable in both Phases 1 and 2 with diffusivity $5\times10^{-4}\text{m}^2/\text{s}$ and $5 \times 10^{-5}\text{m}^2/\text{s}$, respectively, and Component 3 is dissolvable in both Phases 1 and 3 with diffusivity $5 \times 10^{-6}\text{m}^2/\text{s}$ and $2 \times 10^{-5}\text{m}^2/\text{s}$, respectively. The governing equations are non-dimensionalized with a length scale 0.01m, a density scale $1\text{kg}/\text{m}^3$, an acceleration scale $1\text{m}/\text{s}^2$, and a concentration scale $1\text{mol}/\text{m}^3$.

The domain considered is $[1 \times 1]$ with no-slip boundaries. The domain is discretized by $[128 \times 128]$ cells and the time step size is $\Delta t = 10^{-4}$. Initially, a drop of Phase 1 at $(0.3, 0.75)$ with a radius 0.15 is above a tank of Phase 1 filling $0 \leqslant y \leqslant 0.3$. A drop of Phase 2 is at $(0.75, 0.6)$ with a radius 0.1. The rest of the domain is filled by Phase 3. Components 1 and 2 are homogeneously distributed with unity concentration inside the drops of Phases 1 and 2, respectively. Component 3 is distributed between $x = 0.5$ and $x = 0.6$ with unity concentration.

The results are shown in Fig.5.54, and inside each panel, the top-left shows the configuration of the three phases, the top-right, bottom-left, and bottom-right show the concentrations of Components 1, 2, and 3, respectively. Phase 1 is filled by the blue color, Phase 2 is represented by the yellow color, and the white color is used to present Phase 3. The blue lines in the contours of the components represent the interface of Phase 1 and the yellow lines are the interface of Phase 2. The falling of the two drops is very similar to those in Section 5.6. Both drops deform little until they are close to the bottom tank of Phase 1, and the components inside the drops remain homogeneous. The diffusivity of Component 3 in Phase 3 is 4 times larger than that in Phase 1, and the flow in Phase 3 is more significant due to the falling of the drops. Component 3 is more distributed in Phase 3 and some amount of it has entered the drop of Phase 1, while it is still clustered inside the bottom tank of Phase 1. The drop of Phase 2 (the yellow one) first reaches the tank of Phase 1. It is floating on Phase 1 since Phase 2 is lighter than Phase 1. Component 2, carried by the drop of Phase 2, starts to diffuse into the bottom tank of Phase 1. The diffusivity of Component 2 in Phase 1 is 10 times larger than that in Phase 2, and it is the largest among all the diffusivities. As a result, Component 2 becomes homogeneous inside both Phases 1 and 2 in a very short period of time. After the drop of Phase 1 (the blue one) merges to the bottom tank, Com-

ponent 1 is released to the tank. Since it is lighter than that in Section 5.6, it clusters close to the interface between Phases 1 and 3, follows the movement of the interface, and in the meantime keeps diffusing. The surface wave introduced by the merging of the drop of Phase 1 to the bottom tank pushes Phase 2 towards the right wall. After that, the drop of Phase 2 is lifted and then stretched as the surface wave moves up and down. The surface wave is gradually settled down by the viscous effect, and the 135^0 contact angle between Phases 1 and 2 at the right wall is more clearly observable. As time goes on, the phases gradually reach their equilibrium configurations, and Components 1 and 3 keep homogenizing inside their corresponding dissolvable regions. Specifically, Component 1 only exists inside Phase 1 and none of it is observed in Phases 2 and 3 from our results. On the other hand, Component 2 is allowed in both Phases 1 and 3, and it is not observed in Phase 2 from the results. Again, the time histories of the total volumes of individual phases and the total amounts of each component in its corresponding dissolvable region are plotted in Fig.5.55, and they are exactly conserved even though the problem considered is highly complicated and dynamical.

Finally, the effect of the contact angle is illustrated in Fig.5.56 by comparing the present case to the case where all the contact angles are 90^0. It is observed that the effect of the contact angle doesn't change much of the dynamics of the problem while it becomes important for the equilibrium configuration, so only the results at $t = 5$ are shown. It is clear that in the case with contact angles all being 90^0, i.e., in Fig.5.56 b), the interface of Phases 1 and 3 is finally horizontal, and the drop of Phase 2 looks like a section of an ellipse which is symmetric with respect to the interface of Phases 1 and 3. On the other hand, in the case with the 135^0 contact angle between Phases 1 and 2 at the right wall, i.e., in Fig.5.56 a), the interface between Phases 1 and 2 is close to an inclined straight line, and the interface between Phases 1 and 3 is not horizontal.

5.8 Rising bubbles with solidification

Here, a complicated case including interactions among the gas, liquid, and solid phases and solidification is considered, and the thermo-gas-liquid-solid model including solidifica-

tion/melting is used. The material properties of the liquid phase are $\rho_M^L = 2.475 \times 10^3 \text{kg/m}^3$, $\mu_M^L = 1.4 \times 10^{-3} \text{Pa} \cdot \text{s}$, $(C_p)_M^L = 1.0424 \times 10^3 \text{J/(K} \cdot \text{kg)}$, and $\kappa_M^L = 91 \text{W/(m} \cdot \text{K)}$. They are $\rho_M^S = 2.70 \times 10^3 \text{kg/m}^3$, $\mu_M^S = 1.4 \times 10^{-3} \text{Pa} \cdot \text{s}$, $(C_p)_M^S = 0.91 \times 10^3 \text{J/(K} \cdot \text{kg)}$, and $\kappa_M^S = 211 \text{W/(m} \cdot \text{K)}$ for the solid phase, and $\rho_G = 0.4 \times 10^3 \text{kg/m}^3$, $\mu_G = 4 \times 10^{-5} \text{Pa} \cdot \text{s}$, $(C_p)_G = 1.1 \times 10^3 \times 10^3 \text{J/(K} \cdot \text{kg)}$, and $\kappa_G = 61 \times 10^{-3} \text{W/(m} \cdot \text{K)}$ for the gas phase. The melting temperature is $T_M = 933.6\text{K}$, latent heat is $L = 3.8384 \times 10^5 \text{J/kg}$, the surface tension is $\sigma = 0.87 \text{N/m}$, the gravity is $\mathbf{g} = (0, -9.8) \text{m/s}^2$, and the Gibbs-Thomson and linear kinetic coefficients are chosen to be $\Gamma_\phi = 1.3 \times 10^{-3} \text{m} \cdot \text{K}$ and $\mu_\phi = 1.3 \times 10^{-3} \text{m/(s} \cdot \text{K)}$, respectively. The governing equations are non-dimensionalized by a density scale 1kg/m^3, a length scale 0.01m, an acceleration scale 1m/s^2, and a temperature scale 933.6K the same as the melting temperature.

A unit domain is considered. Both the left and right boundaries are no-slip and adiabatic walls. The bottom boundary is no-slip with a fixed temperature $T_{bottom} = 0.5$. The top boundary has a fixed pressure $P_{top} = 0$ and a zero heat flux. The domain is discretized by 128×128 cells, and the time step is $\Delta t = 10^{-4}$. The initial condition of the phases is illustrated in the first snapshot of Fig.5.57. Above $y = 0.75$ is the gas phase, while the solid phase is at the bottom below $y = 0.1$. In the middle of the domain is the liquid phase inside which there are three circular gas bubbles. The radii of the bubbles from left to right are 0.075, 0.125, and 0.1, and their centers are at $(0.175, 0.225)$, $(0.5, 0.3)$, and $(0.8, 0.26)$, respectively. The initial temperature is 0.5, the same as T_{bottom}, inside the solid phase while it is 1.1 elsewhere. Note that the non-dimensionalized melting temperature is 1. The initial velocity is zero, and $\eta_\varphi = \eta_\phi = h$ and $M_\varphi \lambda_\varphi = 10^{-9}$ are set.

Results are shown in Fig.5.57. The gas, liquid, and solid phases are filled by the white, orange, and blue colors, and the solid phase becomes green when the phase change is finished. The bubbles are moving upward due to the buoyancy effect, and, at the same time, the liquid is solidified as its temperature is cooled down by the bottom wall. The motion of the bubbles drives the liquid and produces melt convection. As a result, the liquid below the bubbles is solidified faster than its neighbor, and the liquid-solid interface first "catches" the left bubble then the right one. As the largest bubble at the middle rises, the gas-liquid interface above starts to be perturbed, which, in turn, deviates the bubble rising from its vertical line.

When the middle bubble merges the gas-liquid interface, a strong capillary wave is produced due to the surface tension. As the capillary wave travels back and forth, the liquid-solid interface keeps moving upward. Since the heat conductivity of the gas is much smaller than the liquid or solid, the solidification is slower right above the two trapped gas bubbles, and the liquid-solid interface forms a "V" shape there. As the liquid-solid interface gets closer to the gas-liquid one, the capillary wave is quickly attenuated by the viscosity, due to the zero velocity of the solid. At the end of the simulation, the liquid is completely solidified with two hollows formed by the right and left bubbles.

5.9 Melting and solidification

Here, melting a solid rectangle and then solidifying it again are presented, and the thermo-gas-liquid-solid model including solidification/melting is used. The material properties and setup are identical to those in Section 5.8, except that the thermal conductivity of the gas is $\kappa_G = 100\mathrm{W}/(\mathrm{m}\cdot\mathrm{K})$ and that the bottom wall becomes adiabatic, and the temperature at the other boundaries is 2 before $t = 2$ then 0.5. The initial condition of the phases is illustrated in the first snapshot of Fig.5.58. A rectangular solid with width 0.6 and height 0.4 is sitting above the bottom wall, and it traps two circular gas bubbles whose radii are 0.075 and 0.1, and centers are located at $(0.65, 0.1)$ and $(0.35, 0.25)$, respectively. The initial temperature is 0.8 inside the solid rectangle including the gas bubbles, while it is 2 elsewhere. Recall that the non-dimensionalized melting temperature is 1. The initial velocity is zero, and $\eta_\varphi = \eta_\phi = h$ and $M_\varphi \lambda_\varphi = 10^{-9}$ are set.

Results are shown in Fig.5.58. The two top corners of the solid rectangle first melt, and then the lateral edges. The gas in the larger bubble is released to the ambient, and the melted liquid covers the solid and flows downward to the bottom wall. The solid phase gradually disappears and the smaller gas bubble is finally released. The smaller bubble slides on the bottom wall back and forth, following the capillary wave above, and finally reaches the right wall. As the temperature at the boundaries becomes lower than the melting temperature, solidification first appears at the lateral walls, and the front of the liquid-solid interface moves towards the middle, along with the capillary wave moving up and down. At the end of the

simulation, the melted liquid is completely solidified with a gas bubble at the bottom-right corner.

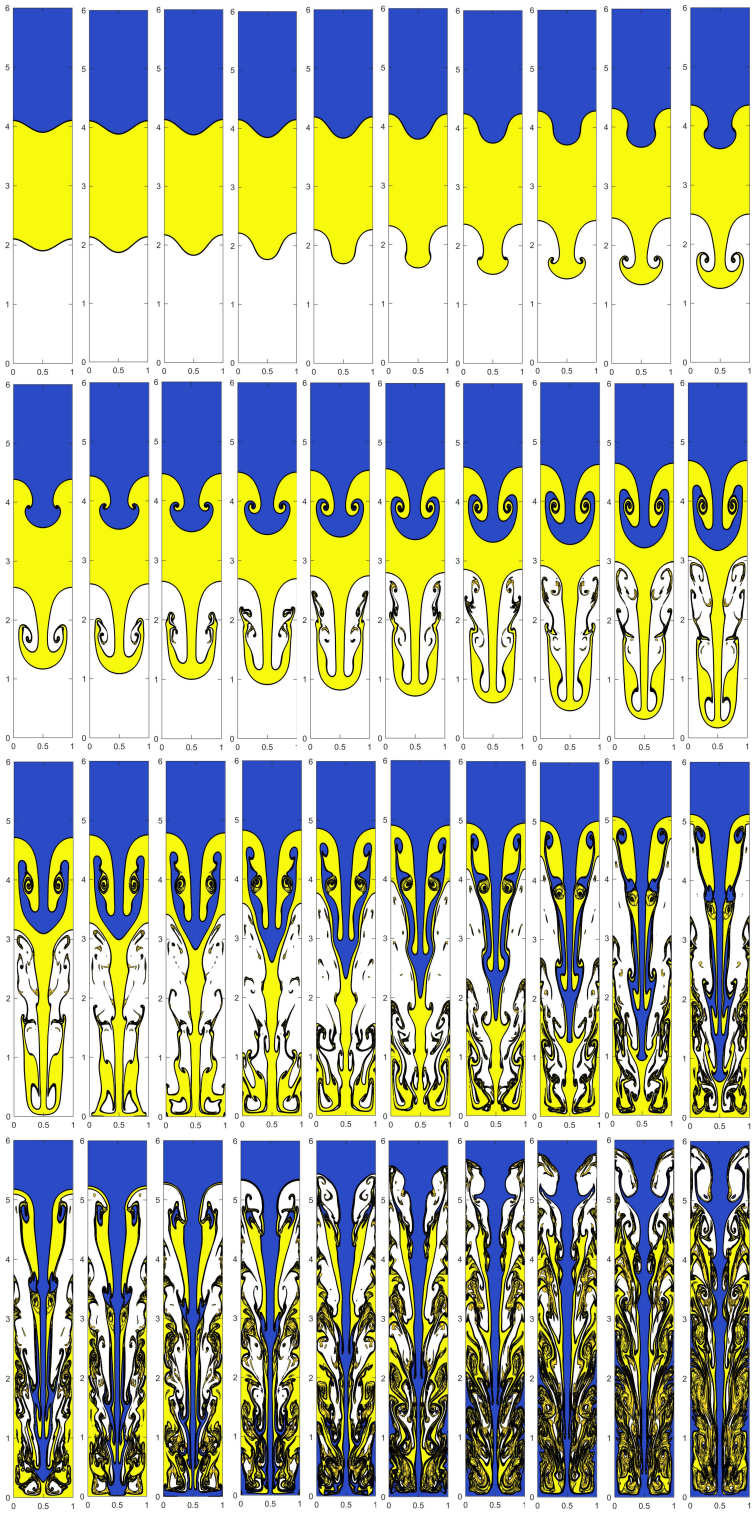

Figure 5.11. Evolutions of the three phases in the three-phase Rayleigh-Taylor instability problem using CH. From left to right, top to bottom, t is 0.00, 0.50, 0.75, 1.00, ..., 10.00. Blue: Phase1, Yellow: Phase2, and White: Phase3.

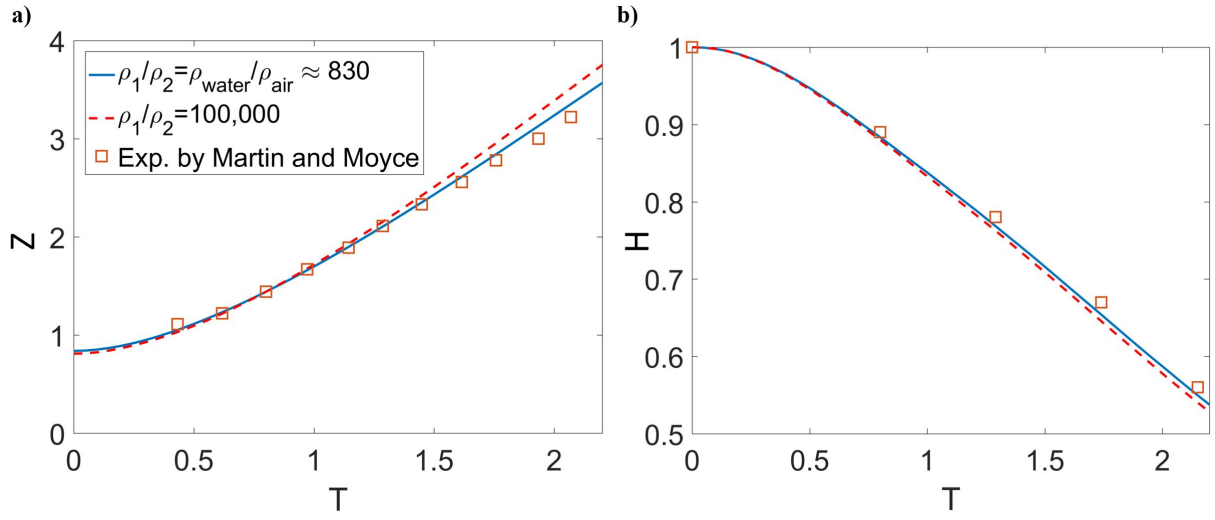

Figure 5.12. Results of the dam break using two-phase CH-B. a) Location of the front Z vs. T, and b) location of the height H vs. T.

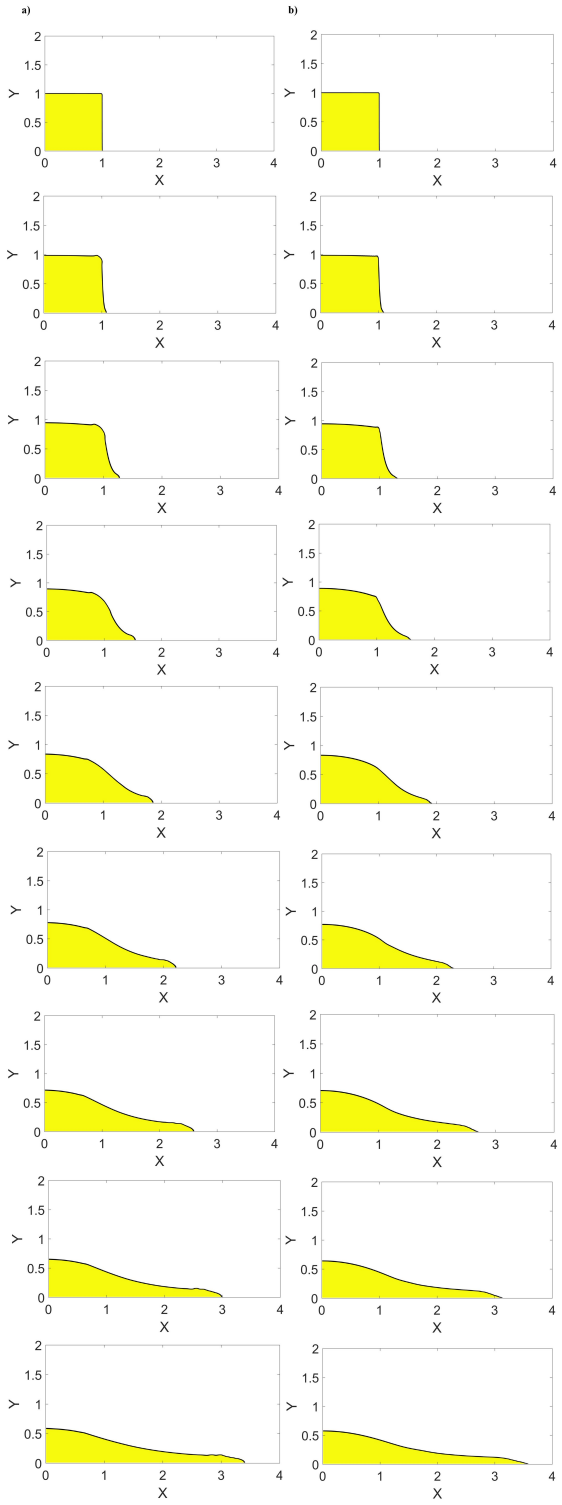

Figure 5.13. Snapshots of the dam break using two-phase CH-B with density ratio a) $\rho_1 = \rho_2 = \rho_{water}/\rho_{air} \approx 830$, and b) $\rho_1/\rho_1 = 100,000$. From top to bottom, $t = 0, 0.25, 0.5, 0.75, 1, 1.25, 1.5, 1.75, 2$.

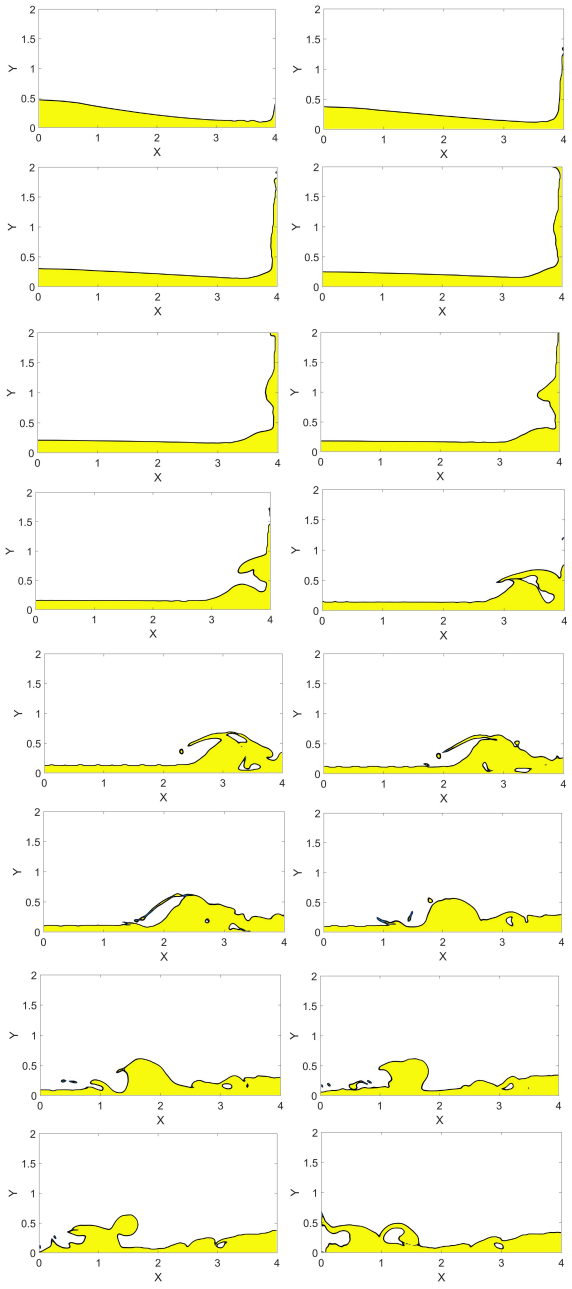

Figure 5.14. Snapshots of the dam break using two-phase CH-B with density ratio $\rho_1 = \rho_2 = \rho_{water}/\rho_{air} \approx 830$ (continued from Fig.5.13 a)). From left to right, and top to bottom, t is from 2.5 to 10 with 0.5 increment.

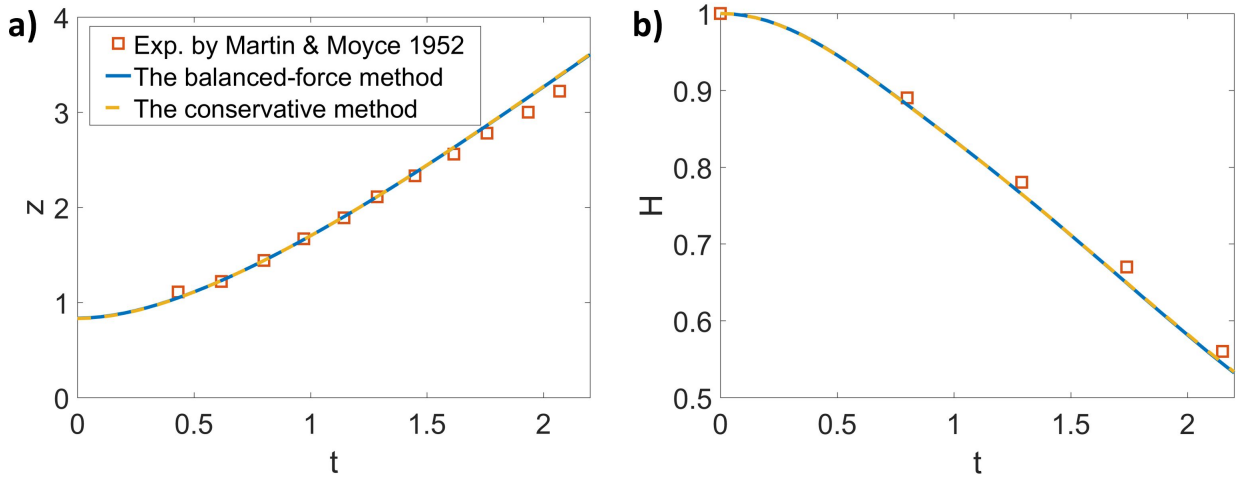

Figure 5.15. The front and the height of the water column versus time using two-phase CAC-B and CAC-C. a) The front of the water column versus time, b) the height of the water column versus time

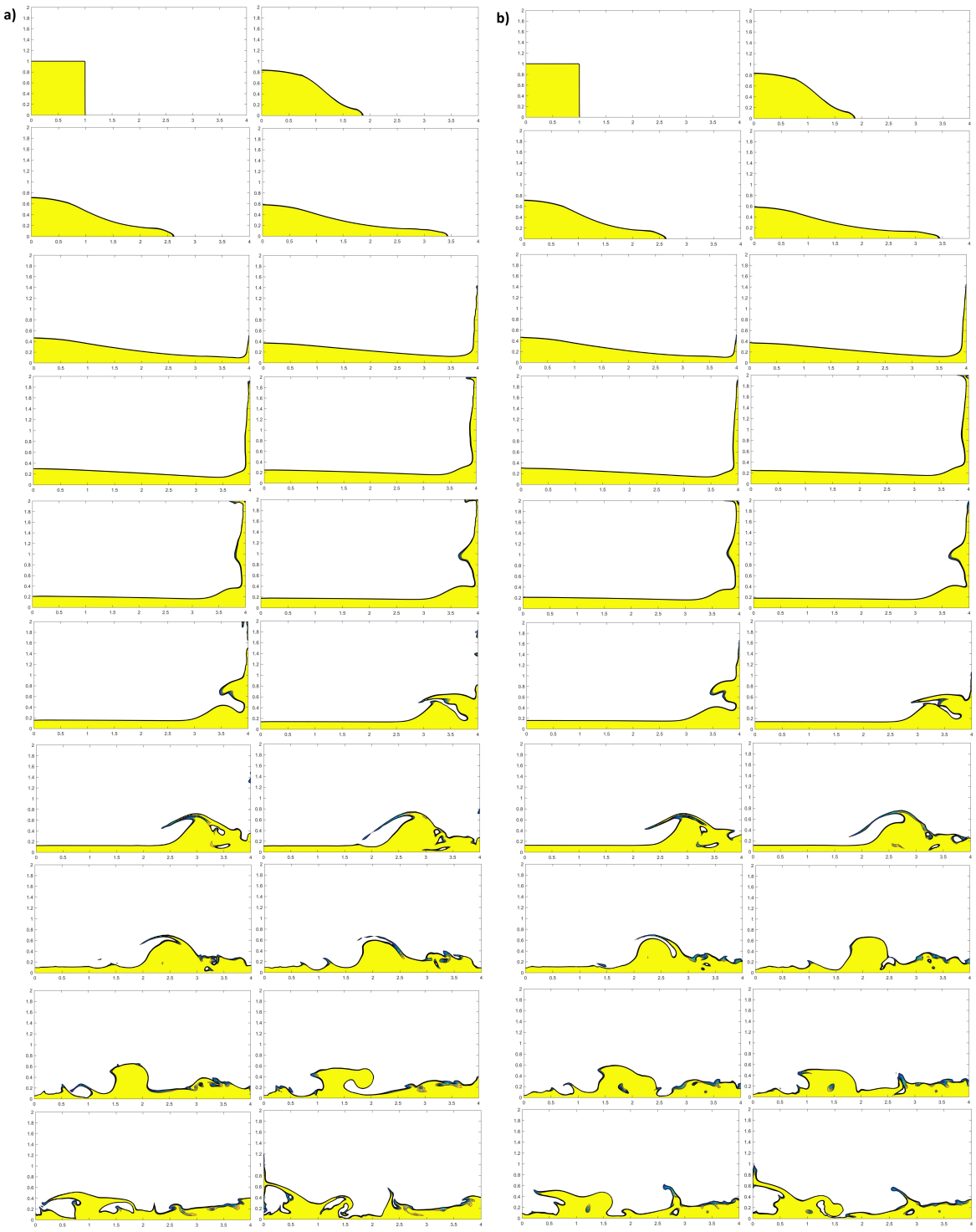

Figure 5.16. The evolution of the interface of the dam break problem using two-phase CAC-B and CAC-C at $t = 0$, $t = 1$, $t = 1.5$, $t = 2$, $t = 2.5$,..., $t = 10$ from left to right and from top to bottom. a) The balanced-force method (two-phase CAC-B), b) the conservative method (two-phase CAC-C).

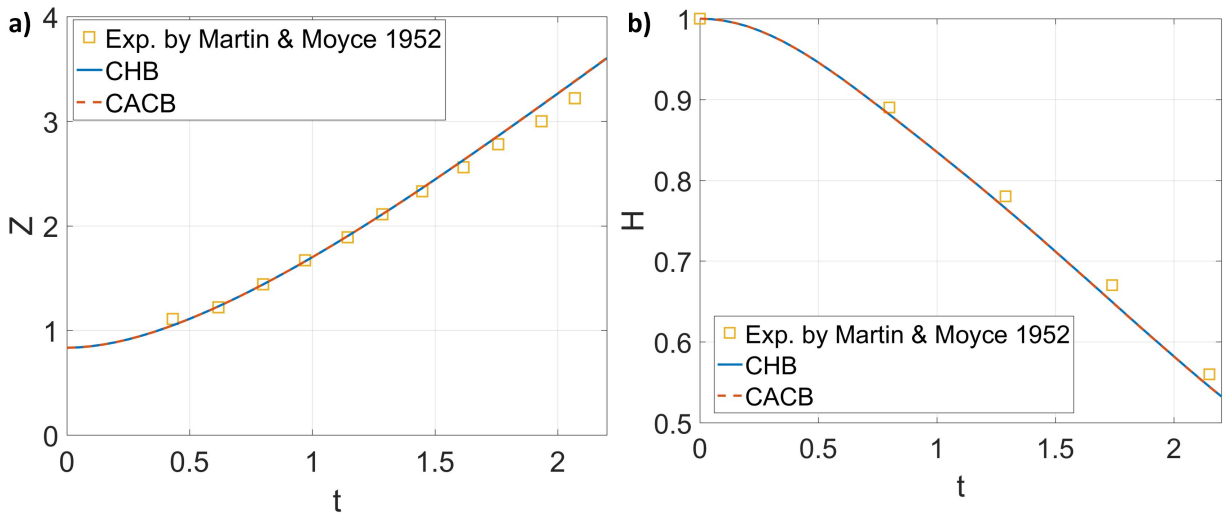

Figure 5.17. Front and height of the water column vs. t using CHB-B and CACB-B. a) Front of the water column. b) Height of the water column.

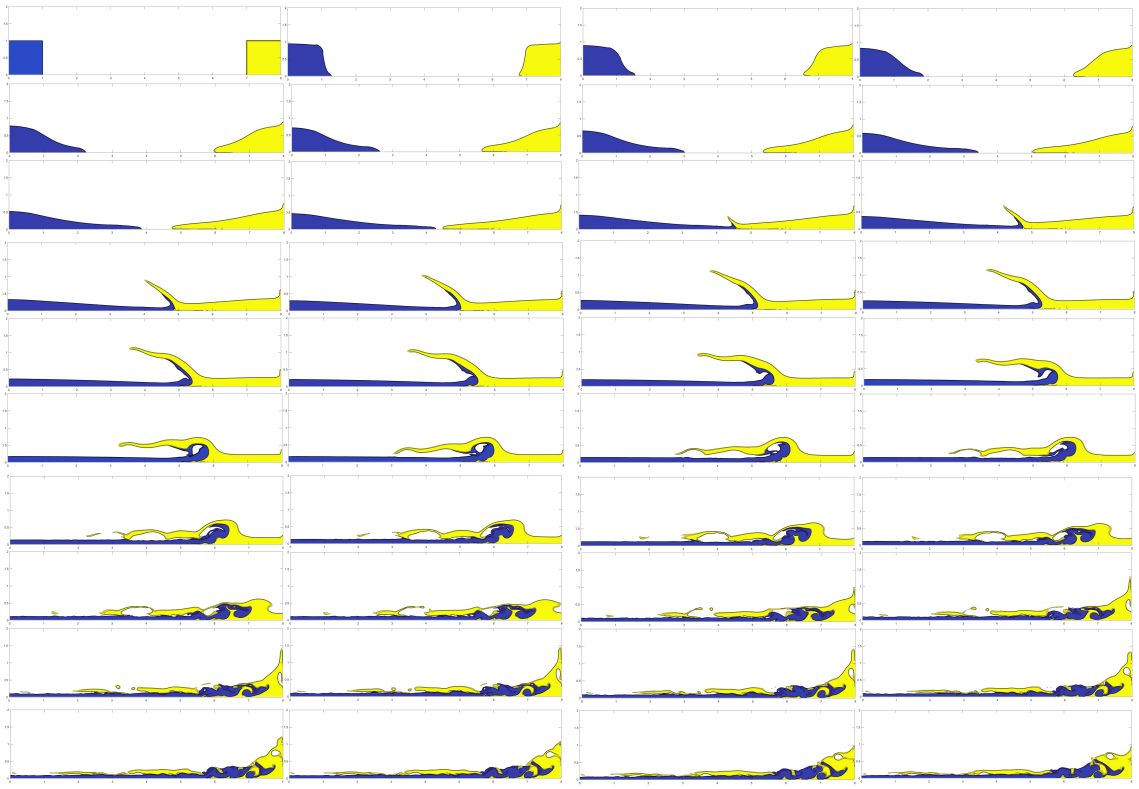

Figure 5.18. Configurations of the three-phase dam break from CHB-B at $t = 0.00, 0.50, 0.75, 1.00, ..., 10.00$. Blue: Water (phase 1). Yellow: Oir (phase 2). White: Air (phase 3).

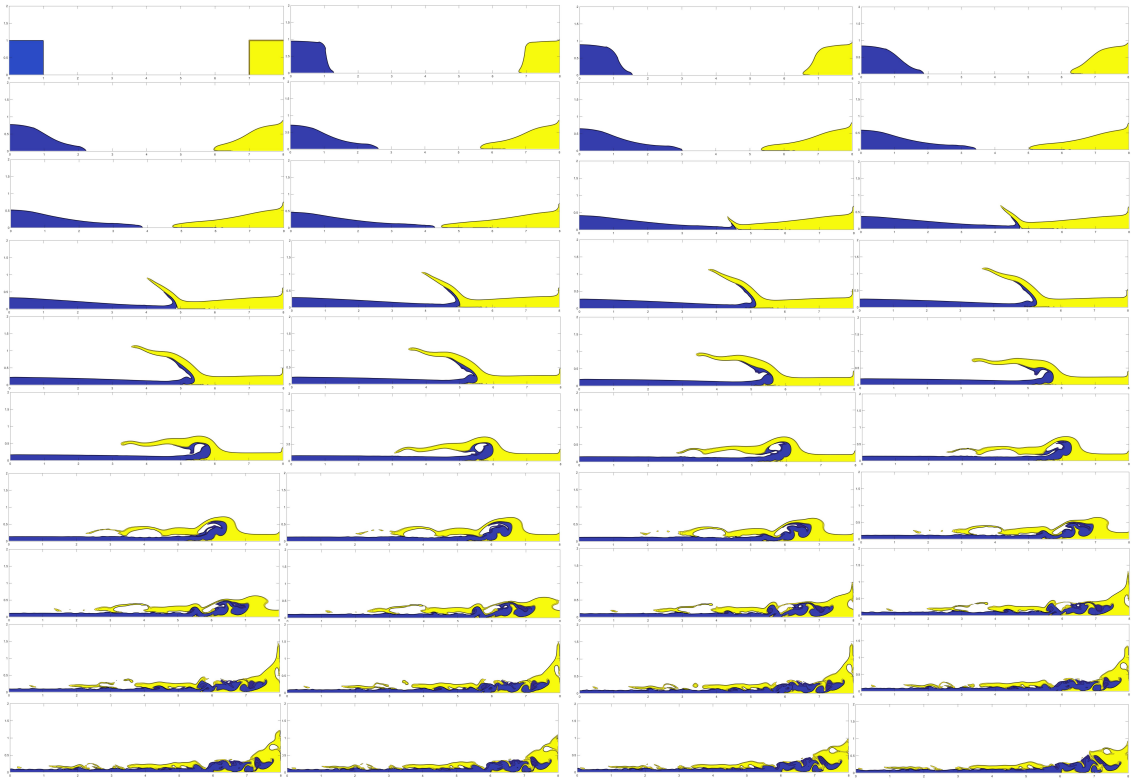

Figure 5.19. Configurations of the three-phase dam break from CACB-B at $t = 0.00, 0.50, 0.75, 1.00,...,10.00$. Blue: Water (phase 1). Yellow: Oir (phase 2). White: Air (phase 3).

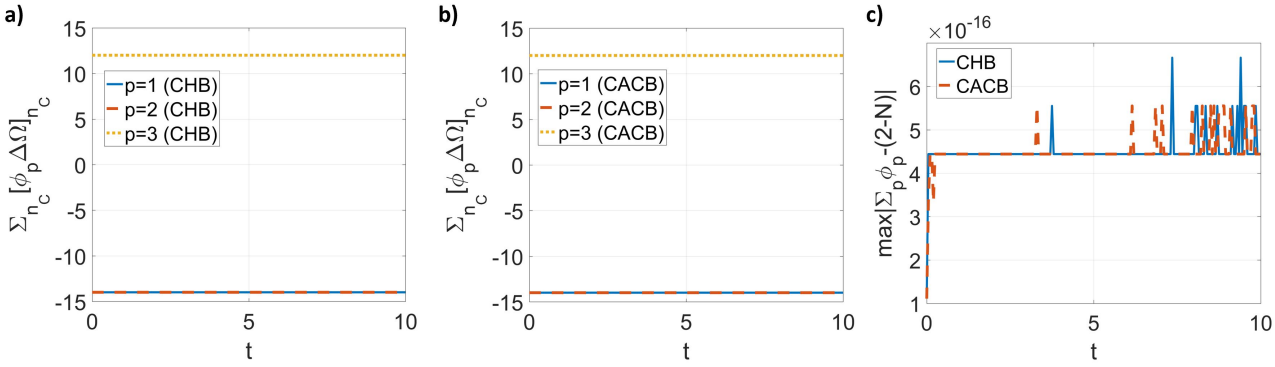

Figure 5.20. Results of the three-phase dam break. a) Mass conservation of individual phases from CHB-B. b) Mass conservation of individual phases from CACB-B. c) Error of the summation constraint for the order parameters from CHB-B and CACB-B.

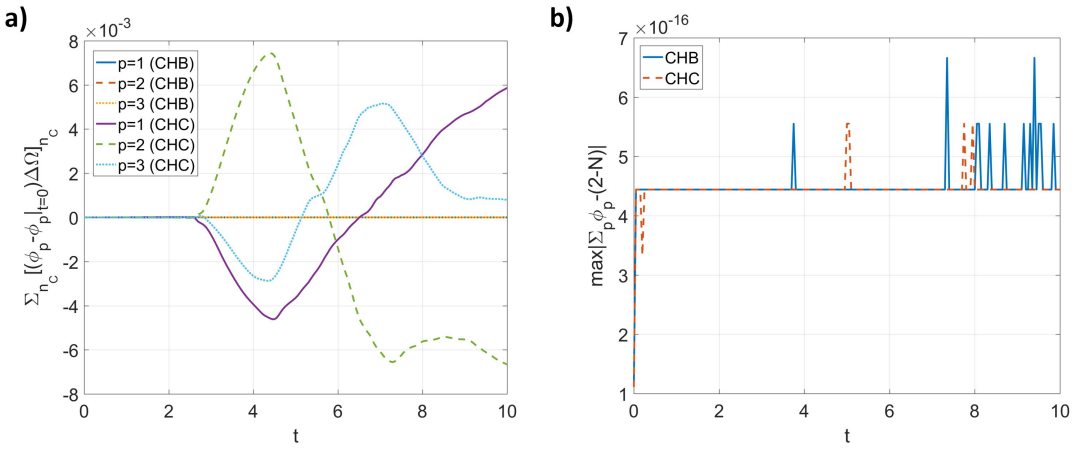

Figure 5.21. Results of the three-phase dam break from CHB-B and CHC-B (which is CH-B but including the clipping and rescaling steps in the boundedness mapping). a) Errors of mass conservation of individual phases. b) The Error of the summation constraint for the order parameters.

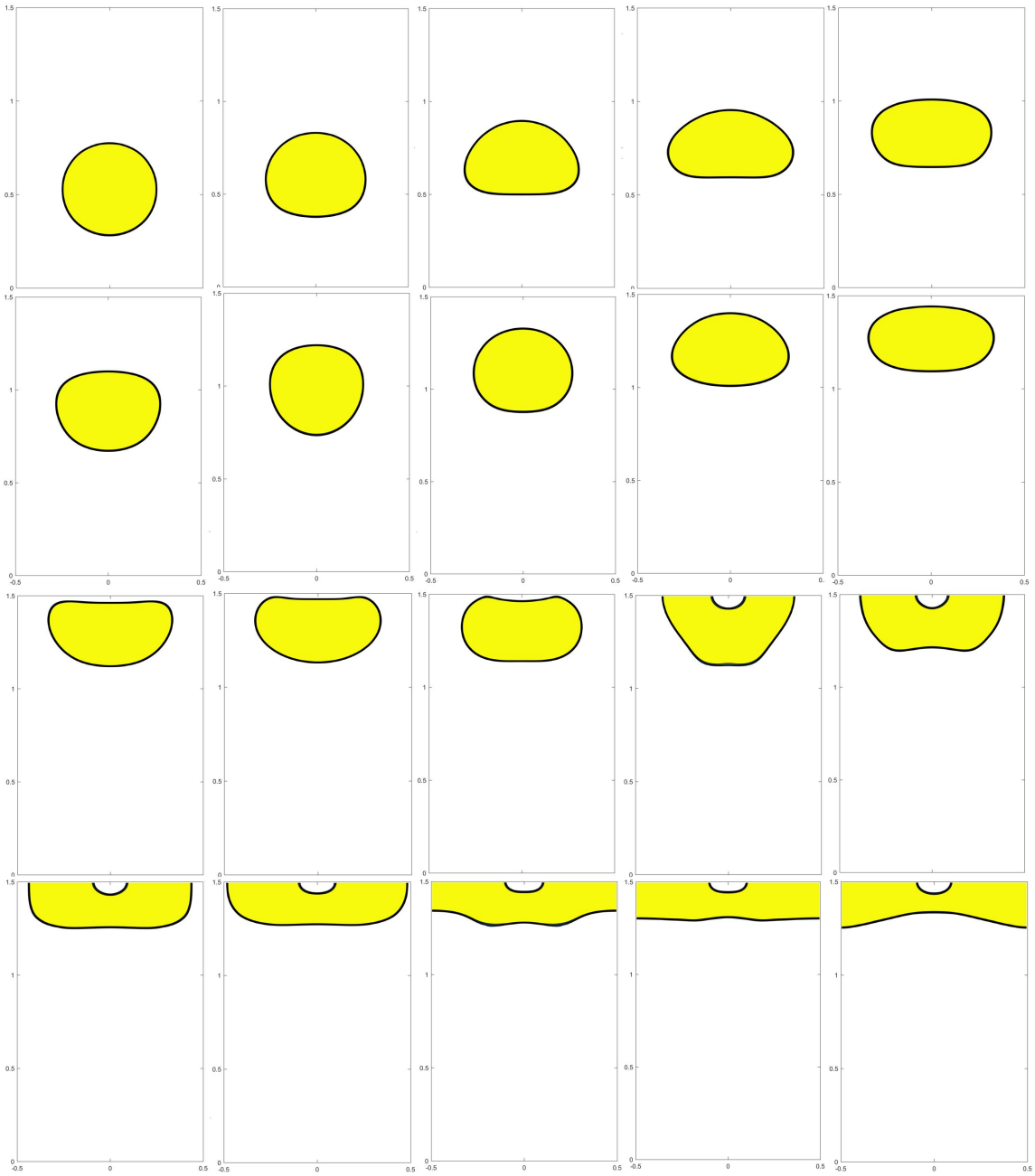

Figure 5.22. Snapshots of the rising bubble using two-phase CH-B in R90L90T90. From left to right, top to bottom, t changes from 0.1 to 2 with 0.1 increment.

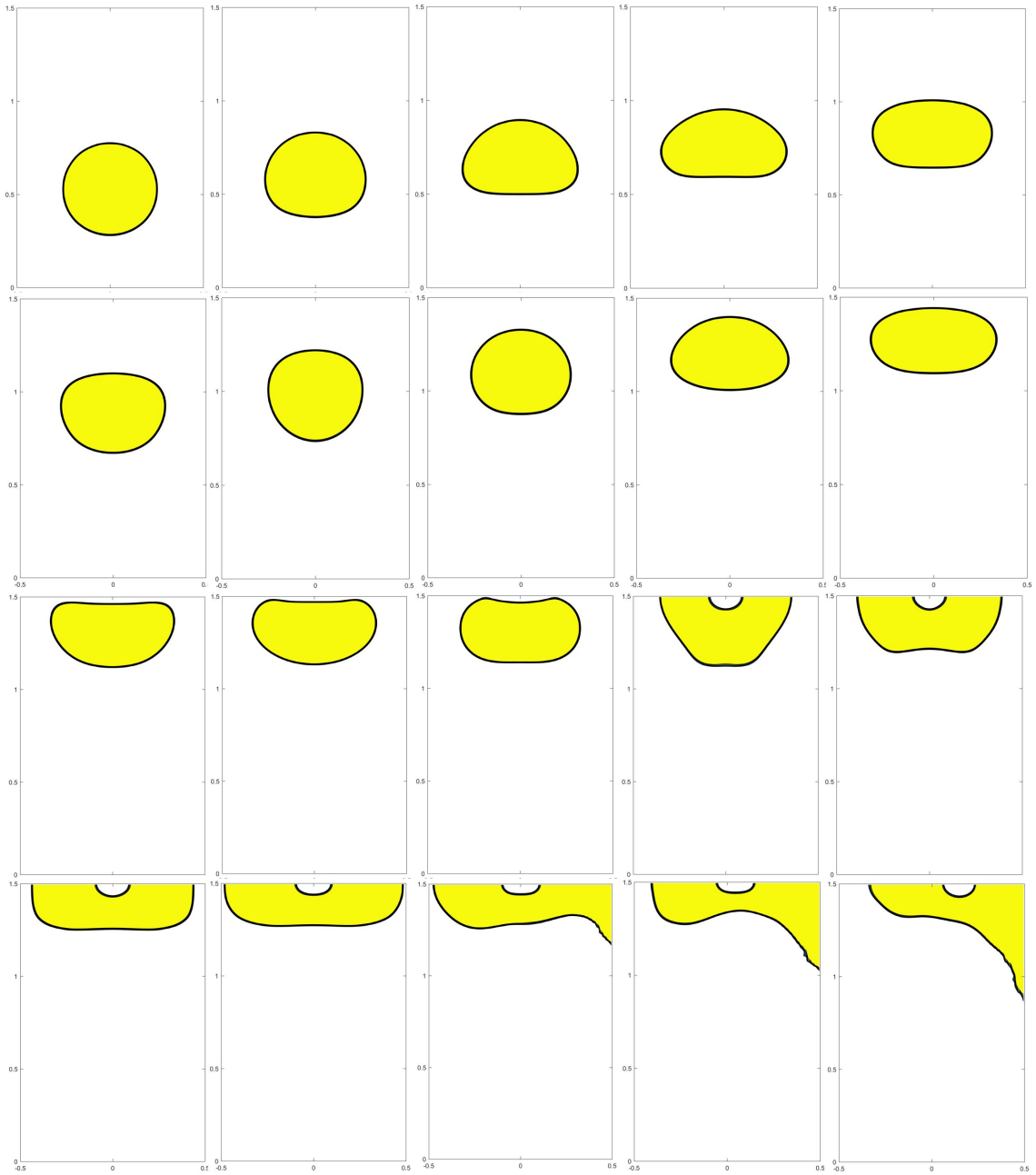

Figure 5.23. Snapshots of the rising bubble using two-phase CH-B in R30L150T90. From left to right, top to bottom, t changes from 0.1 to 2 with 0.1 increment.

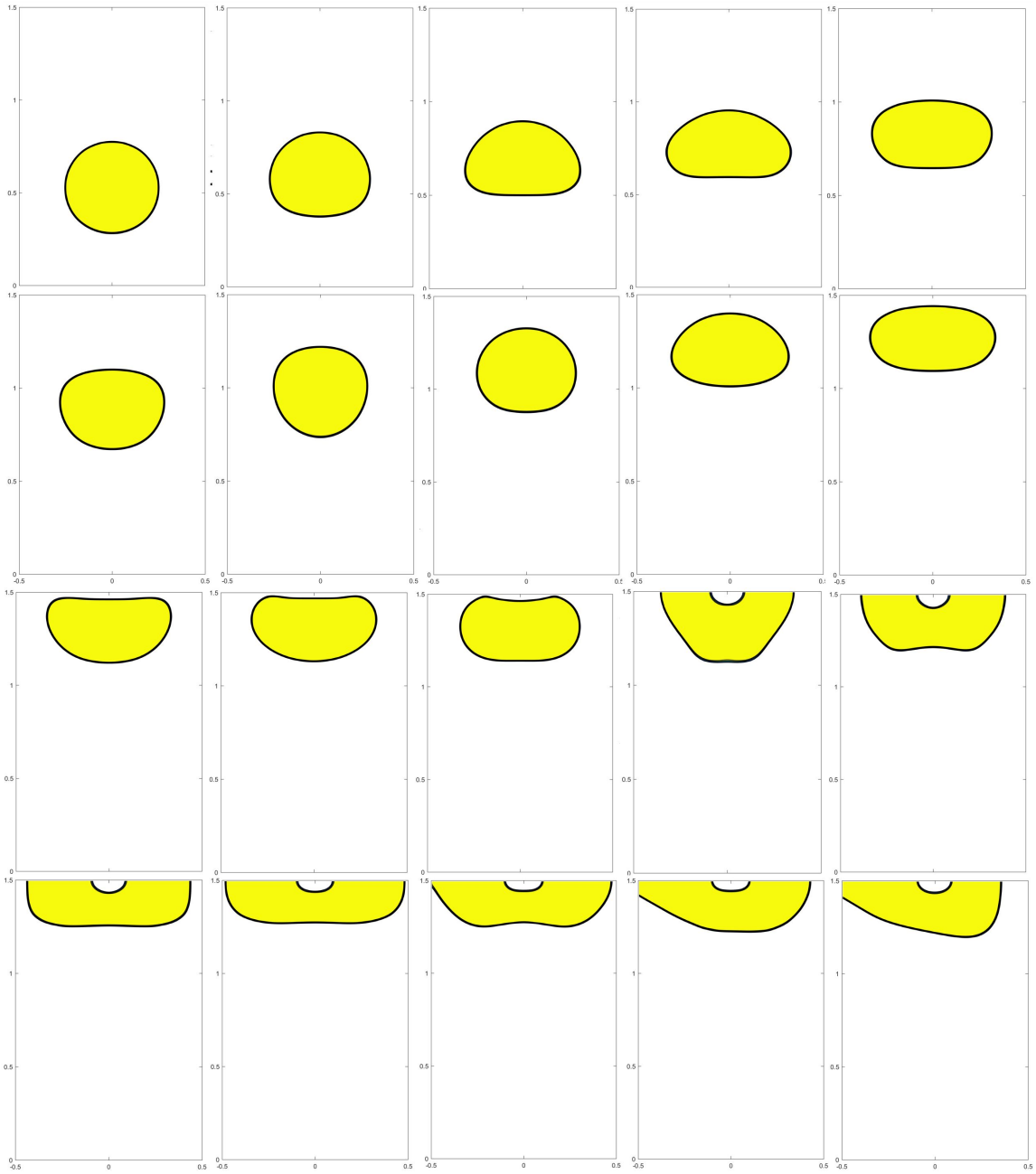

Figure 5.24. Snapshots of the rising bubble using two-phase CH-B in R150L120T90. From left to right, top to bottom, t changes from 0.1 to 2 with 0.1 increment.

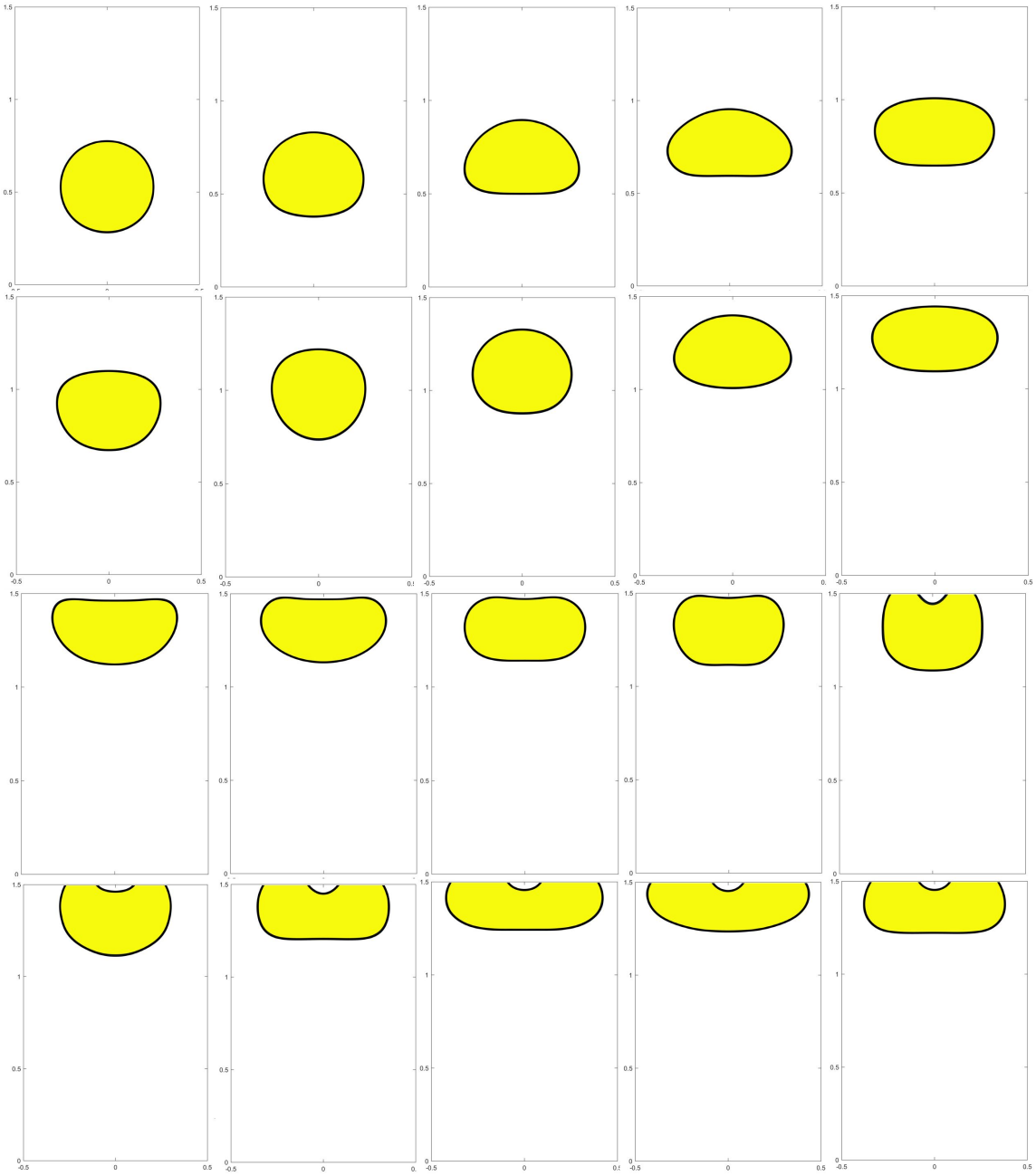

Figure 5.25. Snapshots of the rising bubble using two-phase CH-B in R30L60T120. From left to right, top to bottom, t changes from 0.1 to 2 with 0.1 increment.

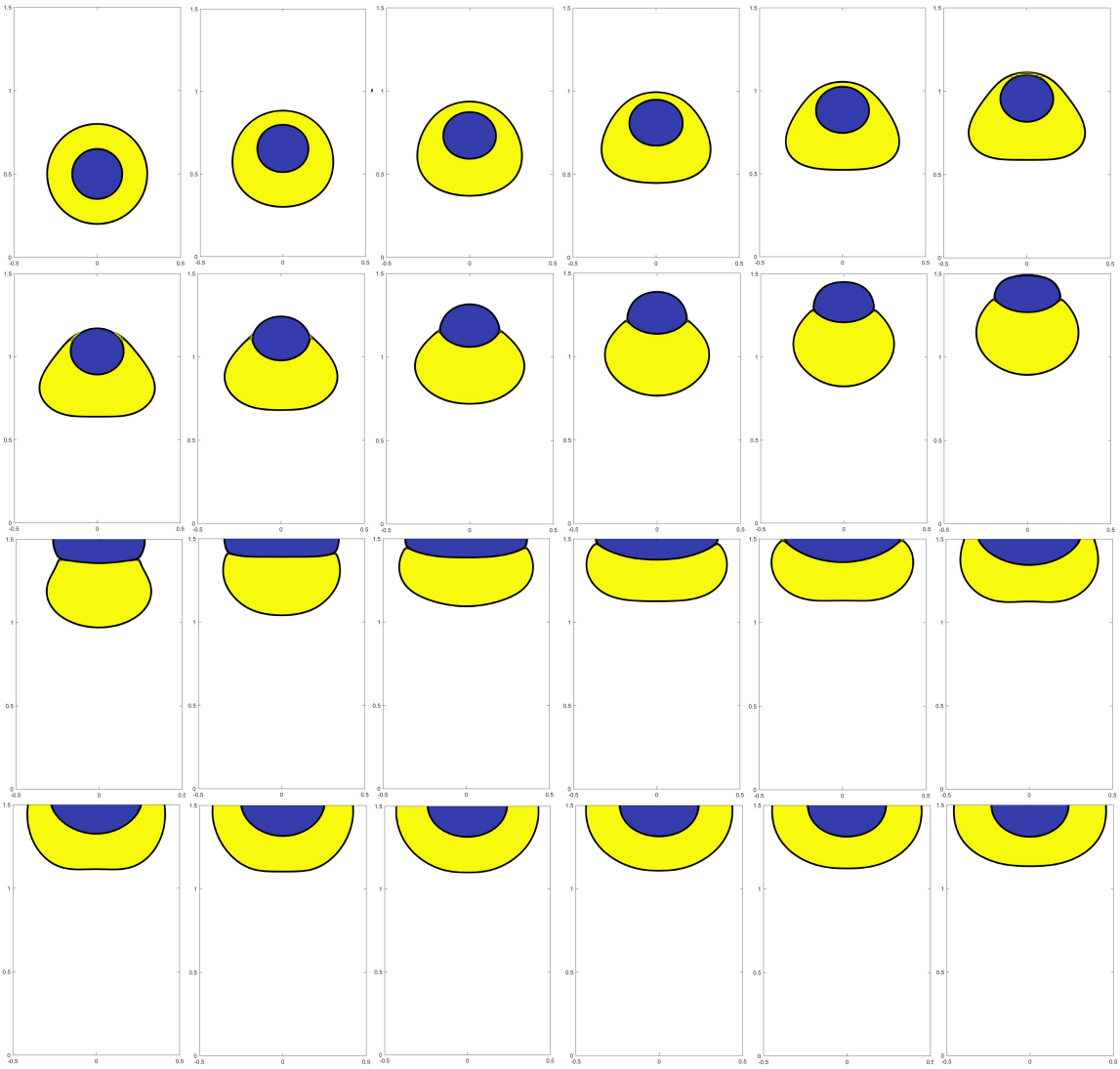

Figure 5.26. Evolution of the three phases using CH-B in the three-phase rising bubble with moving contact lines, where $\theta^T_{water-oil} = \pi/2$, $\theta^T_{oil-air} = \pi/2$. From left to right, top to bottom, t is 0.00, 0.3, 0.4, 0.5, ..., 2.5. Blue: Air, Yellow: Oil, and White: Water.

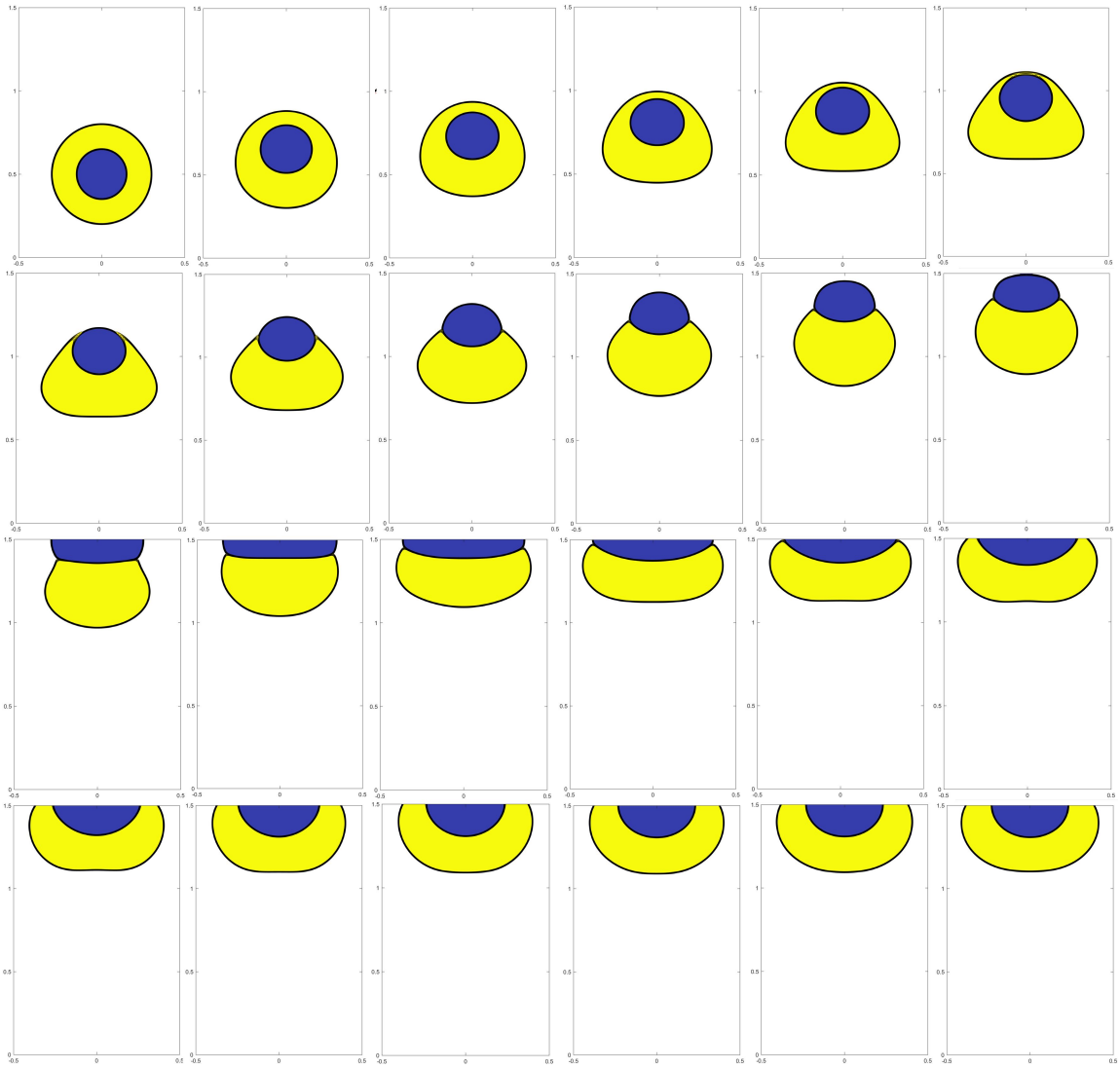

Figure 5.27. Evolution of the three phases using CH-B in the three-phase rising bubble with moving contact lines, where $\theta^T_{water-oil} = \boldsymbol{\pi}/2$, $\theta^T_{oil-air} = 2\boldsymbol{\pi}/3$. From left to right, top to bottom, t is 0.00, 0.3, 0.4, 0.5, ..., 2.5. Blue: Air, Yellow: Oil, and White: Water.

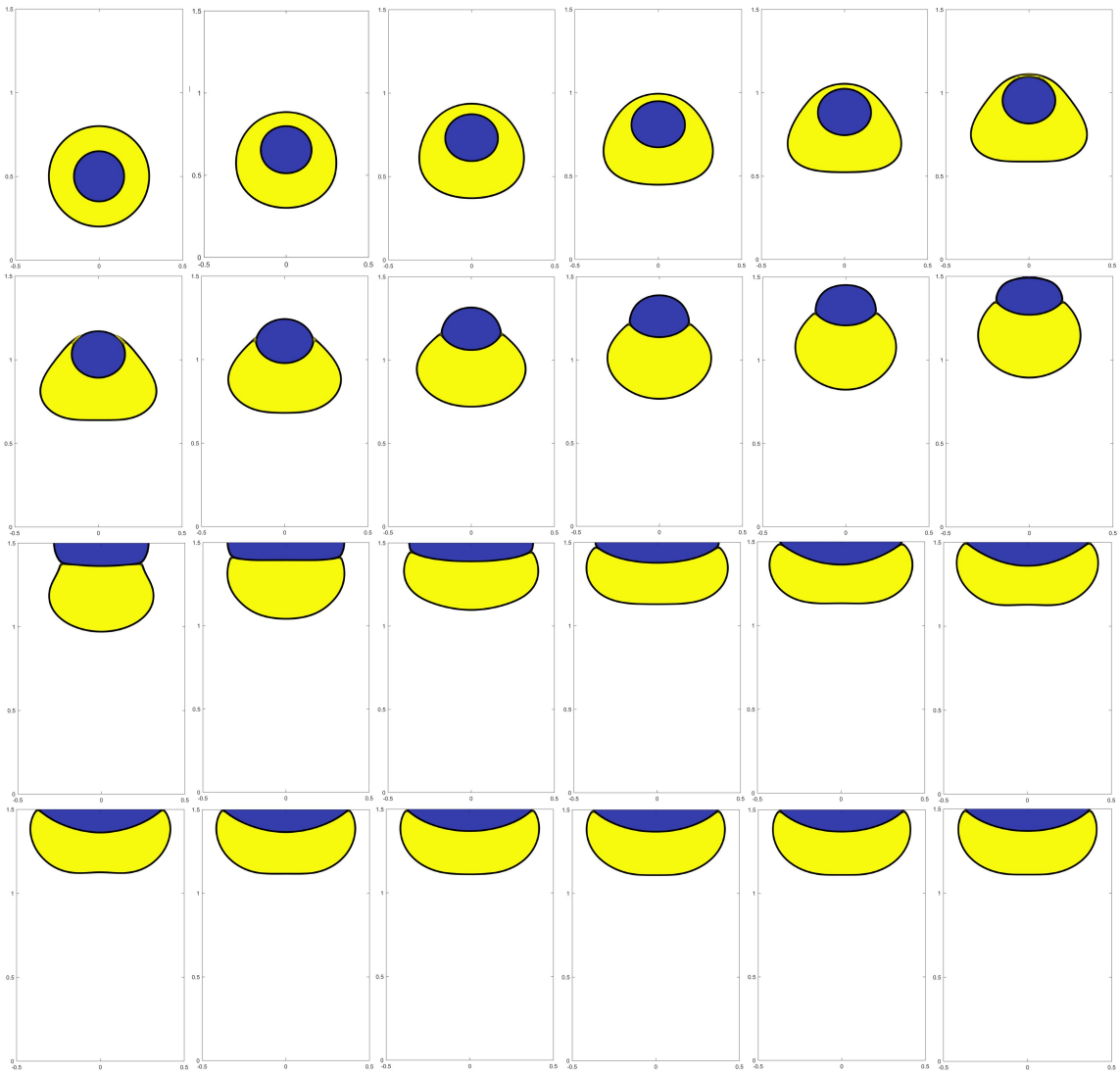

Figure 5.28. Evolution of the three phases using CH-B in the three-phase rising bubble with moving contact lines, where $\theta^T_{water-oil} = \boldsymbol{\pi}/6$, $\theta^T_{oil-air} = 2\boldsymbol{\pi}/3$. From left to right, top to bottom, t is 0.00, 0.3, 0.4, 0.5, ..., 2.5. Blue: Air, Yellow: Oil, and White: Water.

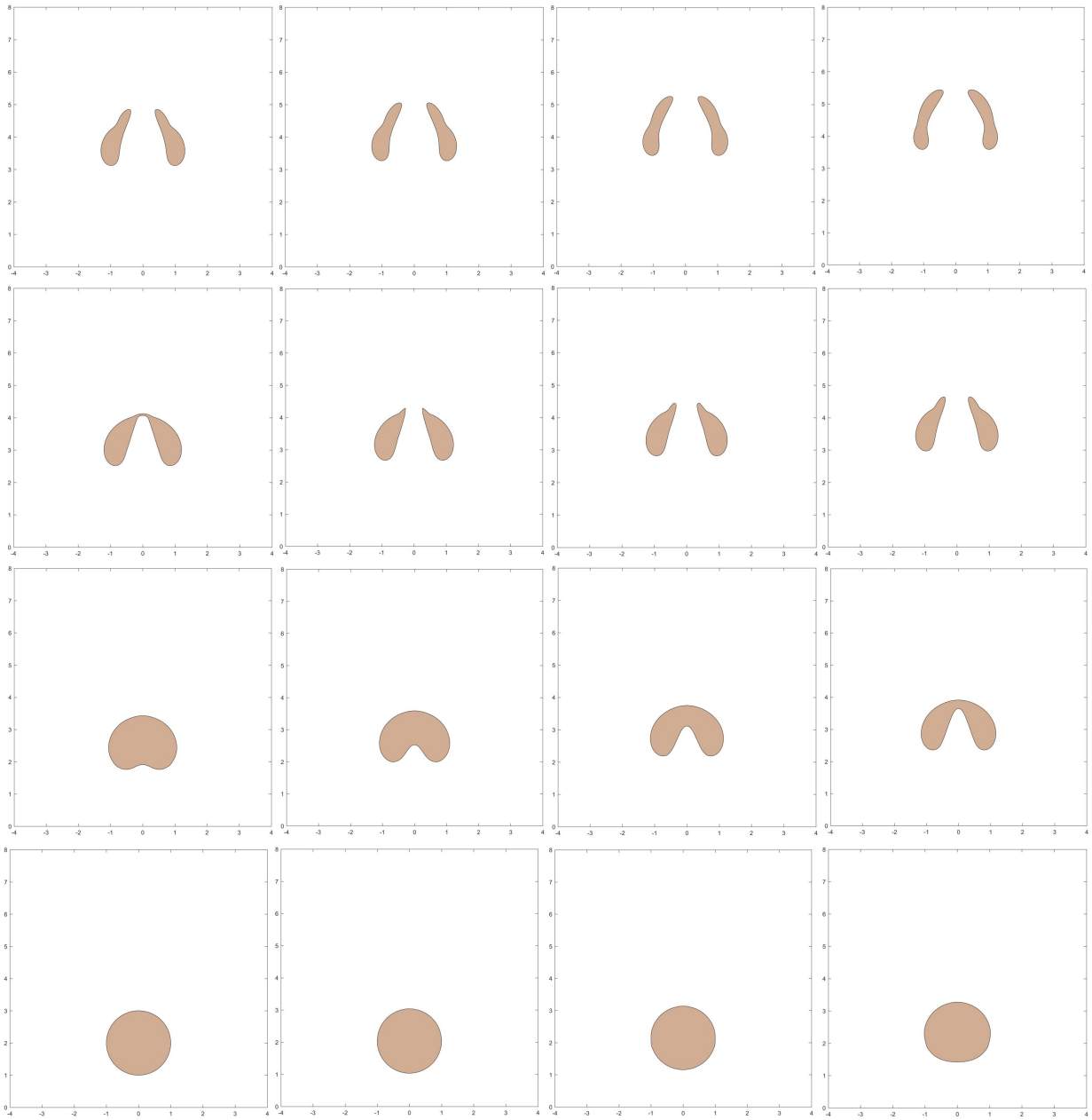

Figure 5.29. Results of the axisymmetric rising bubble using the balanced-force method (two-phase CACB-B) from $t = 0$ to $t = 3$ with 0.2 increment, from left to right and from bottom to top.

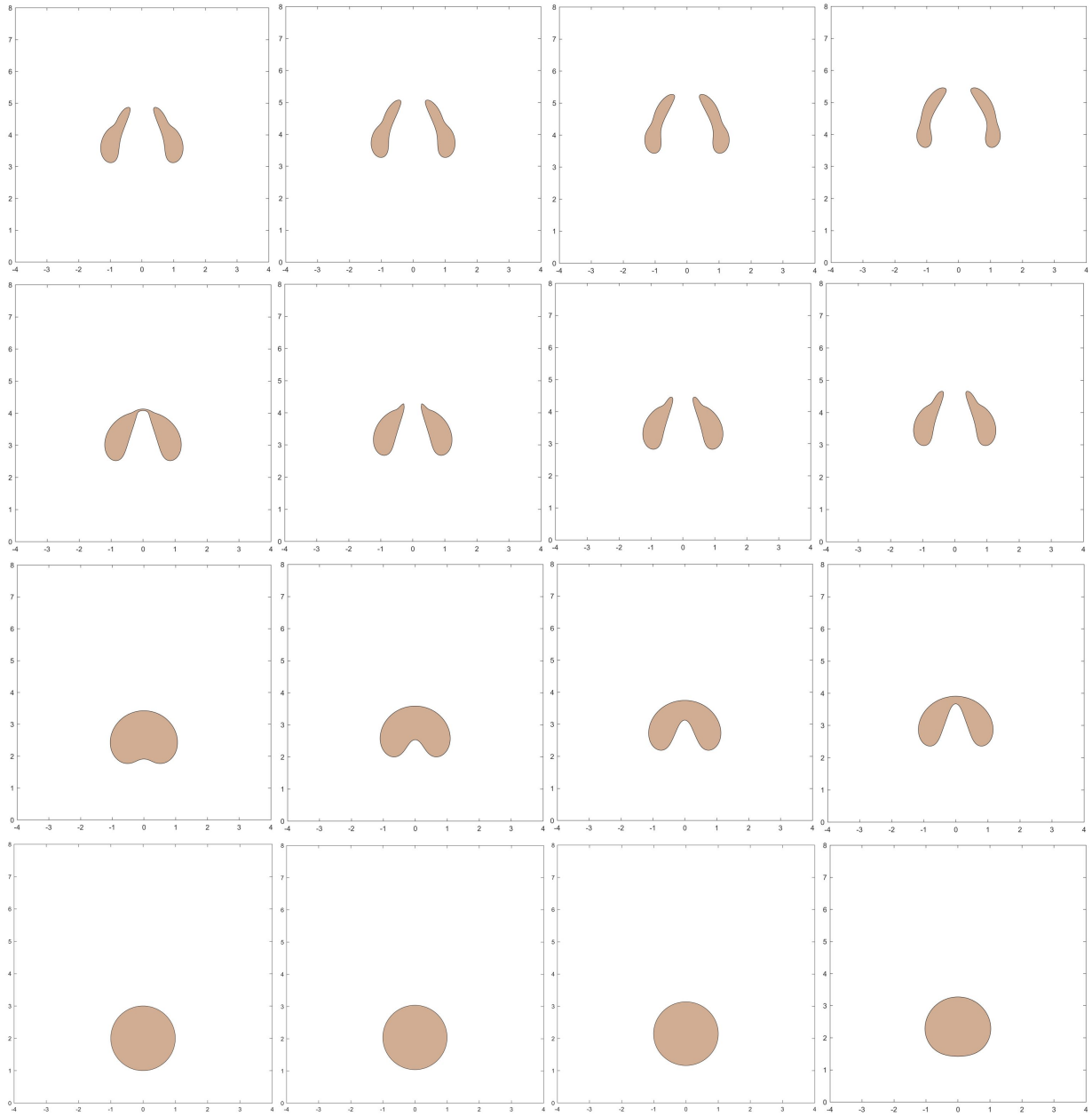

Figure 5.30. Results of the axisymmetric rising bubble using the conservative method (two-phase CACB-C) from $t = 0$ to $t = 3$ with 0.2 increment, from left to right and from bottom to top.

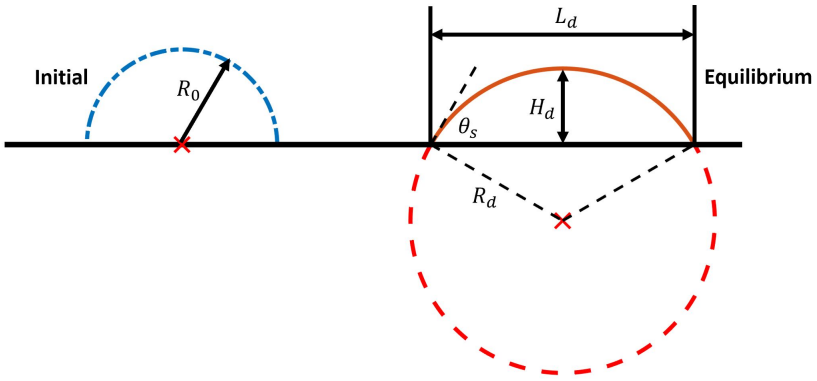

Figure 5.31. Schematic of a drop on a homogeneous flat surface.

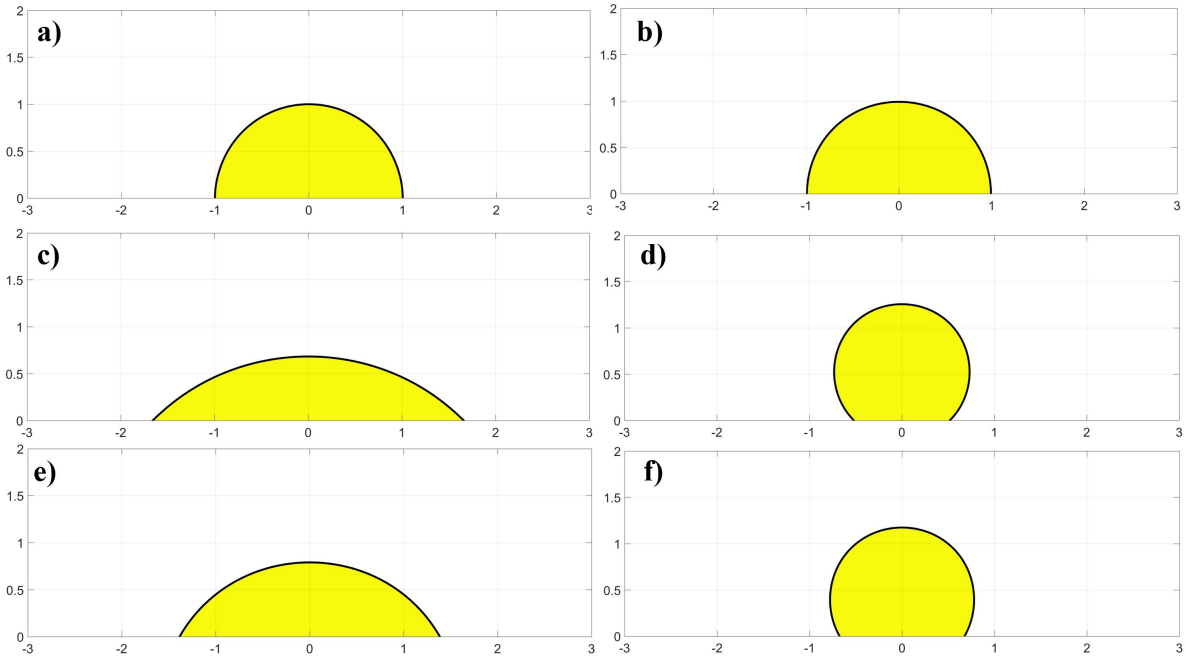

Figure 5.32. Results of the equilibrium drop using two-phase CH-B. a) Initial shape of the drop, b) $\theta^W = 90^0$, c) $\theta^W = 45^0$, d) $\theta^W = 135^0$, e) $\theta^W = 60^0$, and f) $\theta^W = 120^0$.

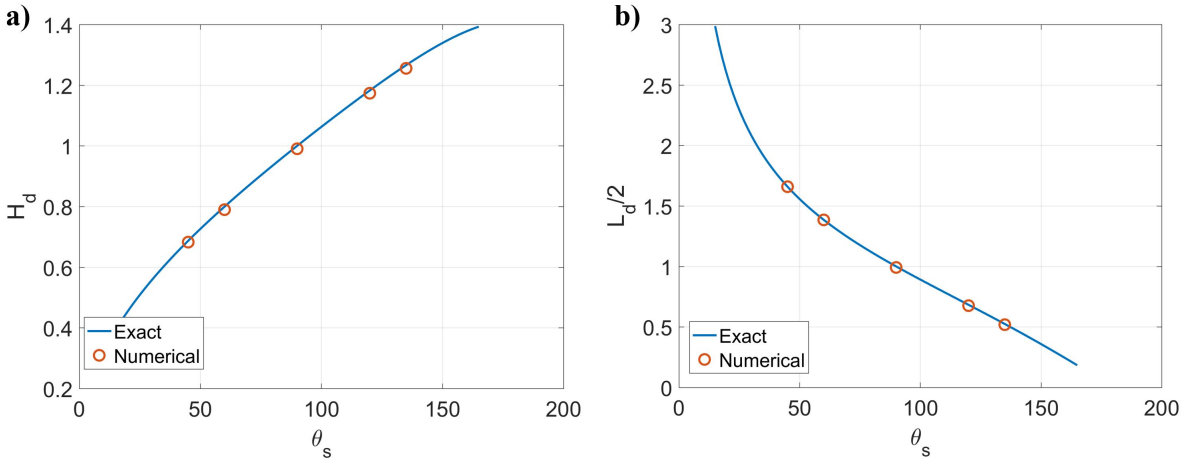

Figure 5.33. Results of the height and length of the drop using two-phase CH-B. a) Height of the drop, b) half length of the drop.

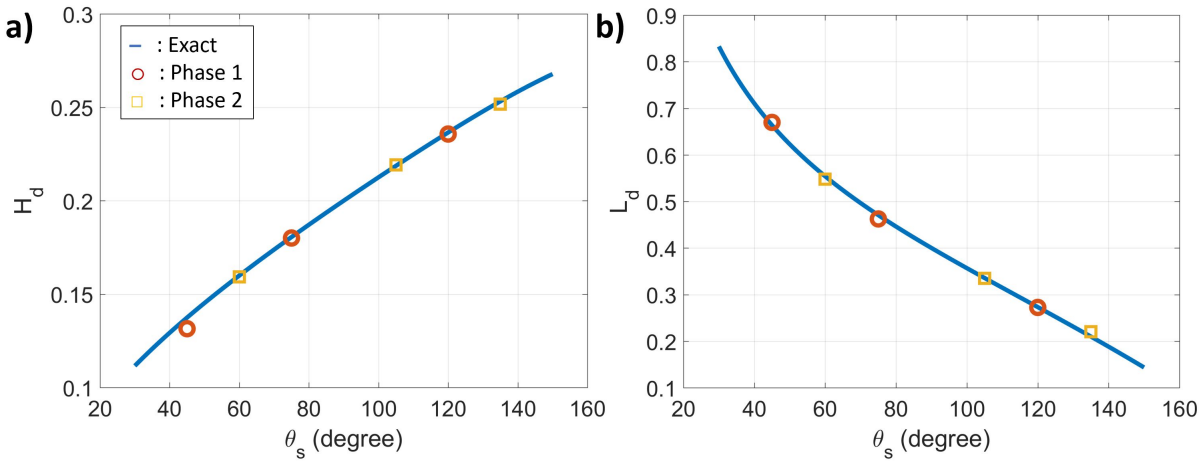

Figure 5.34. Heights and spreading lengths of drop on a surface using CH-B. a) Height (H_d) vs. contact angle (θ_s). b) Spreading length (L_d) vs. contact angle (θ^W). a) and b) share the same legend.

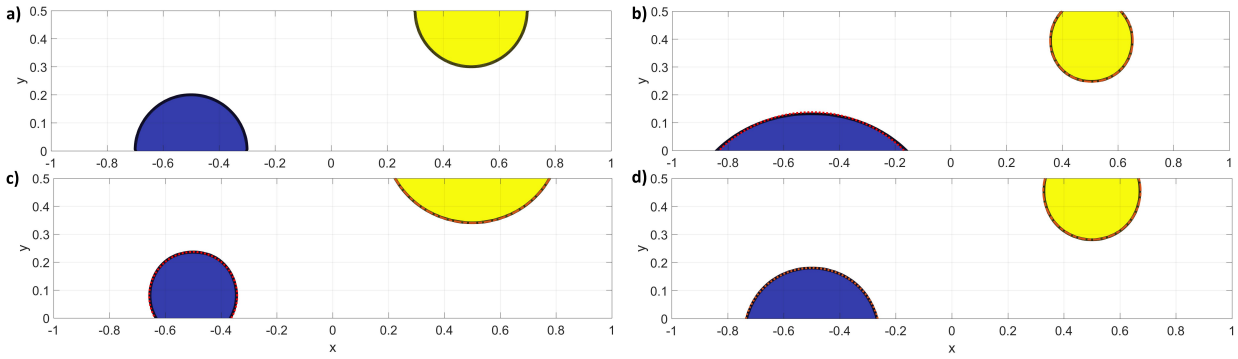

Figure 5.35. Initial and final shapes of the drops on a surface using CH. a) Initial shapes. b) Final shapes with contact angles $(45^0, 135^0)$. c) Final shapes with contact angles $(120^0, 60^0)$. d) Final shapes with contact angles $(75^0, 105^0)$. Blue: Phase 1, Yellow: Phase 2, White: Phase 3. Red dotted line: Exact shape of Phase 1, Orange dash-dotted line: Exact shape of Phase 2.

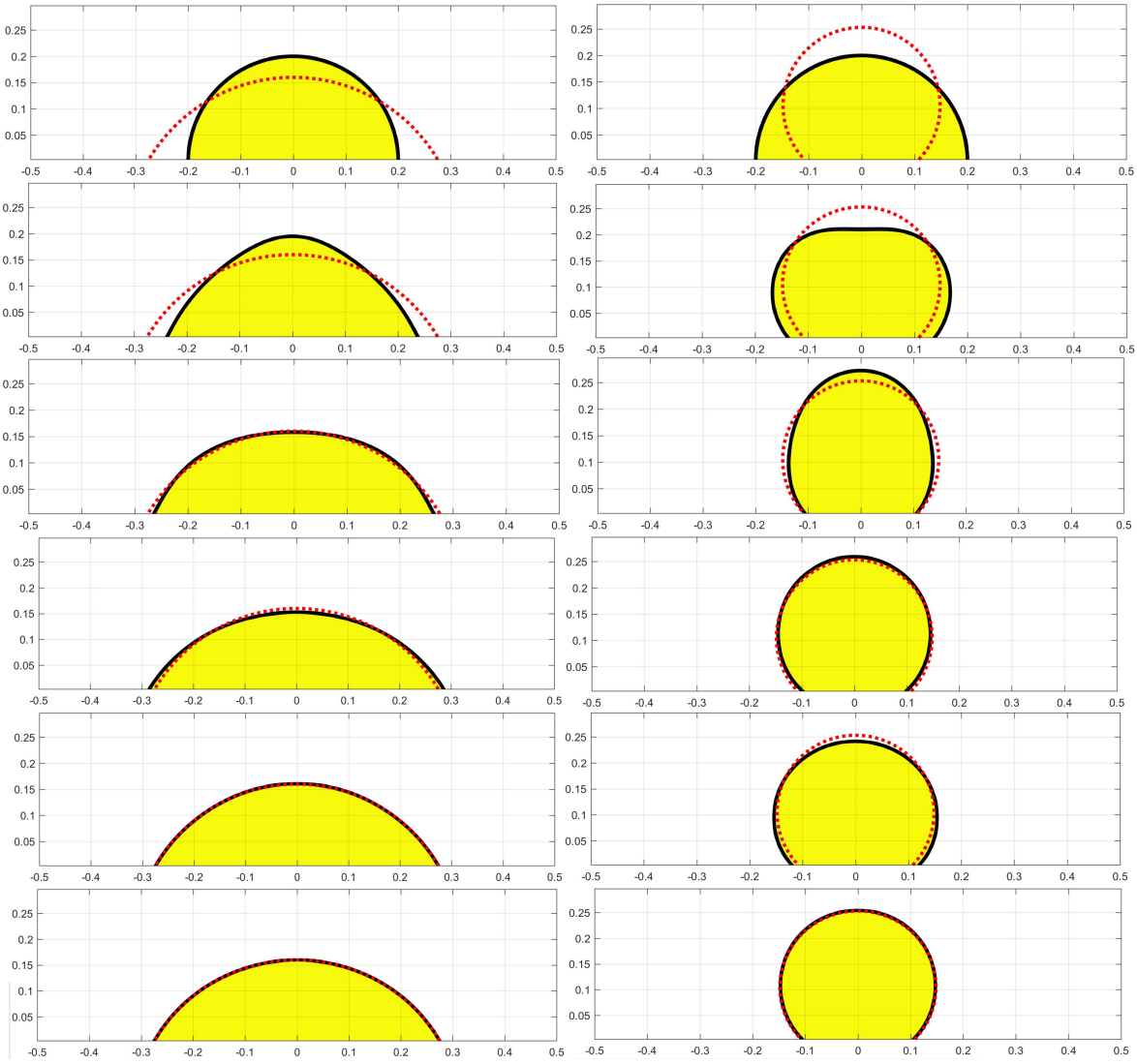

Figure 5.36. Evolution of the water drop using two-phase CAC-B with $|\mathbf{g}| = 0$. Yellow: water (Phase 1); White: air (Phase 2); Red dotted line: exact solution. Left column: $\theta^W = 60^0$; Right column: $\theta^W = 135^0$. From top to bottom, $t = 0.0$, $t = 0.2$, $t = 0.4$, $t = 1.0$, $t = 1.4$, and $t = 2.0$ (left) and $t = 3.0$ (right).

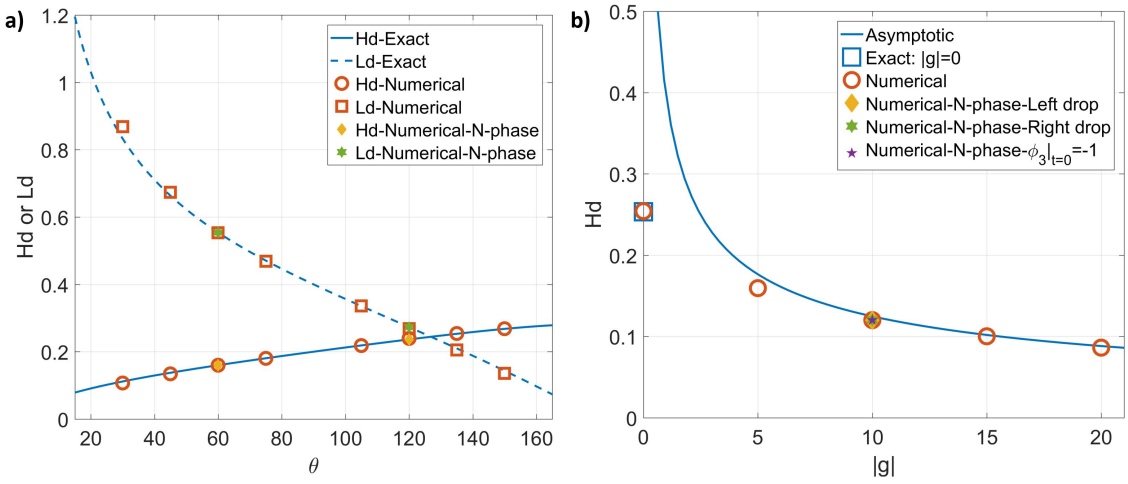

Figure 5.37. Height and spreading length of the drop using CAC-B and two-phase CAC-B. a) H_d and L_d versus θ with $|\mathbf{g}| = 0$. b) H_d versus $|\mathbf{g}|$ with $\theta^W = 135^0$.

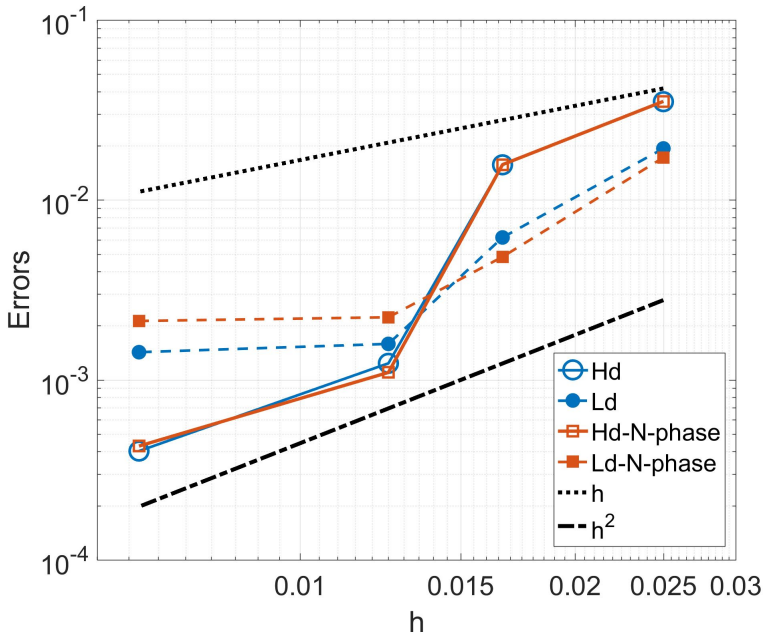

Figure 5.38. Errors of the height and spreading length of the water drop using CAC-B and two-phase CAC-B versus the grid size with $\theta^W = \theta^W_{1,2} = 60^0$ and $|\mathbf{g}| = 0$.

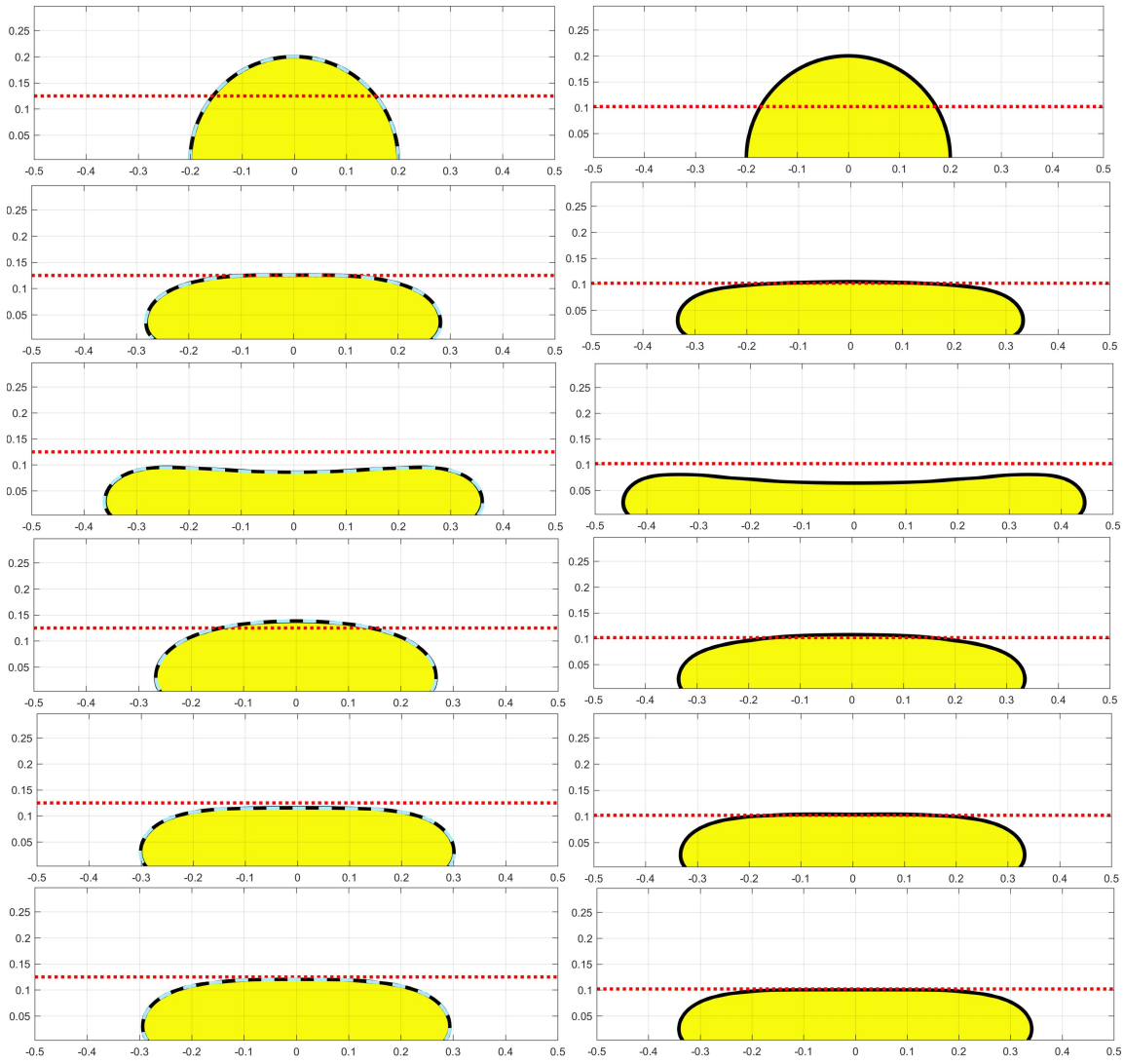

Figure 5.39. Evolution of the water drop using two-phase CAC-B with $\theta^W = 135^0$. Yellow: water (Phase 1); White: air (Phase 2); Red dotted line: asymptotic solution for gravity dominance; Cyan dashed line: N-phase solution from CAC-B with $\phi_3|_{t=0} = -1$. Left column: $|\mathbf{g}| = 10$; Right column: $|\mathbf{g}| = 15$. From top to bottom, $t = 0.0$, $t = 0.2$, $t = 0.4$, $t = 1.0$, $t = 1.4$, and $t = 3.0$.

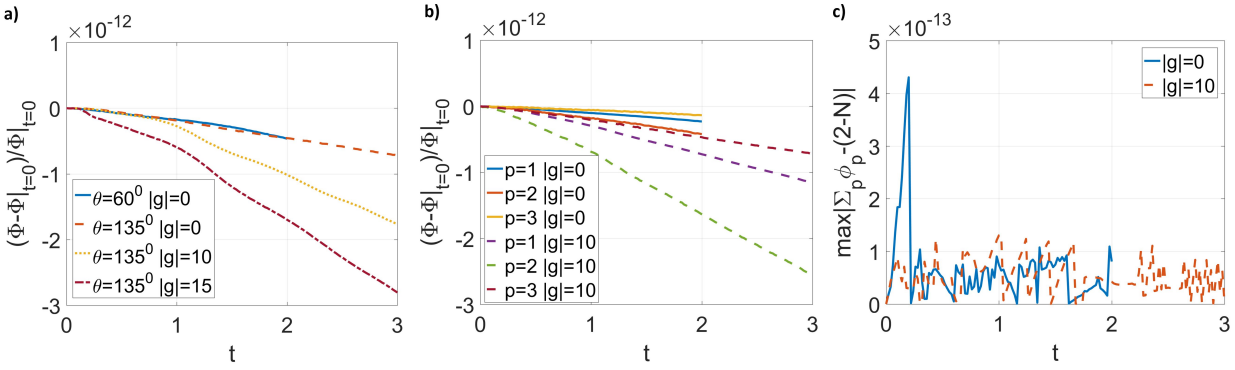

Figure 5.40. a) Relative changes of Φ ($= \int_\Omega \phi d\Omega$) from two-phase CAC-B versus time. b) Relative changes of Φ from CAC-B versus time (p is the phase index). c) $\max|\sum_p \phi_p - (2-N)|$ from CAC-B versus time.

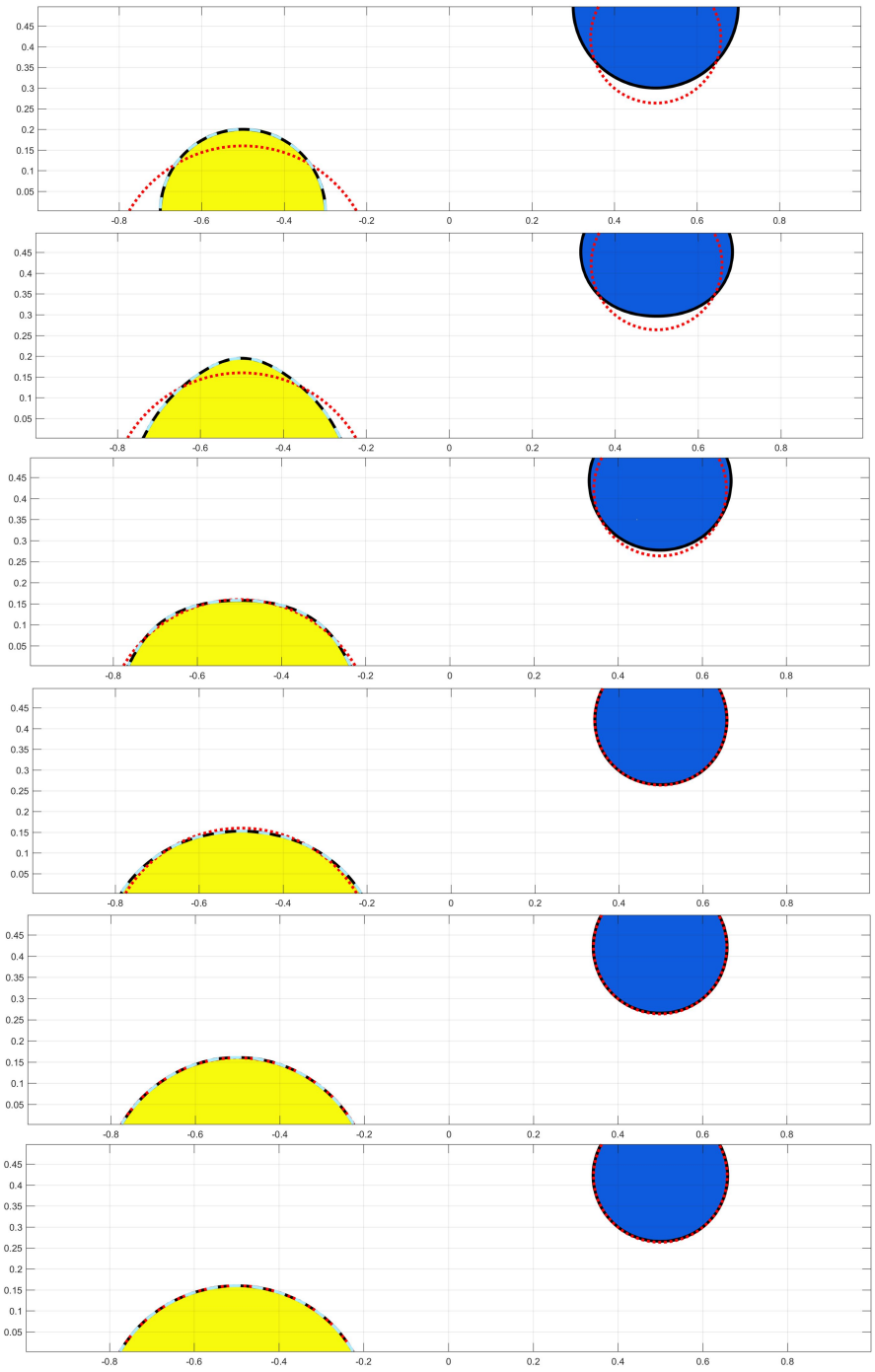

Figure 5.41. Evolution of the water and oil drops using CAC-B with $|\mathbf{g}| = 0$, $\theta_{1,2}^W = 60^0$, and $\theta_{3,2}^W = 120^0$. Yellow: water (Phase 1); White: air (Phase 2); Blue: oil (Phase 3); Red dotted line: exact solution; Cyan dashed line: two-phase solution from two-phase CAC-B in the left column of Fig.5.36. From top to bottom, $t = 0.0$, $t = 0.2$, $t = 0.4$, $t = 1.0$, $t = 1.4$, and $t = 2.0$.

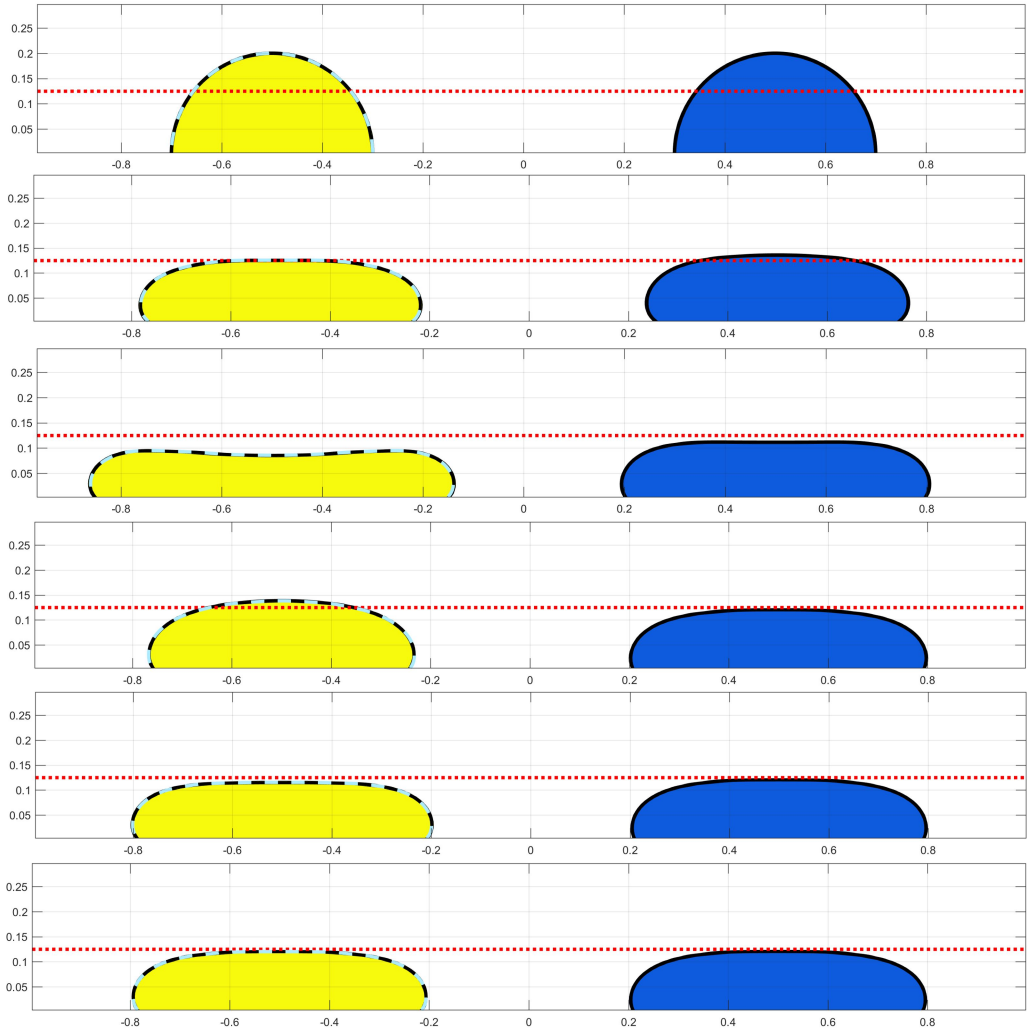

Figure 5.42. Evolution of the water and oil drops using CAC-B with $|\mathbf{g}| = 10$, $\theta_{1,2}^W = 135^0$, and $\theta_{3,2}^W = 120^0$. Yellow: water (Phase 1); White: air (Phase 2); Blue: oil (Phase 3); Red dotted line: asymptotic solution; Cyan dashed line: two-phase solution from two-phase CAC-B in the left column of Fig.5.39. From top to bottom, $t = 0.0$, $t = 0.2$, $t = 0.4$, $t = 1.0$, $t = 1.4$, and $t = 3.0$.

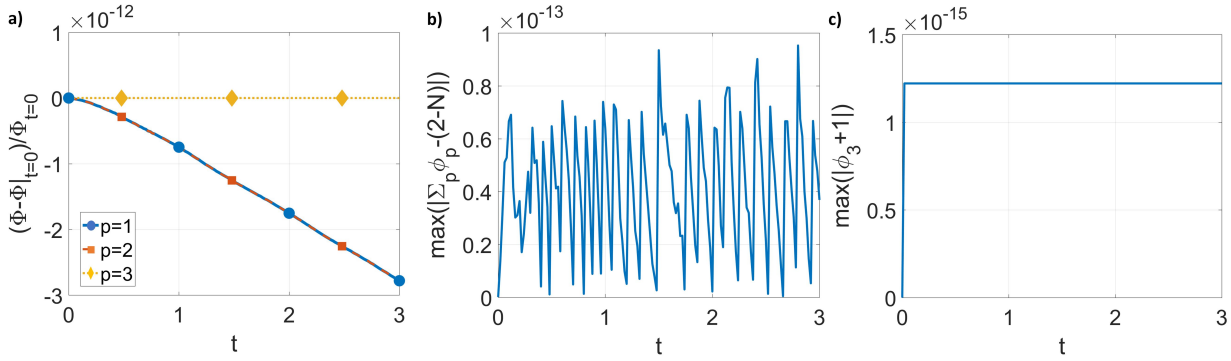

Figure 5.43. a) Relative changes of Φ ($= \int_\Omega \phi d\Omega$) from CAC-B versus time (p is the phase index) with $\phi_3|_{t=0} = -1$. b) $\max|\sum_p \phi_p - (2-N)|$ from CAC-B versus time with $\phi_3|_{t=0} = -1$. c) $\max|\phi_3 + 1|$ from CAC-B versus time with $\phi_3|_{t=0} = -1$.

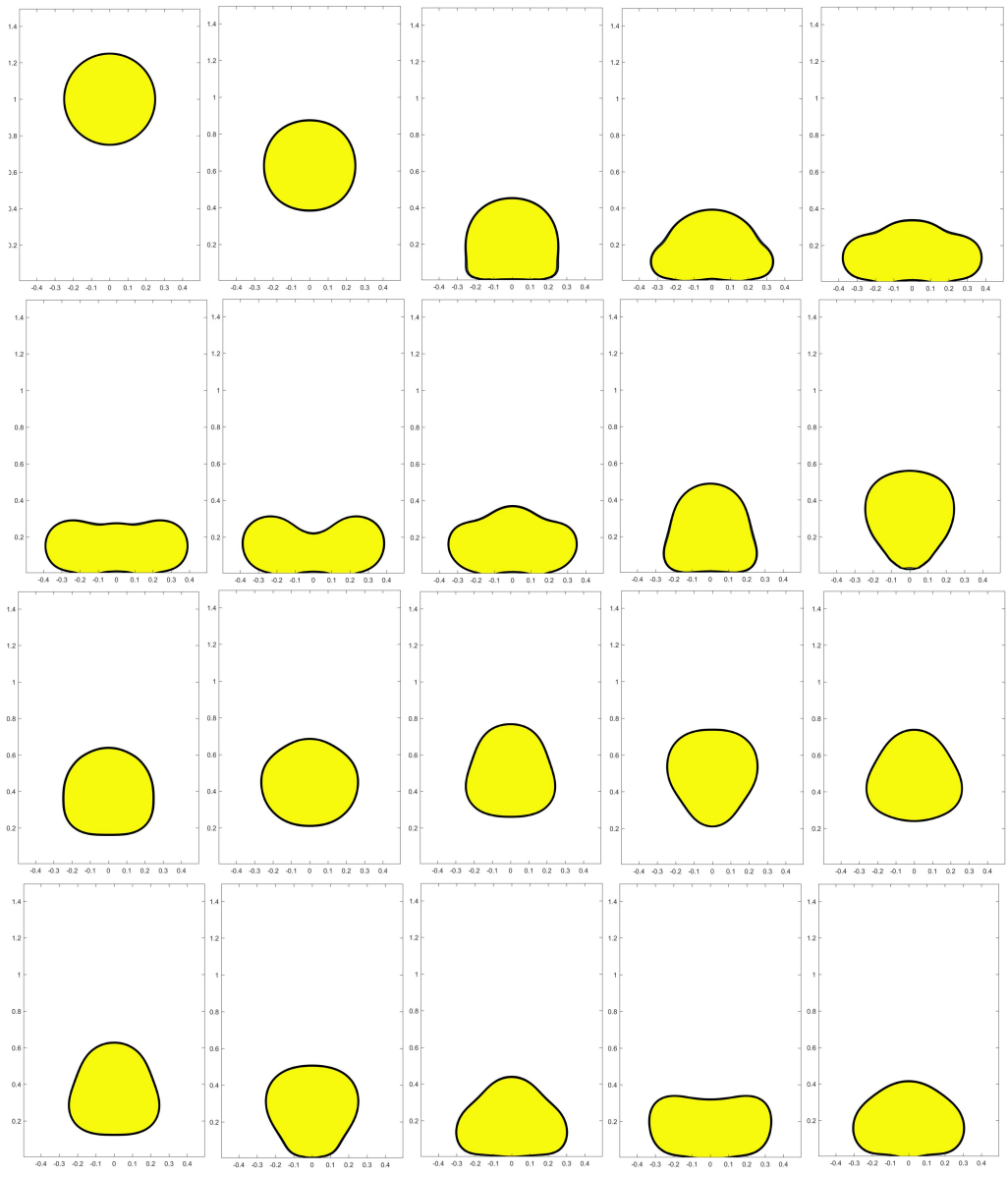

Figure 5.44. Results of the bouncing drop using the two-phase CAC-B with $\theta^W = 165^0$. Yellow: water (Phase 1); White: air (Phase 2); From left to right and top to bottom: $t = 0.00$, $t = 0.30$, $t = 0.44$, $t = 0.46$, $t = 0.48$, $t = 0.50$, $t = 0.52$, $t = 0.56$, $t = 0.60$, $t = 0.64$, $t = 0.68$, $t = 0.72$, $t = 0.80$, $t = 0.85$, $t = 0.90$, $t = 1.00$, $t = 1.05$, $t = 1.10$, $t = 1.15$, and $t = 1.20$.

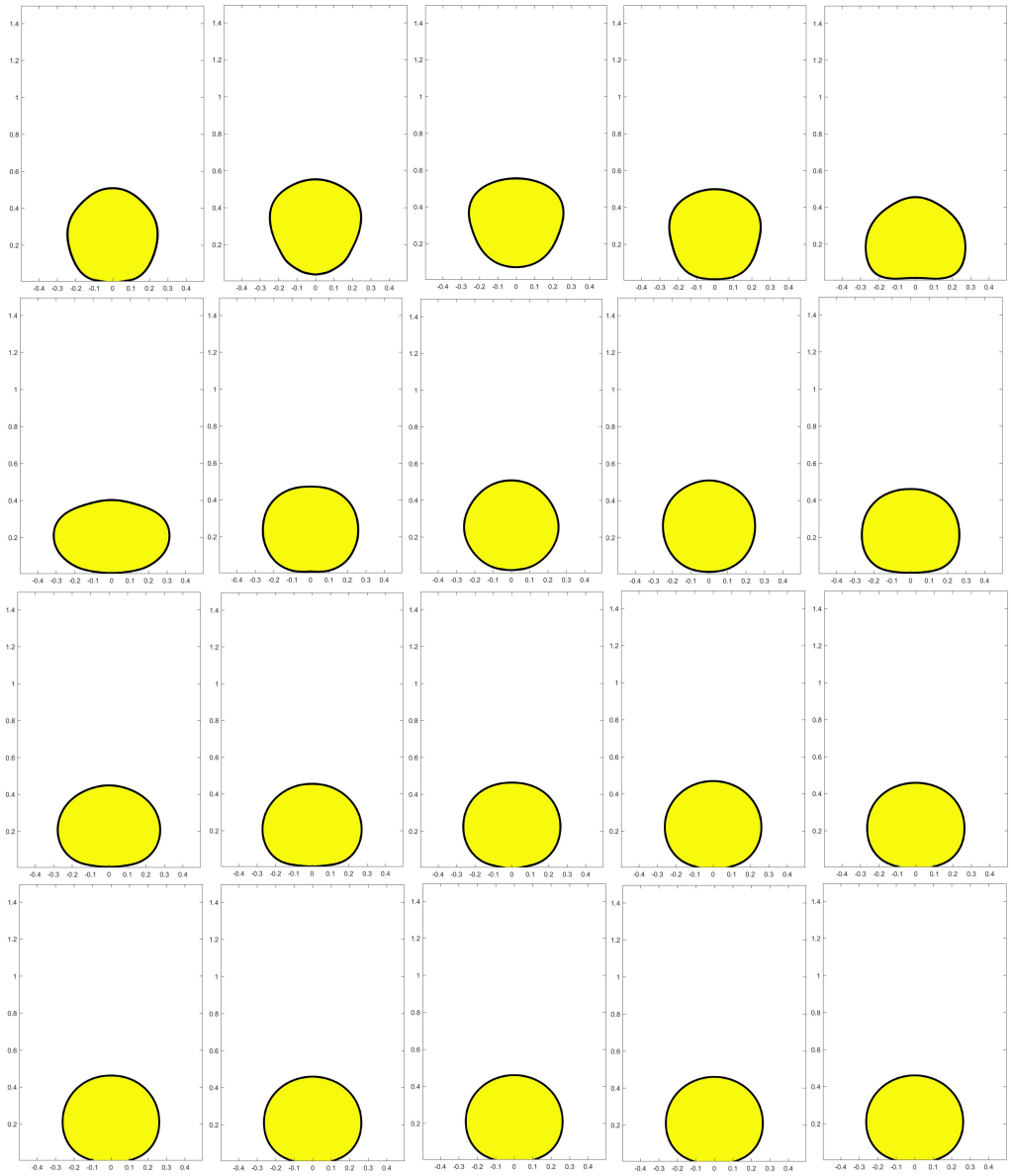

Figure 5.45. (continued from Fig.5.44) From left to right and top to bottom: $t = 1.25$, $t = 1.30$, $t = 1.40$, $t = 1.50$, $t = 1.55$, $t = 1.60$, $t = 1.70$, $t = 1.75$, $t = 1.80$, $t = 1.90$, $t = 1.95$, $t = 2.00$, $t = 2.05$, $t = 2.15$, $t = 2.20$, $t = 2.35$, $t = 2.50$, $t = 3.00$, $t = 3.50$, and $t = 4.00$.

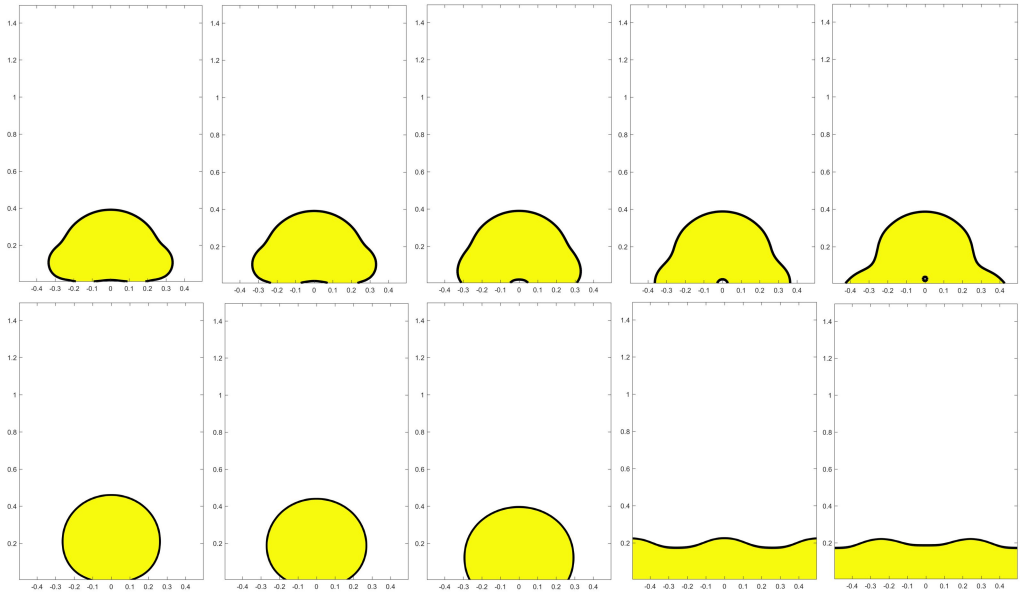

Figure 5.46. Shapes of the drops with different contact angles using two-phase CAC-B. Yellow: water (Phase 1); White: air (Phase 2); From left to right: $\theta = 165^0$, $\theta = 150^0$, $\theta = 120^0$, $\theta = 90^0$, and $\theta = 60^0$. Top: $t = 0.46$; Bottom: $t = 4.00$.

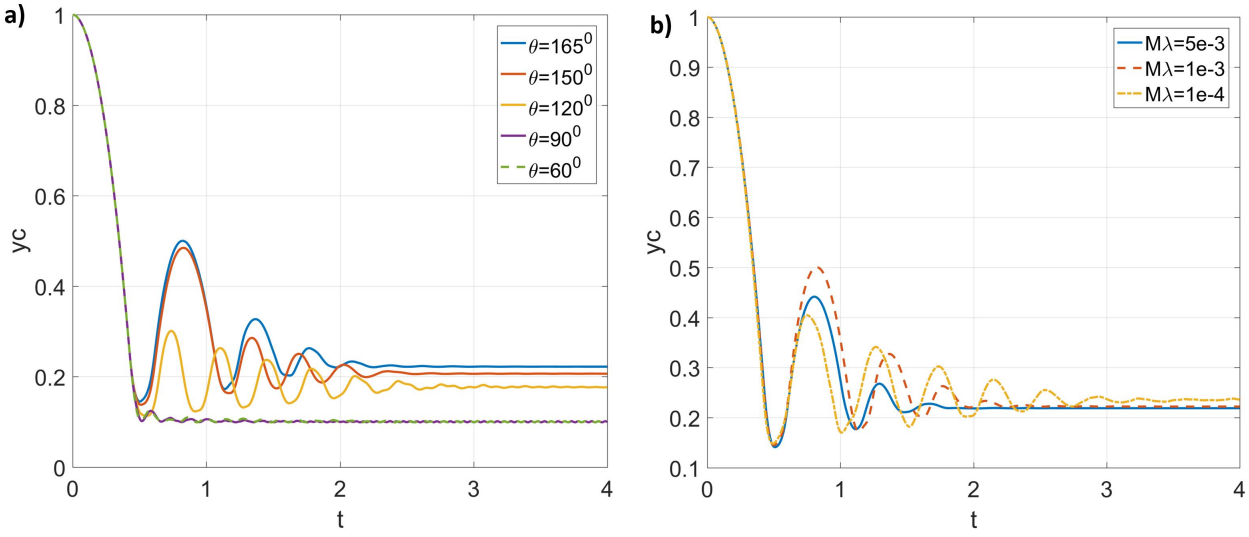

Figure 5.47. Mass center (y component) of the drop versus time using two-phase CAC-B a) with different contact angles, b) with different mobilities.

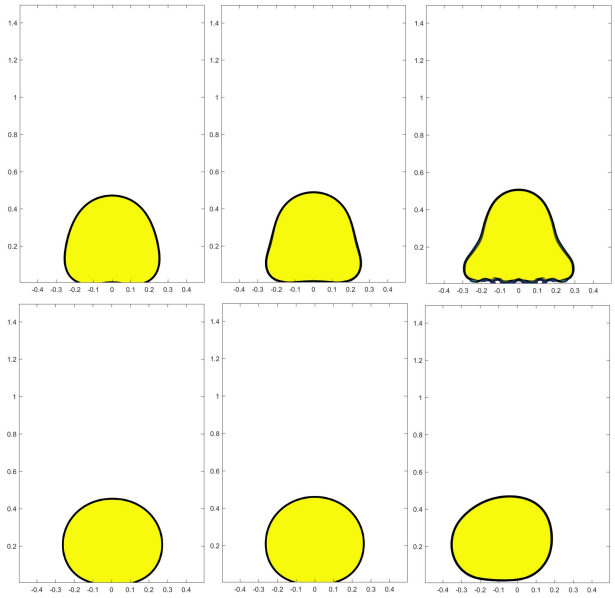

Figure 5.48. Shapes of the drops with different mobilities using two-phase CAC-B. Yellow: water (Phase 1); White: air (Phase 2); From left to right: $M_0\lambda_0 = 5 \times 10^{-3}$, $M_0\lambda_0 = 1 \times 10^{-3}$, and $M_0\lambda_0 = 1 \times 10^{-4}$. Top: $t = 0.60$; Bottom: $t = 4.00$.

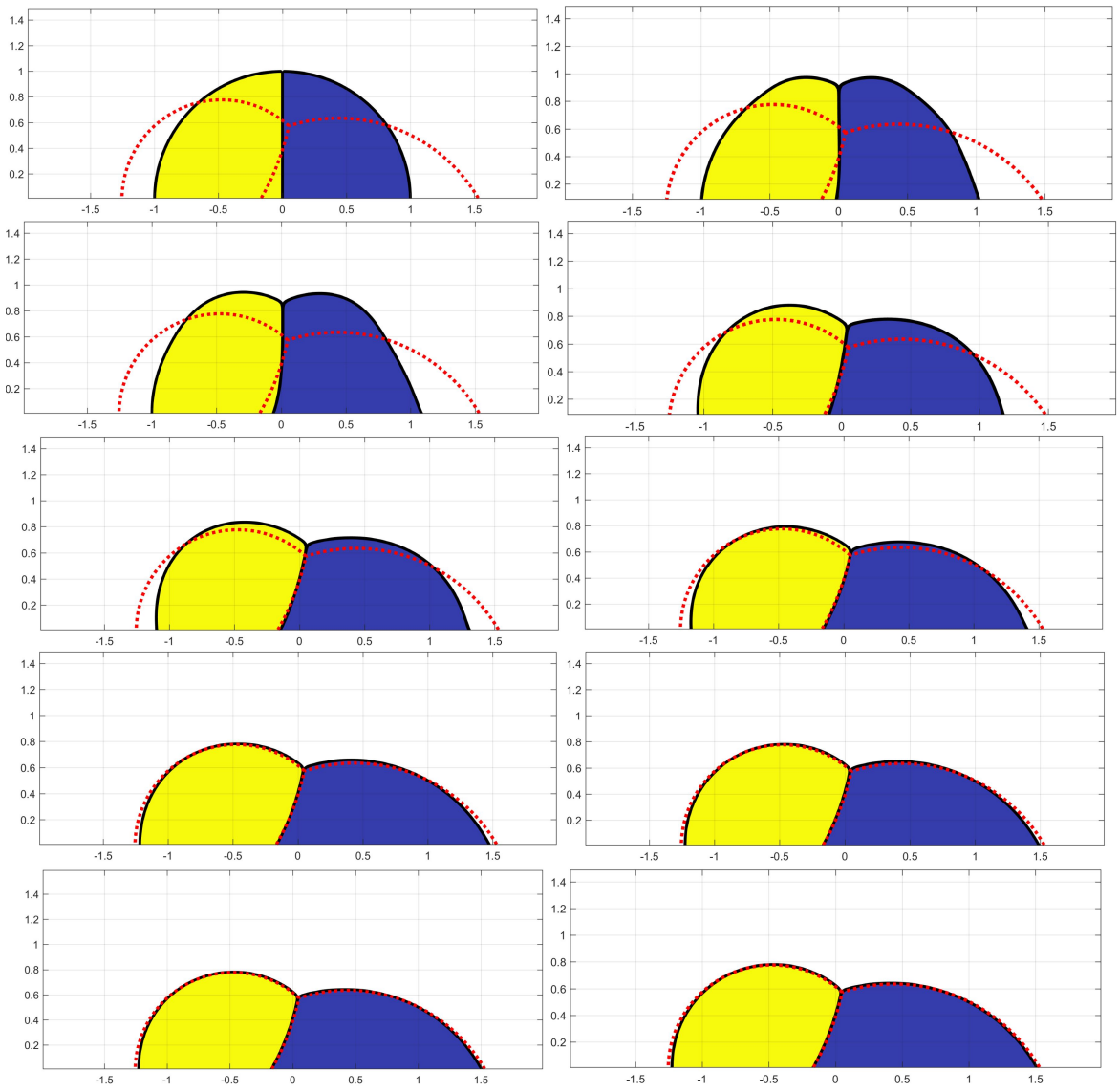

Figure 5.49. Evolution of the compound drops using CAC-B with a stationary bottom wall. Yellow: Phase 1; Blue: Phase 2; White: Phase 3; Red dotted line: exact solution from [90]. From top to bottom and left to right: $t = 0.0$, $t = 0.2$, $t = 0.4$, $t = 1.0$, $t = 1.4$, $t = 2.0$, $t = 3.0$, $t = 4.0$, $t = 5.0$ and $t = 6.0$.

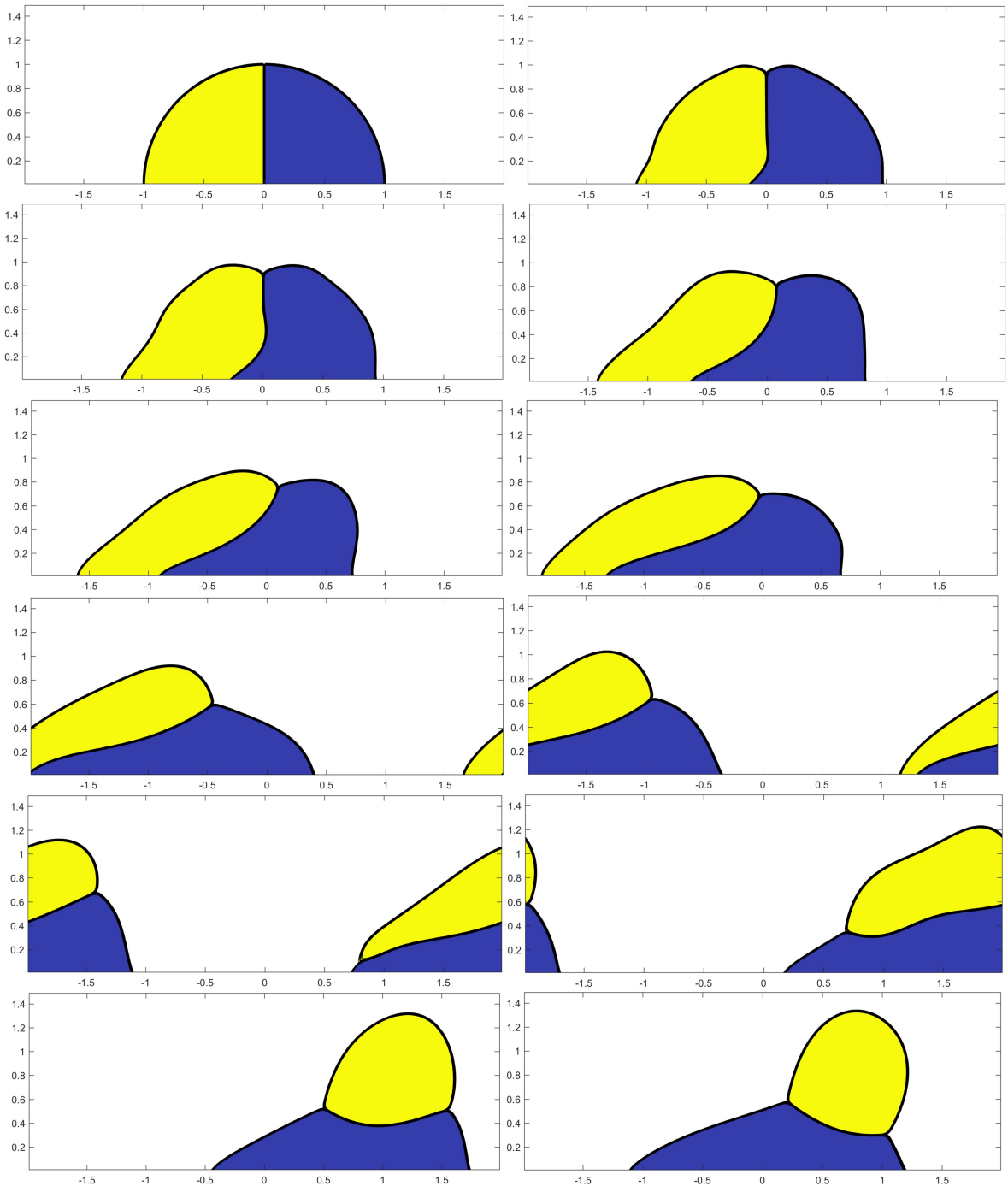

Figure 5.50. Evolution of the compound drops using CAC-B with a translating bottom wall. Yellow: Phase 1; Blue: Phase 2; White: Phase 3. From top to bottom and left to right: $t = 0.0$, $t = 0.2$, $t = 0.4$, $t = 1.0$, $t = 1.4$, $t = 2.0$, $t = 3.0$, $t = 4.0$, $t = 5.0$, $t = 6.0$, $t = 7.0$, and $t = 8.0$.

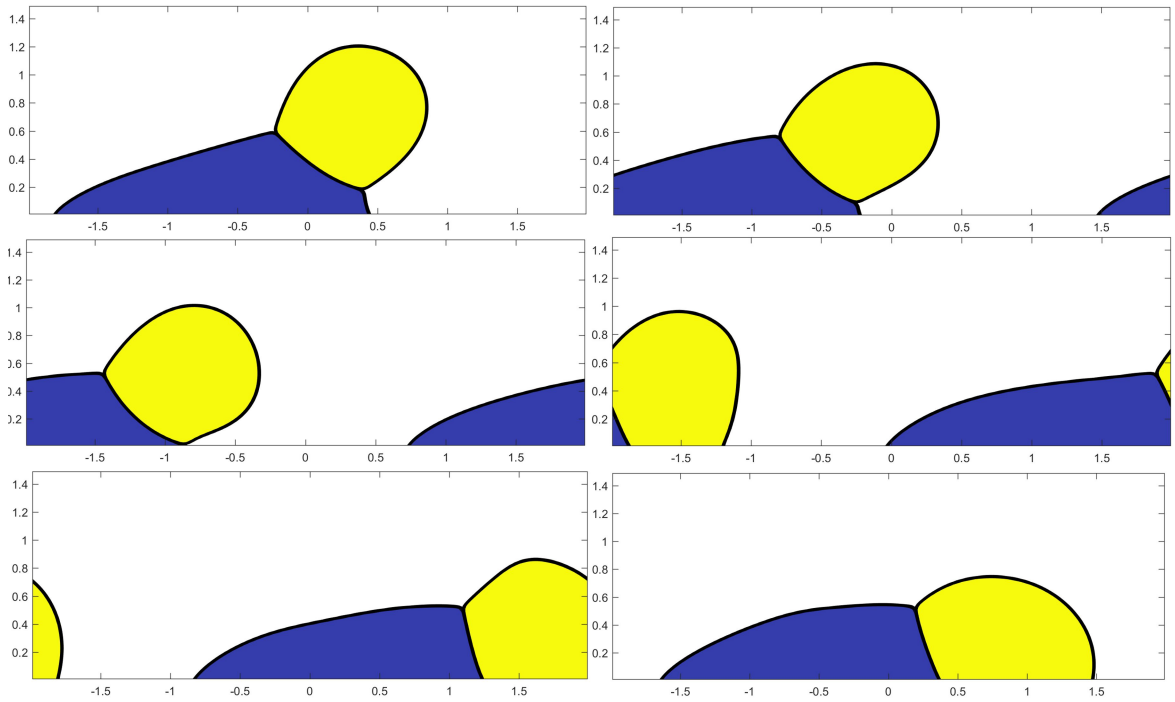

Figure 5.51. (continued from Fig.5.50) From top to bottom and left to right: $t = 9.0$, $t = 10.0$, $t = 11.0$, $t = 12.0$, $t = 13.0$, and $t = 14.0$.

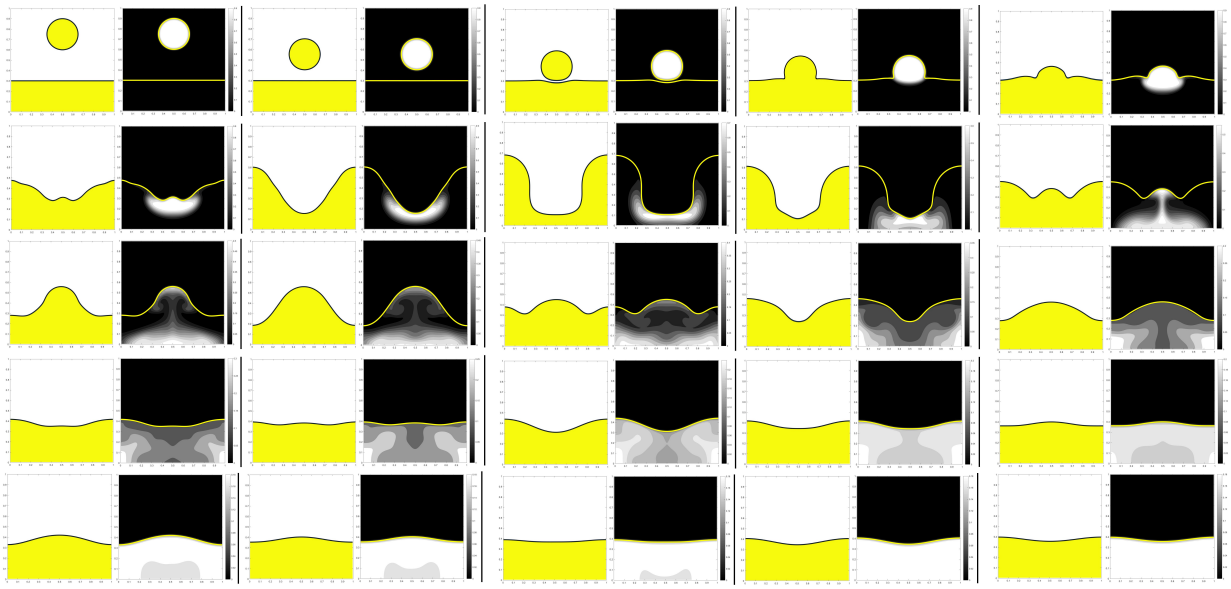

Figure 5.52. Results of the miscible falling drop, from left to right and top to bottom, $t = 0.00$, 0.20, 0.25, 0.27, 0.30, 0.35, 0.40, 0.50, 0.60, 0.70, 0.80, 0.90, 1.00, 1.20, 1.40, 1.60, 1.80, 2.20, 2.60, 3.00, 3.40, 3.80, 4.20, 4.60, 5.00. Left of each panel: configuration of the phases, yellow: Phase 1, white: Phase 2. Right of each panel: configuration of Component 1, yellow solid lines: interfaces of Phase 1.

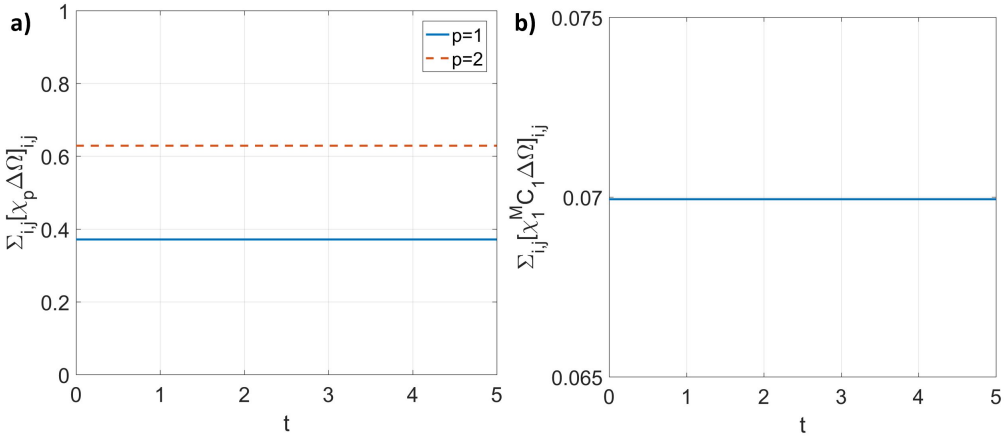

Figure 5.53. Time histories of the total volumes of individual phases and the total amount of Component 1 in its dissolvable region in the miscible falling drop. a) Time histories of the total volumes of individual phases. b) Time histories of the total amount of Component 1 in its dissolvable region.

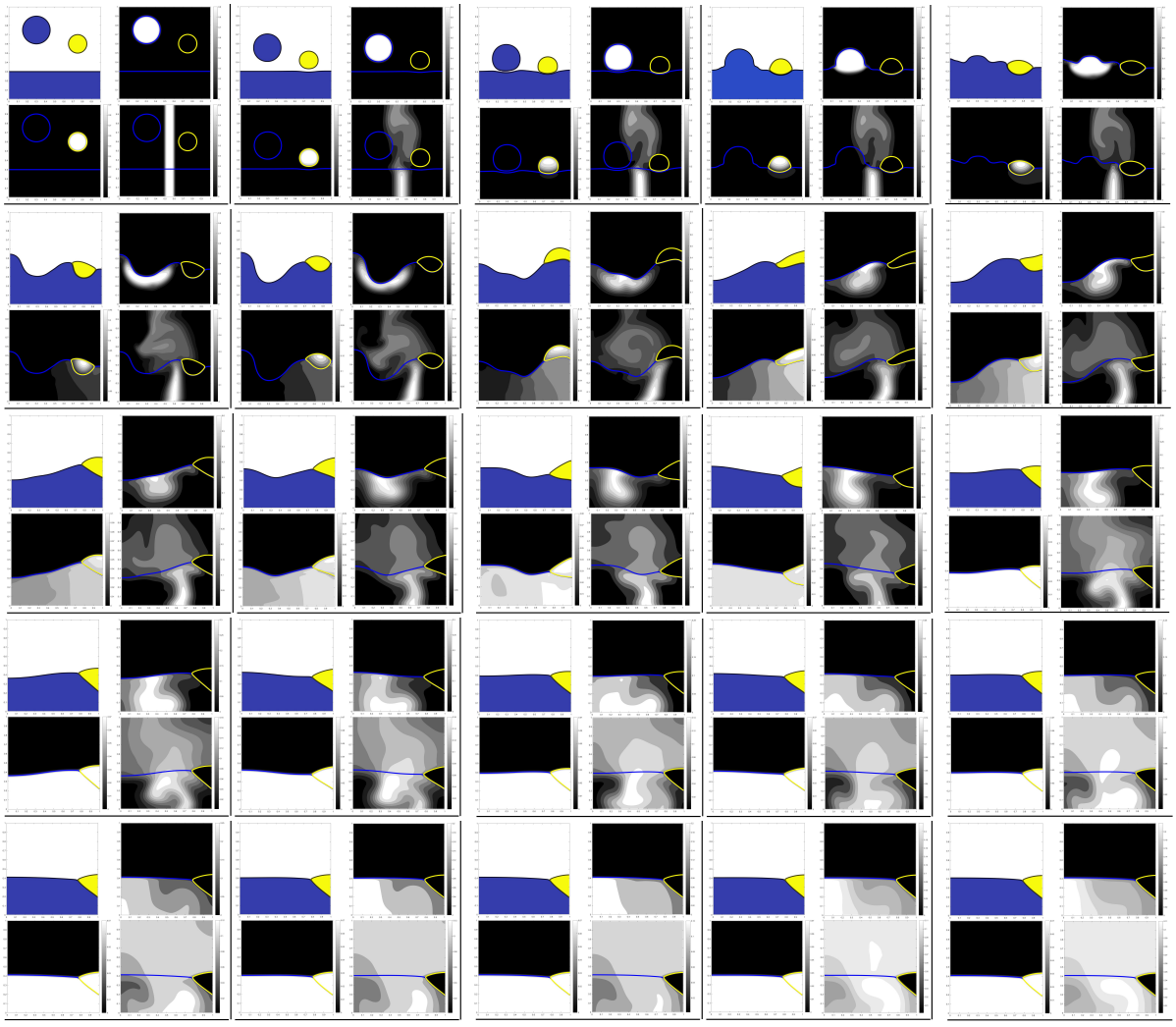

Figure 5.54. Results of the falling drops with moving contact lines, from left to right and top to bottom, t = 0.00, 0.20, 0.25, 0.27, 0.30, 0.35, 0.40, 0.50, 0.60, 0.70, 0.80, 0.90, 1.00, 1.20, 1.40, 1.60, 1.80, 2.20, 2.60, 3.00, 3.40, 3.80, 4.20, 4.60, 5.00. Top-left of each panel: configuration of the phases, blue: Phase 1, yellow: Phase 2, white: Phase 3. Top-right of each panel: configuration of Component 1. Bottom-left: configuration of Component 2. Bottom-right: configuration of Component 3. In the top-right, bottom-left, and bottom right of each panel, blue solid lines: interfaces of Phase 1, yellow solid lines: interfaces of Phase 2.

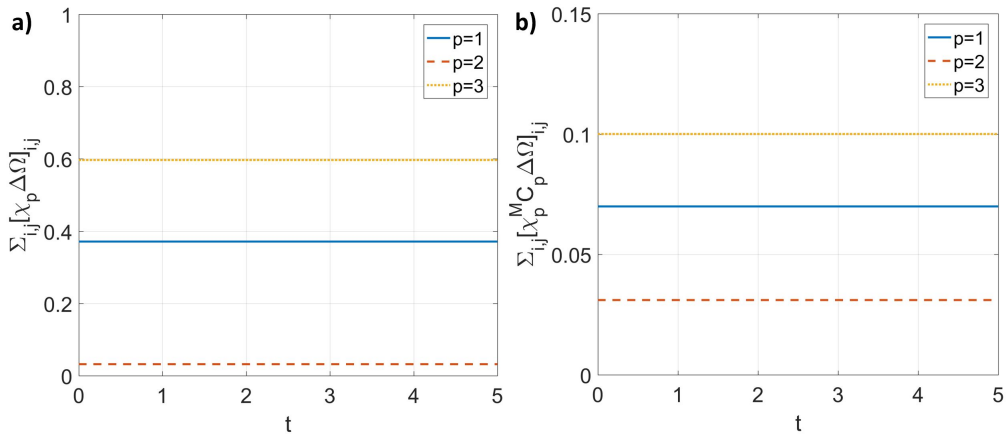

Figure 5.55. Time histories of the total volumes of individual phases and the total amounts of each component in its corresponding dissolvable region in the falling drops with moving contact lines. a) Time histories of the total volumes of individual phases. b) Time histories of the total amounts of each component in its corresponding dissolvable region.

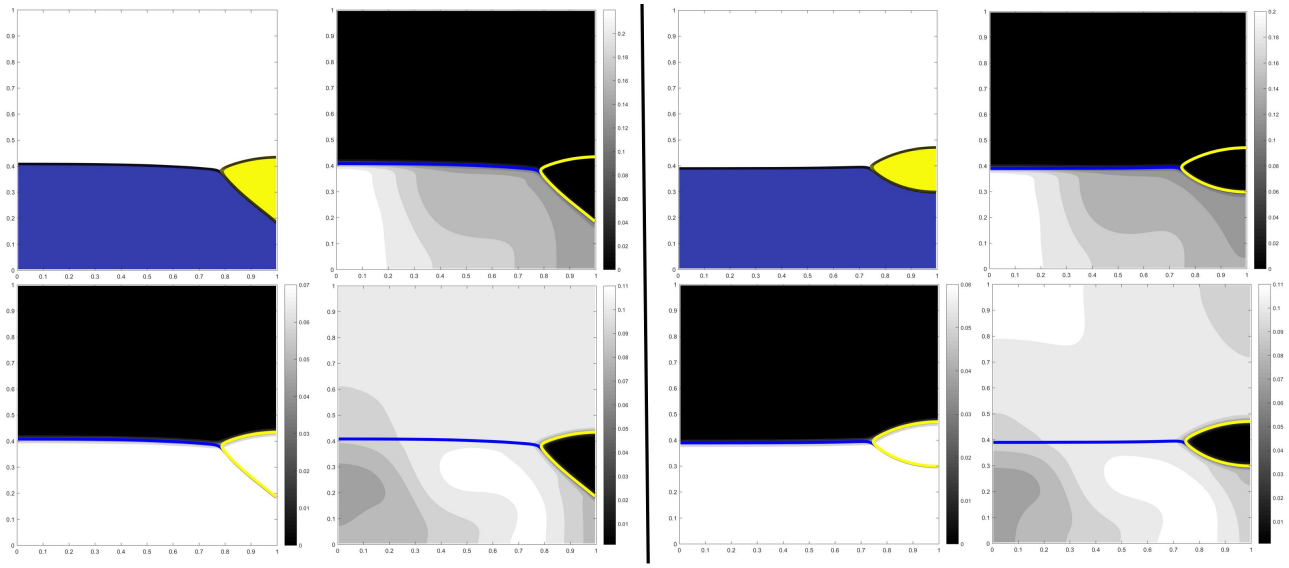

Figure 5.56. Comparison with different contact angle set-ups at $t = 5$ in the falling drop with moving contact lines. Left: the contact angle between Phases 1 and 2 is 135^0 at the right wall. Right: the contact angle between Phases 1 and 2 is 90^0 at the right wall. Top-left of each panel: configuration of the phases, blue: Phase 1, yellow: Phase 2, white: Phase 3. Top-right of each panel: configuration of Component 1. Bottom-left: configuration of Component 2. Bottom-right: configuration of Component 3. In the top-right, bottom-left, and bottom-right of each panel, blue solid lines: interfaces of Phase 1, yellow solid lines: interfaces of Phase 2.

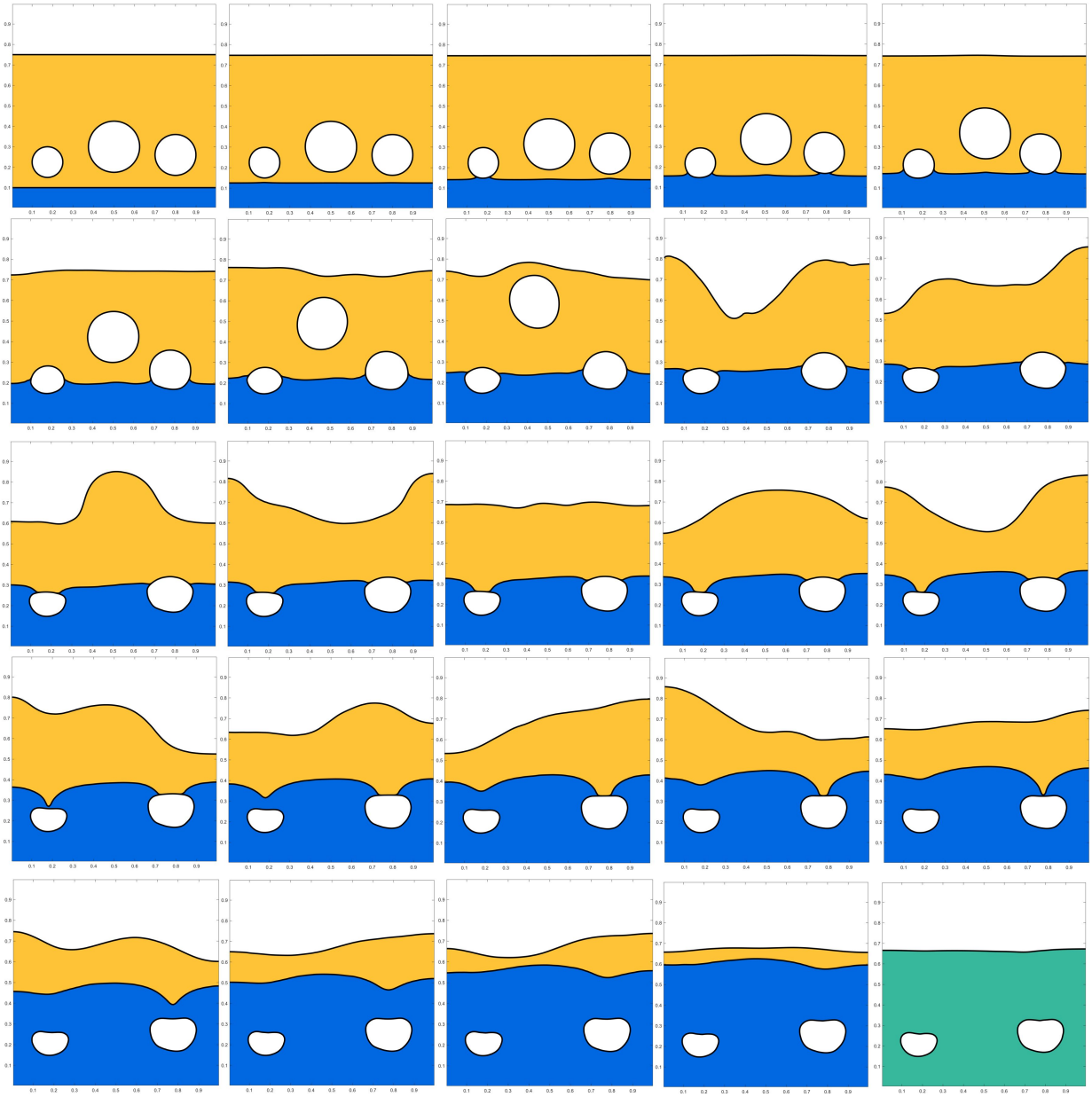

Figure 5.57. Results of rising bubbles with solidification. White: the gas phase, Orange: the liquid phase, Blue: the solid phase, Green: the solid phase when the phase change is finished. From left to right and top to bottom, $t = 0.00$, $t = 0.05$, $t = 0.10$, $t = 0.15$, $t = 0.20$, $t = 0.30$, $t = 0.40$, $t = 0.50$, $t = 0.60$, $t = 0.70$, $t = 0.80$, $t = 0.90$, $t = 1.00$, $t = 1.10$, $t = 1.20$, $t = 1.40$, $t = 1.60$, $t = 1.80$, $t = 2.00$, $t = 2.20$, $t = 2.50$, $t = 3.00$, $t = 3.50$, $t = 4.00$, and $t = 5.00$.

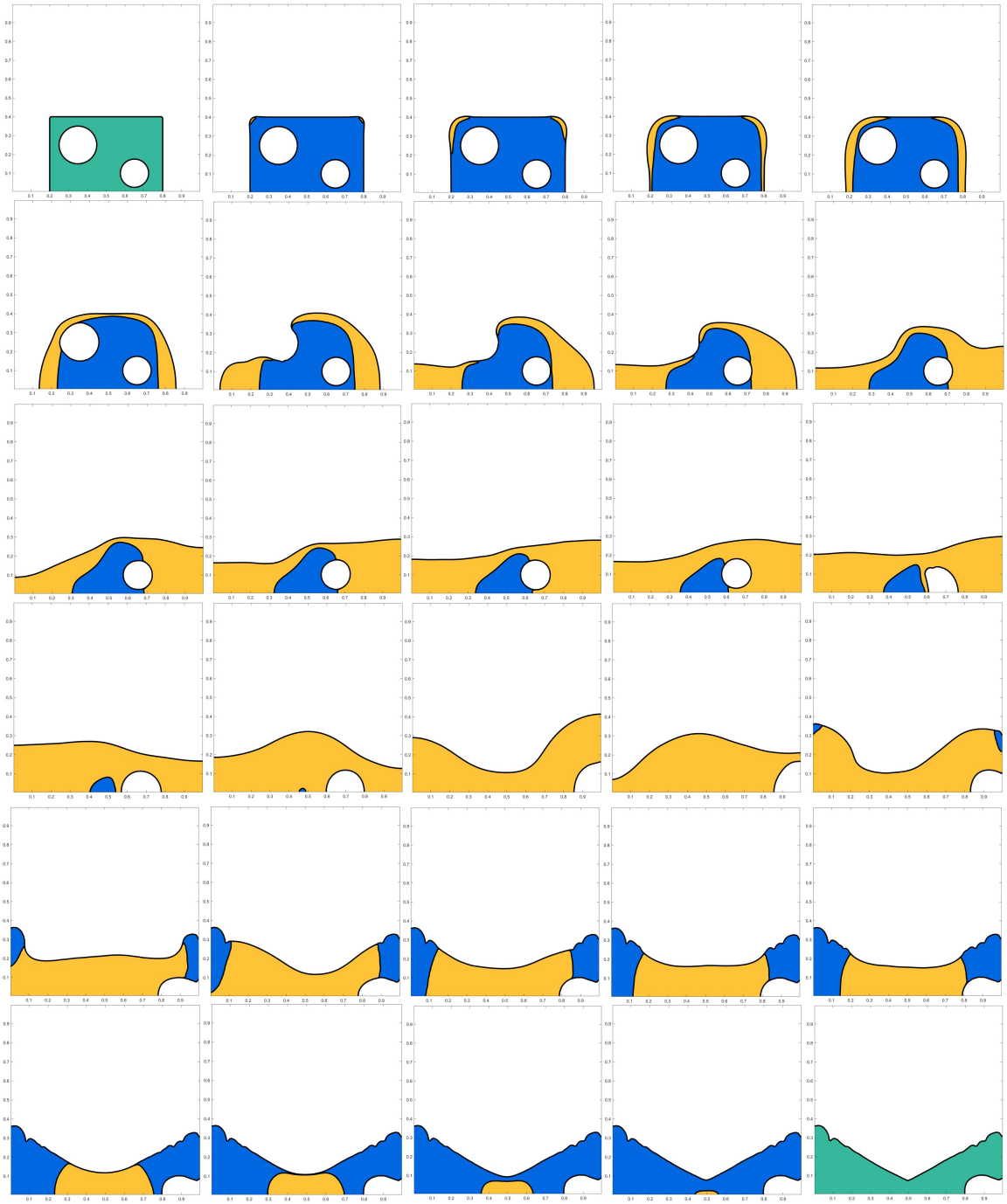

Figure 5.58. Results of rising bubbles with solidification. White: the gas phase, Orange: the liquid phase, Blue: the solid phase, Green: the solid phase when the phase change is finished. From left to right and top to bottom, $t = 0.00$, $t = 0.05$, $t = 0.10$, $t = 0.15$, $t = 0.20$, $t = 0.30$, $t = 0.40$, $t = 0.50$, $t = 0.60$, $t = 0.70$, $t = 0.80$, $t = 0.90$, $t = 1.00$, $t = 1.10$, $t = 1.20$, $t = 1.40$, $t = 1.60$, $t = 1.80$, $t = 2.00$, $t = 2.10$, $t = 2.20$, $t = 2.30$, $t = 2.40$, $t = 2.50$, $t = 2.60$, $t = 3.00$, $t = 3.25$, $t = 3.50$, $t = 3.75$, and $t = 4.00$.

6. SUMMARY[1]

In the present study, a consistent and conservative Phase-Field method for multiphase flow problems is proposed. It consists of the general modeling principles, i.e., the consistency conditions, and the consistent and conservative numerical framework. This method is independent of the specific form of the Phase-Field equation and the numerical scheme to solve it. Problems including an arbitrary number of immiscible and incompressible phases are considered. Each phase has its own constant density and viscosity, and each pair of phases has an interfacial tension at their interfaces and a contact angle at a wall. The proposed consistency conditions provide a practical and convenient way to directly obtain "mixture-level" models for multiphase problems, and individual ingredients of the models are physically connected. The proposed numerical framework preserves most of the physical properties of the multiphase flows in a discrete sense, and therefore they are accurate, robust, and effective for complicated multiphase dynamics, even when there are large differences in material properties. A schematic of the consistent and conservative Phase-Field method is shown in Fig.6.1.

6.1 Development of the Phase-Field equation

In the present work, the general multiphase volume distribution problem, which is an important component of developing multiphase Phase-Field equations, is addressed consistently and conservatively by the proposed consistent and conservative volume distribution algorithm in Section 2.2.2. This algorithm honors the summation constraint, conservation constraint, and *consistency of reduction*, so that no fictitious phases, voids, or overfilling are

[1]This chapter was partly published in Journal of Computational Physics, Vol 387, Ziyang Huang, Guang Lin, Arezoo M. Ardekani, A mixed upwind/central WENO scheme for incompressible two-phase flows, Page 455-480, Copyright Elsevier (2019); in Journal of Computational Physics, Vol 406, Ziyang Huang, Guang Lin, Arezoo M. Ardekani, Consistent, essentially conservative and balanced-force Phase-Field method to model incompressible two-phase flows, Page 109192, Copyright Elsevier (2019); in Journal of Computational Physics, Vol 420, Ziyang Huang, Guang Lin, Arezoo M. Ardekani, Consistent and conservative scheme for incompressible two-phase flows using the conservative Allen-Cahn model, Page 109718, Copyright Elsevier (2020); in Journal of Computational Physics, Vol 434, Ziyang Huang, Guang Lin, Arezoo M. Ardekani, A consistent and conservative model and its scheme for N-phase-M-component incompressible flows, Page 110229, Copyright Elsevier (2021); and in International Journal of Multiphase Flow, Vol 142, Ziyang Huang, Guang Lin, Arezoo M. Ardekani, A consistent and conservative volume distribution algorithm and its applications to multiphase flows using Phase-Field models, Page 103727, Copyright Elsevier (2021).

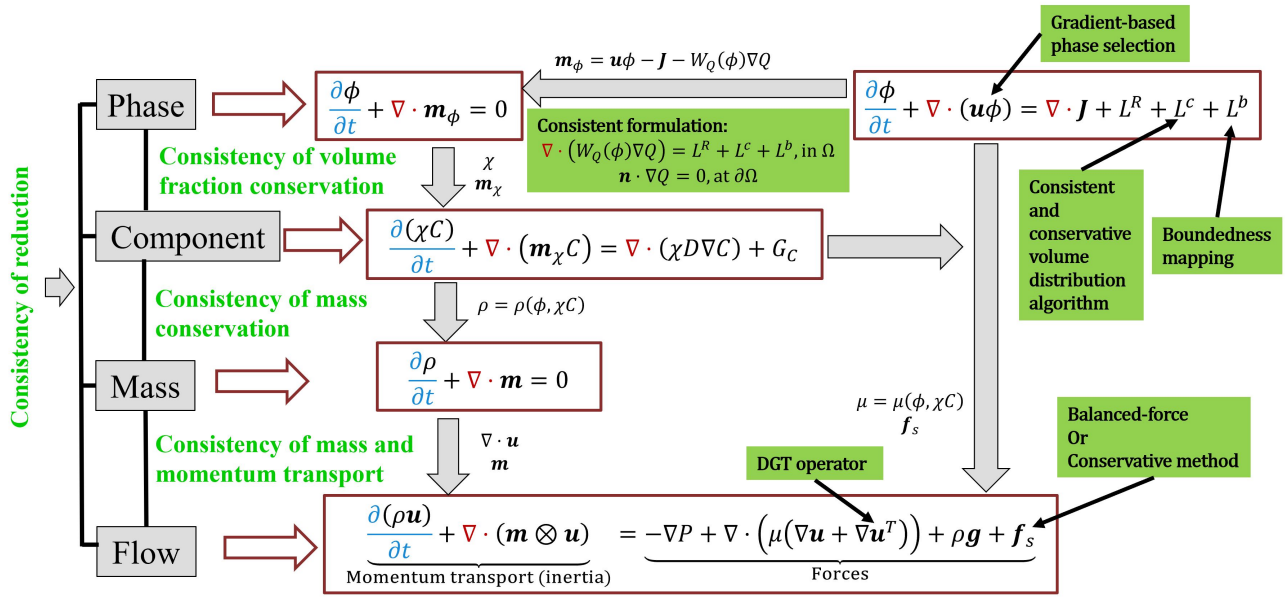

Figure 6.1. Schematic of the consistent and conservative Phase-Field method for multiphase flow problems. Colors highlight the correspondences of the numerical operators in different equations.

generated after the volume distribution. It is challenging to satisfy all the constraints in a general multiphase setup, and the two-phase phase-wise formulation is not feasible. Then the problem is turned into a linear system representing the interactions among different phases. A weight function for volume distribution is carefully selected, so that the aforementioned constraints are satisfied and the coefficient matrix of the linear system is not only symmetric but also diagonally dominant. A scaling argument is supplemented so that the solution of the linear system is admissible. This is the first volume distribution algorithm that is general for an arbitrary number of phases and satisfies all the physical constraints mentioned.

The proposed volume distribution algorithm is successfully applied to determine the Lagrange multipliers that enforce the mass conservation for general multiphase Phase-Field equations. As an example of this application, a multiphase conservative Allen-Cahn equation Eq.(2.19) that honors the summation constraint for the order parameters, the mass conservation, and the *consistency of reduction*, simultaneously, is developed in Section 2.2.3. Such a kind of conservative Allen-Cahn equation is first reported in the present study. In ad-

dition, the multiphase conservative Allen-Cahn equation exactly reduces to the one proposed in [96] for two-phase problems.

The *consistency of reduction* is an important property of a multiphase Phase-Field equation, since it eliminates any generation of fictitious phases. The numerical studies in Chapter 4 show that fictitious phases are unphysically produced at interfacial regions by the multiphase equation in [68] that violates the *consistency of reduction*. On the other hand, there are no fictitious phases generated by either the multiphase conservative Allen-Cahn equation Eq.(2.19), proposed in the present work, or the multiphase Cahn-Hilliard model Eq.(2.17), proposed in [75] and further studied in the present work, since both the Phase-Field equations are reduction consistent. A comparison study is also performed and it is shown that the conservative Allen-Cahn equation Eq.(2.19) has a better ability than the Cahn-Hilliard one Eq.(2.17) to preserve under-resolved structures.

Another application of the proposed volume distribution algorithm is the development of a general formulation to implement the contact angle boundary conditions for the second-order Phase-Field equations. The original second-order Phase-Field equations are modified by adding a Lagrange multiplier that enforces the mass conservation but does not change the summation of the order parameters and the *consistency of reduction*. The newly introduced Lagrange multiplier is determined by the consistent and conservative volume distribution algorithm in Section 2.2.2. The proposed formulation is applicable to not only two-phase but also N-phase ($N \geqslant 2$) cases, and is independent of the specific form of the second-order Phase-Field equations or the contact angle boundary conditions.

Therefore, the consistent and conservative volume distribution algorithm is an important tool for modeling and simulating multiphase flows.

6.2 Coupling to the hydrodynamics

Compared to the progress of developing Phase-Field equations (or models) for multiphase problems, the coupling to the hydrodynamics is usually less discussed. It is illustrated in the present study that the mixture density can be governed by an equation different from the sharp-interface mass conservation equation Eq.(1.1), especially when the divergence-free

"volume-averaged" velocity is considered. As a result, the Navier-Stokes equation Eq.(1.2) needs to be modified to describe the motion of the fluid mixture. In addition to the *consistency of reduction*, two more consistency conditions, which are the *consistency of mass conservation* and *consistency of mass and momentum transport*, are proposed. The *consistency of mass conservation* is implemented to obtain the "actual" mass conservation equation, as well as the consistent mass flux. Then, the *consistency of mass and momentum transport* is applied to finalized the momentum equation, which guarantees the physical coupling between the mass and momentum transport. The direct consequence of satisfying these two consistency conditions is that the resulting momentum equation implies the kinetic energy conservation (if all the forces except the contribution from the pressure gradient are absent) and is Galilean invariant. This conclusion is generally true without the need to consider the detail of the Phase-Field equation. More information of the Phase-Field equation is needed when the 2nd law of thermodynamics and *consistency of reduction* of the entire mulitphase model are considered. The present study shows that the same will be true for the entire multiphase system if the Phase-Field equation on its own enjoys energy dissipation or is reduction consistent. Notice that the above statement is valid only when the other two consistency conditions are implemented in the coupling. Finally, the consistency conditions as well as the formulations derived from them can be physically explained using the control volume analysis and mixture theory. Specifically, the present study considers the conservative Allen-Cahn Eq.(2.19) and Cahn-Hilliard Eq.(2.17) equations because they are fully reduction consistent. The entire multiphase model additionally satisfies the mass conservation of each phase, and the momentum conservation including interfacial tensions.

The *consistency of mass conservation* can not be directly implemented when the Phase-Field equation is not written in a conservative form, like the conservative Allen-Cahn equation Eq.(2.19). To resolve this issue, the consistent formulation is proposed in Section 2.3.1, where the reaction terms and Lagrange multipliers in the Phase-Field equation are reformulated in a conservative form, with the help of defining an auxiliary variable. The auxiliary variable is governed by a Poisson equation, whose source term is compatible with its boundary condition. As a result, the consistency analysis based on the Phase-Field equations

written in a conservative form is again valid for those including reaction terms and Lagrange multipliers.

6.3 Consistent and conservative numerical framework and its results

Another important task finished in the present study is to preserve the physical properties of the proposed mulitphase system after discretization, in addition to considering the accuracy of the schemes. Several novel techniques are developed, and careful numerical analyses are performed to achieve the goal. As a result, the proposed numerical framework is consistent and conservative.

It is first illustrated that the convection term in the Phase-Field equation can be a source of producing local voids, overfilling, or fictitious phases, due to using non-linear interpolation schemes. To fix this issue, the gradient-based phase selection procedure is proposed to correct the numerical convection flux, which is valid regardless of the method used to compute the numerical flux. The conservative method is developed to compute the surface force, which preserves that the integral of the surface force over a periodic domain is zero. The "DGT" numerical operator is developed for the viscous force so that the viscous force exactly reduces to its single-phase discrete counterpart. This is critical for both the *consistency of reduction* and momentum conservation on the discrete level. Achieving consistency on the discrete level is more involved and is not guaranteed by just using the continuous formulations, without carefully considering the numerical implementations. New general theorems are proposed in Section 3.2 to address this difficulty. Those theorems illustrate the numerical correspondences that should be followed in the discrete Phase-Field and momentum equations, and therefore do not rely on the details of the Phase-Field equation and its scheme. Violations of those theorems introduce inconsistent errors (approximately) proportional to the density ratio. Thus, satisfying the consistency conditions on the discrete level becomes more significant for large-density-ratio problems. The boundedness mapping in Section 3.3.2, which is another application of the proposed volume distribution algorithm, maps the out-of-bound order parameters, numerically solved from the Phase-Field equation, into their physical interval, but does not change the physical properties of the order pa-

rameters, i.e., their summation constraint, mass conservation, and *consistency of reduction*. This is essential to avoid negative density and/or viscosity of the fluid mixture, especially when ratios of phase densities and/or viscosities are large. It should be noted that a negative mixture density and/or viscosity results in ill-posedness of the multiphase system. The boundedness mapping is finally modeled as a discrete Lagrange multiplier and is included in the implementation of the consistent formulation in Section 3.3.5. As a result, the discrete consistent mass flux that satisfies the *consistency of mass conservation* is obtained, following the theorems in Section 3.2.

With the help of these novel techniques, the mass conservative and reduction consistent schemes are developed for the Phase-Field equations considered (Eq.(2.17) and Eq.(2.19)). The present study proofs that the order parameters solved from those schemes are reduction consistent, mass conservative, and bounded, and their summation follows the constraints in Eq.(2.2) at every grid point. A projection scheme is constructed to solve the momentum equation for the fluid mixture. This scheme conserves the momentum when the surface force is either neglected or computed by the conservative method. It also satisfies the *consistency of reduction*, and therefore recovers the single-phase dynamics inside each bulk-phase region. It solves advection (or translation) problems exactly (neglecting the gravity and interfacial tensions) regardless of the material properties or interface shapes, thanks to satisfying the *consistency of mass conservation* and *consistency of mass and momentum transport* on the discrete level. All those properties are rigorously proved. Therefore, the schemes are consistent and conservative. In addition, they are decoupled, semi-implicit, and formally 2nd-order accurate.

Various numerical experiments are performed to validate all the aforementioned properties of the schemes, and the results are consistent with the numerical analyses. The formal order of accuracy of the proposed schemes is 2nd-order. It is observed that the out-of-bound error can grow as the computation goes on, contaminate the physical solution, and in the end, trigger numerical instability, although it is small in every time step. The boundedness mapping removes the out-of-bound error while preserves the physical properties of the order parameters, which is beneficial to improve the robustness of the scheme and to provide a physical solution. In the steady drop problem, the strengths of the spurious cur-

rent are small and insensitive to the density ratio, viscosity ratio and surface tension. The balanced-force method gives a smaller spurious current and faster convergence rate than the conservative method. As illustrated in the large-density-ratio advection problem, violating the consistency conditions results in unphysical velocity and pressure fluctuations and interface deformations, and finally triggers numerical instability, while the physical result is well reproduced by the proposed schemes even with an extremely large density ratio like 10^9. This demonstrates the significance of satisfying the consistency conditions on the discrete level. Careful and systematic convergence tests are performed based on the rising bubble case including a large density ratio (1000), a large viscosity ratio (100), and surface tension and gravity forces. Such convergence tests have not yet been done with the Phase-Field method applied to multiphase flows. The results suggest the interface thickness to be in the order of the grid size, while they are insensitive to the magnitude of M_0. The convergence of the numerical solution of the Phase-Field method to the sharp interface one is observed and the convergence rate is between 1.5th- and 2nd-order, no matter whether the Cahn-Hilliard or conservative Allen-Cahn equation is used to capture the interface, or the balanced-force or conservative method is used to discretize the surface force. Including the boundedness mapping does not influence either the order of accuracy of the schemes or the convergence behavior to the sharp-interface solution. In the horizontal shear layer problem, the generation of fictitious phases, local voids, or overfilling is observed when the gradient-based phase selection procedure is not implemented. These unphysical behaviors disappear after the procedure is activated. Different from using the conservative method, the momentum is only essentially conserved with the balanced-force method, while the non-conservation is very small and is reduced after grid refinement. Although it is not shown in the analyses, the numerical results reproduce the total energy decay in both inviscid and viscous cases. The conservative method performs better in the inviscid case when the grid is coarse, while the difference between the two methods is not significant in the fine-grid solution or in the viscous case. Therefore, both the balanced-force method and the conservative method are practical and effective for multiphase flows.

Several realistic multiphase flow problems, which include strong interactions between the fluid phases, large differences in material properties, interfacial tensions, and topological

changes, are performed. The present results agree well with the exact/asymptotic solutions from the sharp-interface methods and with existing numerical and experimental data. The cases with a density ratio of 3000 in the Rayleigh-Taylor instability and with a density ratio of $100,000$ in the dam break are explored, which shows the robustness of the present schemes to deal with practical multiphase problems with large density ratios. Strong interactions among different phases in the long-time dynamics are captured and the interface configuration becomes very complicated. In these applications, it is observed that the balanced-force method has a larger tendency to break to small interfacial structures, resulting in more topological changes, while the conservative method is more stable, i.e., allowing a larger time step. The consistent formulation can be easily applied in different coordinate systems, e.g., the axisymmetric coordinate, and the axisymmetic rising bubble is solved to show this flexibility. The mass conservation and the summation constraint for the order parameters are always satisfied even though the problem considered is highly dynamic. The results also show that simply clipping and rescaling the order parameters, instead of performing the boundedness mapping in Section 3.3.2, leads to significant mass changes. The present results also show that the setup of the contact angles highly influences the dynamics of multiphase problems after the contact lines are formed. The equilibrium shapes and locations of the fluid phases can be very different under different set of contact angles. As a representative of the 2nd-order Phase-Field equations, the conservative Allen-Cahn equation Eq.(2.19) is implemented in moving contact line problems with the help of the proposed formulation. The results agree well with the exact and/or asymptotic solutions for equilibrium problems, and similar dynamical behaviors reported in, e.g., [74], [79], [90] using the fourth-order Cahn-Hilliard equations, are captured by the conservative Allen-Cahn equations.

With the proposed consistent and conservative Phase-Field method, one is able to further quantitatively compare the performances of various categories of Phase-Field equations, like the conservative Phase-Field equation and modified Cahn-Hilliard equation [58], [114], [233]–[236], and even the algebraic Volume-of-Fluid method, e.g., [237], on reproducing the multiphase flow dynamics. Another attractive future direction is to extend the present consistent and conservative numerical framework to the adaptive time and space refinements, which would be especially beneficial for the problems including a wide range of time and length

scales. However, preserving the consistent and conservative properties can be non-trivial. The present study leaves open the possibility of using the 2nd-order Phase-Field equations for moving contact line problems, which has never been considered before. Therefore, it provides plenty of new opportunities to study in the future. Since the pool of plausible Phase-Field equations for moving contact line problems is greatly expanded, it is now not only possible but also desirable to investigate and clarify their performance. Unlike the Cahn-Hilliard equations, there is little theoretical analysis of the 2nd-order Phase-Field equations in moving contact line problems, e.g., the asymptotic analysis as the interface thickness tends to zero. Such an analysis is important to provide physical insights of determining the parameters in the Phase-Field equations.

6.4 N-phase-M-component model

The aforementioned modeling principles and numerical frameworks are extended to multiphase and multicomponent, or N-phase-M-component, incompressible flows with $N \geqslant 1$ and $M \geqslant 0$. Components are newly introduced and dissolvable in some specific phases. This model allows arbitrary numbers of phases and components appearing simultaneously. Each component can exist in different phases. Each phase is a "solution" of its pure phase (which is the background fluid of the phase) as the "solvent" and there can be multiple components as the "solutes" dissolved in that phase . The dissolvability matrix is defined to indicate these relations between phases and components. Individual pure phases and components have their own densities and viscosities. Each pair of a phase and a component has a diffusivity. A new consistency condition: *consistency of volume fraction conservation* is proposed to help to model such a kind of problem.

Each component has its own concentration governed by the convection-diffusion equation in its dissolvable regions, and its flux at the phase boundaries is either zero if it is not dissolvable in the neighboring phases or continuous otherwise. The concentrations represent the local amounts of the components and are generally interpreted as the "molar concentrations", while they can be considered as the "volume fractions" in some special problems. Since all the phases are evolving and deforming, it is challenging to solve the equation and

assign the boundary condition of the components. The diffuse domain approach [143] is applied, which turns the locally defined equation into an equivalent one defined in the entire domain of interest. Then, the phase indicator functions are replaced by the smoothed ones, which makes the volume fractions from the Phase-Field model a directly available candidate. The component equation is finalized by implementing the *consistency of volume fraction conservation* which incorporates the thermodynamical effects from the Phase-Field equation. The density and viscosity of the fluid mixture include both the contributions from the phases and components. The *consistency of mass conservation* and the *consistency of mass and momentum transport* are again applied to ensure the physical coupling between the mass conservation equation and the momentum equation. The *consistency of reduction* is extended such that fictitious components are not produced. With the help of the *consistency of volume fraction conservation* and other consistency conditions, one can show that the proposed N-phase-M-component model honors a physical energy law and the Galilean invariance.

In addition to multiphase and multicomponent problems, the proposed model is also applicable to some multiphase problems, where the miscibilities between each pair of phases are different. It is also flexible to different circumstances of cross-interface transport of a component that is dissolvable in both sides of the interface. More importantly, the present study proposes a general framework that physically connects the dynamics of the phases, the components, and the fluid flows, using the proposed consistency conditions, see Fig.6.1.

The consistent and conservative numerical framework is implemented to solve the proposed N-phase-M-component model. The capability of the model for different circumstances of cross-interface transport of a component which is dissolvable in both sides of the interface is demonstrated. The effect of the *consistency of volume fraction conservation* on eliminating unphysical fluctuations of the components around phase interfaces is illustrated. Finally, the proposed model and scheme are successfully applied to two challenging problems, including multiple materials and various miscibility relations among the materials, and having many critical factors in multiphase and multicomponent flows, i.e., significant differences of the material properties, gravitation, interfacial tensions, topological changes, large deformation of the interfaces, and the effects of contact angles and moving contact lines. In summary,

the proposed model and scheme are general, effective, and robust for multiphase and multi-component incompressible flows.

6.5 Thermo-gas-liquid-solid model with solidification/melting

The aforementioned modeling principles and numerical frameworks are extended to the thermo-gas-liquid-solid flows, where the liquid and solid phases are experiencing solidification/melting. The ingredients of the proposed model include the consistent and conservative Phase-Field method for two-phase flows, the fictitious domain Brinkman penalization (FD/BP) method for fluid-structure interactions [160], [161], and the Phase-Field model of solidification in [163]. These successful models are physically coupled using the proposed consistency conditions. The Cahn-Hilliard equation Eq.(2.22) is applied to locate the gas and phase change material. The phase change equation Eq.(2.59) is derived from the solidification model in [163] using the diffuse domain approach [143]. Then the *consistency of volume fraction conservation* is applied to admit the fully liquid/solid-state of the phase change material. The interpolation function in [163] is also modified so that the equilibrium states of the order parameter in the model depend on the temperature in a physical sense, which resolves the issue of initiating the phase change when the phase change material is fully liquid/solid at the beginning. After applying the *consistency of mass conservation*, not only the consistent mass flux, which appears in the momentum equation following the *consistency of mass and momentum transport*, but also the divergence of the velocity Eq.(2.63), which quantifies the volume change induced by the solidification/melting, is obtained. Isothermal (or temperature equilibrium) solutions are admissible by the proposed energy equation Eq.(2.64) when the phase change is absent, after incorporating the *consistency of mass conservation* and the *consistency of volume fraction conservation*. To confine the surface tension effect on the gas-liquid interface only, a new continuous surface tension force is proposed based on the Phase-Field formulation [54], [55], [113]. The Carman-Kozeny equation [162] is modified to enforce zero velocity in the solid phase. These two additional forces are added to the momentum equation Eq.(2.34). The proposed model defines the volume fractions of the gas, liquid, and solid phases unambiguously, and the volume change due to

solidification/melting is included. The mass and energy conservation is always true. The momentum conservation is honored if the solid phase is absent, since additional forces may appear at the domain boundary to immobilize the solid phase. The proposed model also satisfies the Galilean invariance, and moreover it is reduction consistent.

The proposed model is numerically solved with the consistent and conservative numerical framework, and various numerical tests are performed to validate and demonstrate it. The results not only agree very well with the exact solutions but also match the expectations from the theorems of the model. The volume change resulting from the phase change is illustrated, and it is quantitatively demonstrated to be consistent with the mass conservation. This physical behavior has not been captured in many existing models by assuming the divergence-free velocity all the time. The numerical error of mass conservation is very small, and therefore the present scheme conserves the mass satisfactorily, although not exactly. Finally, two challenging problems, including a wide range of material properties and strong interactions among different phases, are set up and successfully solved, which illustrates the capability of the model.

The present study proposes a practical framework to incorporate the solidification/melting of a pure material into liquid-gas flows. This method can be extended to include more complicated physics, e.g., the thermo-capillary effect, anisotropy or dendritic growth, and solute transport during the solidification.

REFERENCES

[1] U. S. C. Guard and N. R. T. (US), *On Scene Coordinator Report: Deepwater Horizon Oil Spill*. US Department of Homeland Security, US Coast Guard, 2011.

[2] S. Aramideh, P. Vlachos, and A. Ardekani, "Unstable displacement of non-aqueous phase liquids with surfactant and polymer," *Transport in Porous Media*, vol. 126, no. 2, pp. 455–474, 2019.

[3] S. Wang, K. Ellett, and A. Ardekani, "Assessing the utility of high-level co2 storage and utilization resource estimates for ccs system modelling," *Energy Procedia*, vol. 114, pp. 4658–4665, 2017.

[4] V. Alvarado and E. Manrique, "Enhanced oil recovery: An update review," *Energies*, vol. 3, no. 9, pp. 1529–1575, 2010.

[5] H.-C. Kan, H. S. Udaykumar, W. Shyy, and R. Tran-Son-Tay, "Hydrodynamics of a compound drop with application to leukocyte modeling," *Physics of fluids*, vol. 10, no. 4, pp. 760–774, 1998.

[6] P. Gao and J. Feng, "Spreading and breakup of a compound drop on a partially wetting substrate," *Journal of fluid mechanics*, vol. 682, pp. 415–433, 2011.

[7] S. Zhu, A. Kherbeche, Y. Feng, and M.-J. Thoraval, "Impact of an air-in-liquid compound drop onto a liquid surface," *Physics of Fluids*, vol. 32, no. 4, p. 041 705, 2020.

[8] L. Leal, *Advanced Transport Phenomena: Fluid Mechanics and Convective Transport Processes*. Cambridge University Press, 2007.

[9] G. Tryggvason, R. Scardovelli, and S. Zaleski, *Direct Numerical Simulations of Gas-Liquid Multiphase Flows*. Cambridge University Press, 2011.

[10] A. Prosperetti and G. Tryggvason, *Computational Methods for Multiphase Flow*. Cambridge University Press, 2007.

[11] S. Unverdi and G. Tryggvason, "A front-tracking method for viscous, incompressible, multi-fluid flows," *J. Comput. Phys.*, vol. 100, pp. 25–37, 1992.

[12] G. Tryggvason, B. Bunner, A. Esmaeeli, D. Juric, N. Al-Rawahi, W. Tauber, J. Han, S. Nas, and Y. Jan, "A front-tracking method for the computations of multiphase flow," *J. Comput. Phys.*, vol. 169, pp. 708–759, 2001.

[13] S. Manservisi and R. Scardovelli, "A variational approach to the contact angle dynamics of spreading droplets," *Computers & fluids*, vol. 38, no. 2, pp. 406–424, 2009.

[14] M. Muradoglu and S. Tasoglu, "A front-tracking method for computational modeling of impact and spreading of viscous droplets on solid walls," *Computers & Fluids*, vol. 39, no. 4, pp. 615–625, 2010.

[15] S. Osher and A. Sethian, "Fronts propagating with curvature-dependent speed: Algorithms based on hamilton-jacobi formulations," *J. Comput. Phys.*, vol. 79, pp. 12–49, 1988.

[16] M. Sussman, P. Smereka, and S. Osher, "A level set approach for computing solutions to incompressible two-phase flow," *J. Comput. Phys.*, vol. 114, pp. 146–159, 1994.

[17] J. Sethian and P. Smereka, "Level set method for fluid interfaces," *Annu. Rev. Fluid Mech.*, vol. 35, pp. 341–372, 2003.

[18] F. Gibou, R. Fedkiw, and S. Osher, "A review of level-set methods and some recent applications," *J. Comput. Phys.*, vol. 353, pp. 82–109, 2018.

[19] P. Spelt, "A level-set approach for simulations of flows with multiple moving contact lines with hysteresis," *Journal of Computational physics*, vol. 207, no. 2, pp. 389–404, 2005.

[20] J. Zhang and P. Yue, "A level-set method for moving contact lines with contact angle hysteresis," *Journal of Computational Physics*, vol. 418, p. 109 636, 2020.

[21] E. Olsson and G. Kreiss, "A conservative level set method for two phase flow," *J. Comput. Phys.*, vol. 210, pp. 225–246, 2005.

[22] E. Olsson, G. Kreiss, and S. Zahedi, "A conservative level set method for two phase flow ii," *J. Comput. Phys.*, vol. 225, pp. 785–807, 2007.

[23] R. Chiodi and O. Desjardins, "A reformulation of the conservative level set reinitialization equation for accurate and robust simulation of complex multiphase flows," *J. Comput. Phys.*, vol. 343, pp. 186–200, 2017.

[24] S. Zahedi, K. Gustavsson, and G. Kreiss, "A conservative level set method for contact line dynamics," *Journal of Computational Physics*, vol. 228, no. 17, pp. 6361–6375, 2009.

[25] Y. Sato and B. Niceno, "A new contact line treatment for a conservative level set method," *Journal of computational physics (Print)*, vol. 231, no. 10, pp. 3887–3895, 2012.

[26] C. Hirt and B. Nichols, "Volume of fluid (vof) method for the dynamics of free boundaries," *J. Comput. Phys.*, vol. 39, pp. 201–225, 1981.

[27] R. Scardovelli and S. Zaleski, "Direct numerical simulation of free-surface and interfacial flow," *Annu. Rev. Fluid Mech.*, vol. 31, pp. 567–603, 1999.

[28] M. Owkes and O. Desjardins, "A mass and momentum conserving unsplit semi-lagrangian framework for simulating multiphase flows," *J. Comput. Phys.*, vol. 332, pp. 21–46, 2017.

[29] M. Renardy, Y. Renardy, and J. Li, "Numerical simulation of moving contact line problems using a volume-of-fluid method," *Journal of Computational Physics*, vol. 171, no. 1, pp. 243–263, 2001.

[30] S. Afkhami, S. Zaleski, and M. Bussmann, "A mesh-dependent model for applying dynamic contact angles to vof simulations," *Journal of computational physics*, vol. 228, no. 15, pp. 5370–5389, 2009.

[31] K. Yokoi, "Numerical studies of droplet splashing on a dry surface: Triggering a splash with the dynamic contact angle," *Soft Matter*, vol. 7, no. 11, pp. 5120–5123, 2011.

[32] F. Xiao, Y. Honma, and T. Kono, "A simple algebraic interface capturing scheme using hyperbolic tangent function," *Int. J. Numer. Meth. Fluids*, vol. 48, no. 9, pp. 1023–1040, 2005.

[33] S. Ii, K. Sugiyama, S. Takeuchi, S. Takagi, Y. Matsumoto, and F. Xiao, "An interface capturing method with a continuous function: The thinc method with multi-dimensional reconstruction," *J. Comput. Phys.*, vol. 231, no. 5, pp. 2328–2358, 2012.

[34] B. Xie and F. Xiao, "Toward efficient and accurate interface capturing on arbitrary hybrid unstructured grids: The thinc method with quadratic surface representation and gaussian quadrature," *J. Comput. Phys.*, vol. 349, pp. 415–440, 2017.

[35] L. Qian, Y. Wei, and F. Xiao, "Coupled thinc and level set method: A conservative interface capturing scheme with high-order surface representations," *J. Comput. Phys.*, vol. 373, pp. 284–303, 2018.

[36] S. Mirjalili, S. Jain, and D. M.S., "Interface-capturing methods for two-phase flows: An overview and recent developments," *Center for Turbulence Research Annual Research Briefs*, pp. 117–135, 2017.

[37] Y. Sui, H. Ding, and P. Spelt, "Numerical simulations of flows with moving contact lines," *Annual Review of Fluid Mechanics*, vol. 46, pp. 97–119, 2014.

[38] D. Gueyffier, J. Li, A. Nadim, R. Scardovelli, and S. Zaleski, "Volume-of-fluid interface tracking with smoothed surface stress methods for three-dimensional flows," *J. Comput. Phys.*, vol. 152, pp. 423–456, 1999.

[39] J. Brackbill, D. Kothe, and C. Zemach, "A continuum method for modeling surface tension," *J. Comput. Phys.*, vol. 100, pp. 335–354, 1992.

[40] R. Fedkiw, T. Aslam, B. Merriman, and S. Osher, "A non-oscillatory eulerian approach to interfaces in multimaterial flows (the ghost fluid method)," *J. Comput. Phys.*, vol. 152, pp. 457–492, 1999.

[41] B. Lalanne, L. Villegas, S. Tanguy, and F. Risso, "On the computation of viscous terms for incompressible two-phase flows with level set/ghost fluid method," *J. Comput. Phys.*, vol. 301, pp. 289–307, 2015.

[42] A.-A.-S. M.O., S. Popinet, and H. Tchelepi, "A conservative and well-balanced surface tension model," *J. Comput. Phys.*, vol. 371, pp. 896–931, 2018.

[43] M. Francois, J. Cummins, E. Dendy, D. Kothe, M. Sicilian, and W. Williams, "A balanced-force algorithm for continuous and sharp interfacial surface tension models within a volume tracking framework," *J. Comput. Phys.*, vol. 213, pp. 141–173, 2006.

[44] S. Popinet, "Numerical models for surface tension," *Annu. Rev. Fluid Mech.*, vol. 50, pp. 49–75, 2018.

[45] S. Schofield, R. Garimella, M. Francois, and R. Loubere, "A second-order accurate material-order-independent interface reconstruction technique for multi-material flow simulations," *J. Comput. Phys.*, vol. 228, pp. 731–745, 2009.

[46] S. Schofield, C. M.A., V. Dyadechko, R. Garimella, R. Lowrie, and B. Swartz, "Multi-material incompressible flow simulation using the moment-of-fluid method," *Int. J. Numer. Meth. Fluids*, vol. 63, pp. 931–952, 2010.

[47] M. Francois, "Recent numerical and algorithmic advances within the volume tracking framework for modeling interfacial flows," *Procedia IUTAM*, vol. 15, pp. 270–277, 2015.

[48] A. Pathak and M. Raessi, "A three-dimensional volume-of-fluid method for reconstructing and advecting three-material interfaces forming contact lines," *J. Comput. Phys.*, vol. 307, pp. 550–573, 2016.

[49] K. Smith, F. Solis, and D. Chopp, "A projection method for motion of triple junctions by level sets," *Interfaces Free Bound.*, vol. 4, pp. 263–276, 2002.

[50] F. Losasso, T. Shinar, A. Selle, and R. Fedkiw, "Multiple interacting liquids," *ACM Transactions on Graphics (TOG)*, vol. 25, no. 3, pp. 812–819, 2006.

[51] D. Starinshak, S. Karni, and P. Roe, "A new level set model for multimaterial flows," *Interface and free boundaries*, vol. 4, pp. 263–276, 2002.

[52] D. Starinshak, S. Karni, and P. Roe, "A new level set model for multimaterial flows," *Interface and free boundaries*, vol. 4, pp. 263–276, 2002.

[53] D. Anderson, G. McFadden, and A. Wheeler, "Diffuse-interface methods in fluid mechanics," *Annu. Rev. Fluid Mech.*, vol. 30, pp. 139–165, 1998.

[54] D. Jacqmin, "Calculation of two-phase navier-stokes flows using phase-field modeling," *J. Comput. Phys.*, vol. 155, pp. 96–127, 1999.

[55] J. Shen, "Modeling and numerical approximation of two-phase incompressible flows by a phase-field approach," *Multiscale Modeling and Analysis for Materials Simulation*, vol. 22, pp. 147–195, 2011.

[56] H. Abels, H. Garcke, and G. Grun, "Thermodynamically consistent, frame indifferent diffuse interface models for incompressible two-phase flows with different densities," *Mathematical Models and Methods in Applied Sciences*, vol. 22, p. 1 150 013, 2012.

[57] D. Jeong and J. Kim, "Conservative allen–cahn–navier–stokes system for incompressible two-phase fluid flows," *Comput. Fluids*, vol. 156, pp. 239–246, 2017.

[58] P.-H. Chiu and Y.-T. Lin, "A conservative phase-field method for solving incompressible two-phase flows," *J. Comput. Phys.*, vol. 230, pp. 185–204, 2011.

[59] P. Yue, J. Feng, C. Liu, and J. Shen, "A diffuse-interface method for simulating two-phase flows of complex fluids," *J. Fluid Mech.*, vol. 515, pp. 293–317, 2004.

[60] F. Boyer and C. Lapuerta, "Study of a three component cahn-hilliard flow model," *ESAIM: Mathematical Modelling and Numerical Analysis*, vol. 40, no. 4, pp. 653–687, 2006.

[61] F. Boyer, C. Lapuerta, S. Minjeaud, B. Piar, and M. Quintard, "Cahn-hilliard/navier-stokes model for the simulation of three-phase flows," *Transport in Porous Media*, vol. 82, no. 3, pp. 463–483, 2010.

[62] J. Kim, "Phase field computations for ternary fluid flows," *Comput. Methods Appl. Mech. Engre.*, vol. 196, pp. 4779–4788, 2007.

[63] A. R.H.H., M. Rahimian, and A. Fakhari, "Conservative phase-field lattice-boltzmann model for ternary fluids," *J. Comput. Phys.*, vol. 374, pp. 668–691, 2018.

[64] F. Boyer and S. Minjeaud, "Hierarchy of consistent n-component cahn–hilliard systems," *Math. Models Methods Appl. Sci.*, vol. 24, pp. 2885–292, 2014.

[65] J. Kim, "A generalized continuous surface tension force formulation for phase-field models for multi-component immiscible fluid flows," *Comput. Methods Appl. Mech. Engre.*, vol. 198, pp. 3105–3112, 2009.

[66] H. Lee and J. Kim, "An efficient numerical method for simulating multiphase flows using a diffuse interface model," *Physica A*, vol. 423, pp. 33–50, 2015.

[67] J. Kim, "Phase-field models for multi-component fluid flows," *Commun. Comput. Phys.*, vol. 12, pp. 613–661, 2012.

[68] J. Kim and H. Lee, "A new conservative vector-valued allen-cahn equation and its fast numerical method," *Comput. Phys. Commun.*, vol. 221, pp. 102–108, 2017.

[69] S. Aihara, T. Takaki, and N. Takada, "Multi-phase-field modeling using a conservative allen–cahn equation for multiphase flow," *Computers & Fluids*, vol. 178, pp. 141–151, 2019.

[70] Y. Hu, D. Li, and Q. He, "Generalized conservative phase field model and its lattice boltzmann scheme for multicomponent multiphase flows," *International Journal of Multiphase Flow*, vol. 132, p. 103 432, 2020.

[71] S. Wu and J. Xu, "Multiphase allen-cahn and cahn-hilliard models and their discretizations with the effect of pairwise surface tensions," *J. Comput. Phys.*, vol. 343, pp. 10–32, 2017.

[72] S. Dong, "An efficient algorithm for incompressible n-phase flows," *J. Comput. Phys.*, vol. 276, pp. 691–728, 2014.

[73] S. Dong, "Physical formulation and numerical algorithm for simulating n immiscible incompressible fluids involving general order parameters," *J. Comput. Phys.*, vol. 836, pp. 98–128, 2015.

[74] S. Dong, "Wall-bounded multiphase flows of n immiscible incompressible fluids: Consistency and contact-angle boundary condition," *J. Comput. Phys.*, vol. 338, pp. 21–67, 2017.

[75] S. Dong, "Multiphase flows of n immiscible incompressible fluids: A reduction-consistent and thermodynamically-consistent formulation and associated algorithm," *J. Comput. Phys.*, vol. 361, pp. 1–49, 2018.

[76] P. Seppecher, "Moving contact lines in the cahn-hilliard theory," *International journal of engineering science*, vol. 34, no. 9, pp. 977–992, 1996.

[77] D. Jacqmin, "Contact-line dynamics of a diffuse fluid interface," *J. Fluid Mech.*, vol. 402, pp. 57–88, 2000.

[78] T. Qian, X. Wang, and P. Sheng, "A variational approach to moving contact line hydrodynamics," *J. Fluid Mech.*, vol. 564, pp. 333–360, 2006.

[79] S. Dong, "On imposing dynamic contact-angle boundary conditions for wall-bounded liquid-gas flows," *Comput. Methods Appl. Mech. Engrg.*, vol. 247-248, pp. 179–200, 2012.

[80] F. Bai, X. He, X. Yang, R. Zhou, and C. Wang, "Three dimensional phase-field investigation of droplet formation in microfluidic flow focusing devices with experimental validation," *Int. J. Multiph. Flow*, vol. 93, pp. 130–141, 2017.

[81] L. Shen, H. Huang, P. Lin, Z. Song, and S. Xu, "An energy stable c0 finite element scheme for a quasi-incompressible phase-field model of moving contact line with variable density," *Journal of Computational Physics*, vol. 405, p. 109 179, 2020.

[82] G. Zhu, J. Kou, J. Yao, A. Li, and S. Sun, "A phase-field moving contact line model with soluble surfactants," *J. Comput. Phys.*, vol. 405, p. 109 170, 2020.

[83] P. Yue, "Thermodynamically consistent phase-field modelling of contact angle hysteresis," *Journal of Fluid Mechanics*, vol. 899, 2020.

[84] Y. Shi and X.-P. Wang, "Modeling and simulation of dynamics of three-component flows on solid surface," *Japan Journal of Industrial and Applied Mathematics*, vol. 31, no. 3, pp. 611–631, 2014.

[85] J. Shen, X. Yang, and H. Yu, "Efficient energy stable numerical schemes for a phase field moving contact line model," *J. Comput. Phys.*, vol. 284, pp. 617–630, 2015.

[86] Q. Zhang and X. Wang, "Phase field modeling and simulation of three-phase flow on solid surfaces," *J. Comput. Phys.*, vol. 319, pp. 79–107, 2016.

[87] H. Ding and P. Spelt, "Wetting condition in diffuse interface simulations of contact line motion," *Phys. Rev. E*, vol. 75, p. 046 708, 2007.

[88] H. Lee and J. Kim, "Accurate contact angle boundary conditions for the cahn–hilliard equations," *Comput. Fluids*, vol. 44, pp. 178–186, 2011.

[89] J.-C. Loudet, M. Qiu, J. Hemauer, and J. Feng, "Drag force on a particle straddling a fluid interface: Influence of interfacial deformations," *The European Physical Journal E*, vol. 43, no. 2, pp. 1–13, 2020.

[90] C. Zhang, H. Ding, P. Gao, and Y. Wu, "Diffuse interface simulation of ternary fluids in contact with solid," *J. Comput. Phys.*, vol. 309, pp. 37–51, 2016.

[91] J. Cahn and J. Hilliard, "Free energy of a nonuniform system, i interfacial free energy," *J. Chem. Phys.*, vol. 28, pp. 258–267, 1958.

[92] P. Yue, C. Zhou, and J. Feng, "Sharp-interface limit of the cahn–hilliard model for moving contact lines," *J. Fluid Mech.*, vol. 645, pp. 279–294, 2010.

[93] P. Yue and J. Feng, "Wall energy relaxation in the cahn–hilliard model for moving contact lines," *Physics of Fluids*, vol. 23, no. 1, p. 012 106, 2011.

[94] X. Xu, Y. Di, and H. Yu, "Sharp-interface limits of a phase-field model with a generalized navier slip boundary condition for moving contact lines," *Journal of Fluid Mechanics*, vol. 849, pp. 805–833, 2018.

[95] U. Lācis, P. Johansson, T. Fullana, B. Hess, G. Amberg, S. Bagheri, and S. Zaleski, "Steady moving contact line of water over a no-slip substrate," *The European Physical Journal Special Topics*, vol. 229, no. 10, pp. 1897–1921, 2020.

[96] M. Brassel and E. Bretin, "A modified phase field approximation for mean curvature flow with conservation of the volume," *Math. Methods Appl. Sci.*, vol. 34, pp. 1157–1180, 2011.

[97] J. Rubinstein and P. Sternberg, "Nonlocal reaction—diffusion equations and nucleation," *IMA Journal of Applied Mathematics*, vol. 48, no. 3, pp. 249–264, 1992.

[98] J. Kim, S. Lee, and Y. Choi, "A conservative allen–cahn equation with a space–time dependent lagrange multiplier," *Int. J. Eng. Sci.*, vol. 84, pp. 11–17, 2014.

[99] D. Lee and J. Kim, "Comparison study of the conservative allen–cahn and the cahn–hilliard equations," *Math. Comput. Simulation*, vol. 119, pp. 35–56, 2016.

[100] S. Mirjalili, C. Ivey, and A. Mani, "A conservative diffuse interface method for two-phase flows with provable boundedness properties," *J. Comput. Phys.*, vol. 401, p. 109 006, 2020.

[101] S. Mirjalili and A. Mani, "Consistent, energy-conserving momentum transport for simulations of two-phase flows using the phase field equations," *Journal of Computational Physics*, vol. 426, p. 109 918, 2021.

[102] V. Joshi and R. Jaiman, "A positivity preserving and conservative variational scheme for phase-field modeling of two-phase flows," *J. Comput. Phys.*, vol. 360, pp. 137–166, 2018.

[103] V. Joshi and R. Jaiman, "An adaptive variational procedure for the conservative and positivity preserving allen–cahn phase-field model," *J. Comput. Phys.*, vol. 336, pp. 478–504, 2018.

[104] Z. Chai, D. Sun, H. Wang, and B. Shi, "A comparative study of local and nonlocal allen-cahn equations with mass conservation," *J. Fluid Mech.*, vol. 122, pp. 631–642, 2018.

[105] P. Yue, C. Zhou, and J. Feng, "Spontaneous shrinkage of drops and mass conservation in phase-field simulations," *J. Comput. Phys.*, vol. 223, pp. 1–9, 2007.

[106] G. Tierra and F. Guillen-Gonzalez, "Numerical methods for solving the cahn-hilliard equation and its applicability to related energy-based models," *Arch Computat Methods Eng*, vol. 22, pp. 269–289, 2015.

[107] W. Chen, C. Wang, X. Wang, and S. Wise, "Positivity-preserving, energy stable numerical schemes for the cahn-hilliard equation with logarithmic potential," *J. Comput. Phys. X*, vol. 3, p. 100 031, 2019.

[108] F. Frank, A. Rupp, and D. Kuzmin, "Bound-preserving flux limiting schemes for dg discretizations of conservation laws with applications to the cahn-hilliard equation," *Comput. Methods Appl. Mech. Engrg.*, vol. 359, p. 112 665, 2020.

[109] F. Magaletti, F. Picano, M. Chinappi, L. Marino, and C. Casciola, "The sharp-interface limit of the cahn-hilliard/navier-stokes model for binary fluids," *J. Fluid Mech.*, vol. 714, pp. 95–126, 2013.

[110] J. Shen, T. Tang, and J. Yang, "On the maximum principle preserving schemes for the generalized allen–cahn equation," *Commun. Math. Sci.*, vol. 14, pp. 1517–1534, 2016.

[111] S. Allen and J. Cahn, "A microscopic theory for antiphase boundary motion and its application to antiphase domain coarsening," *Acta Metallurgica*, vol. 27, pp. 1085–1095, 1979.

[112] S. Dong and J. Shen, "A time-stepping scheme involving constant coefficient matrices for phase-field simulations of two-phase incompressible flows with large density ratios," *J. Comput. Phys.*, vol. 231, pp. 5788–5804, 2012.

[113] Z. Huang, G. Lin, and A. Ardekani, "A mixed upwind/central weno scheme for incompressible two-phase flows," *J. Comput. Phys.*, vol. 387, pp. 455–480, 2019.

[114] T. Zhang, J. Wu, and X. Lin, "An interface-compressed diffuse interface method and its application for multiphase flows," *Physics of Fluids*, vol. 31, p. 122 102, 2019.

[115] A. Baraldi, M. Dodd, and A. Ferrante, "A mass-conserving volume-of-fluid method: Volume tracking and droplet surface-tension in incompressible isotropic turbulence," *Comput. Fluids*, vol. 96, pp. 322–337, 2014.

[116] T. Arrufat, M. Crialesi-Esposito, D. Fuster, Y. Ling, L. Malan, S. Pal, R. Scardovelli, G. Tryggvason, and S. Zaleski, "A mass-momentum consistent, volume-of-fluid method for incompressible flow on staggered grids," *Computers & Fluids*, vol. 215, p. 104 785, 2021.

[117] J. Guermond and L. Quartapelle, "A projection fem for variable density incompressible flows," *J. Comput. Phys.*, vol. 165, pp. 167–188, 2000.

[118] S. Kim, "A continuous surface tension force formulation for diffuse-interface models," *J. Comput. Phys.*, vol. 204, pp. 784–804, 2005.

[119] H. Ding, P. Spelt, and C. Shu, "Diffuse interface model for incompressible two-phase flows with large density ratios," *J. Comput. Phys.*, vol. 226, pp. 2078–2095, 2007.

[120] P. Hohenberg and B. Halperin, "Theory of dynamic critical phenomena," *Reviews of Modern Physics*, vol. 49, pp. 435–479, 1977.

[121] M. Rudman, "A volume-tracking method for incompressible multifluid flows with large density variations," *Int. J. Numer. Methods. Fluids*, vol. 28, pp. 357–378, 1998.

[122] M. Bussmann, D. Kothe, and J. Sicilian, "Modeling high density ratio incompressible interfacial flows," in *Proceedings of the ASME 2002 Joint U.S.-European Fluids Engineering Division Conference*, ser. Volume 1: Fora, Parts A and B. Montreal, Quebec, Canada. July 14–18, 2002, ASME, 2002, pp. 707–713.

[123] V. Chenadec and H. Pitsch, "A monotonicity preserving conservative sharp interface flow solver for high density ratio two-phase flows," *J. Comput. Phys.*, vol. 249, pp. 185–203, 2013.

[124] M. Raessi and H. Pitsch, "Consistent mass and momentum transport for simulating incompressible interfacial flows with large density ratios using the level set method.," *Comput. Fluids*, vol. 63, pp. 70–81, 2012.

[125] N. Nangia, E. Boyce, N. Patankar, and A. Bhalla, "A robust incompressible navier-stokes solver for high density ratio multiphase flows," *J. Comput. Phys.*, vol. 390, pp. 548–594, 2019.

[126] B. Xie, J. P., D. Y., and S. Liao, "A consistent and balanced-force model for incompressible multiphase flows on polyhedral unstructured grids," *International Journal of Multiphase Flow*, vol. 122, p. 103 125, 2020.

[127] J. Lowengrub and L. Truskinovsky, "Quasi-incompressible cahn-hilliard fluids and topological transitions," *Proceedings of the Royal Society of London. Series A: Mathematical, Physical and Engineering Sciences*, vol. 454, no. 1978, pp. 2617–2654, 1998.

[128] J. Shen, X. Yang, and Q. Wang, "Mass and volume conservation in phase field models for binary fluids," *Communications in Computational Physics*, vol. 13, no. 4, pp. 1045–1065, 2013.

[129] Z. Guo, P. Lin, and J. Lowengrub, "A numerical method for the quasi-incompressible cahn–hilliard–navier–stokes equations for variable density flows with a discrete energy law," *Journal of Computational Physics*, vol. 276, pp. 486–507, 2014.

[130] Z. Guo and P. Lin, "A thermodynamically consistent phase-field model for two-phase flows with thermocapillary effects," *Journal of Fluid Mechanics*, vol. 766, pp. 226–271, 2015.

[131] Z. Guo, P. Lin, J. Lowengrub, and S. Wise, "Mass conservative and energy stable finite difference methods for the quasi-incompressible navier–stokes–cahn–hilliard system: Primitive variable and projection-type schemes," *Computer Methods in Applied Mechanics and Engineering*, vol. 326, pp. 144–174, 2017.

[132] J. Kim and J. Lowengrub, "Phase field modeling and simulation of three-phase flows," *Interfaces Free Bound.*, vol. 7, pp. 435–466, 2005.

[133] J. Li and Q. Wang, "A class of conservative phase field models for multiphase fluid flows," *Journal of Applied Mechanics*, vol. 81, no. 2, p. 021 004, 2014.

[134] J. Oden, A. Hawkins, and S. Prudhomme, "General diffuse-interface theories and an approach to predictive tumor growth modeling," *Mathematical Models and Methods in Applied Sciences*, vol. 20, no. 03, pp. 477–517, 2010.

[135] J. Shen and X. Yang, "A phase-field model and its numerical approximation for two-phase incompressible flows with different densities and viscosities," *SIAM J. SCI. COMPUT.*, vol. 32, pp. 1159–1179, 2010.

[136] C. Liu, J. Shen, and X. Yang, "Decoupled energy stable schemes for a phase-field model of two-phase incompressible flows with variable density," *J Sci Comput*, vol. 62, pp. 601–622, 2015.

[137] J. Shen and X. Yang, "Decoupled, energy stable schemes for phase-field models of two-phase incompressible flows," *SIAM J. NUMER. ANAL*, vol. 53, pp. 279–296, 2015.

[138] K. Teigen, P. Song, J. Lowengrub, and A. Voigt, "A diffuse-interface method for two-phase flows with soluble surfactants," *J. Comput. Phys.*, vol. 230, pp. 375–393, 2011.

[139] Y. Shi, G. Tang, L. Cheng, and H. Shuang, "An improve d phase-field-base d lattice boltzmann model for droplet dynamics with soluble surfactant," *Comput. Fluids*, vol. 179, pp. 508–520, 2019.

[140] G. Soligo, A. Roccon, and A. Soldati, "Coalescence of surfactant-laden drops by phase field method," *J. Comput. Phys.*, vol. 376, pp. 1292–1311, 2019.

[141] F. Giussani, F. Piscaglia, G. Saez-Mischlich, and J. Hèlie, "A three-phase vof solver for the simulation of in-nozzle cavitation effects on liquid atomization," *J. Comput. Phys.*, vol. 406, p. 109 068, 2020.

[142] N. Scapin, P. Costa, and L. Brandt, "A volume-of-fluid method for interface-resolved simulations of phase-changing two-fluid flows," *J. Comput. Phys.*, vol. 407, p. 109 251, 2020.

[143] X. Li, J. Lowengrub, A. Ratz, and A. Voigt, "Solving pdes in complex geometries: A diffuse domain approach," *Commun. Math. Sci.*, vol. 1, pp. 81–107, 2009.

[144] H. Shmueli, G. Ziskind, and R. Letan, "Melting in a vertical cylindrical tube: Numerical investigation and comparison with experiments," *International Journal of Heat and Mass Transfer*, vol. 53, no. 19-20, pp. 4082–4091, 2010.

[145] J. Vogel and A. Thess, "Validation of a numerical model with a benchmark experiment for melting governed by natural convection in latent thermal energy storage," *Applied Thermal Engineering*, vol. 148, pp. 147–159, 2019.

[146] W. Pitscheneder, T. DebRoy, K. Mundra, and R. Ebner, "Role of sulfur and processing variables on the temporal evolution of weld pool geometry during multikilowatt laser beam welding of steels," *Welding Journal (Miami, Fla)*, vol. 75, no. 3, 71s–80s, 1996.

[147] C. Chan, J. Mazumder, and M. Chen, "A two-dimensional transient model for convection in laser melted pool," *Metallurgical Transactions A*, vol. 15, no. 12, pp. 2175–2184, 1984.

[148] H. Zhao, W. Niu, B. Zhang, Y. Lei, M. Kodama, and T. Ishide, "Modelling of keyhole dynamics and porosity formation considering the adaptive keyhole shape and three-phase coupling during deep-penetration laser welding," *Journal of Physics D: Applied Physics*, vol. 44, no. 48, p. 485 302, 2011.

[149] Z. S. Saldi, "Marangoni driven free surface flows in liquid weld pools," PhD thesis, Delft University of Technology, 2012.

[150] J. Dantzig and M. Rappaz, *Solidification: -Revised & Expanded*. EPFL press, 2016.

[151] T.-H. Huang, T.-H. Huang, Y.-S. Lin, C.-H. Chang, P.-Y. Chen, S.-W. Chang, and C.-S. Chen, "Phase-field modeling of microstructural evolution by freeze-casting," *Advanced Engineering Materials*, vol. 20, no. 3, p. 1 700 343, 2018.

[152] C. Panwisawas, C. Qiu, M. Anderson, Y. Sovani, R. Turner, M. Attallah, J. Brooks, and H. Basoalto, "Mesoscale modelling of selective laser melting: Thermal fluid dynamics and microstructural evolution," *Computational Materials Science*, vol. 126, pp. 479–490, 2017.

[153] Q. He, H. Xia, J. Liu, X. Ao, and S. Lin, "Modeling and numerical studies of selective laser melting: Multiphase flow, solidification and heat transfer," *Materials & Design*, vol. 196, p. 109 115, 2020.

[154] S. Lin, Z. Gan, J. Yan, and G. Wagner, "A conservative level set method on unstructured meshes for modeling multiphase thermo-fluid flow in additive manufacturing processes," *Computer Methods in Applied Mechanics and Engineering*, vol. 372, p. 113 348, 2020.

[155] V. Voller, M. Cross, and N. Markatos, "An enthalpy method for convection/diffusion phase change," *International journal for numerical methods in engineering*, vol. 24, no. 1, pp. 271–284, 1987.

[156] V. Voller and C. Prakash, "A fixed grid numerical modelling methodology for convection-diffusion mushy region phase-change problems," *International Journal of Heat and Mass Transfer*, vol. 30, no. 8, pp. 1709–1719, 1987.

[157] A. Brent, V. Voller, and K. Reid, "Enthalpy-porosity technique for modeling convection-diffusion phase change: Application to the melting of a pure metal," *Numerical Heat Transfer, Part A Applications*, vol. 13, no. 3, pp. 297–318, 1988.

[158] V. Voller and C. Swaminathan, "Eral source-based method for solidification phase change," *Numerical Heat Transfer, Part B Fundamentals*, vol. 19, no. 2, pp. 175–189, 1991.

[159] F. Rösler and D. Brüggemann, "Shell-and-tube type latent heat thermal energy storage: Numerical analysis and comparison with experiments," *Heat and mass transfer*, vol. 47, no. 8, p. 1027, 2011.

[160] P. Angot, C.-H. Bruneau, and P. Fabrie, "A penalization method to take into account obstacles in incompressible viscous flows," *Numerische Mathematik*, vol. 81, no. 4, pp. 497–520, 1999.

[161] M. Bergmann and A. Iollo, "Modeling and simulation of fish-like swimming," *Journal of Computational Physics*, vol. 230, no. 2, pp. 329–348, 2011.

[162] P. Carman, "Fluid flow through granular beds," *Chemical Engineering Research and Design*, vol. 75, S32–S48, 1997.

[163] W. Boettinger, J. Warren, C. Beckermann, and A. Karma, "Phase-field simulation of solidification," *Annual review of materials research*, vol. 32, no. 1, pp. 163–194, 2002.

[164] L.-Q. Chen, "Phase-field models for microstructure evolution," *Annual review of materials research*, vol. 32, no. 1, pp. 113–140, 2002.

[165] B. Echebarria, R. Folch, A. Karma, and M. Plapp, "Quantitative phase-field model of alloy solidification," *Physical review E*, vol. 70, no. 6, p. 061 604, 2004.

[166] S. Kim and W. Kim, "Phase-field modeling of solidification," in *Handbook of materials modeling*, Springer, 2005, pp. 2105–2116.

[167] W. Tan, N. Bailey, and Y. Shin, "A novel integrated model combining cellular automata and phase field methods for microstructure evolution during solidification of multi-component and multi-phase alloys," *Computational Materials Science*, vol. 50, no. 9, pp. 2573–2585, 2011.

[168] Y. Ji, L. Chen, and L.-Q. Chen, "Understanding microstructure evolution during additive manufacturing of metallic alloys using phase-field modeling," in *Thermo-Mechanical Modeling of Additive Manufacturing*, Elsevier, 2018, pp. 93–116.

[169] L.-X. Lu, N. Sridhar, and Y.-W. Zhang, "Phase field simulation of powder bed-based additive manufacturing," *Acta Materialia*, vol. 144, pp. 801–809, 2018.

[170] B. Nestler, A. Wheeler, L. Ratke, and C. Stöcker, "Phase-field model for solidification of a monotectic alloy with convection," *Physica D: Nonlinear Phenomena*, vol. 141, no. 1-2, pp. 133–154, 2000.

[171] C. Beckermann, H.-J. Diepers, I. Steinbach, A. Karma, and X. Tong, "Modeling melt convection in phase-field simulations of solidification," *Journal of Computational Physics*, vol. 154, no. 2, pp. 468–496, 1999.

[172] C. Chen and X. Yang, "Efficient numerical scheme for a dendritic solidification phase field model with melt convection," *Journal of Computational Physics*, vol. 388, pp. 41–62, 2019.

[173] J. Zhang and X. Yang, "A fully decoupled, linear and unconditionally energy stable numerical scheme for a melt-convective phase-field dendritic solidification model," *Computer Methods in Applied Mechanics and Engineering*, vol. 363, p. 112 779, 2020.

[174] M. Salcudean and Z. Abdullah, "On the numerical modelling of heat transfer during solidification processes," *International journal for numerical methods in engineering*, vol. 25, no. 2, pp. 445–473, 1988.

[175] A. Samarskii, P. Vabishchevich, O. Iliev, and A. Churbanov, "Numerical simulation of convection/diffusion phase change problems—a review," *International journal of heat and mass transfer*, vol. 36, no. 17, pp. 4095–4106, 1993.

[176] W. Voller, "An overview of numerical methods for solving phase change problems," *Advances in numerical heat transfer*, vol. 1, p. 341, 1996.

[177] H. Hu and S. Argyropoulos, "Mathematical modelling of solidification and melting: A review," *Modelling and Simulation in Materials Science and Engineering*, vol. 4, no. 4, p. 371, 1996.

[178] Y. Dutil, D. Rousse, N. Salah, S. Lassue, and L. Zalewski, "A review on phase-change materials: Mathematical modeling and simulations," *Renewable and sustainable Energy reviews*, vol. 15, no. 1, pp. 112–130, 2011.

[179] N. Dhaidan and J. Khodadadi, "Melting and convection of phase change materials in different shape containers: A review," *Renewable and Sustainable Energy Reviews*, vol. 43, pp. 449–477, 2015.

[180] K. Sultana, S. Dehghani, K. Pope, and Y. Muzychka, "Numerical techniques for solving solidification and melting phase change problems," *Numerical Heat Transfer, Part B: Fundamentals*, vol. 73, no. 3, pp. 129–145, 2018.

[181] Y. Kim, A. Hossain, and Y. Nakamura, "Numerical study of melting of a phase change material (pcm) enhanced by deformation of a liquid–gas interface," *International Journal of Heat and Mass Transfer*, vol. 63, pp. 101–112, 2013.

[182] W. Yan, W. Ge, Y. Qian, S. Lin, B. Zhou, W. Liu, F. Lin, and G. Wagner, "Multi-physics modeling of single/multiple-track defect mechanisms in electron beam selective melting," *Acta Materialia*, vol. 134, pp. 324–333, 2017.

[183] J. Yan, W. Yan, S. Lin, and G. Wagner, "A fully coupled finite element formulation for liquid–solid–gas thermo-fluid flow with melting and solidification," *Computer Methods in Applied Mechanics and Engineering*, vol. 336, pp. 444–470, 2018.

[184] A. Zhang, J. Du, X. Zhang, Z. Guo, Q. Wang, and S. Xiong, "Phase-field modeling of microstructure evolution in the presence of bubble during solidification," *Metallurgical and Materials Transactions A*, vol. 51, no. 3, pp. 1023–1037, 2020.

[185] J. Ramirez, C. Beckermann, A. Karma, and H.-J. Diepers, "Phase-field modeling of binary alloy solidification with coupled heat and solute diffusion," *Physical Review E*, vol. 69, no. 5, p. 051 607, 2004.

[186] V. Shatikian, G. Ziskind, and R. Letan, "Numerical investigation of a pcm-based heat sink with internal fins," *International journal of heat and mass transfer*, vol. 48, no. 17, pp. 3689–3706, 2005.

[187] S. Hosseinizadeh, F. Tan, and S. Moosania, "Experimental and numerical studies on performance of pcm-based heat sink with different configurations of internal fins," *Applied Thermal Engineering*, vol. 31, no. 17-18, pp. 3827–3838, 2011.

[188] H. Brenner, "Is the tracer velocity of a fluid continuum equal to its mass velocity?" *Physical Review E*, vol. 70, no. 6, p. 061 201, 2004.

[189] H. Brenner, "Kinematics of volume transport," *Physica A: Statistical Mechanics and its Applications*, vol. 349, no. 1-2, pp. 11–59, 2005.

[190] H. Brenner, "Navier–stokes revisited," *Physica A: Statistical Mechanics and its Applications*, vol. 349, no. 1-2, pp. 60–132, 2005.

[191] H. Brenner, "Fluid mechanics revisited," *Physica A: Statistical Mechanics and its Applications*, vol. 370, no. 2, pp. 190–224, 2006.

[192] J. Feng, C. Liu, J. Shen, and P. Yue, "An energetic variational formulation with phase field methods for interfacial dynamics of complex fluids: Advantages and challenges," in *Modeling of soft matter*, Springer, 2005, pp. 1–26.

[193] X. Chen, D. Hilhorst, and E. Logak, "Mass conserving allen-cahn equation and volume preserving mean curvature flow," *Interfaces and Free Boundaries*, vol. 12, pp. 527–549, 2010.

[194] X. Yang, J. Feng, C. Liu, and J. Shen, "Numerical simulations of jet pinching-off and drop formation using an energetic variational phase-field method," *J. Comput. Phys.*, vol. 218, pp. 417–428, 2006.

[195] H. Öttinger, *Beyond equilibrium thermodynamics*. John Wiley & Sons, 2005.

[196] S. Mirjalili, "A novel diffuse interface method for two-phase flows and application in simulation of micro-bubble entrainment," Stanford University, 2019.

[197] A. Howard and A. Tartakovsky, "A conservative level set method for n-phase flows with a free-energy-based surface tension model," *Journal of Computational Physics*, p. 109 955, 2020.

[198] R. Bowen, *Theory of Mixtures, Part I. Continuum Physics*, Eringen, A.C. Academic Press, New York, 1976.

[199] W. Gray and S. Hassanizadeh, "Unsaturated flow theory including interfacial phenomena," *Water Resources Research*, vol. 27, no. 8, pp. 1855–1863, 1991.

[200] S. Achanta, J. Cushman, and M. Okos, "On multicomponent, multiphase thermomechanics with interfaces," *International Journal of Engineering Science*, vol. 32, no. 11, pp. 1717–1738, 1994.

[201] L. Bennethum and J. Cushman, "Multicomponent, multiphase thermodynamics of swelling porous media with electroquasistatics: Ii. constitutive theory," *Transport in Porous Media*, vol. 47, no. 3, pp. 337–362, 2002.

[202] D. Drew, "Mathematical modeling of two-phase flow," *Annual review of fluid mechanics*, vol. 15, no. 1, pp. 261–291, 1983.

[203] Y. Sun and C. Beckermann, "Diffuse interface modeling of two-phase flows based on averaging: Mass and momentum equations," *Physica D: Nonlinear Phenomena*, vol. 198, no. 3-4, pp. 281–308, 2004.

[204] M. Szulczewski and R. Juanes, "The evolution of miscible gravity currents in horizontal porous layers," *Journal of Fluid Mechanics*, vol. 719, pp. 82–96, 2013.

[205] E. Javierre, C. Vuik, F. Vermolen, and S. Van der Zwaag, "A comparison of numerical models for one-dimensional stefan problems," *Journal of Computational and Applied Mathematics*, vol. 192, no. 2, pp. 445–459, 2006.

[206] D. Jamet, D. Torres, and J. Brackbill, "On the theory and computation of surface tension: The elimination of parasitic currents through energy conservation in the second-gradient method," *J. Comput. Phys.*, vol. 182, pp. 262–276, 2002.

[207] G.-S. Jiang and C.-W. Shu, "Efficient implementation of weighted eno schemes," *J. Comput. Phys.*, vol. 126, pp. 202–228, 1996.

[208] Z. Lilek and M. Peric, "A fourth-order finite volume method with colocated variable arrangement," *Comput. Fluids*, vol. 24, pp. 239–252, 1995.

[209] Y. Morinishi, T. Lund, O. Vasilyev, and P. Moin, "Fully conservative higher order finite difference schemes for incompressible flow," *J. Comput. Phys.*, vol. 143, pp. 90–124, 1998.

[210] O. Desjardins, G. Blanquart, G. Balarac, and H. Pitsch, "High order conservative finite difference scheme for variable density low mach number turbulent flows," *J. Comput. Phys.*, vol. 227, pp. 7125–7159, 2008.

[211] M. Alfaro and P. Alifrangis, "Convergence of a mass conserving allen–cahn equation whose lagrange multiplier is nonlocal and local," *Interfaces Free Bound.*, vol. 16, pp. 243–268, 2014.

[212] Z. Weng and Q. Zhuang, "Numerical approximation of the conservative allen–cahn equation by operator splitting method," *Math Method Appl. Sci.*, vol. 40, pp. 4462–4480, 2017.

[213] C. Rhie and W. Chow, "A numerical study of the turbulent flow past an isolated airfoil with trailing edge separation," in *AIAA/ASME 3rd Joint Thermophysics, Fluids, Plasma and Heat Transfer Conference*, 1982, AIAA-82–0998.

[214] J. H. Ferziger and M. Perić, *Computational Methods for Fluid Dynamics*, 3rd ed. Springer, 2002.

[215] S. Popinet, "An accurate adaptive solver for surface-tension-driven interfacial flows," *J. Comput. Phys.*, vol. 228, pp. 5838–5866, 2009.

[216] H. Rusche, "Computational fluid dynamics of dispersed two-phase flows at high phase fractions," PhD thesis, Imperial College London, Exhibition Road, London SW7 2BX, 2002.

[217] V. Badalassi, H. Ceniceros, and S. Banerjee, "Computation of multiphase systems with phase field models," *J. Comput. Phys.*, vol. 190, pp. 371–397, 2003.

[218] M. Sussman, K. Smith, M. Hussaini, M. Ohta, and R. Zhi-Wei, "A sharp interface method for incompressible two-phase flows," *Journal of computational physics*, vol. 221, no. 2, pp. 469–505, 2007.

[219] W. Rider and D. Kothe, "Reconstructing volume tracking," *J. Comput. Phys.*, vol. 141, pp. 112–152, 1998.

[220] S. Zalesak, "Fully multidimensional flux-corrected transport algorithms for fluids," *J. Comput. Phys.*, vol. 31, pp. 335–362, 1979.

[221] S. Mirjalili, C. Ivey, and A. Mani, "Comparison between the diffuse interface and volume of fluid methods for simulating two-phase flows," *Int. J. Multiph. Flow*, vol. 116, pp. 221–238, 2019.

[222] H. Akhlaghi Amiri and A. Hamouda, "Evaluation of level set and phase field methods in modeling two phase flow with viscosity contrast through dual-permeability porous medium," *International Journal of Multiphase Flow*, vol. 52, pp. 22–34, 2013.

[223] M. Boger, J. Schlottke, C. Munz, and B. Weigand, "Reduction of parasitic currents in the dns vof code fs3d," in *12th Workshop on Two-Phase Flow Predictions*, 2010.

[224] K. Yokoi, "A practical numerical framework for free surface flows based on clsvof method, multi-moment methods and density-scaled csf model: Numerical simulations of droplet splashing," *J. Comput. Phys.*, vol. 232, pp. 252–271, 2013.

[225] J. Bell and P. Colella, "A second-order projection method for the incompressible navier-stokes equations," *J. Comput. Phys.*, vol. 85, pp. 257–283, 1989.

[226] S. Hysing, S. Turek, D. Kuzmin, N. Parolini, E. Burman, S. Ganesan, and L. Tobiska, "Quantitative benchmark computations of two-dimensional bubble dynamics," *Int. J. Numer. Methods. Fluids*, vol. 60, pp. 1259–1288, 2009.

[227] M. James, *One-dimensional Stefan problems: an introduction*. Longman Sc & Tech, 1987, vol. 31.

[228] I. Langmuir, "Oil lenses on water and the nature of monomolecular expanded films," *J. Chem. Phys.*, vol. 1, pp. 756–776, 1933.

[229] P.-G. de Gennes, F. Brochard-Wyart, and D. Quere, *Capillarity and Wetting Phenomena*. Springer, 2003.

[230] G. Tryggvason, "Numerical simulations of the rayleigh-taylor instability," *J. Comput. Phys.*, vol. 75, pp. 253–282, 1988.

[231] J. Martin and W. Moyce, "An experimental study of the collapse of liquid columns on a rigid horizontal plane," *Philosophical Transactions of the Royal Society of London, Series A*, vol. 244, pp. 312–324, 1952.

[232] M. Sussman and P. Smereka, "Axisymmetric free boundary problems," *J. Fluid Mech.*, vol. 341, pp. 269–294, 1997.

[233] Y. Wang, C. Shu, J. Shao, J. Wu, and X. Niu, "A mass-conserved diffuse interface method and its application for incompressible multiphase flows with large density ratio," *J. Comput. Phys.*, vol. 290, pp. 336–351, 2015.

[234] Y. Li, J. Choi, and J. Kim, "A phase-field fluid modeling and computation with interfacial profile correction term," *Commun. Nonlinear Sci. Numer. Simulat.*, vol. 30, pp. 84–100, 2016.

[235] Y. Zhang and W. Ye, "A flux-corrected phase-field method for surface diffusion," *Commun. Comput. Phys.*, vol. 22, pp. 422–440, 2017.

[236] Y. Hu, Q. He, D. Li, Y. Li, and X. Niu, "On the total mass conservation and the volume preservation in the diffuse interface method," *Comput. Fluids*, vol. 193, p. 104 291, 2019.

[237] D. Zhang, C. Jiang, D. Liang, Z. Chen, Y. Yang, and Y. Shi, "A refined volume-of-fluid algorithm for capturing sharp fluid interfaces on arbitrary meshes," *J. Comput. Phys.*, vol. 274, pp. 709–736, 2014.

VITA

Education

- **Doctor of Philosophy** Aug. 2016 – Jul. 2021
  in Mechanical Engineering

School of Mechanical Engineering,

Purdue University, West Lafayette, IN, USA

Dissertation: Consistent and Conservative Phase-Field Method
for Multiphase Flow Problems

Advisors: Arezoo M. Ardekani & Guang Lin

- **Master of Engineering** Sep. 2014 – Jun. 2016
  in Mechanical Manufacture and Automation

School of Mechanical and Automotive Engineering,

South China University of Technology, Guangzhou, Guangdong, China

Thesis: Characteristics of MHD Flow Coupling with Outer Resistant Circuit
and MHD Fluid Hammer

Advisor: Yajun Liu

- **Bachelor of Engineering** Sep. 2010 – Jul. 2014
  in Mechanical Engineering and Automation

School of Mechanical and Automotive Engineering,

South China University of Technology, Guangzhou, Guangdong, China

GPA: 3.95/4

Thesis: Skin-Friction Coefficient and RANS Simulation for Fuel Dispensing System
(**Thesis Award at South China University of Technology**)

Advisor: Yajun Liu

Research Experiences

- **Research Assistant** Aug. 2016 – Jul. 2021

  at Complex Flow Lab with Prof. Arezoo M. Ardekani,

  School of Mechanical Engineering,

  Purdue University, West Lafayette, IN, USA

  Project: Modeling and Simulation of Multiphase and Multimaterial Flows

- **Research Assistant** Aug. 2016 – Jul. 2021

  at Predictive Modeling & Machine Learning Laboratory with Prof. Guang Lin,

  Department of Mathematics,

  Purdue University, West Lafayette, IN, USA

  Project: Numerical Methods for Multiphase and Multimaterial Flows

- **Research Assistant** Sep. 2013 – Jun. 2016

  at Liu's Lab with Prof. Yajun Liu,

  School of Mechanical and Automotive Engineering,

  South China University of Technology, Guangzhou, Guangdong, China

  Project: MHD Flows and Fluid Hammer

Conference/Symposium/Invited Presentations

- **Z. Huang**, G. Lin, A.M. Ardekani, Consistent and conservative Phase-Field method for two-phase incompressible flows, *Research Group Seminar-Computational Math*, Clemson University, November 16, 2020, Clemson, SC, USA.
- **Z. Huang**, G. Lin, A.M. Ardekani, Modeling and simulation of N-phase-M-component incompressible flows, *73rd Annual Meeting of the APS Division of Fluid Dynamics*, November 22-24, 2020.
- **Z. Huang**, G. Lin, A.M. Ardekani, A mixed upwind/central WENO scheme for incompressible two-phase flows, *The Burgers Program 2019 Summer Research School on Fluid dynamics: Topics in Multiphase flow and Thermal Transport*, Poster Section, June 3-7, 2019, College Park, MD, USA.

- **Z. Huang**, I.C. Christov, G. Lin, A.M. Ardekani, Transport and mixing of miscible fluids inside a capillary tube, *71st Annual Meeting of the APS Division of Fluid Dynamics*, November 18-20, 2018, Atlanta, GA, USA.
- **Z. Huang**, G. Lin, A.M. Ardekani, A WENO-Projection Scheme for Solving the Conservative Form of the Two-Phase Navier-Stokes Equations, *30th International Conference on Parallel Computational Fluid Dynamics*, May 14-17, 2018, Indianapolis, IN, USA.
- **Z.Y. Huang**, Z.Y. Wang, Y.J. Liu, A study of the relationship between MHD flow regimes and efficiency of MHD generator with power extraction, *Conference of China Theoretical and Applied Mechanics 2013*, August 2013, Xi'an, Shanxi, China.

Services

- **Reviewer** of *Journal of Computational Physics*.
- **Reviewer** of *Computer Methods in Applied Mechanics and Engineering*.

Teaching Experiences

- **Teaching assistant** Spring 2020
  of Machine Design
  School of Mechanical Engineering,
  Purdue University, West Lafayette, IN, USA.

Fellowships & Scholarships

- **Lynn Fellowship**, Aug. 2016
  Purdue University
- **National Scholarship** of 2014-2015 Academic Year (top 5%), Dec. 2015
  Ministry of Education of the People's Republic of China
- **Scholarship for Admitted Graduate Students**, Sep. 2014
  South China University of Technology
- **National Scholarship** (top 5%), Nov. 2011-Nov. 2013
  Ministry of Education of the People's Republic of China

PUBLICATION(S)

Peer Reviewed Journal Papers

- **Z. Huang**, G. Lin, A.M. Ardekani, A consistent and conservative volume distribution algorithm and its applications to multiphase flows using Phase-Field models, *International Journal of Multiphase Flow* 142 (2021): 103727.
DOI: https://doi.org/10.1016/j.ijmultiphaseflow.2021.103727
- **Z. Huang**, G. Lin, A.M. Ardekani, A consistent and conservative model and its scheme for N-phase-M-component incompressible flows, *Journal of Computational Physics* 434 (2021): 110229.
DOI: https://doi.org/10.1016/j.jcp.2021.110229
- **Z. Huang**, G. Lin, A.M. Ardekani, Consistent and conservative scheme for incompressible two-phase flows using the conservative Allen-Cahn model, *Journal of Computational Physics* 420 (2020): 109718.
DOI: https://doi.org/10.1016/j.jcp.2020.109718
- **Z. Huang**, G. Lin, A.M. Ardekani, Consistent, essentially conservative and balanced-force Phase-Field method to model incompressible two-phase flows, *Journal of Computational Physics* 406 (2020): 109192.
DOI: https://doi.org/10.1016/j.jcp.2019.109192
- **Z. Huang**, G. Lin, A.M. Ardekani, A mixed upwind/central WENO scheme for incompressible two-phase flows, *Journal of Computational Physics* 387 (2019): 455-480.
DOI: http://dx.doi.org/10.1016/j.jcp.2019.02.043
- **Z.Y. Huang**, Y.J. Liu, Characteristics of laminar MHD fluid hammer in pipe, *Journal of Magnetism and Magnetic Materials* 397 (2016): 213–224.
DOI: http://dx.doi.org/10.1016/j.jmmm.2015.08.100
- **Z.Y. Huang**, Y.J. Liu, Y.Q. Chen and Z.L. Peng, Energy Structure of MHD flow Coupling with Outer Resistance, *Journal of Magnetism and Magnetic Materials* 387 (2015): 186–201.
DOI: http://dx.doi.org/10.1016/j.jmmm.2015.04.001

- **Z.Y. Huang**, Y.J. Liu, Z.Y. Wang and J. Cai, Three-dimensional simulations of MHD generator coupling with outer resistance circuit, *Simulation Modelling Practice and Theory* 54 (2015): 1–18.
DOI: http://dx.doi.org/10.1016/j.simpat.2015.02.006

- Y. Liu, J. Cai, Z.Y. Wang, **Z.Y. Huang**, A new preset refueling mode for gasoline dispenser using frequency converter and flow rate signals, *Proc IMechE Part E: Journal of Process Mechanical Engineering* 230 (2016): 440-446.
DOI: http://dx.doi.org/10.1177/0954408914562596

Preprints and Submitted Papers:

- **Z. Huang**, G. Lin, A.M. Ardekani, Implementing contact angle boundary conditions for second-order Phase-Field models of wall-bounded multiphase flows, *arXiv preprint (2021).*
arXiv:2103.07839

- **Z. Huang**, G. Lin, A.M. Ardekani, A consistent and conservative Phase-Field model for thermo-gas-liquid-solid flows including liquid-solid phase change, *arXiv preprint (2021).*
arXiv:2102.06863

- **Z. Huang**, G. Lin, A.M. Ardekani, A consistent and conservative Phase-Field method for multiphase incompressible flows, *arXiv preprint (2020).*
arXiv:2010.01099

Peer Reviewed Conference Proceedings

- Y.J. Liu, **Z.Y. Huang**, C. C. Jiang, Characteristics of water hammer induced by valve-valve systems, *IEEE: 2015 International Conference on Fluid Power and Mechatronics*, Paper ID: 1698, August 2015, Harbin, Heilongjiang, China.

- Y.J. Liu, Z.Y. Wang, **Z.Y. Huang**, J. Lumkes Jr., New designs in fuel dispensing system to reduce water hammer, *ASME/BATH 2013 Symposium on Fluid Power and Motion Control*, October 2013, Sarasota, FL, USA.